

AD

USAAVLABS TECHNICAL REPORT 66-30

SINGLE ROTOR HELICOPTER DYNAMICS FOLLOWING POWER FAILURE AT HIGH SPEEDS

By

D. Cooper

K. C. Hansen

T. T. Kaplita

June 1966

CLEARINGHOUSE
FOR FEDERAL SCIENTIFIC AND
TECHNICAL INFORMATION

Hardcopy

Microfiche

\$ 6.00

\$ 1.25

261 pp as

1 ARCHIVE COPY

U. S. ARMY AVIATION MATERIEL LABORATORIES
FORT EUSTIS, VIRGINIA

CONTRACT DA 44-177-AMC-195(T)

UNITED AIRCRAFT CORPORATION
SIKORSKY AIRCRAFT DIVISION
STRATFORD, CONNECTICUT

Distribution of this
document is unlimited



DDC
RECEIVED
JUL 14 1966
B

Disclaimers

The findings in this report are not to be construed as an official Department of the Army position unless so designated by other authorized documents.

When Government drawings, specifications, or other data are used for any purpose other than in connection with a definitely related Government procurement operation, the United States Government thereby incurs no responsibility nor any obligation whatsoever; and the fact that the Government may have formulated, furnished, or in any way supplied the said drawings, specifications, or other data is not to be regarded by implication or otherwise as in any manner licensing the holder or any other person or corporation, or conveying any rights or permission, to manufacture, use, or sell any patented invention that may in any way be related thereto.

Trade names cited in this report do not constitute an official endorsement or approval of the use of such commercial hardware or software.

Disposition Instructions

Destroy this report when no longer needed. Do not return it to originator.

COPY SENT TO	
CFSTI	WHITE SECTION
DDC	BUFF SECTION
UNANNOUNCED	
JUSTIFICATION	
1473	
DISTRIBUTION/AVAILABILITY CODES	
DIST.	AVAIL. ORG. or SPECIAL
1	



DEPARTMENT OF THE ARMY
U. S. ARMY AVIATION MATERIEL LABORATORIES
FORT EUSTIS, VIRGINIA 23604

This report has been reviewed by the U. S. Army Aviation Materiel Laboratories and is considered to be technically sound.

As rotary-wing aircraft operations advance into higher speed regimes such as 200 knots, the dynamic pressure, proportional to the velocity squared, becomes increasingly important. This report shows analytically that the vehicle dynamics at such speeds will be determined in large measure by fuselage aerodynamics as a consequence of high dynamic pressure. The aerodynamic forces on the fuselage will determine how long a pilot has to recover from an emergency such as powerplant failure, if he can recover at all. Recovery from powerplant failure is shown to be far easier where only one engine in multiengine installations fails and/or where the forward propulsive force required of the rotor is minimized, as by use of auxiliary propulsion.

The report is published for the exchange of information and the stimulation of ideas.

Task 1D121401A14203
Contract DA 44-177-AMC-195(T)
USAAVLABS Technical Report 66-30
June 1966

SINGLE ROTOR HELICOPTER DYNAMICS FOLLOWING
POWER FAILURE AT HIGH SPEEDS

SER-50414

by

D. Cooper, K. C. Hansen, T. T. Kaplita

Prepared by

United Aircraft Corporation
Sikorsky Aircraft Division
Stratford, Connecticut

for

U. S. ARMY AVIATION MATERIEL LABORATORIES
FORT EUSTIS, VIRGINIA

Distribution of this
document is unlimited

BLANK PAGE

ABSTRACT

An exploratory study has been conducted to investigate the effects of a loss of power on a single rotor helicopter at high speeds. A normal mode flexible blade analysis was combined with generalized helicopter equations of motion on a hybrid computer. Six mode shapes represented blade flexibility, and nonlinear differential equations of motion described the helicopter and blade motions and loading in fifteen degrees of freedom. This analytical method was verified by correlation with flight test data at 143 knots. The method was then used to predict the effects of rotor design variables and corrective control inputs on the transient response of a helicopter following a full and partial loss of main rotor power at 200 and 235 knots. This report presents the results of that study.

A full loss of power can seriously affect the safety of a 200 - 235 knot helicopter unless there is a rapid and appropriate application of main rotor and tail rotor controls. The power loss is less critical when a partial loss of power occurs or for a reduced rotor propulsive force. Hence, the time available for corrective action is increased.

Rotor propulsive force, hinge offset, and rotor blade inertia were found to be important design considerations which affect helicopter and blade motion and loading following a loss of power. Blade pitch-motion feedback concepts were not effective in reducing the aircraft motion. Large vertical and horizontal tail surfaces, however, provide improved stability in the event of an abrupt loss of power. The aircraft response is due primarily to the fuselage aerodynamic characteristics associated with the sideslip and yaw motion generated by the unbalanced tail rotor yawing moment. The weathercock stability provided by a large vertical tail will reduce the sideslip angle and resultant rolling motion due to fuselage and rotor dihedral effect. The stable longitudinal motion observed in this study demonstrates the advantages of a large horizontal tail.

The effects of the rotor design variables on aircraft and blade motion following a full loss of power are summarized in Table I. In the table, the rotor systems are compared with the articulated rotor. The design variables within each box are listed in descending order of importance.

Although these qualitative trends were established using the S-61F (NH-3A) helicopter which has very good longitudinal and directional stability, they are expected to apply, in general, to less stable helicopters.

Further studies are recommended to investigate additional design variables and control inputs, and to conduct research on the pilot delay time problem to provide experimental data on reactions of an unalerted pilot to power loss in flight.

TABLE I
EFFECT OF ROTOR DESIGN VARIABLES ON
AIRCRAFT AND BLADE RESPONSE AT
200 KNOTS WITH A STABLE FUSELAGE

Response Characteristic	Effect of Rotor Design Variable		
	Beneficial	Negligible	Detrimental
Rotor Speed Decay	Low Lock Number	Hingeless Rotor Floating Hub	Zero Offset Delta-three Tip Path Plane Feedback
Fuselage Roll Amplitude	Hingeless Rotor Low Lock Number		Floating Hub Zero Offset Delta-three Tip Path Plane Feedback
Blade Flapping Increase	Floating Hub Low Lock Number Delta-three	Tip Path Plane Feedback Zero Offset	
Flapwise Vibratory Moment			Hingeless Rotor Low Lock Number Delta-three Tip Path Plane Feedback Zero Offset
Chordwise Vibratory Moment	Zero Offset		Hingeless Rotor Low Lock Number Delta-three Tip Path Plane Feedback
Torsion Vibratory Moment			Delta-three Tip Path Plane Feedback Hingeless Rotor Zero Offset Low Lock Number
Fuselage Pitch Amplitude		Low Lock Number Delta-three Tip Path Plane Feedback Zero Offset Hingeless Rotor	Floating Hub

FOREWORD

This report, conducted by Sikorsky Aircraft with the cooperation of UAC Research Laboratories, describes an analytic investigation of the effects of power loss on a helicopter at high speeds. The program was sponsored by the U. S. Army Aviation Materiel Laboratories, Fort Eustis, Virginia, under the technical direction of Mr. R. Piper.

Appreciation is due to Messrs. E. S. Carter, Jr., D. S. Jenney, K. C. Mard, and D. J. Carnese, of Sikorsky Aircraft, for their guidance. Particular credit is due to Mr. P. Acidiacano of the Aerophysics Group of UAC Laboratories for the development of the equations of motion. Messrs. G. Paquette, E. A. Galligan, D. H. Sorenson, and Miss K. A. Derek of the Analog Computing Group of the UAC Laboratories, are also commended for their assistance in programing and conducting this study.

BLANK PAGE

CONTENTS

	<u>Page</u>
ABSTRACT	iii
FOREWORD	v
LIST OF ILLUSTRATIONS	viii
LIST OF TABLES	xiv
LIST OF SYMBOLS	xv
INTRODUCTION	1
SCOPE OF PROGRAM	3
DEVELOPMENT OF COMPUTER PROGRAM	6
DISCUSSION OF RESULTS	10
A. EFFECT OF ROTOR DESIGN PARAMETERS ON HELICOPTER AND BLADE MOTION PEAK VALUE CHARACTERISTICS FOLLOWING POWER LOSS	10
B. EFFECT OF ROTOR DESIGN PARAMETERS, ROTOR PROPULSIVE FORCE, AND CORRECTIVE CONTROL IN- PUTS ON HELICOPTER AND BLADE MOTION TIME HISTORY FOLLOWING POWER LOSS	12
C. EFFECT OF ROTOR DESIGN PARAMETERS, ROTOR PRO- PULSIVE FORCE, AND CORRECTIVE CONTROL INPUTS ON BLADE BENDING MOMENTS	19
CONCLUSIONS	127
RECOMMENDATIONS	137
REFERENCES	138
DISTRIBUTION	139
APPENDIXES	
I. ROTOR SYSTEM AND AIRCRAFT PHYSICAL PROPERTIES	140
II. EQUATIONS OF MOTION AND DESCRIPTION OF FLEXIBLE BLADE AND HYBRID COMPUTER SIMULATION	191
III. PROGRAM EQUATIONS	204

ILLUSTRATIONS

<u>Figure</u>		<u>Page</u>
1	Comparison of Calculated Aircraft Response Due to a Simulated Power Loss With Flight Test Data at 143 Knots	8
2	Simulated Pilot Control Inputs	9
3	Fully Articulated Rotor ($e/R = 0.034$), Full Power Loss, $D/L = 0.15$, No Corrective Control Input	26
4	Fully Articulated Rotor ($e/R = 0.034$), Full Power Loss, $D/L = 0.15$, With Corrective Control Input 6B	29
5	Effect of Lock Number on Rotor Speed Two Seconds After Power Loss	32
6	Effect of Lock Number on Flapping Disturbance Following Power Loss	33
7	Effect of Lock Number on Blade Lead-Lag Motion Following Power Loss	34
8	Effect of Lock Number on the First Peak Roll Following Power Loss	35
9	Effect of Pitch-Blade Motion Feedback on Rotor Speed Two Seconds After Power Loss	36
10	Effect of Pitch-Blade Motion Feedback on Flapping Disturbance Following Power Loss	37
11	Effect of Pitch-Blade Motion Feedback on Blade Lead-Lag Motion Following Power Loss	38
12	Effect of Pitch-Blade Motion Feedback on the First Peak Roll Angle Following Power Loss	39
13	Effect of Flapping Hinge Offset on Rotor Speed Two Seconds After Power Loss	40
14	Effect of Flapping Hinge Offset on Flapping Disturbance Following Power Loss	41
15	Effect of Flapping Hinge Offset on Blade Lead-Lag Motion Following Power Loss	42
16	Effect of Flapping Hinge Offset on the First Peak Roll Angle Following Power Loss	43

<u>Figure</u>		<u>Page</u>
17	Aircraft Disturbance Following Power Loss, All Configurations	44
18	Helicopter and Rotor Blade Motion Following Part Power Loss, $D/L = 0.15$, No Corrective Control Inputs, Various Rotor Configurations	45
19	Helicopter and Rotor Blade Motion Following Part Power Loss, $D/L = 0.15$, No Corrective Control Inputs, Various Rotor Configurations	47
20	Helicopter and Rotor Blade Motion Following Full Power Loss, No Corrective Control Inputs, Fully Articulated Rotor ($e/R = 0.034$)	49
21	Helicopter and Rotor Blade Motion Following Full Power Loss, $D/L = 0.15$, No Corrective Control Inputs, Various Rotor Configurations	51
22	Helicopter and Rotor Blade Motion Following Full Power Loss, $D/L = 0.15$, No Corrective Control Inputs, Various Rotor Configurations	53
23	Helicopter and Rotor Blade Motion Following Full Power Loss, $D/L = -0.063$, No Corrective Control Inputs, Various Rotor Configurations	55
24	Helicopter and Rotor Blade Motion Following Part Power Loss, $D/L = 0.15$, With Corrective Control Inputs, Fully Articulated Rotor ($e/R = 0.034$)	57
25	Helicopter and Rotor Blade Motion Following Part Power Loss, $D/L = 0.15$, With Corrective Control Inputs, Rotor With Blade Pitch-Flap Feedback	59
26	Helicopter and Rotor Blade Motion Following Part Power Loss, $D/L = 0.15$, With Corrective Control Inputs, Rotor With Blade Pitch-Tip with Plane Tilt Feedback	61
27	Helicopter and Rotor Blade Motion Following Part Power Loss, $D/L = 0.15$, With Corrective Control Inputs, Rotor With Reduced Lock Number	63
28	Helicopter and Rotor Blade Motion Following Part Power Loss, $D/L = 0.15$, With Corrective Control Inputs, Rotor With Zero Flapping Hinge Offset	65

<u>Figure</u>		<u>Page</u>
29	Helicopter and Rotor Blade Motion Following Part Power Loss, $D/L = 0.15$, With Corrective Control Inputs, Hingeless Rotor	67
30	Helicopter and Rotor Blade Motion Following Part Power Loss, $D/L = 0.15$, With Corrective Control Input 4B, Various Rotor Configurations	68
31	Helicopter and Rotor Blade Motion Following Part Power Loss, $D/L = 0.15$, With Corrective Control Input 4B, Various Rotor Configurations	70
32	Helicopter and Rotor Blade Motion Following Full Power Loss, $D/L = 0.15$, With Corrective Control Inputs, Fully Articulated Rotor ($e/R = 0.034$)	72
33	Helicopter and Rotor Blade Motion Following Full Power Loss, $D/L = 0.15$, With Corrective Control Inputs, Rotor With Blade Pitch-Flap Feedback	74
34	Helicopter and Rotor Blade Motion Following Full Power Loss, $D/L = 0.15$, With Corrective Control Inputs, Rotor With Blade Pitch-Tip Path Plane Tilt Feedback	76
35	Helicopter and Rotor Blade Motion Following Full Power Loss, $D/L = 0.15$, With Corrective Control Inputs, Rotor With Reduced Lock Number	78
36	Helicopter and Rotor Blade Motion Following Full Power Loss, $D/L = 0.15$, With Corrective Control Inputs, Rotor With Zero Flapping Hinge Offset	80
37	Helicopter and Rotor Blade Motion Following Full Power Loss, $D/L = 0.15$, With Corrective Control Inputs, Fully Articulated Rotor ($e/R = 0.034$)	82
38	Helicopter and Rotor Blade Motion Following Full Power Loss, $D/L = 0.15$, With Corrective Control Inputs, Hingeless Rotor	84
39	Helicopter and Rotor Blade Motion Following Full Power Loss, $D/L = 0.15$, With Corrective Control Input 6B, Various Rotor Configurations	85
40	Helicopter and Rotor Blade Motion Following Full Power Loss, $D/L = 0.15$, With Corrective Control Input 6B, Various Rotor Configurations	87

<u>Figure</u>		<u>Page</u>
41	Helicopter and Rotor Blade Motion Following Full Power Loss, $D/L = 0$, With Corrective Control Inputs, Fully Articulated Rotor ($e/R = 0.034$)	89
42	Helicopter and Rotor Blade Motion Following Full Power Loss, $D/L = -0.063$, With Corrective Control Inputs, Fully Articulated Rotor ($e/R = 0.034$)	91
43	Helicopter and Rotor Blade Motion Following Full Power Loss, $D/L = -0.063$, With Corrective Control Inputs, Rotor With Blade Pitch-Flap Feedback	93
44	Helicopter and Rotor Blade Motion Following Full Power Loss, $D/L = -0.063$, With Corrective Control Inputs, Rotor With Reduced Lock Number	95
45	Helicopter and Rotor Blade Motion Following Full Power Loss, $D/L = -0.063$, With Corrective Control Inputs, Hingeless Rotor	97
46	Helicopter and Rotor Blade Motion Following Full Power Loss, $D/L = -0.063$, With Corrective Control Input 7B, Various Rotor Configurations	98
47	Helicopter and Rotor Blade Motion Following Full Power Loss, $D/L = -0.063$, With Corrective Control Inputs, Fully Articulated Rotor ($e/R = 0.034$)	100
48	Fully Articulated Rotor ($e/R = 0.034$), Full Power Loss, $D/L = 0.15$, No Corrective Control Input, Multiple Bending Moment Data	102
49	Trim Flapwise Moment Characteristics ($r/R = 56\%$), Various Rotor Configurations and Drag-To-Lift Ratios	105
50	Trim Chordwise Moment Characteristics ($r/R = 56\%$), Various Rotor Configurations and Drag-To-Lift Ratios	106
51	Trim Torsional Moment Characteristics ($r/R = 56\%$), Various Rotor Configurations and Drag-To-Lift Ratios	107
52	Hingeless Rotor Trim Bending Moment Characteristics ($r/R = 22.5\%$), Various Drag-To-Lift Ratios	108
53	Rotor Blade Vibratory and Peak Moment Variation Full Power Loss, $D/L = 0.15$, No Corrective Control Inputs, Pitch-Blade Motion Feedback Rotor Configurations	109

<u>Figure</u>		<u>Page</u>
54	Rotor Blade Vibratory and Peak Moment Variation, Full Power Loss, $D/L = 0.15$, No Corrective Control Inputs, Various Rotor Configurations	112
55	Rotor Blade Vibratory and Peak Moment Variation, Full Power Loss, $D/L = 0.15$, Various Corrective Control Inputs, Fully Articulated Rotor ($e/R = 0.034$)	115
56	Rotor Blade Vibratory and Peak Moment Variation, Full Power Loss, $D/L = -0.063$, Various Corrective Control Inputs, Fully Articulated Rotor	118
57	Hingeless Rotor, Full Power Loss, $D/L = 0.15$, No Corrective Control Input, Multiple Bending Moment Data	121
58	Hingeless Rotor, Full Power Loss, $D/L = -0.063$, No Corrective Control Input, Multiple Bending Moment Data	124
59	Effect of Time Delay for Corrective Control Inputs and Rotor Propulsive Force on Helicopter Roll Angle and Rotor Speed, Fully Articulated Rotor ($e/R = 0.034$), Full Power Loss at 200 Knots	129
60	Effect of Sideslip Angle and Fuselage Aerodynamic Characteristics on Aircraft Motion Following Part Power Loss at 200 Knots	130
61	Effect of Flapping Hinge Offset, Lock Number, and Flapping Hinge Restraint on Helicopter Motion and Blade Torsional Bending Moment Following Full Power Loss at $D/L = 0.15$, 200 Knots	131
62	Effect of Blade Pitch-Flap Coupling on Helicopter Motion, Rotor Speed, and Torsional Bending Moment Following Full Power Loss at 200 Knots	132
63	Response of the Hingeless and Articulated Rotor Following a Part Power Loss at 200 Knots	133
64	Variation of Blade Flapping Angle and Blade Deflection Over the Tail Cone With Time, Both Referenced From the Plane of the Shaft, Fully Articulated Rotor ($e/R = 0.034$), 200 Knots	134
65	Change in Altitude Following Loss of Main Rotor Power, Fully Articulated Rotor ($e/R = 0.034$)	135

<u>Figure</u>		<u>Page</u>
66	Effect of Corrective Control Inputs With 0.2 Second Time Delay on Rotor Blade Bending Moments Following Full Loss of Power at 200 Knots, Fully Articulated Rotor ($e/R = 0.034$)	136
67	CH-3C Rotor Blade Spanwise Structural and Physical Properties	145
68	Articulated Rotor Blade Spanwise Structural and Physical Properties	151
69	Zero Offset Rotor Blade Spanwise Structural and Physical Properties	157
70	Reduced Lock Number Rotor Blade Spanwise Structural and Physical Properties	163
71	Hingeless Blade Spanwise Structural and Physical Properties	169
72	Floating Hub Rotor Blade Spanwise Structural and Physical Properties	175
73	S-61R (CH-3C) Aircraft	181
74	S-61F (NH-3A) Aircraft	182
75	S-61R (CH-3C) Wind Tunnel Data (Wind Axis System)	183
76	S-61F (NH-3A) Wind Tunnel Data (Wind Axis System)	185
77	S-61R (CH-3C) Wind Tunnel Data (Body Axis System)	187
78	S-61F (NH-3A) Wind Tunnel Data (Body Axis System)	189
79	Hybrid Computer Flow Diagram	200
80	Composite 0012 Airfoil Data, Sea Level, Standard Conditions	201
81	Fuselage and Rotor Head Axis Systems	234

TABLES

<u>Table</u>		<u>Page</u>
I	Effect of Rotor Design Variables on Aircraft and Blade Response at 200 Kncts With a Stable Fuselage	iv
II	Study Conditions	5
III	Rotor Operating Conditions	5
IV	Control Input Patterns	23
V	Trim Conditions	24
VI	Spar Section Modulus	25
VII	Rotor Physical Properties	142
VIII	Aircraft Physical Properties	144
IX	Scale Factors	197
X	K Constants	228
XI	C Constants	230

SYMBOLS

A_{ls}	Main rotor lateral cyclic blade pitch angle measured in shaft axis system, cosine term of Fourier series representation of blade pitch angle, positive for stick right, deg.
A'	Area enclosed by blade spar midline, in. ²
AR	Aspect ratio, R/c
B	Tip loss factor
B_{ls}	Main rotor longitudinal cyclic blade pitch angle measured in the shaft axis system, sine term of Fourier series representation of blade pitch angle, positive for stick forward, deg.
$BLCG$	Butt-line of center of gravity, in.
$BLMR$	Butt-line of main rotor, in.
C	Rotary viscous damping, ft.-lb.-sec./rad.
$(C_H/\sigma)_s$	Longitudinal rotor force coefficient perpendicular to the shaft, positive aft, $H/\rho\pi R^2 (\Omega_o R)^2 \sigma$
C_L	Rotor lift coefficient, $L/\rho\pi R^2 (\Omega_o R)^2$
$(C_{l1}/\sigma)_f$	Component of main rotor moment about the fuselage rolling axis, X_f axis, divided by $\rho\pi R^3 (\Omega_o R)^2 \sigma$, positive roll right.
$(C_{l1}/\sigma)_s$	Main rotor rolling moment coefficient, positive roll right, $\mathcal{L}_{MR}/\rho\pi R^3 (\Omega_o R)^2 \sigma$
$(C_m/\sigma)_f$	Component of main rotor moment about the fuselage pitch axis, Y_f axis, divided by $\rho\pi R^3 (\Omega_o R)^2 \sigma$, positive nose up.
$(C_m/\sigma)_s$	Main rotor pitching moment coefficient, positive nose up, $M_{MR}/\rho\pi R^3 (\Omega_o R)^2 \sigma$
$(C_n/\sigma)_f$	Component of main rotor moment about the fuselage yaw axis, Z_f axis, divided by $\rho\pi R^3 (\Omega_o R)^2 \sigma$, positive nose right.
C_o	Non-dimensional lag damper rotary viscous damping coefficient, $C/m_o \Omega_o R^3$
C_{Qd}	Drag torque coefficient for one blade, drag torque/ $\rho\pi R^3 (\Omega_o R)^2$
$(C_Q/\sigma)_e$	Engine torque coefficient, equal to $(C_Q/\sigma)_s$ prior to engine failure.

$(C_Q/\sigma)_S$	Main rotor torque coefficient, $Q_{MR}/\rho \pi R^3 (\Omega_o R)^2 \sigma$
$(C_T/\sigma)_S$	Main rotor thrust coefficient in the shaft axis system, positive up, $T/\rho \pi R^2 (\Omega_o R)^2 \sigma$
$(C_T/\sigma)_T$	Tail rotor thrust coefficient positive right, $T_{TR}/\rho \pi R^2 (\Omega_o R)^2 \sigma$
$(C_X/\sigma)_f$	Component of main rotor force along the fuselage X_f axis, divided by $\rho \pi R^2 (\Omega_o R)^2 \sigma$, positive forward.
$(C_Y/\sigma)_f$	Component of main rotor force along the fuselage Y_f axis, divided by $\rho \pi R^2 (\Omega_o R)^2 \sigma$, positive right.
$(C_Y/\sigma)_S$	Main rotor side-force coefficient perpendicular to the shaft, $Y_{MR}/\rho \pi R^2 (\Omega_o R)^2 \sigma$, positive right.
$(C_Z/\sigma)_f$	Component of main rotor force along the fuselage Z_f axis, divided by $\rho \pi R^2 (\Omega_o R)^2 \sigma$, positive down.
D	Main rotor drag force, positive for forward rotor propulsive force, lb.
D_{ff}	Fuselage drag (body axis), positive along the negative X_f axis, lb.
D_{fw}	Fuselage drag force (wind axis), positive aft, lb.
Dt	Blade tip displacement measured with respect to a plane perpendicular to the shaft, positive up, in.
D_w	Rotor downwash correction factor.
FSAD	Fuselage station of aerodynamic data point, in.
FSCG	Fuselage station of center of gravity, in.
FSHT	Fuselage station of center of pressure of horizontal tail, in.
FSMR	Fuselage station of main rotor, in.
FSVT	Fuselage station of center of pressure of vertical tail, in.
G.W.	Gross weight, lb.
H	Longitudinal rotor force perpendicular to the shaft, positive aft, lb.
I_B	Mass moment of inertia of main rotor blade about the flapping and lagging hinges, slug - ft. ²

I_{hub}	Mass moment of inertia of main rotor hub and all rotating mechanical components about the axis of rotation, including tail rotor, tail rotor shaft and transmission, does not include main rotor blades, slug - ft. ²
I_p	Blade mass moment of inertia about the feathering axis, slug - ft. ²
I_s	Longitudinal shaft tilt with respect to the fuselage, positive forward, radians.
I_{TR}	Mass moment of inertia of tail rotor blade about center of rotation, slug - ft. ²
I_x	Mass moment of inertia of aircraft about the principal fuselage longitudinal axis without main rotor blades, slug - ft. ²
I_y	Mass moment of inertia of aircraft about the principal fuselage lateral axis without main rotor blades, slug - ft. ²
I_z	Mass moment of inertia of aircraft about the principal vertical axis without main rotor blades, slug - ft. ²
I_{yy}	Blade section flapwise moment of inertia, in. ⁴
I_{zz}	Blade section chordwise moment of inertia, in. ⁴
J	Blade section torsional moment of inertia, in. ⁴
K_o	Lag damper spring constant, $\frac{ft. - lb.}{rad.}$
K_r	Control system spring constant, $\frac{ft. - lb.}{rad.}$
$K_o,$	Pitch-lag coupling
L	Rotor lift force, lb.
L_{ff}	Fuselage lift (body axis), positive along the negative Z_f axis, lb.
Z_{ff}	Fuselage rolling moment (body axis), positive right roll, ft. - lb.
L_{fw}	Fuselage lift force (wind axis), positive up, lb.
Z_{fw}	Fuselage rolling moment (wind axis), positive right roll ft. - lb.

ΣMR	Main rotor hub rolling moment, ft. - lb.
M	Mach number
$M(B)$	Rotor blade mass slugs
$M_B(r_{cg})$	Blade mass moment about the flapping and lag hinges, slug - ft. ²
M_C	Main rotor local chordwise blade bending moment, positive leading edge in compression, in. - lb.
M_{eaAe}	Aerodynamic moment about the blade elastic axis, positive nose up, in. - lb.
M_f	Main rotor local flapwise blade bending moment, positive blade upper surface in compression, in. - lb.
m_{ff}	Fuselage pitching moment (body axis), positive nose up, ft. - lb.
m_{fw}	Fuselage pitching moment (wind axis), positive nose up, ft.-lb.
M_L	Main rotor chordwise bending moment in vicinity of lag damper, $x = 12\%$, positive leading edge in compression, in. - lb.
M_{LD}	Moment due to lag damper, ft. - lb.
M_{MR}	Main rotor hub pitching moment, positive nose up, ft. - lb.
M_{damp}	Fuselage pitch damping moment, ft - lb/sec.
$M_{down-wash}$	Fuselage pitching moment increment due to main rotor downwash, ft. - lb.
M_θ	Local main rotor blade torsional moment, positive nose up, in. - lb.
M_{T90°	Tip Mach number of blade at the 90° azimuth position.
M_{Y_3}	Blade root moment about the Y_3 axis, in. - lb.
M_{Z_3}	Blade root moment about the Z_3 axis, in. - lb.
N_{damp}	Fuselage yaw damping moment, ft. - lb./sec.
n_{ff}	Fuselage yawing moment parameter (body axis) positive nose right, ft. - lb.
n_{fw}	Fuselage yawing moment (wind axis) positive nose right, ft. - lb.

P_{Xf}	Propulsive force along fuselage X_f axis divided by $\rho \pi R^4 \Omega_o^2$
Q_{MR}	Main rotor torque, ft.-lb.
R	Rotor radius, ft.
RN	Reynolds number
$S_{X5a,Y5a,Z5a}$	Aerodynamic shear force per unit span in the X_5 , Y_5 and Z_5 directions, lb./in.
$S_{X3,Y3,Z3}$	Total shear forces in X_3 , Y_3 , and Z_3 directions at blade root, lb.
T	Computer cycle time, sec.
T	Main rotor thrust, lb.
T_{TR}	Tail rotor thrust, lb.
$T.F.$	Thrust factor, $\rho b c \Omega_o^2 R^3$, lb.
U	Blade element resultant velocity, ft./sec.
U_p	Component of U perpendicular to the blade span axis, ft./sec.
U_T	Component of U tangent to the blade span axis, ft./sec.
V	Forward speed, knots
$W(B)$	Rotor blade weight, lb.
$WLAD$	Fuselage water line location of aerodynamic data point, in.
$WLCG$	Fuselage water line location of center of gravity, in.
$WLMR$	Fuselage water line location of main rotor center of rotation, in.
$WLTR$	Fuselage water line location of tail rotor center of rotation, in.
X_f	Body principal longitudinal axis, positive forward
X_{MR}	Component of main rotor forces along body X_f axis, lb.
Y_f	Body principal lateral axis, positive to the right
Y_{ff}	Body side force parameter (body axis), positive along the Y_f axis, lb.

Y_{fw}	Body side force (wind axis), positive to the right, lb.
Y_{MR}	Component of main rotor forces along body Y_f axis, positive in the positive Y_f direction, lb.
Z_f	Body principal vertical axis, positive along the positive Z_f axis, lb.
Z_{MR}	Component of main rotor forces along body Z_f axis, lb.
a	Blade section lift curve slope, 1/radian
b	Number of blades
c	Rotor blade chord, ft.
c_d	Blade airfoil section profile drag coefficient, $\frac{d}{\frac{1}{2} \rho U^2 c}$
c_l	Blade airfoil section profile lift coefficient, $\frac{l}{\frac{1}{2} \rho U^2 c}$
$c_{m_{c/4}}$	Blade airfoil section pitching moment coefficient about the quarter-chord, $m_{c/4} + \frac{1}{2} \rho U^2 c^2$
d	Blade section drag force, lb.
e	Flapping hinge offset from center of rotation, ft.
\bar{e}	Flapping hinge offset ratio, e/R
\bar{e}'	Nondimensional distance from flapping hinge to first aerodynamic segment, e/R
e_{LD}	Lag damper moment arm measured from the center of rotation, ft.
$(e/r)_{LD}$	Ratio of lag damper moment arm measured from the center of rotation to lag damper moment arm measured from the lag hinge
g	Acceleration due to gravity, ft./sec. ²
h_a	Vertical distance from center of gravity to fuselage aerodynamic data point, ft.
h_{MR}	Vertical distance from center of gravity to main rotor center of rotation at the center of the hub, ft.

h_{TR}	Vertical distance from center of gravity to tail rotor center of rotation, ft.
l	Blade section lift force, lb.
l_a	Horizontal distance from center of gravity to fuselage aerodynamic data point, ft.
l_{MR}	Horizontal distance from center of gravity to main rotor center of rotation, ft.
l_{TR}	Horizontal distance from center of gravity to tail rotor center of rotation, ft.
m	Blade mass per unit length, slugs/ft.
m_f	Mass, slugs
$m_c/4$	Blade section pitching moment about quarter chord, ft.-lb.
m_o	Blade reference mass per unit length, slugs/ft.
n_z	Normal load factor
p	Aircraft roll angular velocity about the body longitudinal axis, rad./sec.
q_f	Dynamic pressure, $\frac{1}{2} \rho U^2$
q	Aircraft pitch angular velocity about the body lateral axis, positive nose up, rad./sec.
q_{v_n}	Amplitude of $(n)^{th}$ edgewise deflection mode (equals blade tip deflection in y_6 direction divided by R when Y_{v_n} at tip is defined as 1.0)
q_{w_n}	Amplitude of $(n)^{th}$ flapwise deflection mode (equals blade tip deflection in z_6 direction divided by R when y_{w_n} at tip is defined as 1.0)
q_θ	Amplitude of first elastic torsional mode (equals elastic twist angle about x_6 axis in radians at tip when y_θ at tip is defined as 1.0)
r	Distance from center of rotation to local blade station, ft.
r	Fuselage yawing angular velocity about the vertical body axis, positive nose right, rad./sec.

r_a	Distance from flapping hinge to center of aerodynamic section of local blade station, ft.
r_l	Distance from flapping hinge to first aerodynamic segment, ft.
r_{LD}	Moment arm of lag damper force about lag hinge, ft.
Δr	Aerodynamic segment length, ft.
$(r_{cg})_B$	Distance from flapping hinge to blade center of gravity, ft.
t	Blade spar wall thickness, in.
t	Time, sec.
u	Nondimensional blade element resultant velocity, $U/\Omega R$
u_p	Nondimensional component of u perpendicular to the blade span axis, $U_p/\Omega R$
u_T	Nondimensional component of u tangent to the blade span axis, $U_T/\Omega R$
v	Translational velocity of a point on the blade relative to a Newtonian axis system, ft./sec.
v_0	Translational velocity of axis system, ft./sec.
v_{x_1, y_1, z_1}	Translational velocity of a point in the x_1 , y_1 , and z_1 directions, ft./sec.
x	Nondimensional blade radial distance from center of rotation r/R
ΔZ	Change in altitude, positive up, ft.
Ω	Instantaneous rotor angular velocity relative to the "1" axis system, rad./sec.
Ω_0	Trim rotor angular velocity, rad./sec.
$\bar{\Omega}$	Nondimensional rotor angular velocity, Ω/Ω_0
α_f	Fuselage angle of attack, deg.
α_r	Local blade section angle of attack, deg.
β	Rotor blade flapping angle, deg.

β_f	Fuselage sideslip angle, deg.
γ	Rotor blade Lock number, $\rho a c R^4 / I_B$
γ_{v_n}	Blade chordwise normal mode shape function of $(n)^{th}$ mode
γ_{w_n}	Blade flapwise normal mode shape function of $(n)^{th}$ mode
γ_θ	Blade torsional normal mode shape function
δ	Rotor blade lead-lag angle, positive lead forward, deg.
δ_3	Blade pitch-flap coupling angle, deg.
θ	Local blade pitch angle due to control system input and built-in twist, deg.
θ_B	Local blade pitch angle due to built-in twist, deg.
θ_c	Main rotor collective pitch measured at center of rotation, deg.
θ_f	Fuselage pitch angle, deg.
θ_o	Blade pitch at $3/4$ radius including blade motion coupling, deg.
$(\theta_s)_{.75}$	Impressed blade pitch at $3/4$ radius, deg.
θ_t	Tail rotor collective blade pitch angle, deg.
θ_l	Main rotor blade twist angle, positive for leading edge up, deg.
λ	Tail rotor inflow ratio
λ_o	Main rotor inflow ratio
μ	Advance ratio, $1.688 V / \Omega_o R$
μ_{X_f, Y_f, Z_f}	Advance ratios of airspeed components in body axis system
ρ	Mass density of air, slugs/ft. ³
σ	Rotor solidity, $bc / \pi R$
ϕ_f	Fuselage roll angle, deg.

ϕ_w	Local blade inflow angle, $\tan^{-1} (U_p/U_t)$, radians
ψ_f	Fuselage yaw angle, deg.
ψ_R	Rotor blade azimuth angle, measured positive in the direction of rotation and referenced to zero in the full aft blade position, deg.
ω	Angular velocity of axis system, rad./sec.
ω_{v_n}	Frequency of (n) th chordwise mode, rad./sec.
ω_{w_n}	Frequency of (n) th flapwise mode, rad./sec.
ω_θ	Frequency of first torsional mode, rad./sec.

Subscripts

B	Main rotor blade parameter
LD	Lag damper parameter
MR	Main rotor parameter
T	Tail rotor parameter
a	Aerodynamic parameter
bw	Refers to the trailing edge of spar
f	fuselage parameter
i	inertia parameter
le	Refers to the leading edge of the spar
s	Rotor shaft axis parameter
.75	Refers to rotor blade .75 radius ratio station

Miscellaneous

($\bar{\quad}$)	Nondimensional parameter, nondimensionalizing factors employed are $\bar{\Omega}_o$, \bar{R} and \bar{m}_o , thus $\bar{\omega} = \omega / \Omega_o$, $\bar{r} = r / R$, $\bar{M}_B(r_{cg}) = M_B(r_{cg}) / m_o \Omega_o^2 R^3$, etc.
(\quad)'	indicates derivatives of (\quad) with respect to \bar{r}
($\dot{\quad}$)	indicates derivatives of (\quad) with respect to t
(\quad^x)	indicates derivatives of (\quad) with respect to \bar{t}

INTRODUCTION

Present day helicopters, which cruise in the 100 to 150 knot speed regime, can safely negotiate a complete loss of power. However, the larger perturbations created by a sudden power plant failure in future high speed helicopters might result in excessive rotor stresses, both because of the larger applied torque change and because of the decrease in rotor stability associated with the higher speed. Although it is reasonable to expect the problem to be most severe for helicopters that obtain all of their propulsion and lift from the rotor system, it might also exist for high speed helicopters that derive some propulsive force from auxiliary power plants.

In order to reduce the conjecture regarding the seriousness of the stress and blade motion following an abrupt power plant failure on a high speed helicopter, Sikorsky Aircraft has conducted an exploratory analytical investigation under contract to the U. S. Army Aviation Materiel Laboratories (Contract DA 44-177-AMC-195(T)). The goal of this study was to determine the influence of various combinations of design parameters, flight conditions, and corrective control input patterns on the blade stress and motion of a helicopter following complete and partial power loss at high speeds. This report gives results of that study.

The prediction of helicopter and rotor dynamic behavior after a power plant failure involves consideration of a large number of coupled, complex, and nonlinear effects. The classical approach to the analysis of helicopter maneuvering flight considers linear solutions only. This linear approach to certain problems is still very attractive. These solutions, which are useful for generating trends for systems with feedback circuits, are not particularly suited to calculation of helicopter motion following engine malfunction.

A nonlinear method for calculating the applied and inertia loads acting on a helicopter during various maneuvers was developed employing actual force and moment equations. This method describes the aircraft in six degrees of freedom in the body axis system and the rotor in flapping and rotor speed degrees of freedom. With the inclusion of rotor blade inplane motion (lead-lag) and intricate rotor blade aeroelastic characteristics, the method is well suited to the analysis of dynamic response of a helicopter following power plant failure at high speeds.

The Sikorsky Normal Mode Flexible Blade Analysis system was used for the rotor system. It solves the blade equations by time-wise step-by-step integration and is directly applicable to the calculation of rotor transient motion. This analysis represents the blade deflections in a conventional manner by a summation of normal vibratory blade elastic modes to give the fully coupled flapwise, chordwise, and torsional bending response. This analysis provides an accurate representation of the rotor blade aeroelastic characteristics and includes blade inplane (lead-lag) degree of freedom. Essential agreement with test data has been obtained in

correlation studies.

The above analysis was coupled on the hybrid digital analog computer with the general helicopter simulation force and moment equations of motion. This coupling provides a complete and accurate representation of body and blade motions as well as stress levels at critical blade spanwise stations. This combined analysis, representing a significant advancement in analytical techniques, is general and well suited to a variety of VTOL aircraft and maneuvering flight conditions. Good correlation has been achieved with S-61 flight test data.

This report presents the results of the application of this method to the analysis of helicopter rotor and fuselage motion following an exponential reduction of 50% and 100% in power supplied to the rotor system and subsequent insertions of corrective rotor control inputs. The major portion of this study is concerned with flight speeds at 200 and 235 knots of the six-bladed, S-61F (NH-3A) high speed research helicopter, configured with various combinations of flapping hinge offset, twist, tip path plane and flapping feedback, Lock number, and drag-to-lift ratios.

SCOPE OF PROGRAM

The effects of power loss on helicopter behavior and blade structural loading have been studied, for general rotor design parameters, at 200 and 235 knots. The influence of flapping hinge offset, articulation method, twist, Lock number and pitch-blade motion coupling has been investigated for 50% and 100% reduction in the available rotor system driving torque. In this study, a partial power loss or 50% loss in available rotor system driving torque is considered as a loss of one engine. A full power loss assumes the loss of both engines. Auxiliary propulsive force is assumed to be provided by an independent power source. Four values of drag-to-lift ratios, D/L , have been considered in order to determine the influence of auxiliary propulsion. In addition, various types of corrective control inputs were investigated, with delay times ranging from 0.2 second to 0.6 second.

In order to establish qualitatively the interrelation among design combinations, flight conditions, and input patterns, hybrid computer time history data of body and blade motions were recorded for each basic variation. The flight conditions investigated included the following combinations:

200 knots, $D/L = 0.15$, $\theta_1 = -4^\circ$

200 knots, $D/L = 0.075$, $\theta_1 = -4^\circ$

200 knots, $D/L = 0$, $\theta_1 = 0^\circ$

235 knots, $D/L = -0.063$, $\theta_1 = 0^\circ$

where D/L is the ratio of rotor propulsive force to rotor lift (drag-to-lift ratio).

The design combinations were incorporated into seven rotor systems installed on the same base aircraft. The high speed S-61F research aircraft, described in Appendix I, was used as a basis for this study. A gross weight of 11,900 pounds was assumed.

The control input portion of this study was conducted for six rotor configurations and three D/L conditions to determine the influence of rate and magnitude of inputs, and coupling of controls.

Blade structural loading and motion time history data were recorded with and without control inputs for those cases considered to be most severe. Chordwise, flapwise, and torsion bending moments have been computed at three radial stations, utilizing realistic blade structures. In addition, chordwise bending moments have also been calculated in the vicinity of the lag damper. The data have been analyzed to define qualitatively the effects of the design parameters and control inputs on blade loading.

DESCRIPTION OF ROTOR SYSTEMS

The basic design combinations of flapping hinge offset, articulation method, twist, Lock number, and pitch-blade motion coupling were investigated by means of the following seven rotor systems:

- a. Fully articulated six-bladed rotor with a flapping hinge offset ratio (e/R) of 0.0339, $\gamma = 10.62$.
- b. Rotor system (a) above with individual blade pitch-flap coupling $\delta\text{-three} = 30^\circ$.
- c. Rotor system (a) above with individual blade pitch coupling with the integrated flapping of all blades.
- d. Rotor system (a) above with a flapping hinge offset ratio (e/R) of 0.
- e. Rotor system (a) above with a decreased Lock number, $\gamma = 7.88$.
- f. Rotor with four low aspect ratio blades rigidly attached to the hub.
- g. Rotor system (f) above with a floating hub.

The value of $\delta\text{-three}$, used for this study for rotor b, is a typical value considered for use on present day high speed helicopters to reduce the gust sensitivity of the main rotor. A comparable amount of tip path tilt feedback was used for rotor c. For rotor c, the tilt of the tip path plane was sensed by feeding back blade flapping velocity to blade pitch. A stable feedback was used for both rotors.

The physical properties of the various rotor systems are given in Appendix I.

The study conditions investigated for each of those rotor systems are outlined in Table II, and the rotor operating conditions are listed in Table III. With the advancing blade tip Mach number specified contractually, as shown in Table III, a maximum rotor tip speed of 633 fps was selected as providing the best performance characteristics. The most critical operating condition, in terms of stall, is at a drag-to-lift ratio (D/L) of 0.15 at 200 knots. This condition sized each rotor so that a maximum value of rotor lift coefficient (C_L/σ) of 0.044 was available within the "upper stall" limit of (bC_{qd}/σ) = 0.008. This is a reasonable limit for steady flight operation. For the fully articulated rotor with six blades, this operating condition dictated a rotor lift of 11,900 pounds. At 235 knots, however, a $D/L = -0.063$ was selected, in order to provide a reasonable amount of rotor torque within an "onset of stall" limit of (bC_{qd}/σ) = 0.004.

TABLE II
STUDY CONDITIONS

Forward Speed	200 Knots			235 Knots
Blade Twist	-4 Degrees		0 Degrees	
D/L				
Rotor System	0.15	0.075	0.	-0.063
a Fully Articulated	X	X	X	X
b Delta-3 Feedback	X	-	X	X
c Tip Path Plane Tilt Feedback	X	-	X	-
d Zero Offset	X	-	X	-
e Low Lock Number	X	X	X	X
f Hingeless Rotor	X	X	X	X
g Floating Hub	X	X	X	-

TABLE III
ROTOR OPERATING CONDITIONS

V	M_{T90°	Ω_{OR}	μ	$(C_L/\sigma)_{Stall}$	(D/L)
Knots	-	fps	-	-	-
200	0.870	633	0.534	0.044	0.15
200	0.870	633	0.534	0.052	0.075
200	0.870	633	0.534	0.058	0.
235	0.923	633	0.627	0.044	-0.063

DEVELOPMENT OF COMPUTER PROGRAM

The prediction of helicopter and rotor system dynamic response following a power plant failure involves consideration of a large number of coupled, complex, and nonlinear effects. The analysis used, programed on a hybrid computer system, describes the aircraft in six degrees of freedom in the body axis system and the rotor in flapping, lagging, bending, and rotor speed degrees of freedom, and represents the blades by a summation of normal vibratory blade elastic modes to give a fully coupled flapwise, chordwise, and torsional bending response.

The program includes the following:

1. Six degree of freedom fuselage equations of motion with no small angle assumptions.
2. Nonlinear fuselage aerodynamic wind tunnel data.
3. Nonlinear rotor force and moment equations of motion for each blade with no angle of attack or advance ratio restrictions.
4. Nonlinear rotor blade airfoil section aerodynamic data including stall and Mach number effects.
5. Individual blade flapping and lagging degrees of freedom.
6. Rotor speed degree of freedom.
7. Six aerodynamically coupled blade deflection degrees of freedom.
 - A. Three Flapwise Modes
 - B. Two Chordwise Modes
 - C. One Torsional Mode

In the analysis, tail rotor power is assumed small and is not included in the decay of main rotor speed. For the aircraft trimmed for zero roll in the 200-knot range of forward speed, tail rotor power is only about 3% of the main rotor power and, therefore, is a second order effect.

In the blade aeroelastic part of the program, although one reference blade was monitored, a complete aerodynamic and aeroelastic solution was obtained for each blade. This procedure insured accurate calculation of rotor performance and simplified the analysis of the floating hub rotor system.

A description of equations of motion, flexible blade simulation, assumptions and method of solution is given in Appendix II. A list of equations used in this study is given in Appendix III.

PROGRAM CHECK OUT AND CORRELATION

Verification of the hybrid computer program was conducted by correlating calculated data with actual flight test data of a simulated power failure. Flight test data of the Sikorsky CH-3C aircraft, described in Appendix I, was utilized in this study. A comparison with flight test data of the calculated response of the aircraft due to a simulated power loss at 143 knots is presented in Figure 1. Actual pilot control inputs, shown in Figure 2, as well as an exponential decay of power with time were used in the computer program. Engine power was permitted to decay exponentially to 35% of its trim value in 0.5 second. However, as seen in Figure 1, after 1.4 seconds, the power lever was changed to provide more power. This power rise was not simulated in the computer program due to the limited information on the engine response characteristics and the actual power change.

In Figure 1, the calculated response of the aircraft agrees favorably with the flight test data during the time interval that the power lever was held fixed. In particular, calculated rotor speed and blade lag angle show excellent correlation with flight test data. Fuselage angular rates and displacements show good correlation in both trends and magnitudes.

In previous correlation studies conducted in development of stability and control programs, a significant variation in the response of unstabilized helicopters was observed whenever the initial conditions were varied or whenever mild atmospheric turbulence was introduced. It is reasonable to assume that during this test the aircraft was not in as perfect trim, nor in as ideal weather conditions as can be commanded on the computer. These non-ideal conditions will affect the aircraft response following the power reduction. The long term difference between calculated and test value of the aircraft angular rates and displacements is, therefore, attributed to the difference in these conditions.

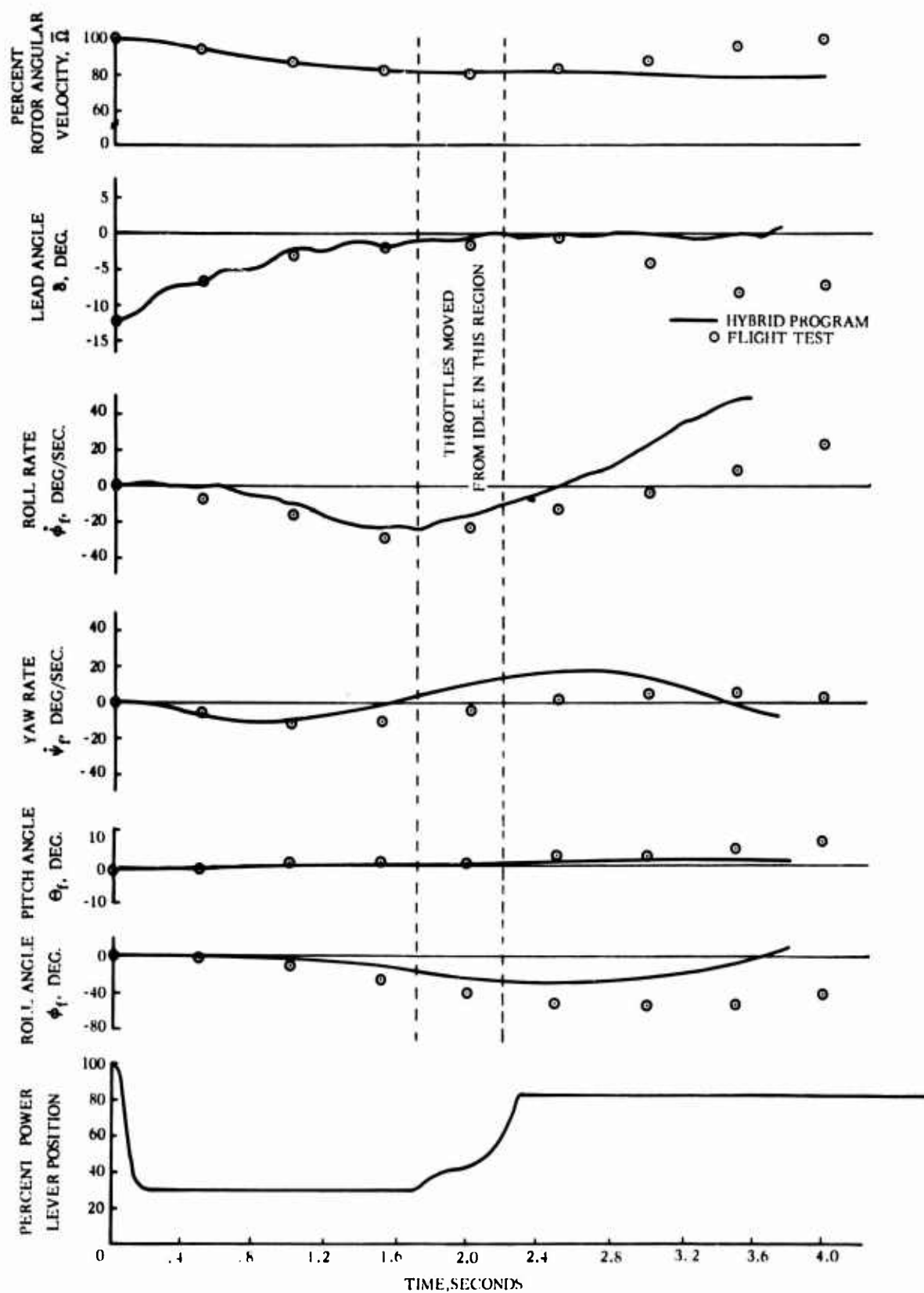


Figure 1. Comparison of Calculated Aircraft Response Due to a Simulated Power Loss With Flight Test Data at 143 Knots

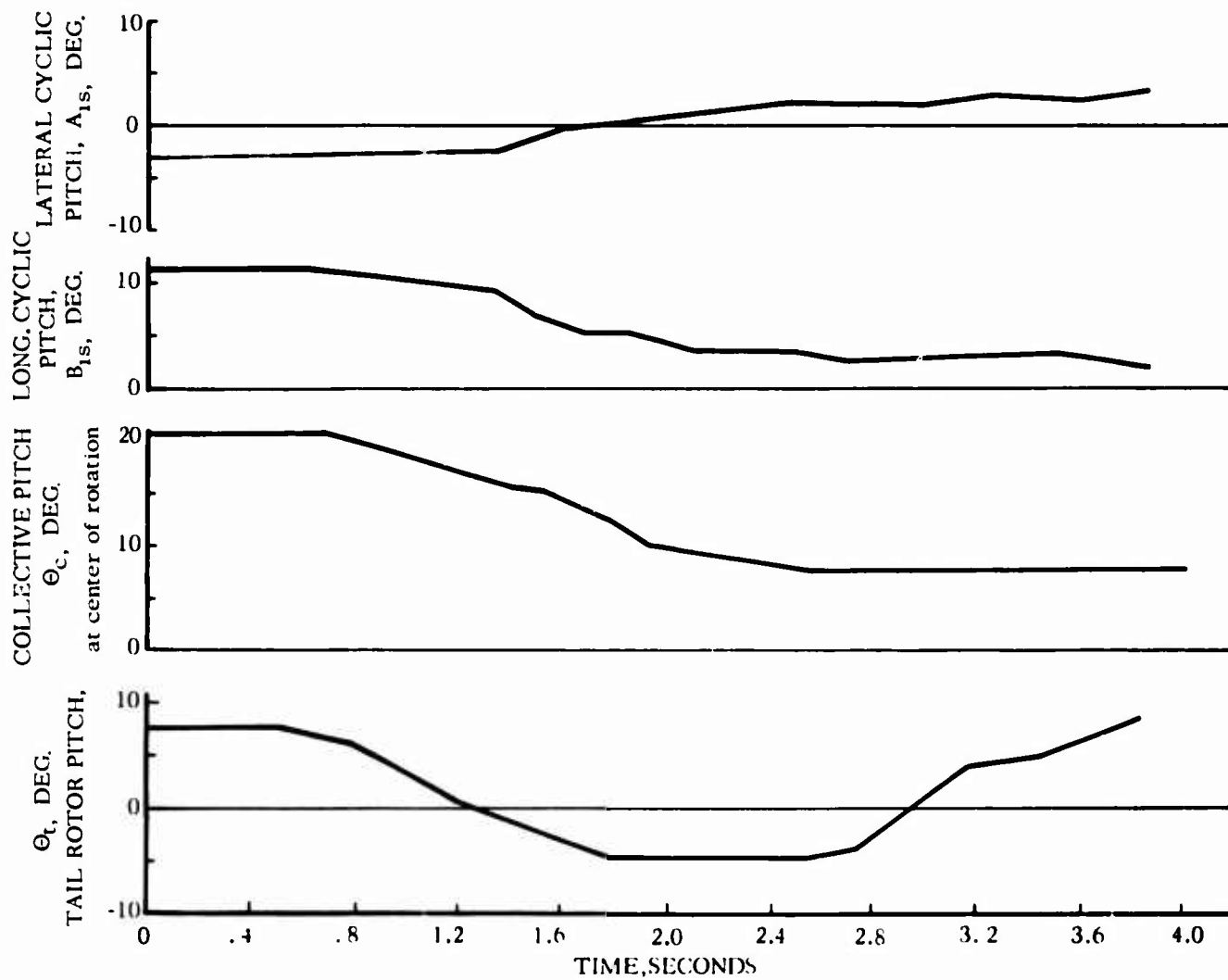


Figure 2. Simulated Pilot Control Inputs

DISCUSSION OF RESULTS

Time history data of body and blade motions were recorded for each rotor configuration in order to establish the interrelation among rotor parameters, flight conditions, and corrective control input patterns. A total of 178 combinations were investigated and the most significant have been analyzed and discussed here. A list of the configurations and flight conditions is given in Table II, and a selected list of the corrective control inputs discussed in this section is presented in Table IV. As seen in the latter table, these inputs include various combinations of step and ramp pedal inputs and ramp inputs of cyclic and collective blade pitch. All ramp inputs are applied at the rate of 7.5 degrees per second. The trim condition for each rotor system is given in Table V.

Typical time history data recorded for this study are presented in Figures 3 and 4. The response of a fully articulated rotor, rotor (a), following a full power loss at 200 knots, ($D/L = 0.15$) with no control input is presented in Figure 3. The effect of a full corrective control input, 6B, initiated 0.2 second after the power loss is shown in Figure 4.

In this section, helicopter and blade motion following a loss of power is discussed and then the blade loading associated with these disturbances is considered. The effects of Lock number, flapping hinge offset, and blade pitch-blade motion feedback on rotor speed, flapping, lagging, and fuselage roll angle with no control inputs are treated first. The discussion is based on values recorded 2 seconds after power loss or on values of the first peak after power loss, section A. This analysis, based on discrete values, is further supplemented by a detailed analysis of helicopter and blade transient response, section B. The time history data were replotted to show the effects of the power loss by a relative comparison of rotor configurations, flight conditions, and corrective control inputs. The blade loading discussion, section C, includes both an analysis of the trim bending moments for all configurations except the floating hub rotor and an analysis of the maximum vibratory moment characteristics for several rotor configurations, control inputs, and main rotor drag to lift ratios, D/L . Note that D/L represents the ratio of rotor propulsive force to rotor lift. This section is then completed by a discussion of the time history of peak and one-half peak-to-peak bending moment envelope for various configurations and control inputs.

A. EFFECT OF ROTOR DESIGN PARAMETERS ON HELICOPTER AND BLADE MOTION PEAK VALUE CHARACTERISTICS FOLLOWING POWER LOSS - NO CORRECTIVE CONTROL APPLIED

Effect of Lock Number

A 26% reduction in Lock number from 10.62 to 7.88 does not significantly affect the rotor speed following loss in power as shown in Figure 5. The rotor speed, as a percentage of trim rotor speed measured two seconds after the loss in power, is used as a criterion for comparison. The rotor speed for each configuration differs only by about 2%. Following a full power

loss, the rotor with the low Lock number blades maintains a higher rotor speed than the standard rotor. Both rotors maintain about the same speed following a partial loss in power.

The higher inertia of the low Lock number blades reduces the flapping disturbance as seen in Figure 6. The change, from trim, in the one-half peak-to-peak maximum vibratory flapping amplitude is used for comparison. Neither rotor experiences a change in blade flapping following a partial loss in power for drag to lift ratios of 0.075, 0, and -0.063. Although the high inertia blades would cause the rotor disk to lag behind the aircraft roll motion and would indicate a larger flapping motion relative to the shaft, the reduction in roll motion reduced the rotor disk lag, thereby reducing blade flapping.

The change in steady lag angle is also reduced as the blade Lock number is decreased, as shown in Figure 7. The tip mass in the centrifugal force field acts as a restoring moment to reduce the initial lagging position of the blades and the blade lead-lag excursion.

The increased hub moment damping provided by the higher inertia of the low Lock number blades reduces the aircraft roll response, as seen in Figure 8. A comparison of the first peak in fuselage roll angle after the power loss is presented in this figure. For both configurations, the severity of the roll disturbance is considerably reduced as the rotor propulsive force requirement is reduced, with lower D/L. At 235 knots, $D/L = -0.063$, the aircraft displays little or no roll disturbance even for a full loss in power. Therefore, increasing the rotor blade moment of inertia will effectively reduce the blade and aircraft disturbance following a loss of power.

Effect of Blade Pitch-Blade Motion Feedback

Delta-three and tip path plane feedback will not be beneficial, as seen in Figures 9 through 12. Compared to a standard fully articulated rotor, rotor speed falls off faster, as seen in Figure 9. Within the first two seconds following loss of power, the delta-three rotor loses more speed than the other configurations. Flapping disturbance, however, is decreased when a full power loss occurs, and is slightly increased following a part power loss (Figure 10). Blade lead-lag motion is also higher with blade motion feedback as seen in Figure 11. The time history data for the delta-three rotor were terminated about 1.5 seconds after the full power loss (Figure 21). The termination occurred because the aircraft motion exceeded reasonable value limits programed in the computer. Blade flapping motion was therefore not fully developed for this flight condition. Of significant interest, however, are the peak roll response characteristics shown in Figure 12.

Delta-three and tip path plane tilt feedback aggravate the roll transient response of a helicopter following a loss of power. Although the peak roll amplitudes are nearly the same for a part power loss, the delta-three rotor experiences a larger roll disturbance than either the tip path plane feedback or standard rotor following a full loss of power. Both feedback rotors experience a larger roll disturbance than the standard rotor. As rotor

propulsive force requirements are reduced, with lower D/L , all rotors have the same reduced response.

Effect of Flapping Hinge Offset

A reduction in flapping hinge offset ratio, e/R , with the associated reduction in hub moment damping, also aggravates the transient response of a helicopter following a power loss at high speeds. This is evident in Figures 13 through 16. Compared with a rotor with a 3.4% flapping hinge offset ratio, a rotor with zero offset will experience a faster decay in rotor speed (Figure 13), a large flapping disturbance (Figure 14), and a larger excursion in lead-lag angle following both full and part power losses (Figure 15). The reduction in hub damping with zero offset also causes the roll disturbances to be larger, as seen in Figure 16. The disturbance, however, is reduced for both configurations as the rotor propulsive force requirements are reduced.

An analysis of the recorded time history data indicates that Lock number, blade motion feedback, and flapping hinge offset do not significantly affect the pitch, yaw, and sideslip motion. The peak values of these quantities are therefore presented in Figure 17 as a single curve. It is seen in this figure that the pitch, yaw, and sideslip response are primarily affected by rotor propulsive force requirements, D/L , and fuselage aerodynamic characteristics, as will be shown in the next section.

B. EFFECT OF ROTOR DESIGN PARAMETERS, ROTOR PROPULSIVE FORCE, AND CORRECTIVE CONTROL INPUTS ON HELICOPTER AND BLADE MOTION TIME HISTORY FOLLOWING POWER LOSS

Although the evaluation of discrete values of helicopter and blade motion presented above does show some distinctive trends, a complete time history of the transient response is required for a thorough appreciation of the effects of rotor parameters and control inputs. For this reason, selected time history data of helicopter and blade motions have been replotted and presented in Figures 18 through 47. The transient response data are presented for various combinations of rotor configurations, corrective control inputs, and drag-to-lift ratios. The data presented include blade flapping and lagging motion, rotor speed, fuselage roll and sideslip angles, and fuselage yaw and pitch rates.

Part Power Loss - No Control Input

The transient helicopter and blade motion following a part power loss at a $D/L = 0.15$, 200 knots, for all rotor configurations is presented in Figures 18 and 19. The response of a helicopter with a blade pitch-blade flap feedback rotor system (rotor b); a blade pitch-tip path plane feedback rotor system (rotor c), and a reduced Lock number rotor system (rotor e) is compared with the response of a fully articulated rotor system (rotor a) in Figure 18. The response of rotor systems with zero flapping hinge offset (rotor d), hingeless blades (rotor f), and floating hub (rotor g) is compared with the response of rotor (a) in Figure 19.

Throughout the recorded time period in Figure 18, Lock number does not appreciably affect rotor speed. Although rotor speed tends to converge to approximately the same value at the end of the period, the delta-three rotor has a higher decay rate and the speed remains below all others. About 4 seconds after the partial loss of power, rotor speed becomes constant at about 90% of its trim value. At this new rotor speed, the power required by the main rotor matches the power available from the remaining single engine. Rotor speed can be increased by reducing forward speed or entering a descending flight condition by lowering collective pitch.

The roll response, however, is quite severe. Rotors (a), (b), and (c) roll left more than 40° in 2.5 seconds after the loss of power. However, the increased hub damping moment associated with the low Lock number blades limits its roll disturbance to about 30° . The stabilization concepts of flapping and tip path plane feedback to blade pitch are seen to be ineffective, because these systems experience a larger roll motion than the standard rotor.

The rapid reduction in main rotor torque without an accompanying reduction in tail rotor thrust creates an unbalanced yawing moment condition on the fuselage. Consequently, the aircraft yaws to the left about -5° to generate a sideslip angle of approximately $+5^\circ$ in 2 seconds. As seen in Figure 3, the aircraft is trimmed at a negative angle of attack of -4° . For this combination of fuselage angle of attack and sideslip, the fuselage rolling moment is negative and yawing moment is positive (Figure 78). The initial yaw motion to the left is reversed in about 1.5 seconds by the fuselage yawing moment, and the aircraft rolls to the left due to the stable fuselage and rotor dihedral effect. The pitch and yaw rates, sideslip angle, and their period of motion, however, are virtually the same for all rotor configurations. The aircraft response is, therefore, due primarily to the fuselage aerodynamic forces and moments associated with the sideslip and yaw motion generated by the unbalanced tail rotor yawing moment.

The blade lead-lag motion for all configurations has a vibratory amplitude of about $\pm 1^\circ$. Blade flapping is relatively constant and then increases markedly at about 4 seconds. The large flapping amplitude of the delta-three rotor in comparison with the fully articulated rotor is evident. Higher harmonics of flapping also occur in the delta-three trace. Since fuselage roll rate peaks at about 4 seconds (Figure 3), the large flapping amplitude is attributed to the angle of attack induced by the roll rate.

The transient response of rotor speed for the hingeless rotor is initially the same as for the fully articulated rotor (Figure 19). About 2 seconds later, however, the hingeless rotor speeds up. The speed-up is attributed to the change in rotor angle of attack distribution induced by the aircraft roll and pitch rates. This rotor maintains a zero roll attitude for about 1 second, then rolls rapidly to -80° in about 3 seconds, and continues to diverge with time. Although the gyroscopic characteristics of the hingeless rotor initially limit the effects of the power loss, the unbalanced tail rotor thrust generates a disturbance on the aircraft, which produces a left roll. The gyroscopic effects generate a nose down moment which increases the negative angle of attack of the fuselage. A larger negative

rolling moment is developed which increases the left roll motion, causing the aircraft to diverge.

The effect of low hub moment damping is evident in the motion of the zero offset rotor. Aircraft motion is larger and rotor speed decays faster. The effect of the aircraft motion on flapping, as well as the increase in vibratory lead-lag motion as rotor speed falls off, is evident in Figure 19.

No automatic stabilization has been assumed in any of the cases shown. The divergence could probably be controlled by an auxiliary stabilization device, but the optimization of proper feedback was beyond the scope of this study.

Full Power Loss - No Control Input

Effects of rotor propulsive force, fully articulated rotor

The effect of a full loss of power on the transient motion of the fully articulated rotor for various drag-to-lift ratios is shown in Figure 20. As D/L increases, the rate of decay of rotor speed also increases for the 200 knot condition ($D/L = 0, 0.075$ and 0.15), because of the increase in power loading with an increase in D/L. Since the rotor at $D/L = -0.063$ (235 knots) has about the same power loading as at $D/L = 0$ (200 knots), the decay in rotor speed is about the same.

As the D/L ratio increases, the fuselage response becomes more severe. This is due to the fuselage aerodynamics. Larger slip angles occur and, therefore, larger roll angles due to fuselage rolling moments. Fuselage roll angles as large as -90° were recorded for $D/L = 0.15$. At $D/L = 0.075$, the fuselage roll angle was reduced to -30° , and at a D/L of 0, the largest roll angle measured was -10° . At 235 knots, there was a very small change in roll attitude with a full power loss. For $D/L = 0$ and -0.063 , the fuselage angle of attack is about 1.5° . As seen in Figure 78, rolling moment is correspondingly small and independent of sideslip. The roll disturbance for these flight conditions will be small.

From Figure 20, it can be seen that as D/L increases, the flapping and lead angles also increase following the loss in power. Since the aircraft roll motion increases with D/L, the rotor disk lags the fuselage and, consequently, blade flapping also increases.

Effects of rotor design parameters, $D/L = 0.15$

The effects of a full power loss at $D/L = 0.15$ for all rotor systems are shown in Figures 21 and 22. The rotor speed for all articulated rotors tends to converge to about 70% of trim speed in Figure 21. The low Lock number rotor maintains a consistently higher rotor speed and the delta-three rotor speed is lowest throughout the time period. The severity of the disturbance can be seen in the yaw rate and sideslip angle curves. The peak values are twice as large as for the part loss of power data shown in Figure 18. This effect is consistent with the twofold increase in unbal-

anced tail rotor yawing moment associated with the full power loss. Roll displacement is doubled so that the flapping amplitude is markedly increased for all configurations. The fuselage motion of the delta-three rotor was so large that reasonable value limits of roll rate (Appendix II) programed on the computer were exceeded. The computer went into a hold mode and the time history recording was terminated 1.5 seconds after the loss of power. This was also true for the zero offset, hingeless, and floating hub rotors as seen in Figure 22. Therefore, the severest condition for a loss of power is at $D/L = 0.15$ (200 knots). Auto-stabilization by means of blade pitch-motion feedback and gyroscopic damping of hingeless blades is not effective in minimizing the effects of the fuselage rolling moment due to sideslip. Increasing the blade inertia of the articulated rotors and decreasing the rotor propulsive force requirements are the only effective means of reducing the initial disturbance following loss of power.

Effects of rotor design parameters, $D/L = -0.063$

A comparison of the effects of a negative rotor propulsive force for several rotor systems is presented in Figure 23. The responses of the fully articulated rotor (rotor a), delta-three rotor (rotor b), low Lock number rotor (rotor e), and hingeless rotor (rotor f) are compared for a full power loss at $D/L = -0.063$ (235 knots). Although the initial yaw and the sideslip disturbance are nearly the same as for $D/L = 0.15$ conditions, the roll motion is negligible. As discussed previously, the fuselage rolling moment is small and roughly independent of sideslip angle, at this fuselage angle of attack, so that all rotor systems have about the same response. Notice that the left roll induces a nose-down pitch motion on the hingeless rotor. Rotor speed also decays fastest for this rotor, and reduces to 70% after 4 seconds. However, the low Lock number rotor maintains a rotor speed slightly higher than the standard rotor, and rotor speed for the delta-three rotor falls slightly below the conventional rotor. Since rotor speed is the only quantity that has changed, the gradual increase in flapping and lead-lag amplitude is due to the reduction in rotor speed.

Part Power Loss With Corrective Control Inputs, $D/L = 0.15$

The effects of control inputs on helicopter and blade transient response following a partial loss of power at $D/L = 0.15$ are shown in Figures 24 through 29 for the following rotor systems: fully articulated rotor (a), delta-three feedback (b), tip path plane tilt feedback (c), reduced Lock number (d), zero flapping hinge offset (e), and hingeless rotor (f).

It has been shown in Figures 18 and 19 that for this flight condition the critical quantity affecting the helicopter disturbance is fuselage roll due to sideslip. Since the primary cause is the unbalanced tail rotor thrust yawing moment, corrective control inputs applied only to tail rotor blade pitch were investigated for this condition. The tail rotor control inputs for this case are listed in Table IV and consisted of two ramp inputs of 7.5 degrees per second applied after a time delay of 0.6 and 0.2 seconds, 4A and 4B respectively, and a step input at 0.2 second, 2B. For all cases, the tail rotor blade pitch angle was reduced to 3 degrees.

The ramp input at 0.6 second, 4A, reduced the roll period and displacement for all rotor systems. Ramp and step inputs at 0.2 second reduced roll angle even further; and the step input, 2B, provided the largest reduction in roll amplitude. For the articulated rotor systems, Figures 24 through 28 show that reducing the roll amplitude also decreases the blade motion, with a maximum reduction occurring when the roll amplitude is minimized. Although rotor speed for the articulated rotors is not significantly affected by the control inputs, the hingeless rotor speed time history shows marked changes, Figure 29. The reduction in aircraft motion caused by input 2B decreased the rotor speed-up and roll motion of the aircraft. By reducing the rolling motion of the aircraft, the nose down pitch rate (caused by gyroscopic coupling) was also decreased.

The strong coupling between fuselage sideslip and roll is clearly evident in these figures. By reducing tail rotor thrust, the fuselage yawing moment reverses the yaw rate, sideslip is rapidly reduced and roll disturbance is correspondingly reduced. Since the ramp input with a 0.2-second time delay, input 4B, provided the least overall sideslip motion, the effects of the fuselage rolling moment should be small. A comparison of rotor configurations with this input will then permit an evaluation of the effects of rotor parameters. This has been done and the results are shown in Figures 30 and 31.

The transient response of the fully articulated rotor (a), delta-three feedback rotor (b), tip path plane feedback rotor (c) and low Lock number rotor (e) are compared in Figure 30. A 7.5 degrees per second ramp tail rotor blade pitch angle input (4B) was applied 0.2 second after the part power loss. The hingeless rotor (f) and zero offset rotor (d) are compared with rotor (a) for the same control input in Figure 31. A comparison of results, shown in Figure 30 indicates that there is no significant difference in the transient response of these articulated rotors. Rotor speed varies slightly and only small differences occur in roll displacement. The low Lock number rotor rolls slightly less than the conventional rotor, and the introduction of blade motion feedback produces a slightly larger roll angle. Flapping amplitude behaves in the same way. The hingeless rotor and zero offset rotor showed the only noticeable difference, as seen in Figure 31. The zero offset rotor time history data was terminated earlier because roll velocity exceeded limit values. The zero offset rotor can, therefore, be considered to respond the most severely to the part power loss at 200 knots.

The hingeless rotor response is also relatively severe. Rotor speed initially falls off and then reverses to a peak value of about 116% in about 3.8 seconds after the power loss. Also, although the hingeless rotor rolls slower than the fully articulated rotor (a), the peak value is larger and the roll motion induces a nose down pitching motion. A direct comparison of the results presented in Figures 30 and 31 indicates that blade inertia and flapping hinge offset are important rotor design parameters which affect helicopter and rotor blade motion following loss of power.

Full Power Loss With Corrective Control Input

Effect of rotor design parameters and 0.2 second delay, D/L = 0.15

Although the transient response of a helicopter following a partial loss of power can be adequately controlled with only tail rotor corrective control inputs, cyclic and collective controls must be applied when a full loss of power occurs. These additional controls are required in order to recover the sharp reduction of rotor speed, as well as to reduce the aircraft motion.

Since a full power loss at $D/L = 0.15$ (200 knots) represents the most severe flight condition, several combinations of control inputs were investigated at this condition. The effects of three control input patterns on the response of rotors (a) through (f) are compared in Figures 32 through 38.

The strong effect of the unbalanced yawing moments following the full power loss is evident in the transient roll and sideslip motion curves for the articulated rotors (Figures 32 through 36). The most effective means of reducing this undesirable roll motion was found to be a step input on tail rotor pitch to 0 degrees at 0.2 second. A tail rotor step input at 0.6 second reduced the roll motion to only 65° . Although roll amplitudes as large as 100 degrees have been flown satisfactorily by pilots, they are considered very undesirable under unalerted situations such as this.

Rotor speed was effectively controlled by reducing collective and pulling back on longitudinal cyclic stick, inputs 5B, 12B, and 12C. Input 5B is not the optimum control input for this flight condition and would require further corrective action by the pilot within 2 seconds (Figures 32 through 37). Input patterns 12B and 12C were found to be the most promising (Figure 37). Figure 37 also shows the input of rotor control (collective and cyclic pitch) can be delayed up to four seconds, following a loss in power, and still control rotor speed satisfactorily. Since all articulated rotor configurations respond in a similar manner to control inputs 1B, 5B, and 6B, it is expected they would all respond similarly to input 12B and 12C. The traces with input 12B terminated at 1.4 seconds because \dot{q}_{w2} exceeded its built-in limit (Appendix II). The value of \dot{q}_{w2} also became very close to its built-in limit for control input 12C. This is not a physical limit but is an expected maximum limit based on test data. Further rescaling would have prevented \dot{q}_{w2} from becoming too large.

Improvement in roll response was achieved by applying right lateral stick, input 6B (Figures 32 through 36). The total effect of this input is an order of magnitude reduction in the roll motion of an articulated rotor following a full power loss at $D/L = 0.15$. In all cases, vibratory flapping amplitude was initially reduced by this input, but was then increased prior to the termination of the run.

The most effective initial control input for the hingeless rotor, input 8B, is almost identical to input 6B for the articulated rotors. The only difference is that collective pitch was reduced to 8° instead of 2° . With this input, the aircraft rolled left only to about -5° and then recovered (Figure 38). Rotor speed also recovered after a mild droop to about 92%. The aircraft, however, pitched nose down to -10° . This nose down tendency contrasts with the sharp nose up effect caused by input 9B. For this input

collective was reduced only to 12° and longitudinal control was changed by 3.75° .

The transient response associated with control input 6B for the articulated rotors and 8B for the hingeless rotor has been redrawn in Figures 39 and 40 in order to obtain a relative comparison for all systems. Lock number and flapping hinge offset consistently stand out as important design parameters. The delta-three rotor shows a smaller recovery of rotor speed than the other articulated rotor systems for the same control input. This is due to the washout of control input with delta-three; therefore, it would require more control input to achieve the same amount of rotor control as the other articulated rotors. Other than the direct effect of the control input on blade flapping, there is little or no relative difference, with or without control inputs, in the response of the articulated rotor systems.

Effect of 0.6 second time delay, fully articulated rotor, $D/L = 0$

The effect of applying control inputs following a full power loss with a 0.6-second time delay was investigated for the fully articulated rotor (a) at $D/L = 0$ (200 knots), and the results are shown in Figure 41. Although the tail rotor input, 3A, ultimately reduced sideslip to zero, the initial effects of rolling moment produced a left roll. As sideslip was reduced to zero no fuselage moment was available to restore the aircraft to a level attitude. However, the aircraft maintained a reasonably level attitude and some rotor speed was recovered with the full control input, 7A. Since this input represents a typical pilot applied input, the pilot should experience no difficulty in recovering from a full loss of power at this flight condition, $D/L = 0$.

Effect of rotor design parameters at 235 knots, $D/L = -0.063$

The effect of control input time delay has also been investigated at 235 knots, and the results are presented in Figures 42 through 47. The effects of ramp tail rotor control inputs with a 0.2-second time delay, input 3B, and a 0.6-second time delay, input 3A, are compared, along with a full control input, 7B, in Figures 42 through 47 for four rotor systems. These rotor systems include the fully articulated rotor (a) in Figure 42, the delta-three rotor (b) in Figure 43, the reduced Lock number rotor (e) in Figure 44, and the hingeless rotor (f) in Figure 45. A relative comparison of the effects of control input 7B is presented in Figure 46 for all of these rotors.

Since the roll disturbance is small following a full power loss at the flight condition $D/L = -0.063$, tail rotor control inputs were applied to reduce the yaw rate and sideslip motion. The rapid application of tail rotor corrective controls, 0.2-second time delay, effectively reduced both the yaw and sideslip disturbance and the flapping amplitude. As the tail rotor thrust is reduced, a left rolling moment is generated. This happens because the main rotor rolling moment is no longer balanced, so the aircraft rolls left. If the tail rotor control input is delayed 0.6 second, the roll motion is smaller. This is true for all configurations. The additional lateral stick motion in input 7E reduced this roll motion, the

yaw rate, sideslip angle, and the rotor speed decay for all the articulated rotors.

The gyroscopic coupling of the hingeless rotor, however, caused a nose down pitching motion following the tail rotor control inputs as shown in Figure 45. Although the roll response was slightly reduced when the delay time was increased to 0.6 second, the pitching motion was not significantly affected. The lateral stick motion of input 10B reduced sideslip. Yaw rate was reduced only at first but then was increased to the right. The pitch response was aggravated by this control input.

The nose down motion of the hingeless rotor is contrasted with the slight pitch up tendency of the fully articulated rotor systems in Figure 46. The hingeless rotor pitched nose down to about 30° in 2.5 seconds and because of this would require further pilot corrective action to maintain attitude control. The delta-three rotor systems response was milder than the other articulated rotor systems. This was due to the washout of control inputs caused by the delta-three coupling.

For the articulated rotor at a $D/L = -0.063$, the most promising control input was found to be a reduction in main rotor collective pitch to 2° and longitudinal change in cyclic pitch of -5.5° , input 13B (Figure 47). Since the low Lock number and articulated rotor responded in a similar manner to control input 3A, 3B, and 10B, the low Lock number rotor would be expected to respond similarly to input 13B. For this high speed flight condition, although roll motion control presents no problem, application of corrective tail rotor control inputs to recover the yaw and sideslip motion must be accompanied by right lateral stick motion. Aft stick and reduced collective will recover the rotor speed droop. The disturbance following a full power loss at 235 knots, $D/L = -0.063$, is mild, and the pilot should have no difficulty in controlling the aircraft. A full power loss at $D/L = 0.15$, however, produces a severe disturbance and an automatic tail rotor control system would probably be required in order to control the aircraft fuselage motion.

C. EFFECT OF ROTOR DESIGN PARAMETERS, ROTOR PROPULSIVE FORCE, AND CORRECTIVE CONTROL INPUTS ON BLADE BENDING MOMENTS

Time history data of blade bending moments were recorded for all rotor systems except for the floating hub rotor. Data were obtained for 27 combinations of rotor configuration and control inputs. Since the most severe aircraft and blade disturbance occurred at the $D/L = 0.15$ condition, thirteen combinations are included at this flight condition. Included is each of the six configurations with no control inputs, and data for three control inputs apiece for the articulated rotor (a) and the delta-three rotor (b). Typical time history data recorded for this study are presented in Figure 48. Multiple moment data are shown for the fully articulated rotor (a) following a full power loss at 200 knots, ($D/L = 0.15$). It is seen in this figure that flapwise, chordwise, and torsional moment data were all recorded at three radial stations. Stations between the nodal points of the first three flapwise bending modes were selected for this study. The

radial stations for the articulated rotor are 41, 56, and 71 percent of the rotor radius. The hingeless rotor was investigated at 22.5, 45, and 70 percent. In addition, chordwise bending moment data in the vicinity of the lag damper, $r/R = 12\%$, were recorded for the articulated rotors. The recorded moments can be converted to stress by means of the section modulus data listed in Table VI. Since the neutral axis is not equidistant from the leading and trailing edges, two values are given for the chordwise section modulus.

Effect of Rotor Design Parameters and Drag-to-Lift Ratio on Trim Bending Moments

The trim bending moments for all the study conditions listed in Table II have been recorded and the results are presented in Figures 49 through 52. The one-half peak-to-peak vibratory moment is plotted as a function of the corresponding steady moment to constitute a bending moment diagram for each of the four drag-to-lift ratios.

The data for flapwise bending of the articulated rotors at $r/R=56\%$ (Figure 49) indicate that the low Lock number rotor consistently has the lowest steady flapwise moment, and has a vibratory flapwise moment slightly higher than the other systems for all drag-to-lift ratios. For the same forward speed, 200 knots, the vibratory and steady moments generally decrease as the rotor propulsive force requirements are reduced from $D/L = 0.15$ to 0. This reduction, however, is due in part to a reduction of blade twist which is -4° at $D/L = 0.15$ and 0.075 and 0° at $D/L = 0$ and -0.063 . The difference in the vibratory bending moment among rotor systems, however, is small. At $D/L = 0.15$, the difference between the vibratory flapwise moment for the low Lock number, highest value, and the delta-three rotor, lowest value, is equivalent to only ± 600 psi of blade stress.

The chordwise steady bending moments for all rotor systems are negative except for the zero offset rotor, as seen in Figure 50. The zero offset rotor also has the smallest vibratory chordwise bending moment; since the chordwise moments presented in this figure correspond to less than 2000 psi steady and vibratory stress, the values are not critical for the trim conditions shown.

The torsional vibratory moment is also smaller at $D/L = 0$ than at $D/L = 0.15$, as seen in Figure 51. For all drag-to-lift ratios the steady and vibratory torsional moment is the smallest for the fully articulated rotor, and generally, the delta-three rotor experiences the largest vibratory torsional moment.

The hingeless rotor trim bending moments are shown in Figure 52. An in-board reference station at $r/R = 22.5\%$ was selected since the maximum moments occur in the inboard section of a hingeless rotor. The negative steady chordwise bending moments could have been minimized if the rotor blades had been swept aft.

Effect of Rotor Design Parameters, Rotor Propulsive Force and Control Inputs on Blade Vibratory and Peak Moment Time History for Full Power Loss

Time history of the peak and vibratory blade bending moment envelopes are presented in Figures 53 through 58 for each of the three spanwise stations. These moment envelopes will provide a thorough appreciation of the effects of rotor parameters and control inputs on blade bending moments.

The peak moment is the variation of the maximum negative or positive moment recorded as a function of time. Therefore, the envelope of the peak moment is defined by these curves. Also shown is the one-half peak-to-peak moment envelope, called the vibratory moment.

Effect of rotor design parameters, $D/L = 0.15$, no control input

Various articulated configurations are compared in Figure 53 at a rotor lift-to-drag ratio of 0.15 for a full power loss. All configurations shown have about the same flapwise and chordwise moment envelope following a full power loss, except in the region from 1 to 3 seconds, where there is an increase in flapwise, chordwise, and torsional steady and vibratory moments with configurations (a) and (c). This moment increase is due to retreating blade stall, which is shown in Figure 48 as peaks in torsional moment at 1.35 and 1.75 seconds. The termination of configuration (b) at 1.7 seconds was due to fuselage roll rate exceeding its built in value of 1 rad./sec. Retreating blade stall causes an increase in flapwise moment on the outboard section of the blade, while the maximum chordwise moment is increased along the entire blade.

The maximum flapwise and chordwise vibratory moments recorded for configurations (a), (b), and (c) were converted to stress, using Table V, and correspond to vibratory stresses below the 5,500 psi allowable vibratory stress of aluminum for effective infinite life. Therefore, this maneuver does not result in a vibratory or peak bending moment which would cause damage to the blades. Blade stress is used here as a criteria to determine the severity of the maneuver. The moment loading in this study can be used for analyzing other rotor systems, provided the EI ratio and blade bending natural frequencies of the other system is the same as that used in this study. In addition, the stress produced by these moments will be the same if the I/C values of the two systems are the same.

The zero offset rotor system and low Lock number rotors are compared to articulated rotor in Figure 54 and at a rotor drag-to-lift ratio of 0.15 for a full loss in driving torque. Reducing Lock number increases the chordwise and flapwise peak and vibratory moments on the blade following a power failure. The flapwise vibratory moment at the outboard radial station, where the maximum moment occurs, corresponds to a stress level of about 10,000 psi. At this stress level the blade could withstand more than 3,000,000 cycles, therefore, it is not considered a serious condition for this blade design. The most pronounced effect of the zero offset rotor, d, is the reduced trim chordwise peak and vibratory moments. Following the power failure, the flapwise and chordwise moments build up in the same manner

as the articulated rotor. The termination of the zero offset rotor after one second was due to the fuselage roll rate exceeding its built in limit. It is of interest to note even with such a violent fuselage motion the flapwise and chordwise blade moments were not exceedingly large; near the end of the trace the torsional moment did show an increase. A typical time history variation of the chordwise moment in the vicinity of the lag damper (12% radial station) is shown in Figure 48 for the articulated rotor. Throughout this study, this moment remained small.

Effect of Control inputs, fully articulated rotor, $D/L = 0.15$

The effect of control inputs on blade bending moments is shown in Figure 55 for the articulated rotor at a rotor D/L of 0.15 for a full loss in power. By reducing fuselage yaw and roll with a step input on tail rotor collective pitch, the maximum torsional moment was reduced. The flapwise and chordwise vibratory moments recorded correspond to stresses below the allowable 5,500 psi for infinite life and, therefore, are not serious. Even the chordwise and flapwise bending moments produced by control input 5B and 6B correspond to stresses below 10,000 psi and are not serious.

The initial effect of the main rotor control input is to reduce chordwise and torsional bending moments. This is due to unloading the blades with the reduction in collective pitch. After one second all bending moments increase as the rotor tilts back and rotor flapping increases.

Effect of Control inputs, fully articulated rotor, $D/L = -0.063$

The effect of control inputs on the articulated rotor blade moments at a rotor drag-to-lift ratio of -0.063 is shown in Figure 56. Introduction of tail rotor pitch, to reduce fuselage sideslip, decreases the flapwise and chordwise bending moments, but has very little effect on the torsional moment. Rotor inputs 11B initially decrease the torsional and flapwise vibratory moments. At 0.5 to 1.0 seconds, the vibratory and peak moments increase with rotor inputs. As in the previous case, these moments will not damage the blades.

Effect of rotor propulsive force

The hingeless rotor bending moments did not show an appreciable change following a full power loss until fuselage motion built up (Figures 57 and 58). The termination of both traces prior to 5 seconds was due to the fuselage roll rate exceeding 1 rad./sec. The sudden build up of blade bending moments in Figure 58 was due to a sudden increase in fuselage roll rate caused by the rigid rotor gyroscopic moment. As the main rotor slows down, the aircraft pitches nose down. This, in turn, causes a violent negative gyroscopic rolling moment. If automatic stabilization had been used, this build up would probably have been prevented.

The moments presented here are those for an aluminum blade. The moments would increase if steel were used, unless the EI distribution and blade bending natural frequencies were kept the same as that of the rotor blade used in this study.

TABLE IV
CONTROL INPUT PATTERNS

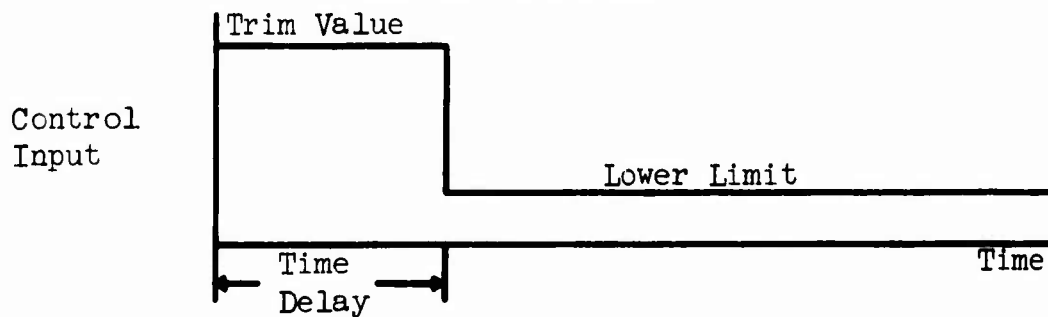
Input Number*	Step Input	Ramp Inputs At 7.5° Per Second			
	Lower Limit	Lower Limit		Input Increment	
	θ_T	θ_T	θ_C	B _{ls}	A _{ls}
1	0°	--	--	--	--
2	3°	--	--	--	--
3	--	0°	--	--	--
4	--	3°	--	--	--
5	0°	--	2°	-7.50°	--
6	0°	--	2°	-7.50°	4°
7	--	0°	2°	-7.50°	4°
8	0°	--	8°	-7.50°	4°
9	0°	--	12°	-3.75°	4°
10	--	0°	2°	-1.00°	4°
11	--	0°	2°	-7.50°	--
12	0°	--	5°	-11.25°	--
13	--	0°	2°	-3.75°	--

* A. Input Applied 0.6 Second After Power Loss.

B. Input Applied 0.2 Second After Power Loss.

C. Main Rotor Input Applied 4.0 Seconds After Power Loss
And Tail Rotor Input 0.2 Second After Power Loss.

STEP INPUT PATTERN



RAMP INPUT PATTERN

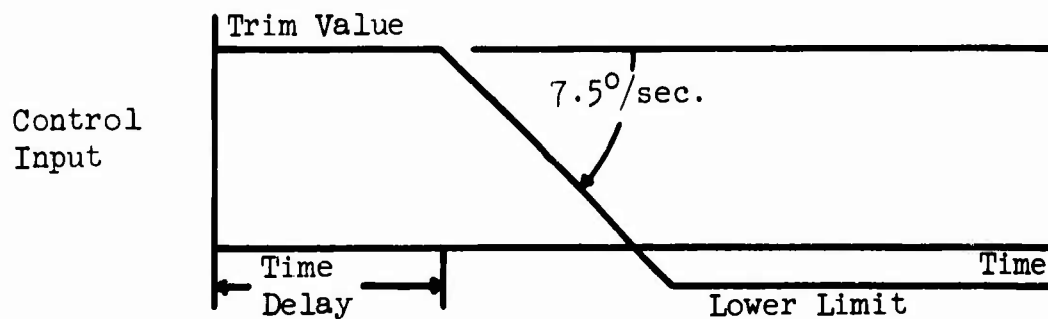


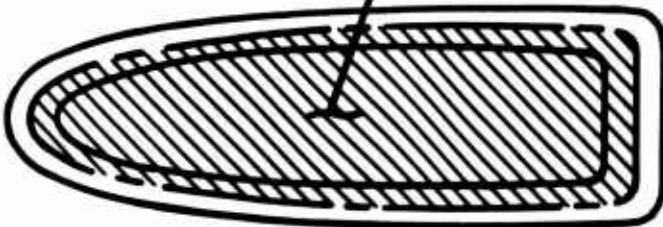
TABLE V

TRIM CONDITIONS

Configuration	D/L	θ_t	θ_c	A _{1s}	B _{1s}	α_f	β_f
Fully Articulated Rotor (a)	0.15	7.4	16.5	-4.9	11.0	-4	1.8
	0.075	6.1	14.3	-4.0	10.5	-1.3	1.2
	0.0	4.9	6.9	-3.6	6.7	1.5	1.0
	-0.063	4.0	4.9	-3.2	3.5	1.5	1.0
Delta-3 Feedback Rotor (b)	0.15	7.8	17.8	-6.5	10.3	-4.5	1.0
	0.0	4.1	8.1	-4.4	6.4	1.5	.0
	-0.063	4.9	7.7	-3.7	4.5	2.0	1.0
Tip Path Plane Tilt Feedback Rotor (c)	0.15	7.5	16.6	-6.2	11.7	-4.2	1.0
	0.0	4.3	7.2	-4.0	7.2	1.6	1.0
Zero Offset Rotor (d)	0.15	9.0	17.6	-7.075	10.2	-6.6	1.2
	0.0	5.0	8.4	-6.8	8.9	2.0	1.0
Low Lock Number Rotor (e)	0.15	7.9	16.7	-3.6	11.7	-4.5	1.0
	0.075	6.4	14.5	-2.9	11.2	-1.5	1.0
	0.0	4.4	7.0	-2.4	6.8	1.5	1.0
	-0.063	4.5	5.8	-2.4	4.8	2.0	1.0
Hingeless Rotor (f)	0.15	7.4	15.6	-2.6	10.0	-5.0	1.0
	0.075	7.1	12.8	-3.2	8.1	-2.0	1.0
	0.0	6.5	6.8	-5.9	5.6	.5	1.0
	-0.063	6.1	3.8	-6.9	2.4	1.5	1.0
Floating Hub Rotor (g)	0.15	8.85	14.6	-3.9	6.5	-6.5	1.0
	0.075	6.8	12.7	-4.1	8.4	-1.0	1.0
	0.0	3.7	5.6	-2.2	4.4	2.5	.5

TABLE VI

SPAR SECTION MODULUS

<u>ARTICULATED ROTOR SYSTEMS</u>				
Radius Rotor, r/R	Flapwise	Chordwise	Torsional	
	$(I/c)_{yy}$	$(I/c)_{zz_{bw}}$	$(I/c)_{zz_{le}}$	$2A't$
12%	--	10.9	8.70	--
41%	2.35	7.5	6.2	4.7704
56%	2.15	6.6	5.7	4.412
71%	1.9	5.55	5.12	3.900
<u>HINGELESS ROTOR SYSTEM</u>				
Radius Ratio, r/R	Flapwise	Chordwise	Torsional	
	$(I/c)_{yy}$	$(I/c)_{zz_{bw}}$	$(I/c)_{zz_{le}}$	$2A't$
22.5%	10.09	27.57	23.05	24.565
45%	6.39	18.2	16.0	13.397
70%	5.51	16.0	14.0	11.395
<p align="center">A' (Blade Spar Midline Area)</p> 				

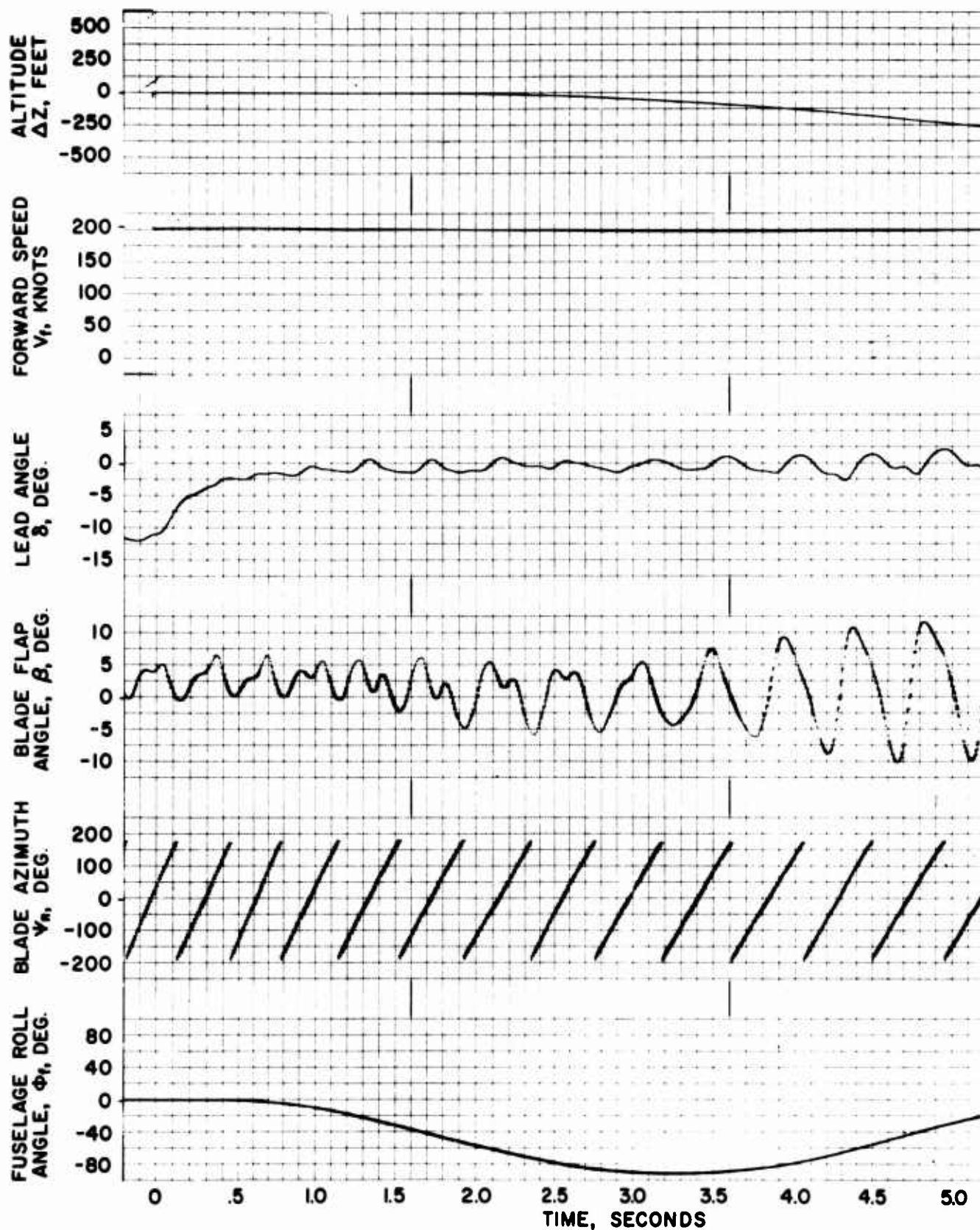


Figure 3. Fully Articulated Rotor ($e/R = 0.034$), Full Power Loss, $D/L = 0.15$, No Corrective Control Input

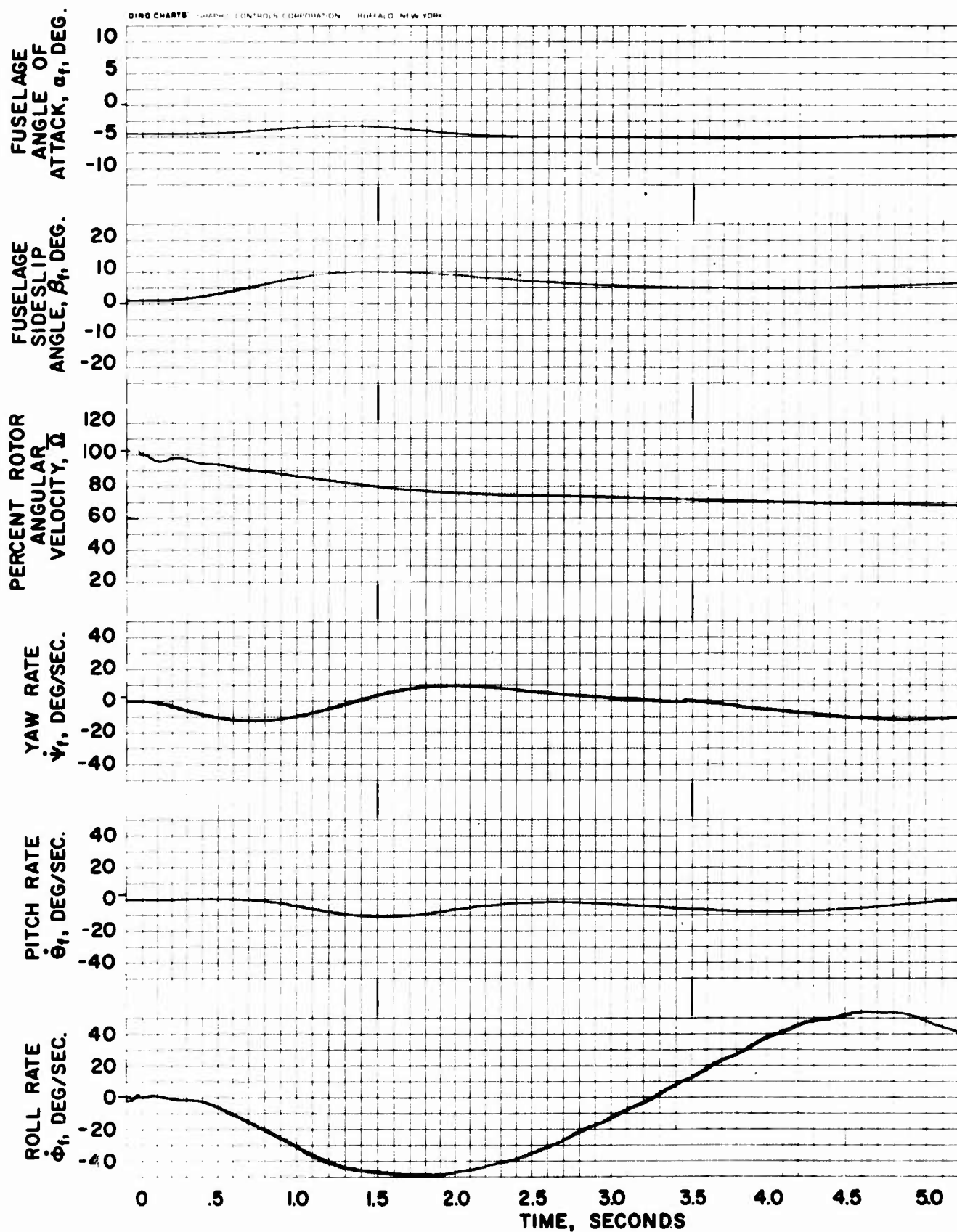


Figure 3. Continued

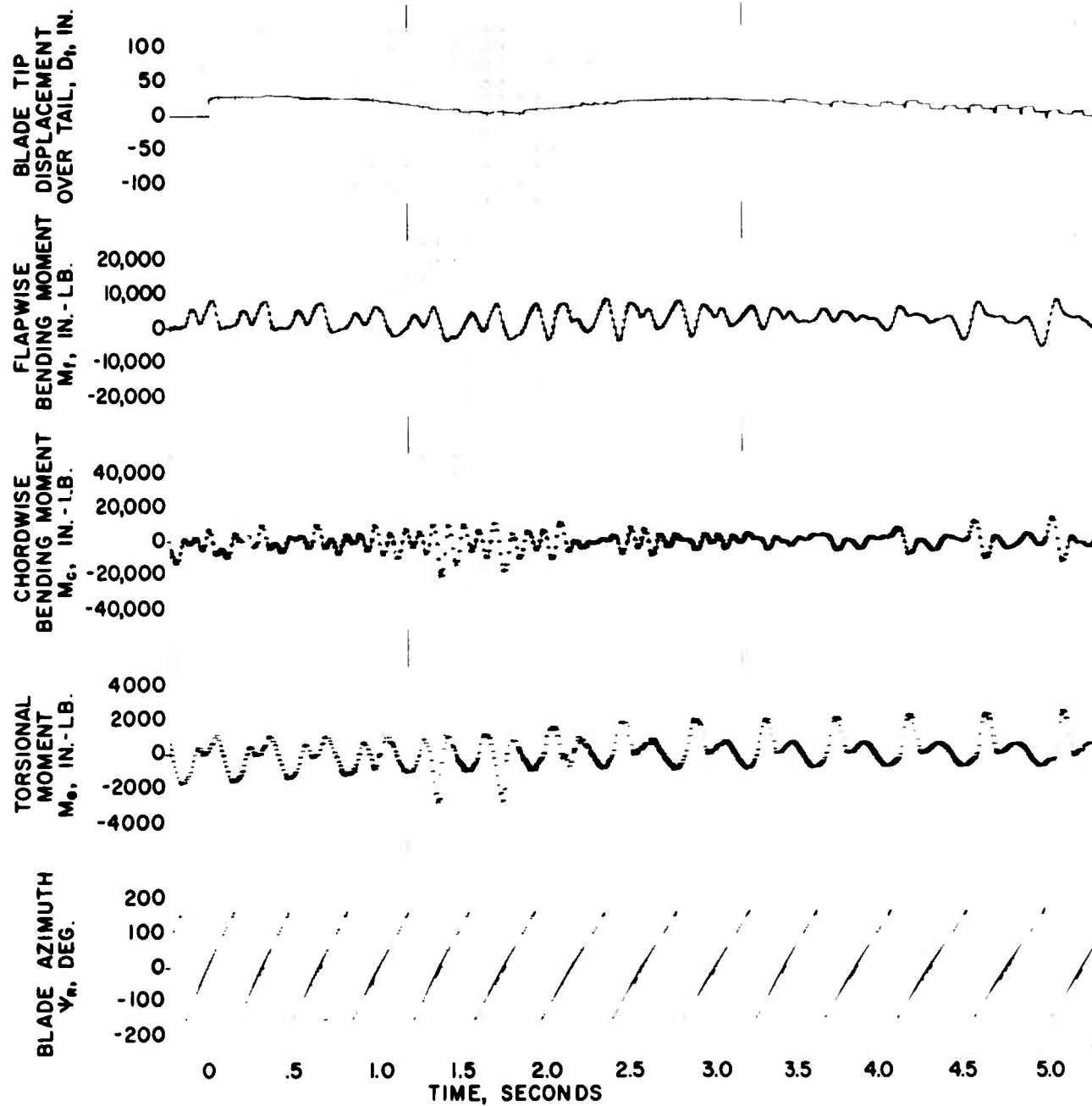


Figure 3. Concluded

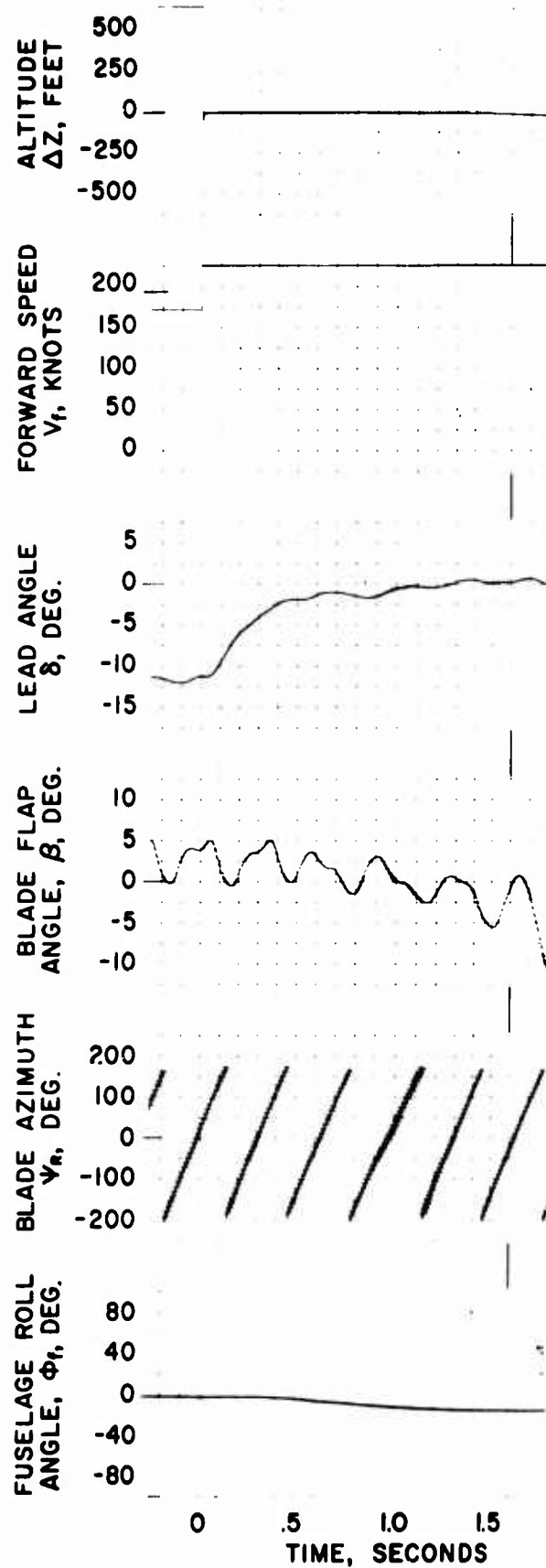


Figure 4. Fully Articulated Rotor ($e/R = 0.034$), Full Power Loss, $D/L = 0.15$, With Corrective Control Input 6B

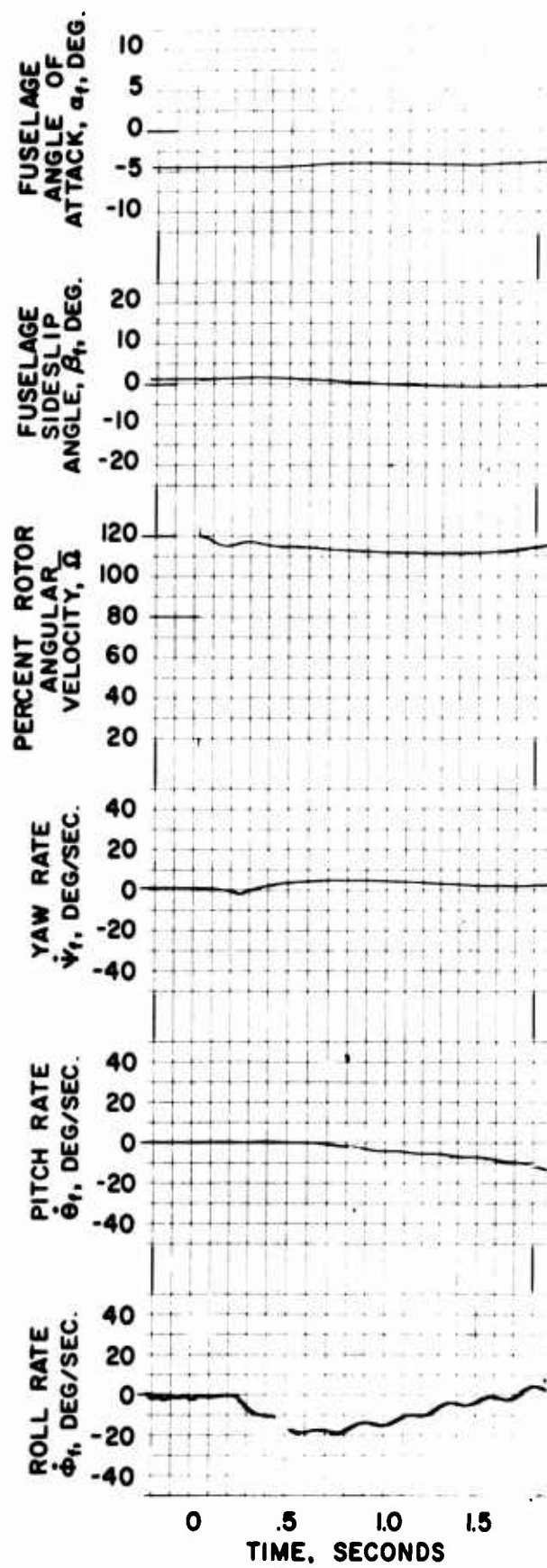


Figure 4. Continued

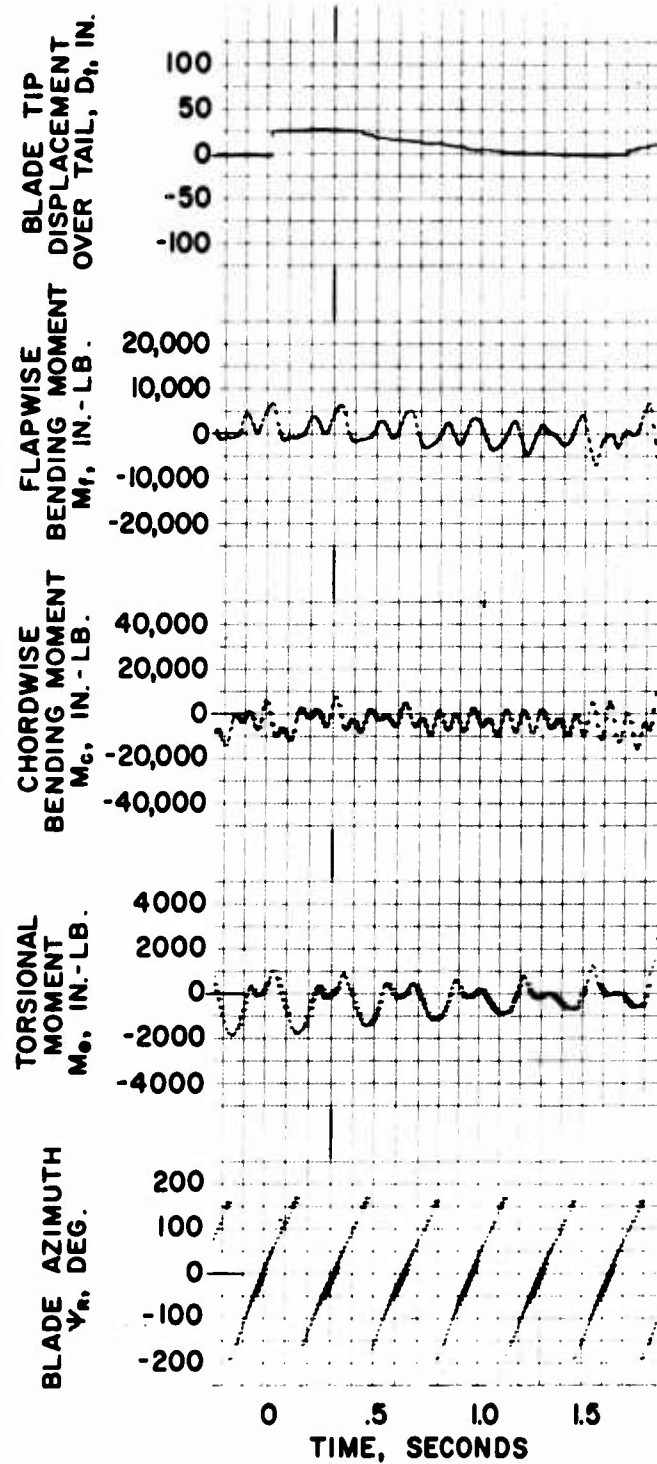


Figure 4. Concluded

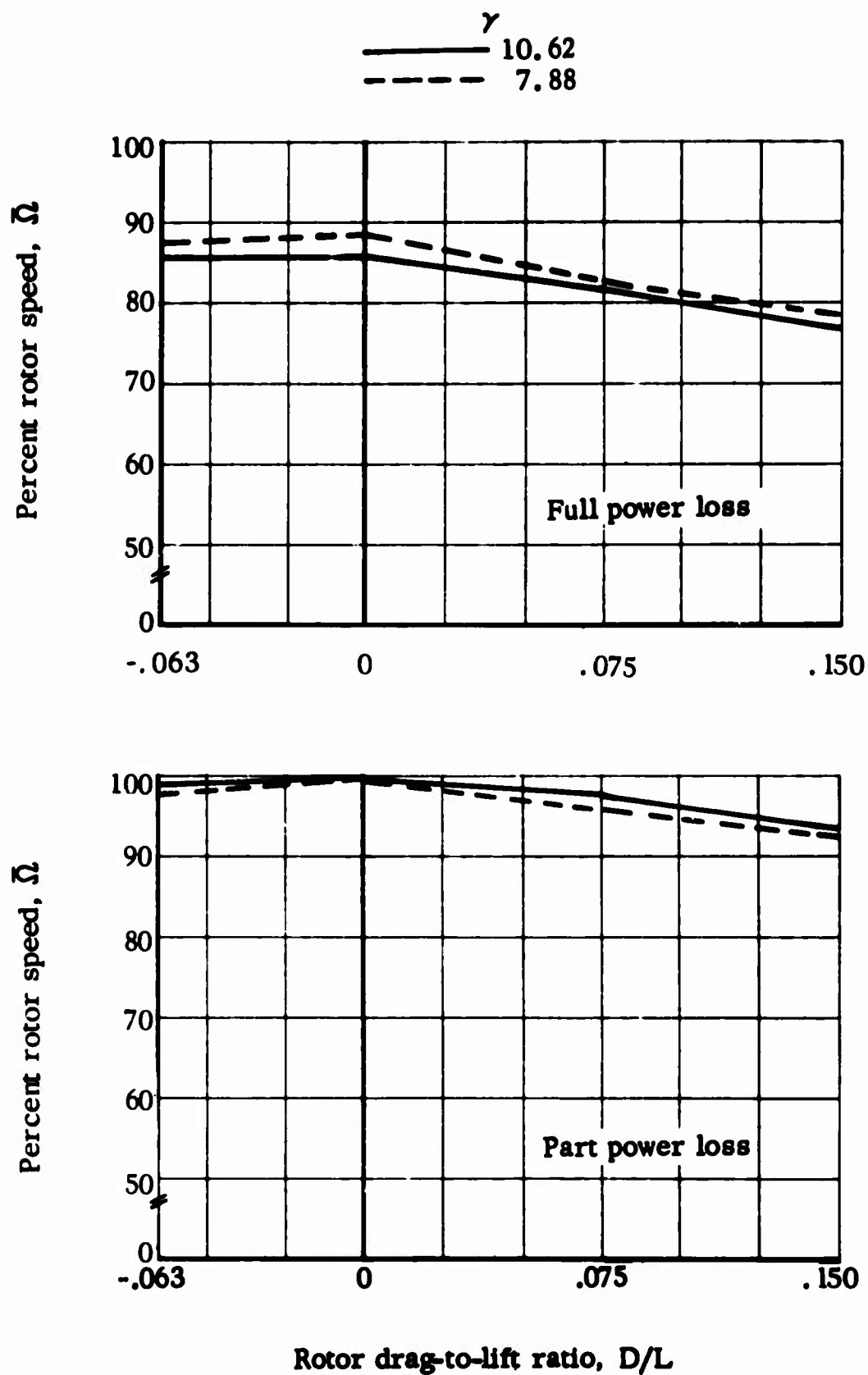


Figure 5. Effect of Lock Number on Rotor Speed
Two Seconds After Power Loss

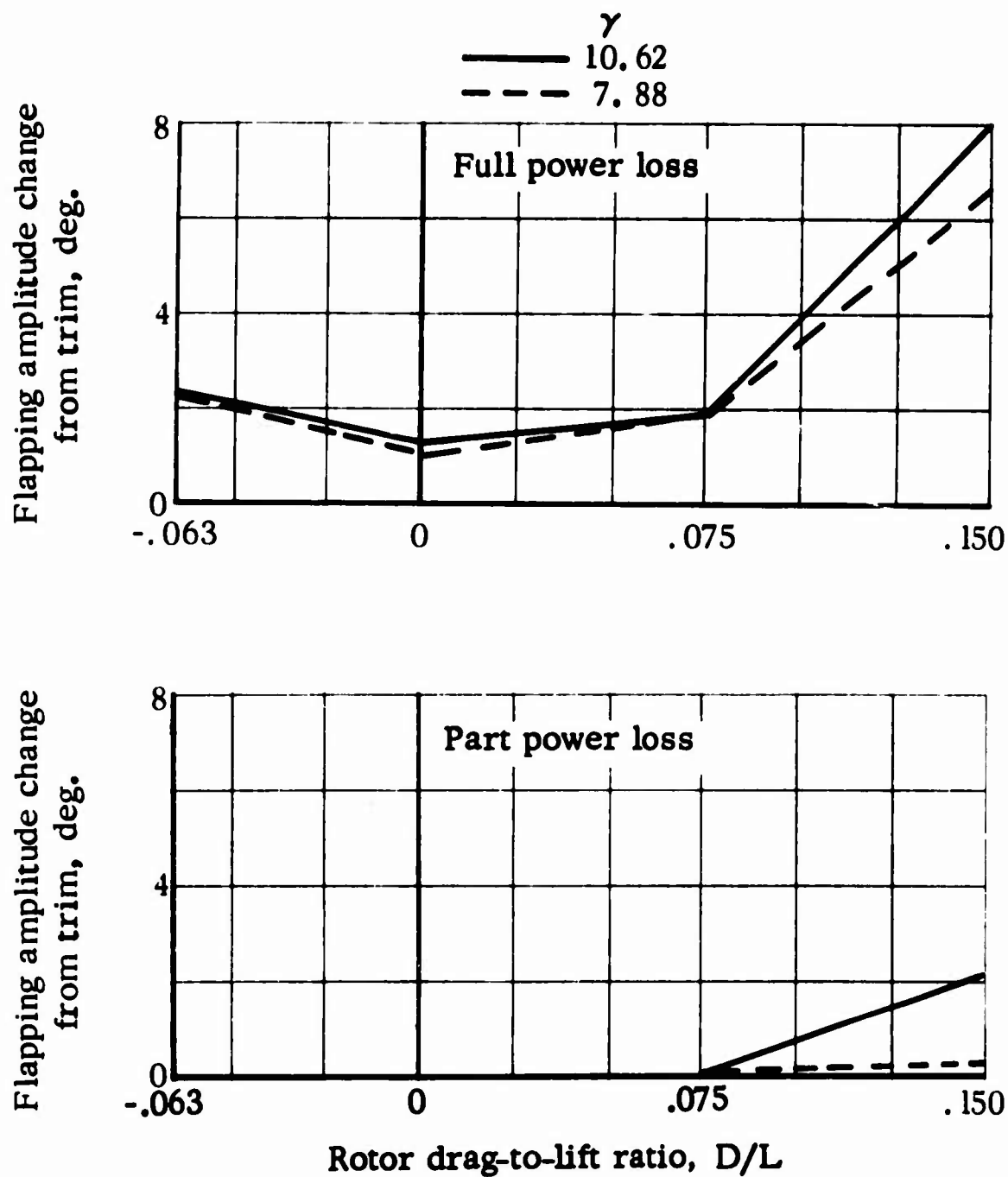


Figure 6. Effect of Lock Number on Flapping Disturbance Following Power Loss

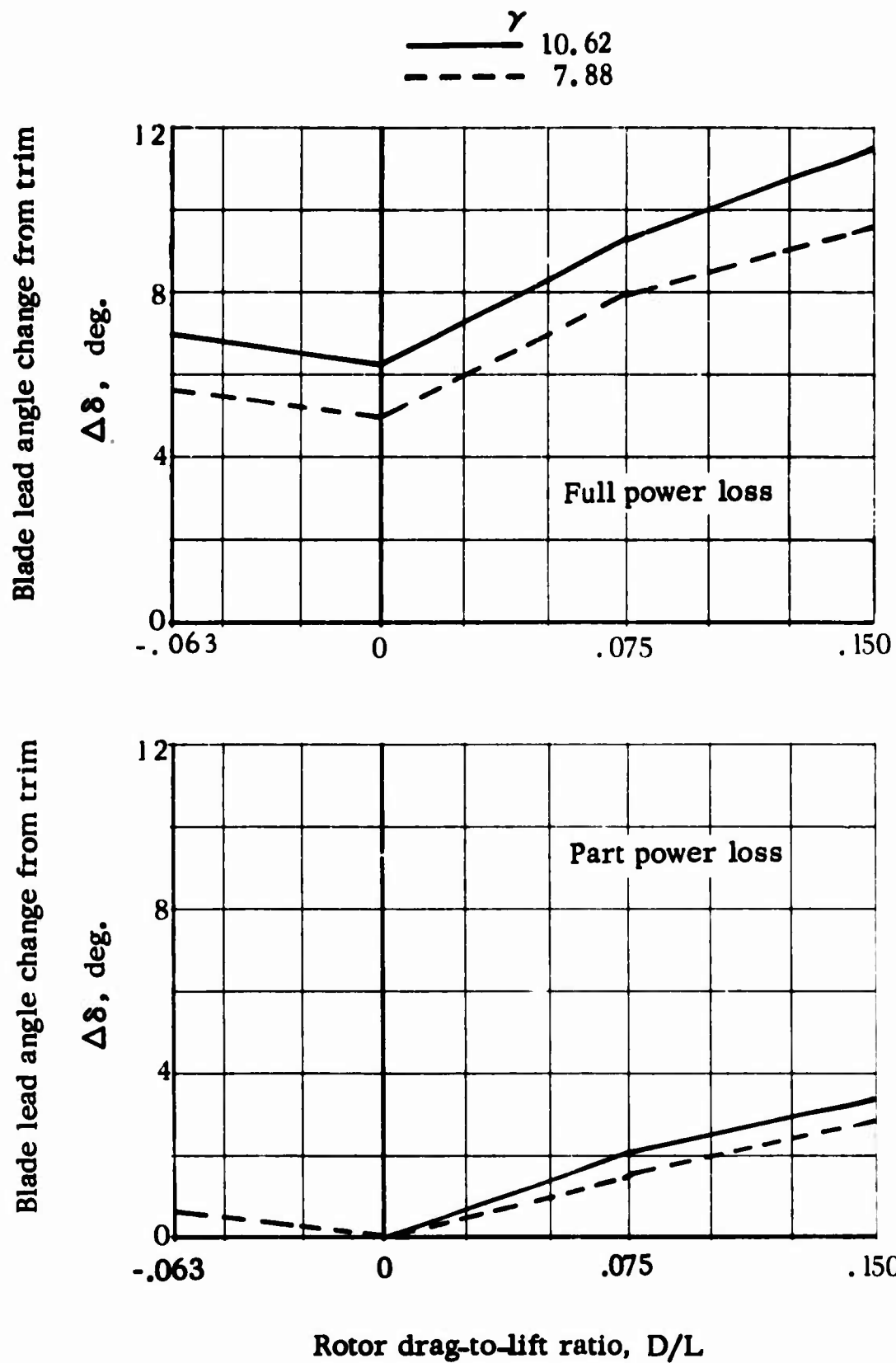


Figure 7. Effect of Lock Number on Blade Lead-Lag Motion Following Power Loss

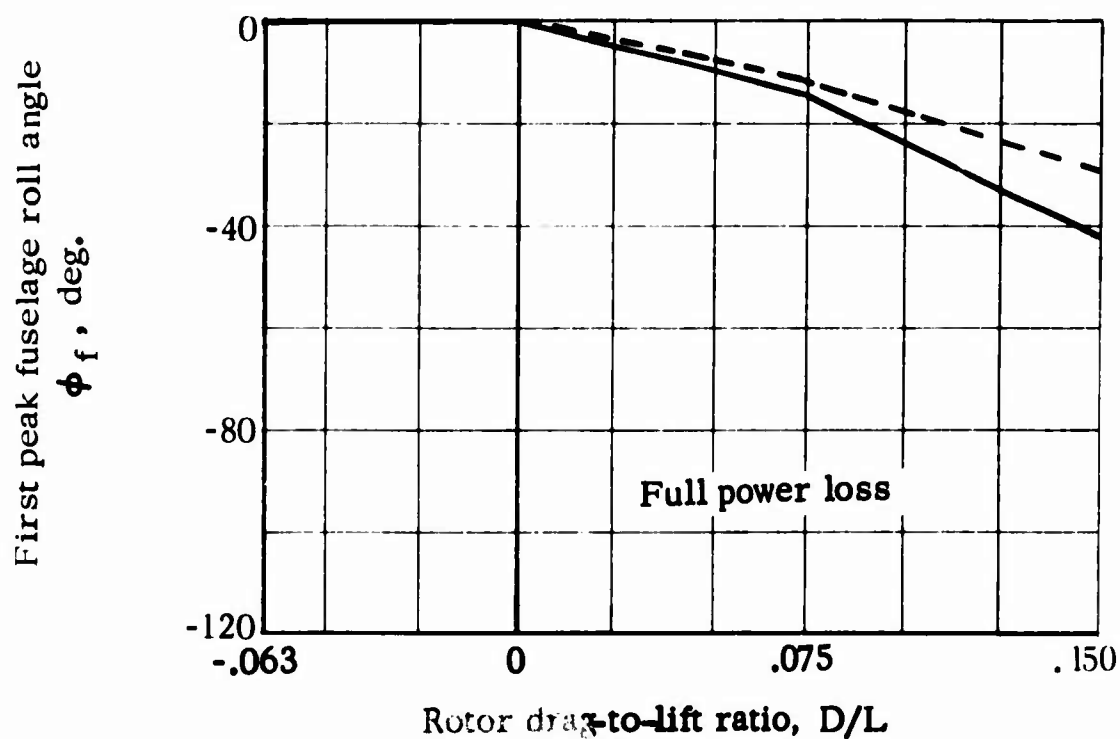
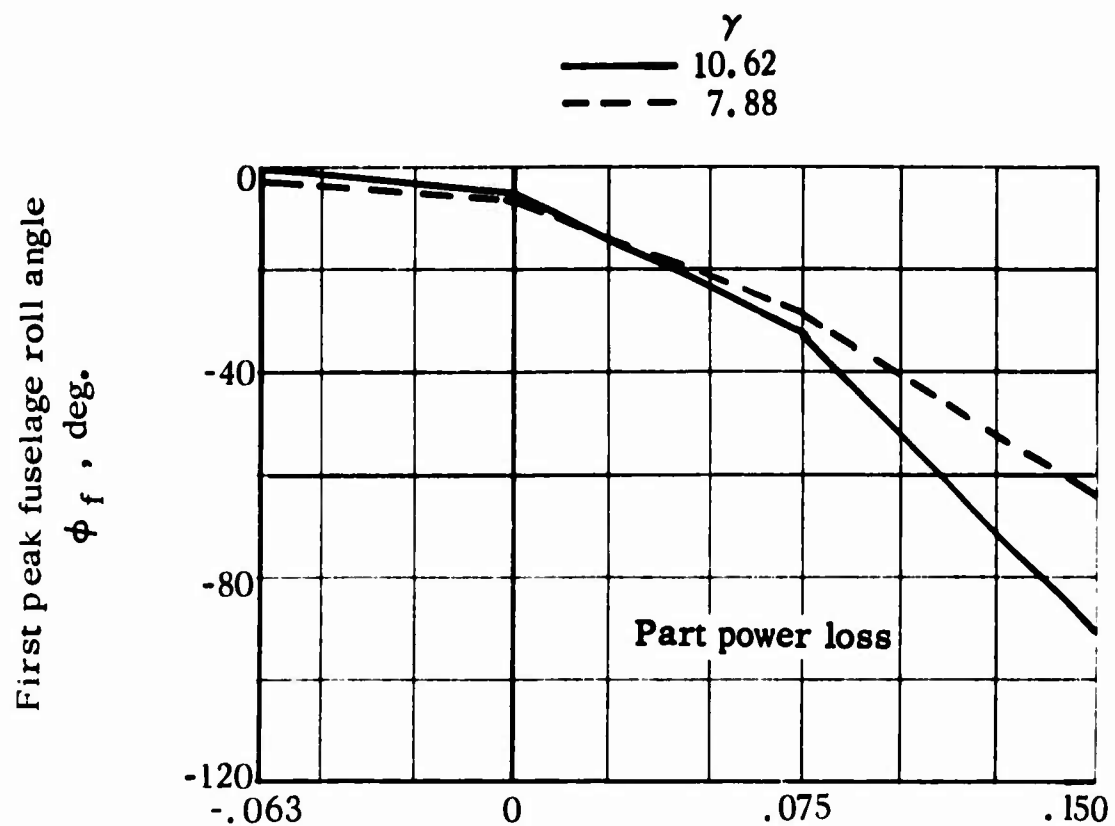


Figure 8. Effect of Lock Number on the First Peak Roll Following Power Loss

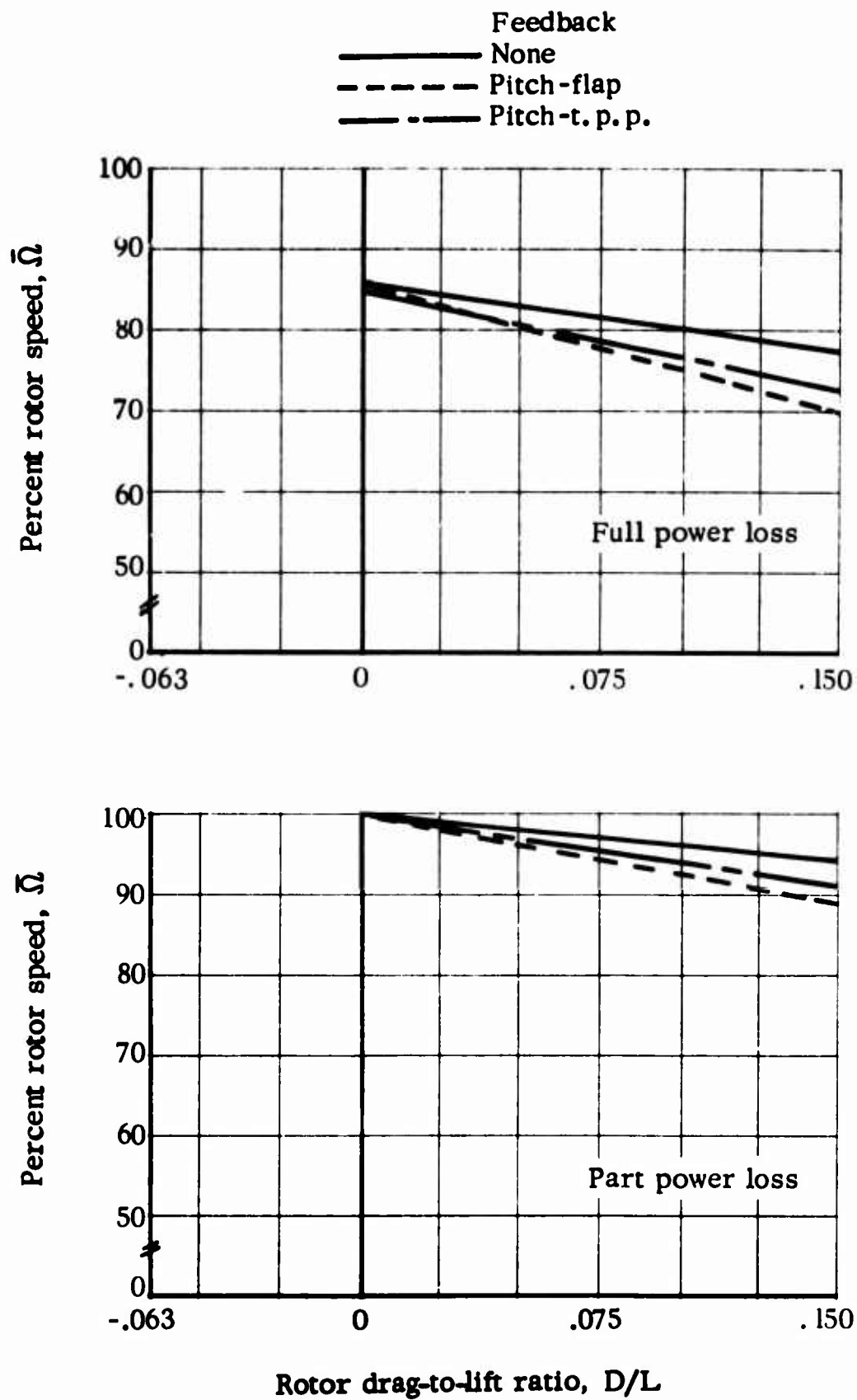


Figure 9. Effect of Pitch-Blade Motion Feedback on Rotor Speed Two Seconds After Power Loss

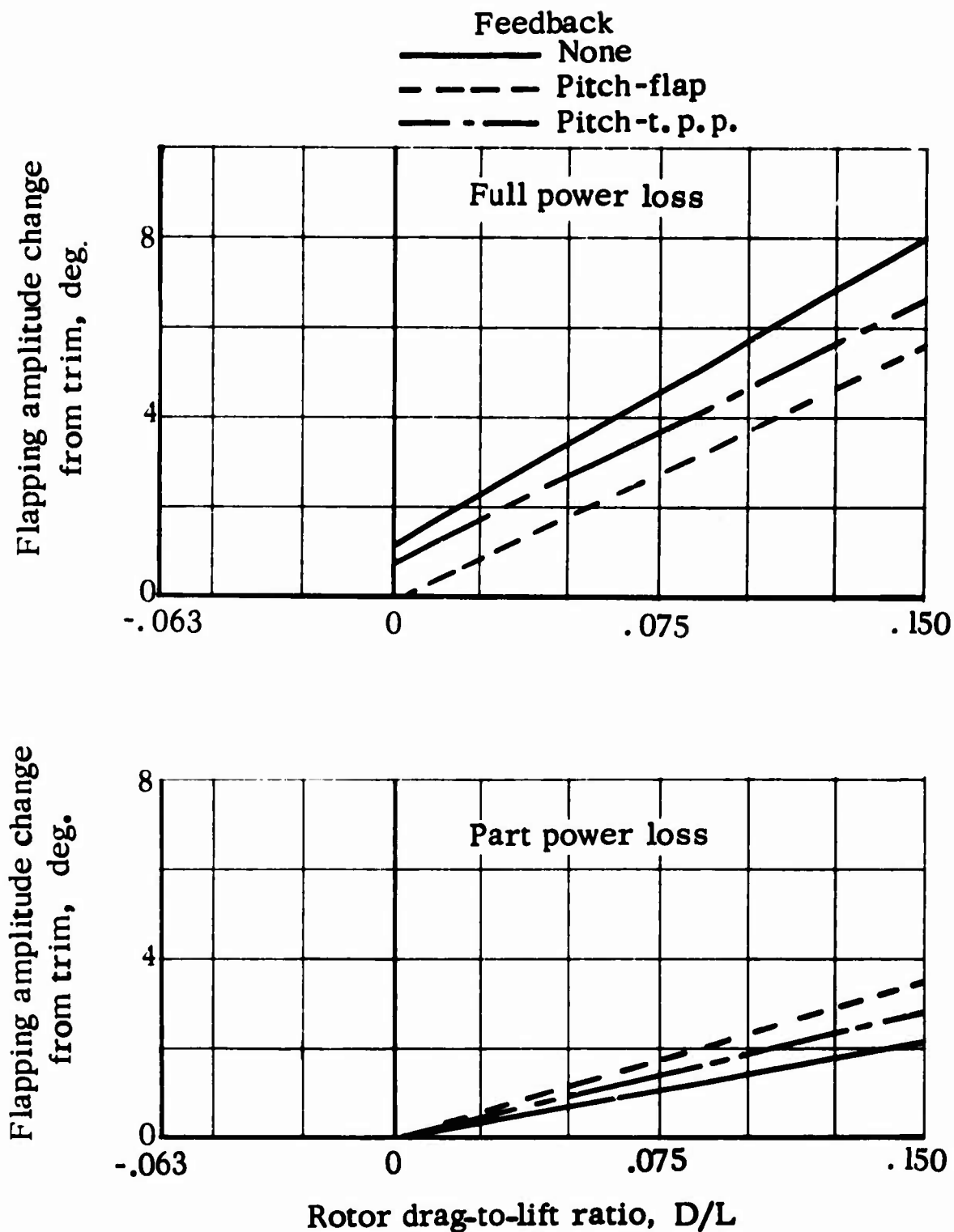


Figure 10. Effect of Pitch-Blade Motion Feedback on Flapping Disturbance Following Power Loss

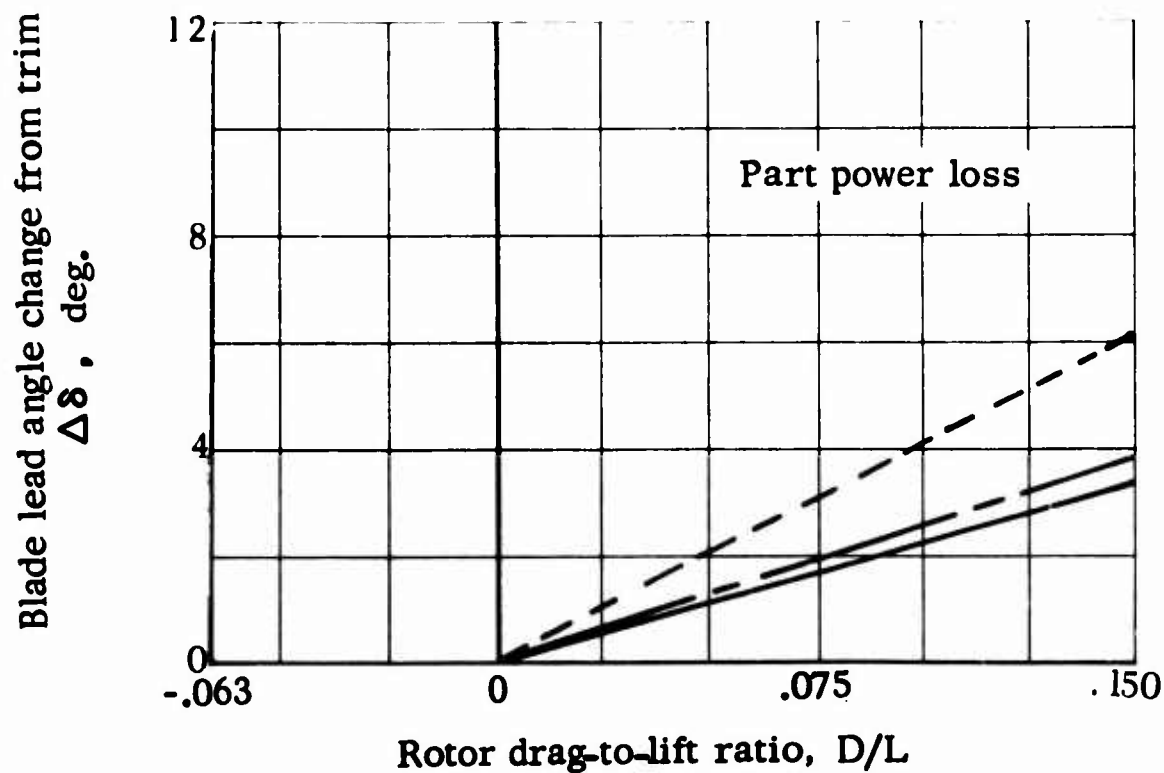
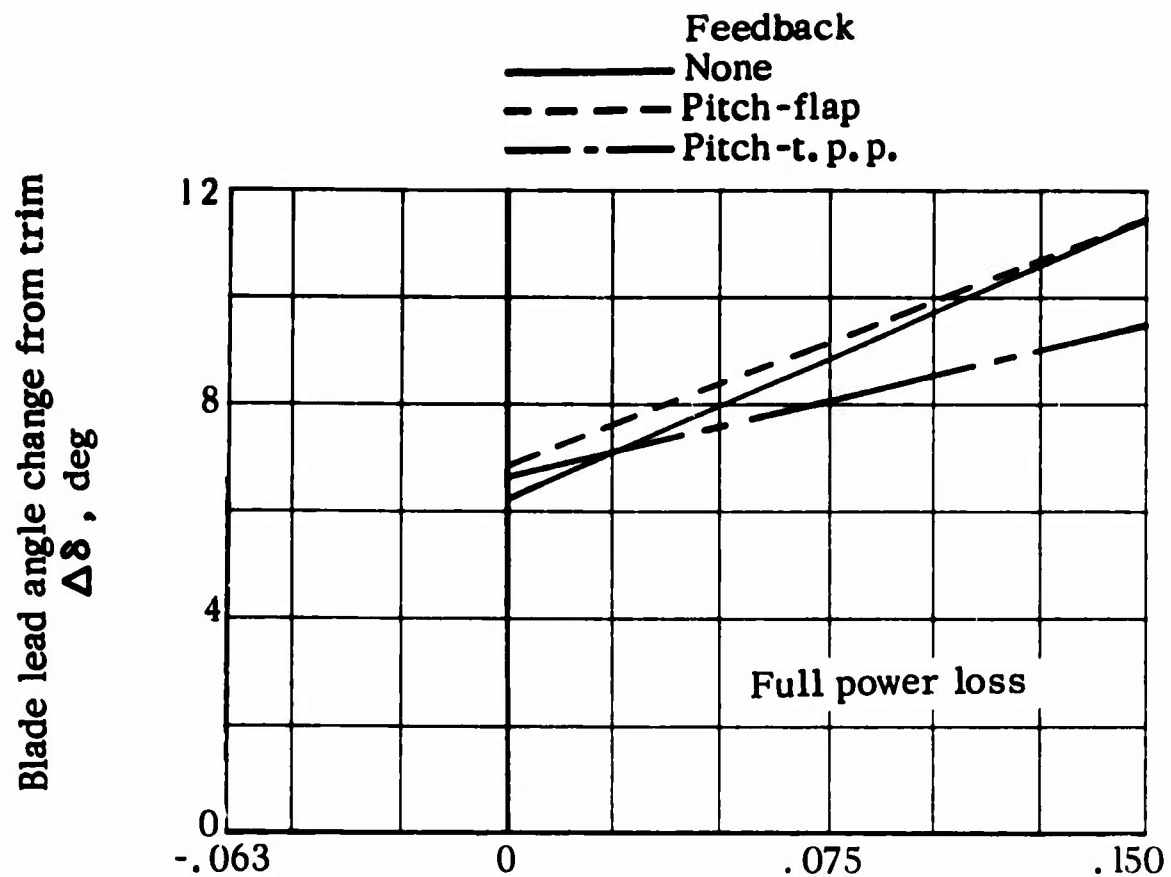


Figure 11. Effect of Pitch-Blade Motion Feedback on Blade Lead-Lag Motion Following Power Loss

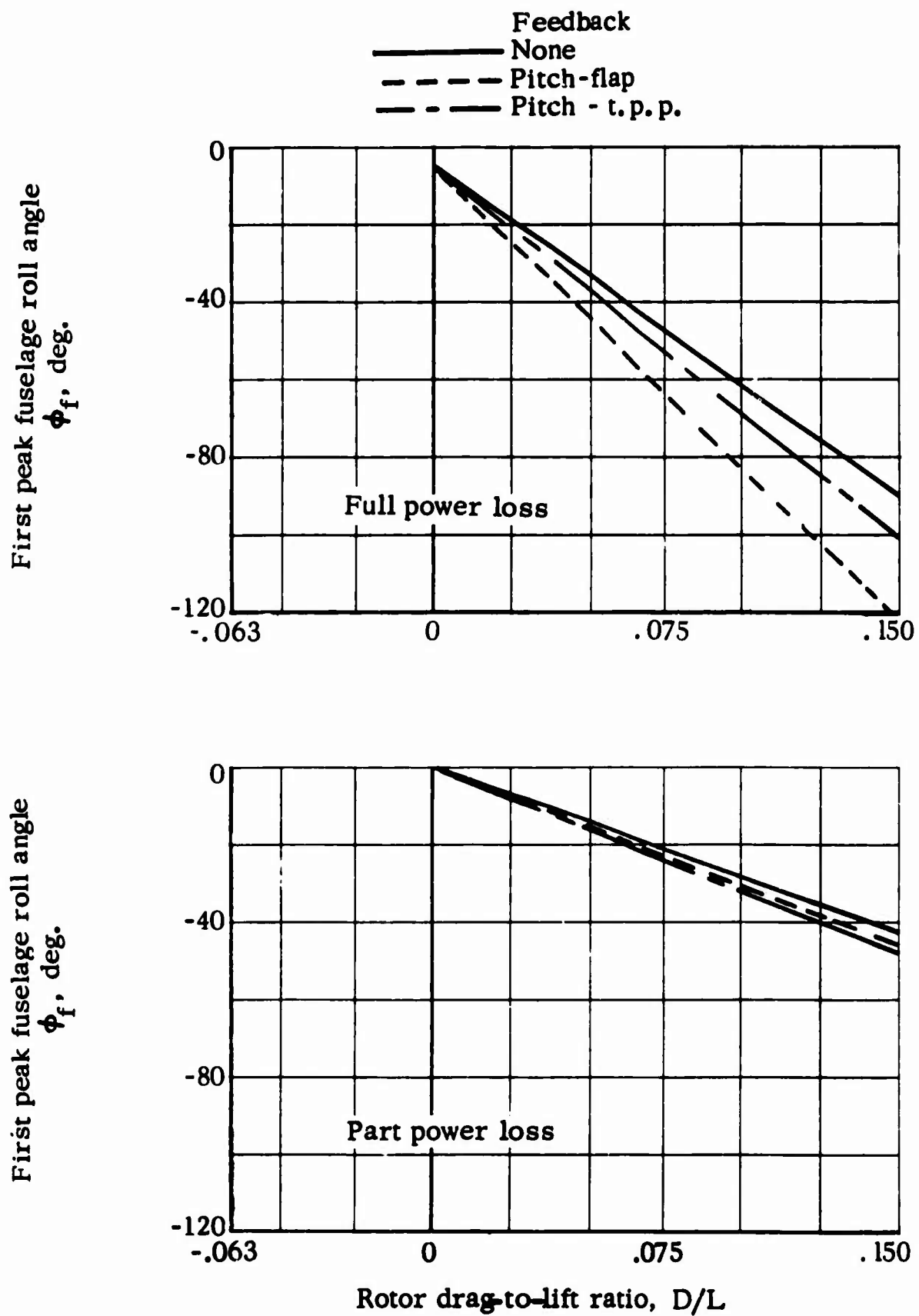


Figure 12. Effect of Pitch-Blade Motion Feedback on the First Peak Roll Angle Following Power Loss

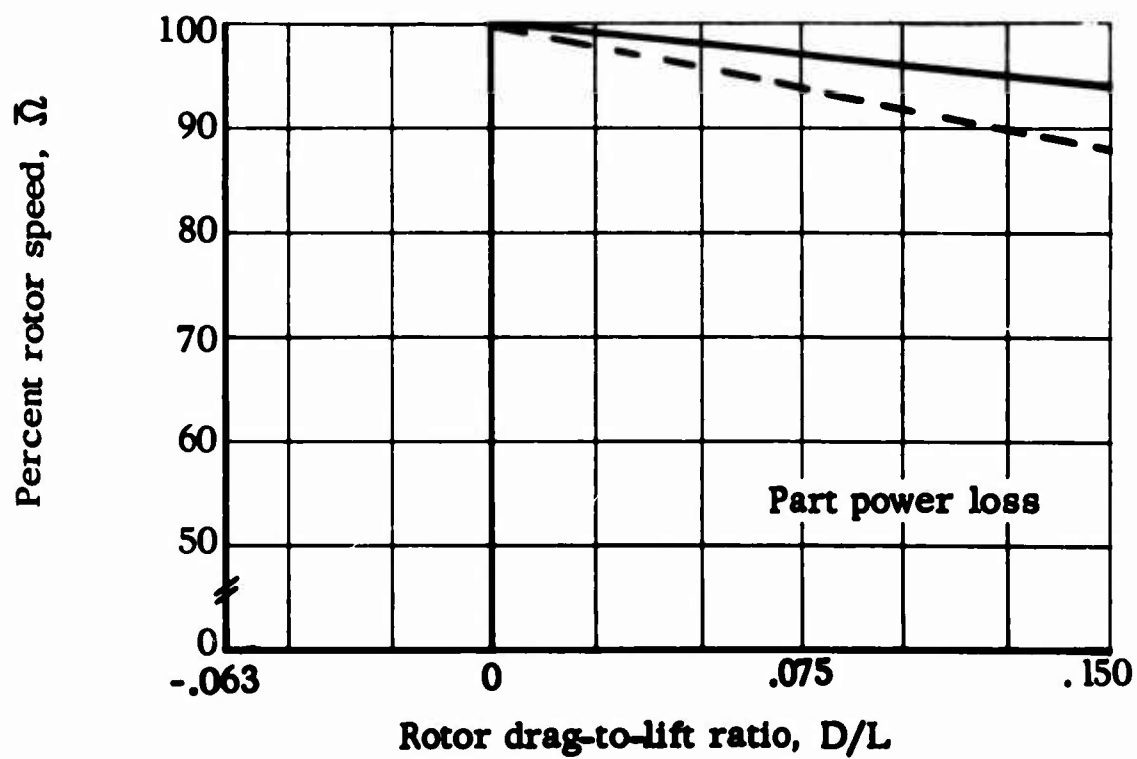
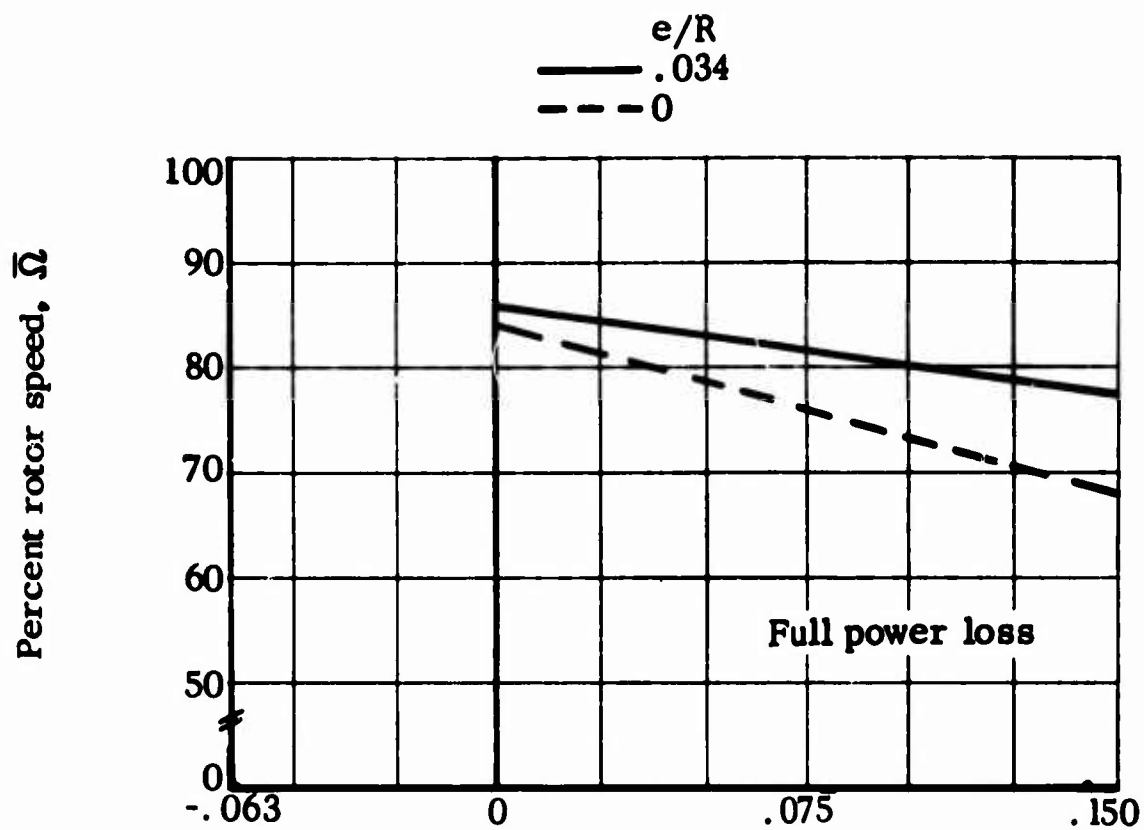


Figure 13. Effect of Flapping Hinge Offset on Rotor Speed
Two Seconds After Power Loss

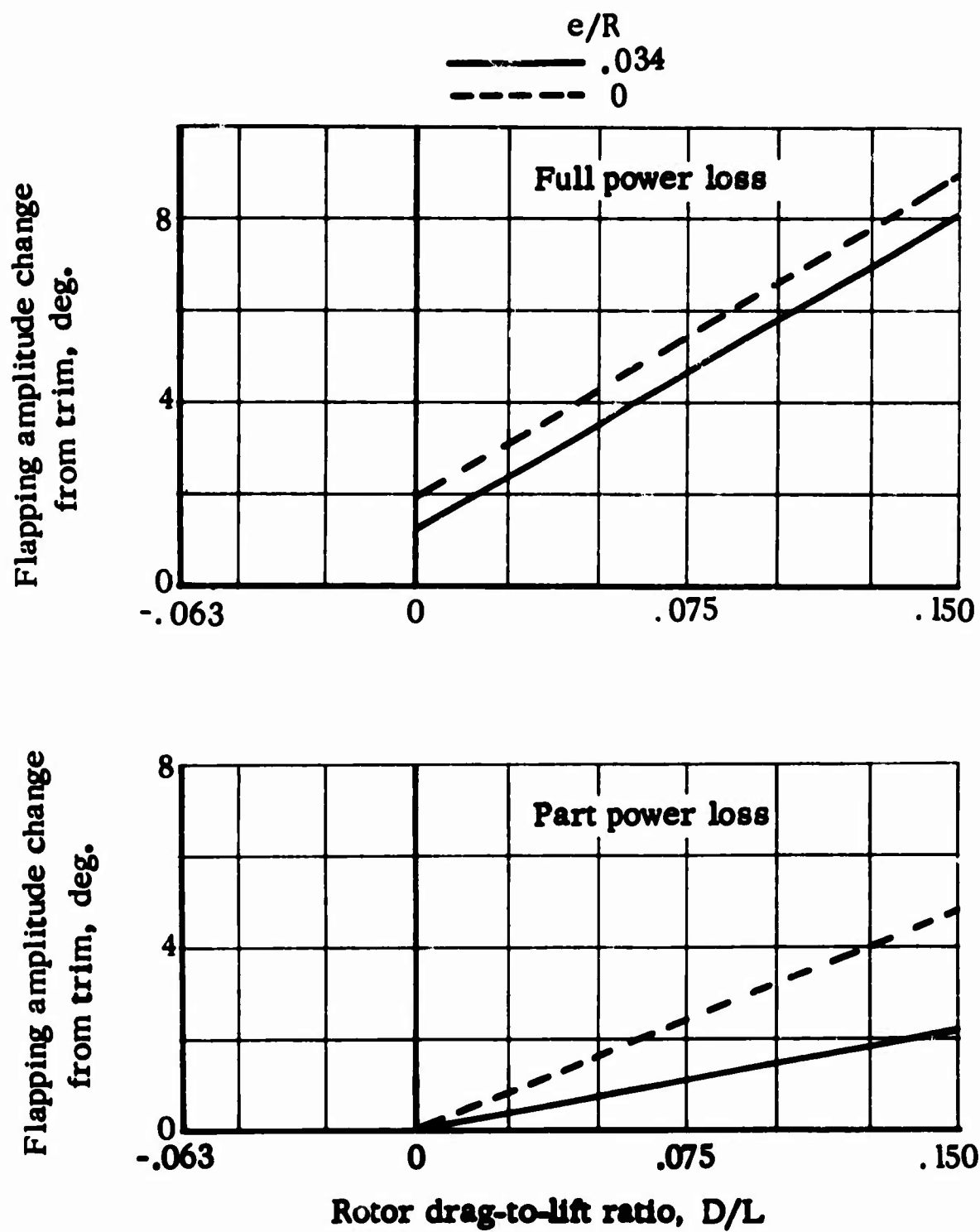


Figure 14. Effect of Flapping Hinge Offset on Flapping Disturbance Following Power Loss

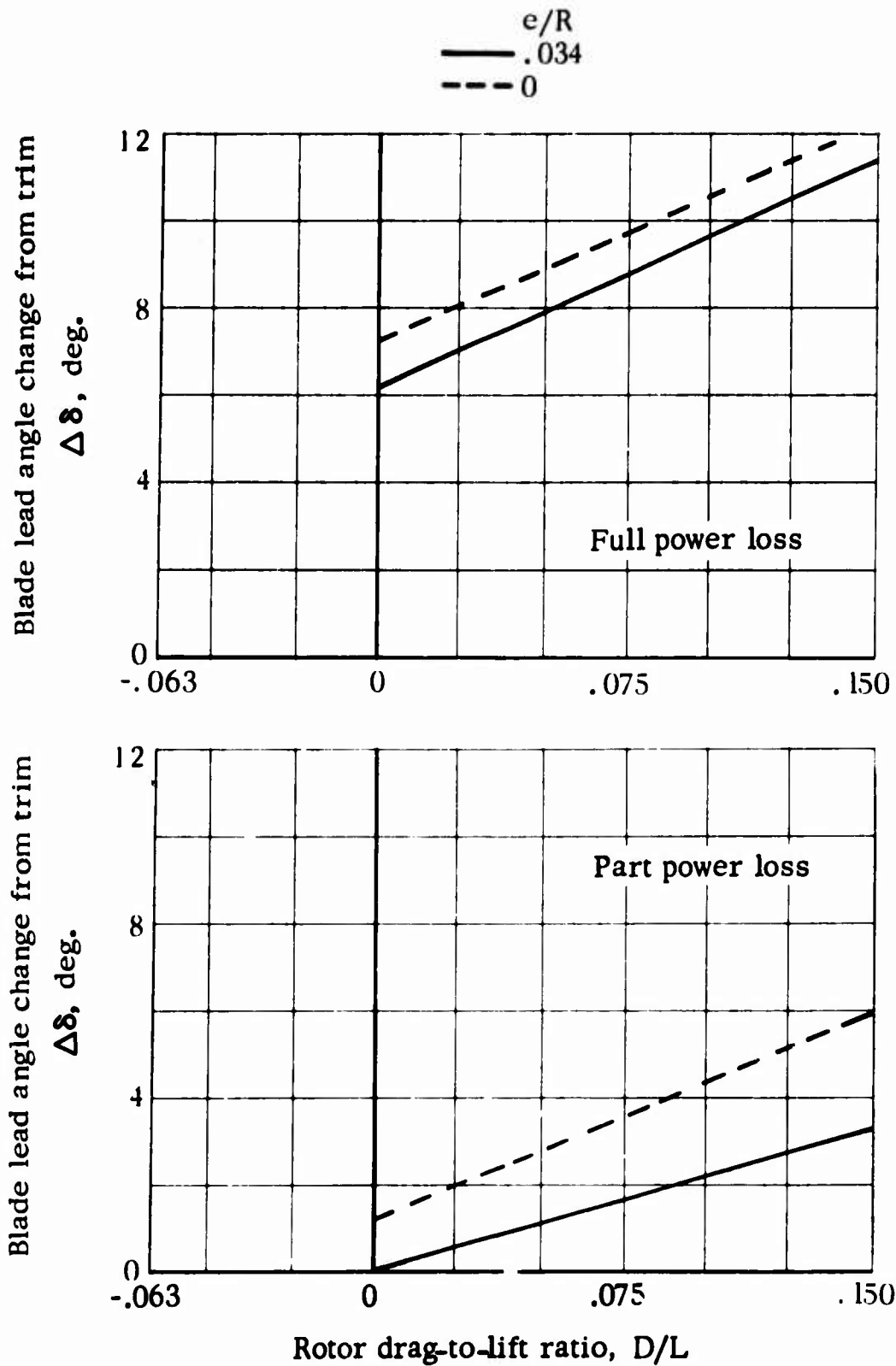


Figure 15. Effect of Flapping Hinge Offset on Blade Lead-Lag Motion Following Power Loss

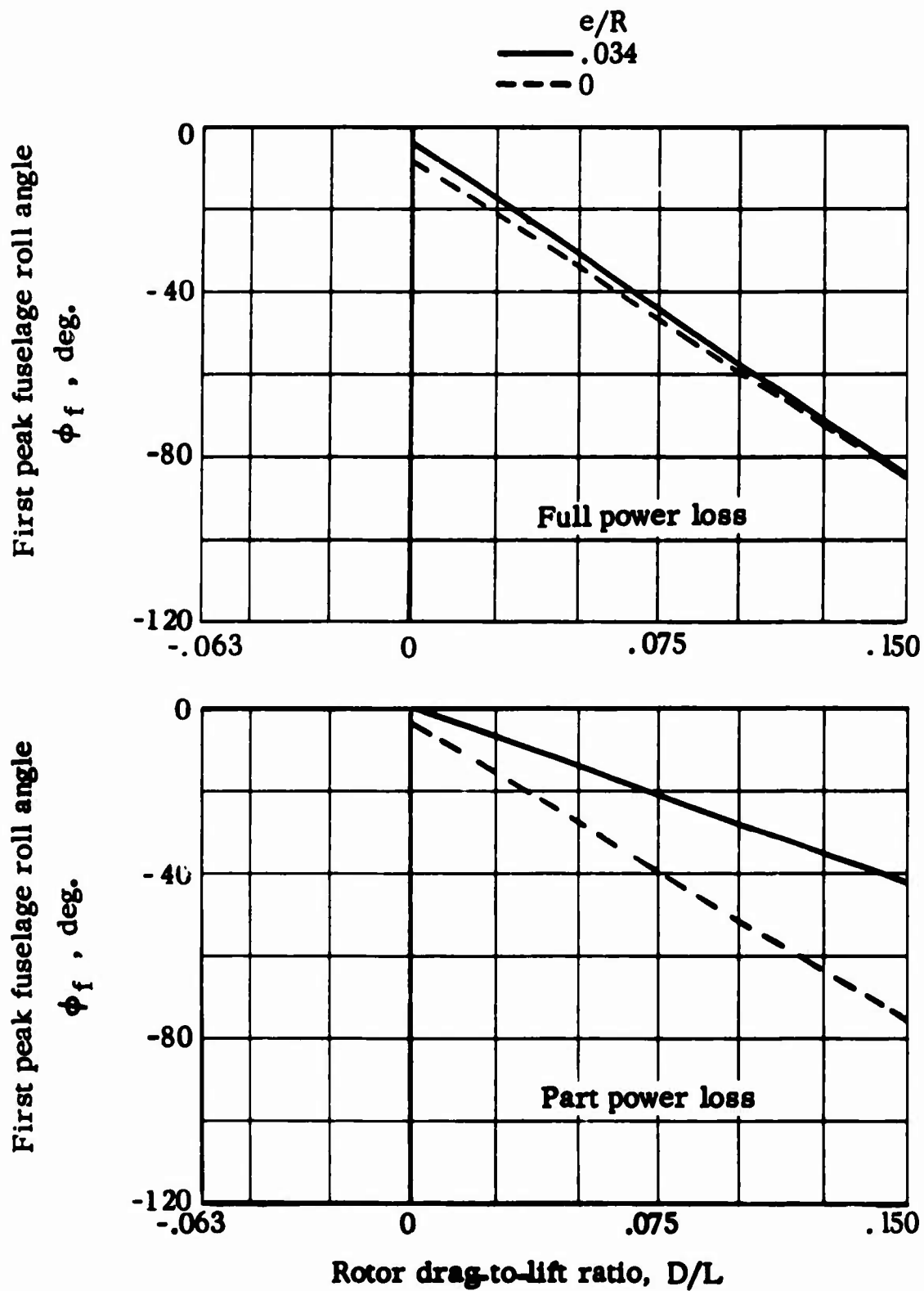


Figure 16. Effect of Flapping Hinge Offset on the First Peak Roll Angle Following Power Loss

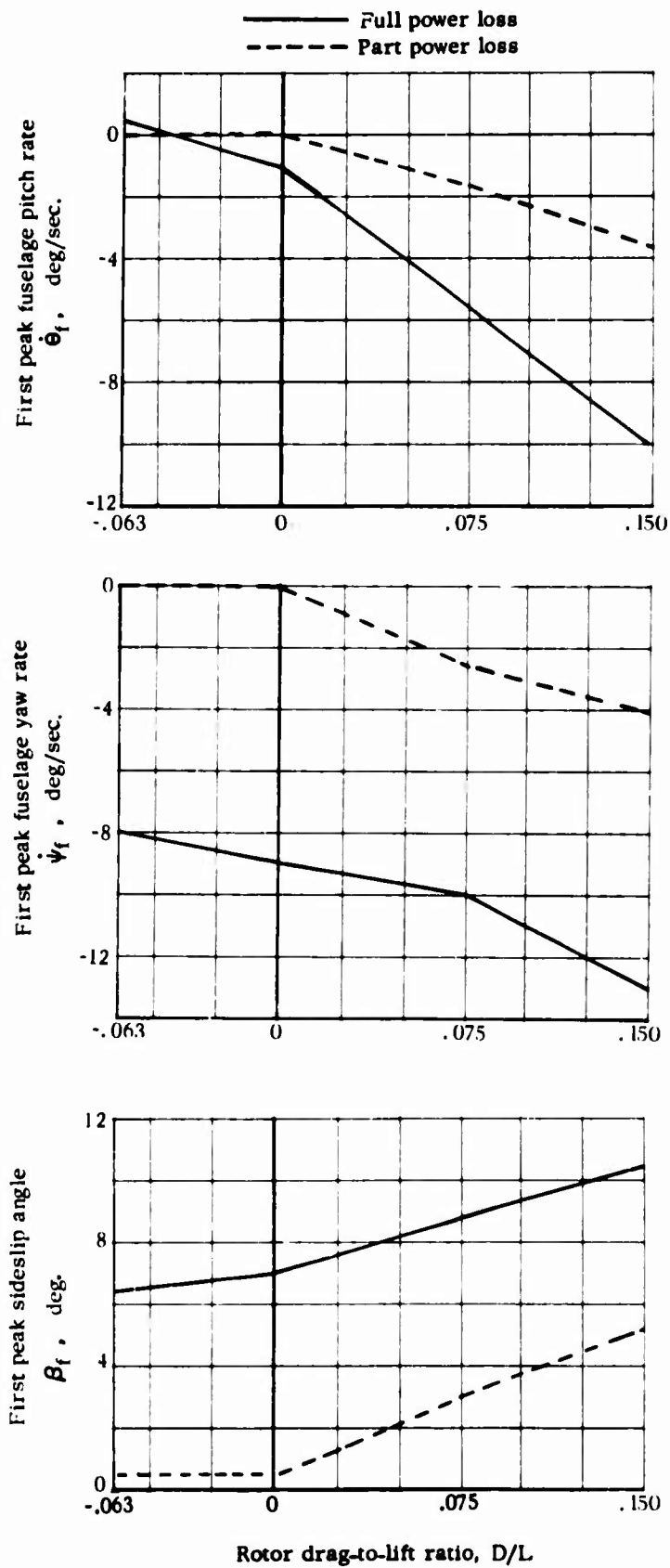


Figure 17. Aircraft Disturbance Following Power Loss, All Configurations

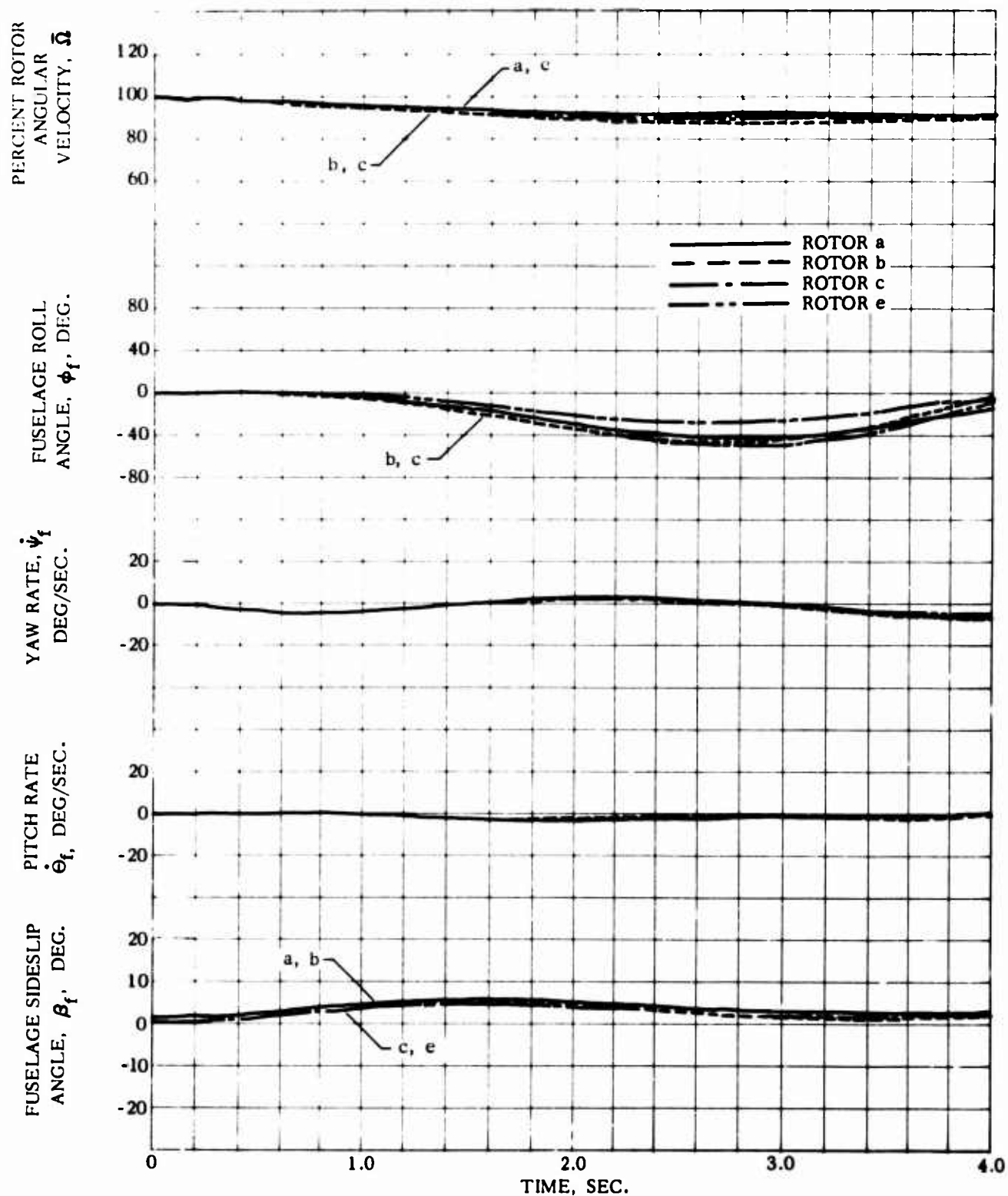


Figure 18. Helicopter and Rotor Blade Motion Following Part Power Loss, $D/L = 0.15$, No Corrective Control Inputs, Various Rotor Configurations

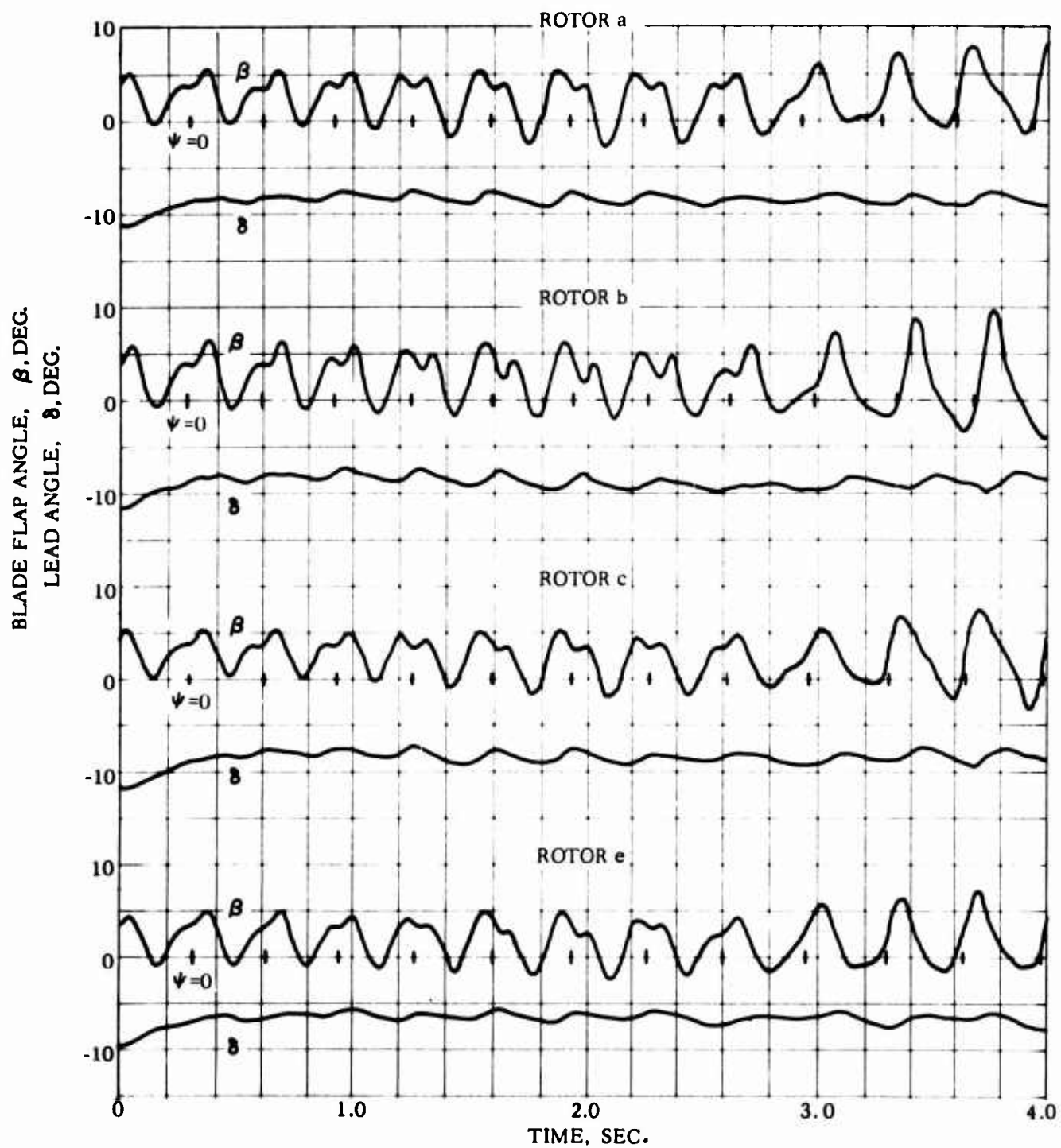


Figure 18. Concluded

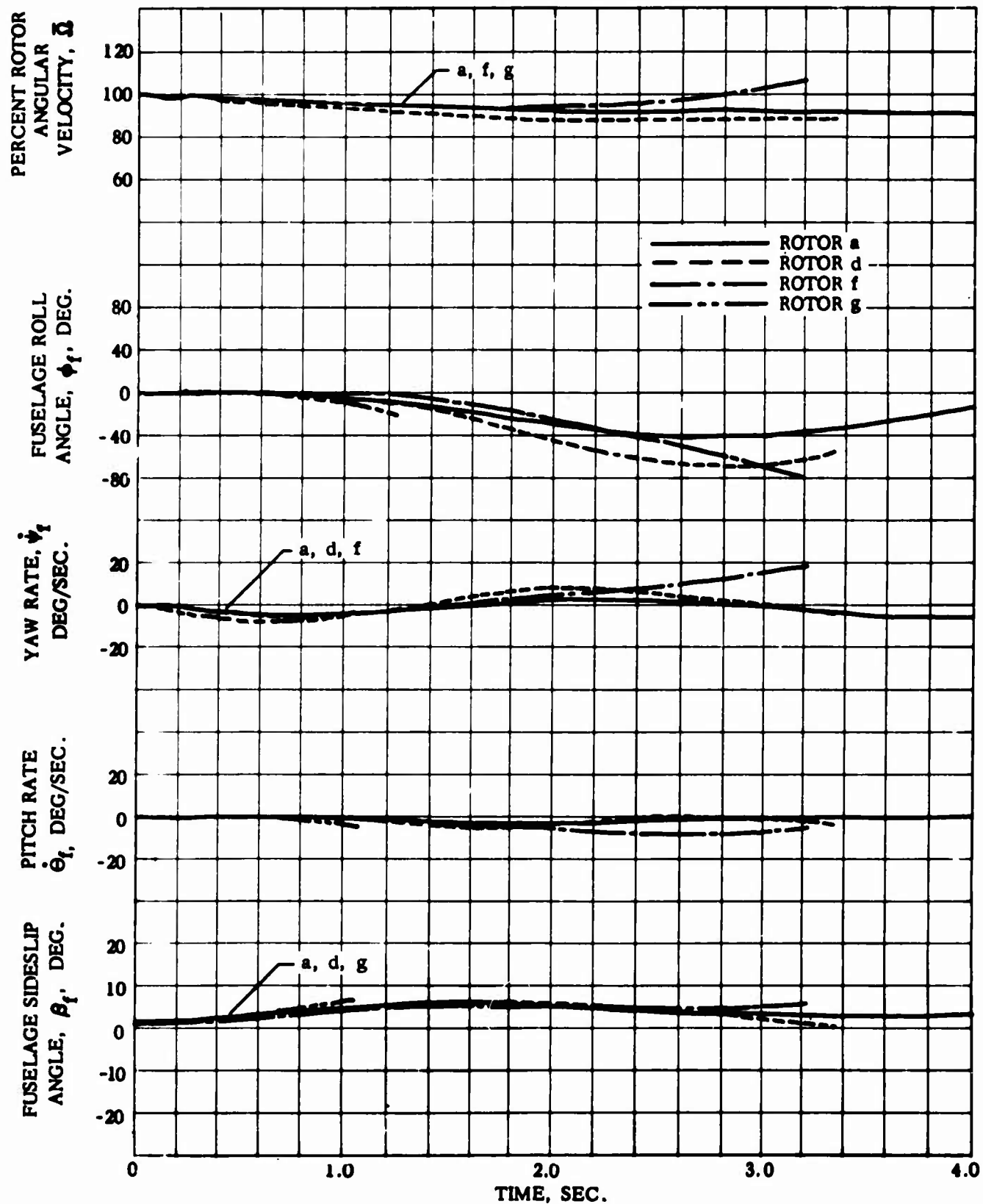


Figure 19. Helicopter and Rotor Blade Motion Following Part Power Loss, $D/L = 0.15$, No Corrective Control Inputs, Various Rotor Configurations

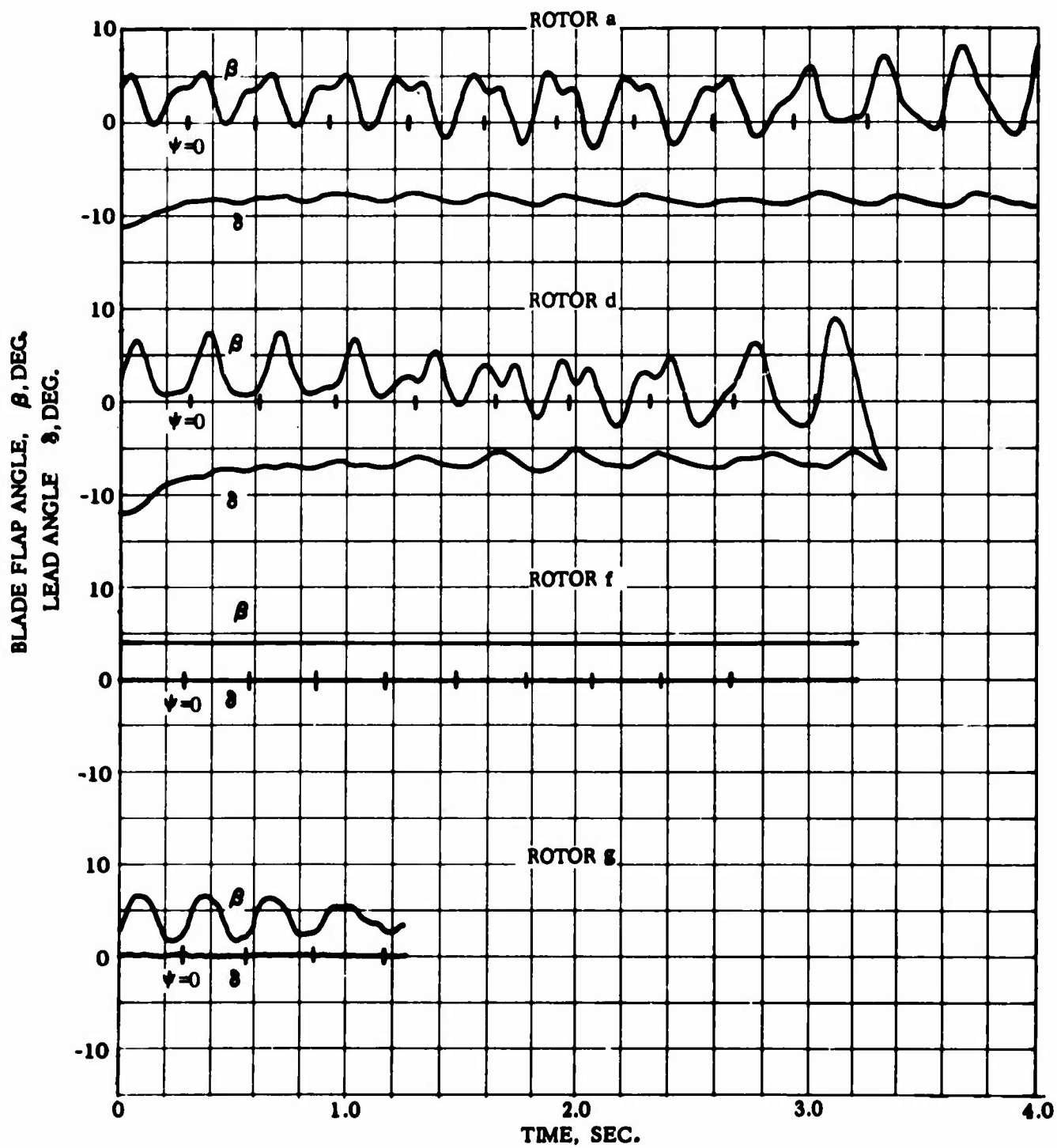


Figure 19. Concluded

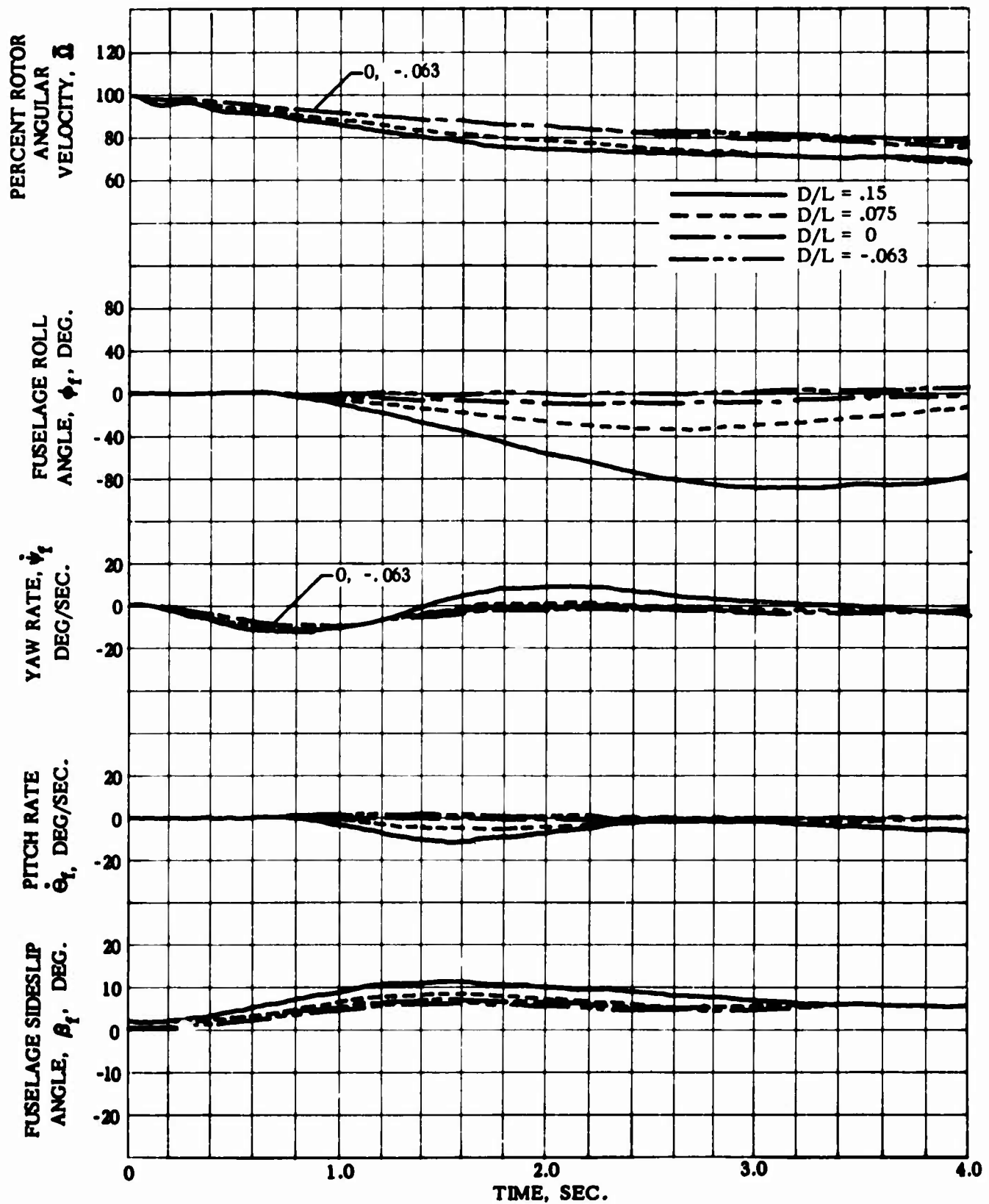


Figure 20. Helicopter and Rotor Blade Motion Following Full Power Loss, No Corrective Control Inputs, Fully Articulated Rotor ($e/R = 0.034$)

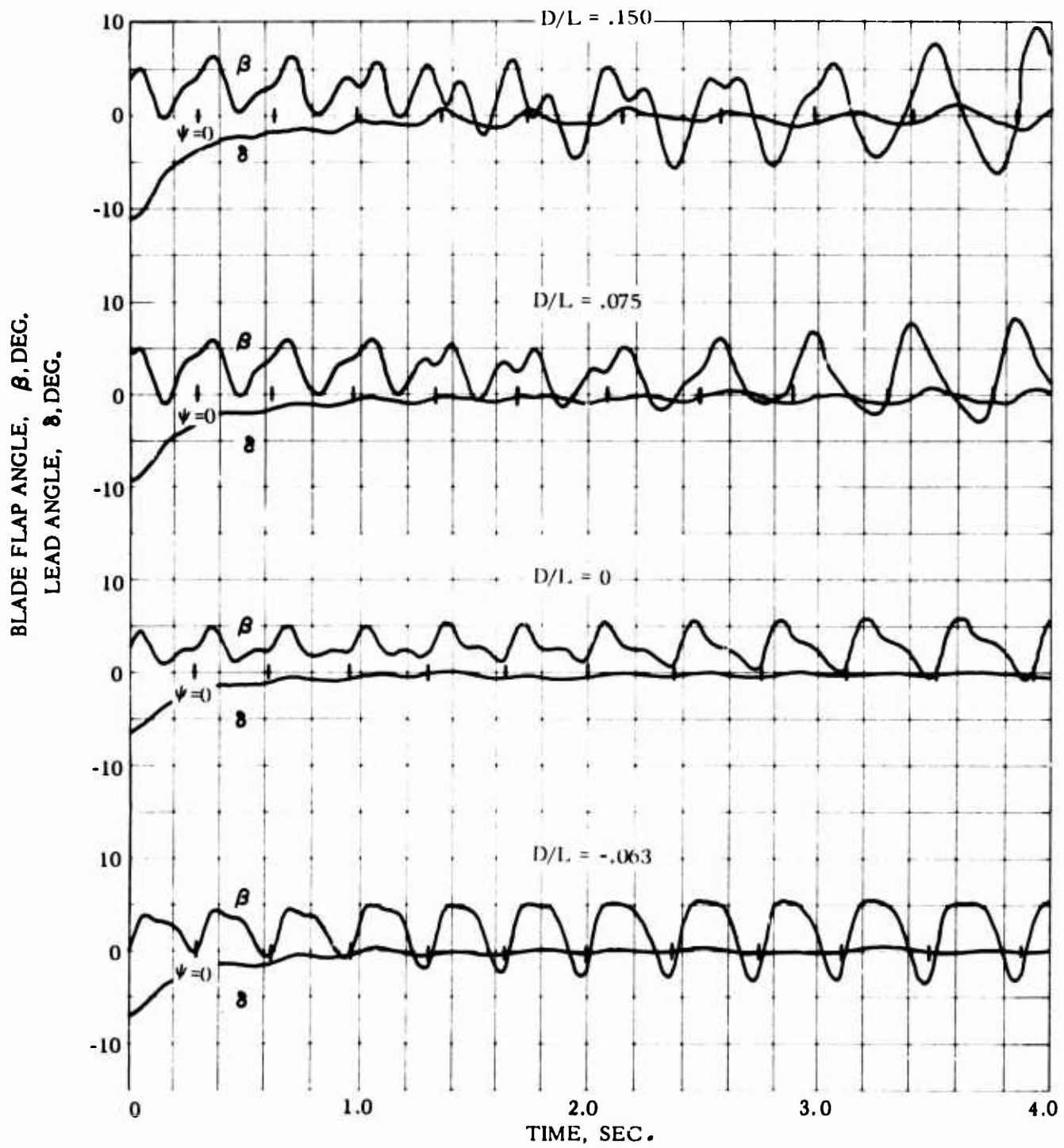


Figure 20. Concluded

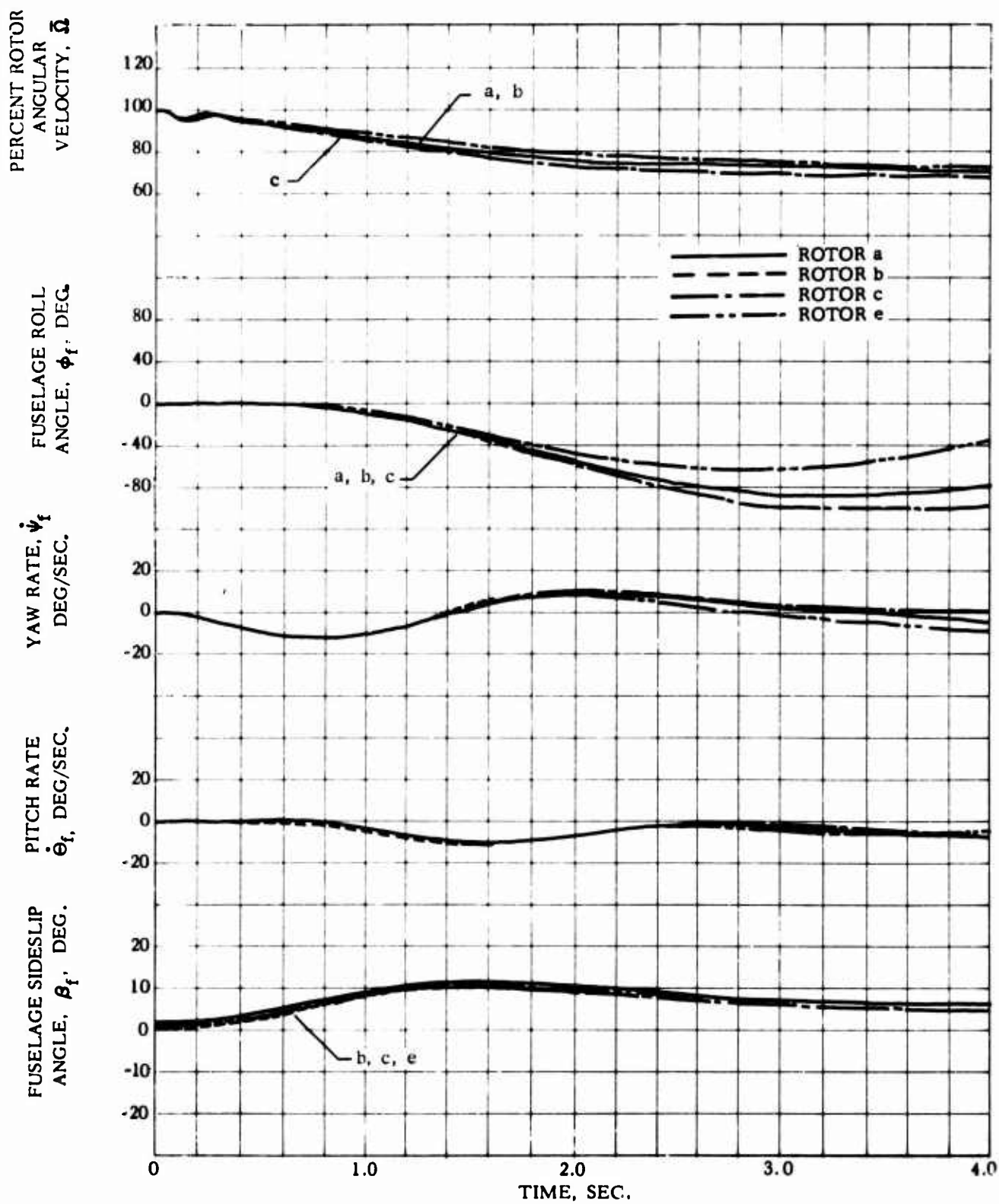


Figure 21. Helicopter and Rotor Blade Motion Following Full Power Loss, $D/L = 0.15$, No Corrective Control Inputs, Various Rotor Configurations

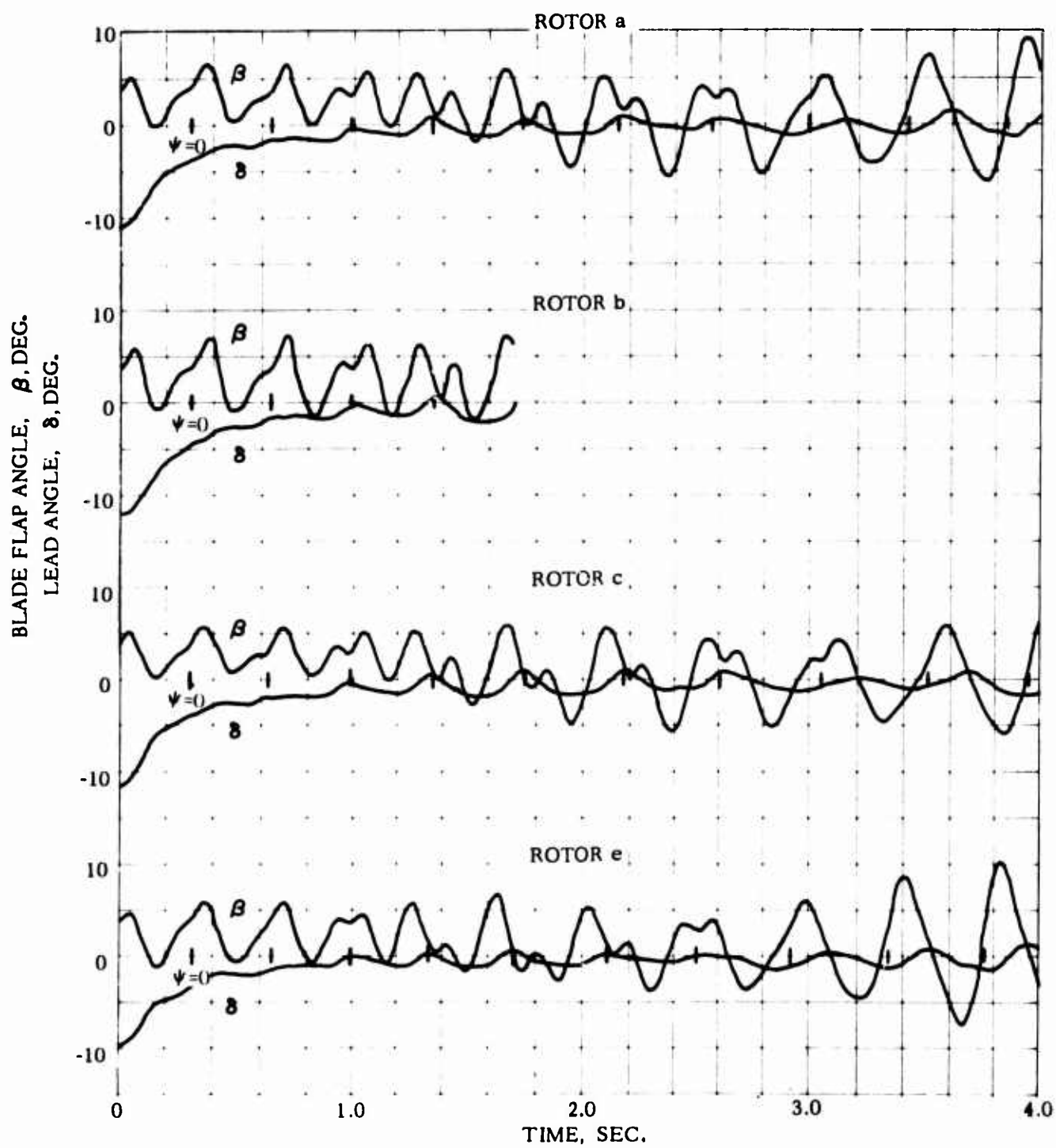


Figure 21. Concluded

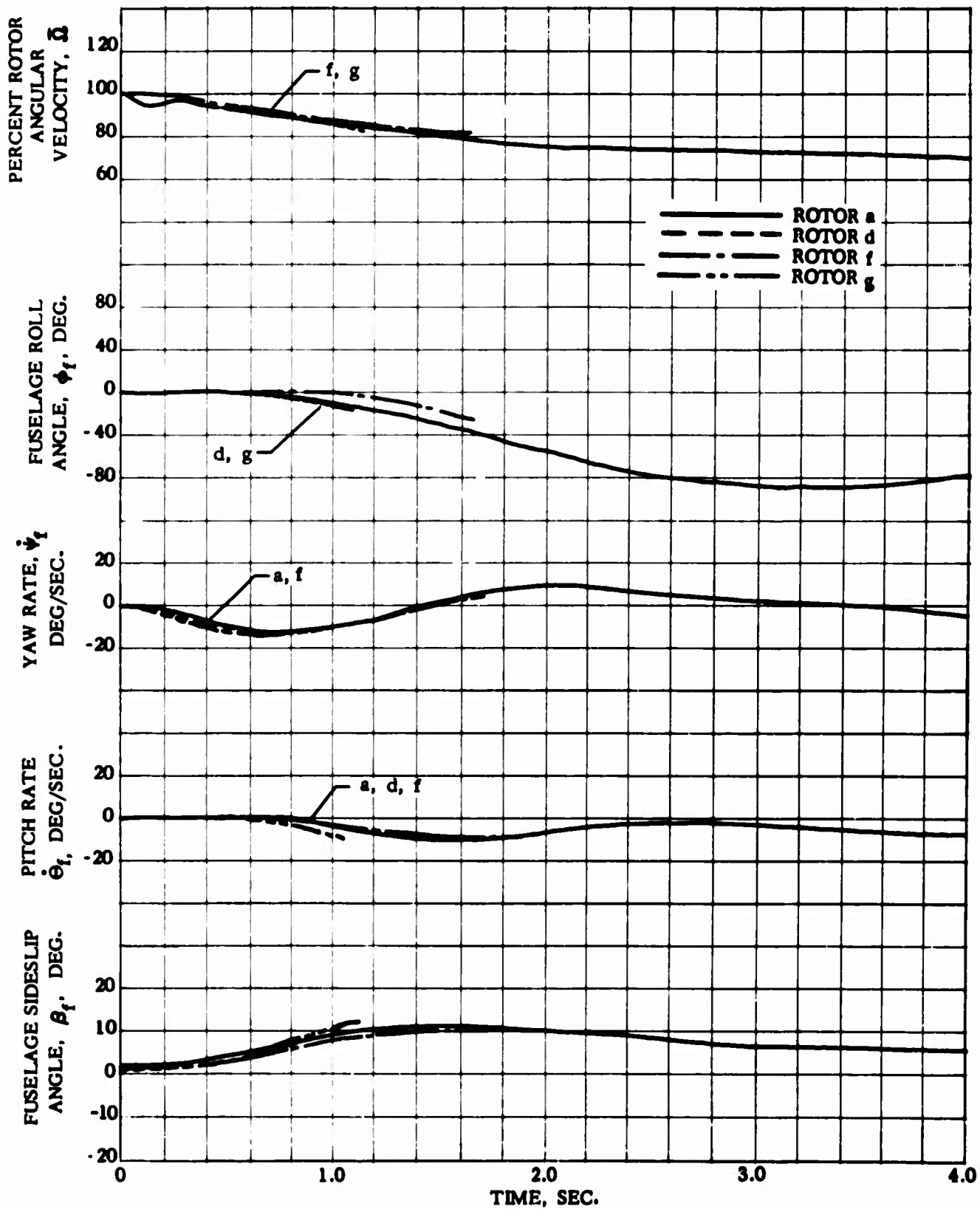


Figure 22. Helicopter and Rotor Blade Motion Following Full Power Loss, $D/L = 0.15$, No Corrective Control Inputs, Various Rotor Configurations

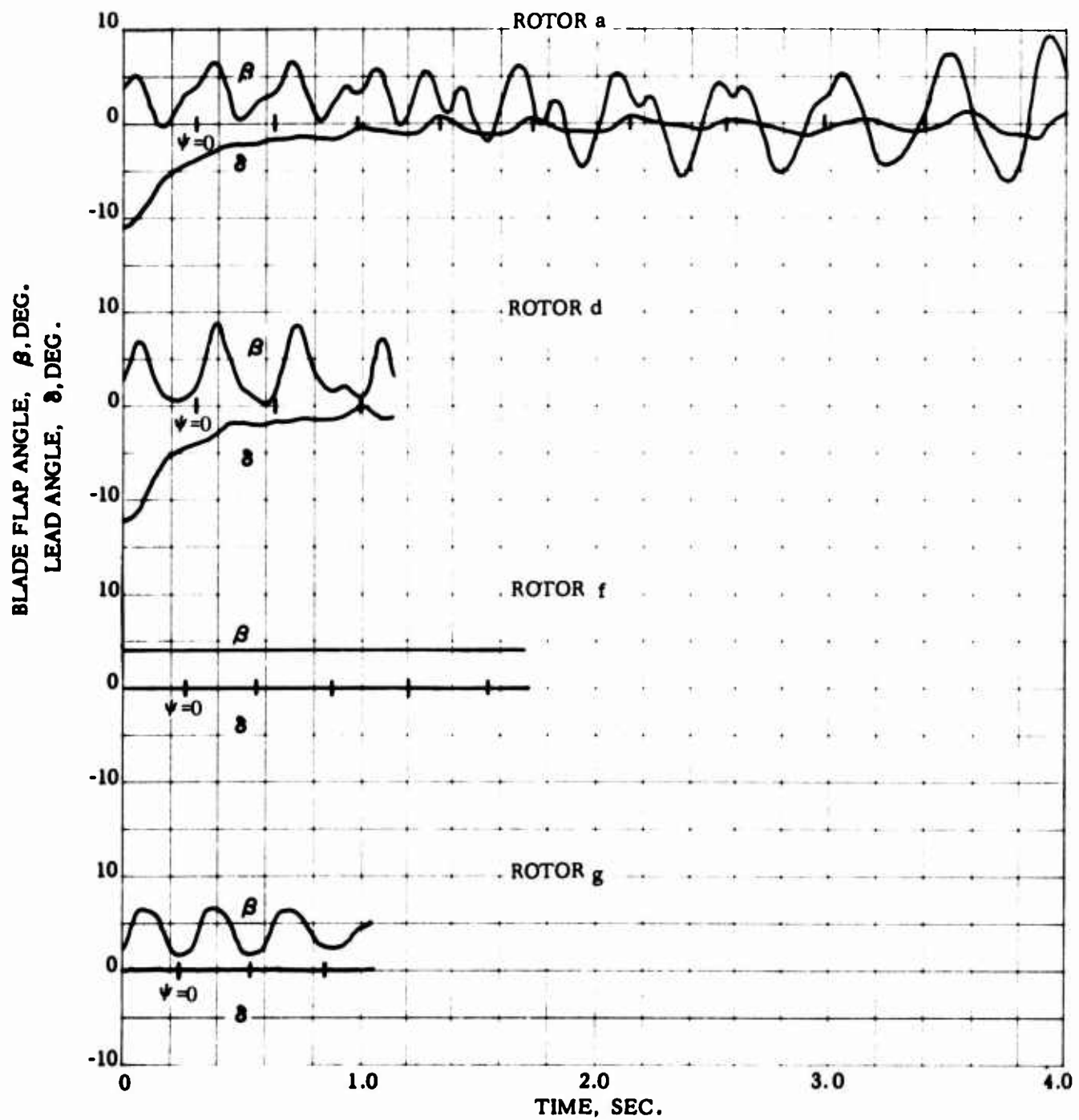


Figure 22. Concluded

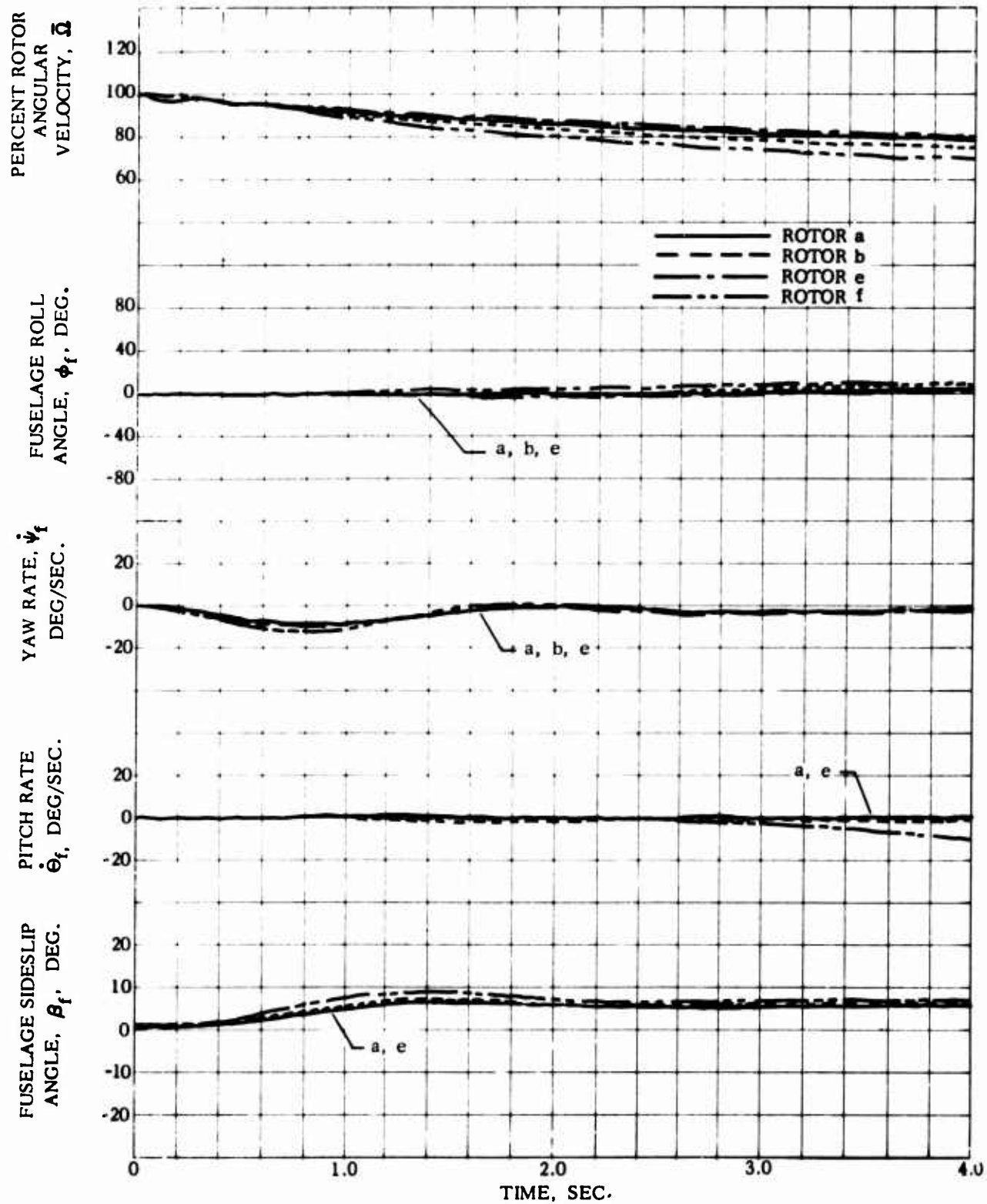


Figure 23. Helicopter and Rotor Blade Motion Following Full Power Loss, $D/L = -0.063$, No Corrective Control Inputs, Various Rotor Configurations

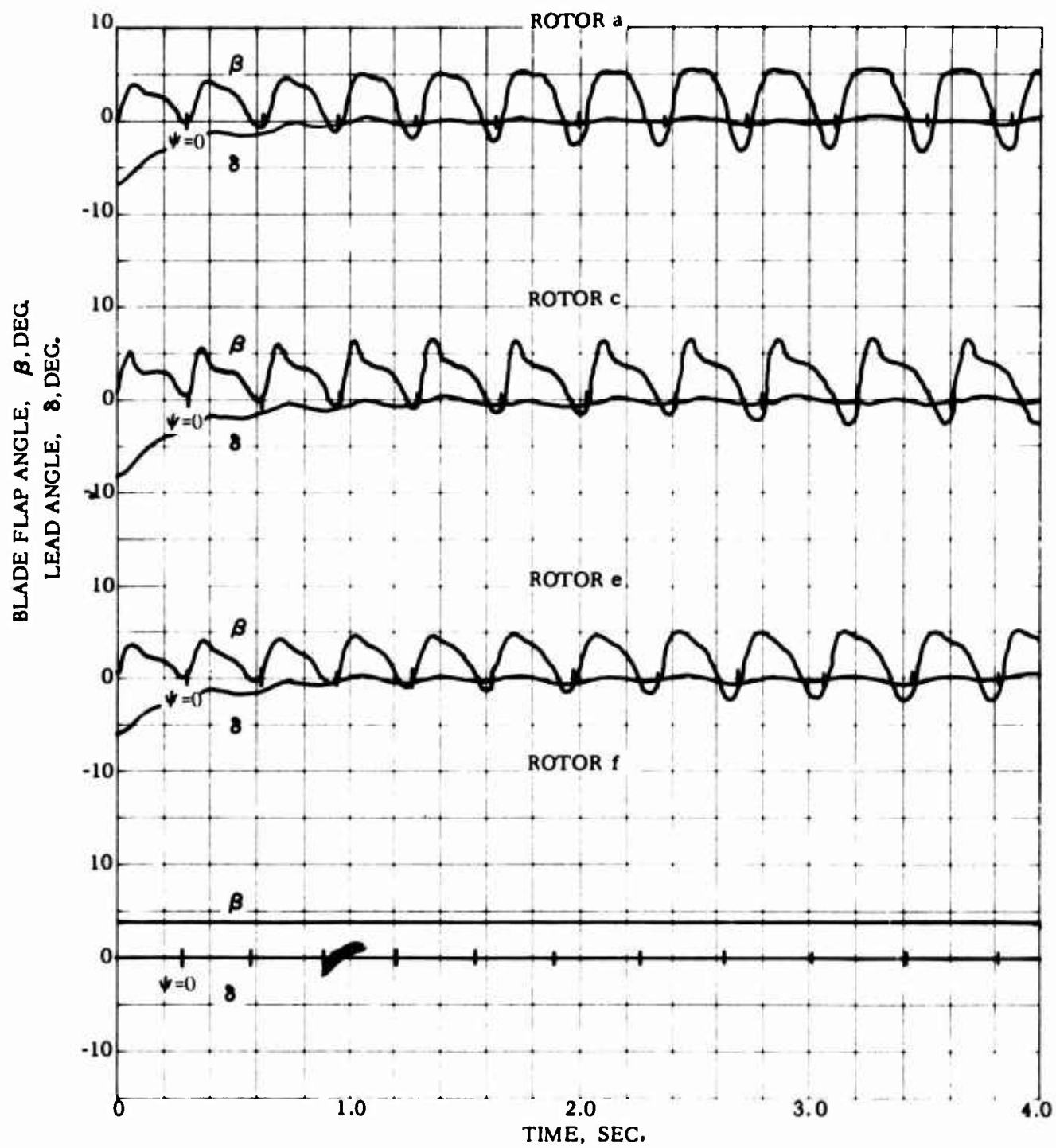


Figure 23. Concluded

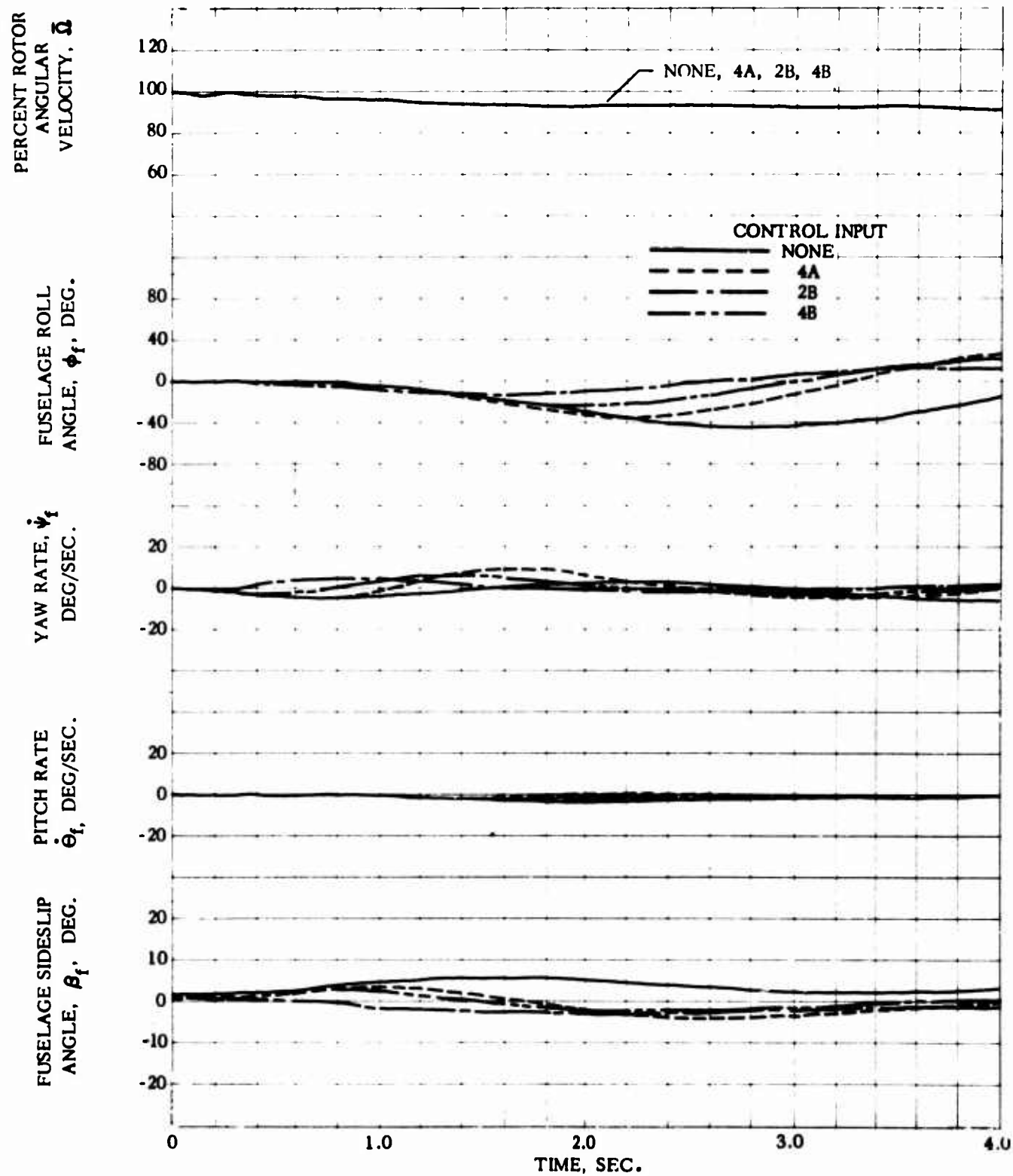


Figure 24. Helicopter and Rotor Blade Motion Following Part Power Loss, $D/L = 0.15$, With Corrective Control Inputs, Fully Articulated Rotor ($e/R = 0.034$)

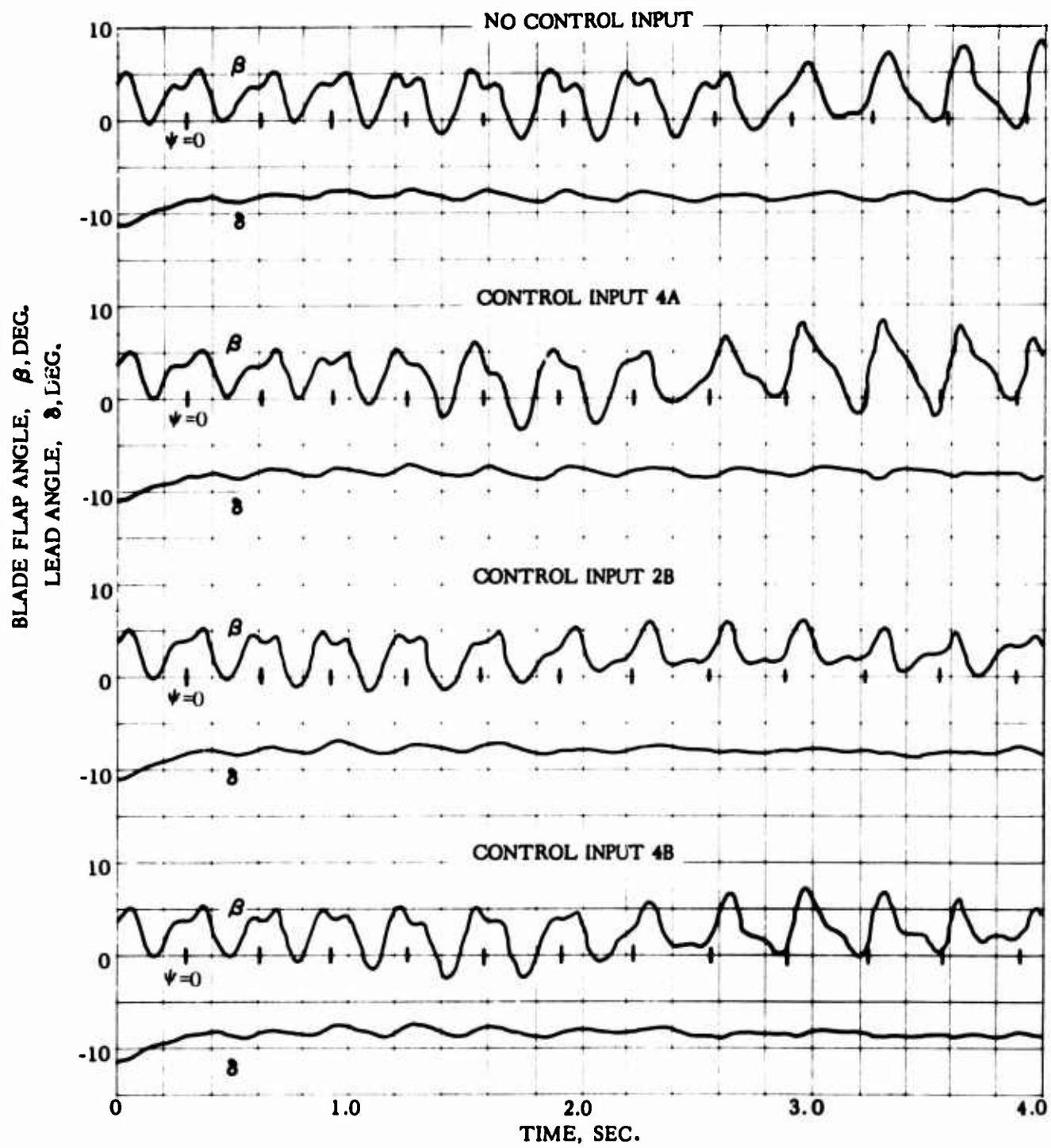


Figure 24. Concluded

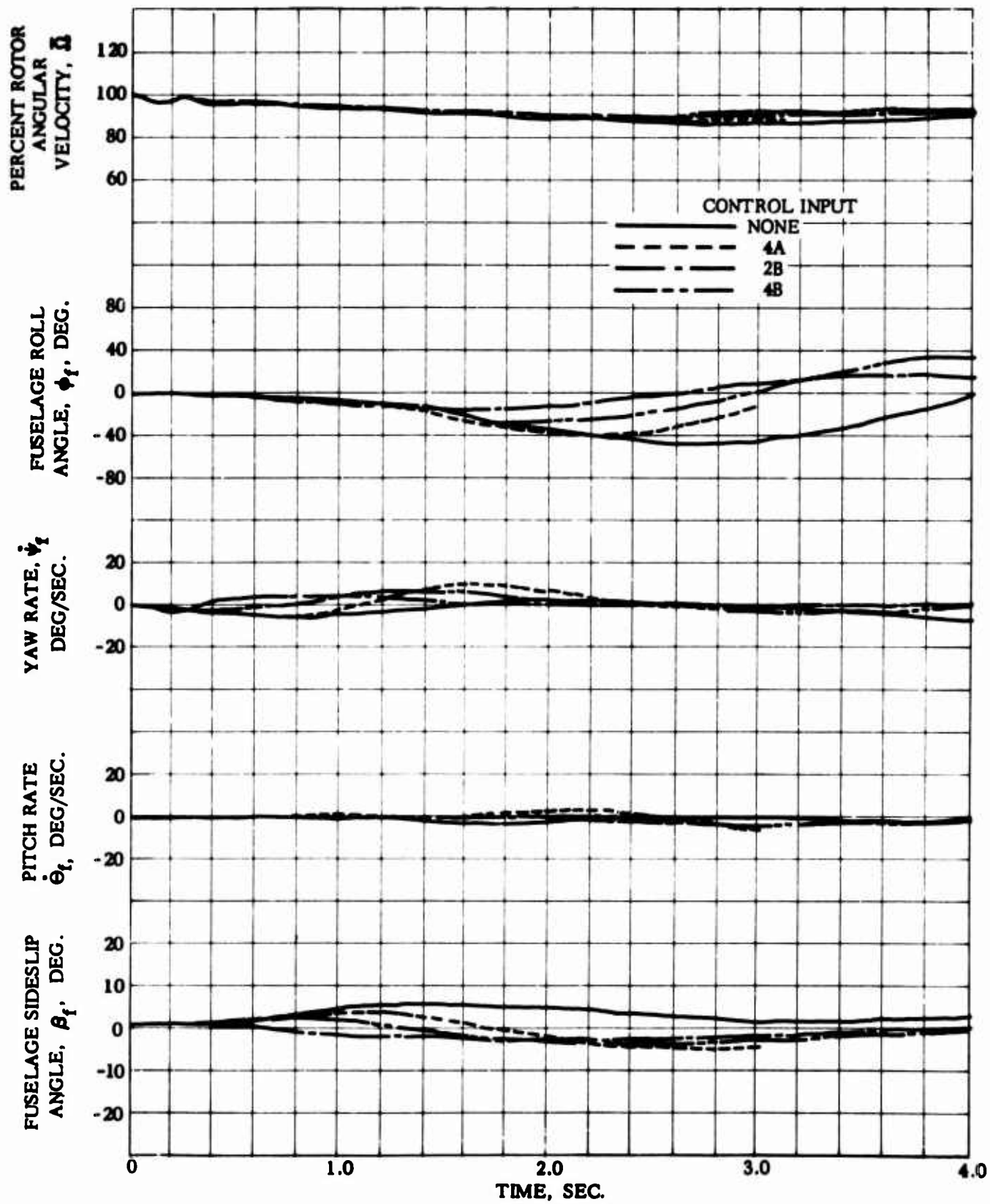


Figure 25. Helicopter and Rotor Blade Motion Following Part Power Loss, $D/L = 0.15$, With Corrective Control Inputs, Rotor With Blade Pitch-Flap Feedback

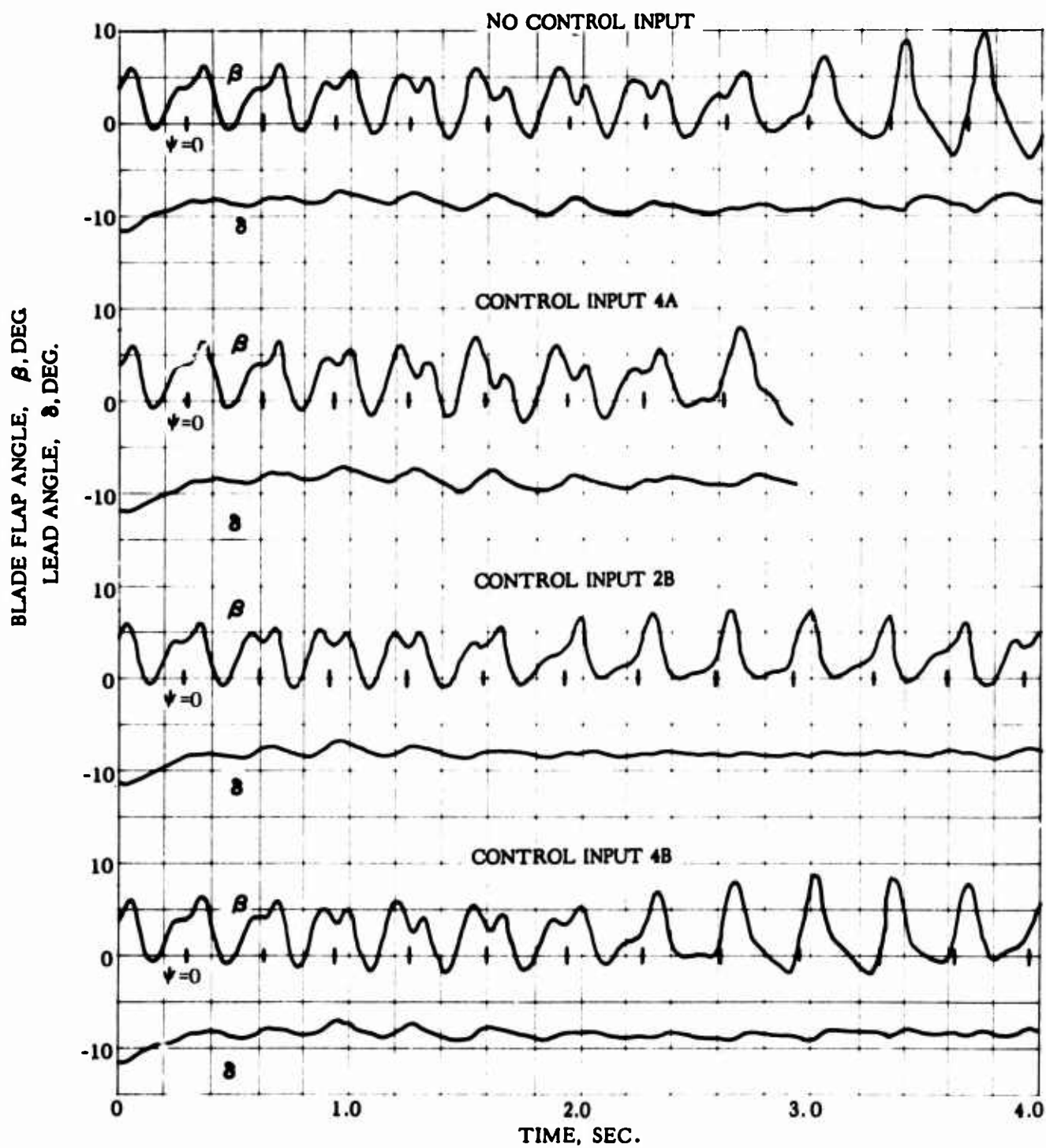


Figure 25. Concluded

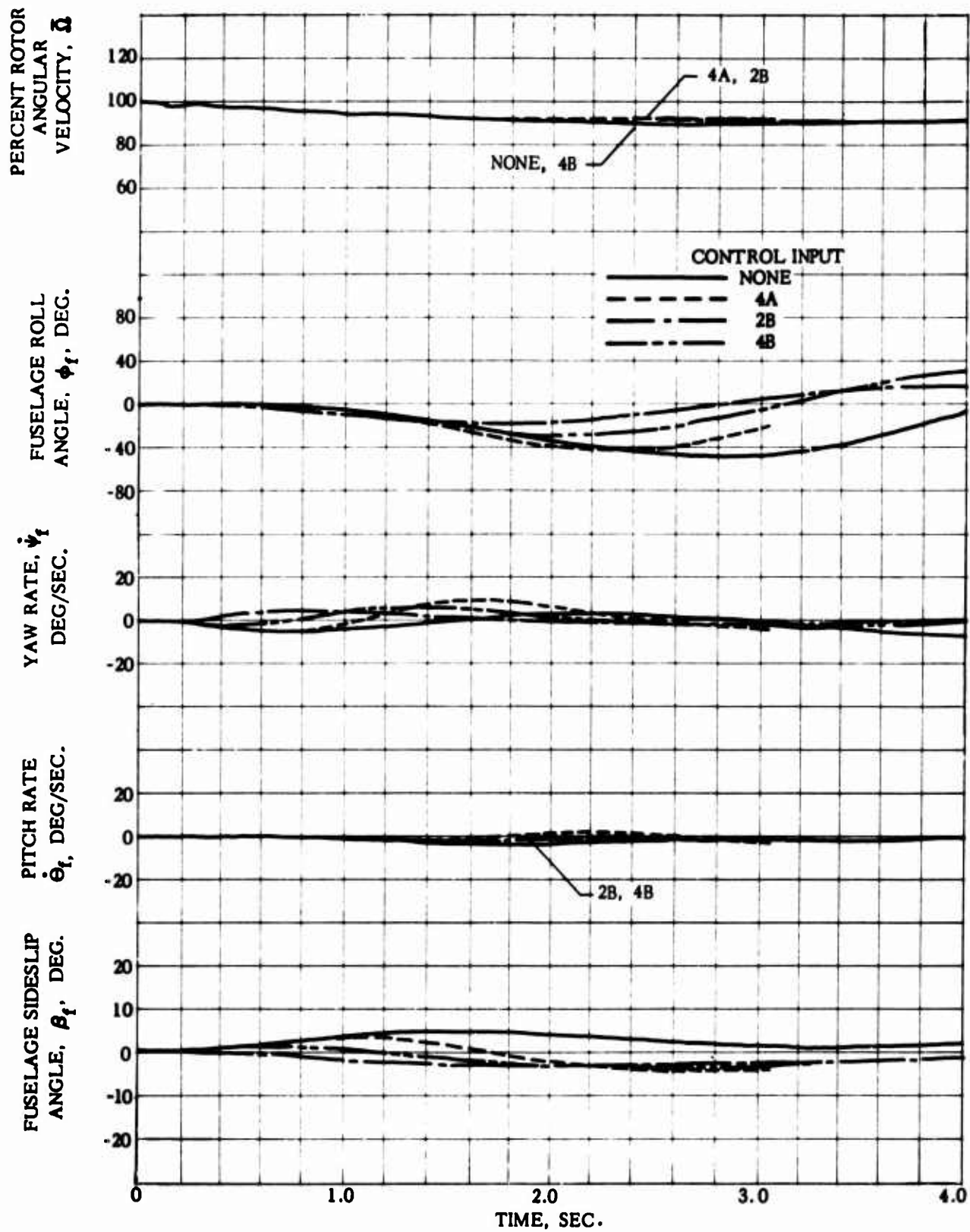


Figure 26. Helicopter and Rotor Blade Motion Following Part Power Loss, $D/L = 0.15$, With Corrective Control Inputs, Rotor With Blade Pitch-Tip Path Plane Tilt Feedback

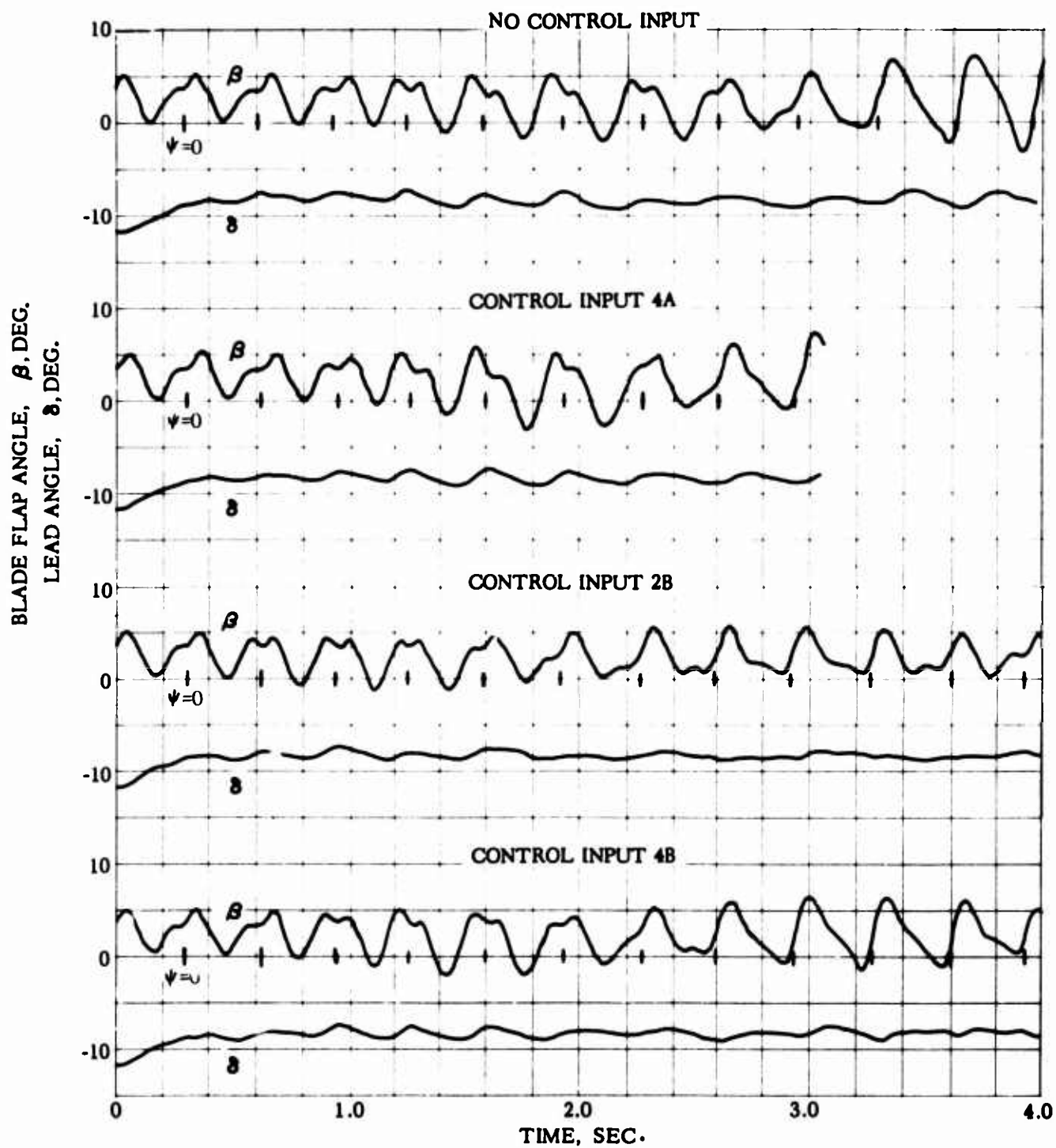


Figure 26. Concluded

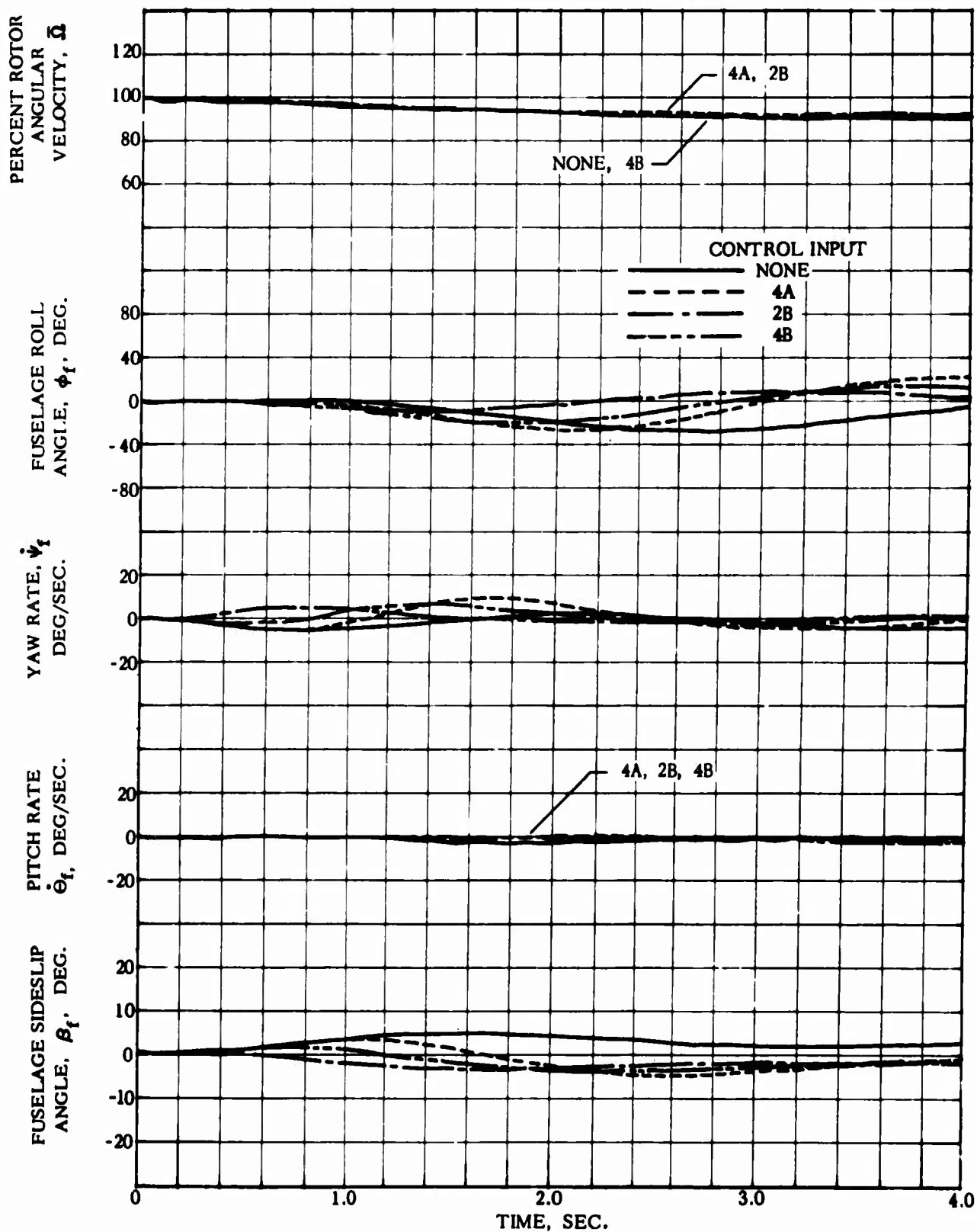


Figure 27. Helicopter and Rotor Blade Motion Following Part Power Loss, $D/L = 0.15$, With Corrective Control Inputs, Rotor With Reduced Lock Number

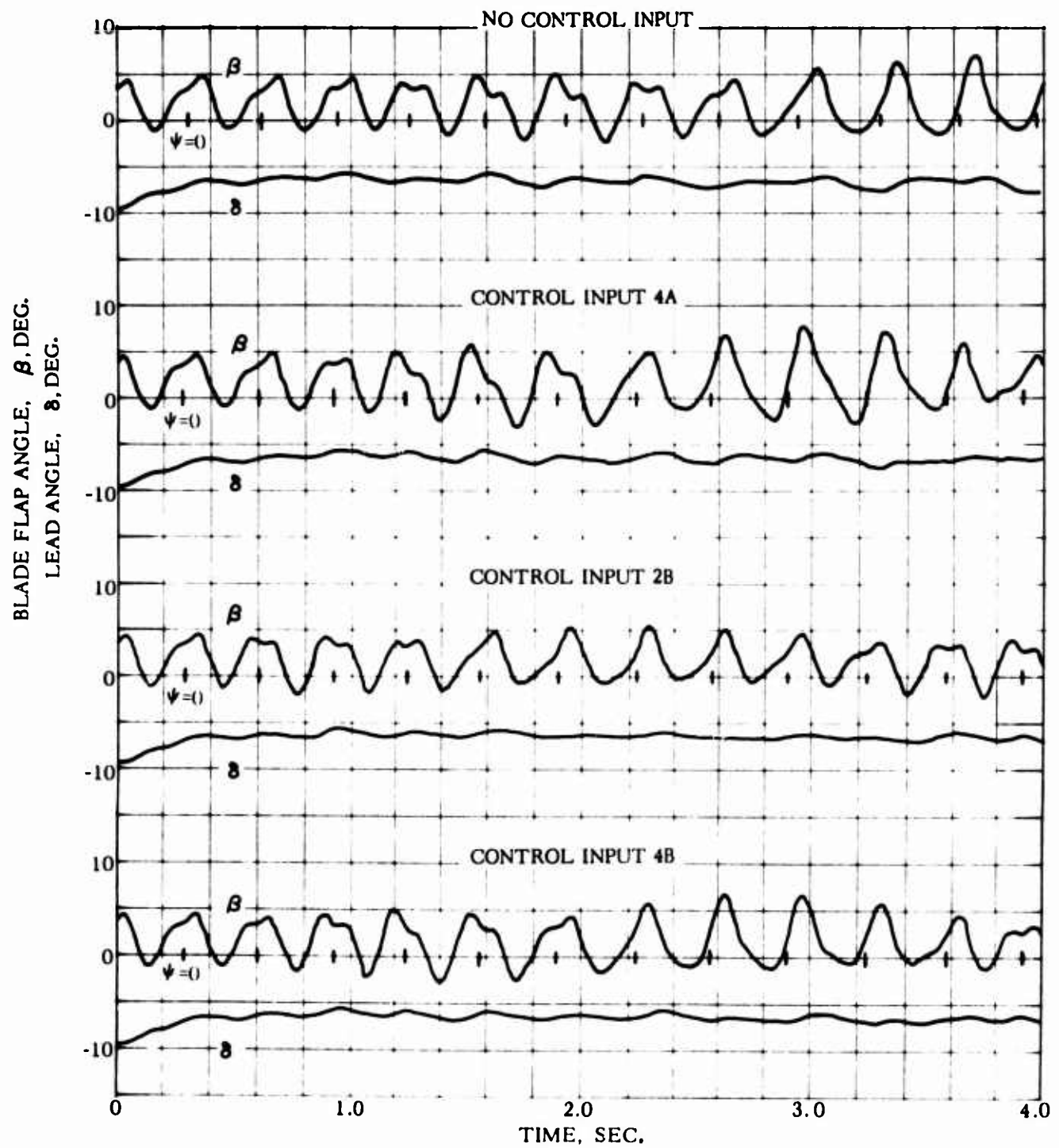


Figure 27. Concluded

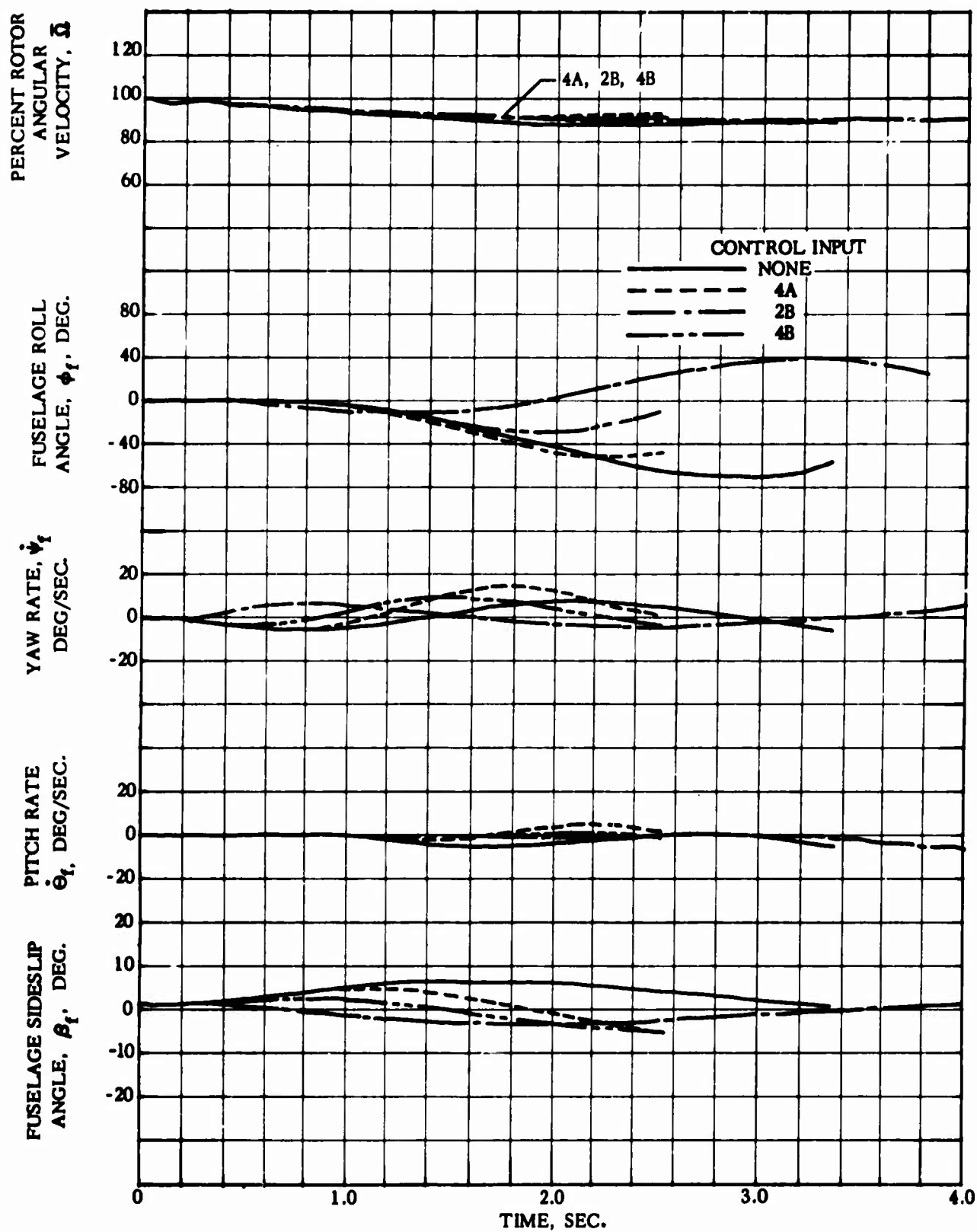


Figure 28. Helicopter and Rotor Blade Motion Following Part Power Loss, $D/L = 0.15$, With Corrective Control Inputs, Rotor With Zero Flapping Hinge Offset

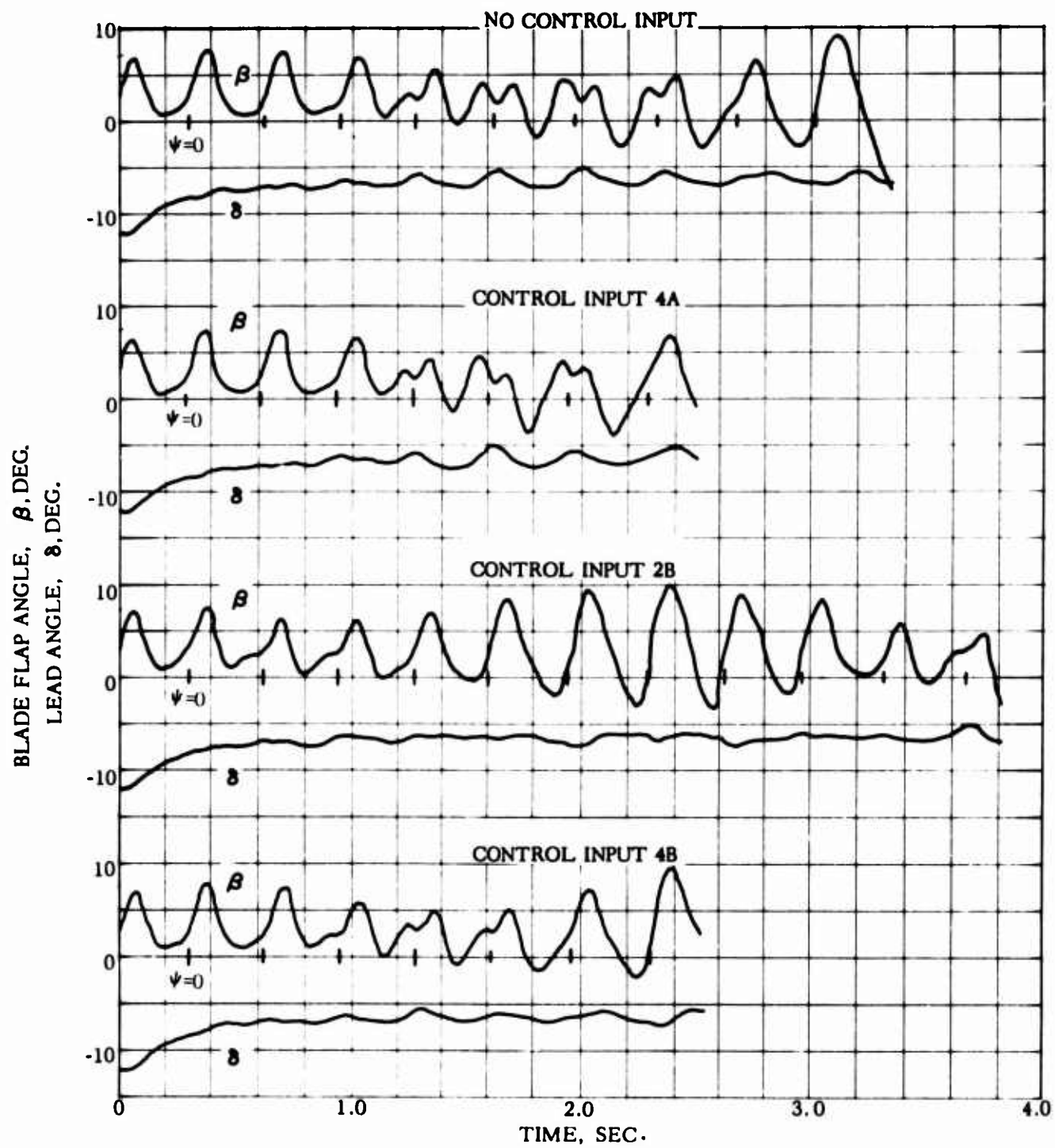


Figure 28. Concluded

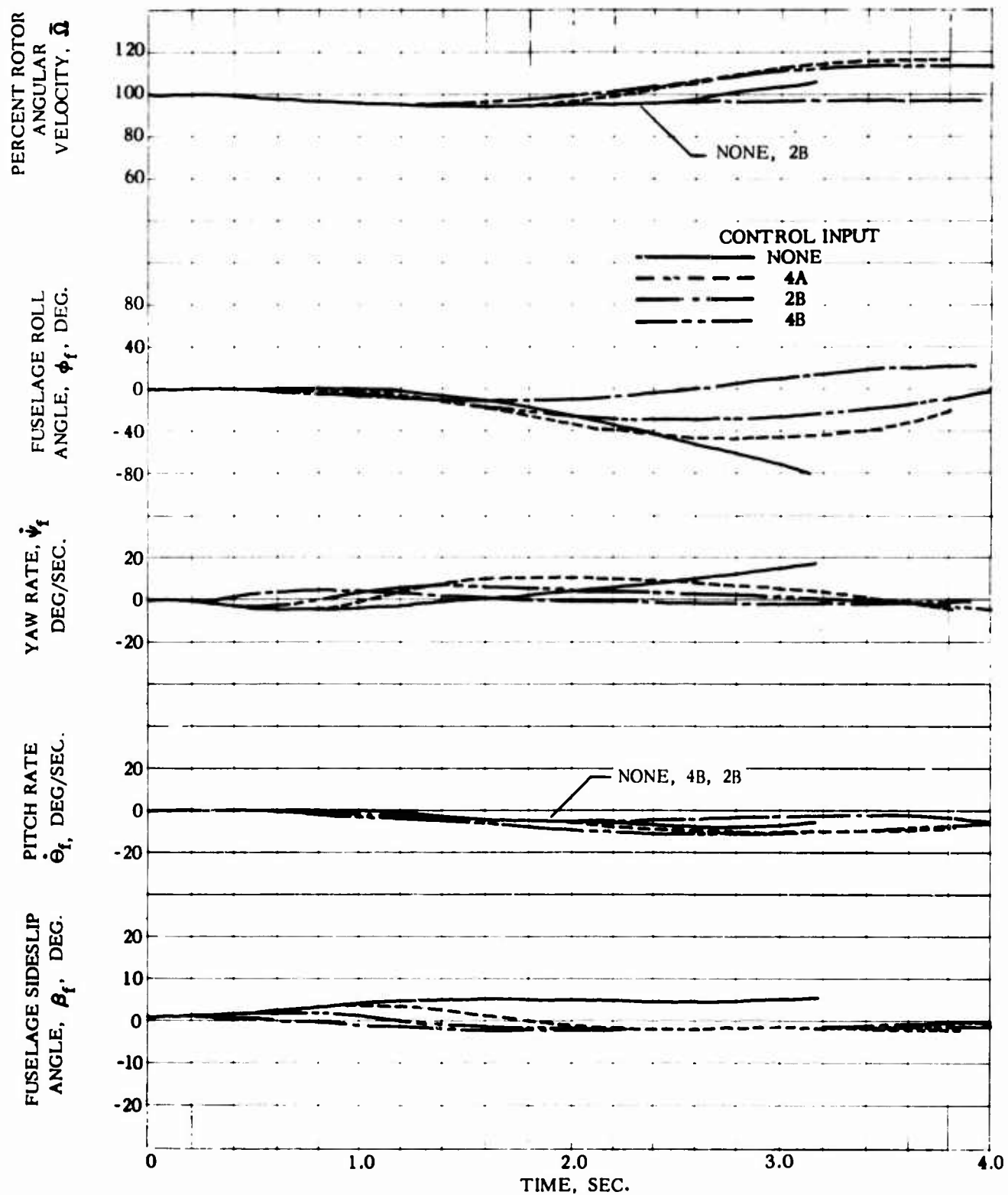


Figure 29. Helicopter and Rotor Blade Motion Following Part Power Loss, $D/L = 0.15$, With Corrective Control Inputs, Hingeless Rotor

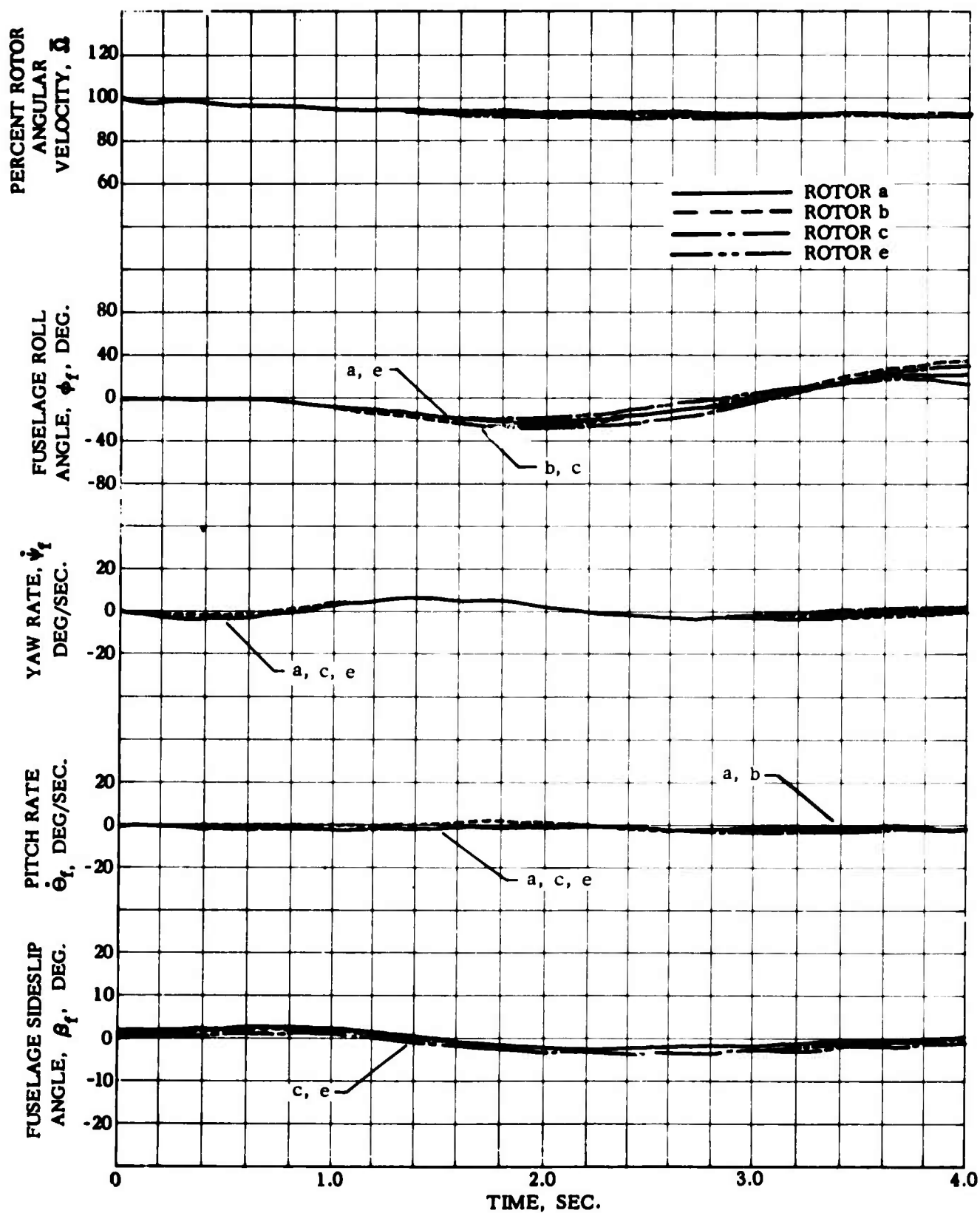


Figure 30. Helicopter and Rotor Blade Motion Following Part Power Loss, $D/L = 0.15$, With Corrective Control Input 4B, Various Rotor Configurations

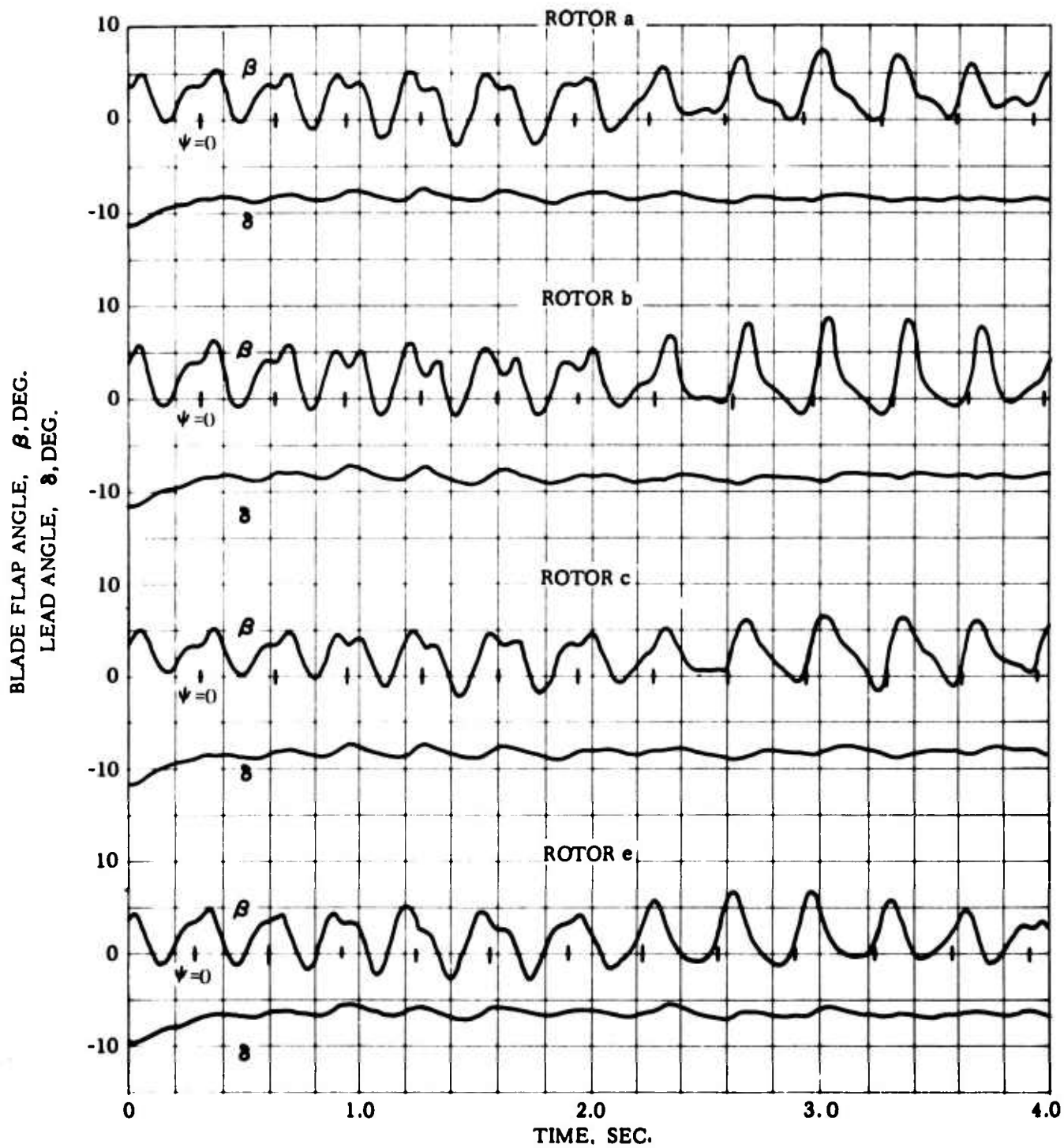


Figure 30 Concluded

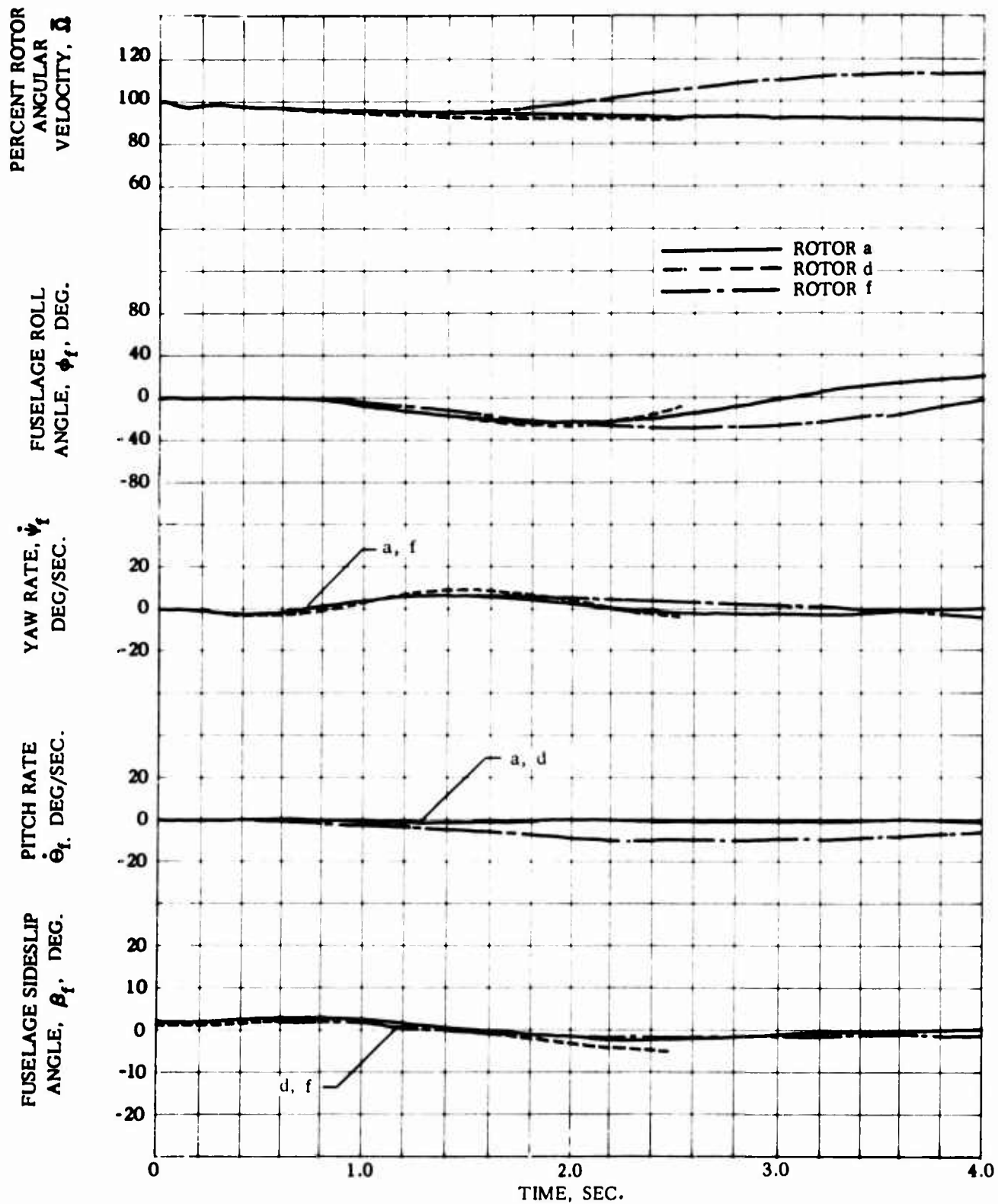


Figure 31. Helicopter and Rotor Blade Motion Following Part Power Loss, $D/L = 0.15$, With Corrective Control Input 4B, Various Rotor Configurations

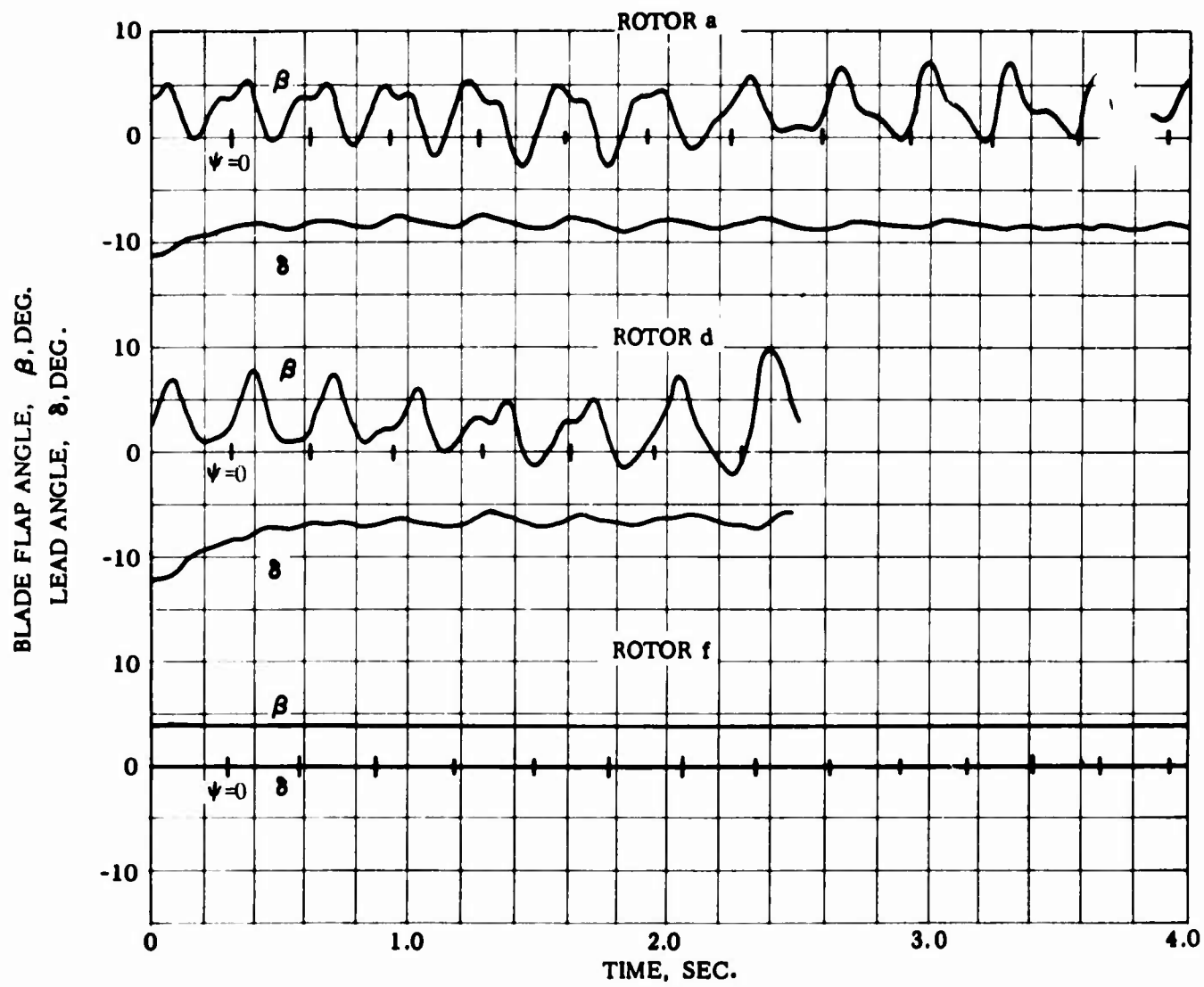


Figure 31. Concluded

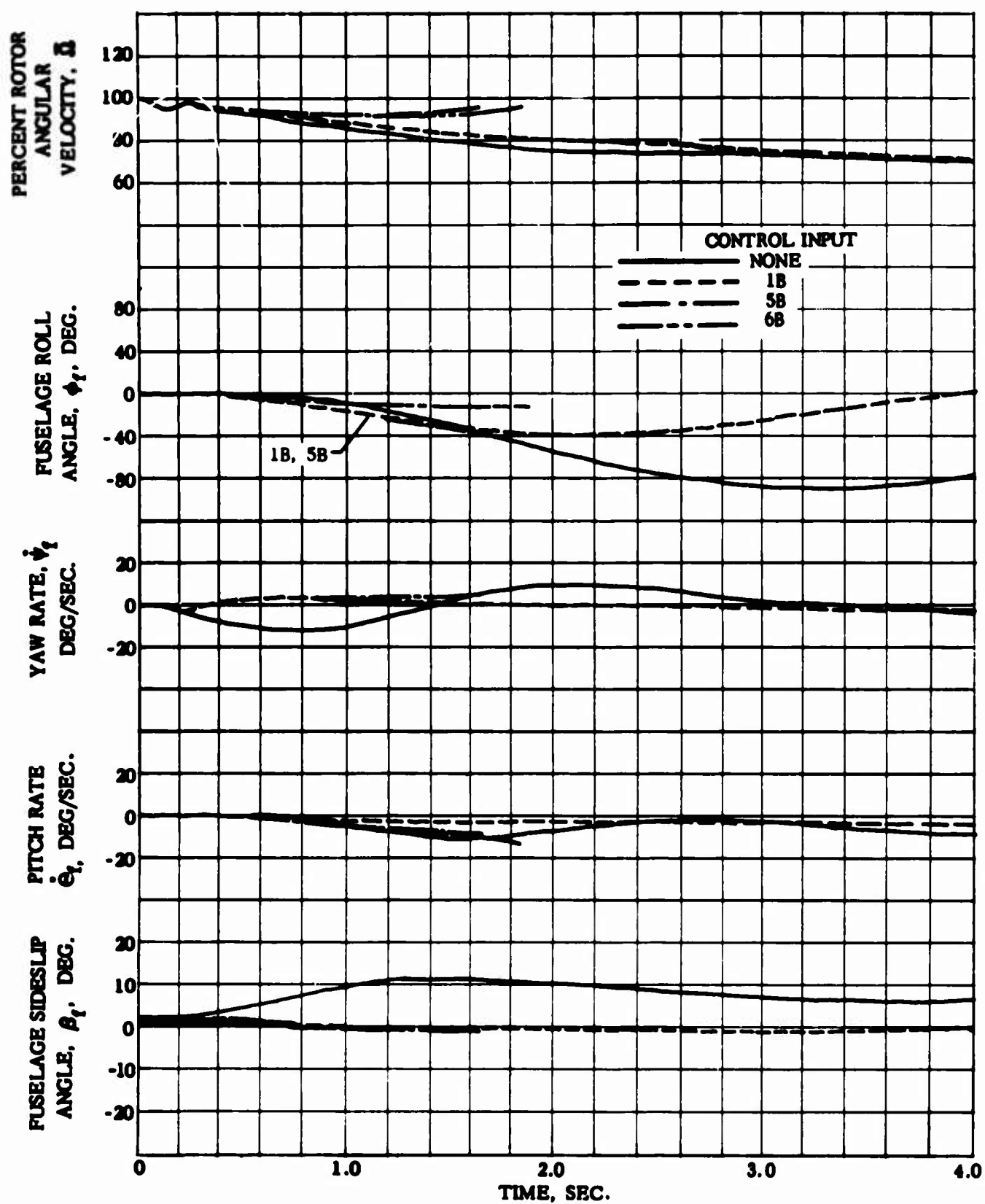


Figure 32. Helicopter and Rotor Blade Motion Following Full Power Loss, $D/L = 0.15$, With Corrective Control Inputs, Fully Articulated Rotor ($e/R = 0.034$)

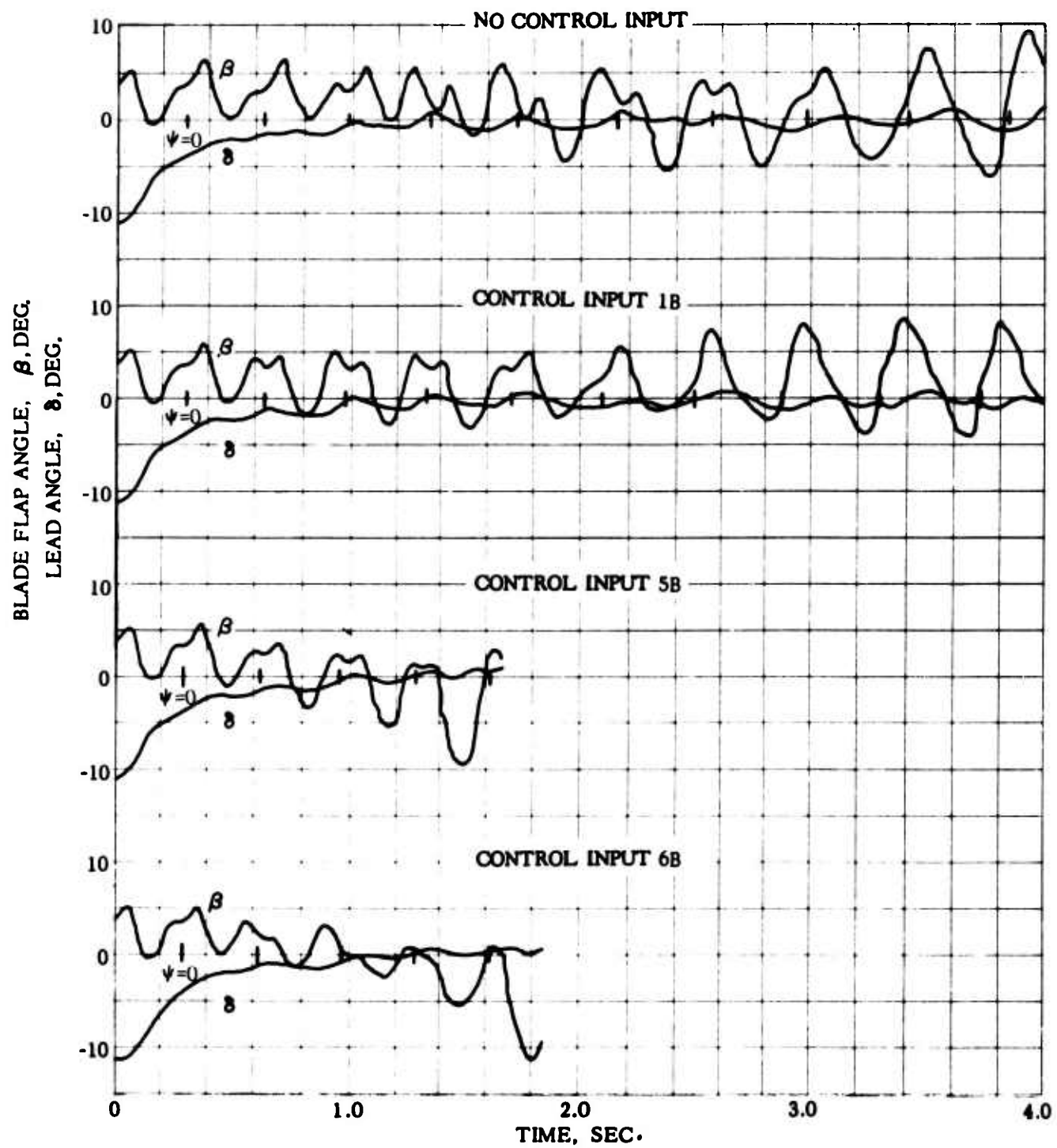


Figure 32. Concluded

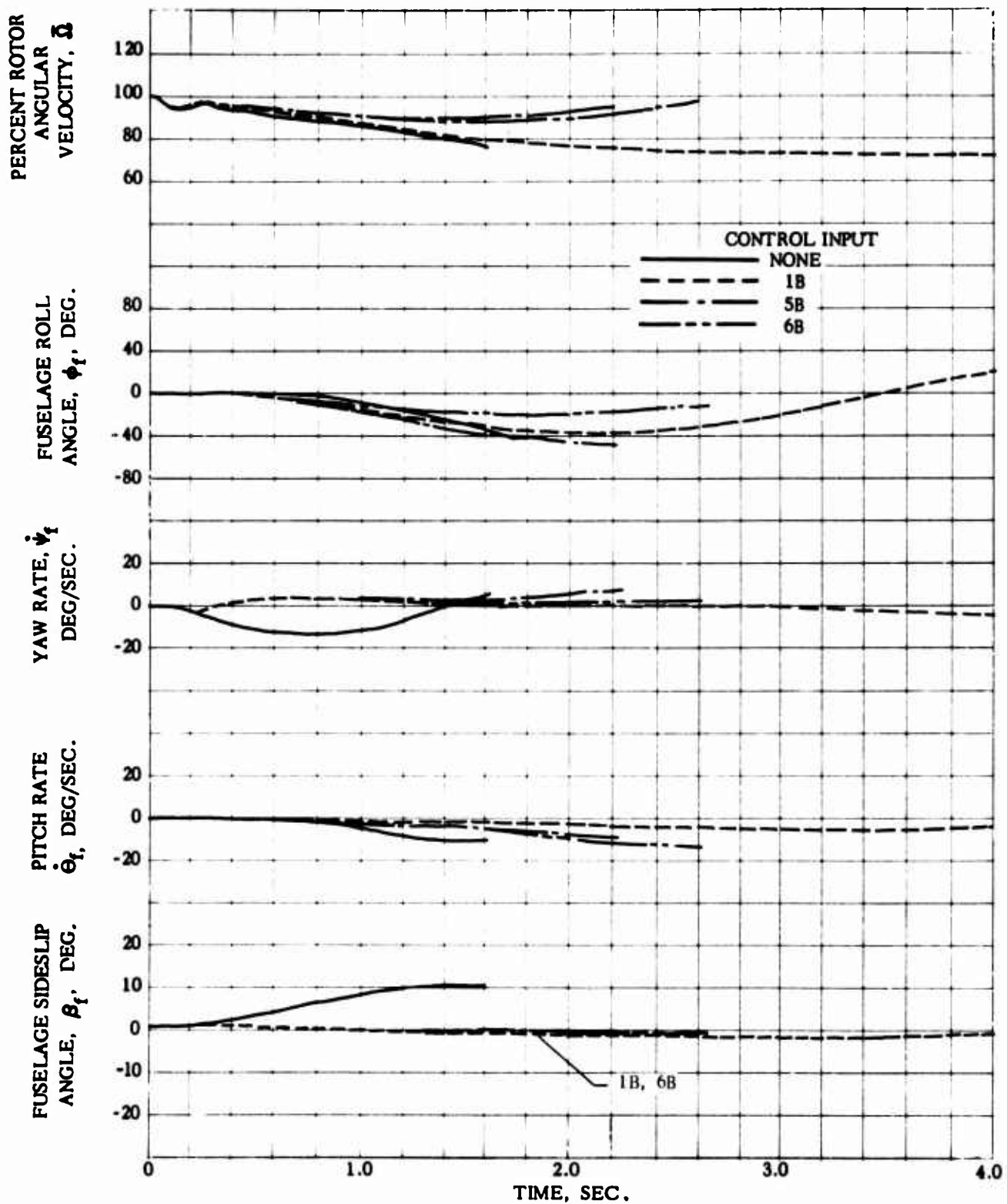


Figure 33. Helicopter and Rotor Blade Motion Following Full Power Loss, $D/L = 0.15$, With Corrective Control Inputs, Rotor With Blade Pitch-Flap Feedback

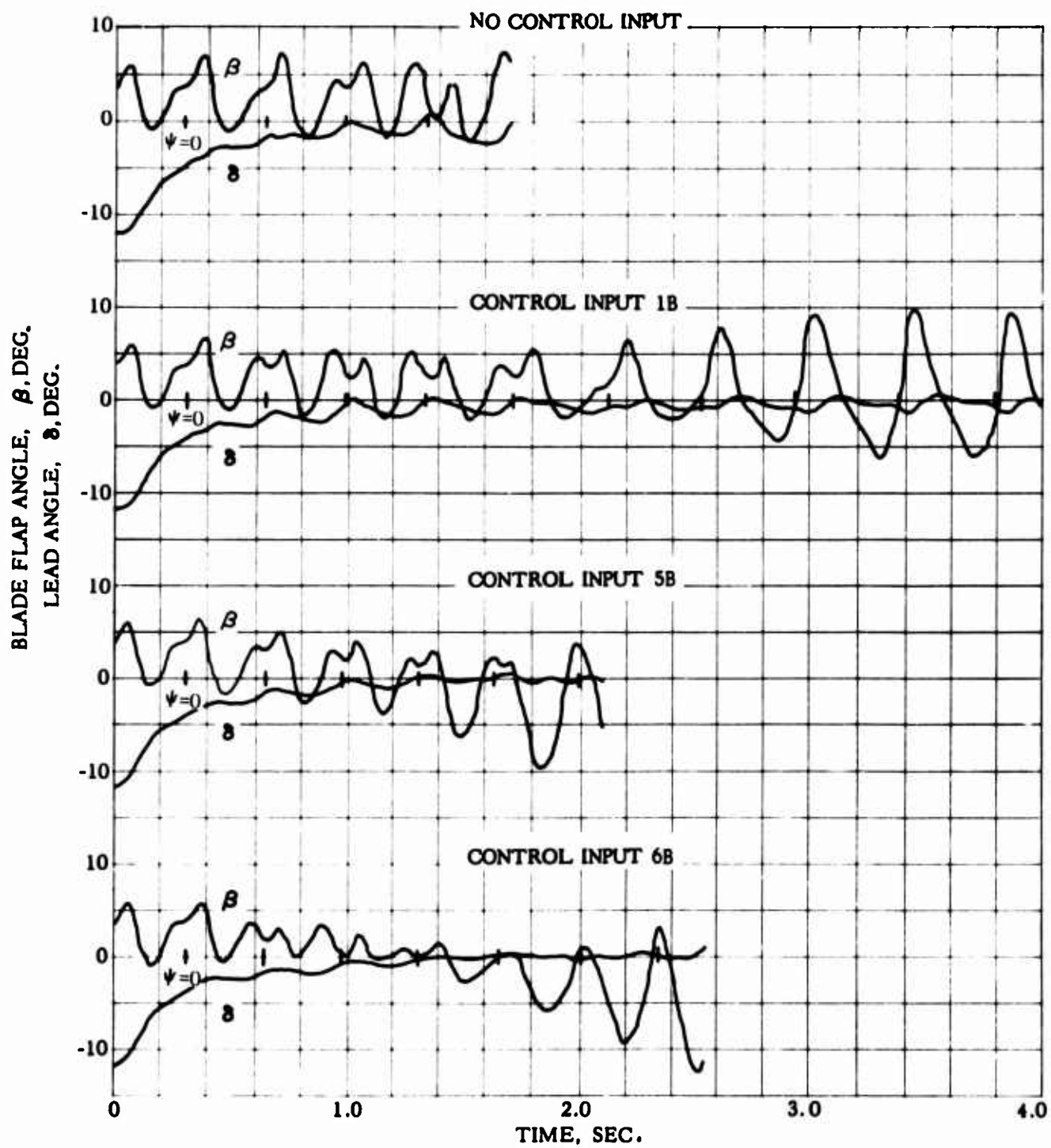


Figure 33. Concluded

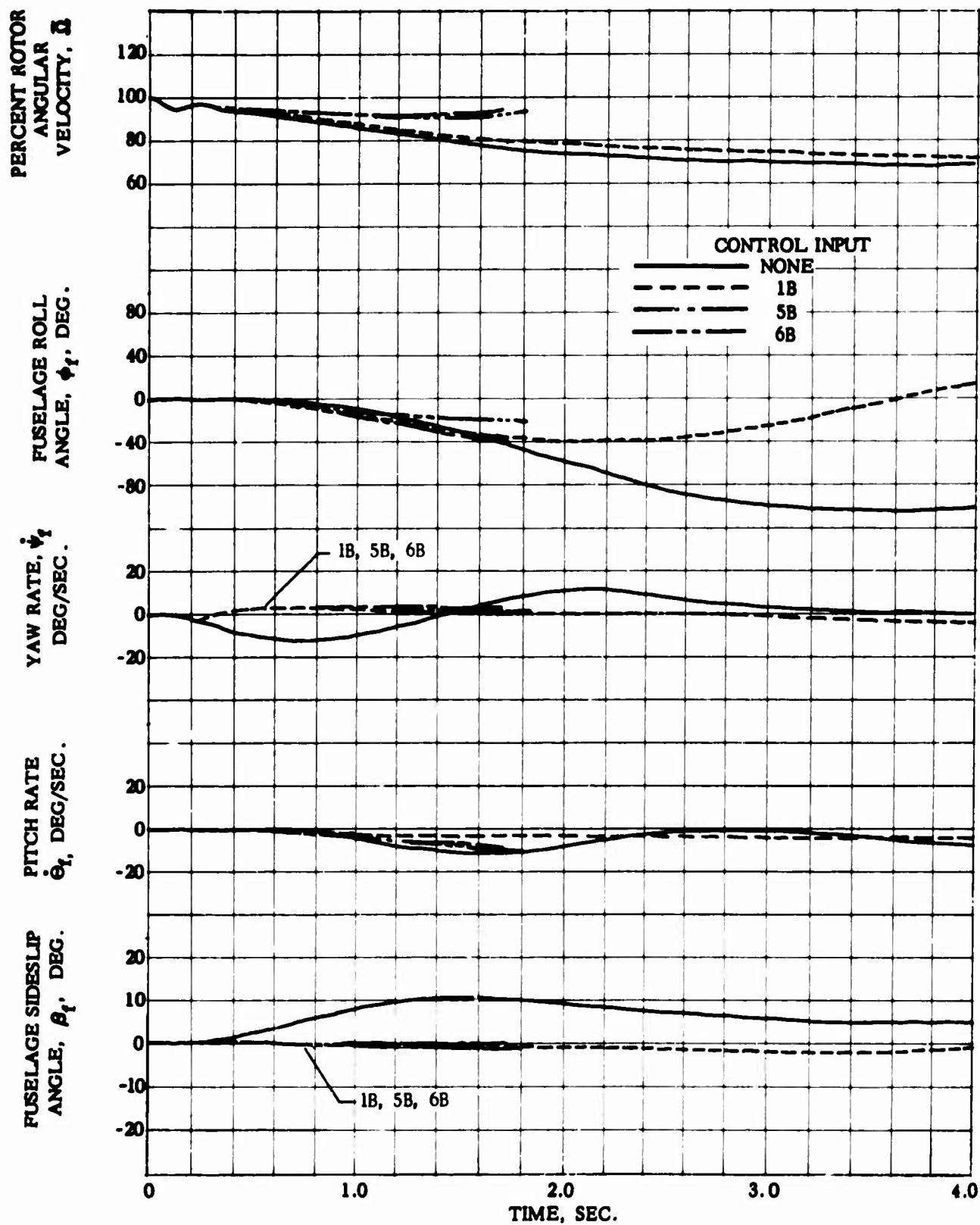


Figure 34. Helicopter and Rotor Blade Motion Following Full Power Loss, $D/L = 0.15$, With Corrective Control Inputs, Rotor With Blade Pitch-Tip Path Plane Tilt Feedback

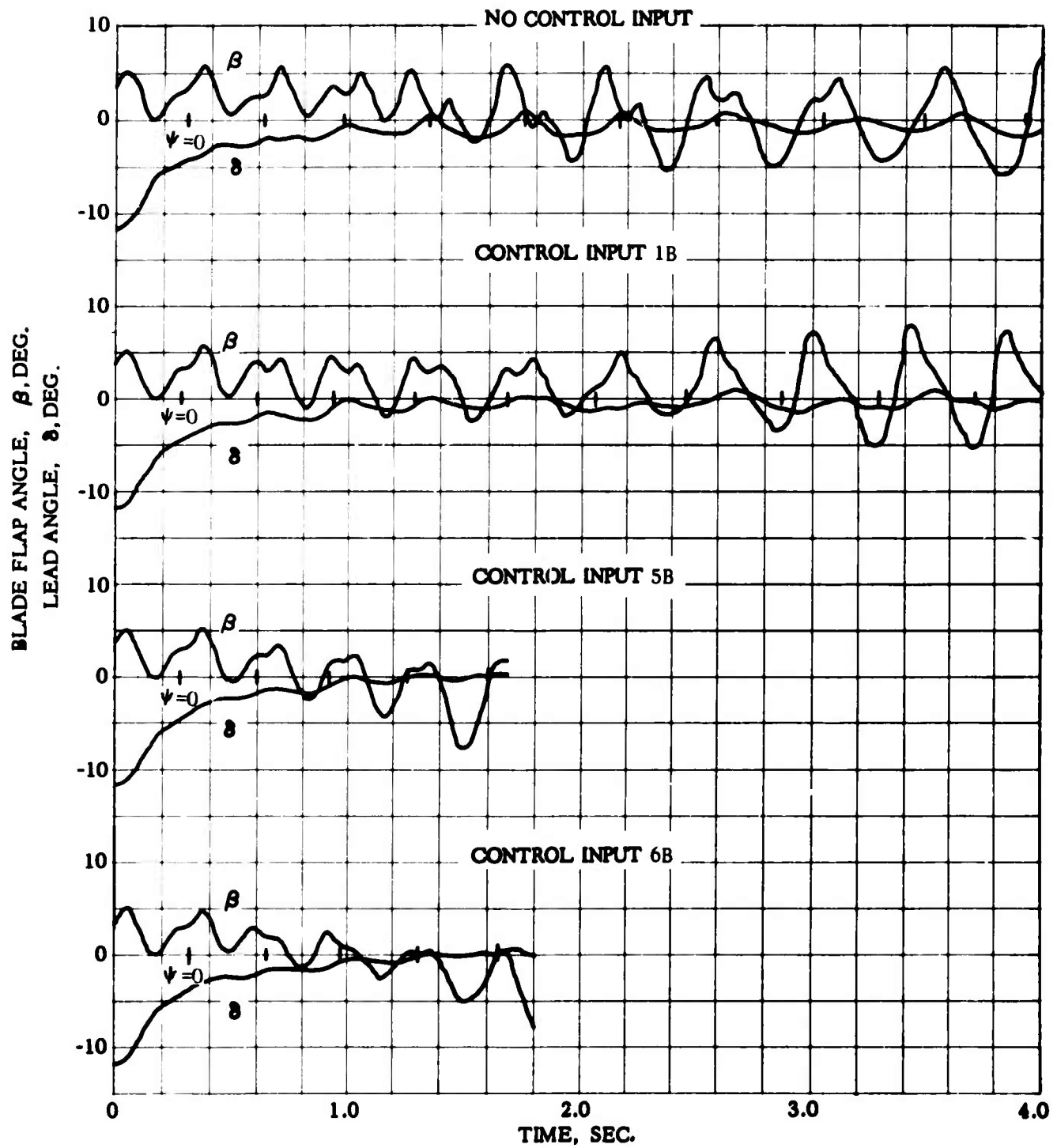


Figure 34. Concluded

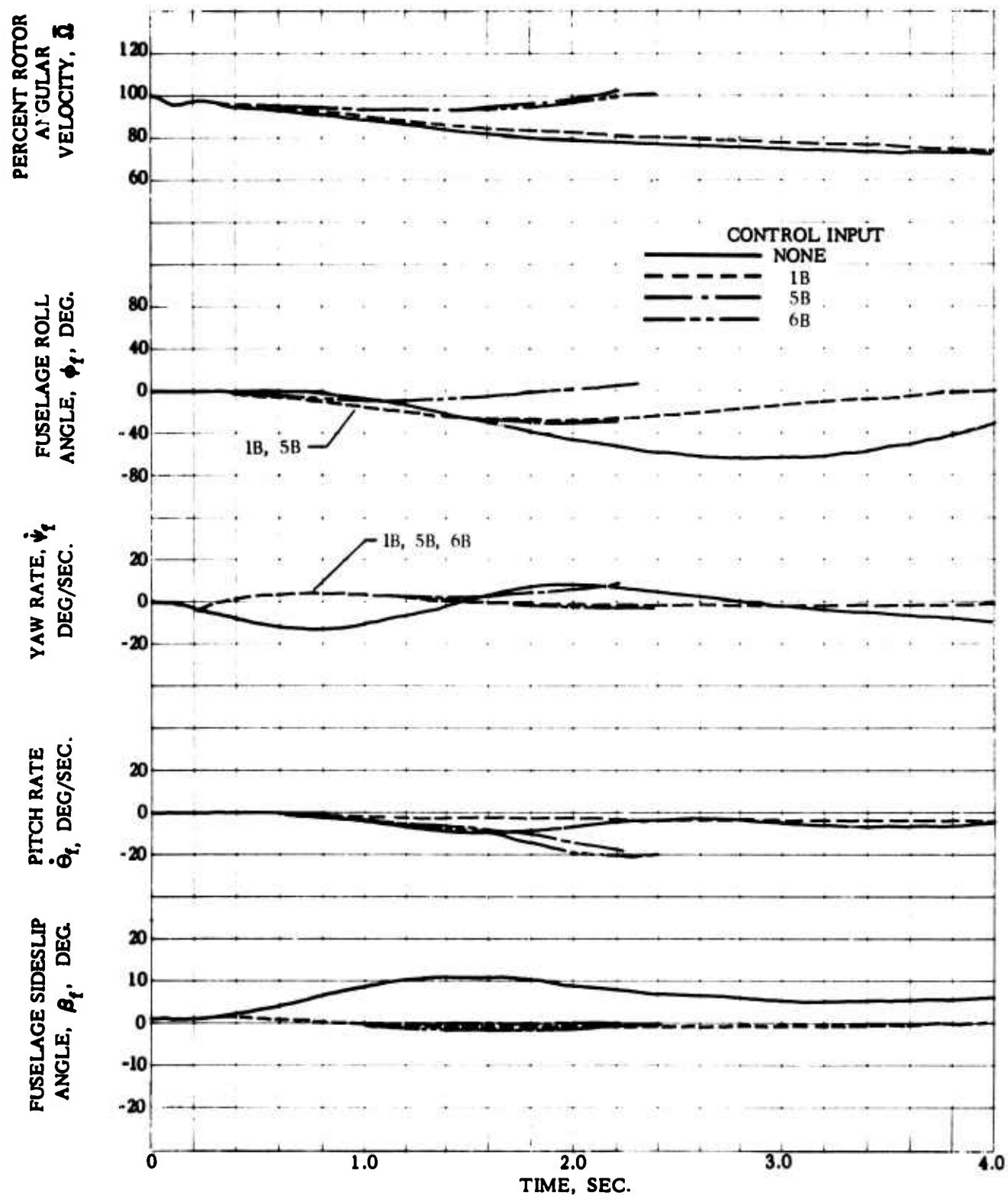


Figure 35. Helicopter and Rotor Blade Motion Following Full Power Loss, $D/L = 0.15$, With Corrective Control Inputs, Rotor With Reduced Lock Number

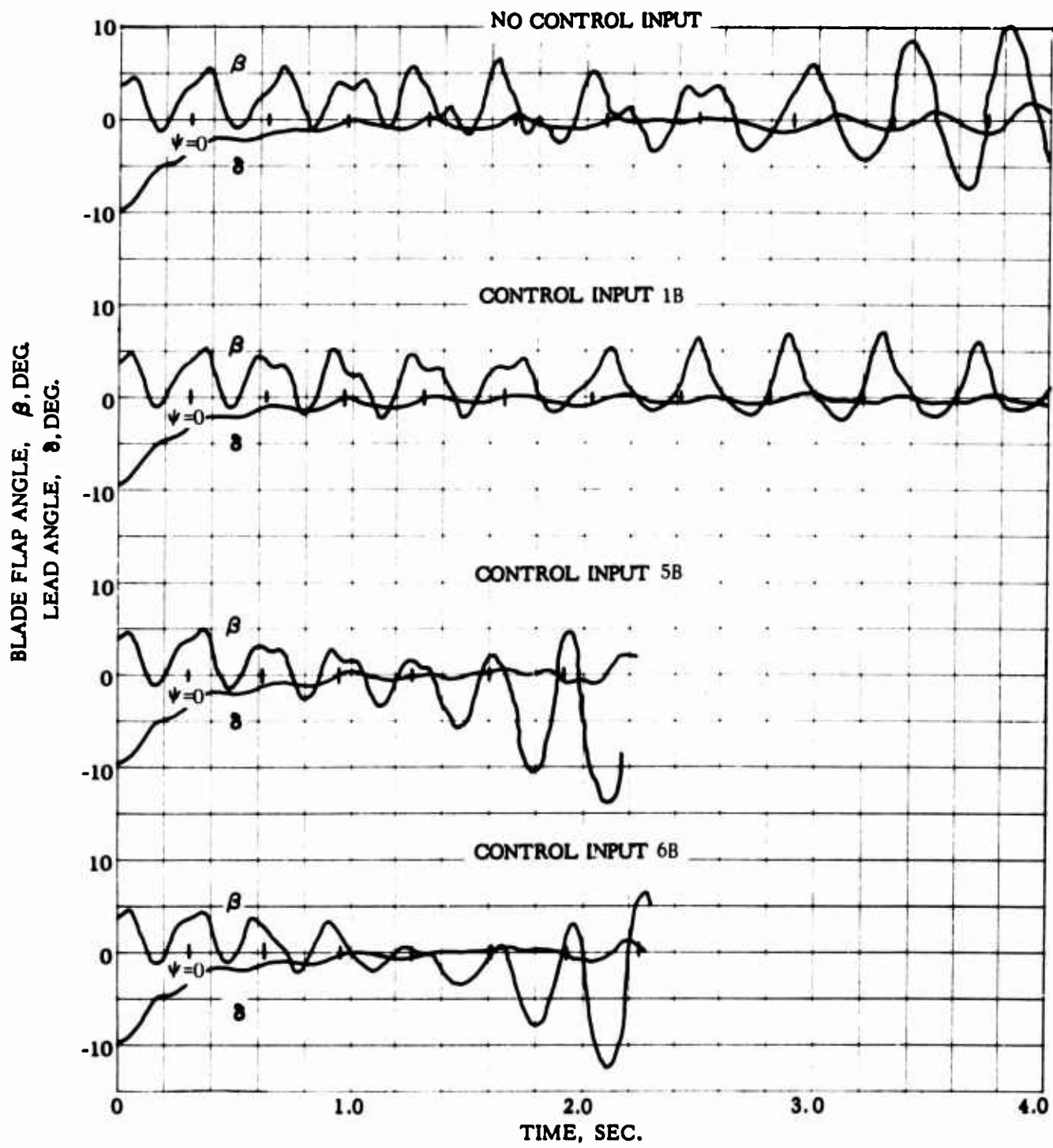


Figure 35. Concluded

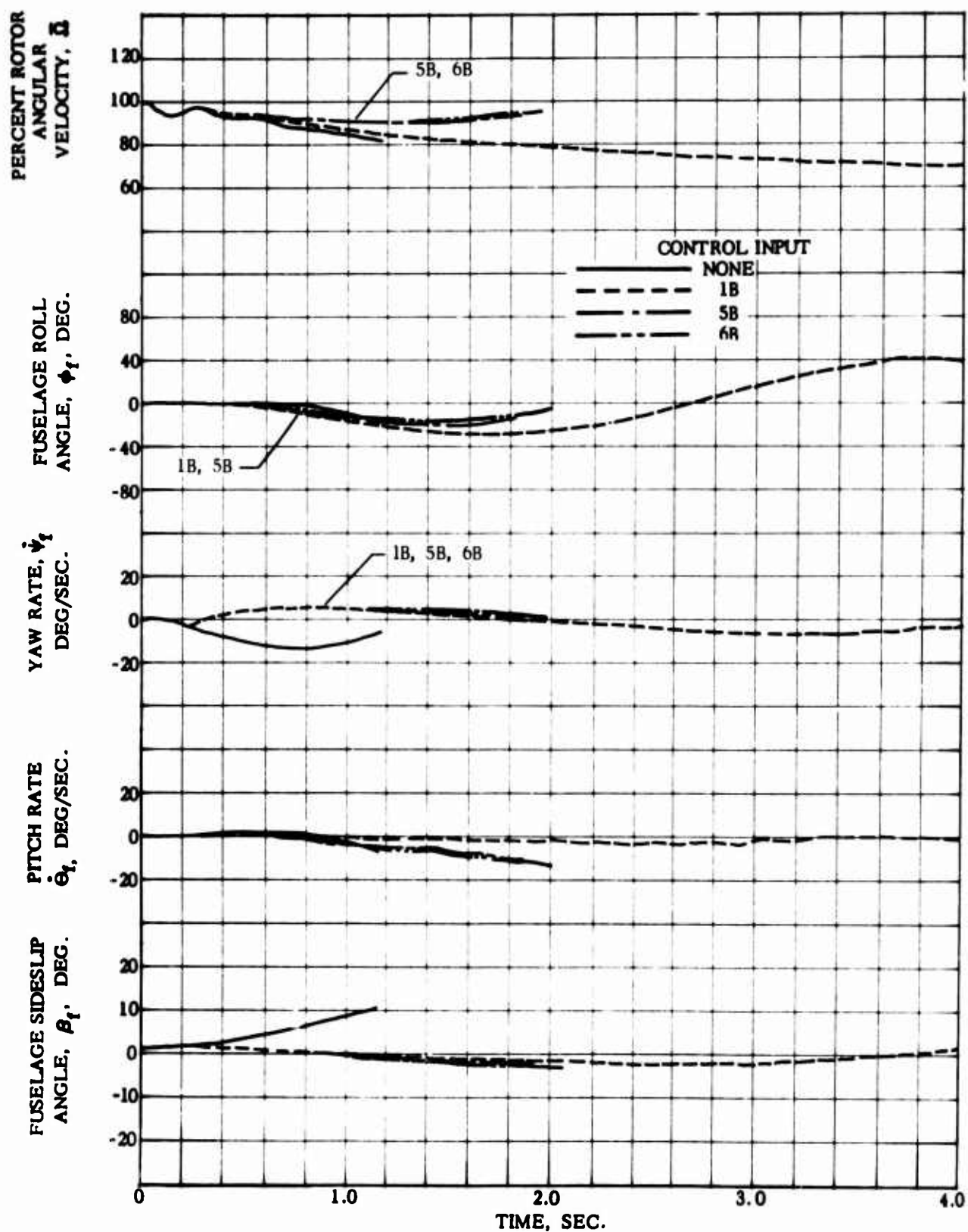


Figure 36. Helicopter and Rotor Blade Motion Following Full Power Loss, $D/L = 0.15$, With Corrective Control Inputs, Rotor With Zero Flapping Hinge Offset

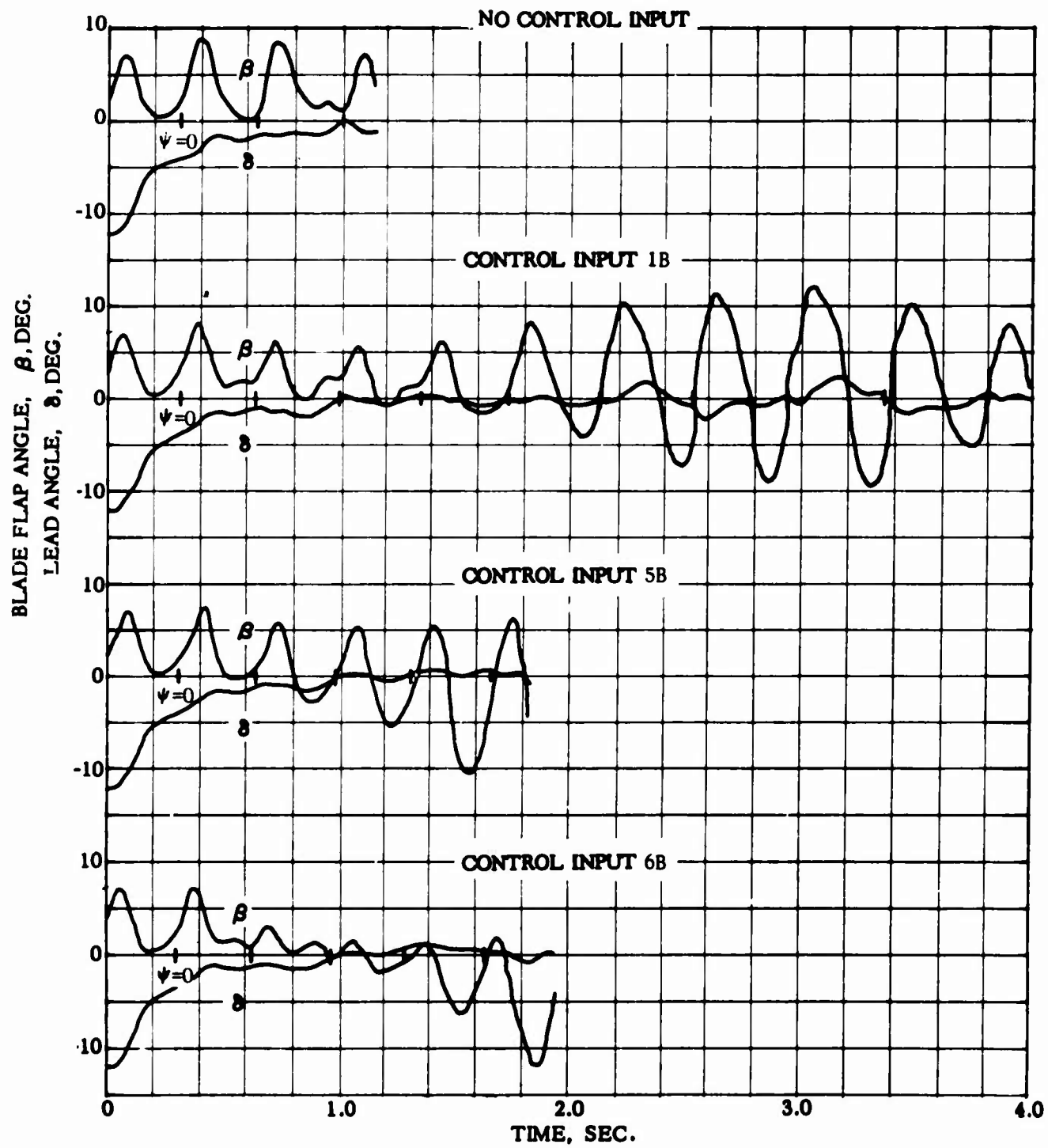


Figure 36. Concluded



Figure 37. Helicopter and Rotor Blade Motion Following Full Power Loss,
 $D/L = 0.15$, With Corrective Control Inputs, Fully Articulated
 Rotor ($e/R = 0.034$)

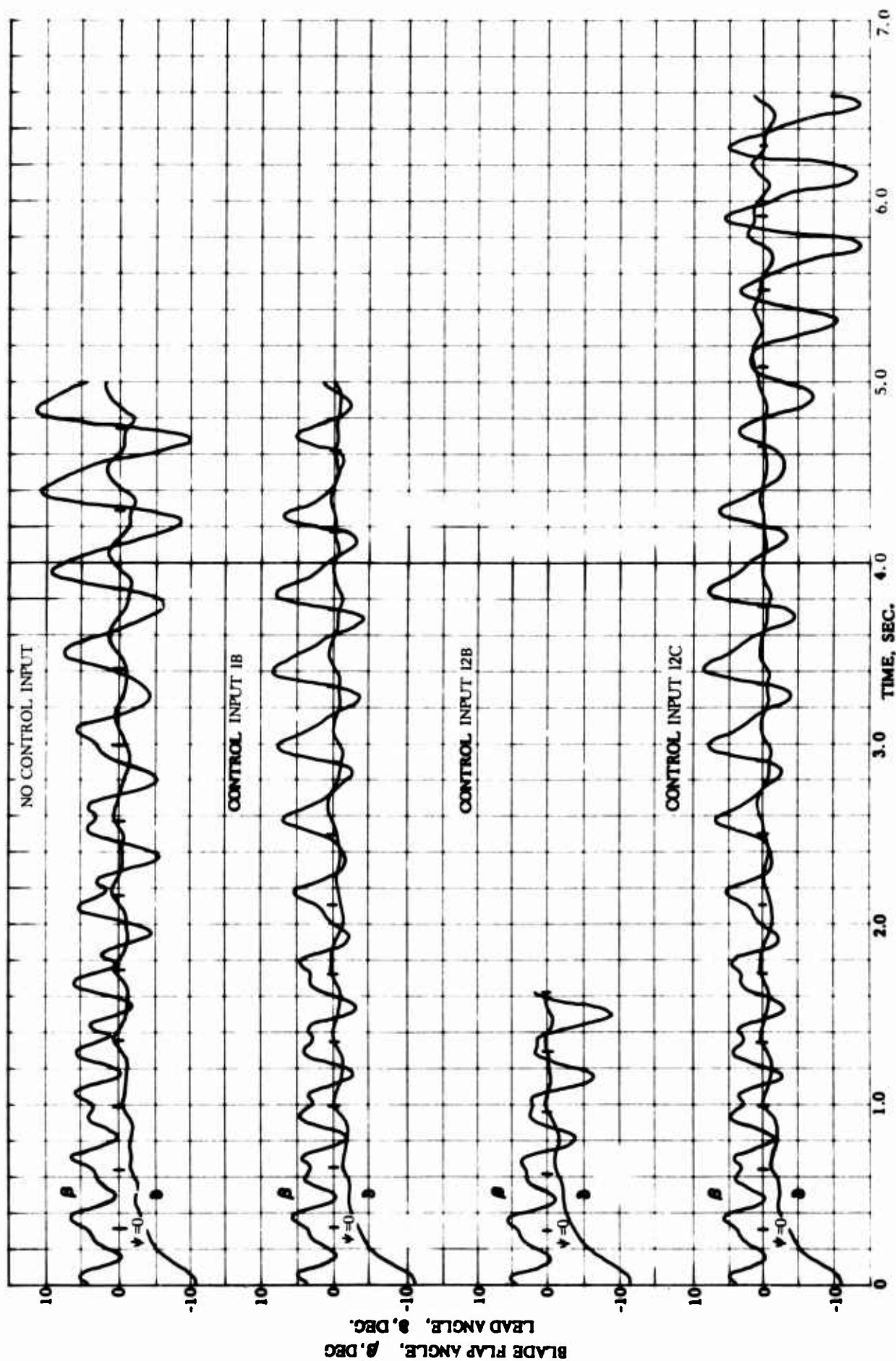


Figure 37. Concluded

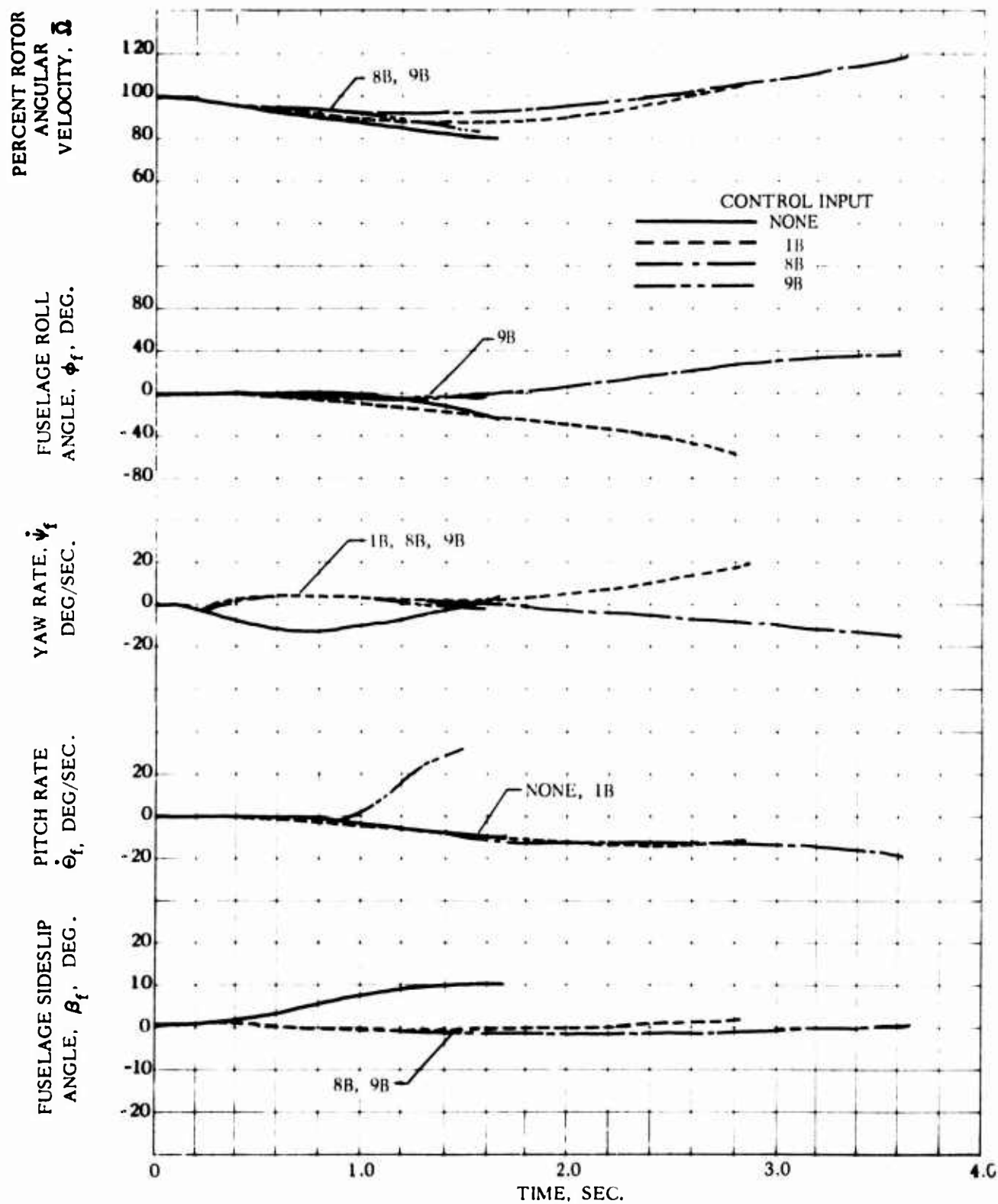


Figure 38. Helicopter and Rotor Blade Motion Following Full Power Loss, $D/L = 0.15$, With Corrective Control Inputs, Hingeless Rotor

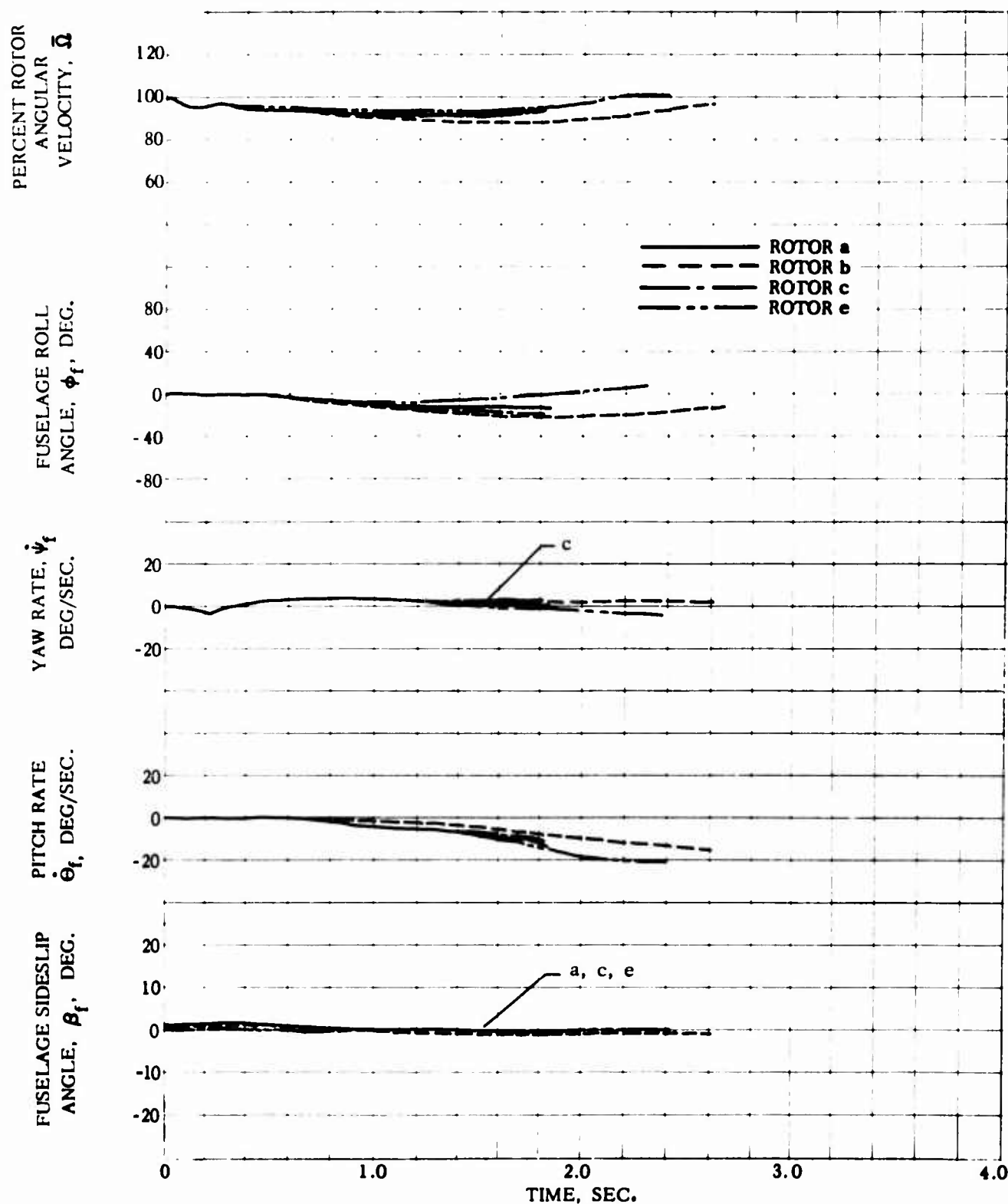


Figure 39. Helicopter and Rotor Blade Motion Following Full Power Loss, $D/L = 0.15$, With Corrective Control Input δB , Various Rotor Configurations

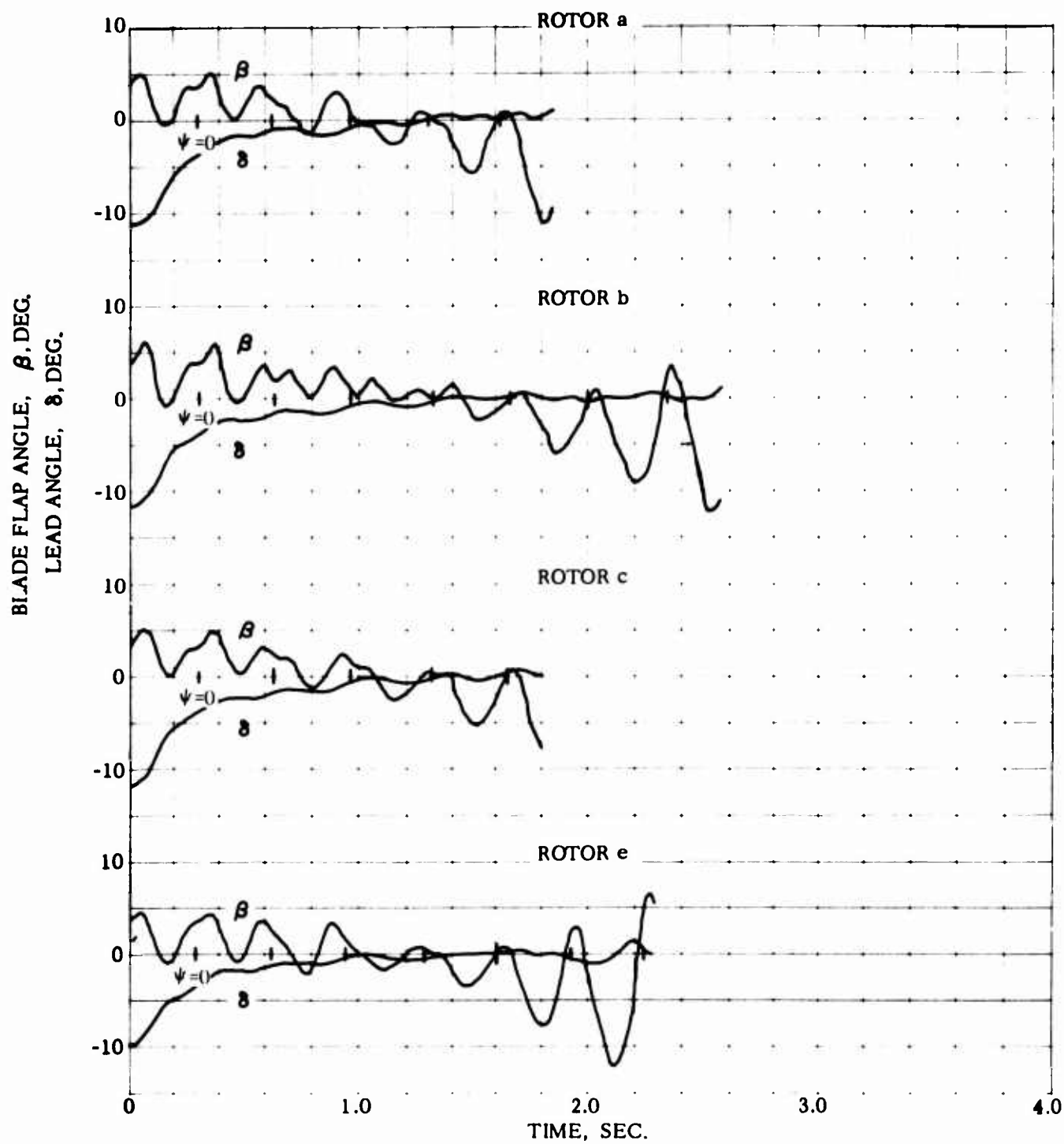


Figure 39. Concluded

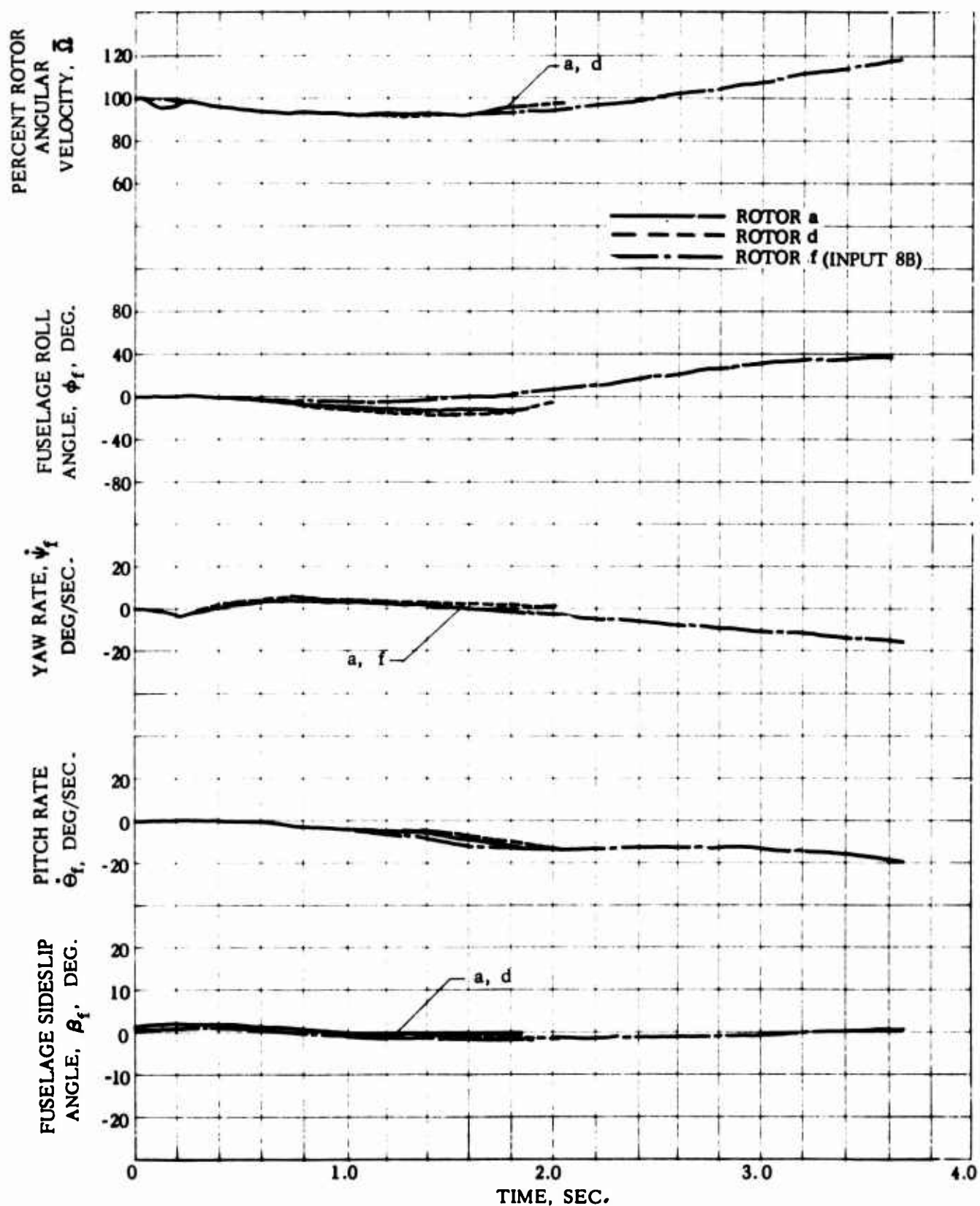


Figure 40. Helicopter and Rotor Blade Motion Following Full Power Loss, $D/L = 0.15$, With Corrective Control Input 6B, Various Rotor Configurations

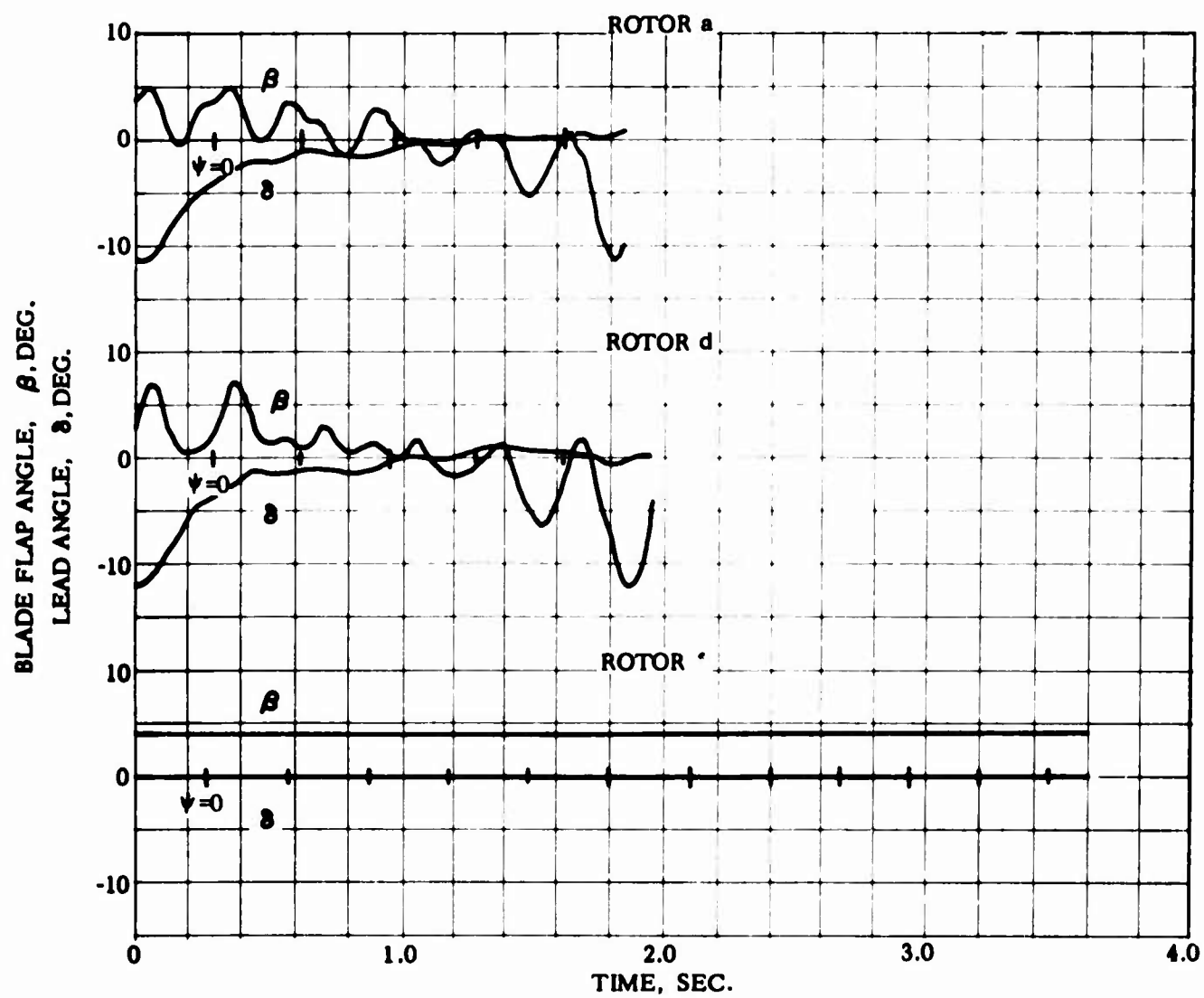


Figure 40. Concluded

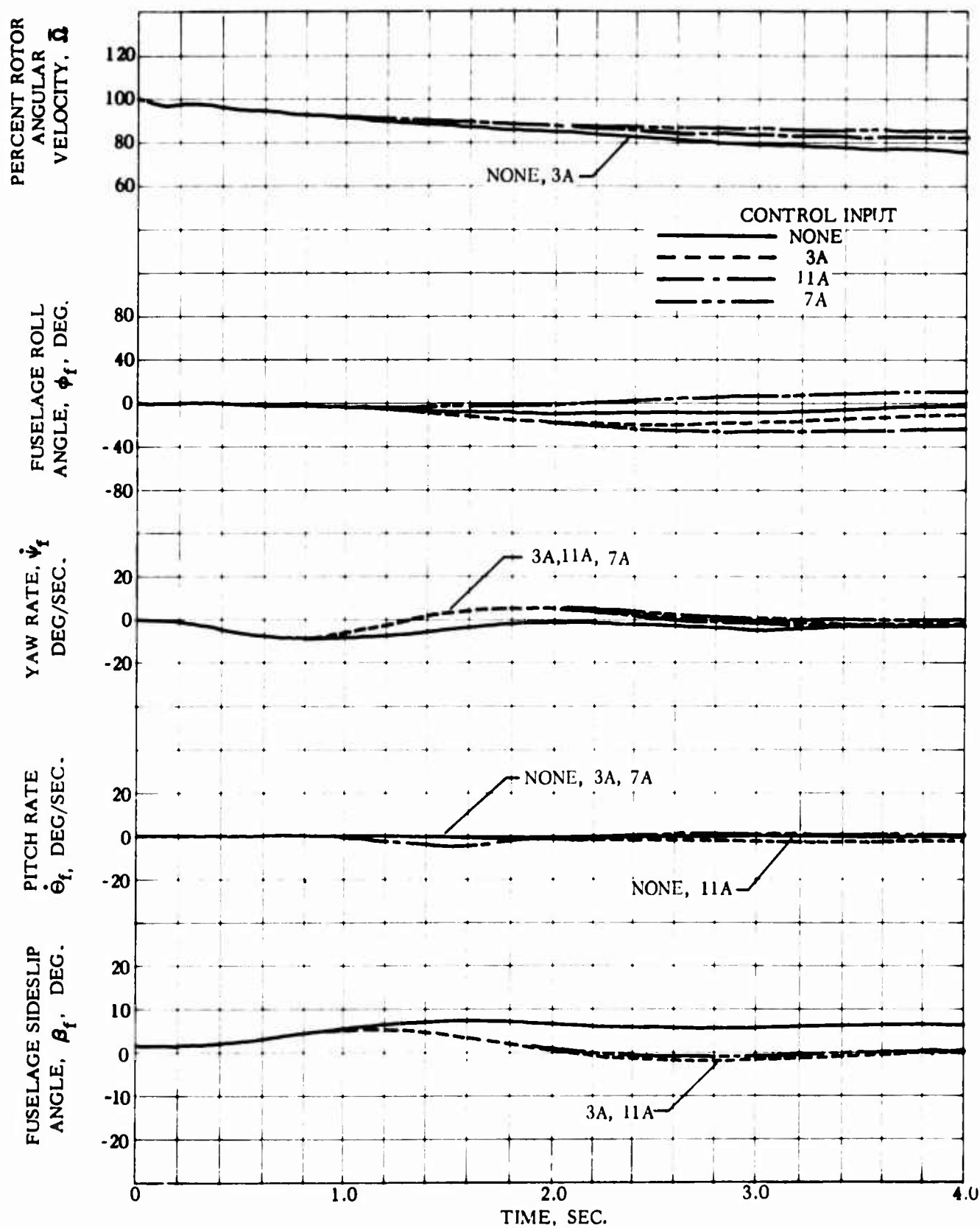


Figure 41. Helicopter and Rotor Blade Motion Following Full Power Loss, $D/L = 0$, With Corrective Control Inputs, Fully Articulated Rotor ($e/R = 0.034$)

BLADE FLAP ANGLE, β , DEG.
LEAD ANGLE, δ , DEG.

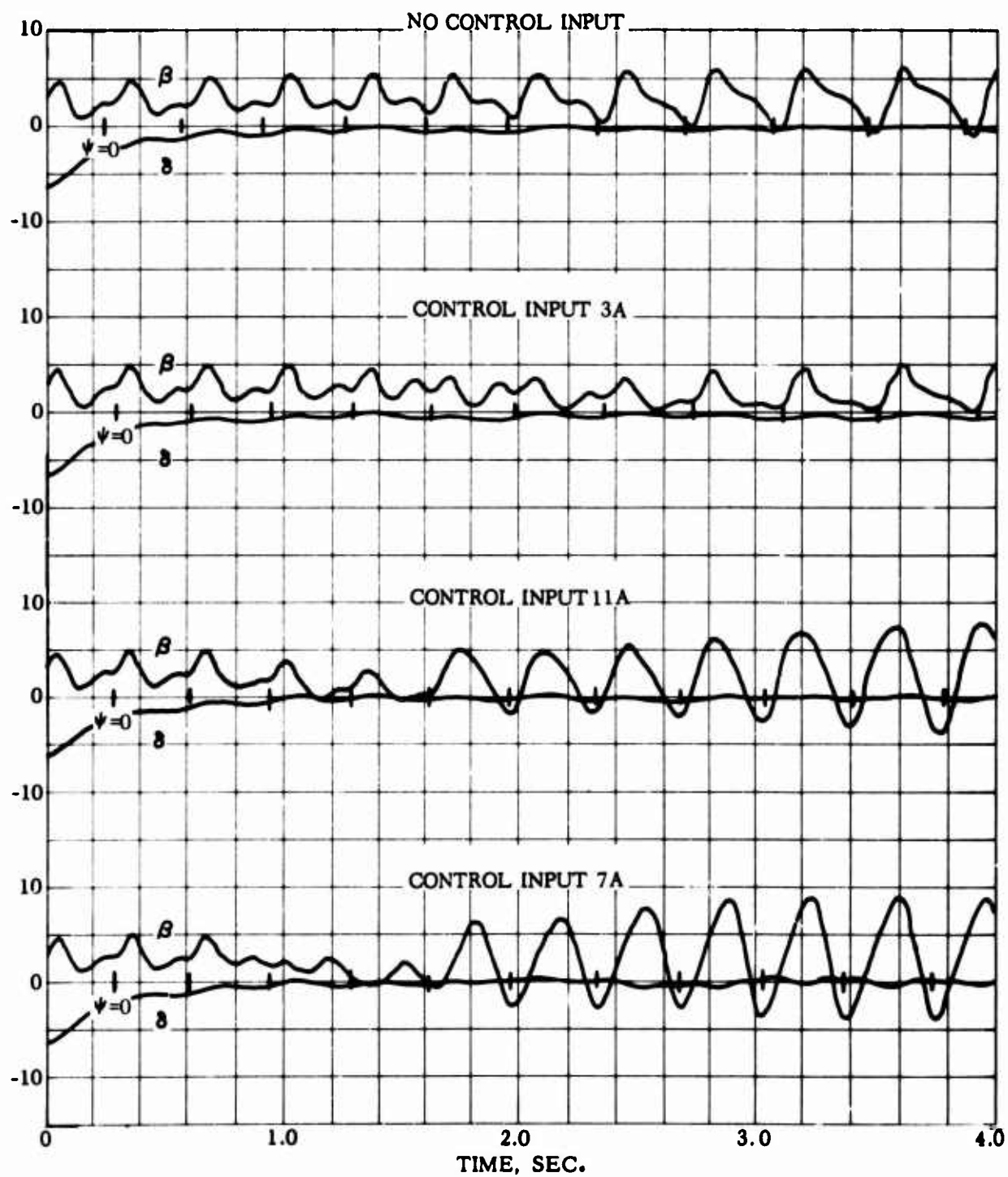


Figure 41. Concluded

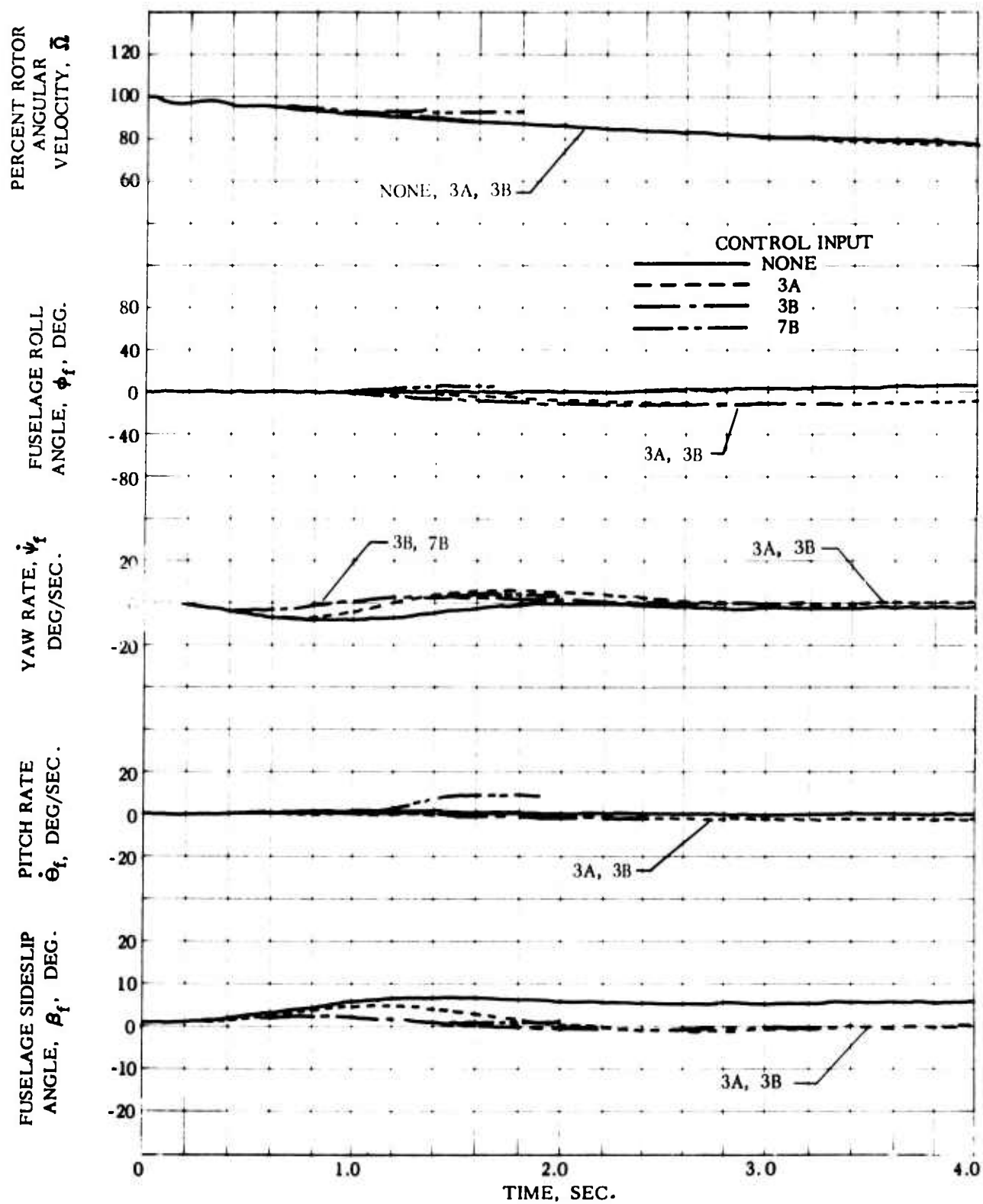


Figure 42. Helicopter and Rotor Blade Motion Following Full Power Loss, $D/L = -0.063$, With Corrective Control Inputs, Fully Articulated Rotor ($e/R = 0.034$)

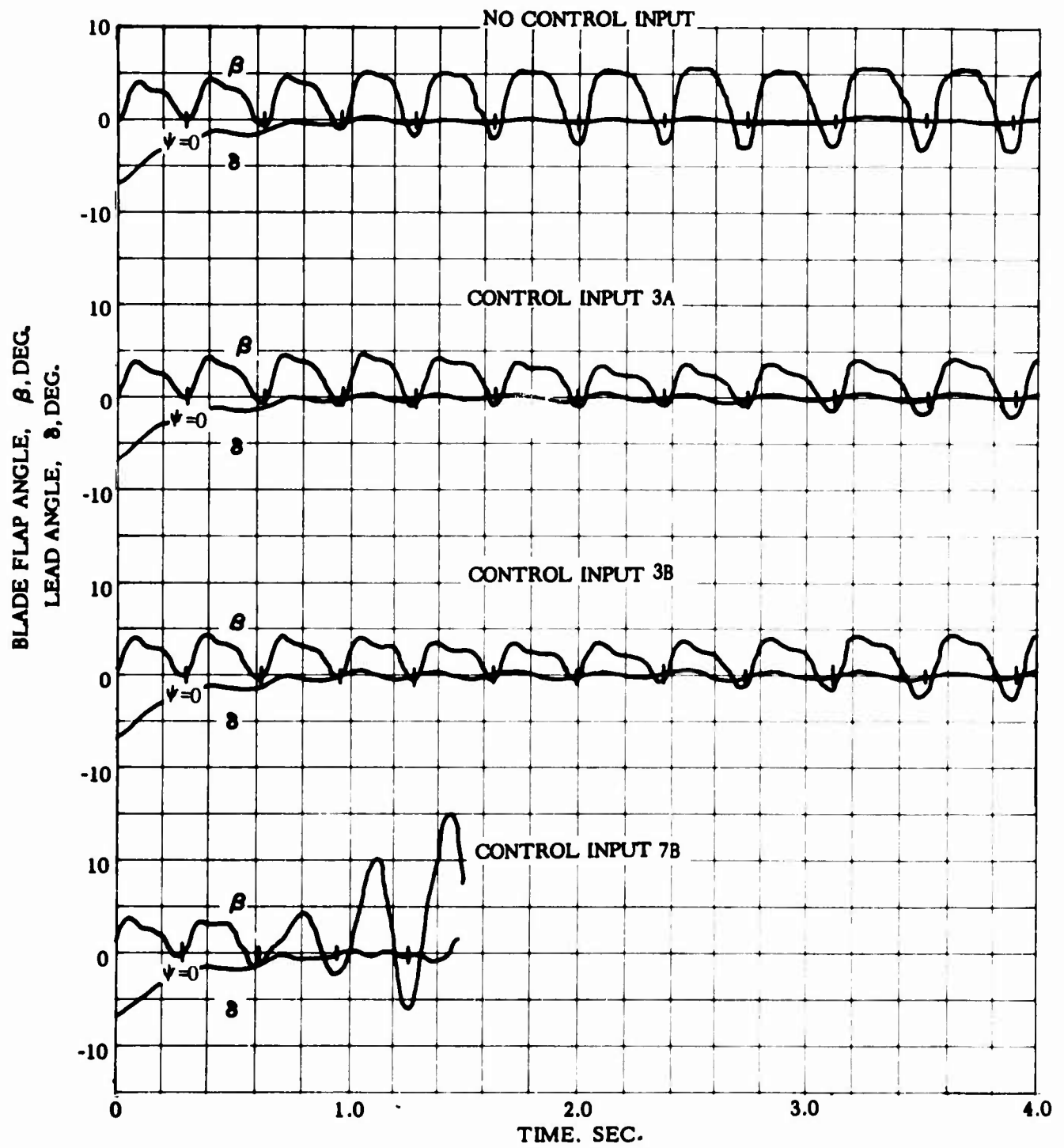


Figure 42. Concluded

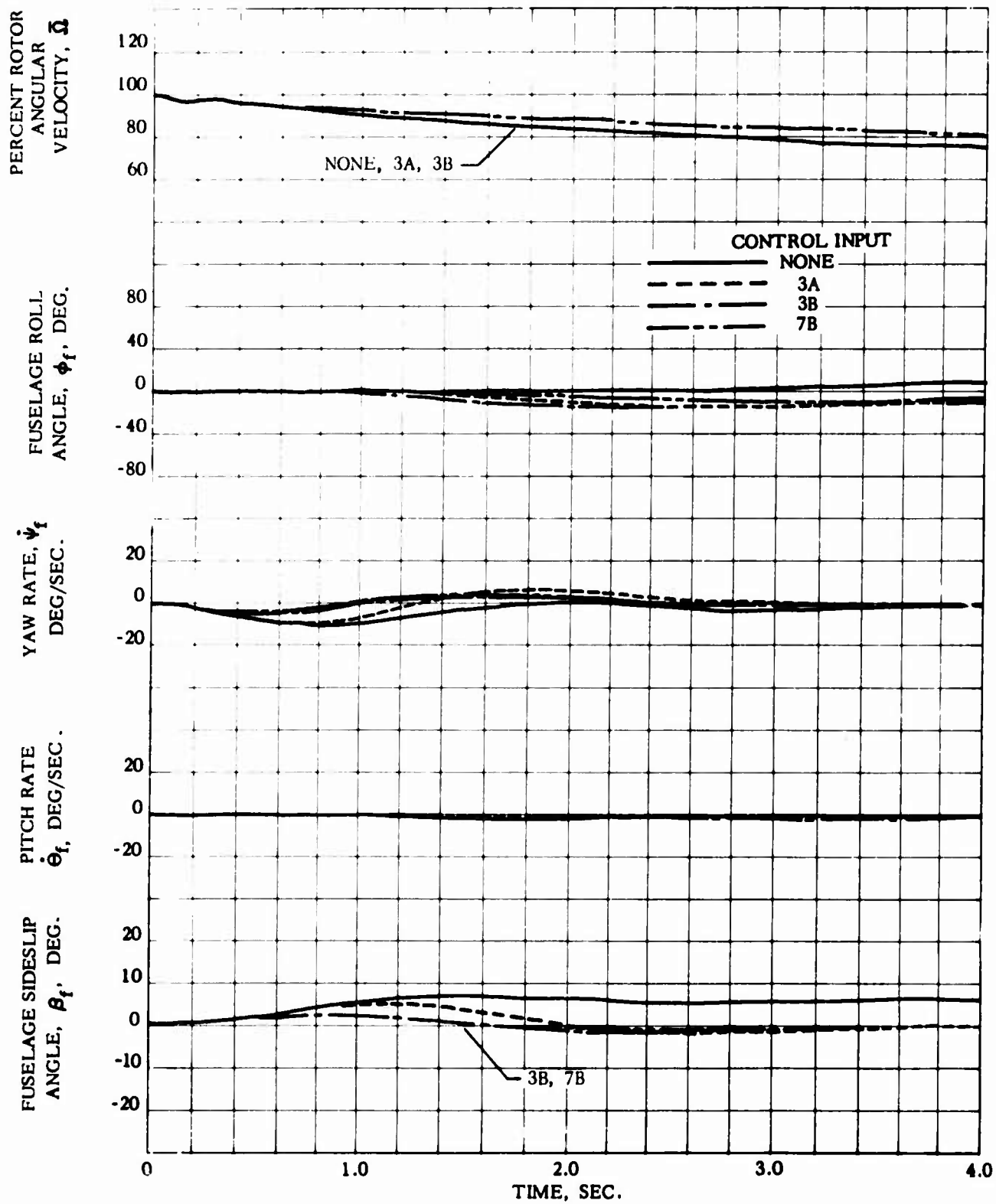


Figure 43. Helicopter and Rotor Blade Motion Following Full Power Loss, $D/L = -0.063$, With Corrective Control Inputs, Rotor With Blade Pitch-Flap Feedback

BLADE FLAP ANGLE, β , DEG.
LEAD ANGLE, δ , DEG.

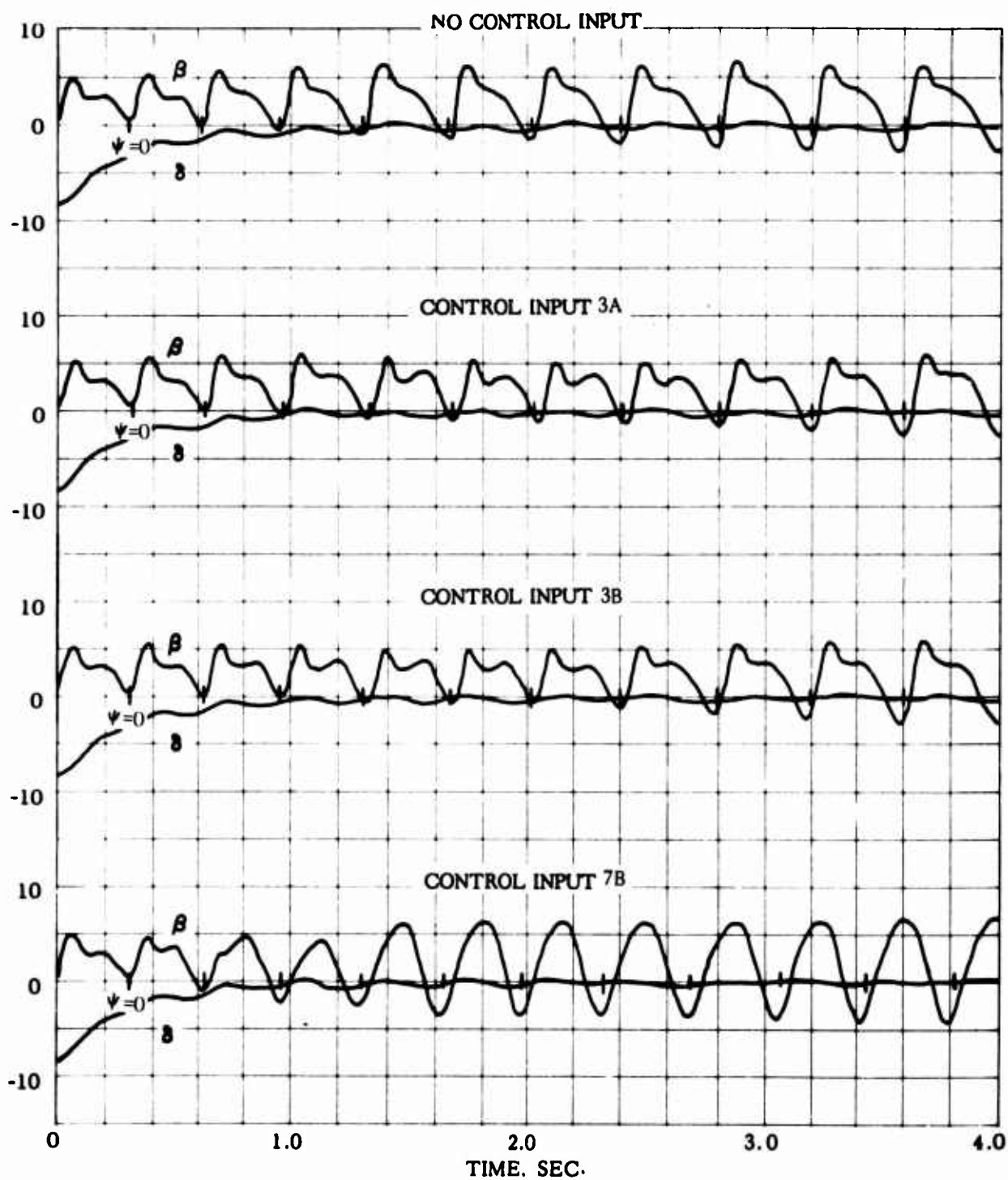


Figure 43. Concluded

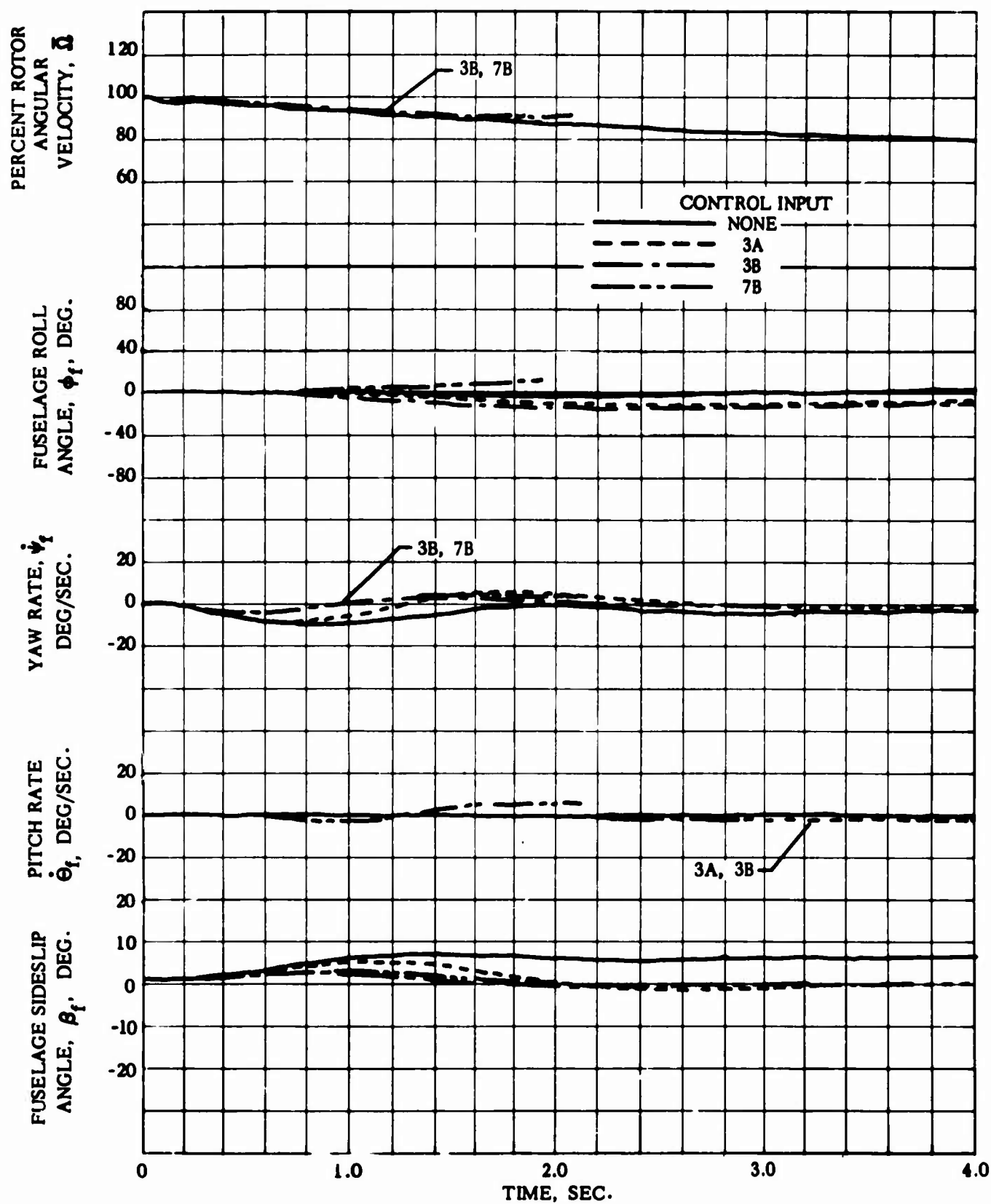


Figure 44. Helicopter and Rotor Blade Motion Following Full Power Loss, $D/L = -0.063$, With Corrective Control Inputs, Rotor With Reduced Lock Number

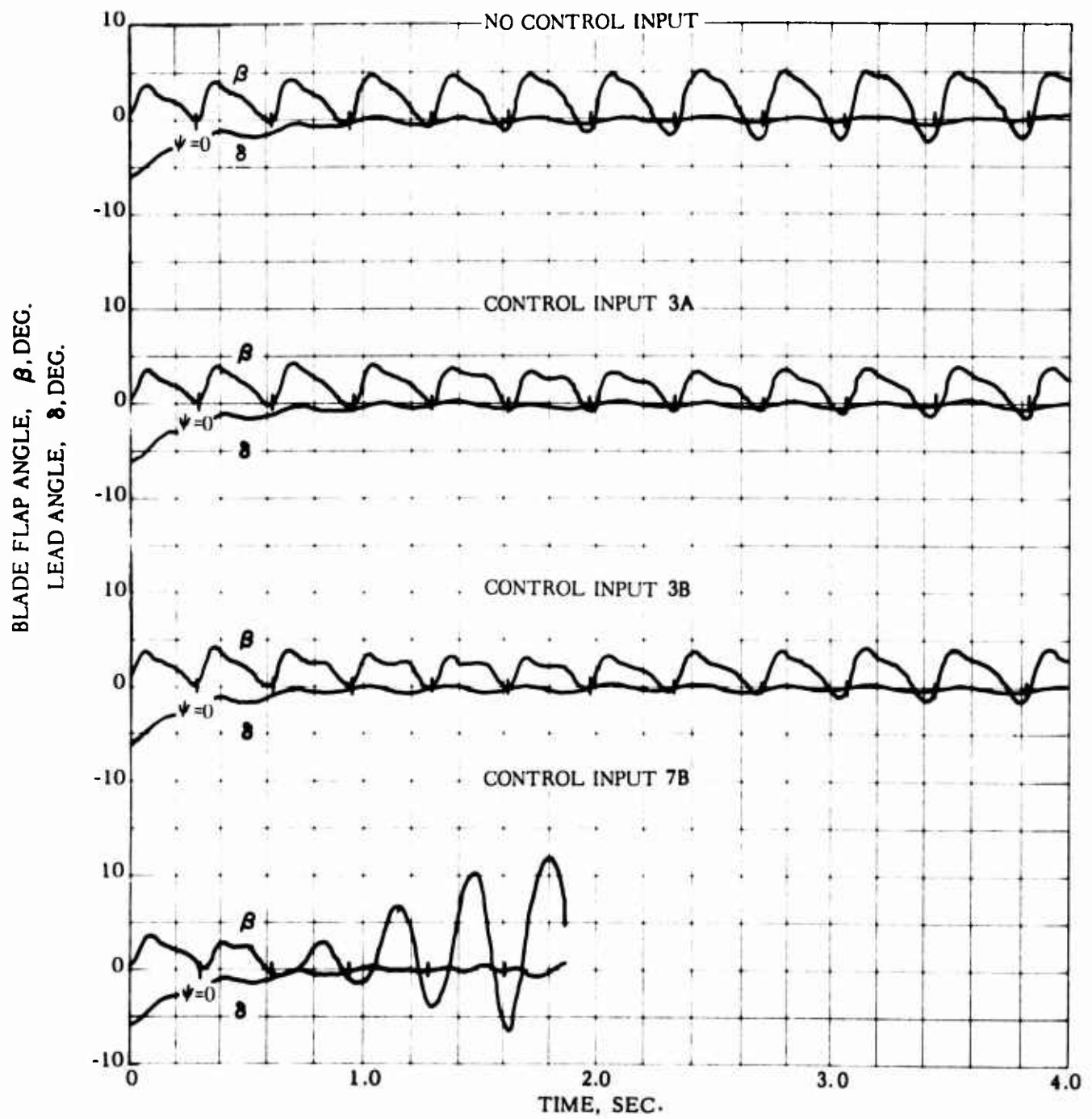


Figure 1'. Concluded

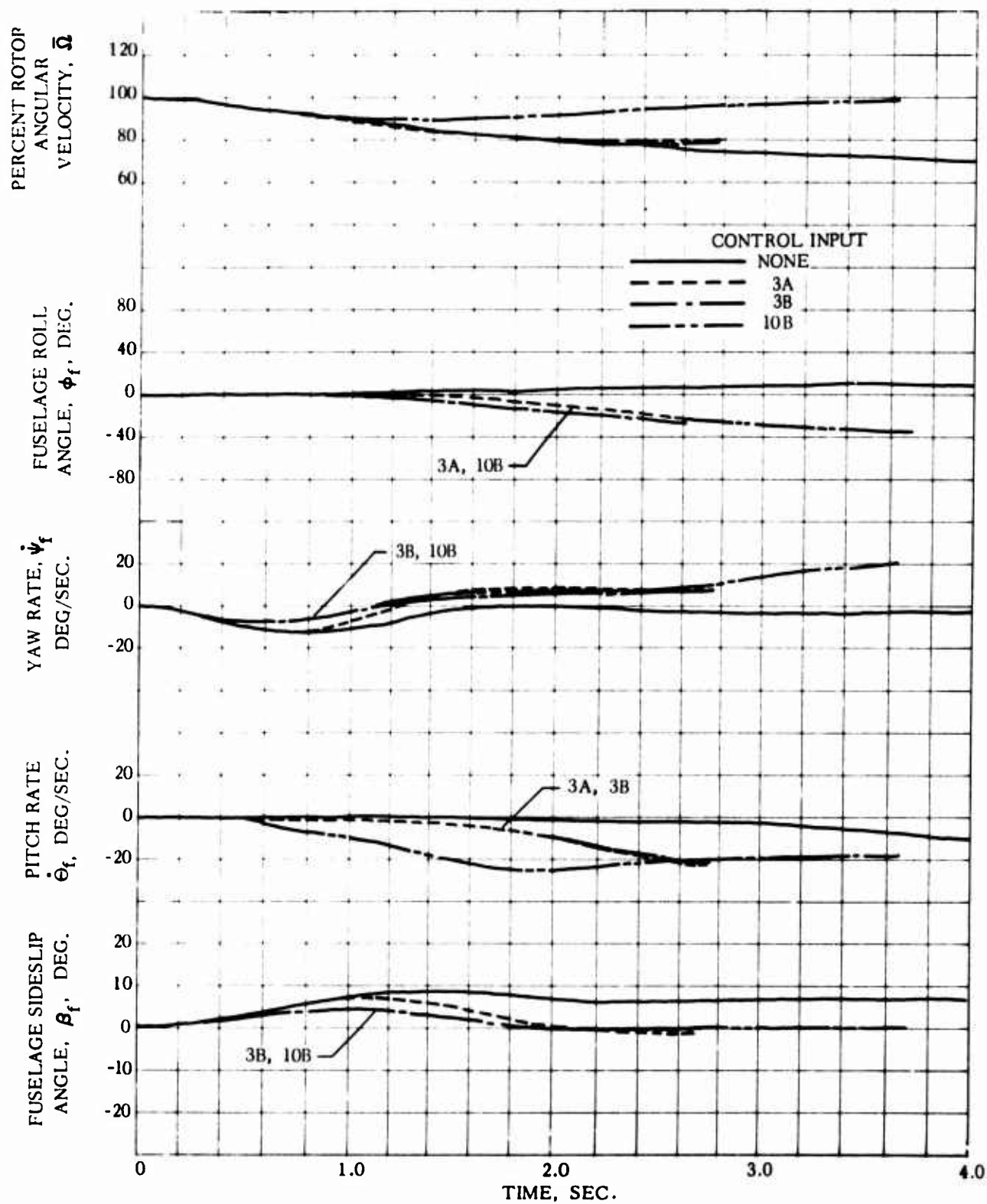


Figure 45. Helicopter and Rotor Blade Motion Following Full Power Loss, $D/L = -0.063$, With Corrective Control Inputs, Hingeless Rotor

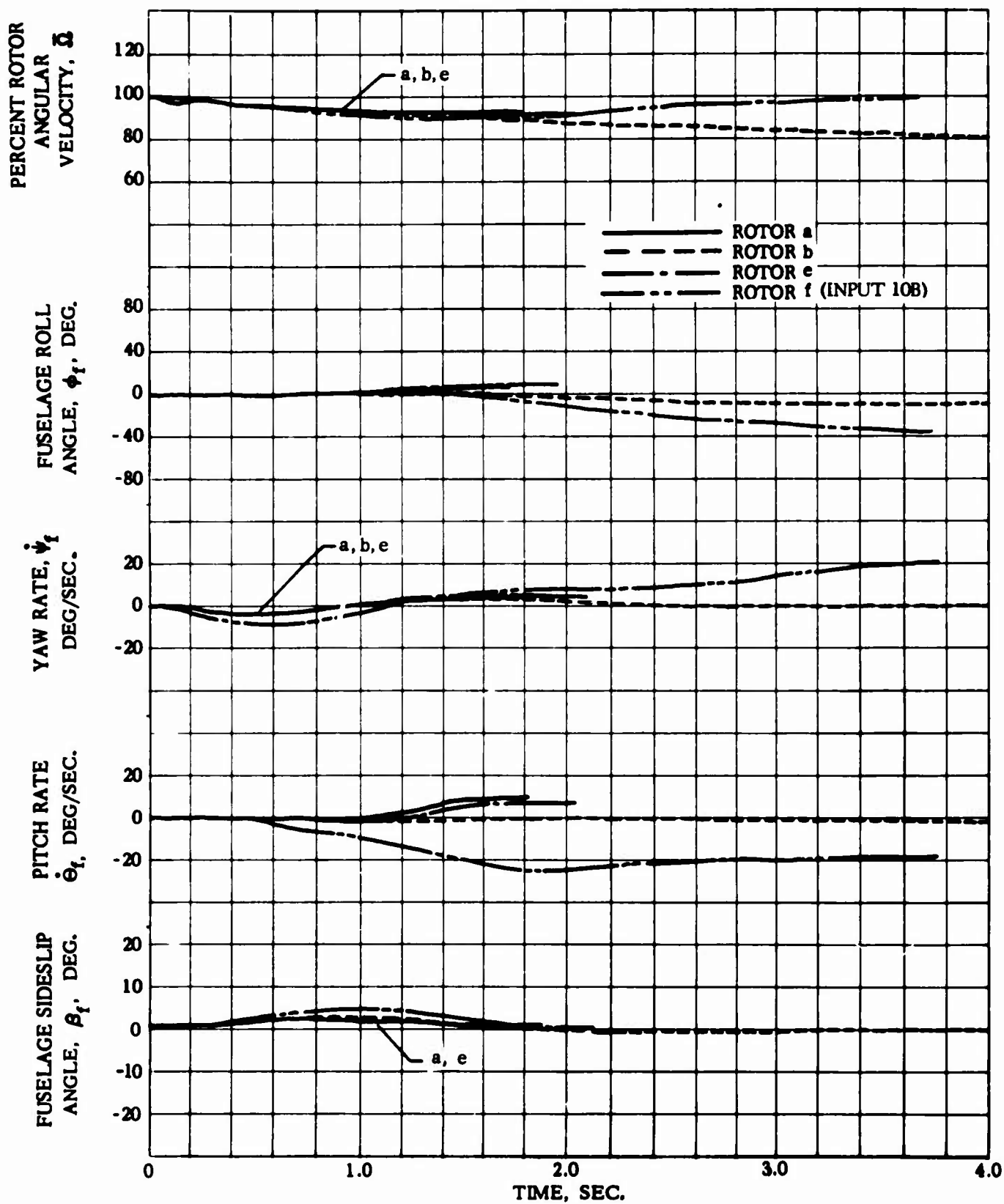


Figure 46. Helicopter and Rotor Blade Motion Following Full Power Loss, $D/L = -0.063$, With Corrective Control Input 7B, Various Rotor Configurations

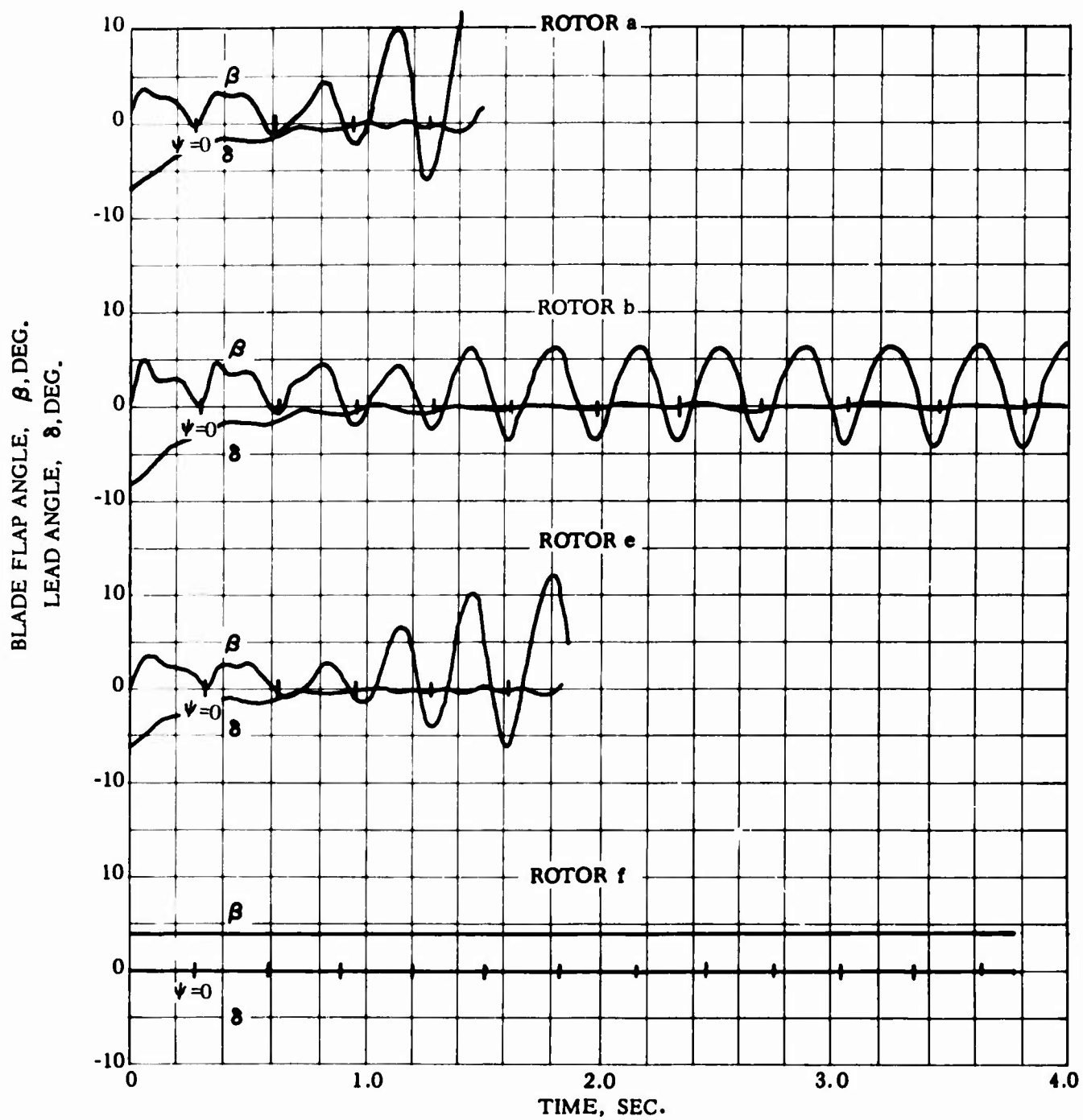


Figure 46. Concluded

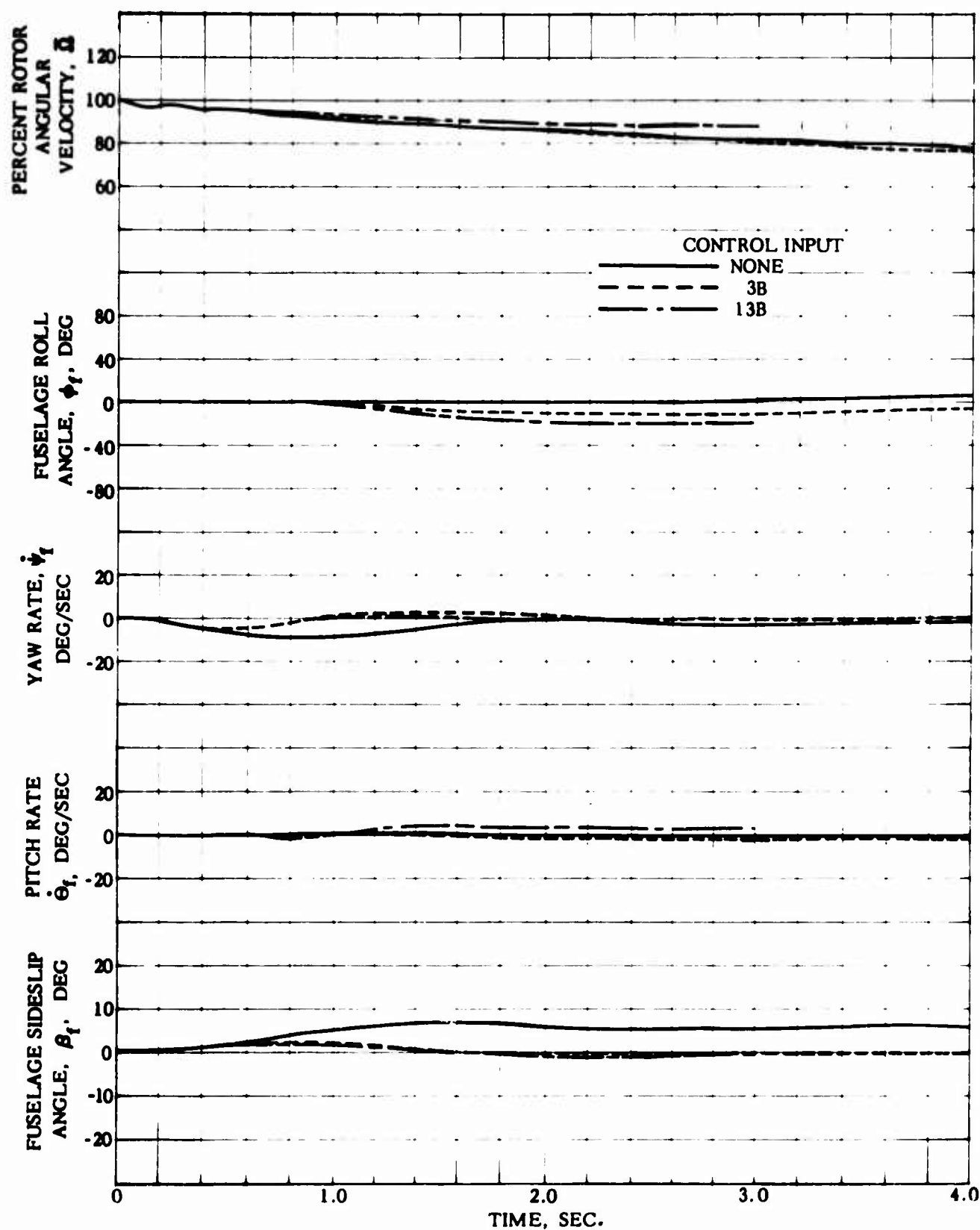


Figure 47. Helicopter and Rotor Blade Motion Following Full Power Loss, $D/L = -0.063$, With Corrective Control Inputs, Fully Articulated Rotor ($e/R = 0.034$)

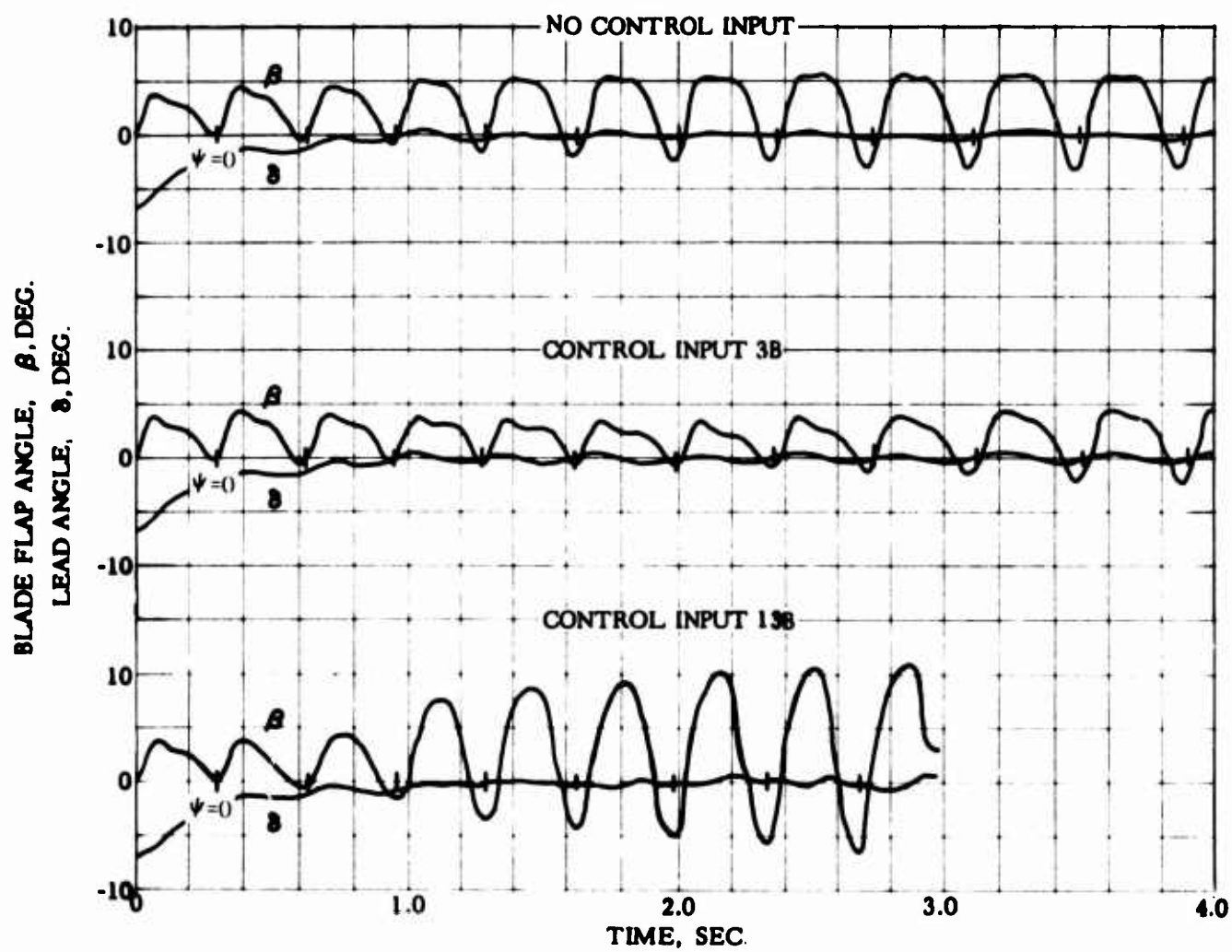


Figure 47. Concluded

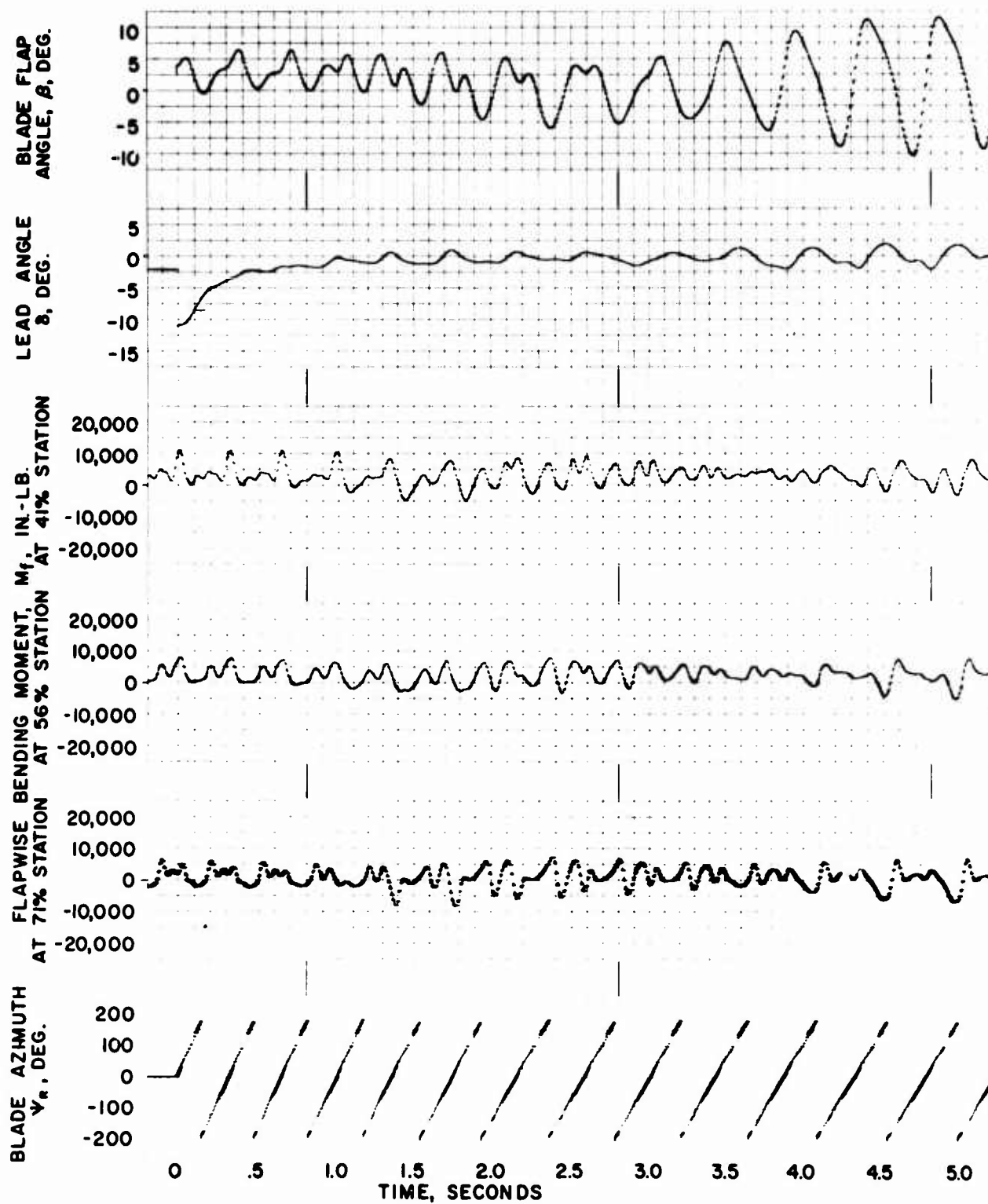


Figure 48. Fully Articulated Rotor ($e/R = 0.034$), Full Power Loss, $D/L = 0.15$, No Corrective Control Input, Multiple Bending Moment Data

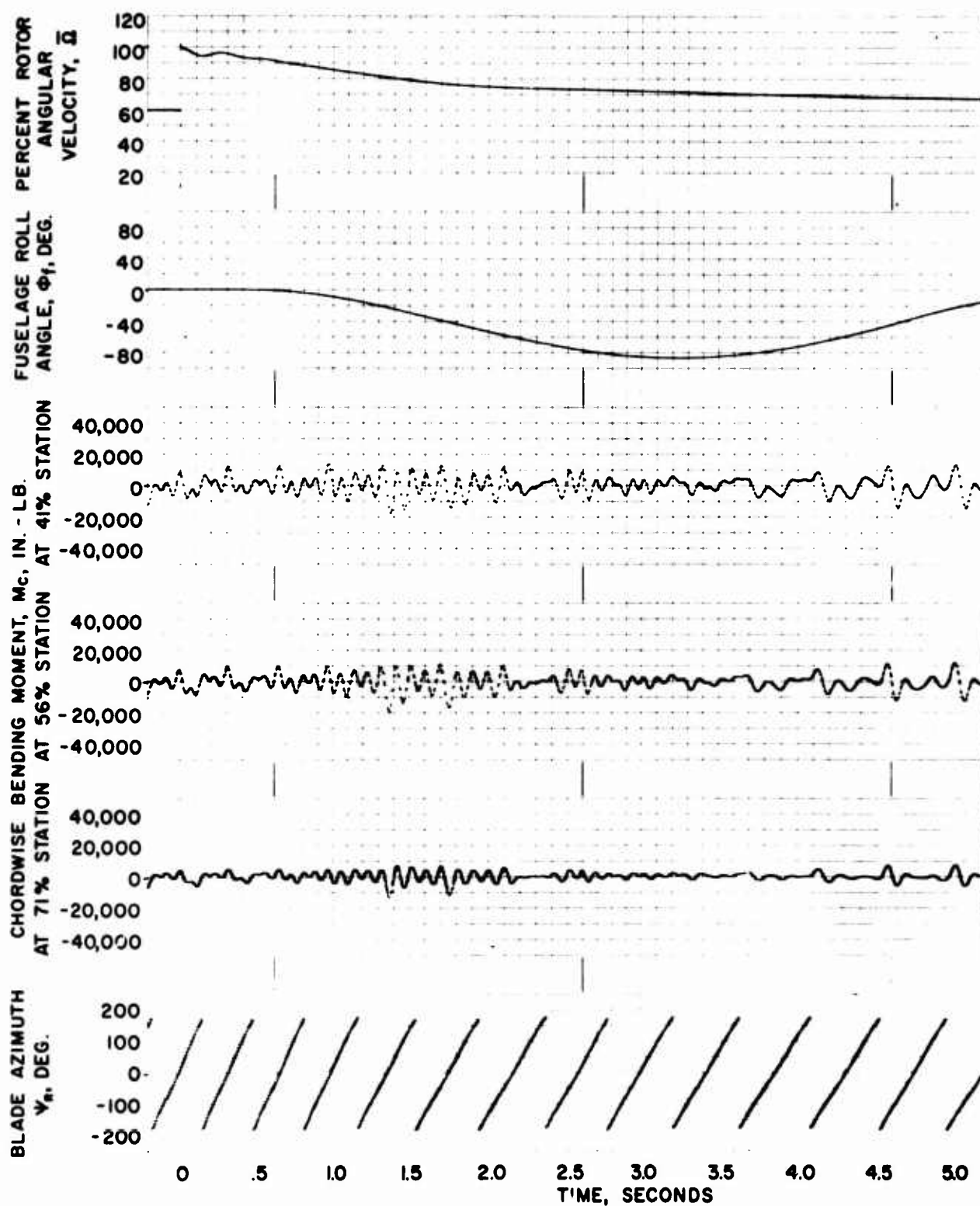


Figure 48. Continued

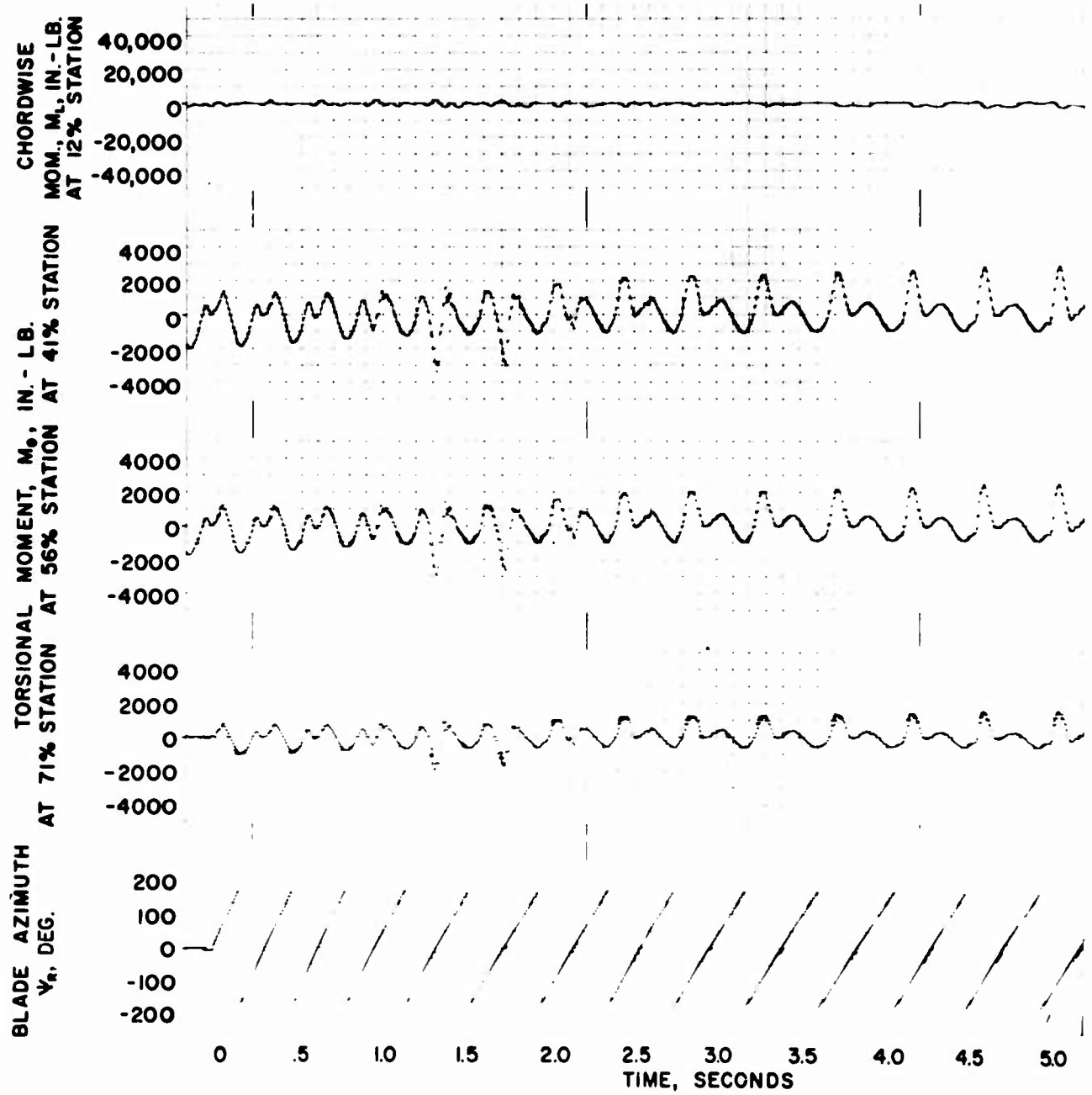


Figure 48. Concluded

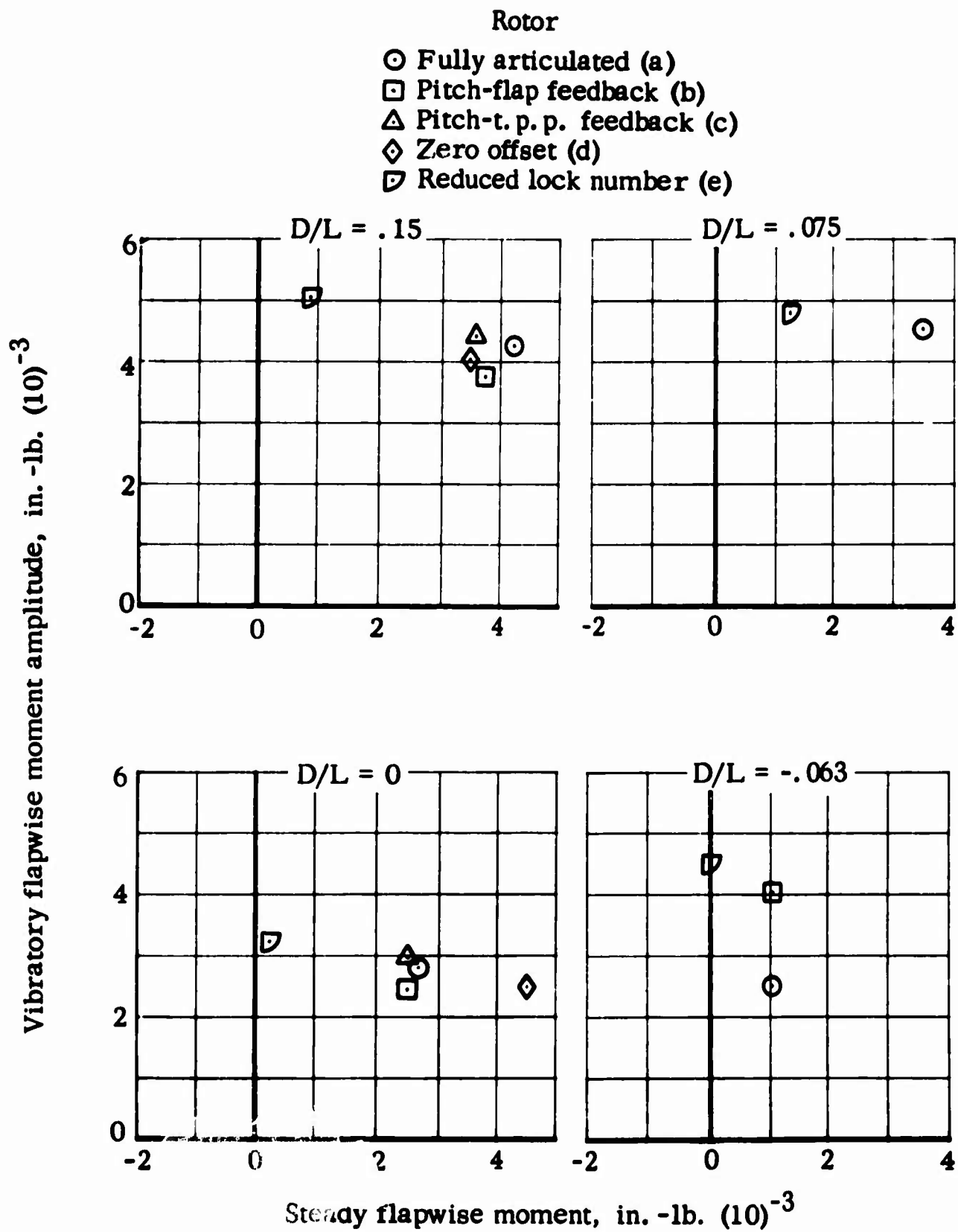


Figure 4.2. Trim Flapwise Moment Characteristics ($r/R = 56\%$), Various Rotor Configurations and Drag-To-Lift Ratios

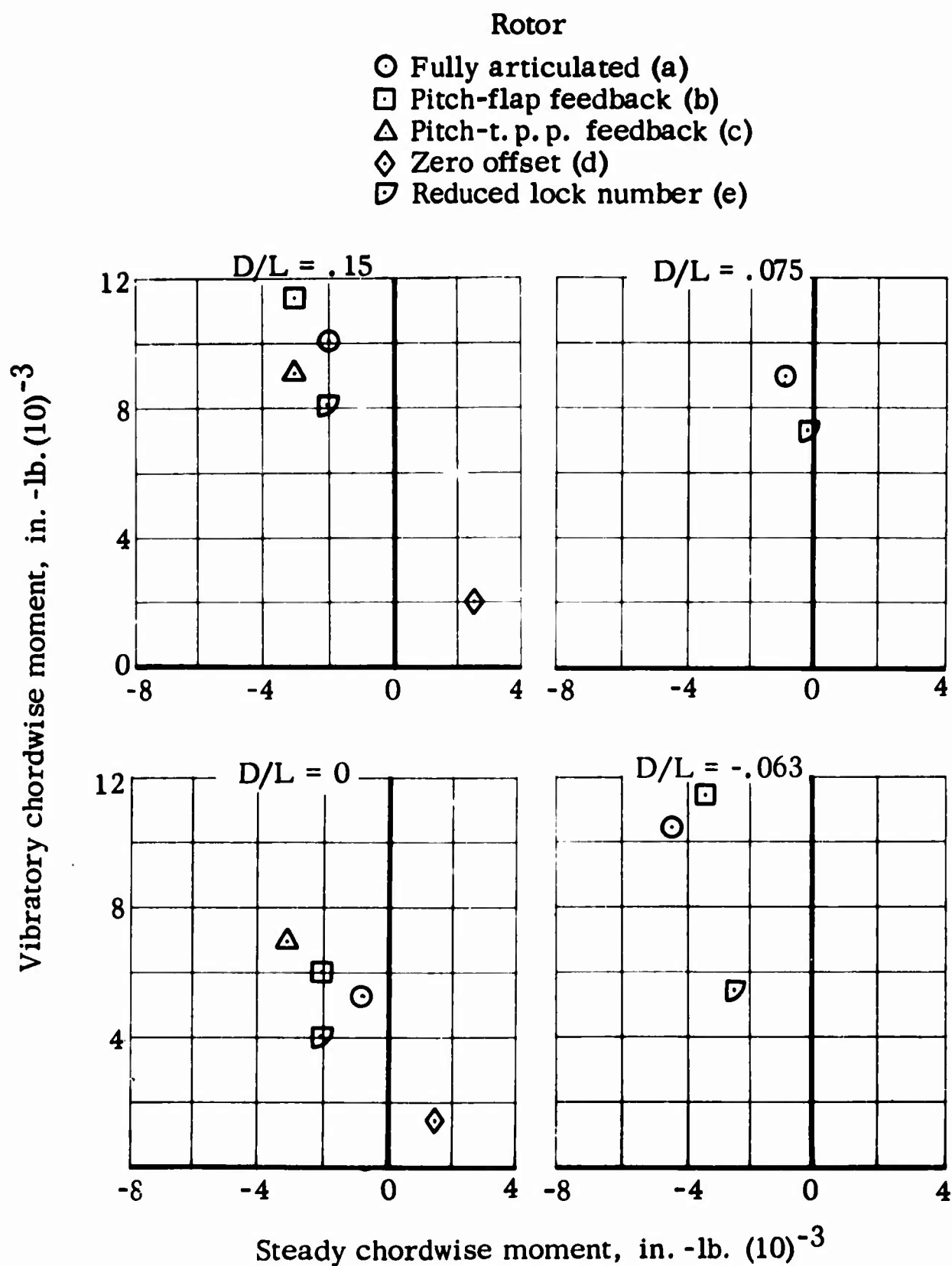


Figure 50. Trim Chordwise Moment Characteristics ($r/R = 56\%$), Various Rotor Configurations and Drag-To-Lift Ratios

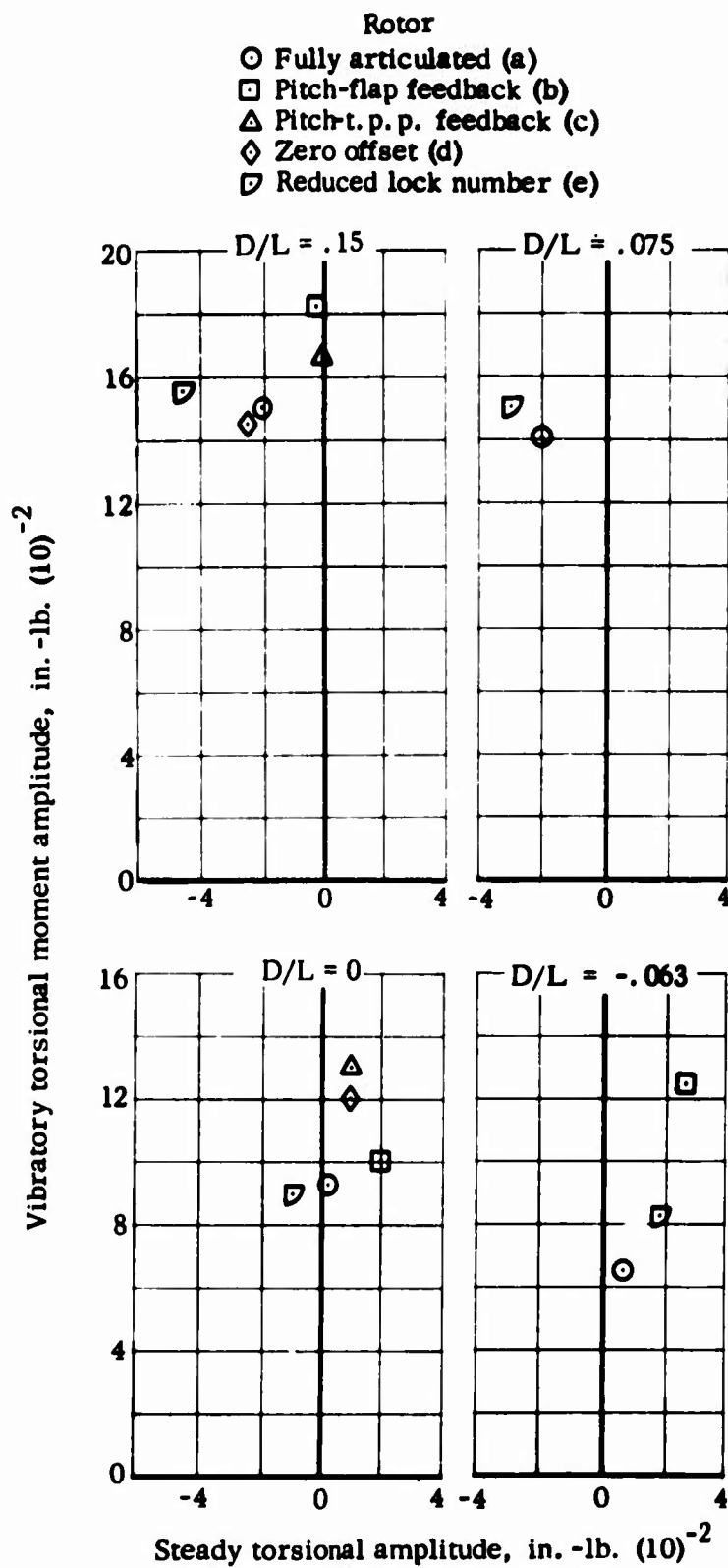


Figure 51. Trim Torsional Moment Characteristics ($r/R = 56\%$), Various Rotor Configurations and Drag-To-Lift Ratios

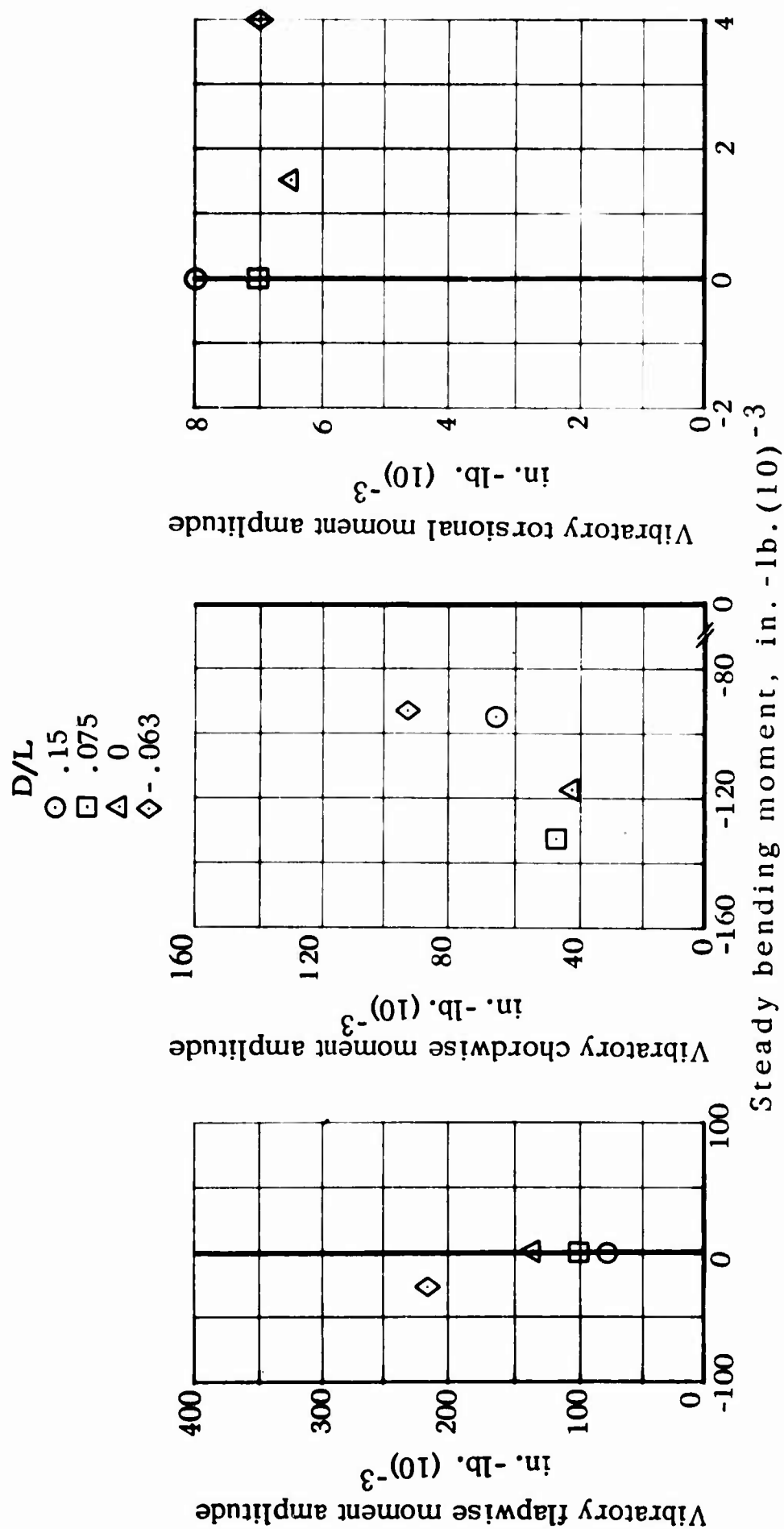


Figure 52. Hingeless Rotor Trim Bending Moment Characteristics
($r/R = 22.5\%$), Various Drag-To-Lift Ratios

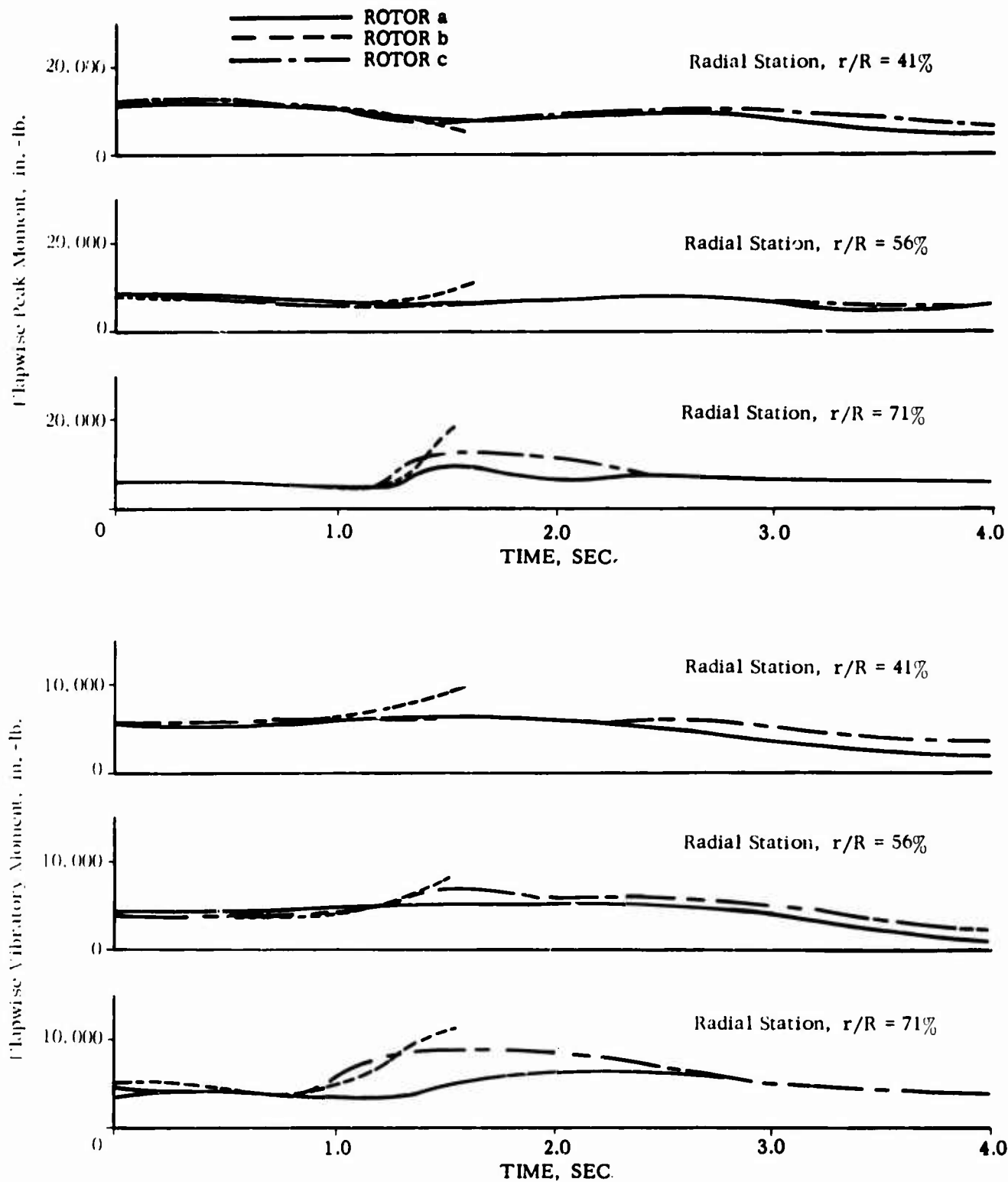


Figure 53. Rotor Blade Vibratory and Peak Moment Variation
Full Power Loss, $D/L = 0.15$, No Corrective Control
Inputs, Pitch-Blade Motion Feedback Rotor
Configurations

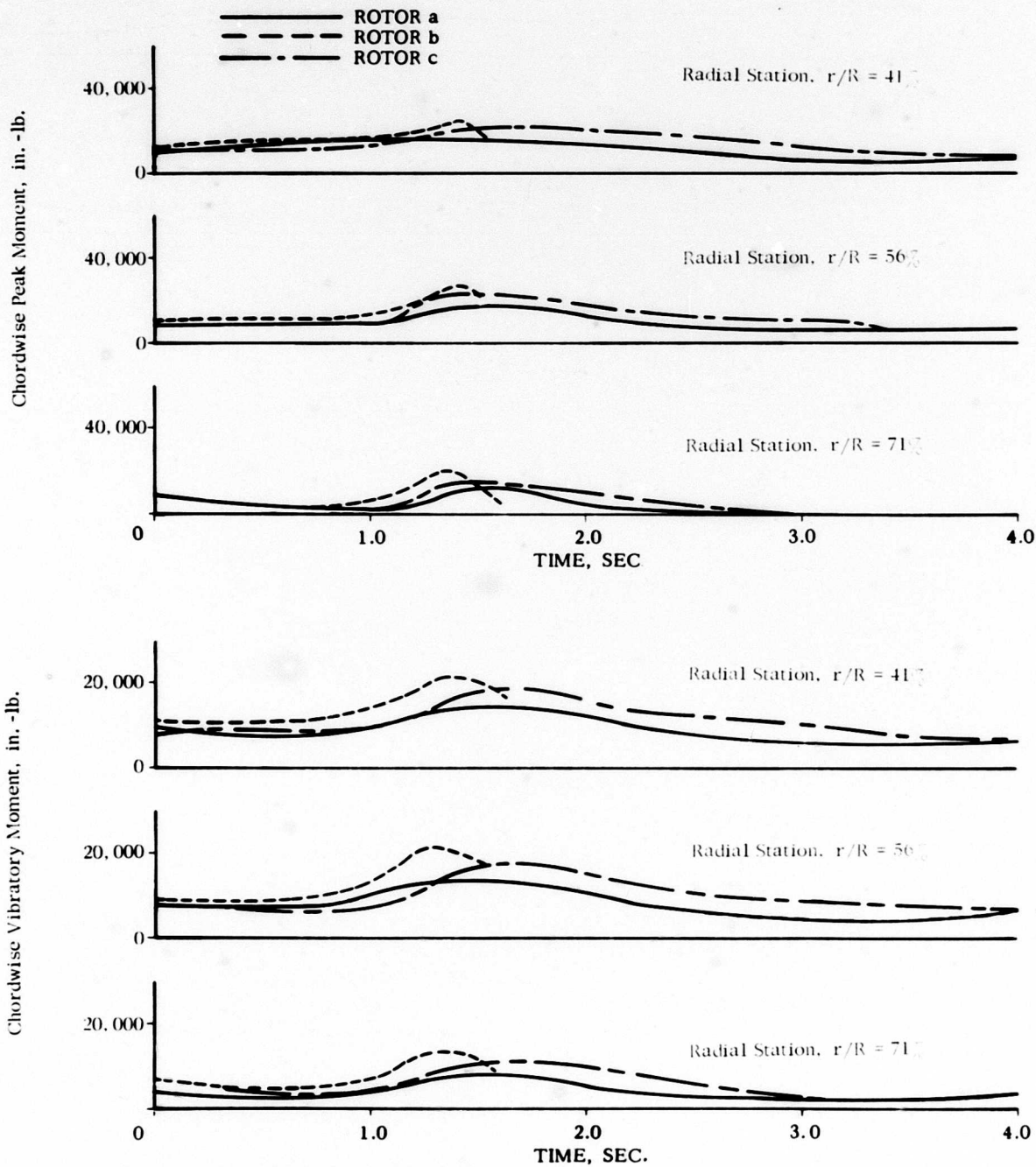


Figure 53. Continued

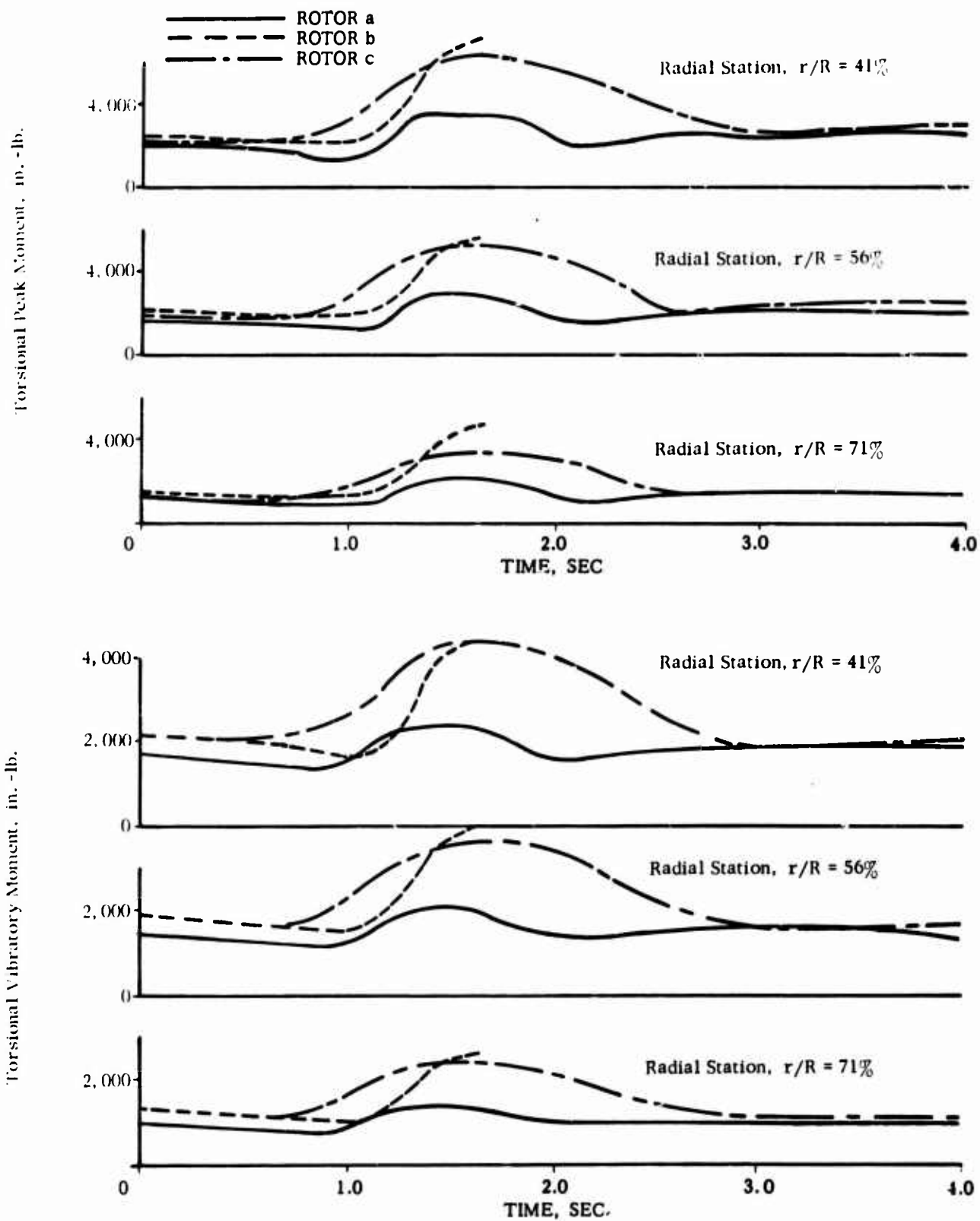


Figure 53. Concluded

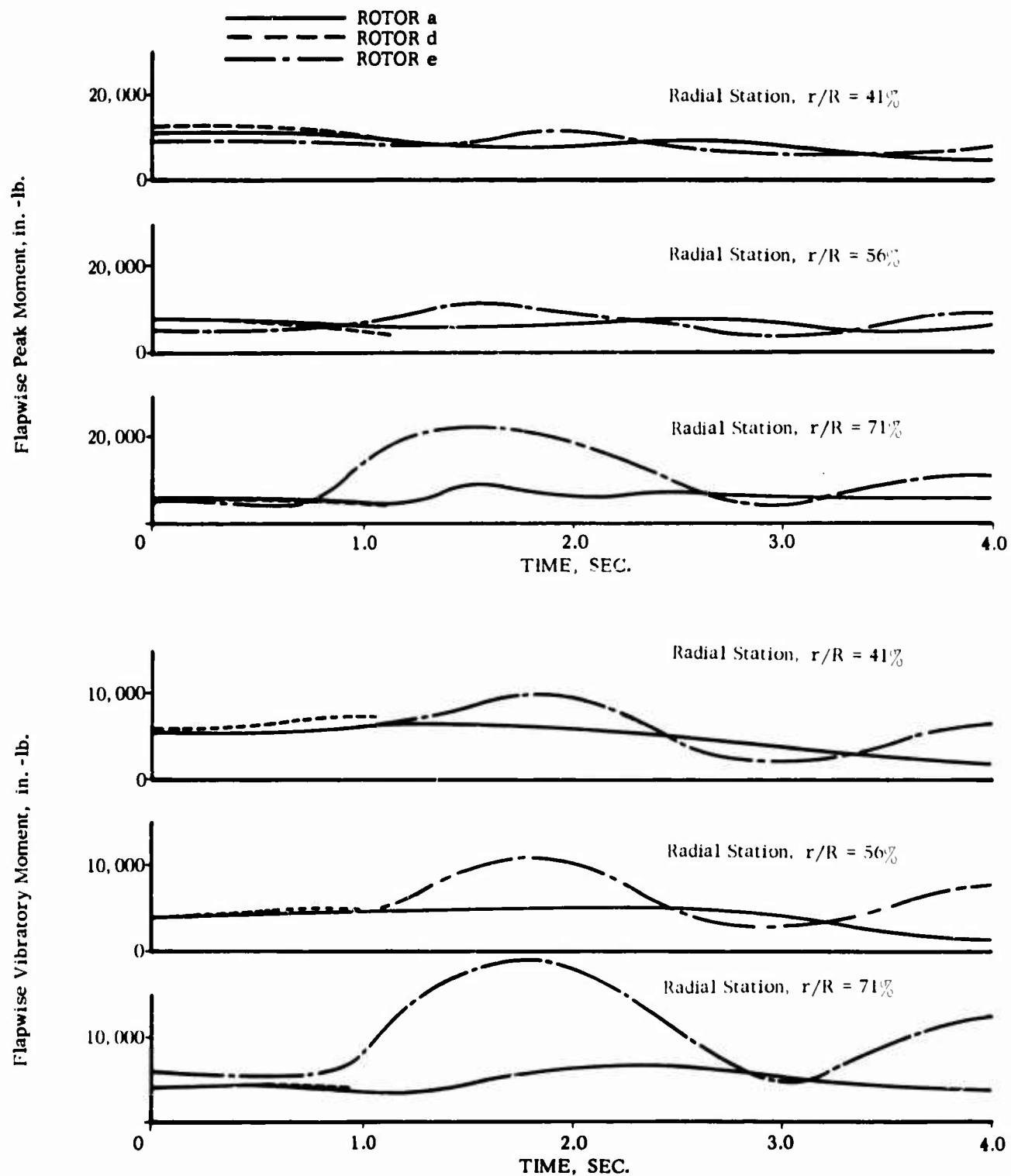


Figure 54. Rotor Blade Vibratory and Peak Moment Variation, Full Power Loss, $D/L = 0.15$, No Corrective Control Inputs, Various Rotor Configurations

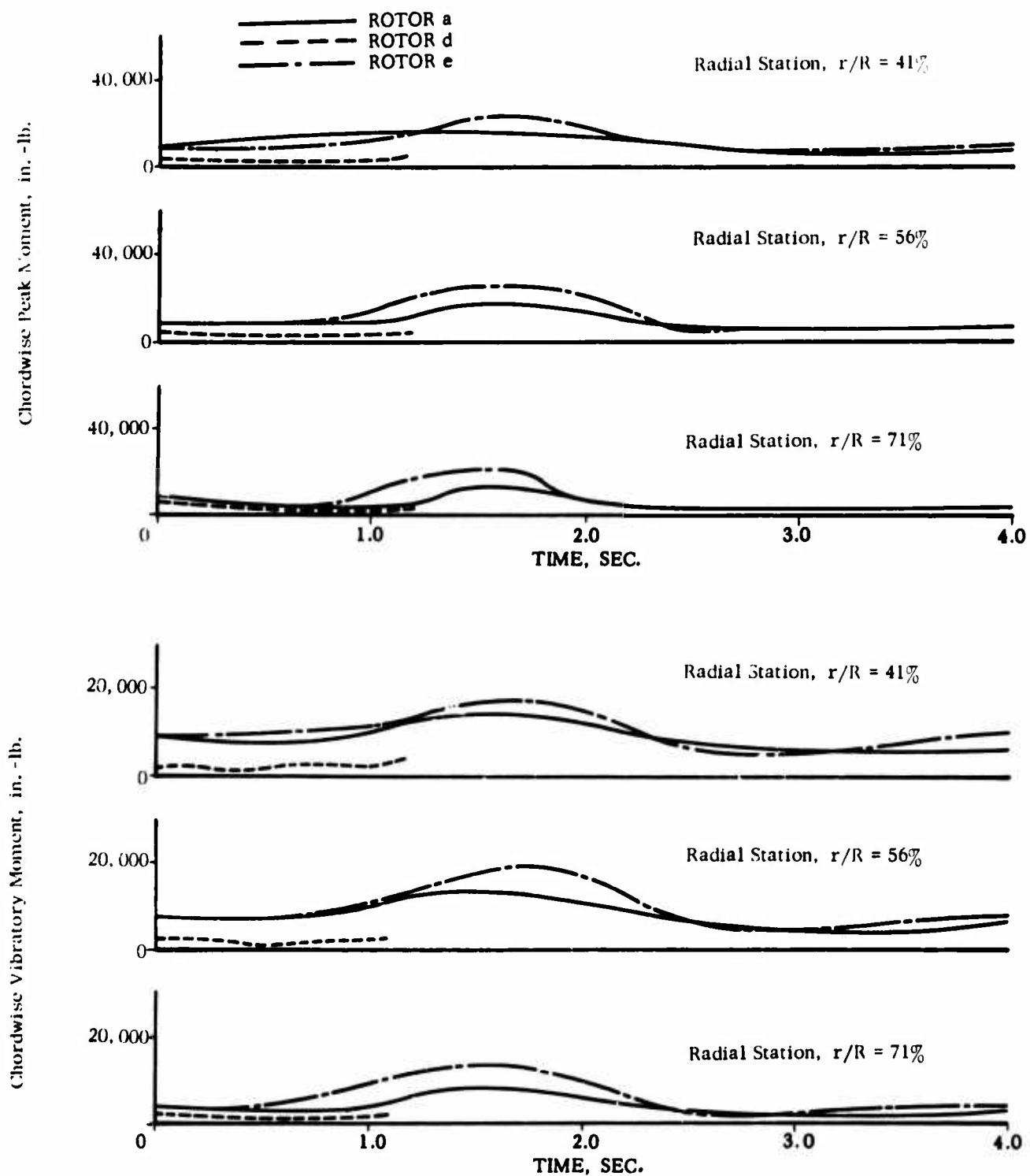


Figure 54. Continued

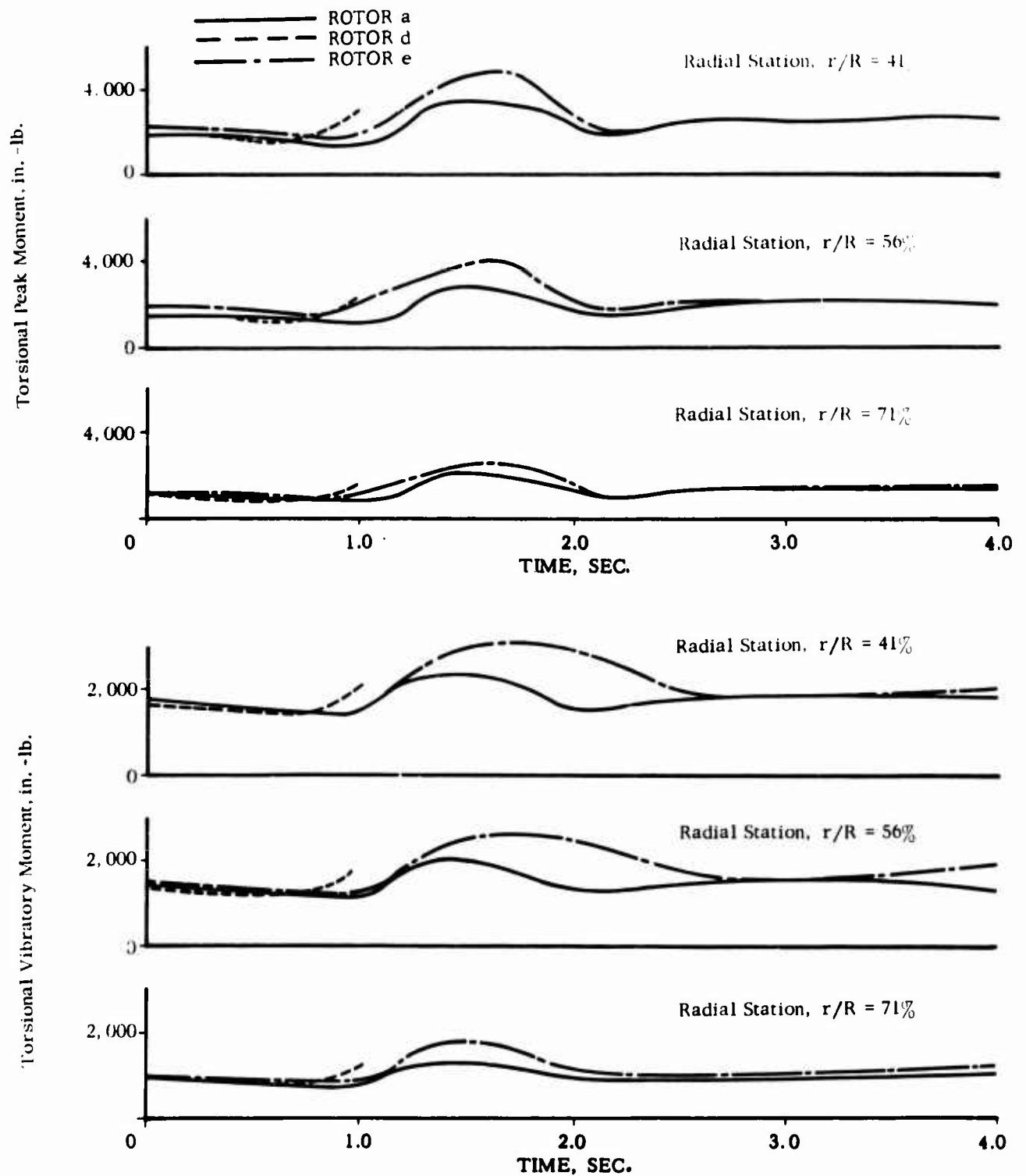


Figure 54. Concluded

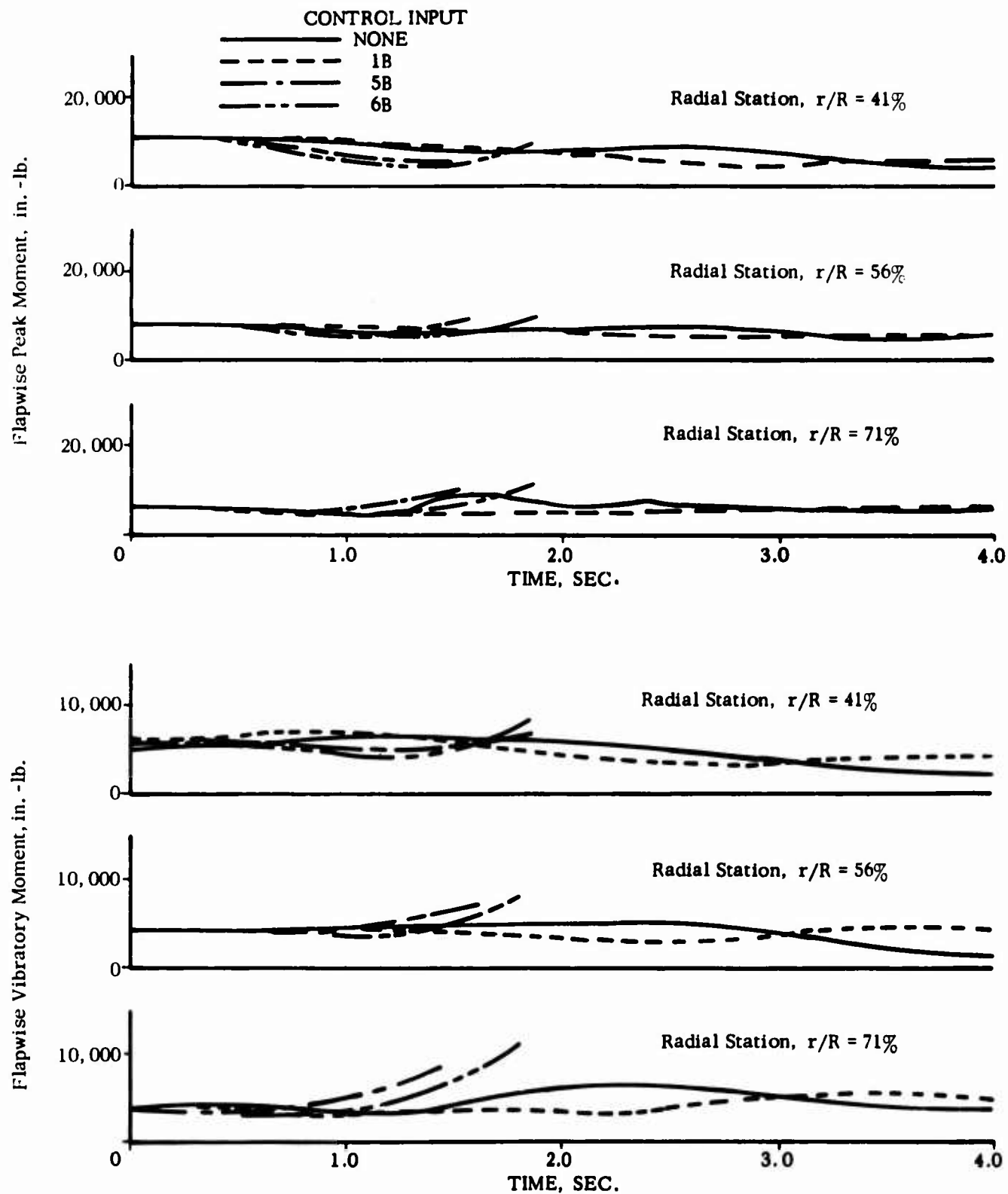


Figure 55. Rotor Blade Vibratory and Peak Moment Variation, Full Power Loss, $D/L = 0.15$, Various Corrective Control Inputs, Fully Articulated Rotor ($e/R = 0.034$)

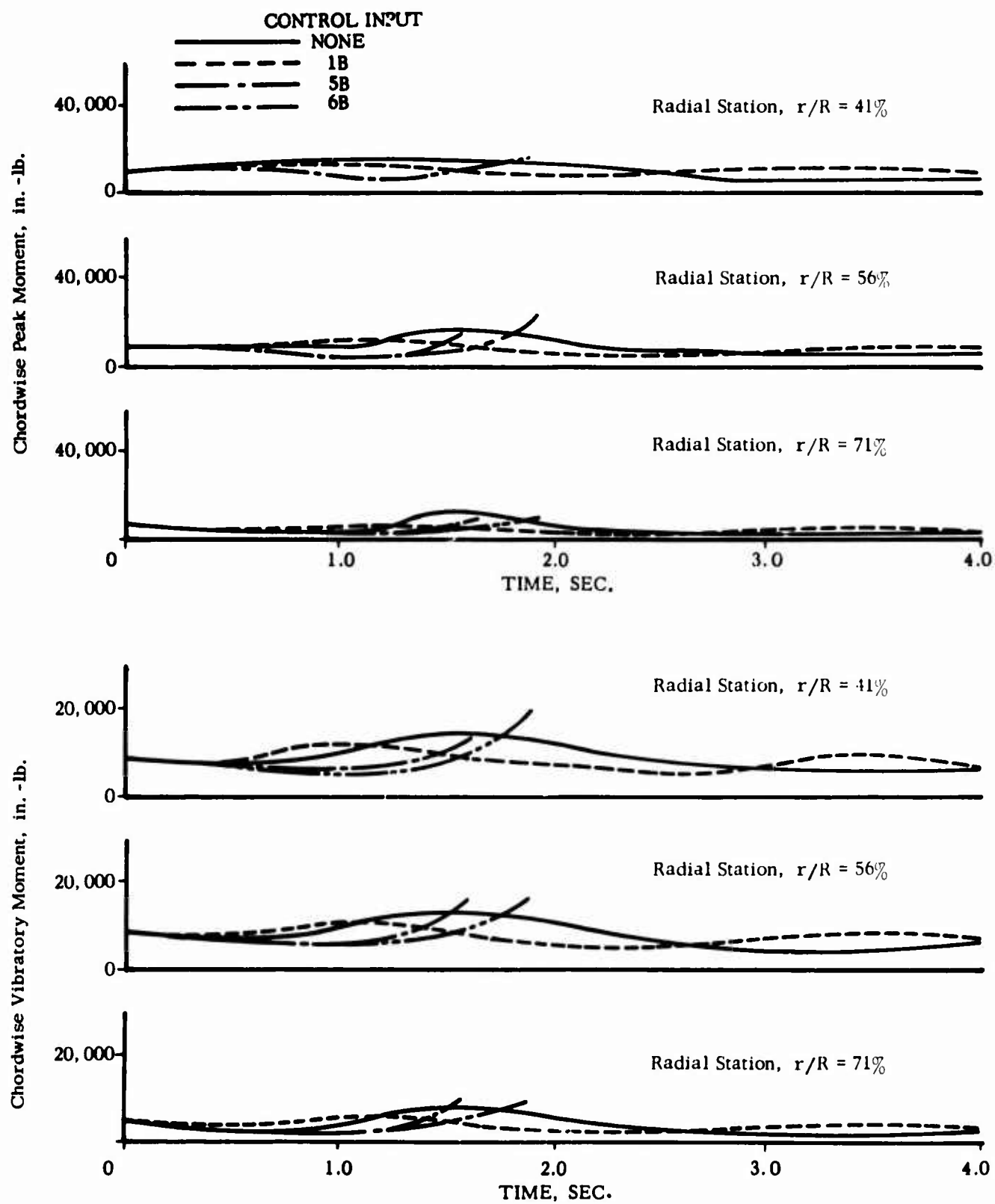


Figure 55. Continued

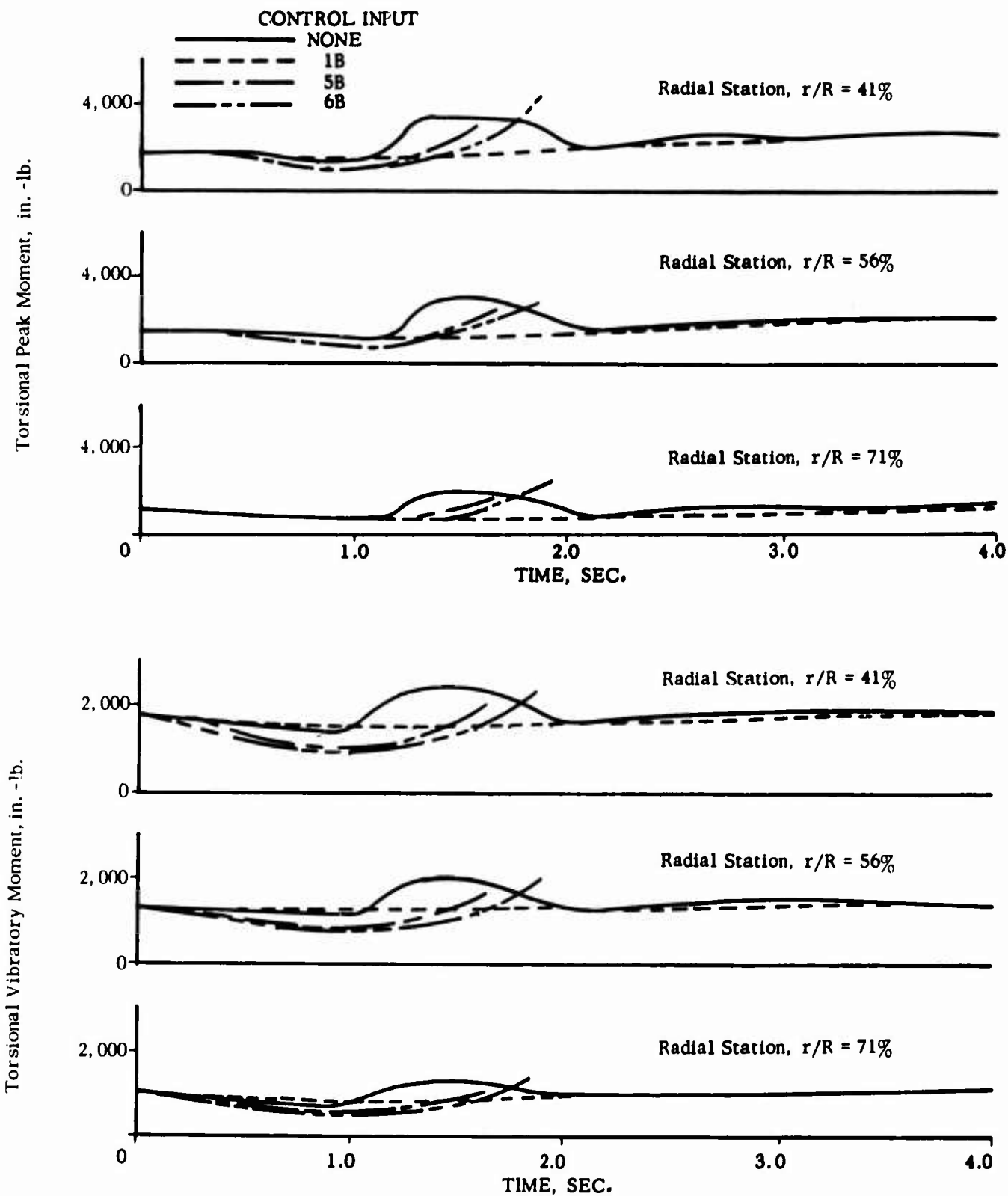


Figure 55. Concluded

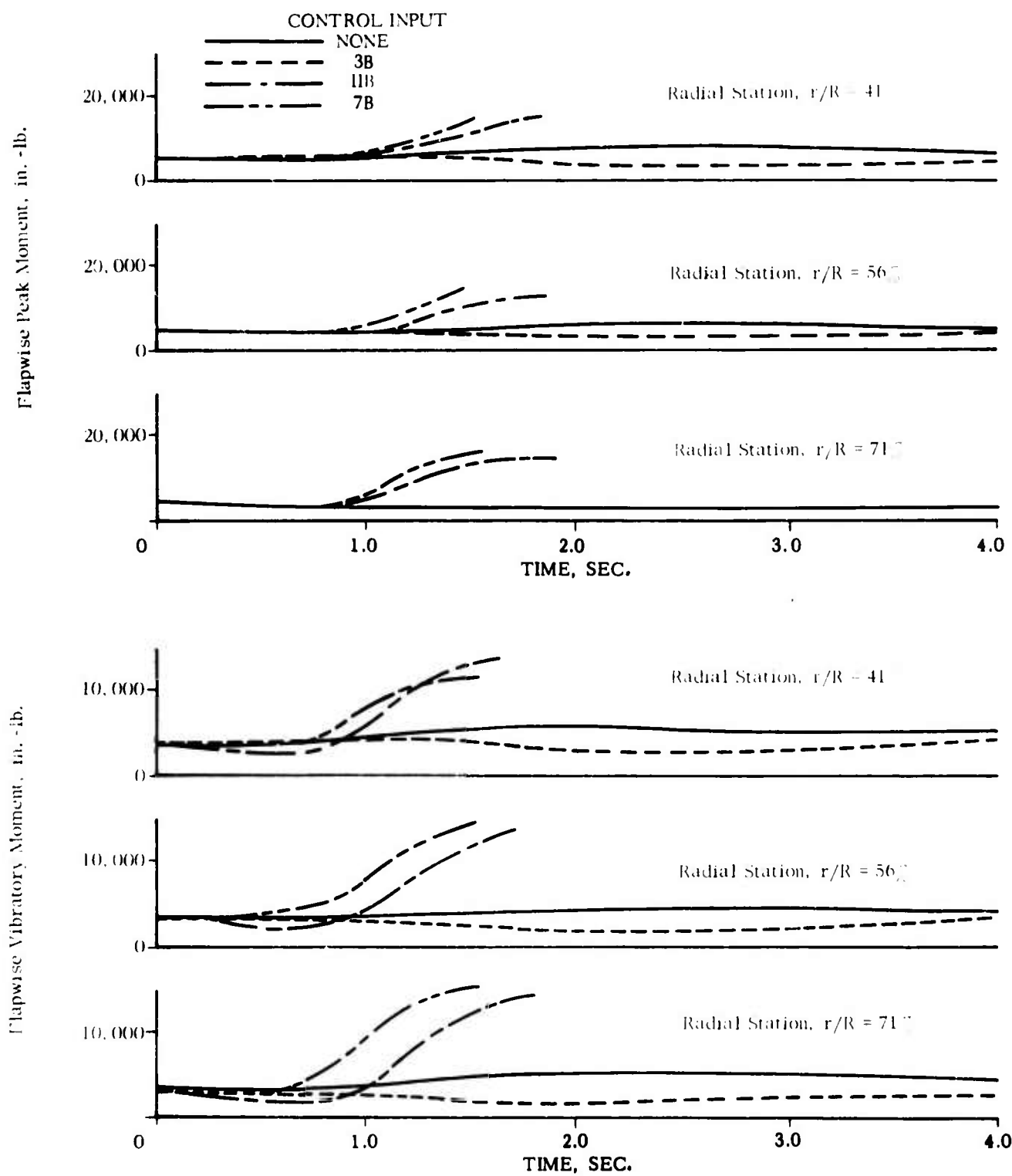


Figure 56. Rotor Blade Vibratory and Peak Moment Variation, Full Power Loss, $D/L = -0.063$, Various Corrective Control Inputs, Fully Articulated Rotor

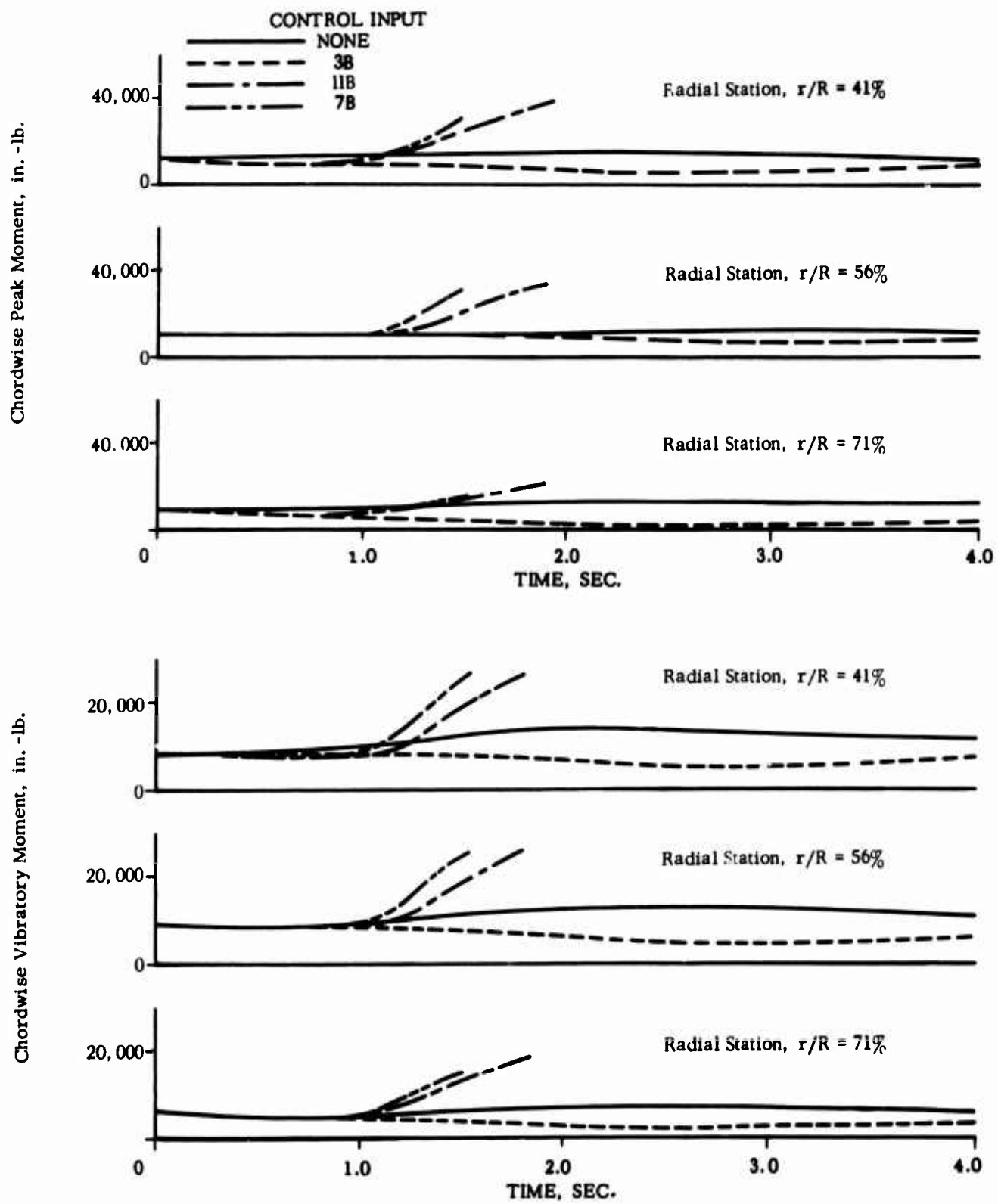


Figure 56. Continued

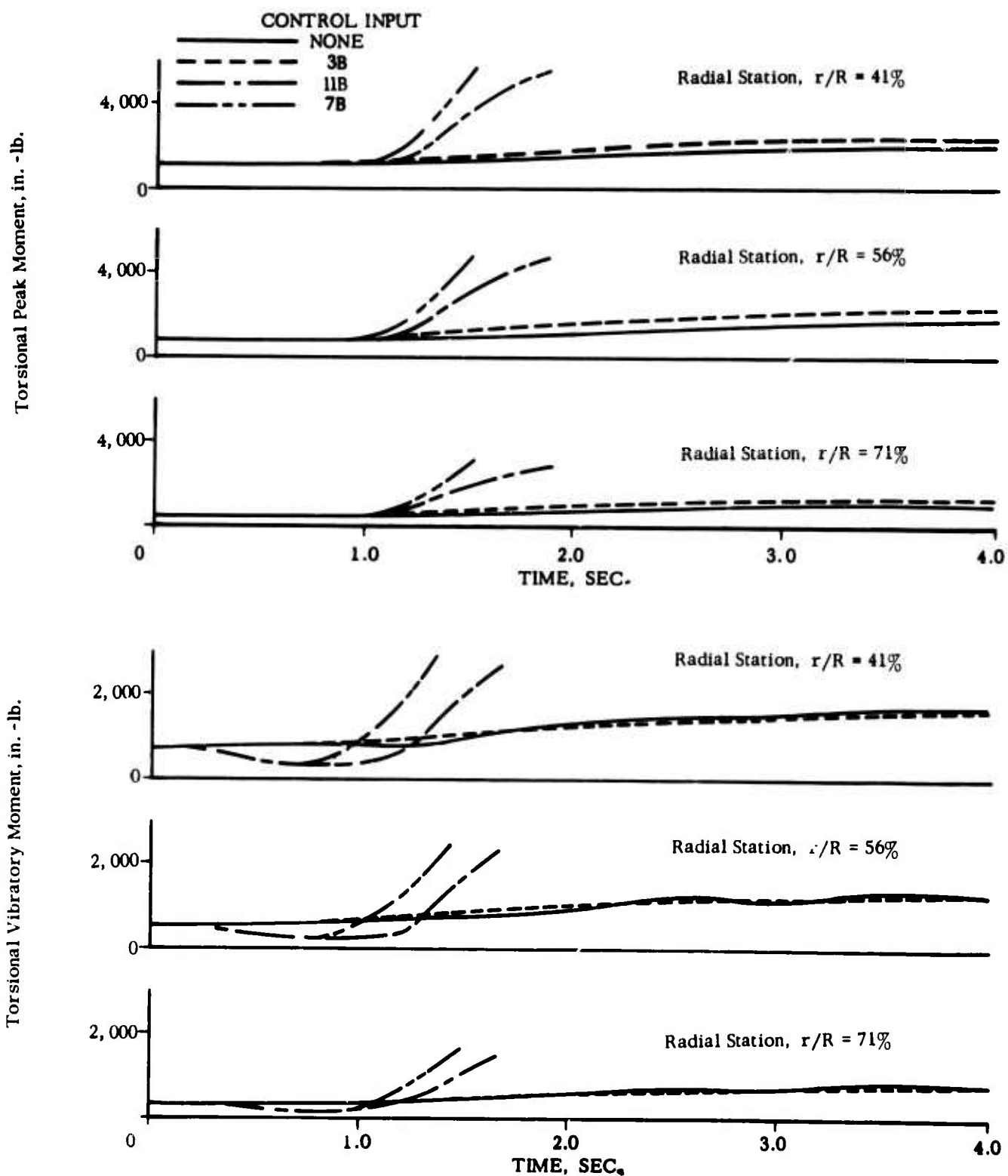


Figure 56. Concluded

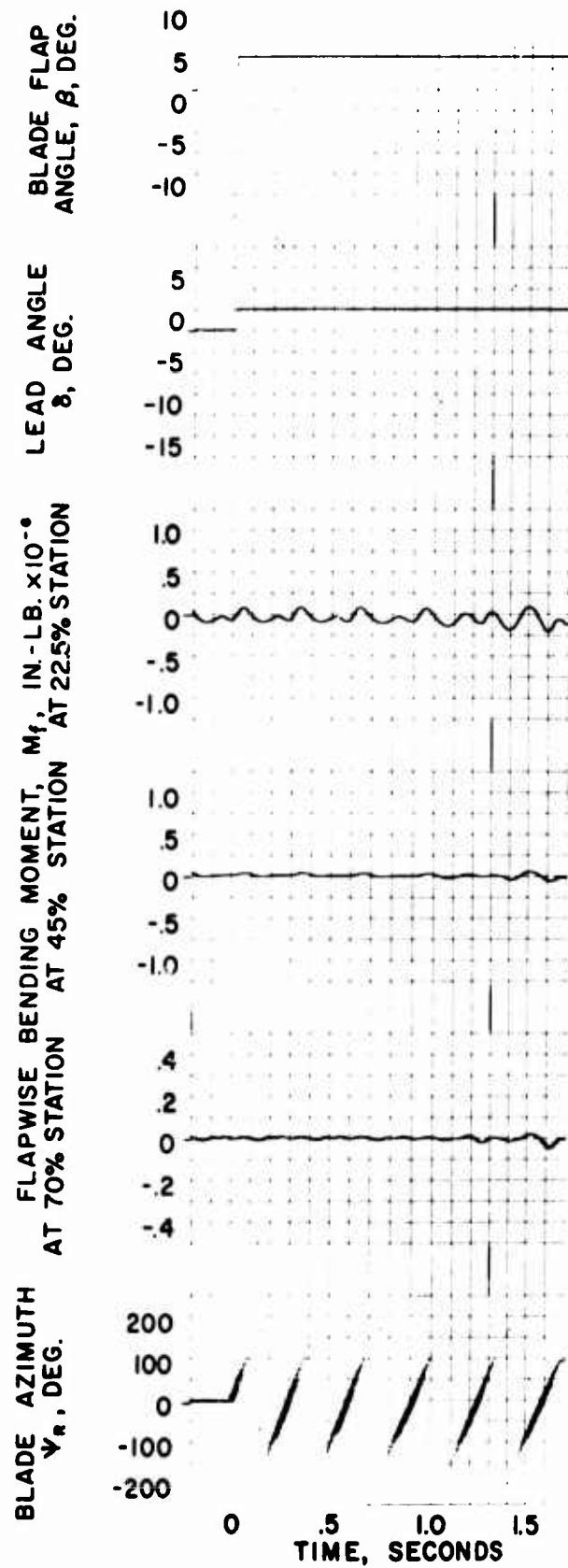


Figure 57. Hingeless Rotor, Full Power Loss, $D/L = 0.15$, No Corrective Control Input, Multiple Bending Moment Data

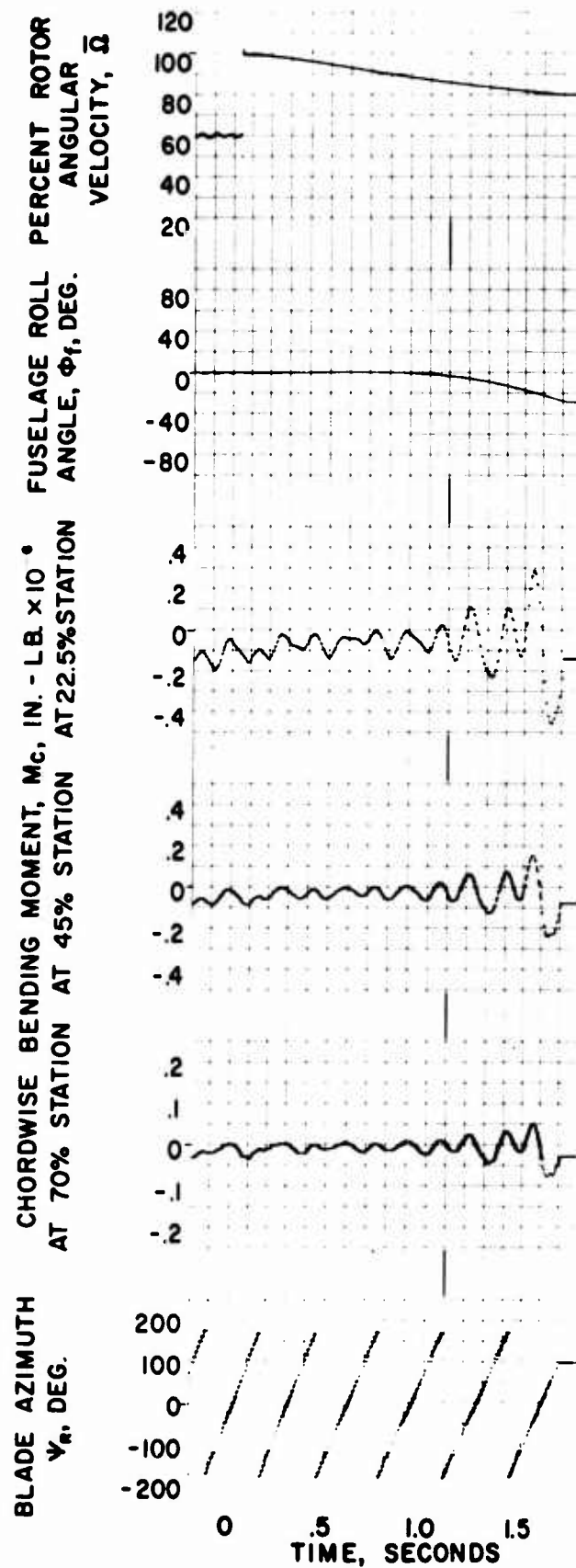


Figure 57. Continued

BLADE AZIMUTH
 ψ_r , DEG.

TORSIONAL MOMENT, M_t , IN. - LB. $\times 10^{-6}$
 AT 70% STATION AT 45% STATION AT 22.5% STATION

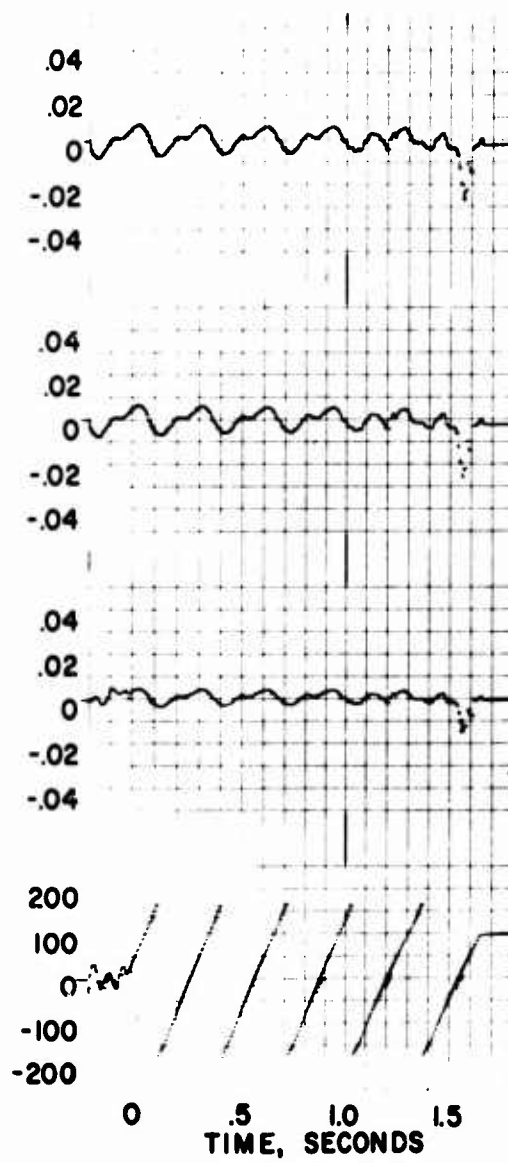


Figure 57. Concluded

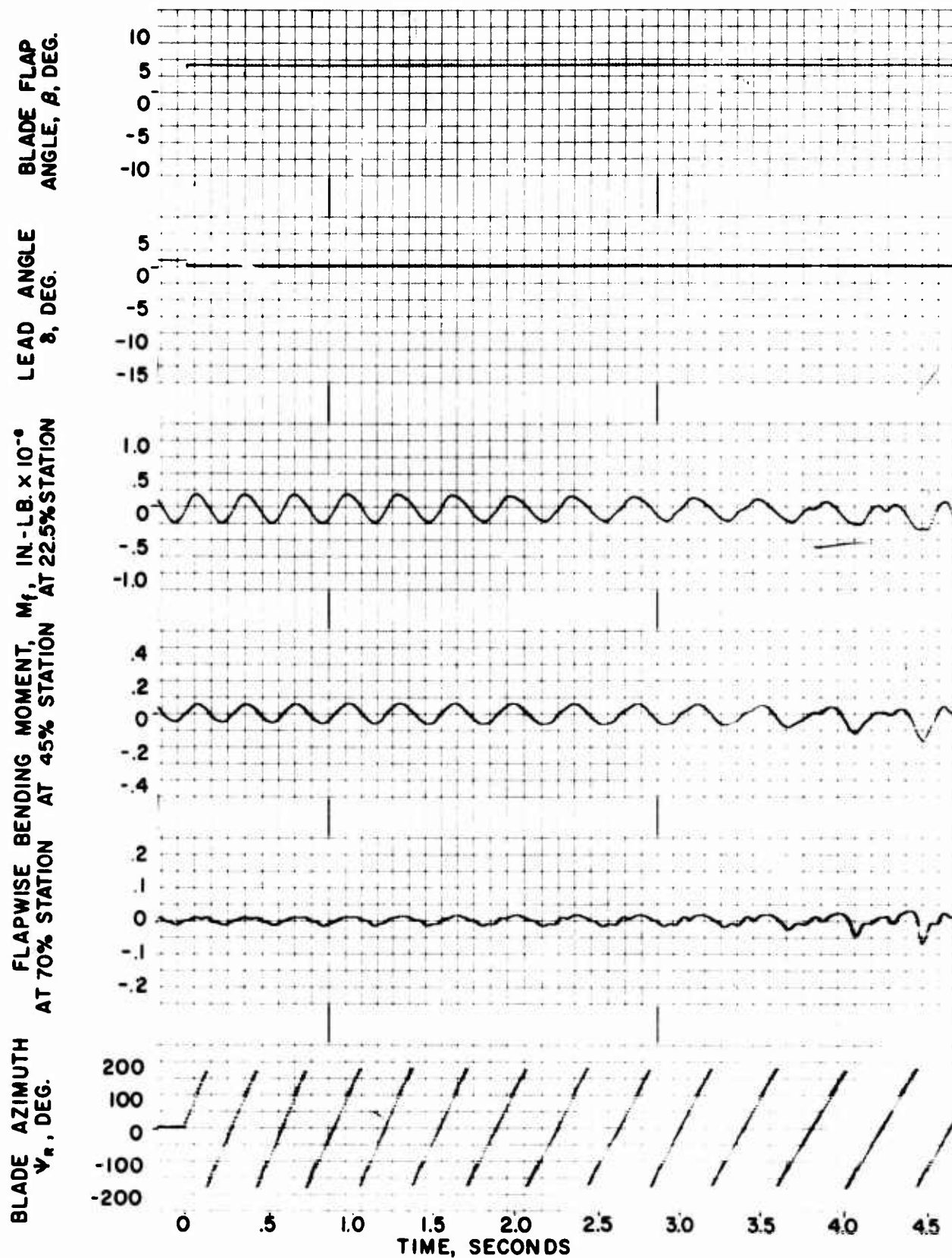


Figure 58. Hingeless Rotor, Full Power Loss, $D/L = -0.063$, No Corrective Control Input, Multiple Bending Moment Data

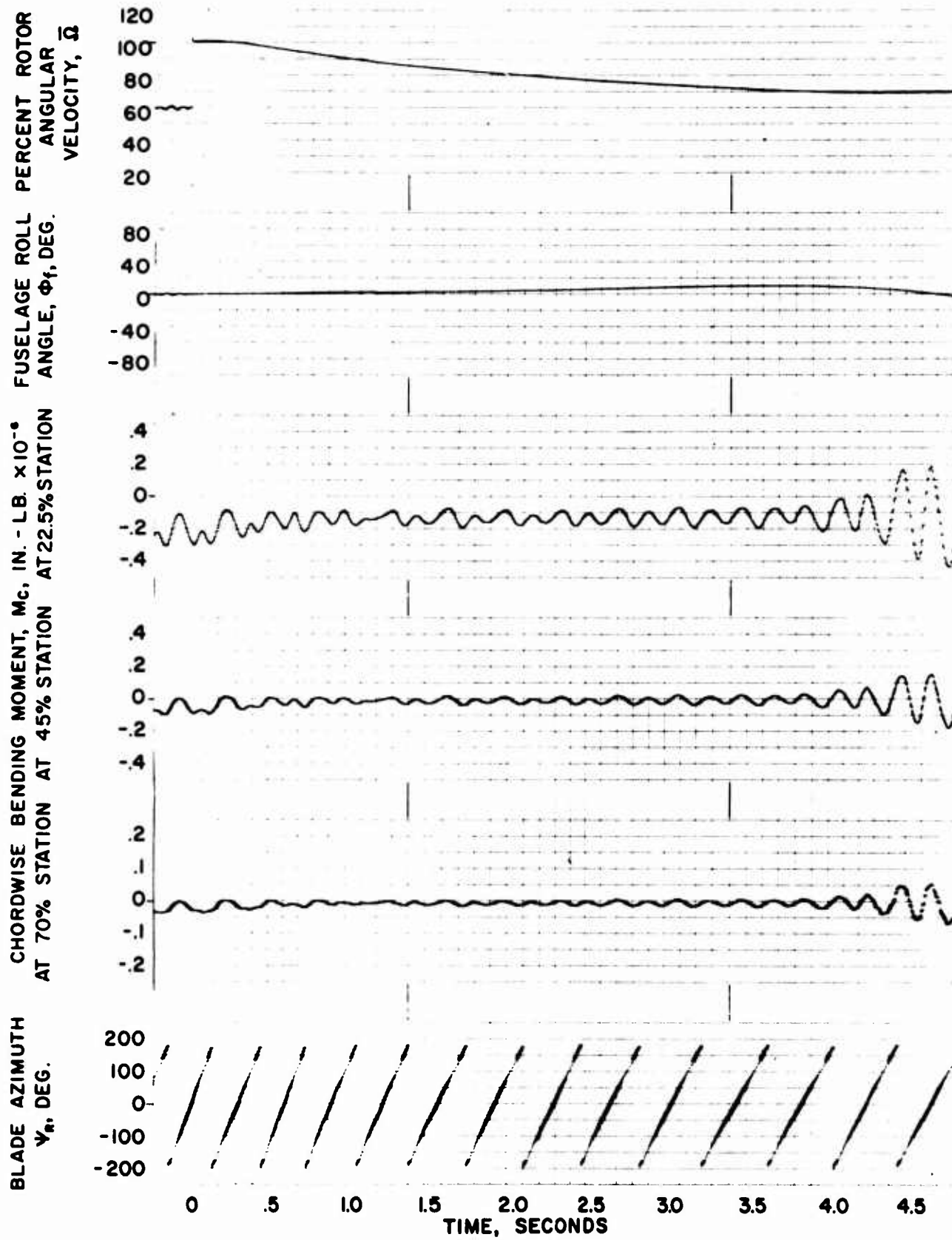


Figure 58. Continued

BLADE AZIMUTH
 ψ_r , DEG.

TORSIONAL MOMENT, M_t , IN. - LB. $\times 10^{-6}$
 AT 70% STATION AT 45% STATION AT 22.5% STATION

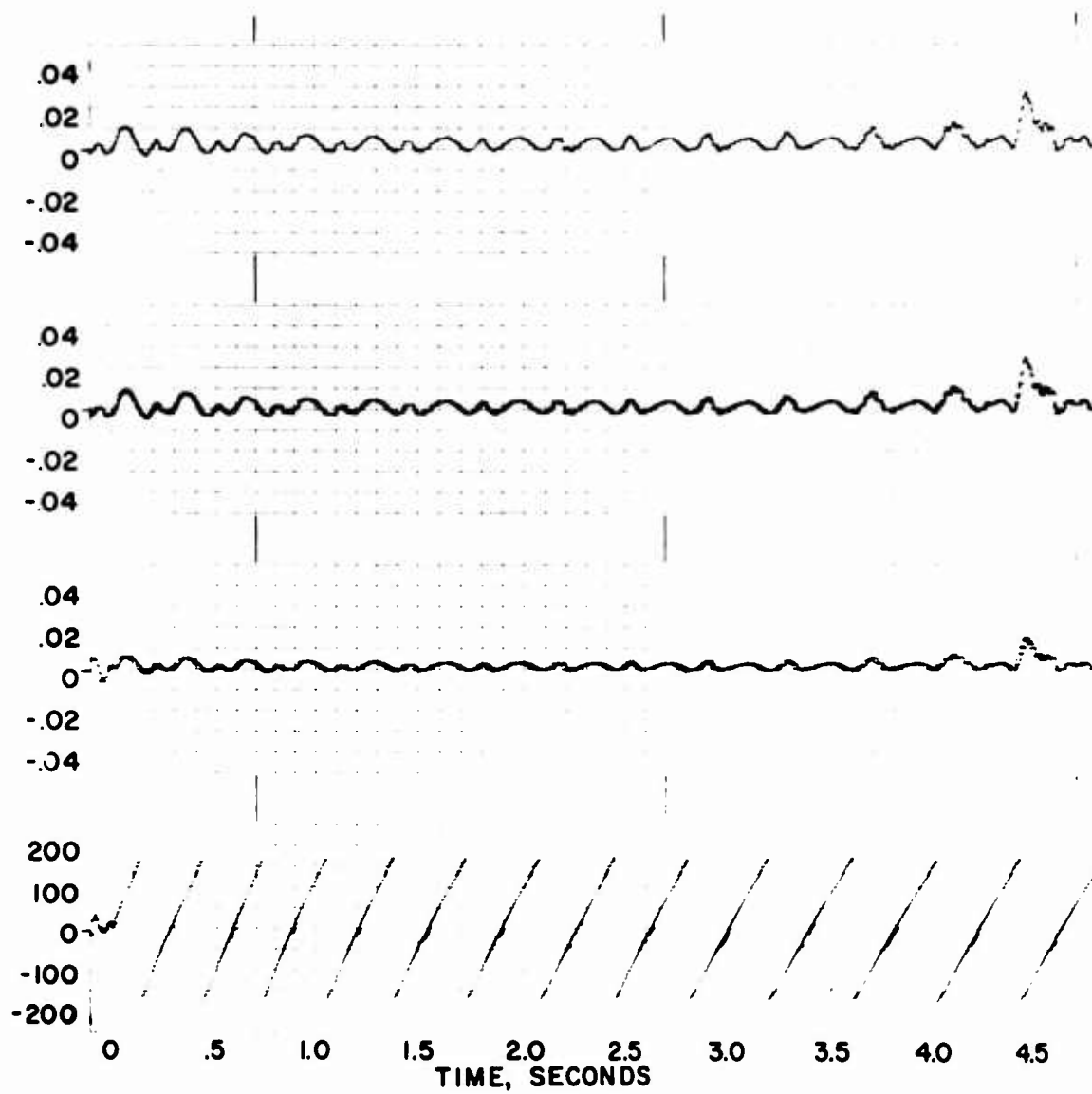


Figure 58. Concluded

CONCLUSIONS

1. A full loss of main rotor power can seriously affect the safety of a 200 - 235 knot helicopter, unless there is a rapid and appropriate application of tail rotor control. For the S-61F helicopter, used in this study, operating at a rotor propulsive force-to-lift ratio, $D/L = 0.15$, tail rotor corrective control action was necessary in less than 0.2 second to retain attitude control. The loss of power is less critical with reduced rotor propulsive force. With all propulsion provided by auxiliary propulsion devices, corrective control input delay times of 0.6 second for both main rotor and tail rotor control inputs can be tolerated. Rotor speed recovery was achieved using collective and cyclic pitch corrective control with time delays up to 4.0 seconds (Figure 59).
2. High speed helicopters should be configured with large vertical and horizontal tail surfaces to insure a stable platform in the event of an abrupt loss of power. The aircraft response is due primarily to the specific fuselage aerodynamic characteristics associated with the sideslip which is created by the unbalanced yawing moment. The weathercock stability provided by a large vertical tail will limit the sideslip angle and hence reduce the resulting rolling moment due to the fuselage and rotor dihedral effect (Figure 60). The beneficial effect of a large horizontal tail is clearly evident in the small fuselage pitch disturbance and stable motion observed for the S-61F base helicopter throughout this study.
3. Flapping hinge offset and rotor blade inertia (Lock number) are important design parameters affecting helicopter and blade motion and loading following a loss of power. A rotor with a moderate flapping hinge offset ratio, 3 to 5 percent, experienced both a smaller roll disturbance than the zero offset rotor and a smaller blade moment excursion than the larger effective offset rotor (hingeless). A reduction in Lock number results in reduced fuselage rolling and blade flapping disturbance. However, for the conditions investigated, the higher inertia of the rotor blades increases the tendency for the blade to stall due to roll rate, and results in higher values of blade bending moments (Figure 61).
4. Blade pitch-flap feedback ($\Delta\text{-three} = 30^\circ$) and blade pitch-tip path plane feedback are not effective concepts for reducing the helicopter roll motion following a loss of power. Rotor blade stall tendency (caused by the larger roll rate) and the corresponding blade bending moments were increased by $\Delta\text{-three}$ and tip path plane tilt feedback. Below stall, both concepts increased this torsional vibratory and peak bending moment (Figure 62).
5. The gyroscopic effects of the hingeless rotor system restrain the initial roll motion following power loss, but, without stability augmentation, the pitch-roll coupling aggravates the long term roll and pitch motion (Figure 63).
6. Blade tip-tail cone clearance will not be a problem for rotor fuselage arrangements typical of the configuration used in this study. The maximum

down flapping angle referenced to the shaft over the tail cone would provide more than adequate margin for all reasonable recovery maneuvers (Figure 64).

7. The loss of altitude becomes more pronounced as the rotor propulsive force increases following a loss in power. This loss in altitude is due in a large part to pitch and roll attitude build up (Figure 65).

8. The marked increase in bending moments generated by the motion following the power loss can be diminished by reducing the resulting roll rate with corrective tail rotor inputs and also by unloading the blades. The bending moments increase as the rotor angle of attack increases with cyclic pitch control inputs. The values of the bending moments recorded during this study, under fixed control inputs, did not produce blade stresses which would result in a loss of the aircraft for the duration of time histories shown (Figure 66). The bending moments for the hingeless rotor tend to be higher than for the other rotors and should be considered in the design of the aircraft.

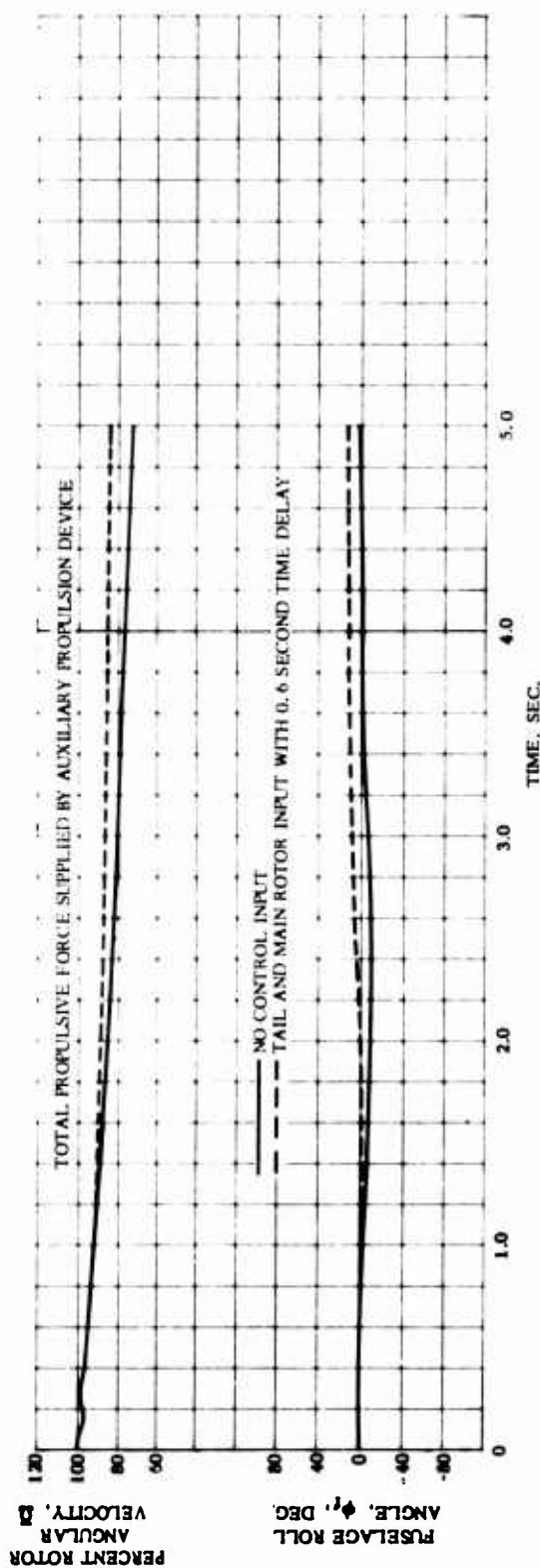
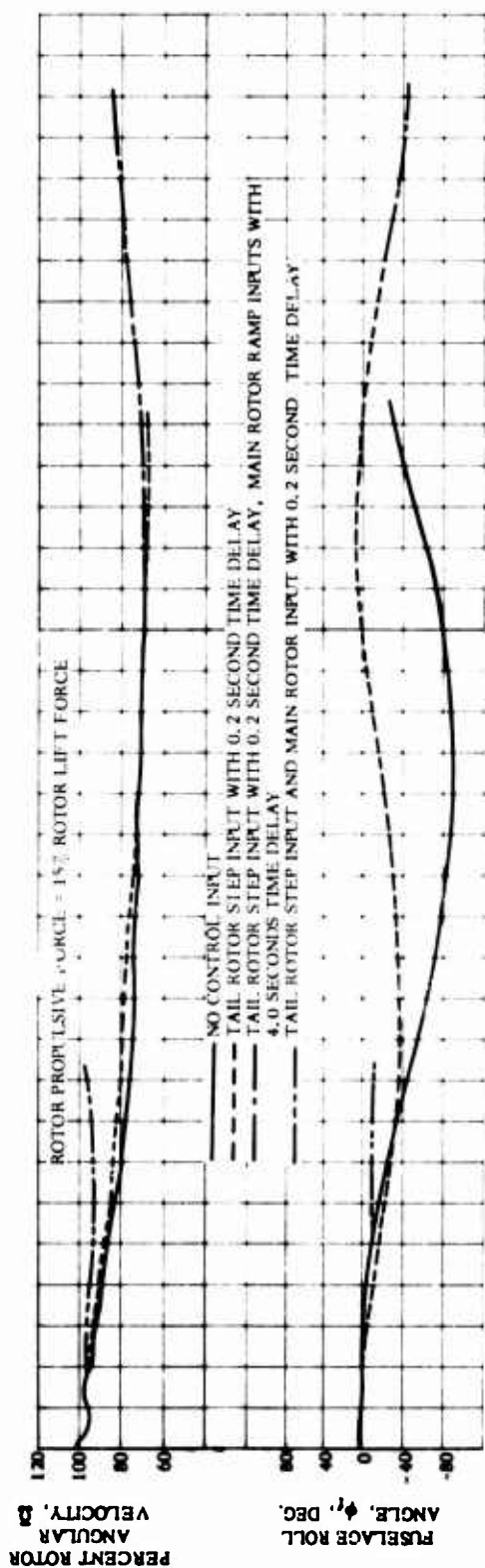


Figure 59. Effect of Time Delay for Corrective Control Inputs and Rotor Propulsive Force on Helicopter Roll Angle and Rotor Speed, Fully Articulated Rotor ($e/R = 0.034$), Full Power Loss at 200 Knots

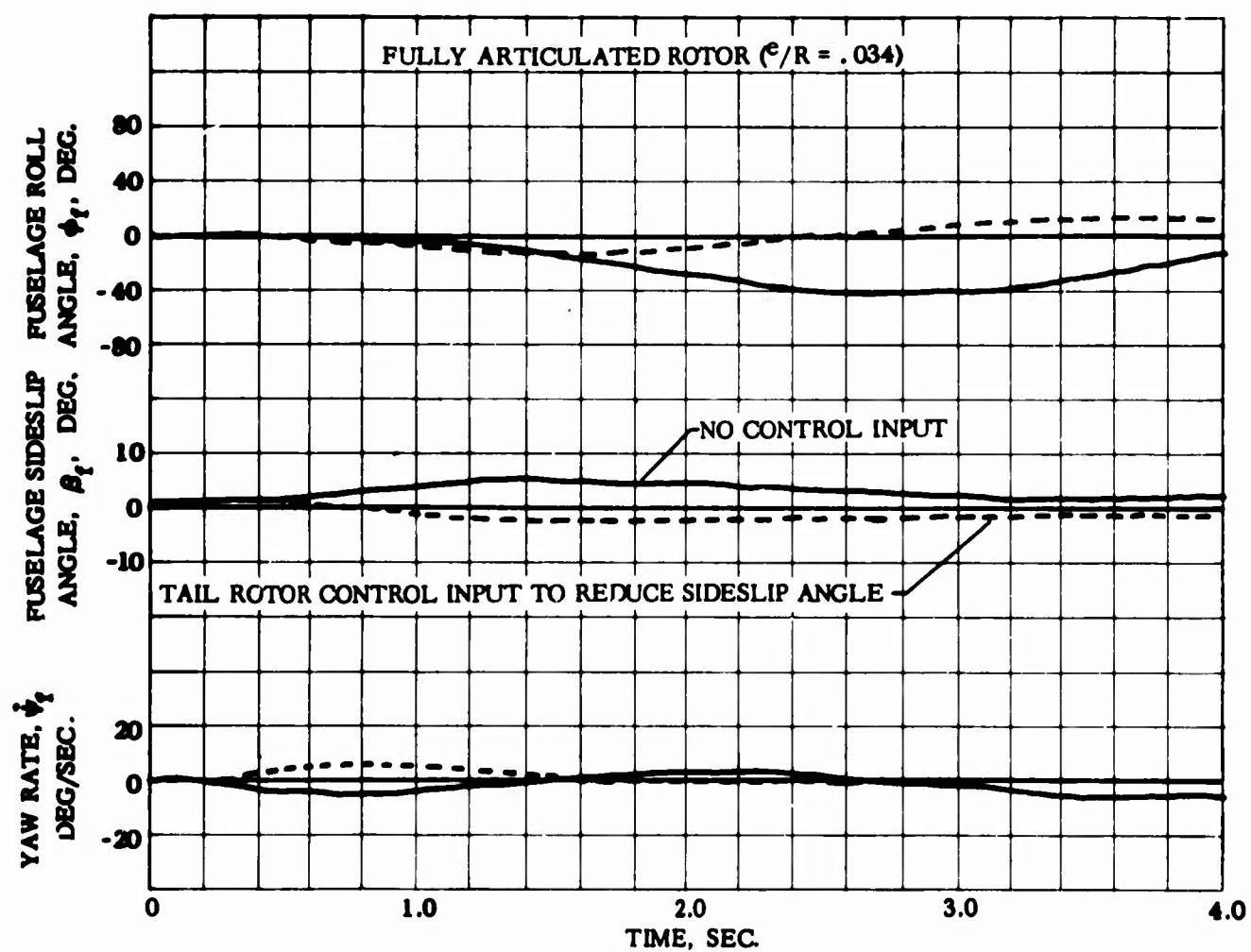


Figure 60. Effect of Sideslip Angle and Fuselage Aerodynamic Characteristics on Aircraft Motion Following Part Power Loss at 200 Knots

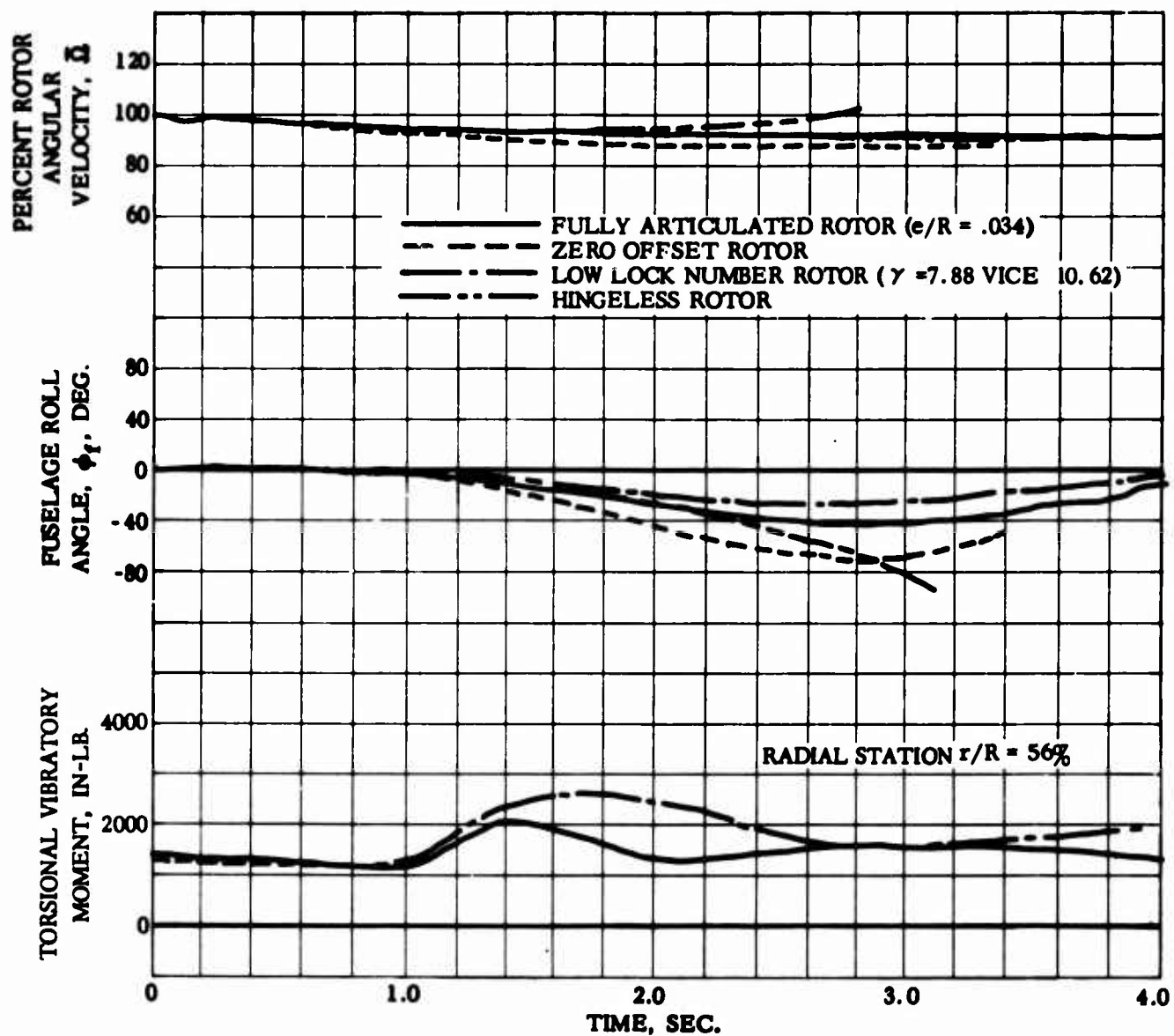


Figure 61. Effect of Flapping Hinge Offset, Lock Number, and Flapping Hinge Restraint on Helicopter Motion and Blade Torsional Bending Moment Following Full Power Loss at $D/L = 0.15$, 200 Knots

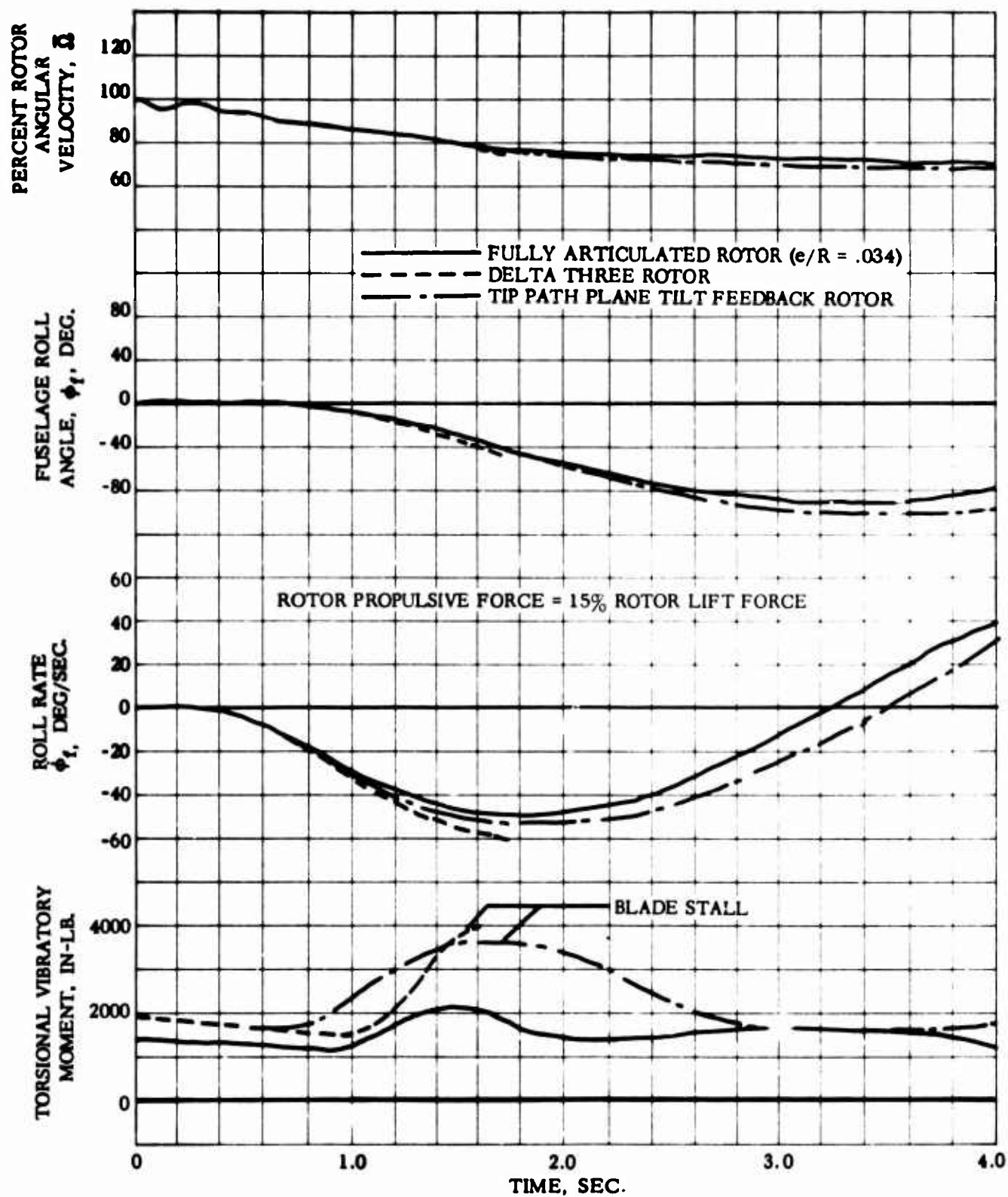


Figure 62. Effect of Blade Pitch-Flap Coupling on Helicopter Motion, Rotor Speed, and Torsional Bending Moment Following Full Power Loss at 200 Knots

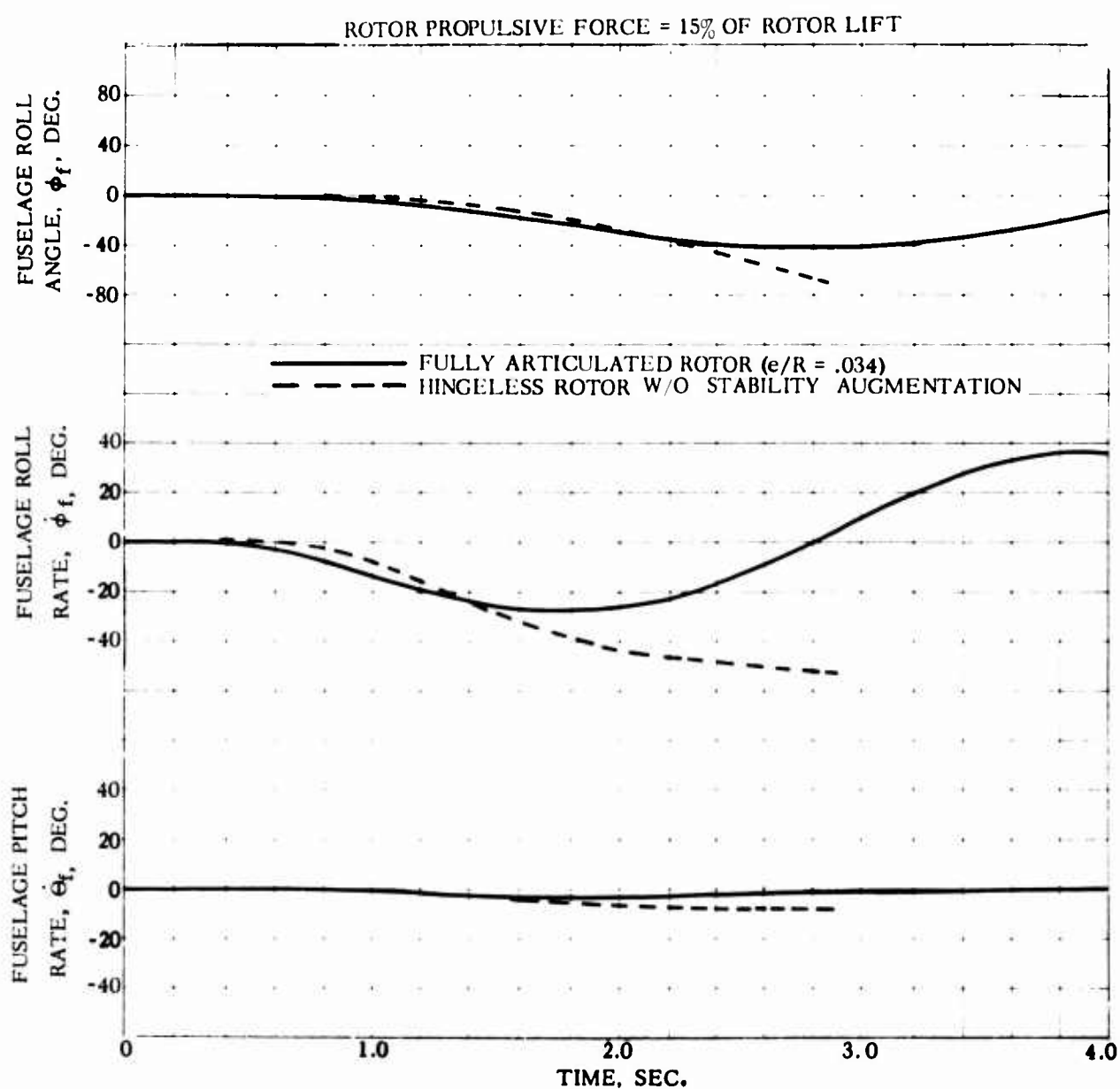


Figure 63. Response of the Hingeless and Articulated Rotor Following a Part Power Loss at 200 Knots

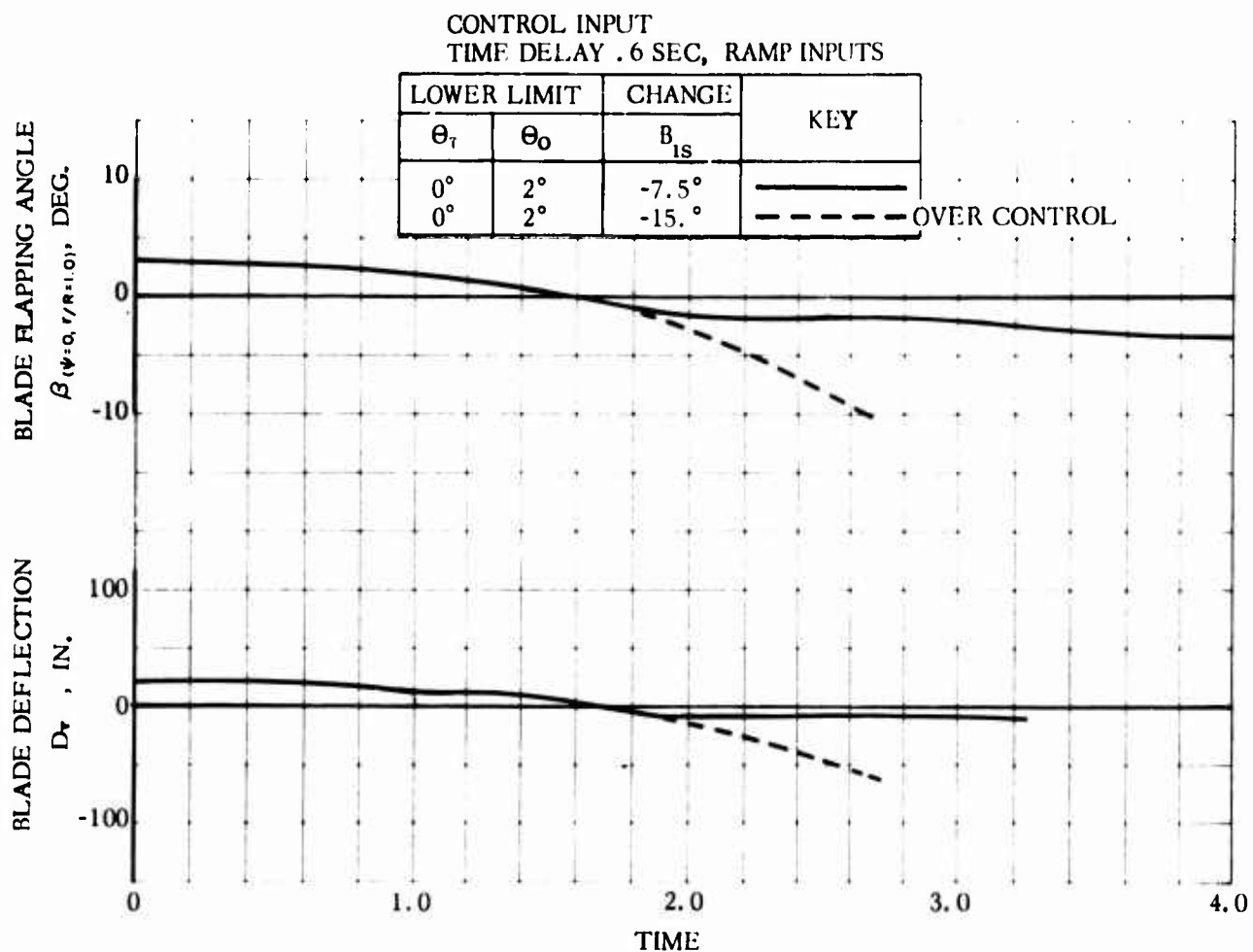


Figure 64. Variation of Blade Flapping Angle and Blade Deflection Over the Tail Cone With Time, Both Referenced From the Plane of the Shaft, Full Articulated Rotor ($e/R = 0.034$), 200 Knots

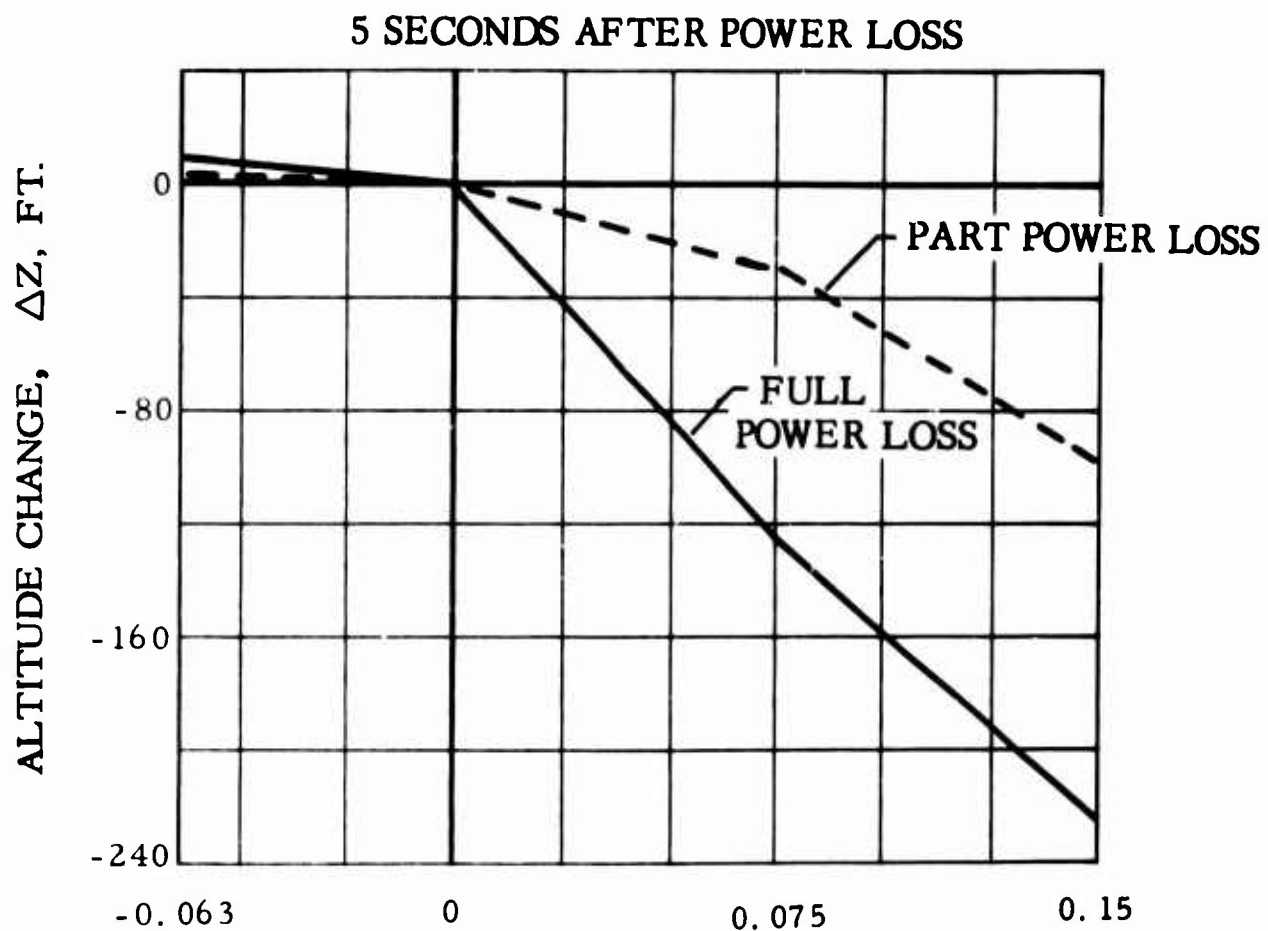


Figure 65. Change in Altitude Following Loss of Main Rotor Power, Fully Articulated Rotor ($e/R = 0.034$)

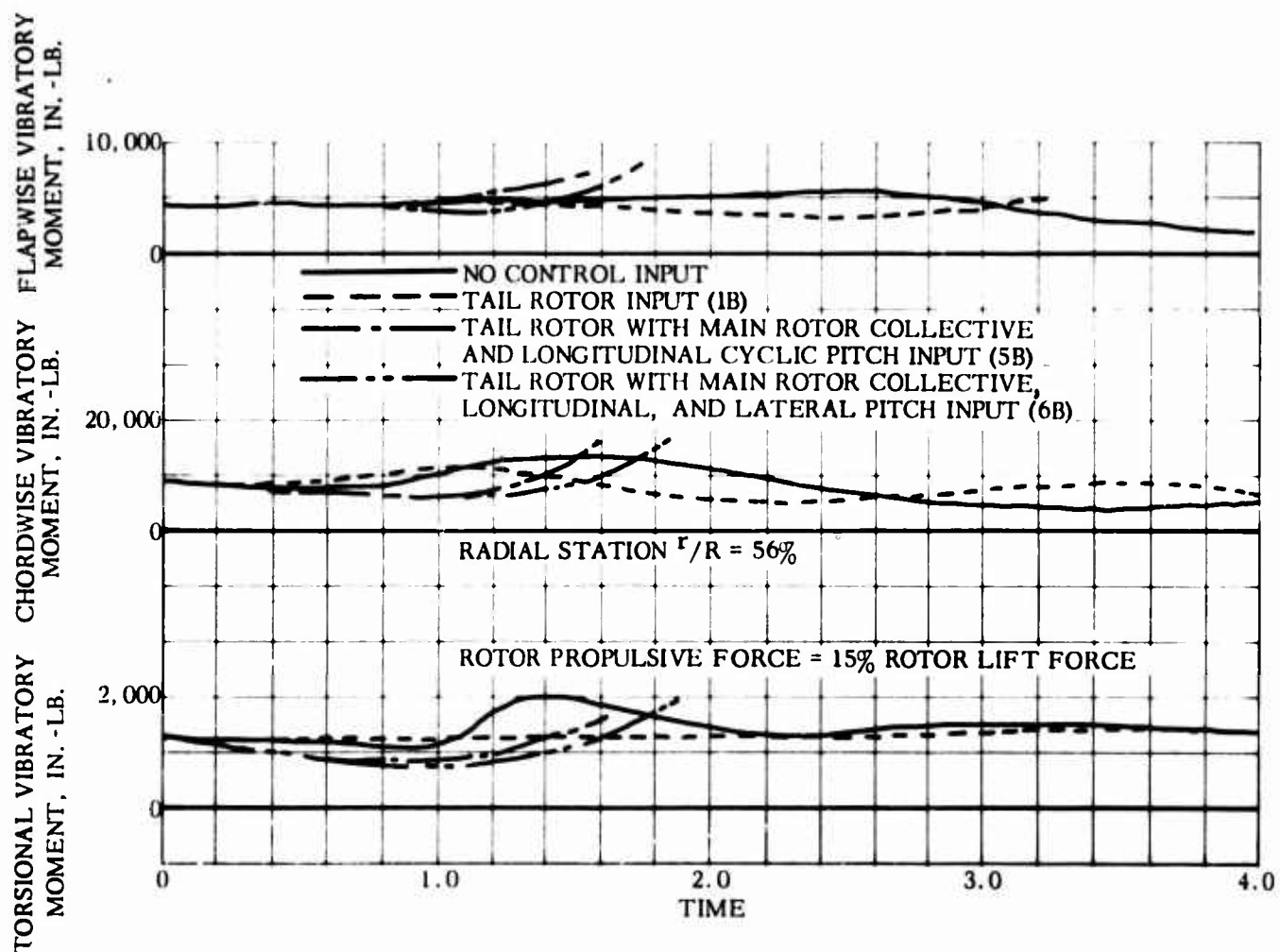


Figure 66. Effect of Corrective Control Inputs With 0.2 Second Time Delay on Rotor Blade Bending Moments Following Full Loss of Power at 200 Knots, Fully Articulated Rotor ($e/R = 0.034$)

RECOMMENDATIONS

1. This exploratory study has disclosed several significant trends concerning the effects of operating conditions, airframe aerodynamics, and corrective control inputs on helicopter and blade motion following a loss of power at high speeds, all of which should be explored in more detail. The fuselage aerodynamic characteristics, in particular, were found to be significant due to the dynamic pressures associated with the high airspeeds. For the flight conditions investigated, the rotor sustained all the aircraft gross weight and was operating near the stall limit. Consideration should be given to alleviating rotor stall by means of wings and flaps. In addition, auxiliary stabilization devices, pilot reaction characteristics, extended time delays, and coupling of rotor and auxiliary propulsion have a profound effect on the helicopter and blade motion and on the corrective control inputs following a loss of power. Since these considerations were beyond the scope of this study, it is recommended that this study be continued to examine in greater detail the effects of the following areas:

- . wing and flap arrangements
- . fuselage aerodynamic and stability characteristics
- . auxiliary stabilization equipment
- . control inputs from a simulated pilot including extended time delays
- . coupled power requirements of rotor and auxiliary propulsion systems

2. This study has re-emphasized the importance of the time delay before corrective control inputs are applied. The problem facing the helicopter pilot experiencing a loss of engine power is complex, both because the cues are complex (noise, accelerations, vibrations, angular rates) and because the decisions he must make involve not only "what" but "how much". Experimental data on pilot reactions to an unalerted power loss in flight are almost nonexistent. Research on the three following parts of the pilot delay time problem is therefore recommended:

- . tests to establish the cues that can be detected by a pilot
- . a specific study of helicopter pilot reaction times
- . flight tests with simulated emergencies

3. Although the method developed in this study has shown good correlation with flight test data at 143 knots, further correlation of fuselage motion, blade motion, and loading are required at higher airspeeds. Flight test data for maneuvers at high airspeeds will be obtained in the S-61F (NH-3A) Maneuvering Flight Test Program to be conducted under Army/Navy sponsorship in 1966. The data obtained from this program should be correlated with the analytical methods developed in this present study.

REFERENCES

1. Carlson, R. G., and Hilzinger, K. D., Analysis and Correlation of Helicopter Rotor Blade Response in a Variable Inflow Environment, TRECOM Technical Report 65-51, Sikorsky Aircraft Engineering Report 50405, U. S. Army Aviation Materiel Laboratories, * Fort Eustis, Virginia, September 1965
2. Gerstenberger, W., and Wood, E. R., Analysis of Helicopter Aeroelastic Characteristics in High Speed Flight, I.A.S. Preprint 63-72, I.A.S., 31st Annual Meeting, New York, N.Y., January 1963.
3. Paquette, G. A., Progress of Hybrid Computation at United Aircraft Research Laboratories, AFIPS Conference Proceedings Volume 26, Part I, 1964 Fall Joint Computer Conference, Spartan Books, Baltimore, Maryland, 1964, pp. 695-705.
4. Scanlan, R. H., and Rosenbaum, R., Introduction to The Study of Aircraft Vibration and Flutter, The MacMillan Company, New York, N.Y., 1951, p. 87.
5. Wood, E. R., and Hilzinger, K. D., A Method for Determining The Fully Coupled Aeroelastic Response of Helicopter Rotor Blades, Proceedings of the 19th Annual Forum of the American Helicopter Society, Washington, D.C., May 1963, pp. 28-37.
6. Wood, E. R., and Buffalano, A. C., Parametric Investigation of the Aerodynamic and Aeroelastic Characteristics of Articulated and Rigid (Hingeless) Helicopter Rotor Systems, TRECOM Technical Report 64-15, Sikorsky Engineering Report 50359, U.S. Army Aviation Materiel Laboratories, Fort Eustis, Virginia, April 1964.

* Formerly Transportation Research Command

DISTRIBUTION

US Army Materiel Command	2
US Army Mobility Command	5
US Army Aviation Materiel Command	6
Chief of R&D, DA	1
US Army Aviation Materiel Laboratories	25
US Army R&D Group (Europe)	2
US Army Human Engineering Laboratories	1
US Army Test and Evaluation Command	1
US Army Combat Developments Command, Fort Belvoir	2
US Army Combat Developments Command Transportation Agency	1
US Army Combat Developments Command Experimentation Command	3
US Army Command and General Staff College	1
US Army Aviation School	1
US Army Aviation Test Board	3
US Army Electronics Command	2
US Army Aviation Test Activity, Edwards AFB	2
Air Force Flight Test Center, Edwards AFB	2
US Army Transportation Engineering Agency	1
US Army Field Office, AFSC, Andrews AFB	1
Air Force Flight Dynamics Laboratory, Wright-Patterson AFB	1
Systems Engineering Group (RTD), Wright-Patterson AFB	3
US Directorate of Flight Safety Research, Norton AFB	1
Bureau of Naval Weapons, DN	7
Office of Naval Research	2
Chief of Naval Research	2
Aero Space Medical Laboratory, Wright-Patterson AFB	1
US Naval Air Station, Norfolk	1
David Taylor Model Basin	1
Commandant of the Marine Corps	1
Marine Corps Liaison Officer, US Army Transportation School	1
Testing and Development Division, US Coast Guard	1
Ames Research Center, NASA	1
NASA Representative, Scientific and Technical Information Facility	2
NAFEC Library (FAA)	2
US Army Aviation Human Research Unit	2
US Army Board for Aviation Accident Research	1
Bureau of Safety, Civil Aeronautics Board	2
US Naval Aviation Safety Center, Norfolk	1
Federal Aviation Agency, Washington, D. C.	1
CARI Library, FAA	1
Bureau of Flight Standards, FAA	1
HQ, US Marine Corps	1
Director of Army Aviation, ODCSOPS	1
Office of Deputy Chief of Staff for Military Operations	1
Office of Deputy Chief of Staff for Personnel	1
National Institutes of Health	1
Defense Documentation Center	20

APPENDIX I

ROTOR SYSTEM AND AIRCRAFT PHYSICAL PROPERTIES

ROTOR SYSTEM PHYSICAL PROPERTIES

The physical properties of all of the rotor systems are listed in Table VII, and the spanwise physical properties and bending mode shapes of their blades are presented in Figures 67 through 72. The aerodynamic characteristics of the blade airfoil sections are presented in the Development of Computer Program Section. The S-61R (CH-3C) rotor was used in the correlation phase, and rotors (a) through (g) were used in the analytical phase of this study. The S-61R main rotor blade, with appropriate modifications, is common to all of the articulated rotor systems, rotors (a) through (e). A scaled-down version of the blades used on the C4-R compound helicopter of Reference 6 was used for the rotor systems, with blades rigidly attached to the hub, rotor systems (f) and (g). These rotors were sized to have the same loading as the articulated rotors.

Since the blade torsional moment of inertia is determined experimentally for the whole blade including the cuff, the spanwise distribution is not known. For this study, the torsional mode shapes were calculated by assuming a constant spanwise distribution of torsional moment of inertia, which was derived from the experimental value for the whole blade.

The bending mode shapes, their derivatives, and the spanwise physical properties of the CH-3C rotor blade are presented in Figure 67. The data include three flapwise mode shapes with their first and second derivatives, two chordwise mode shapes with their first and second derivatives, and one torsional mode shape with its first derivative. The spanwise physical properties include flapwise, chordwise, and torsion moments of inertia as well as section area and mass distribution.

The blades used in rotor systems (a), (b), and (c) are identical, except for twist, to the S-61R blades. Since the tip speed is 633 fps compared with 660 fps for the S-61R, the mode shapes will have slight differences. The mode shapes and spanwise physical properties for these rotors are presented in Figure 68.

The zero offset rotor blade, rotor system (d), was also derived from the S-61R. The root structure and mass were extended to the center of rotation. The resulting structural and physical characteristics are shown in Figure 69.

A reduced Lock number for rotor system (e) was obtained by adding a non-structural tip weight of 24.5 pounds to the blades of rotor system (a). With this weight, a 26% reduction in Lock number from 10.62 to 7.88, was achieved. The spanwise data for these blades are presented in Figure 70. The torsional moment of inertia was increased to account for the blade tip mass.

The torsional moment of inertia for the hingeless blades, shown in Figures 71 and 72, was empirically derived from production blade characteristics and was assumed constant along the span. Since the end conditions are different, the mode shapes for the fixed hub blades, shown in Figure 71, differ from the mode shapes for the floating hub blades presented in Figure 72. The selection of the mode shapes is discussed in the Development of Computer Program Section of this report. In both cases, the blade was cantilevered from an infinitely rigid hub. The hub extended outboard to a 9% spanwise station.

The torsional mode shape for all rotors includes the effect of control system flexibility. The root spring constant for the S-61R push rod-swash-plate system was determined experimentally. The root spring constant for the hingeless blades, however, was increased to maintain the same root to blade spring ratio as the S-61R.

AIRCRAFT PHYSICAL PROPERTIES

The physical properties of the S-61R (CH-3C) aircraft (Figure 73), and the S-61F (NH-3A) high speed research aircraft (Figure 74), used in this study are presented in Table VIII. The loading conditions and mass moments of inertia of the S-61F aircraft, including the effective inertia of the rotor system, were kept constant for all rotor systems.

The weight and balance data are based on a low loading condition. Although the center of gravity position is well aft, the large stabilizing surfaces make the aircraft stable for this condition.

The aerodynamic characteristics of both aircraft, obtained from wind tunnel model tests, are presented in Figures 75 and 76. This data was transformed from the wind axis system to the body axis system for use in this program and resulted in the curves shown in Figures 77 and 78. Since all lift forces were assumed to be generated entirely by the rotor system, the fuselage and stabilizer lifting forces and pitching moments were adjusted for each rotor system and speed to meet the rotor operating conditions listed in Table III.

A conventional helicopter control system of longitudinal and lateral cyclic, collective, and tail rotor blade pitch was assumed. The controls were not coupled with each other, nor with any auxiliary surfaces, such as elevators or rudders. The elevator was assumed to be trim adjustable to provide adequate cyclic stick control range.

TABLE VII
ROTOR PHYSICAL PROPERTIES

Rotor System	CH-3C	a,b,c	d	e	f,g
Radius, ft.	31.0	31.0	31.0	31.0	28.7
Offset Ratio, \bar{e}	.0339	.0339	0	.0339	.0900
Chord, in.	18.25	18.25	18.25	18.25	29.52
b	5	6	6	6	4
θ_1	-8°	0°, -4°	0°, -4°	0°, -4°	0°, -4°
$\Omega_0 R$, ft./sec.	660	633	633	633	633
W_B , lb.	275.5	275.5	332.5	300.0	399.0
$M_B(r_{cg})$, slug-ft.	92.5	92.5	103.0	114.1	110.2
I_B , slug-ft. ²	1800	1800	2002	2430	1918
γ	10.62	10.62	9.56	7.88	11.86
I_{hub} , slug-ft. ²	573.3	573.3	568.8	573.3	625.9
Δr	.07661	.07661	.07661	.07661	.07661
$(e/r)_{LD}$.776	.776	1.000	.776	--
$\bar{e} + \bar{e}'$.2339	.2339	.2339	.2339	.2339
ω_{w1}/Ω_0	2.678	2.689	2.568	2.843	1.300
ω_{w2}/Ω_0	4.889	4.943	4.507	5.303	3.830
ω_{w3}/Ω_0	7.631	7.772	6.959	8.305	8.270
ω_{v1}/Ω_0	3.454	3.530	3.310	2.213	1.433
ω_{v2}/Ω_0	9.105	9.390	8.490	8.440	7.518
ω_{θ}/Ω_0	8.070	8.397	8.397	8.057	8.154

TABLE VII (Continued)

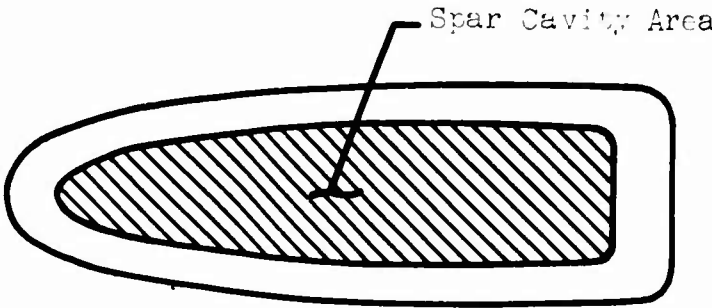
Rotor System	CH-3C	a,b,c	d	e	f,g
$K_r \times 10^{-6}$	1.200	1.200	1.200	1.200	5.300
C_o/I_B	.632	.632	.632	.632	--
AR Blade	20.4	20.4	20.4	20.4	11.7
*Spar Cavity Area, in. ²	11.40	11.40	11.40	11.40	38.49
I_p , lbs.-ft.- sec. ²	.672	.672	.672	.938	2.932
<p>*</p> 					

TABLE VIII
AIRCRAFT PHYSICAL PROPERTIES

	CH-3C	S-61F
* GW, lb.	16,000	11,900
** I _x , slugs - ft. ²	8,650	10,180
** I _y , slugs - ft. ²	52,500	53,100
** I _z , slugs - ft. ²	47,300	51,200
C.G.		
Water Line, in.	153.6	164.0
Fuselage Station, in.	280.0	278.0
Main Rotor		
Water Line, in.	233.0	233.0
Fuselage Station, in.	267.5	267.5
Tail Rotor		
Water Line, in.	225.0	233.5
Fuselage Station, in.	709.5	705.0
Aerodynamic Data Reference		
Water Line, in.	127.4	144.0
Fuselage Station, in.	275.0	275.0
Horizontal Tail		
Water Line, in.	255.0	158.0
Fuselage Station, in.	709.5	701.50
Area, ft. ²	27.0	76.0
Vertical Fin		
Water Line, in.	200.0	186.8
Fuselage Station, in.	672.0	686.2
Area, ft. ²	24.0	42.5
Shaft Incidence, deg., Forward	4.0	3.0
<p>* Including Rotor System.</p> <p>** Including the Effective Inertia of Rotor System.</p>		

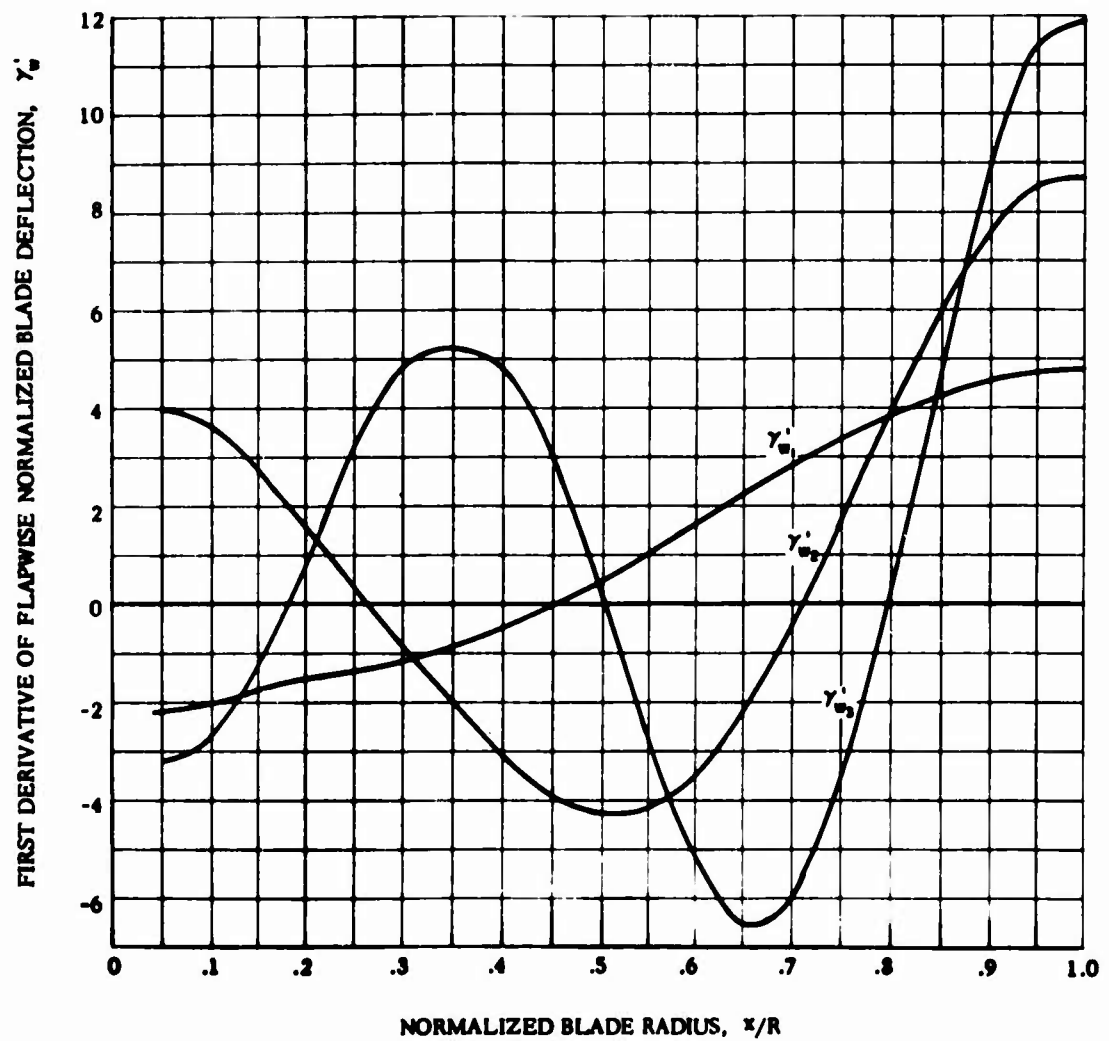
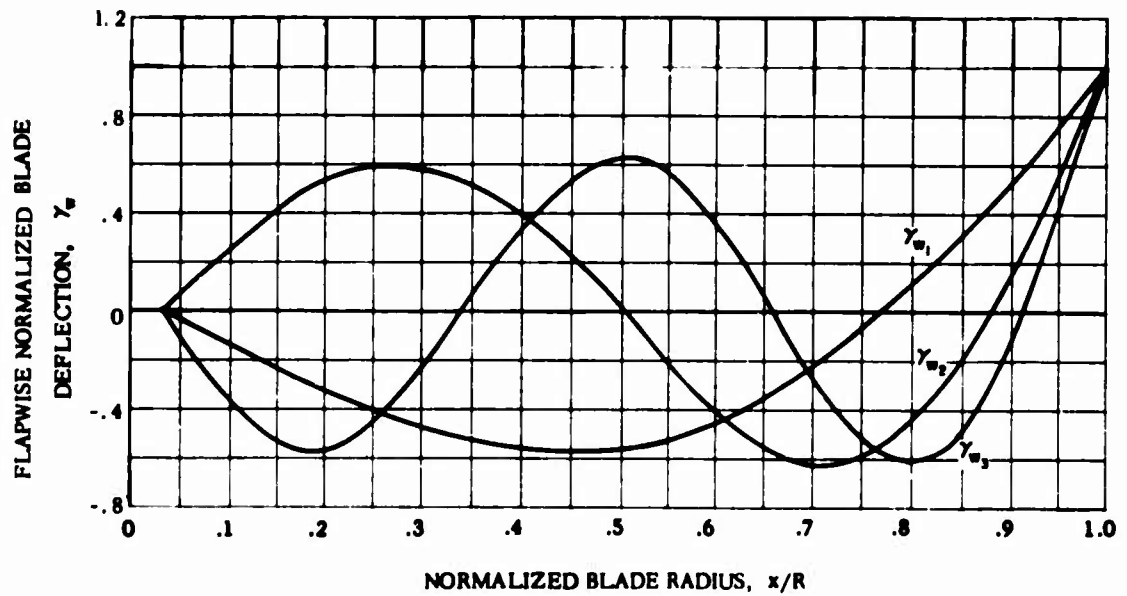


Figure 67. CH-3C Rotor Blade Spanwise Structural and Physical Properties

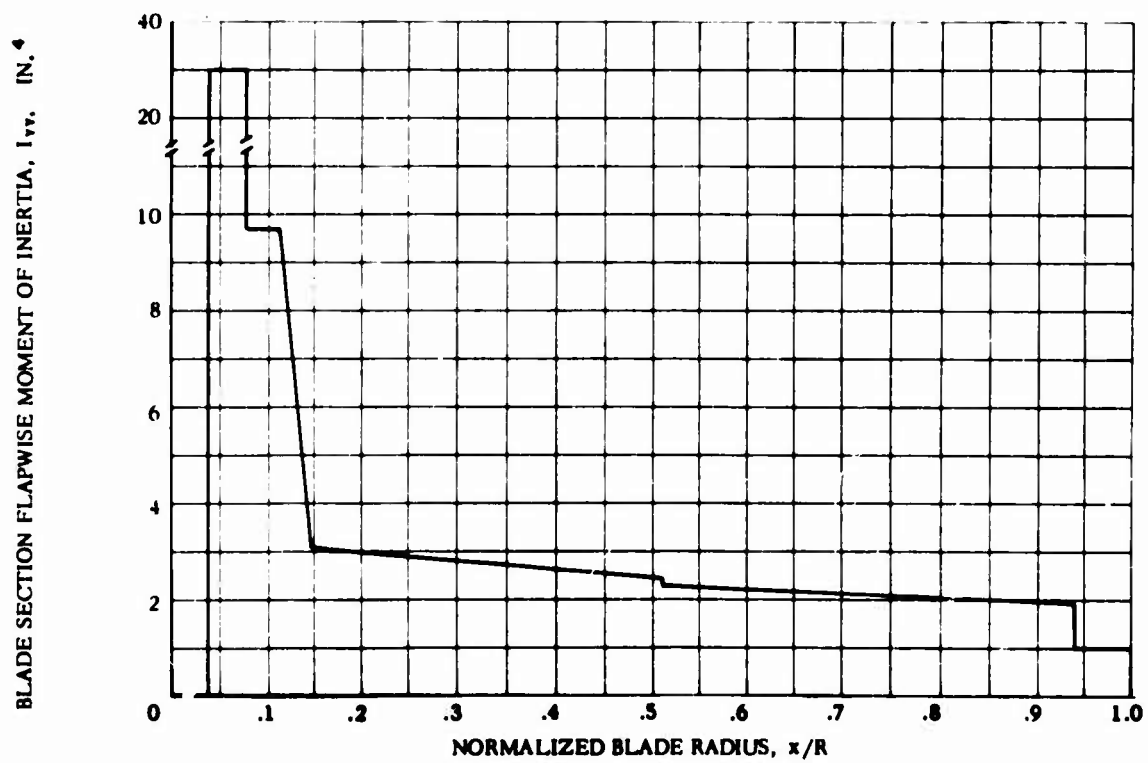
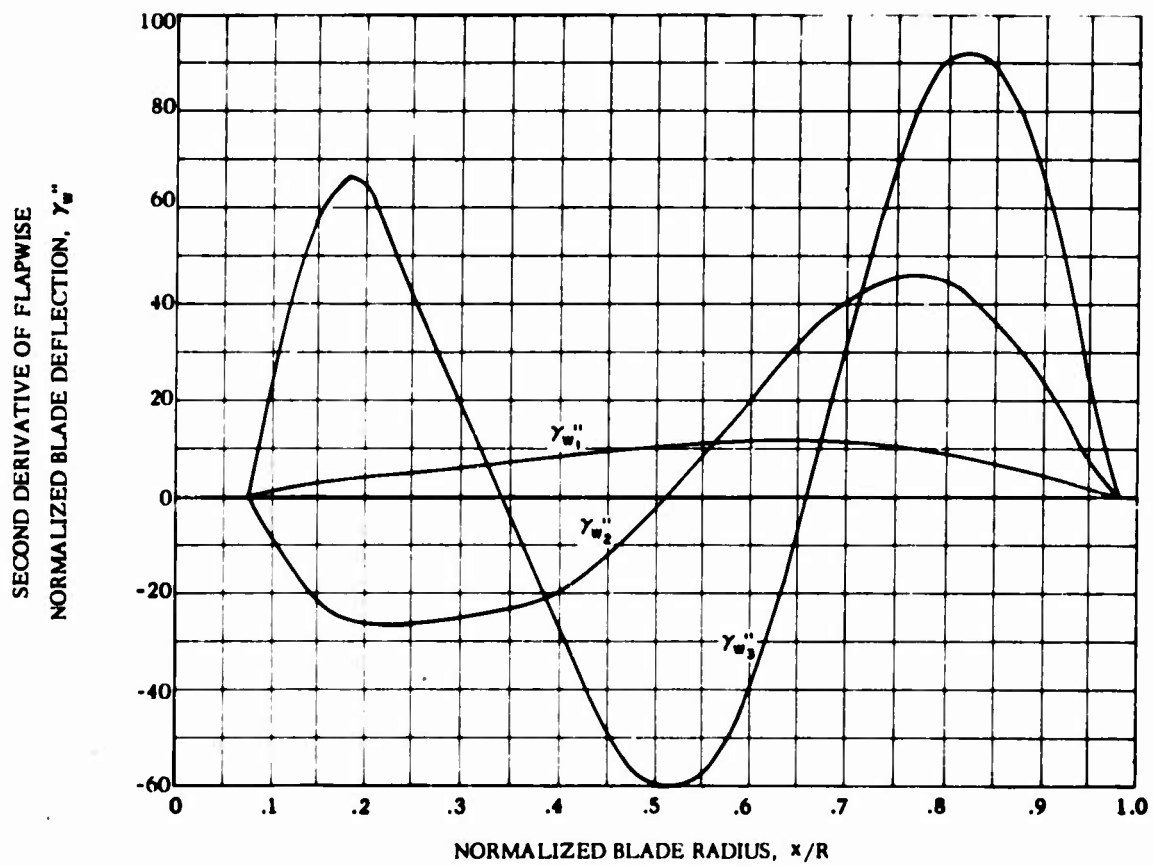


Figure 67. Continued

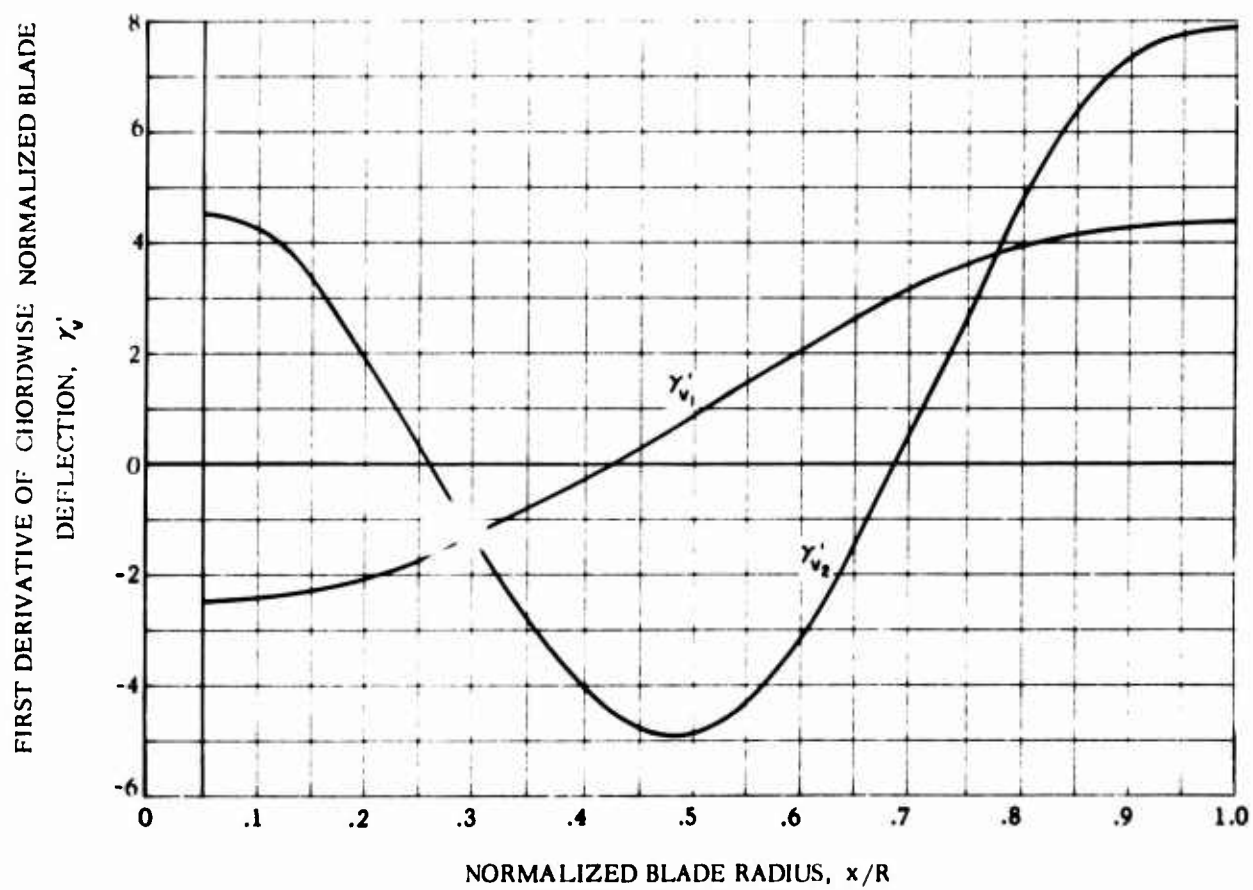
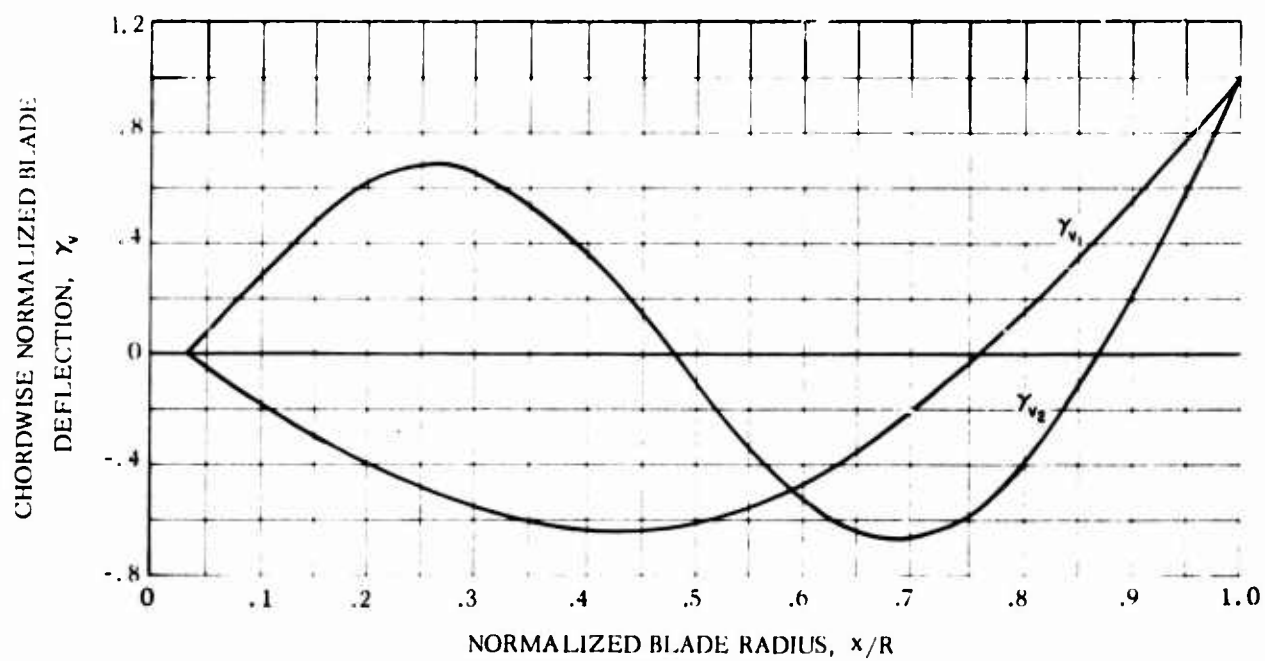


Figure 67. Continued

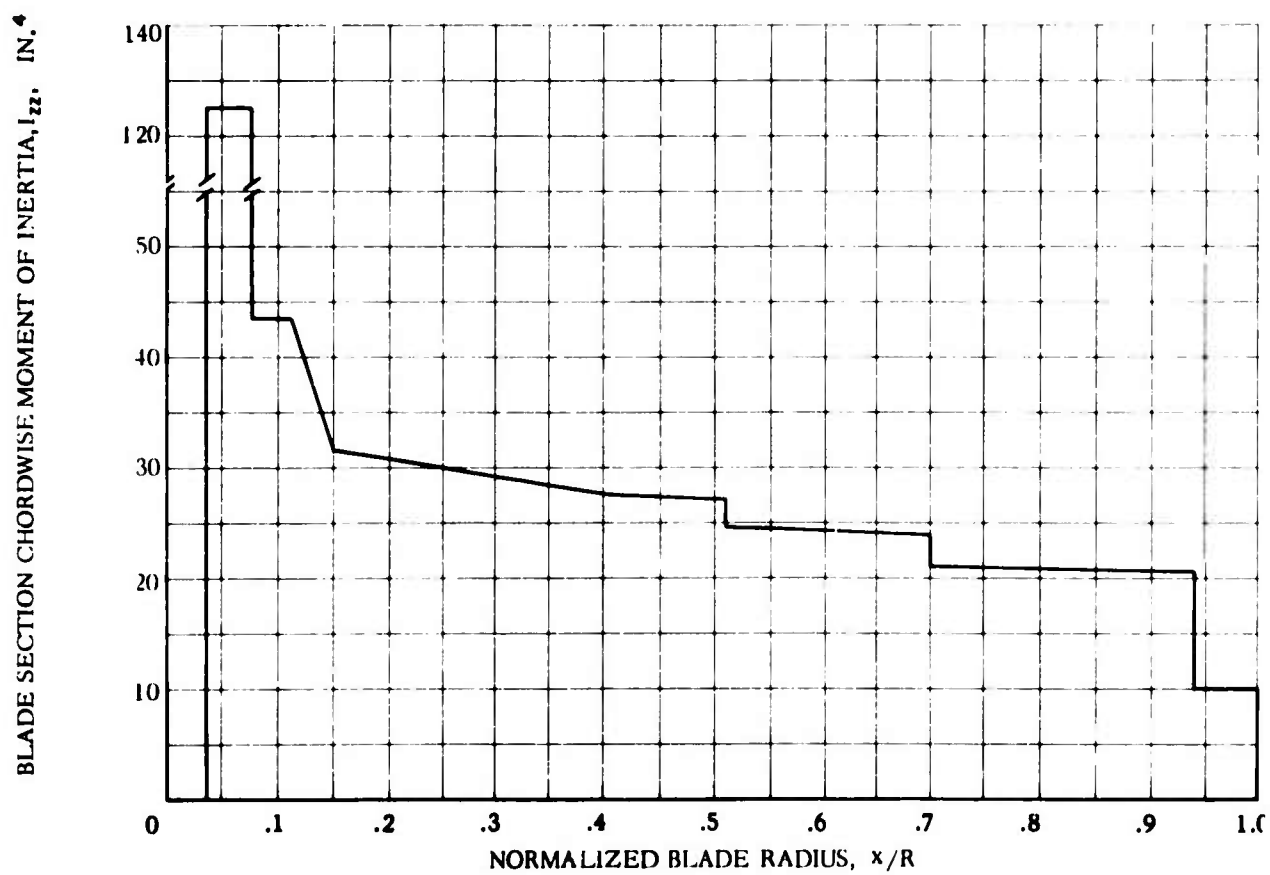
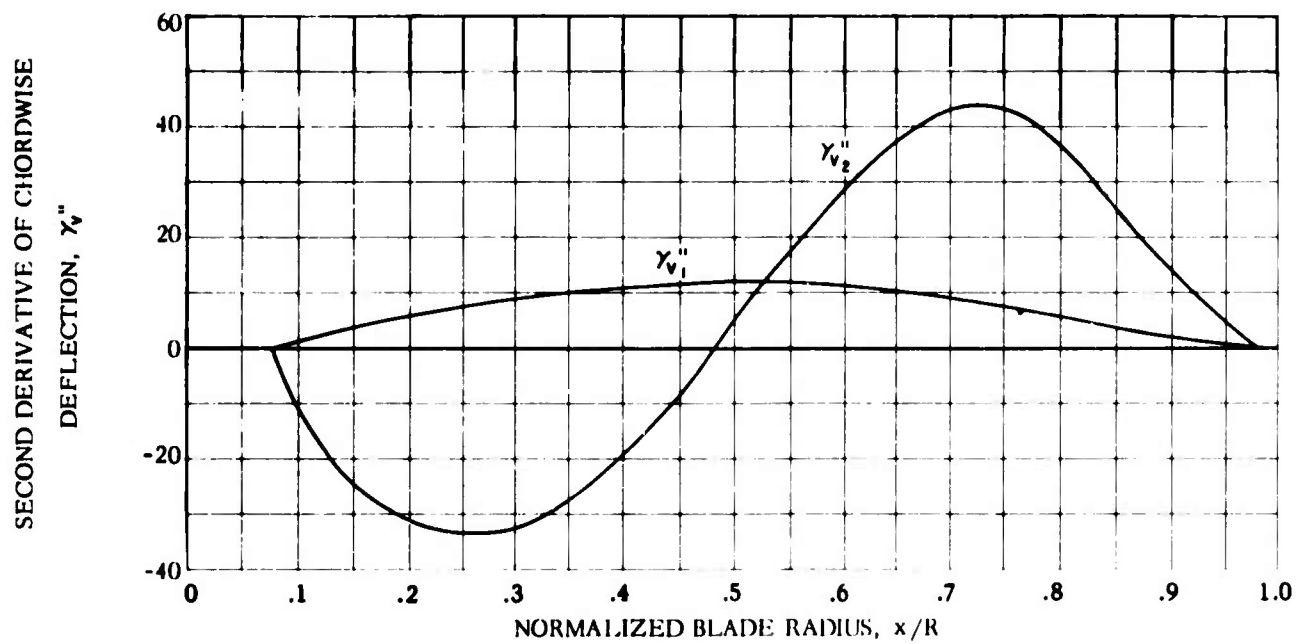


Figure 67. Continued

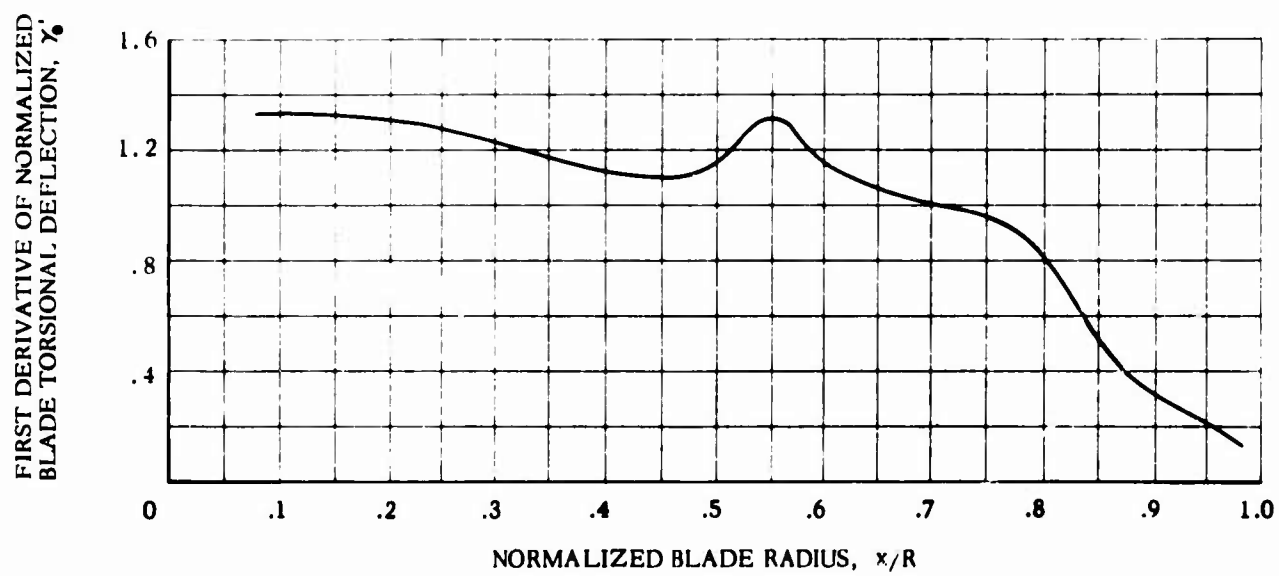
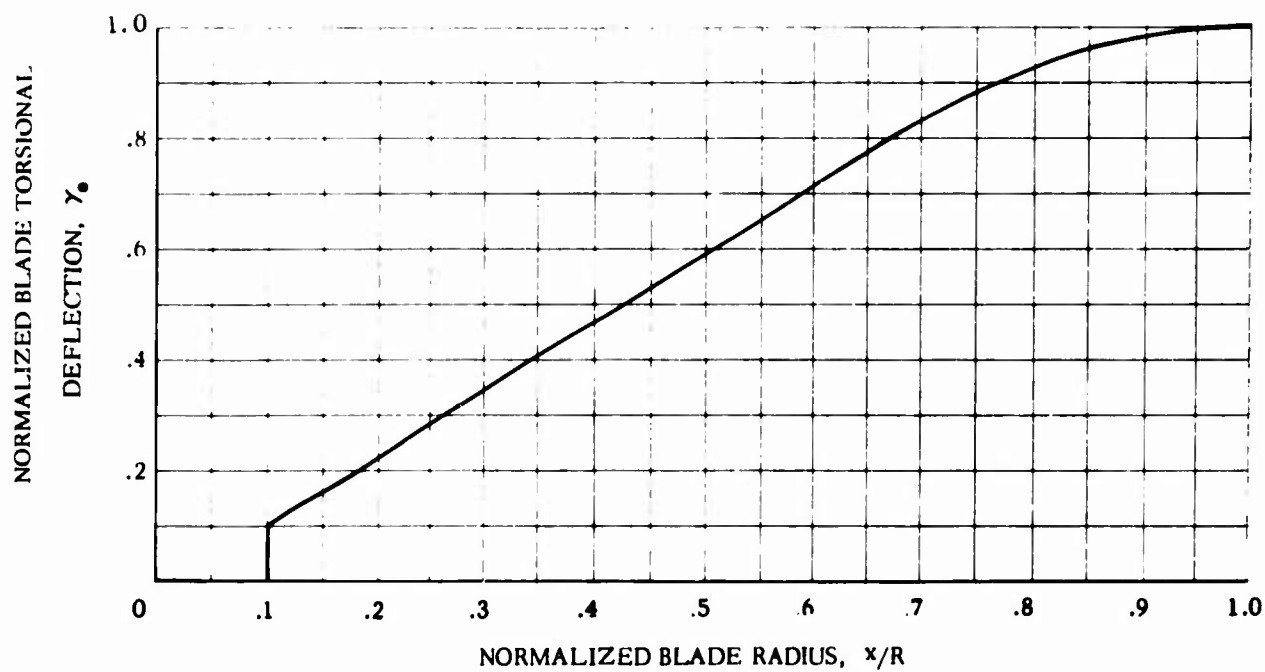


Figure 67. Continued

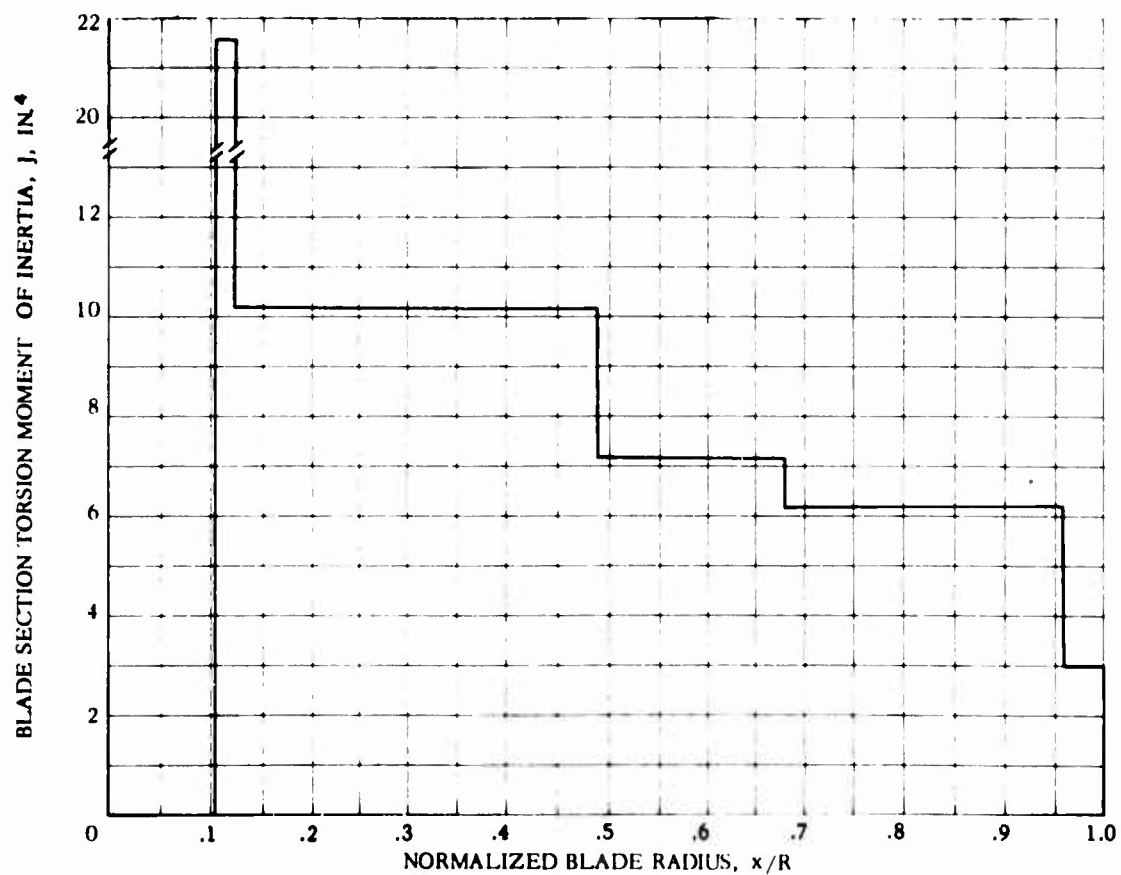
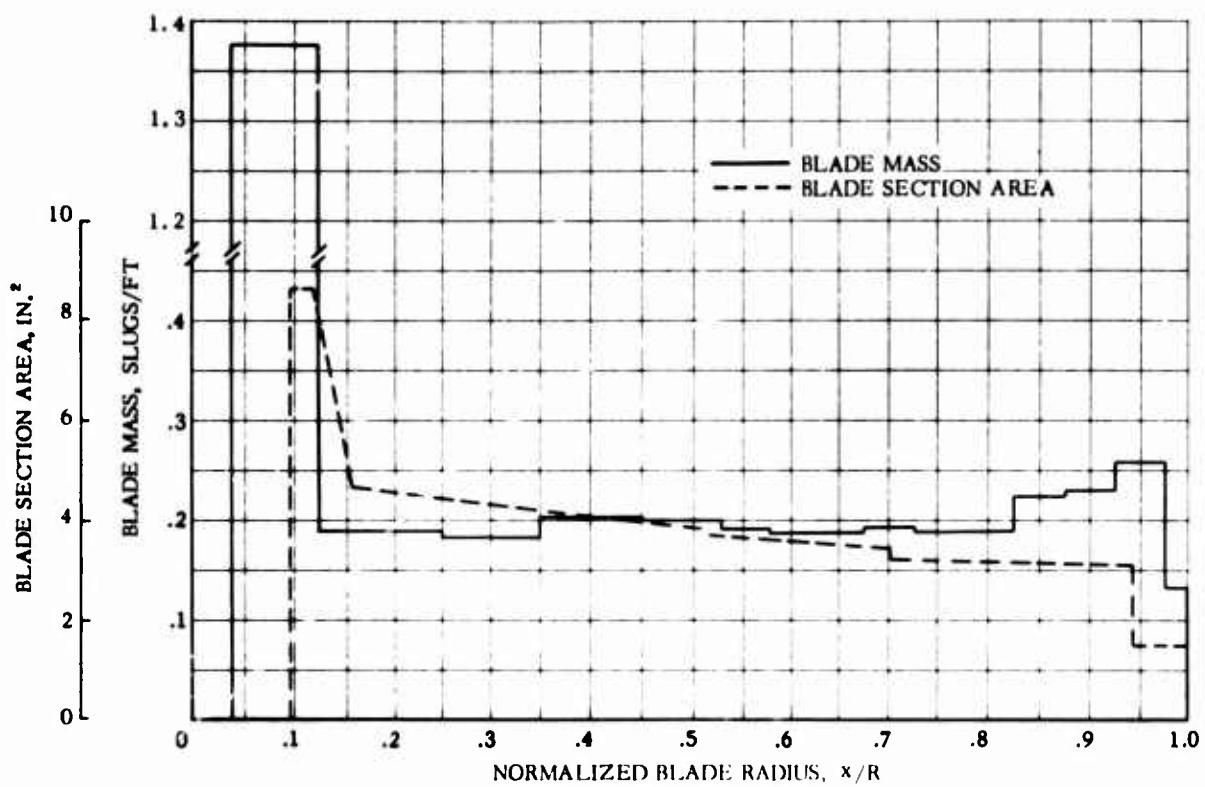


Figure 67. Concluded

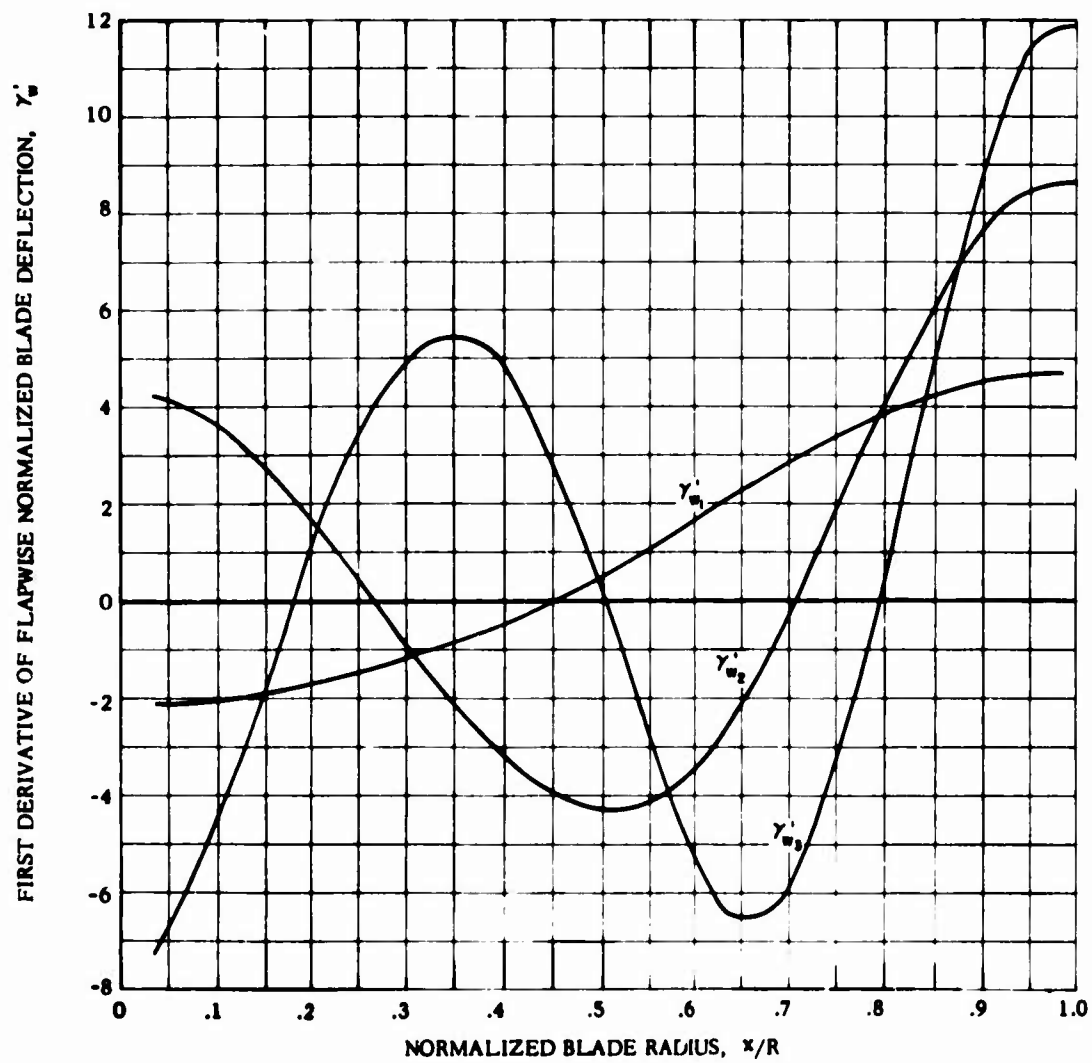
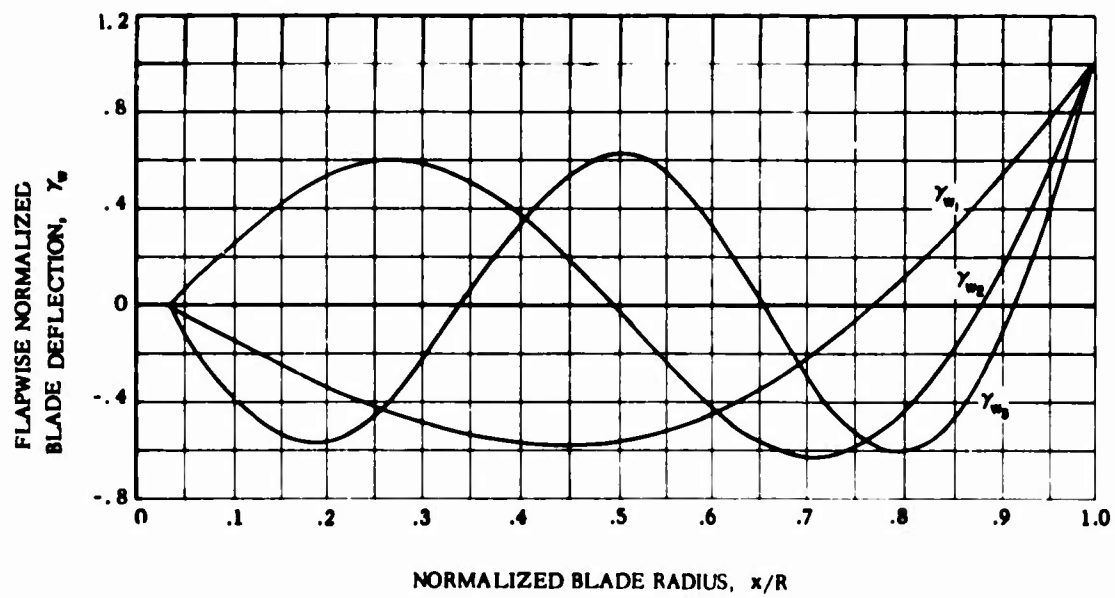


Figure 68. Articulated Rotor Blade Spanwise Structural and Physical Properties

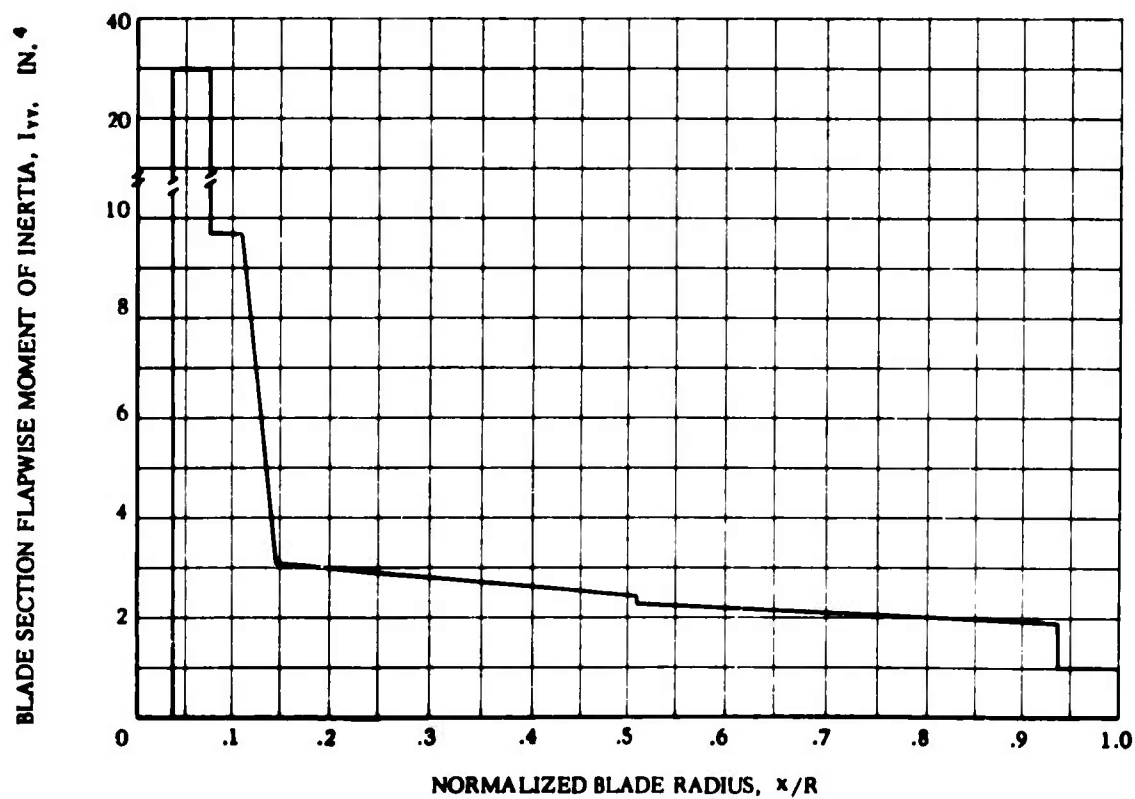
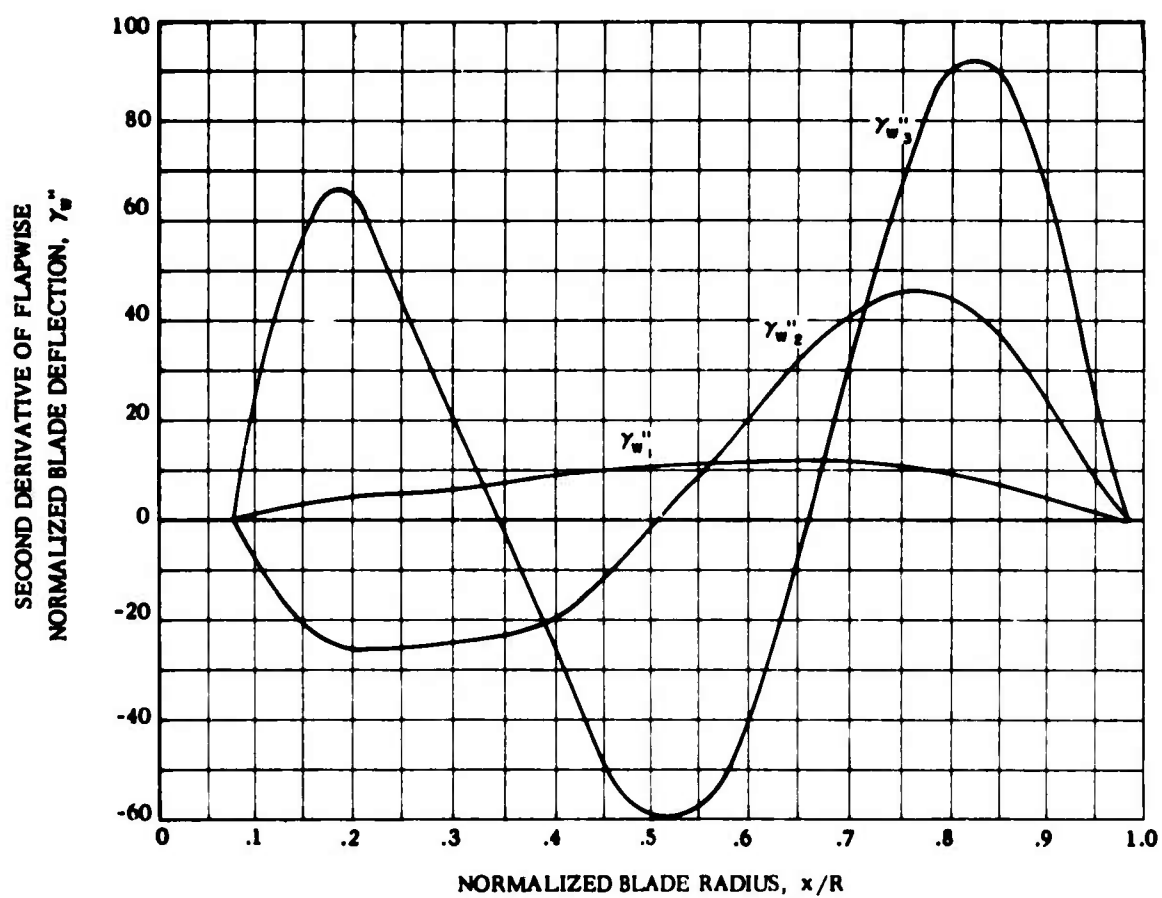


Figure 68. Continued

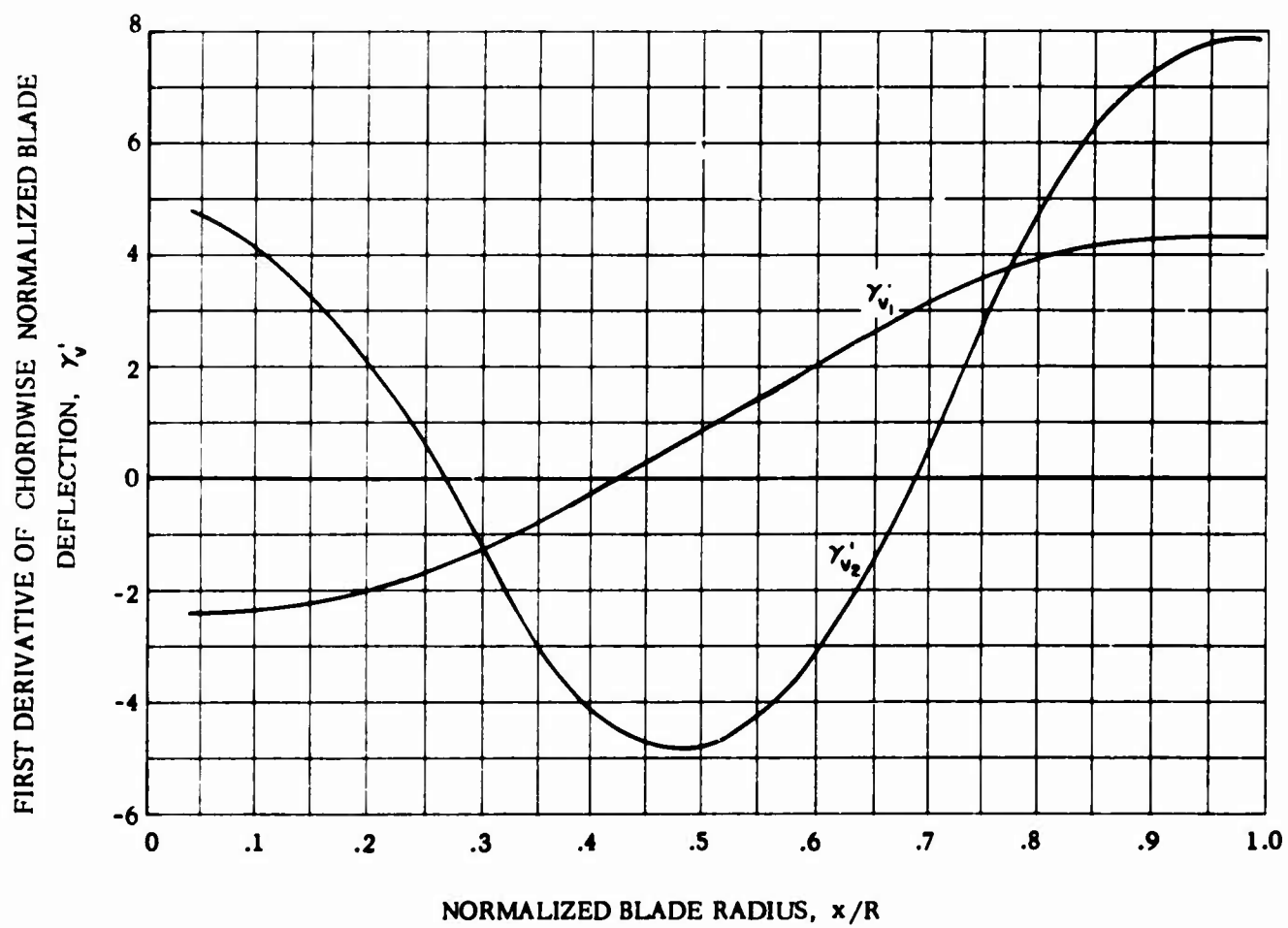
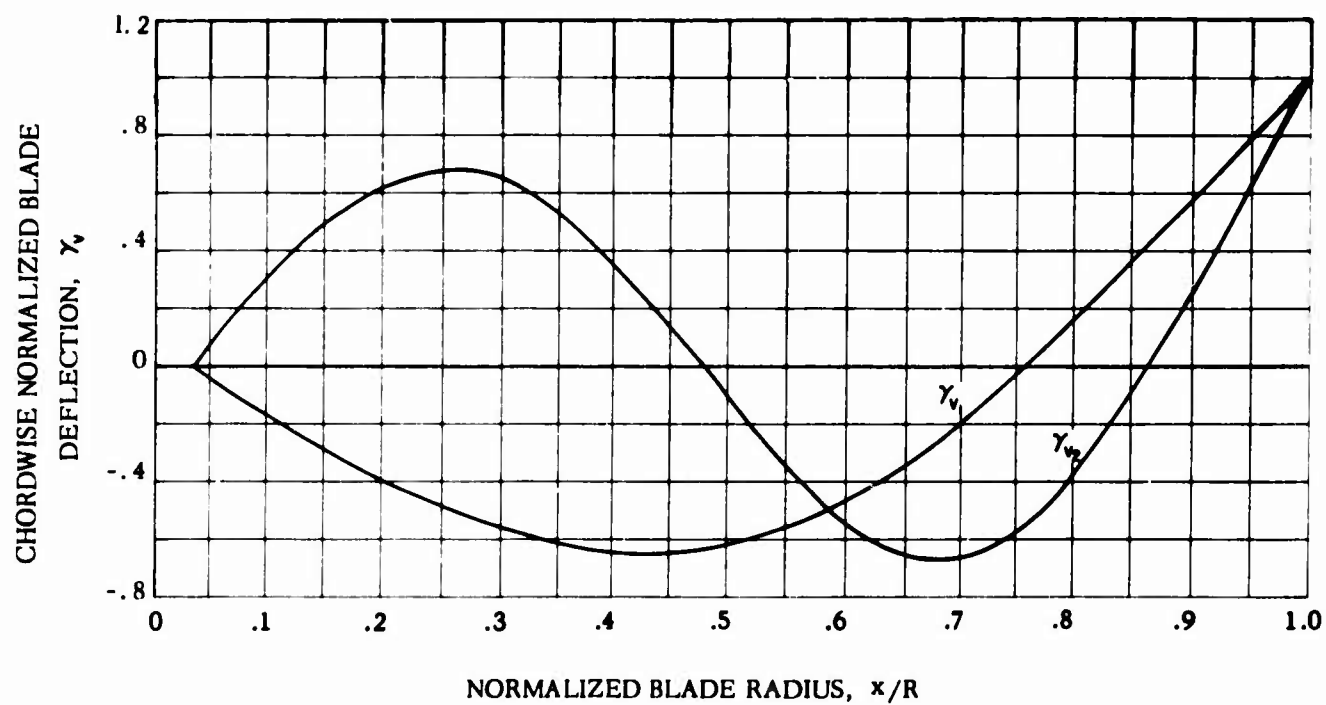


Figure 68. Continued

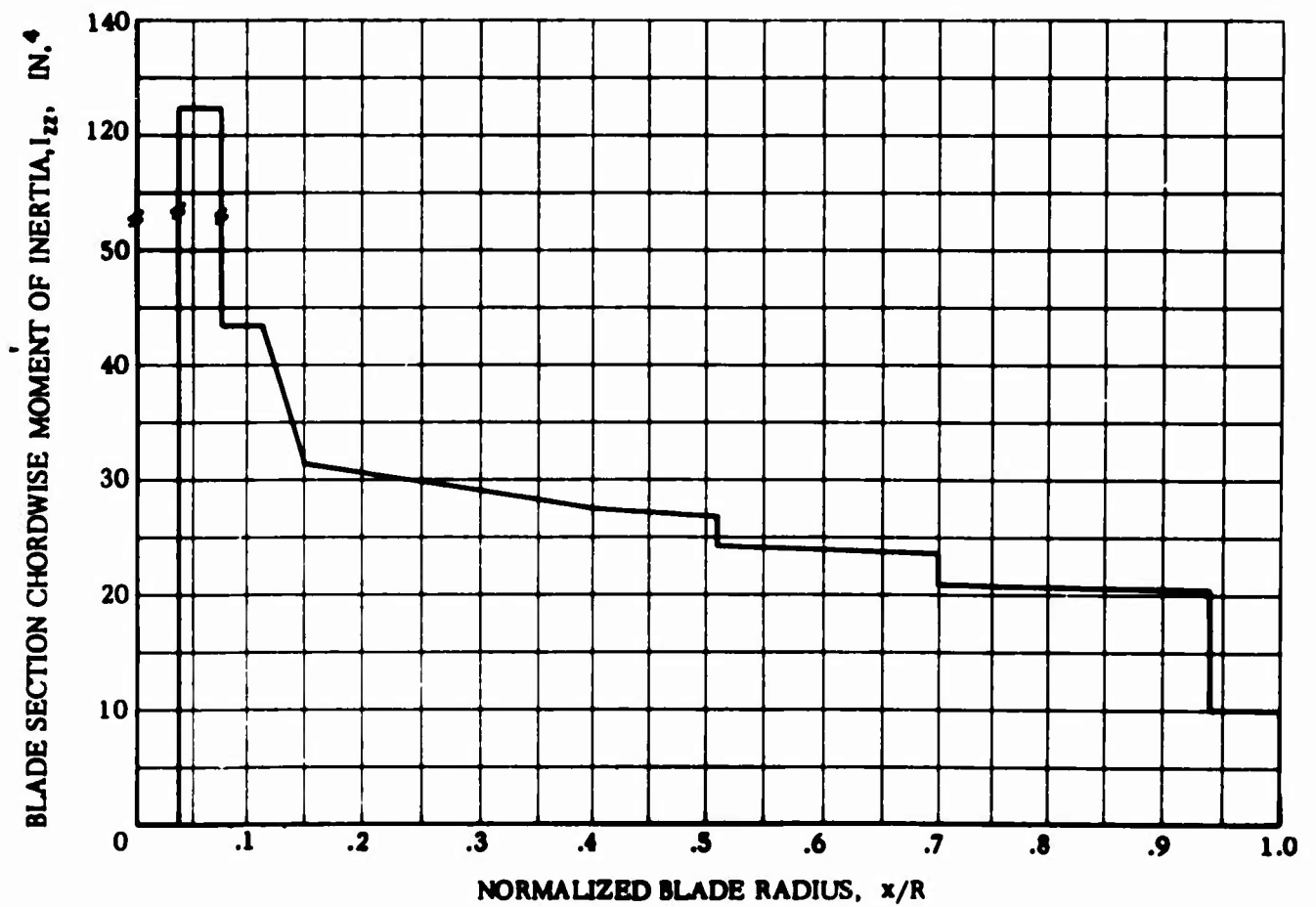
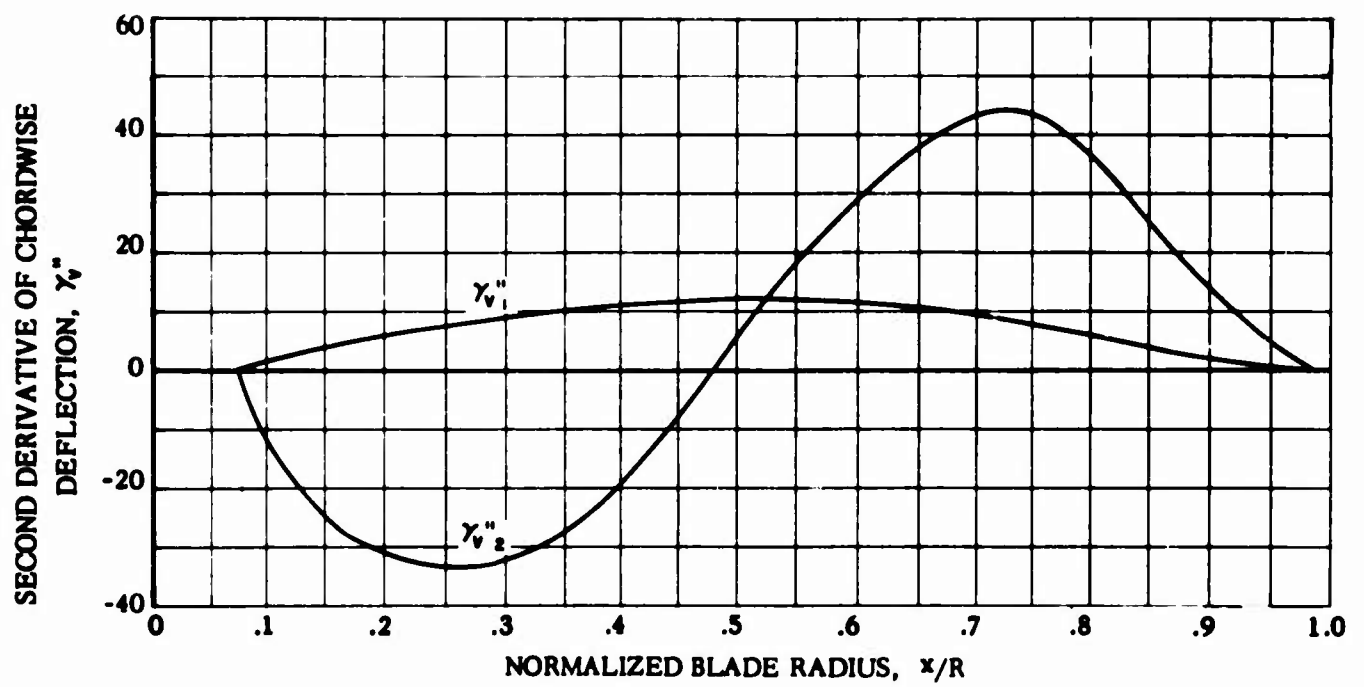


Figure 68. Continued

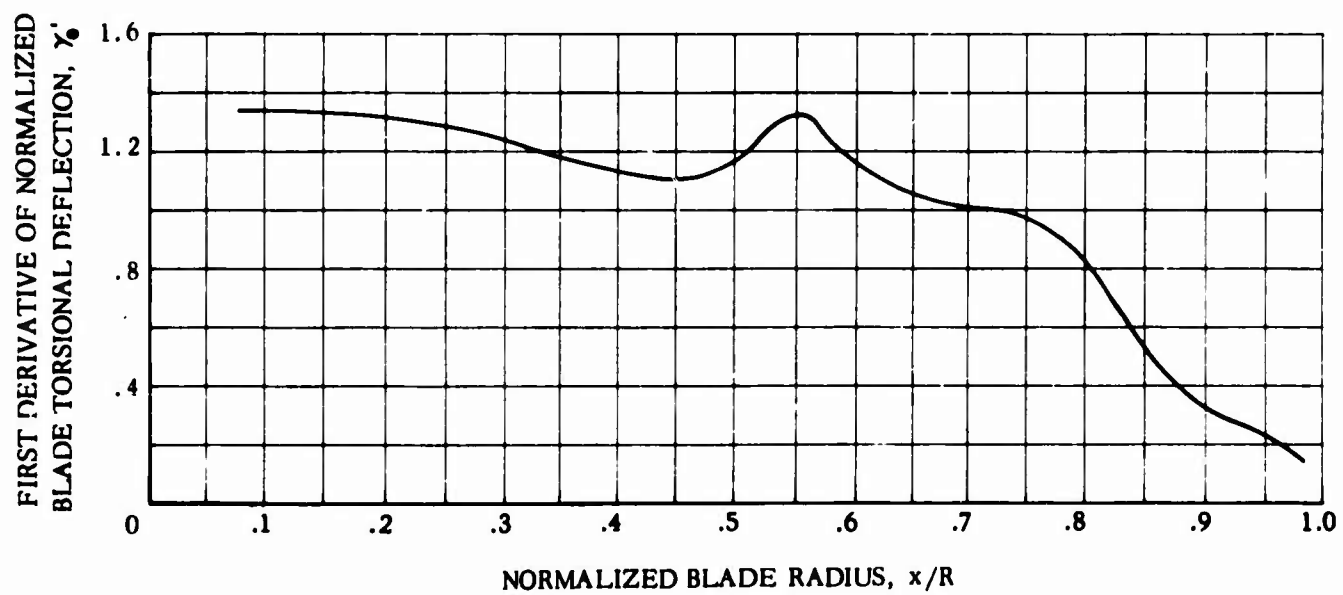
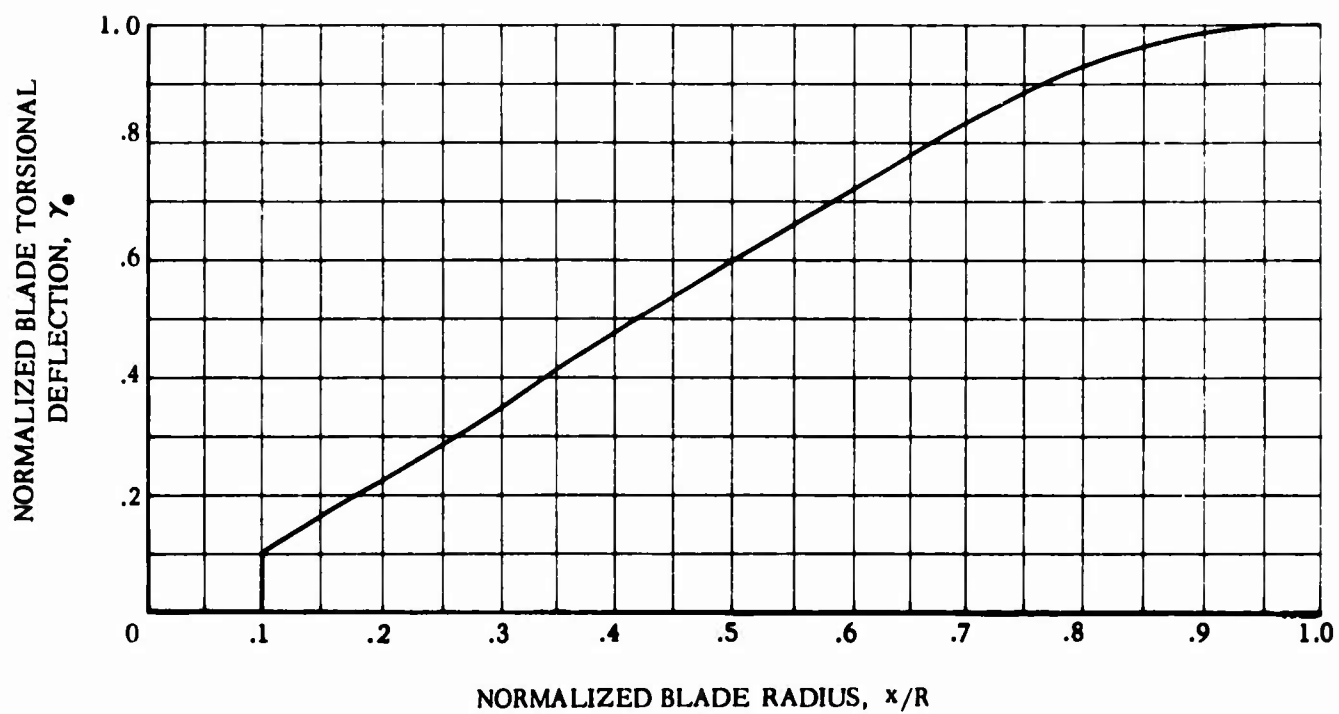


Figure 68. Continued

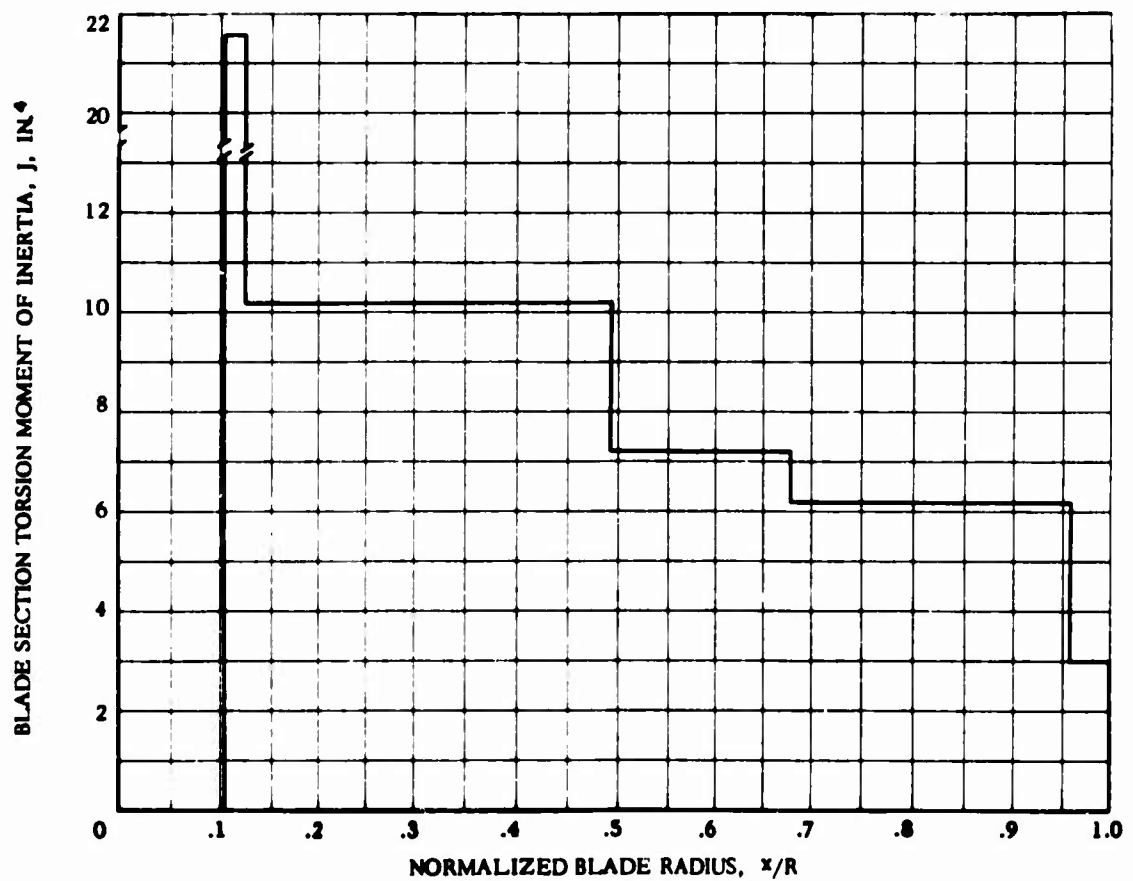
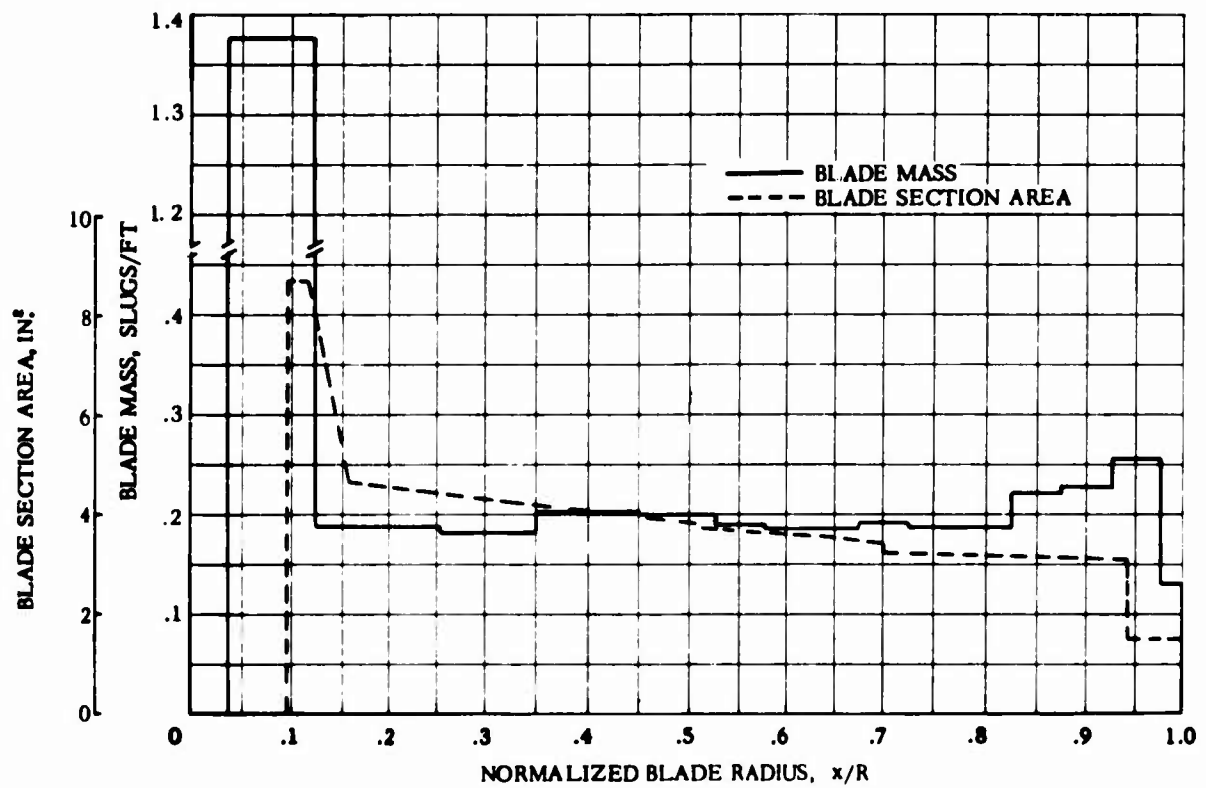


Figure 68. Concluded

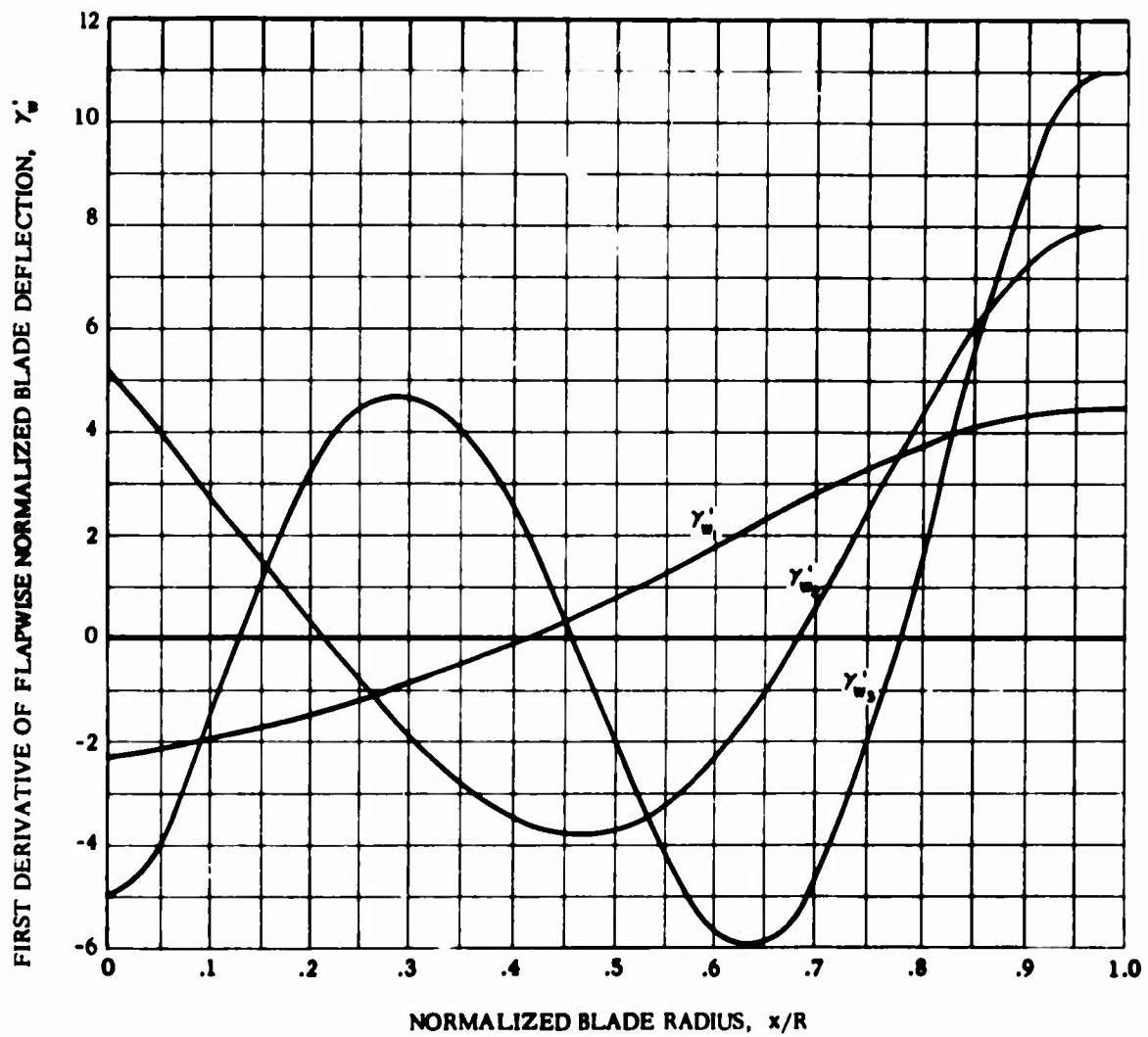
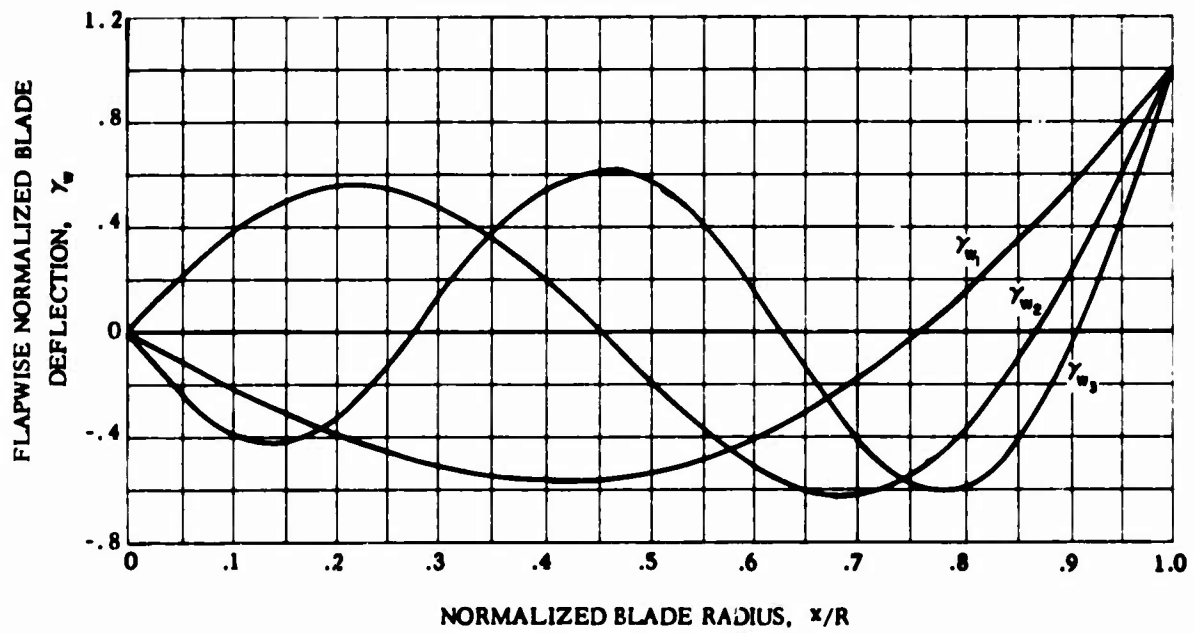


Figure 69. Zero Offset Rotor Blade Spanwise Structural and Physical Properties

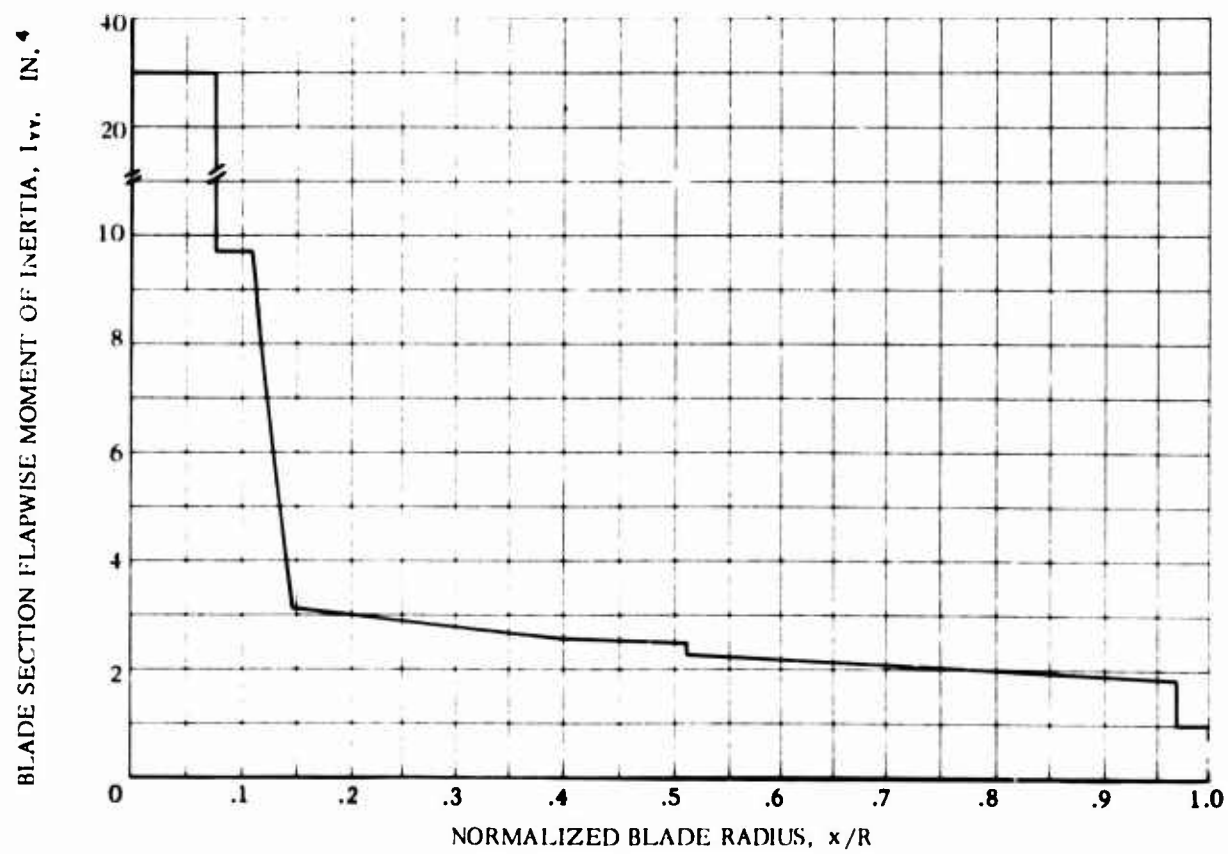
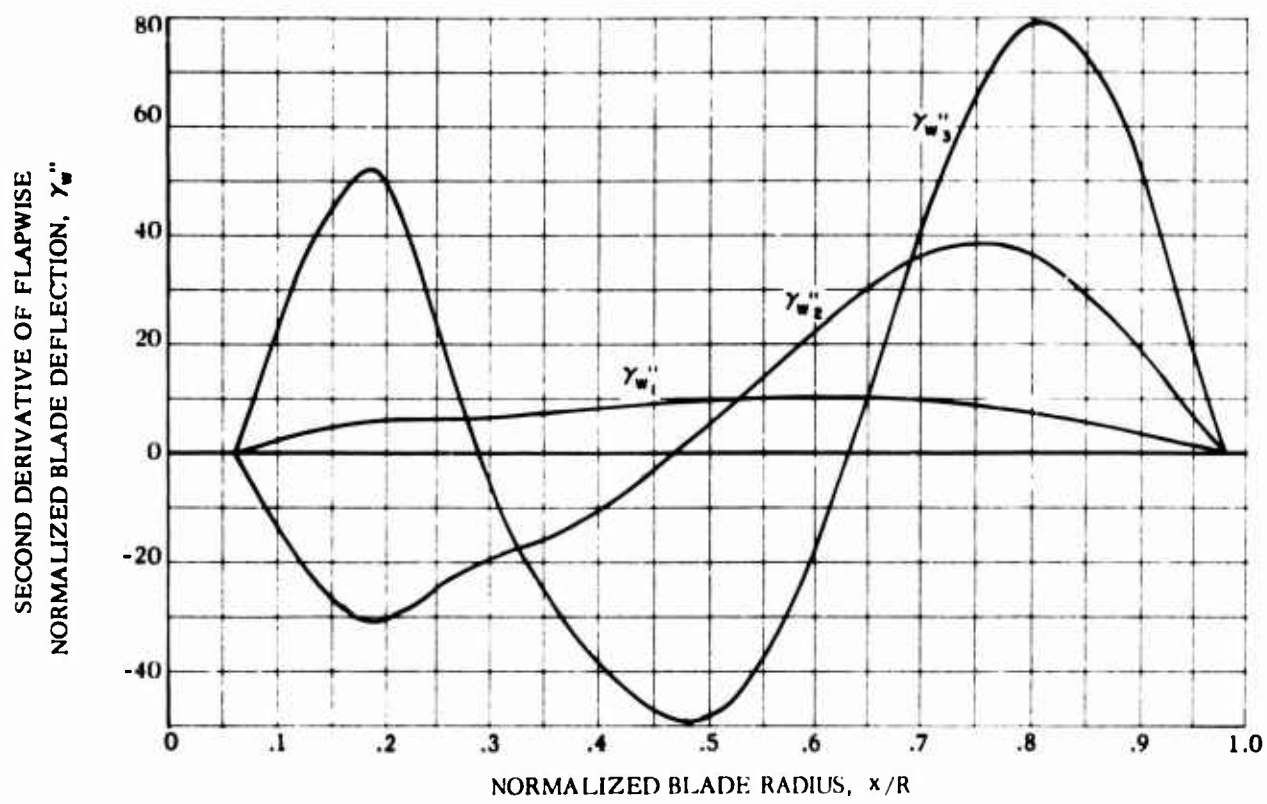


Figure 69. Continued

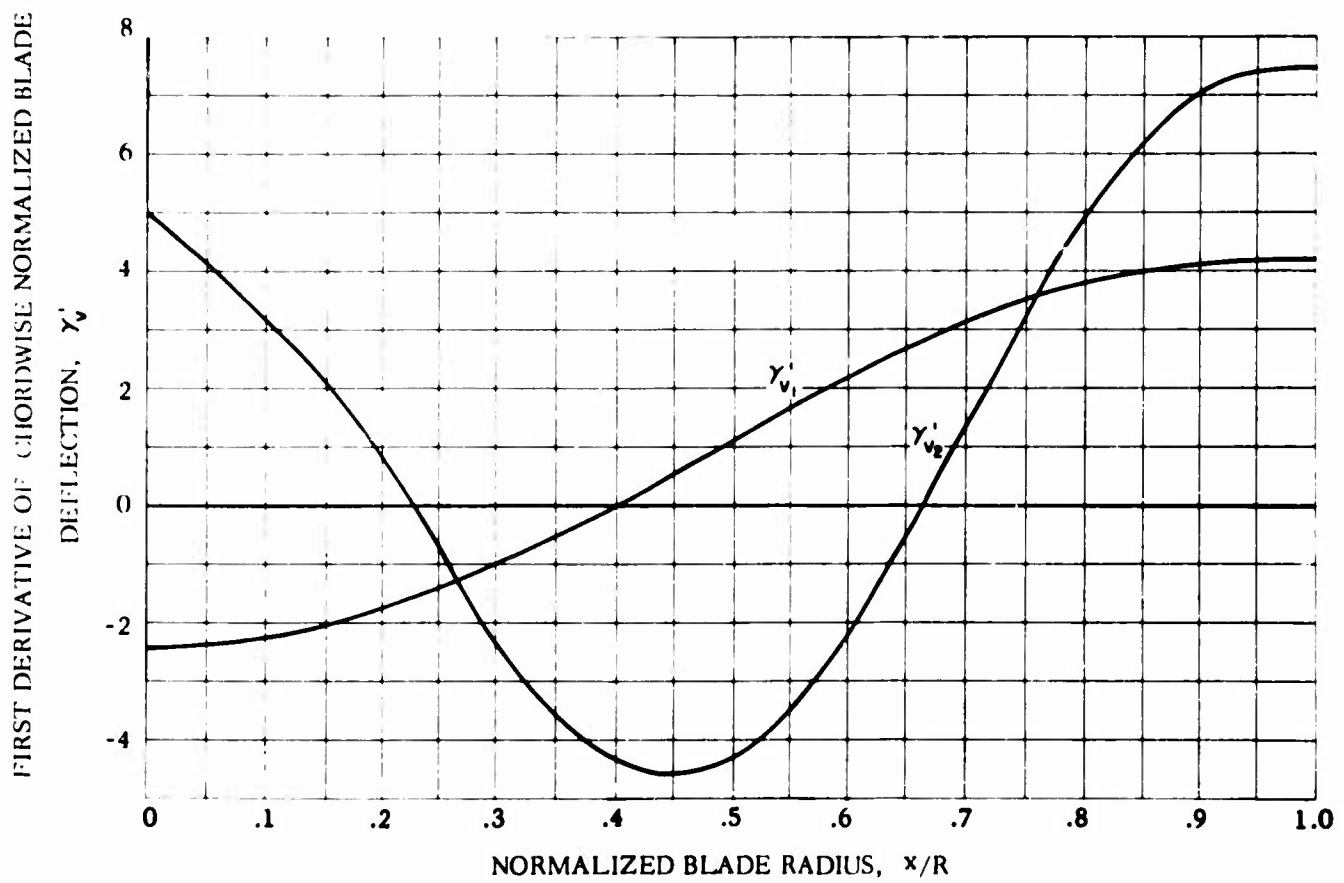
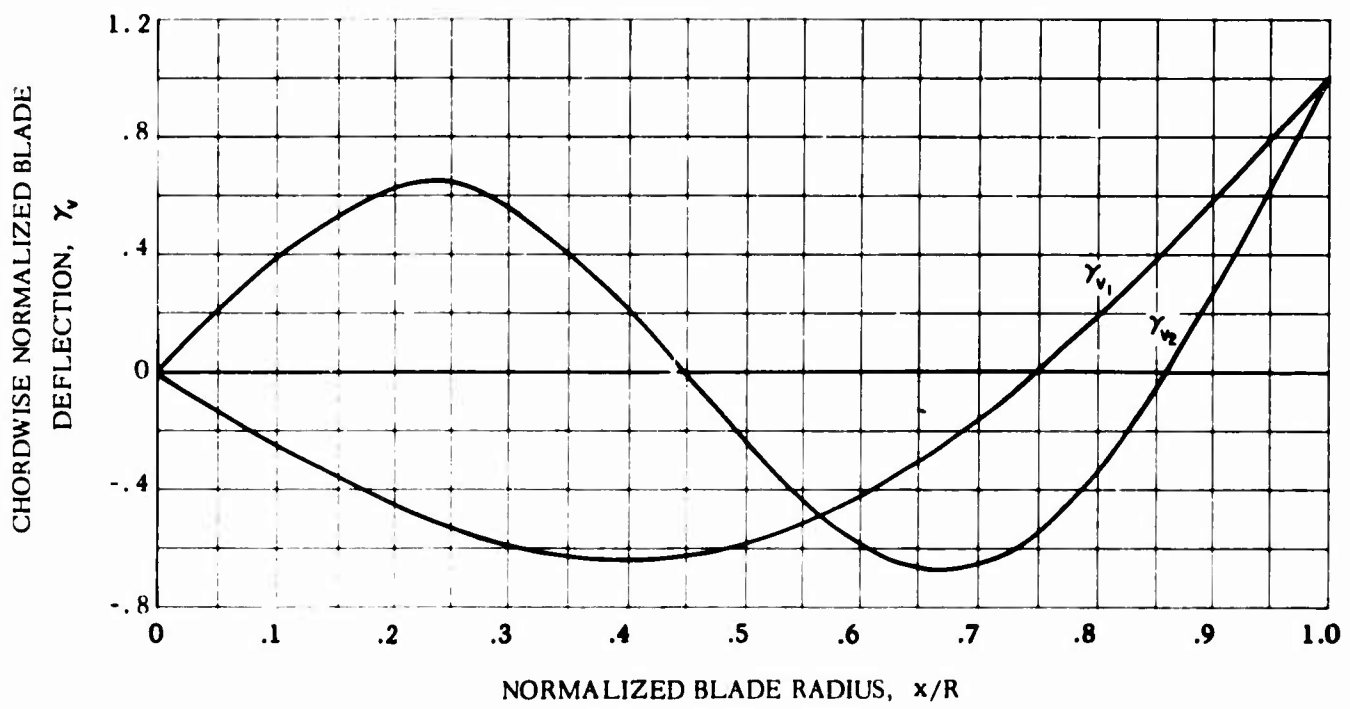


Figure 69. Continued

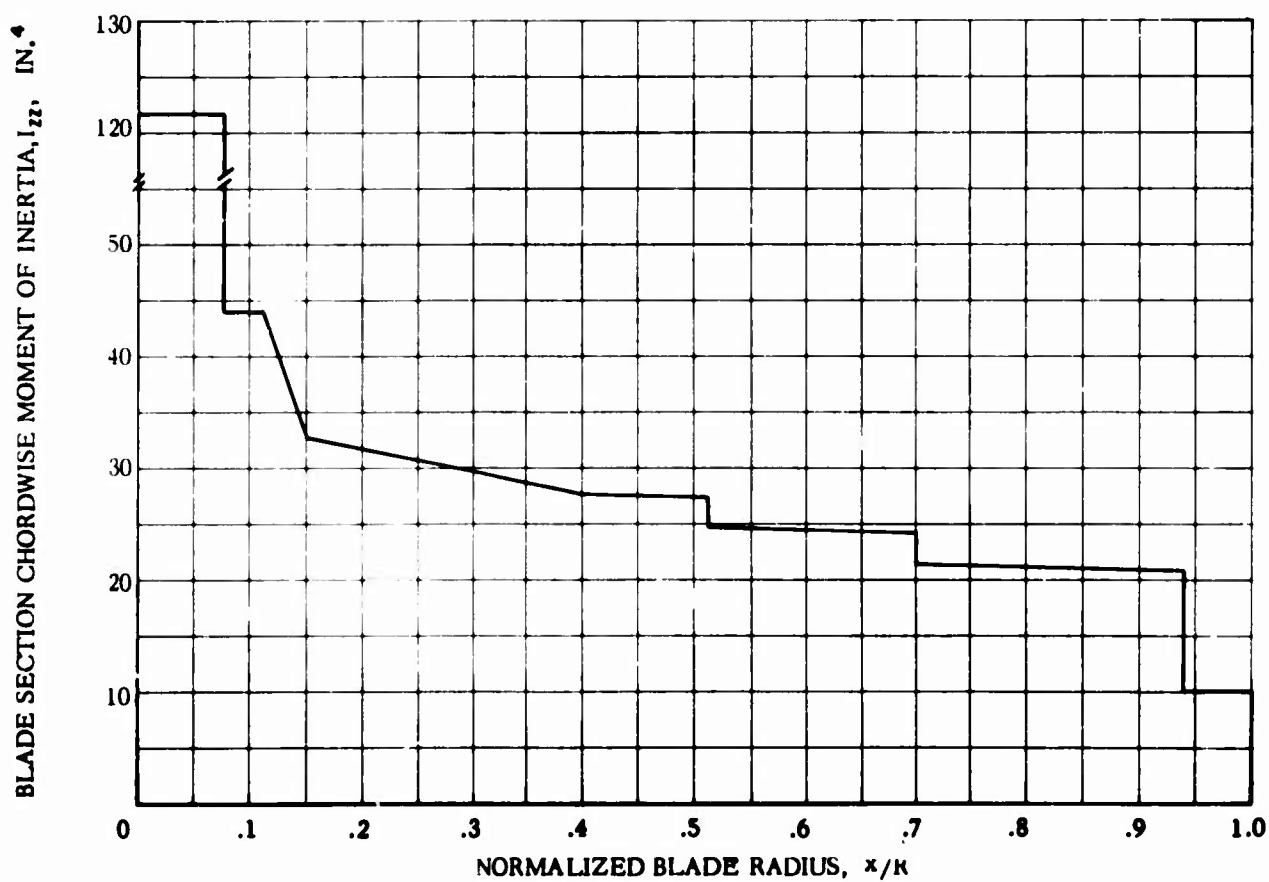
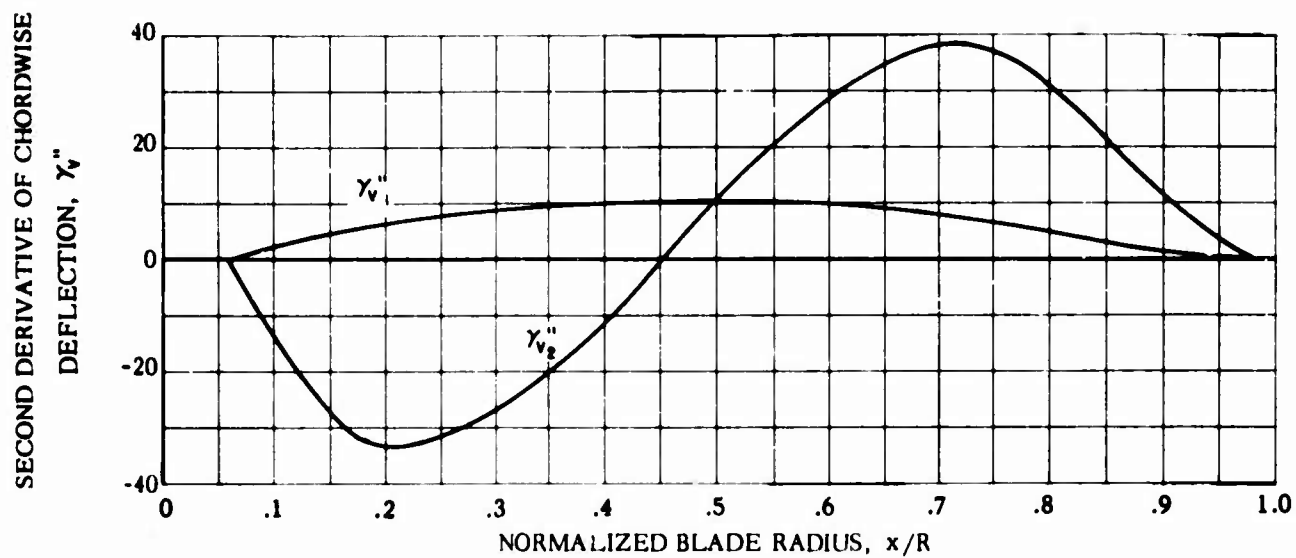


Figure 69. Continued

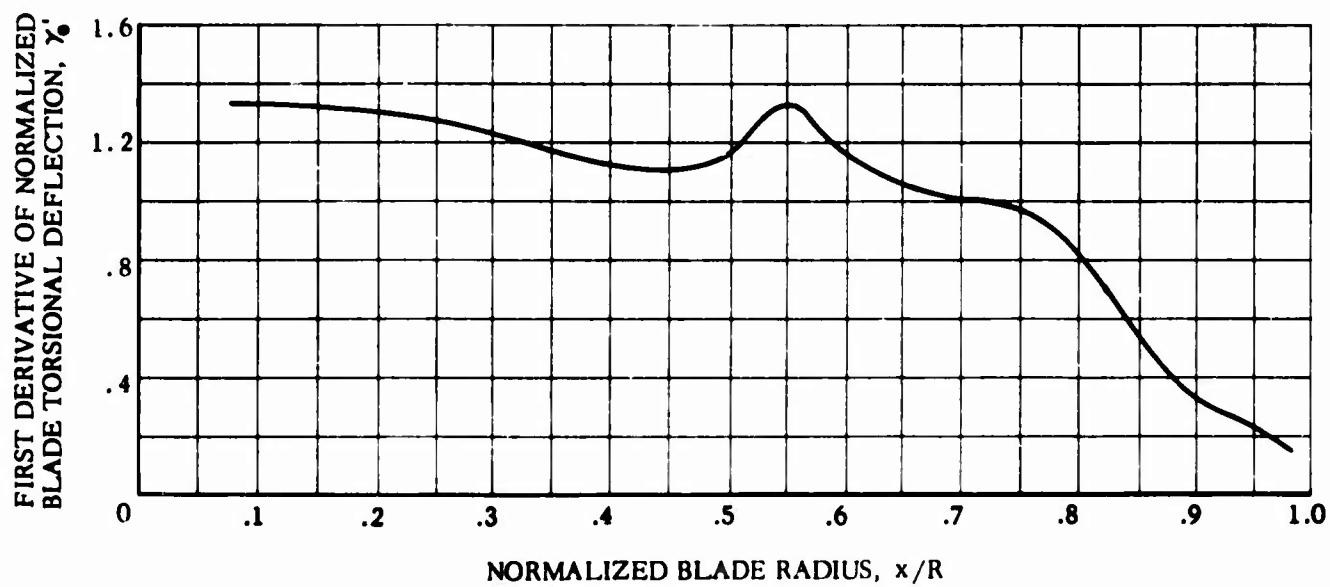
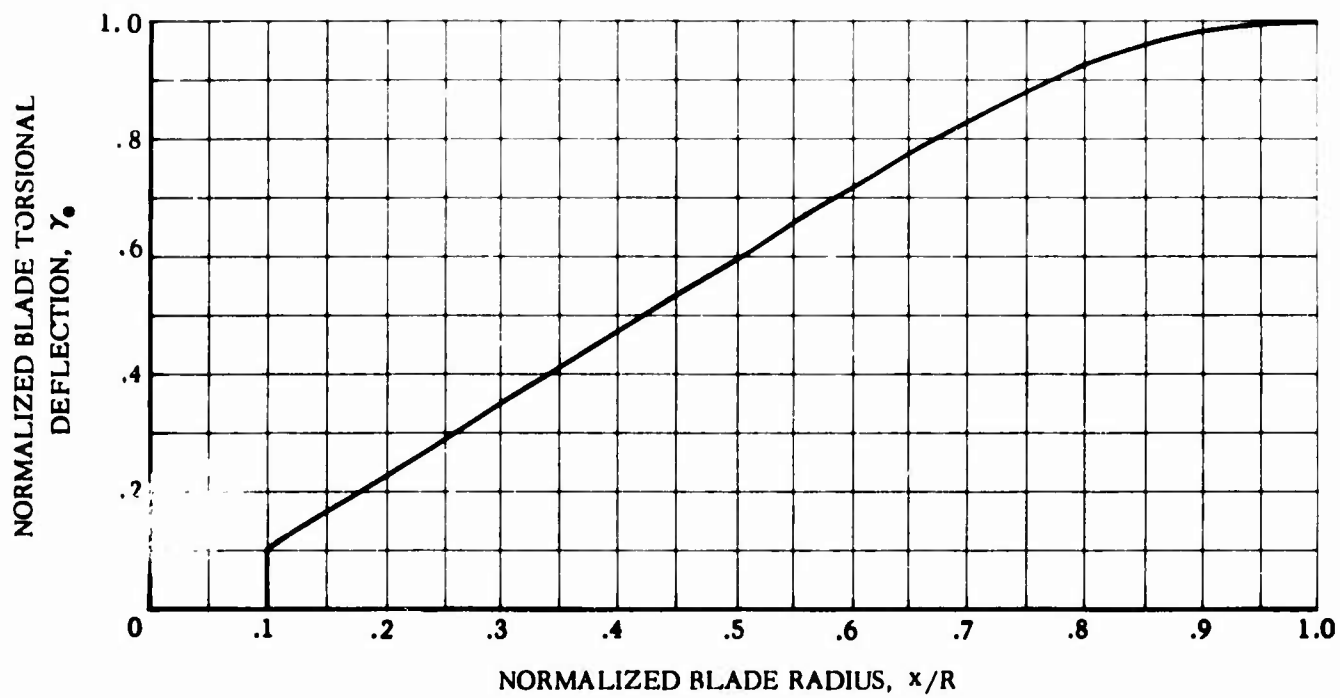


Figure 69. Continued

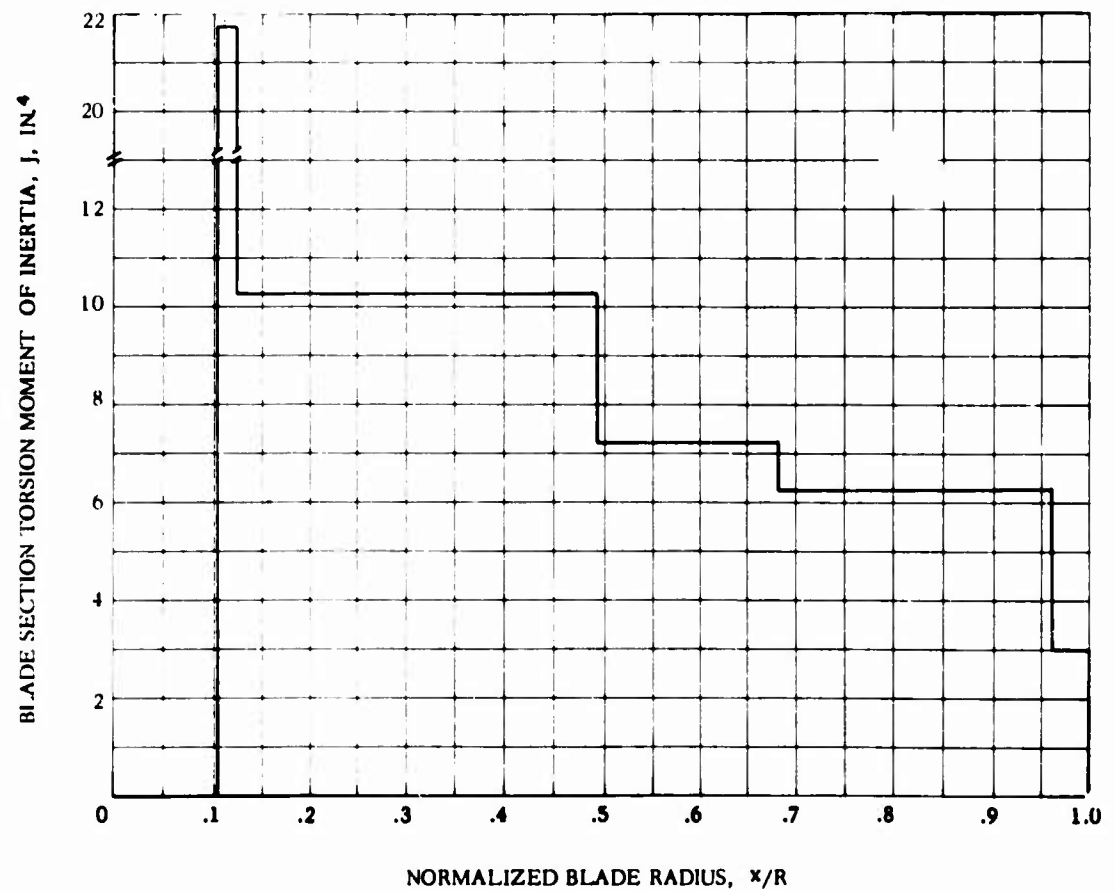
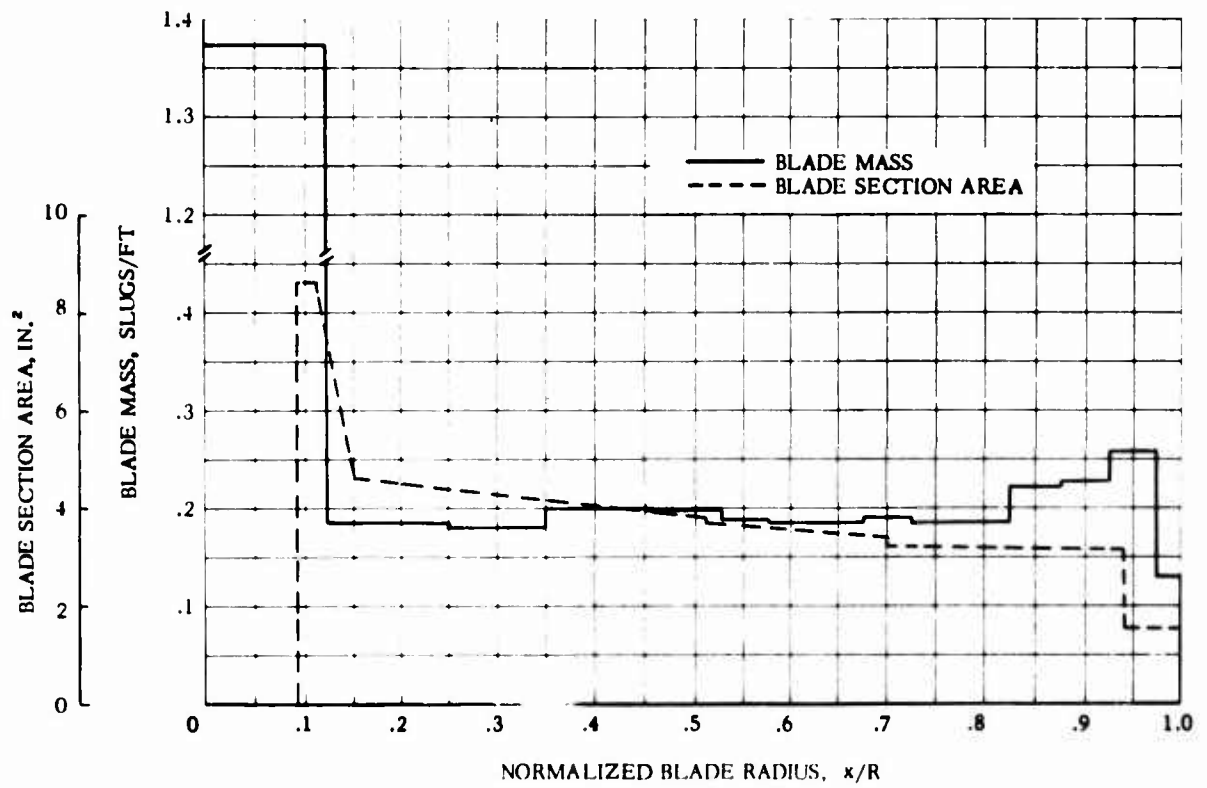


Figure 69. Concluded

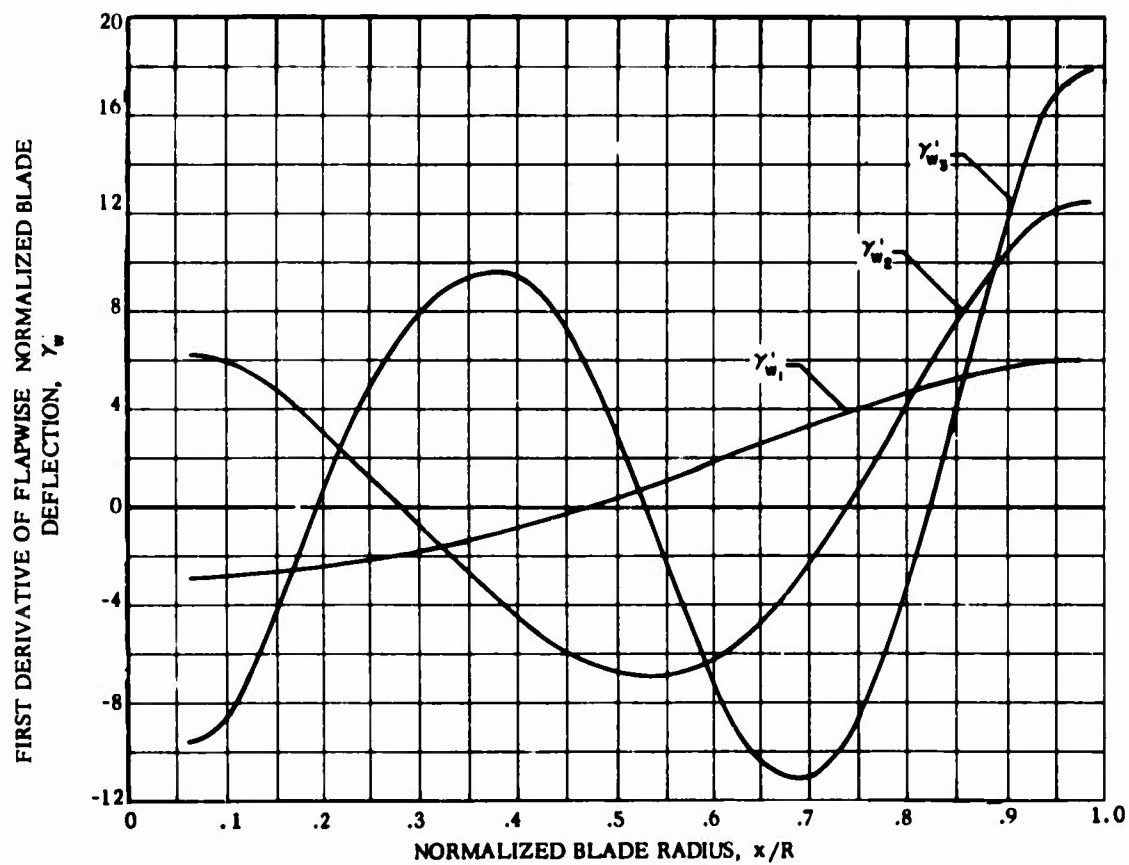
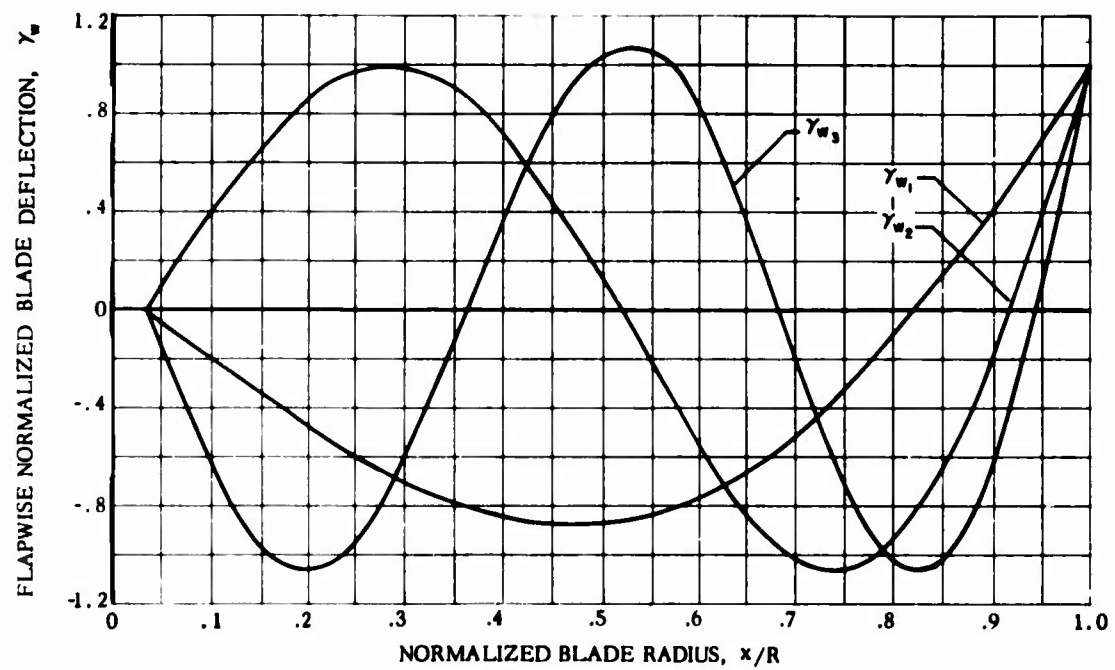


Figure 70. Reduced Lock Number Rotor Blade Spanwise Structural and Physical Properties

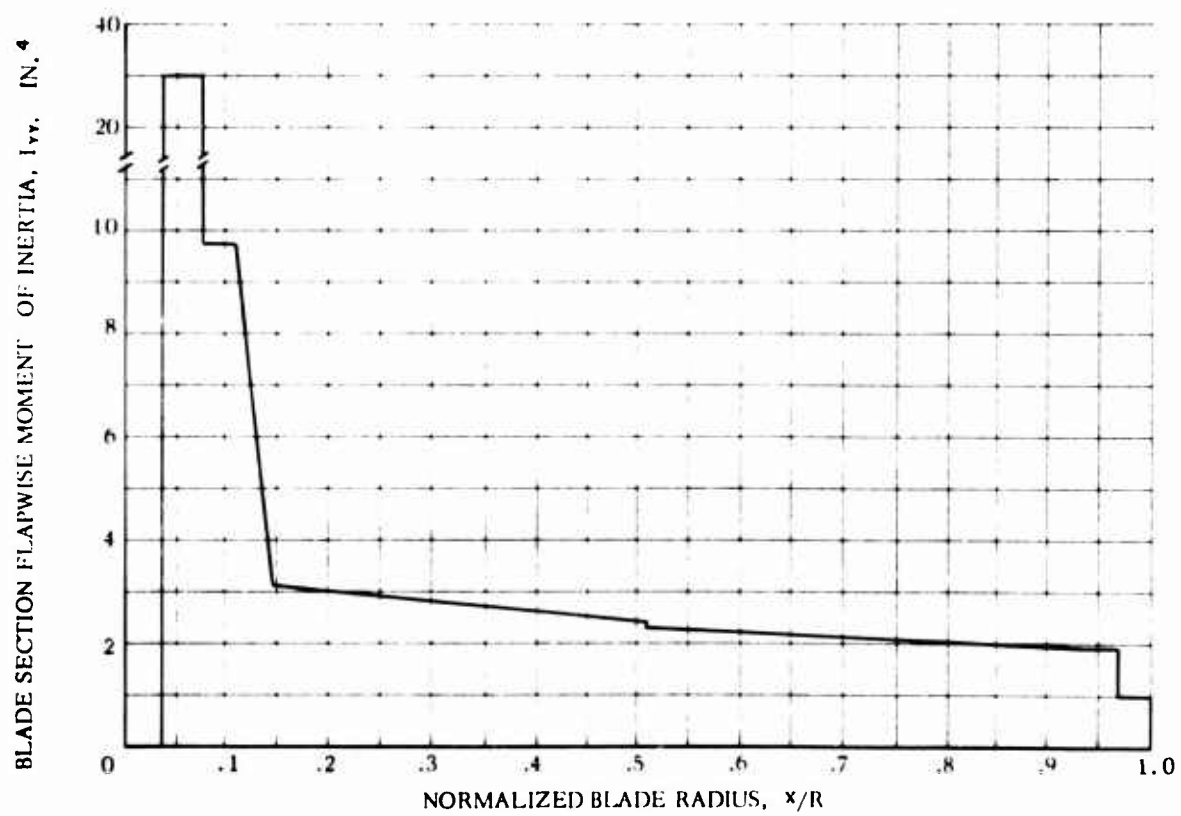
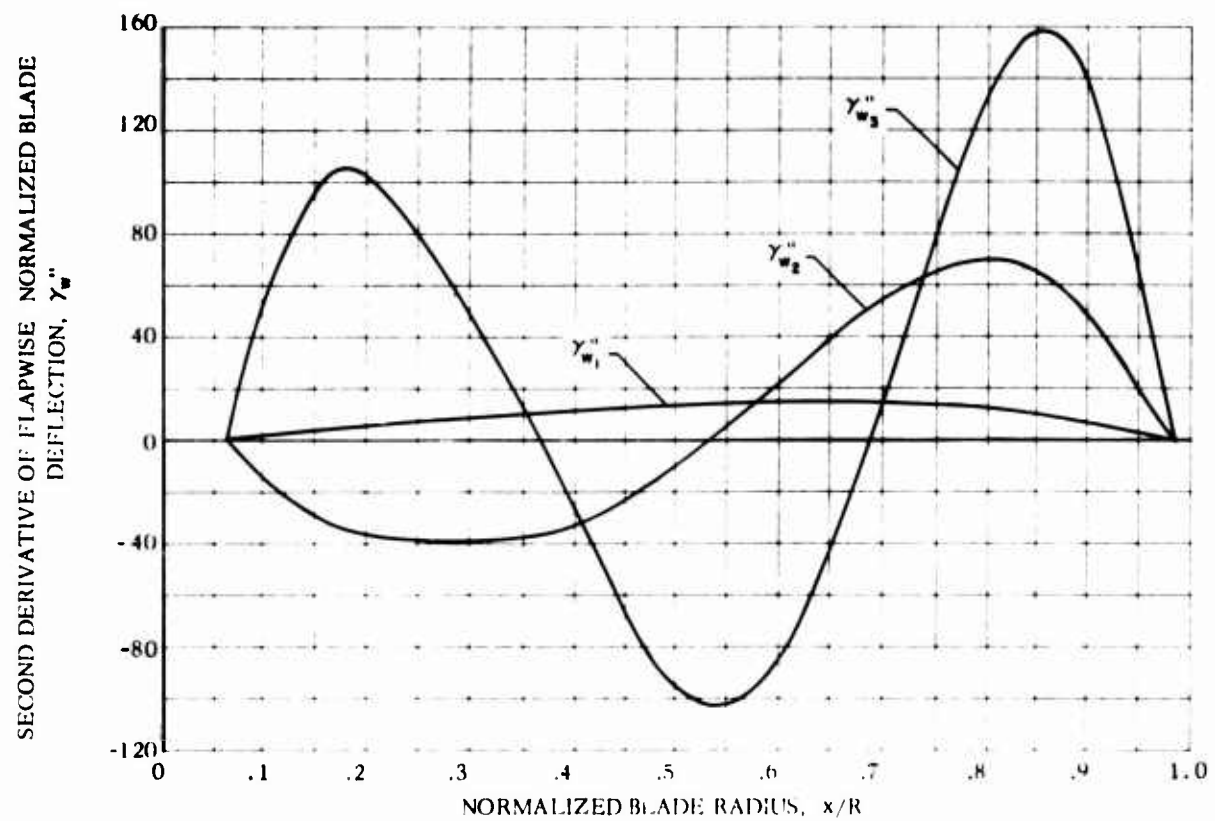


Figure 70. Continued

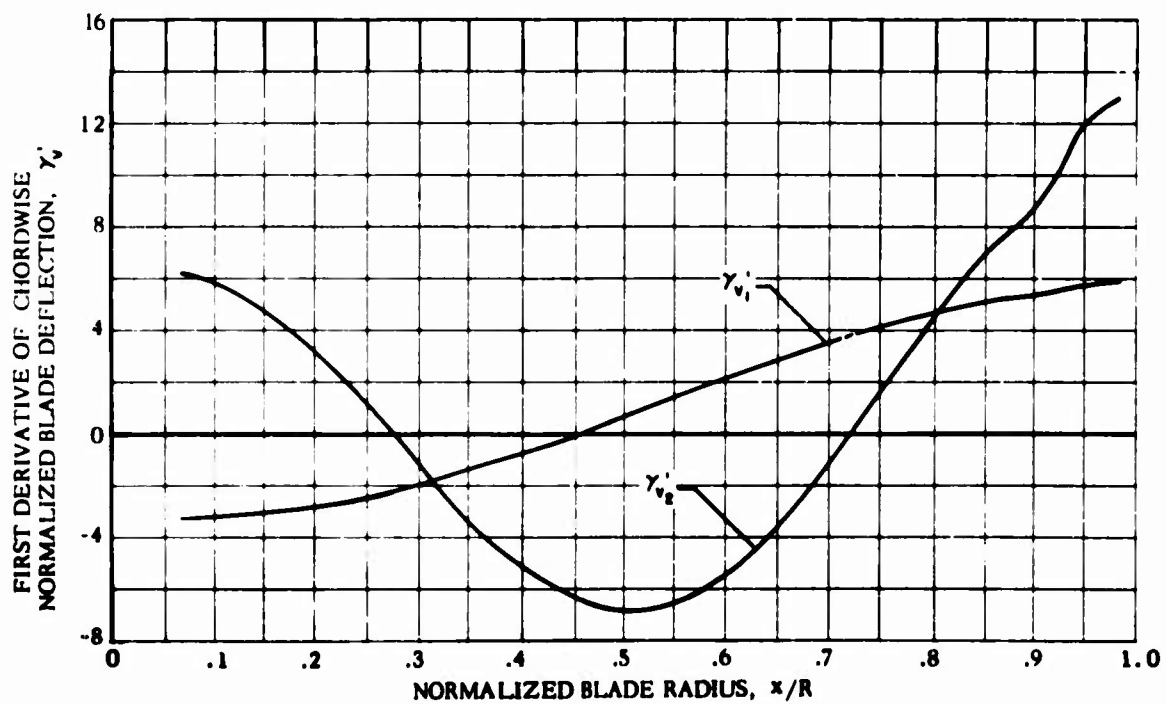
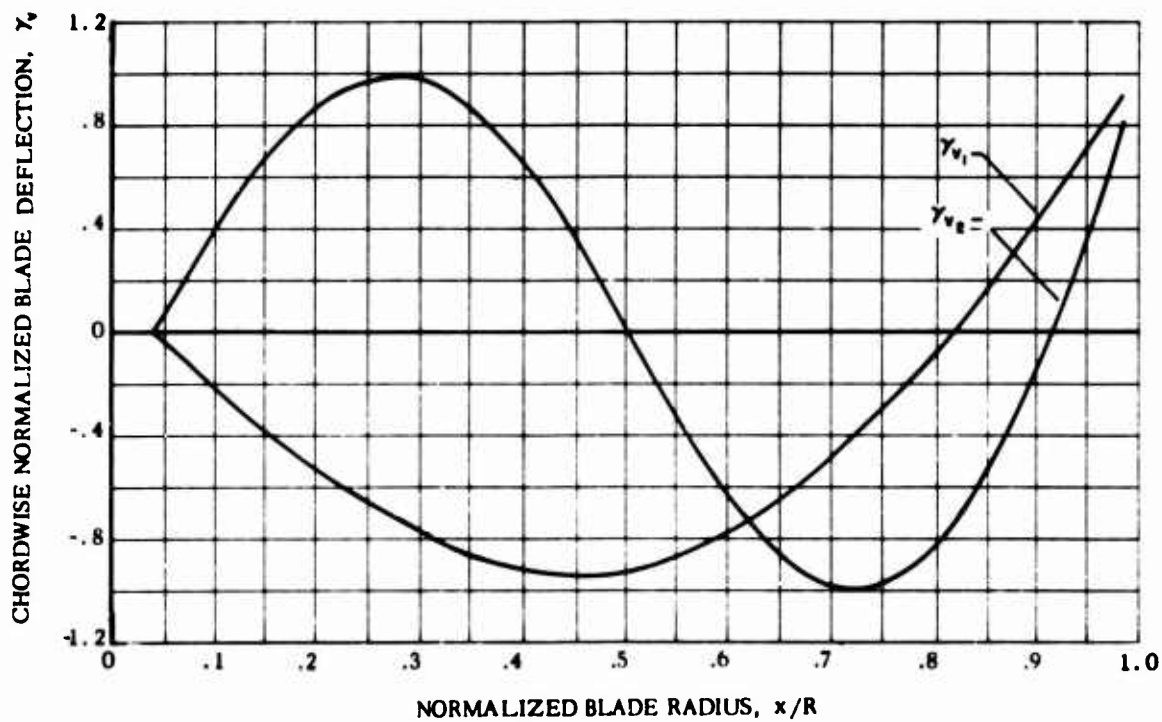


Figure 70. Continued

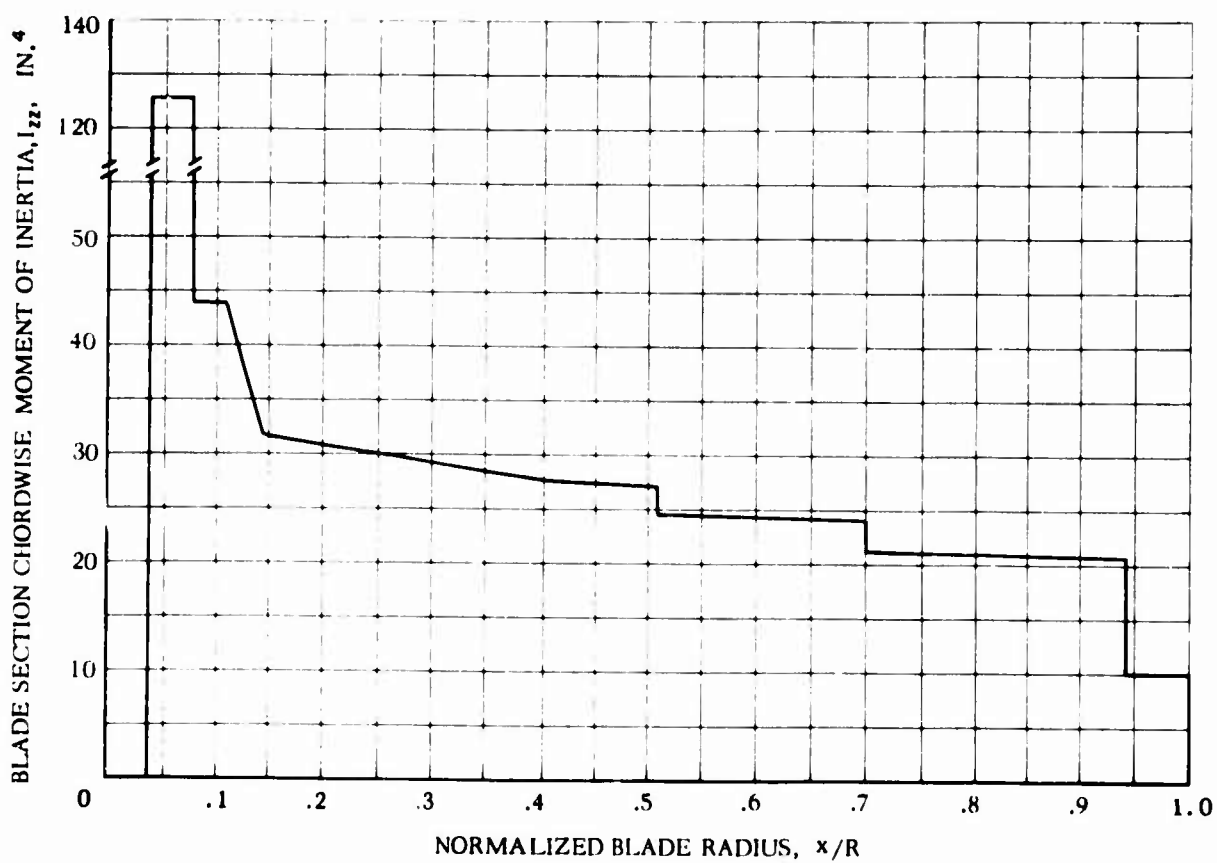
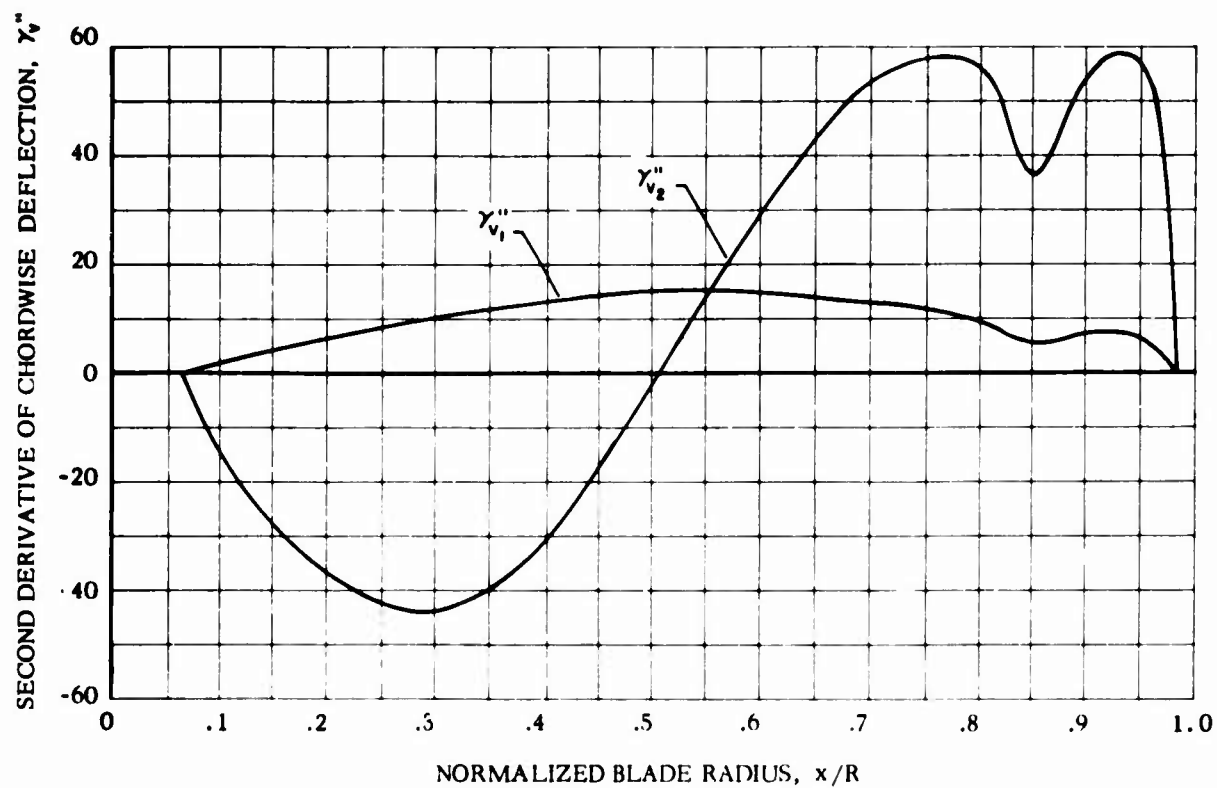


Figure 70. Continued

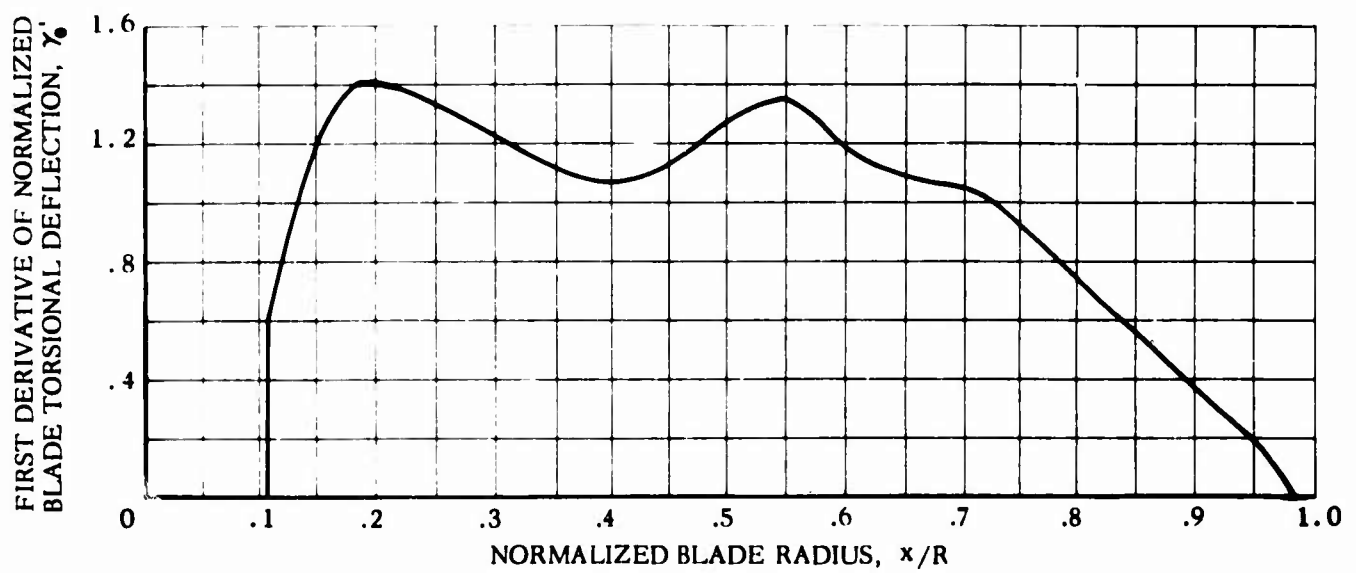
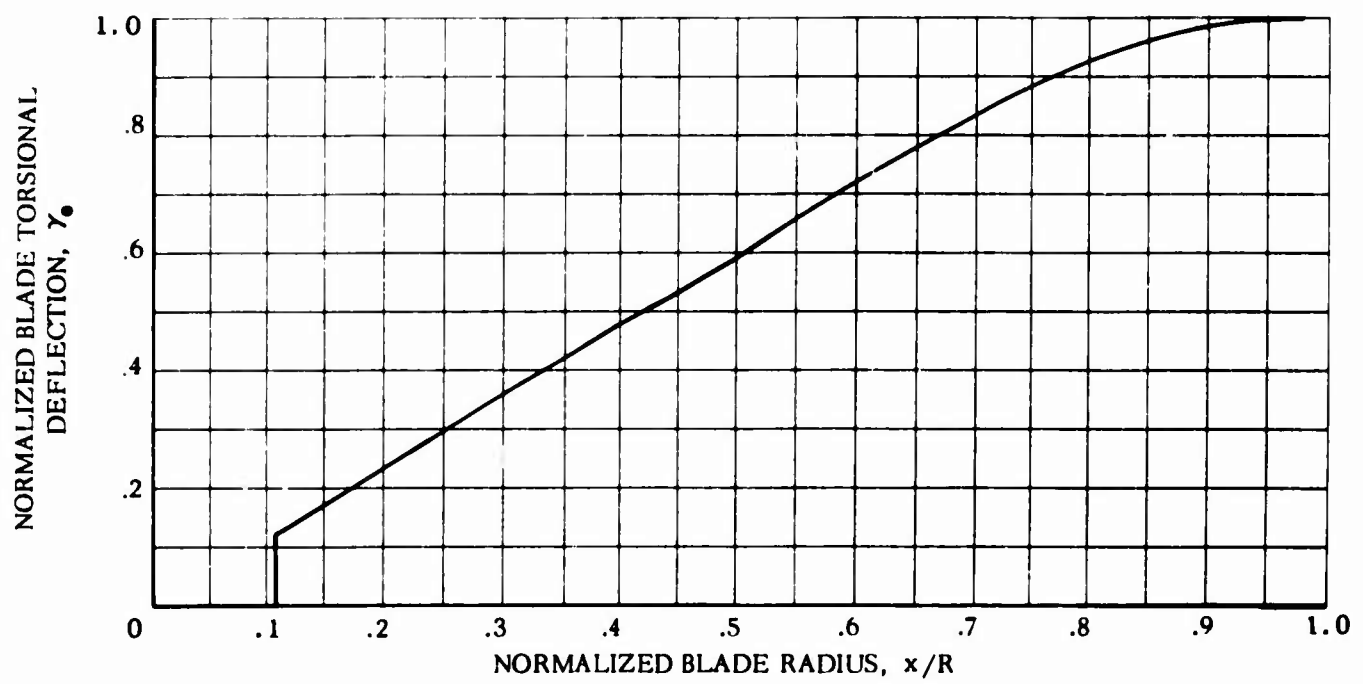


Figure 70. Continued

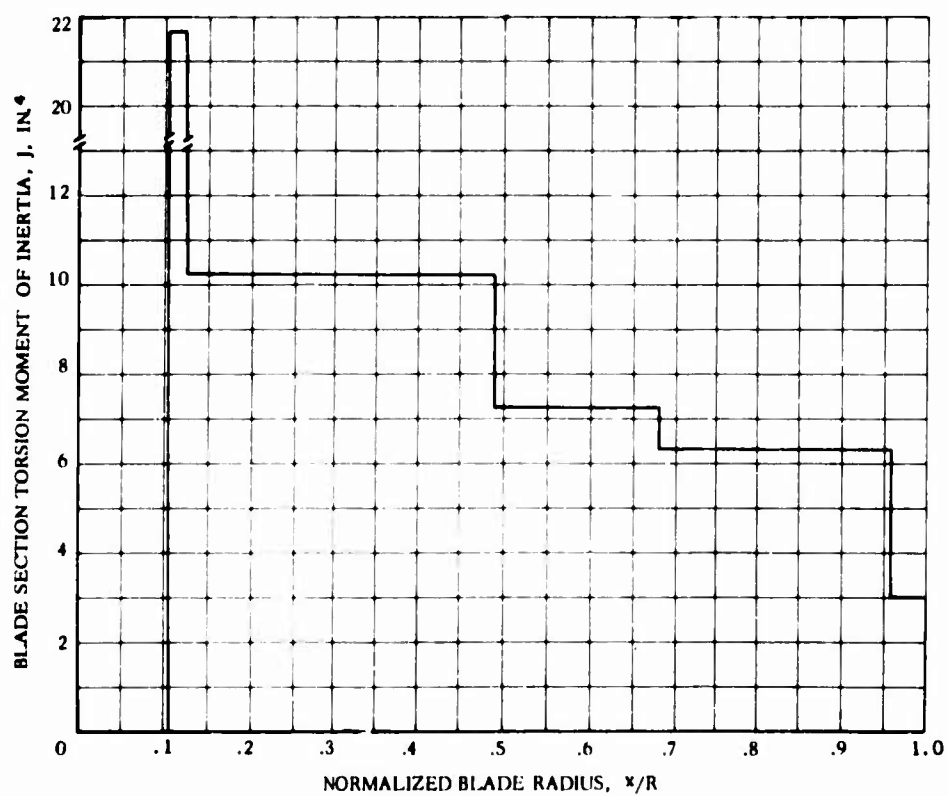
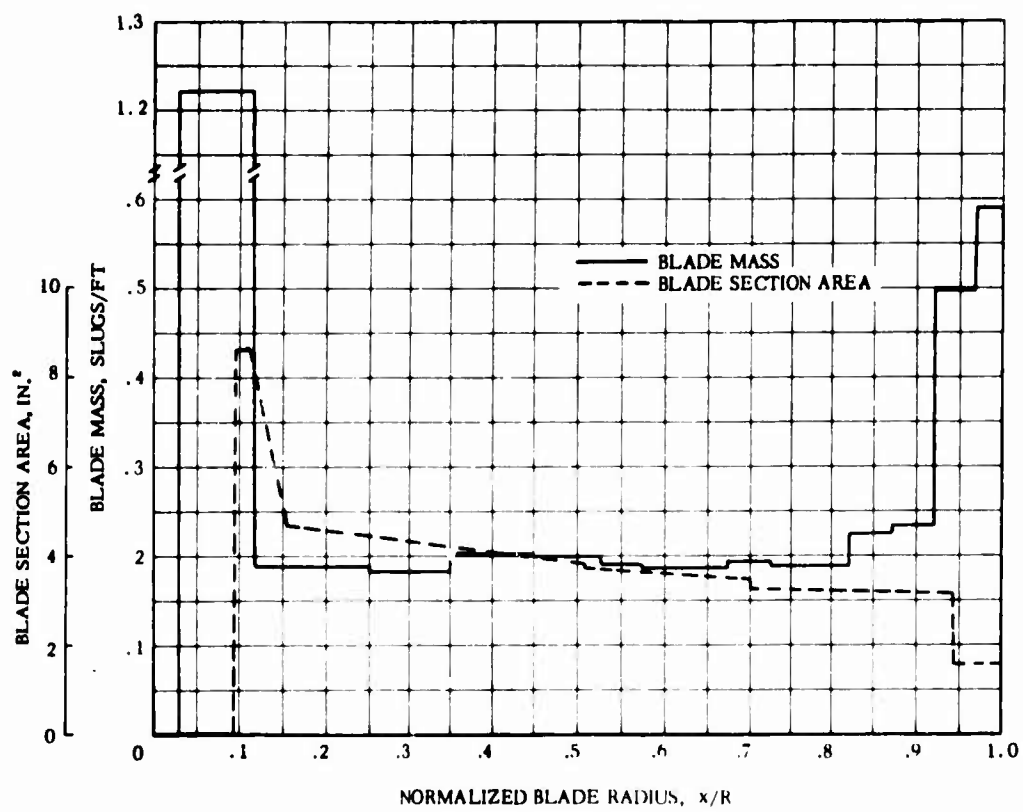


Figure 70. Concluded

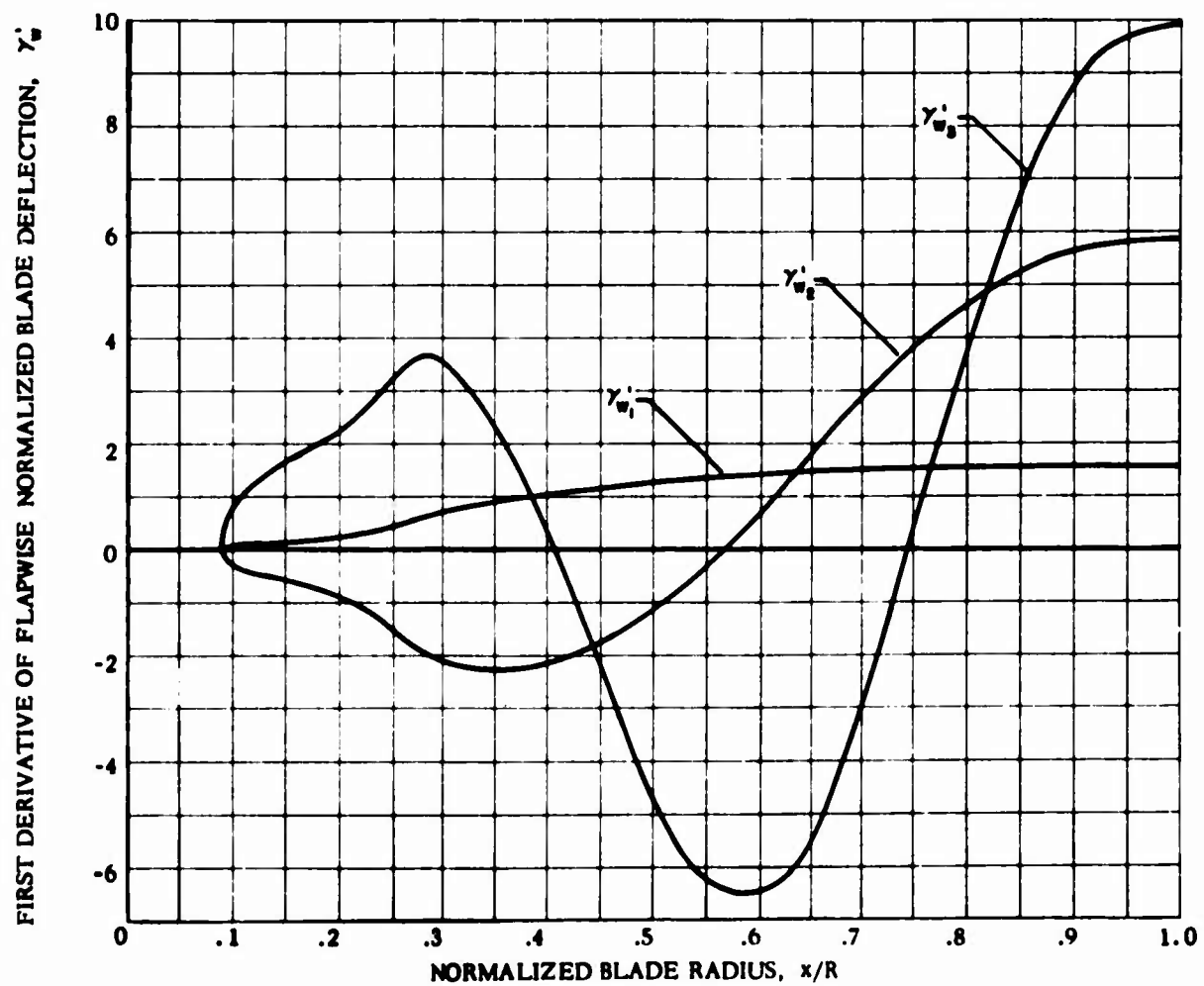
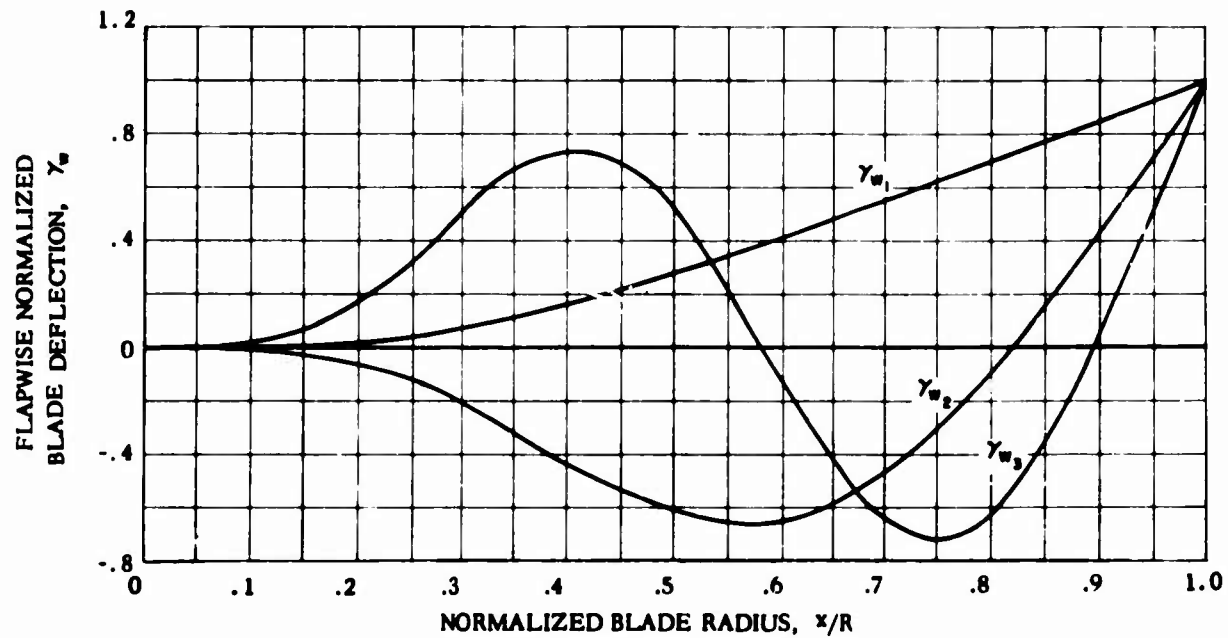


Figure 71. Hingeless Blade Spanwise Structural and Physical Properties

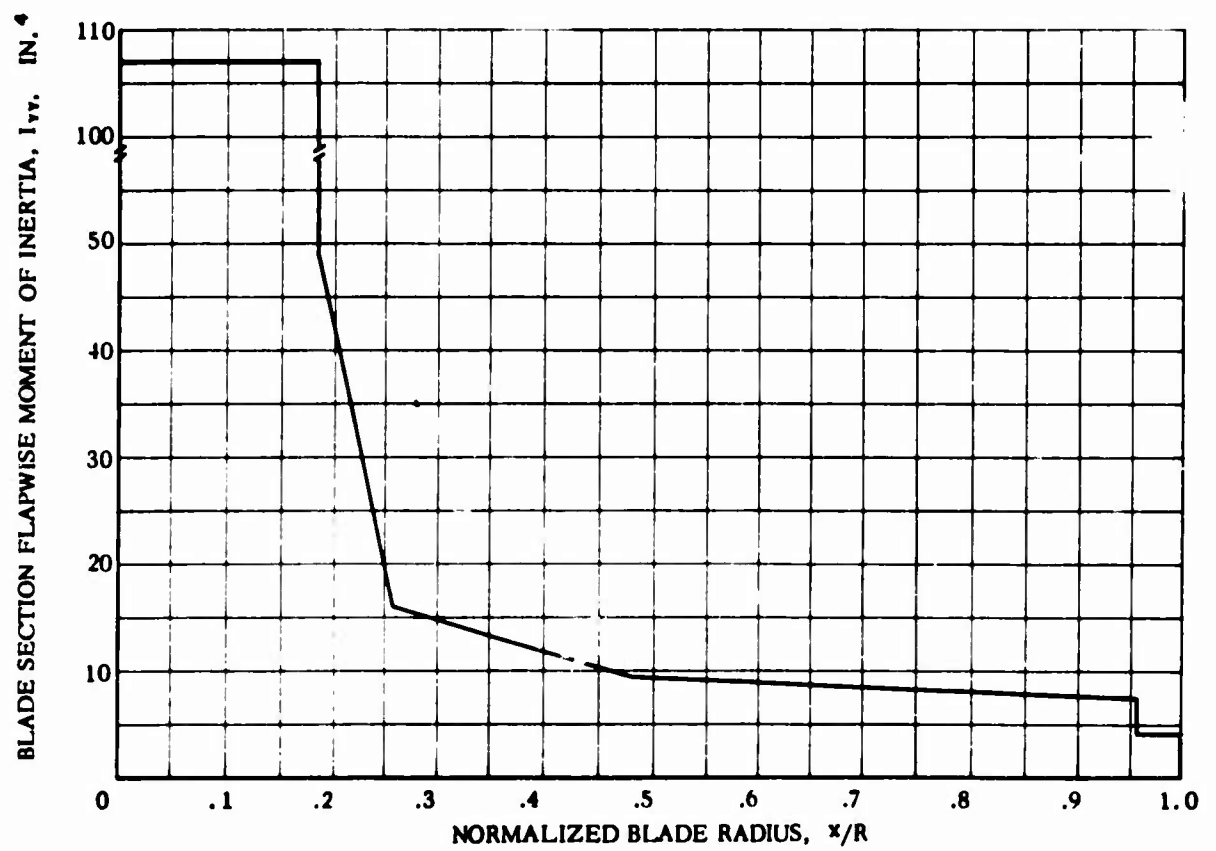
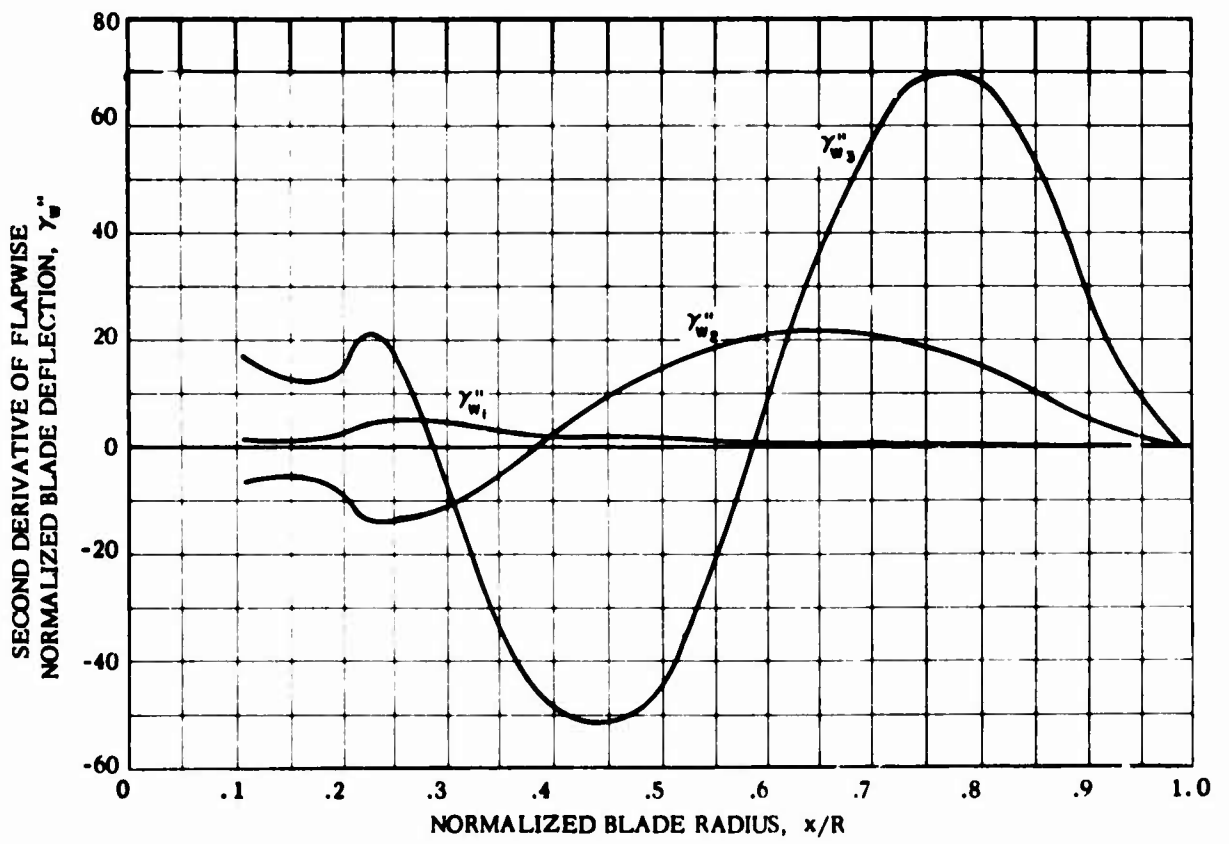


Figure 71. Continued

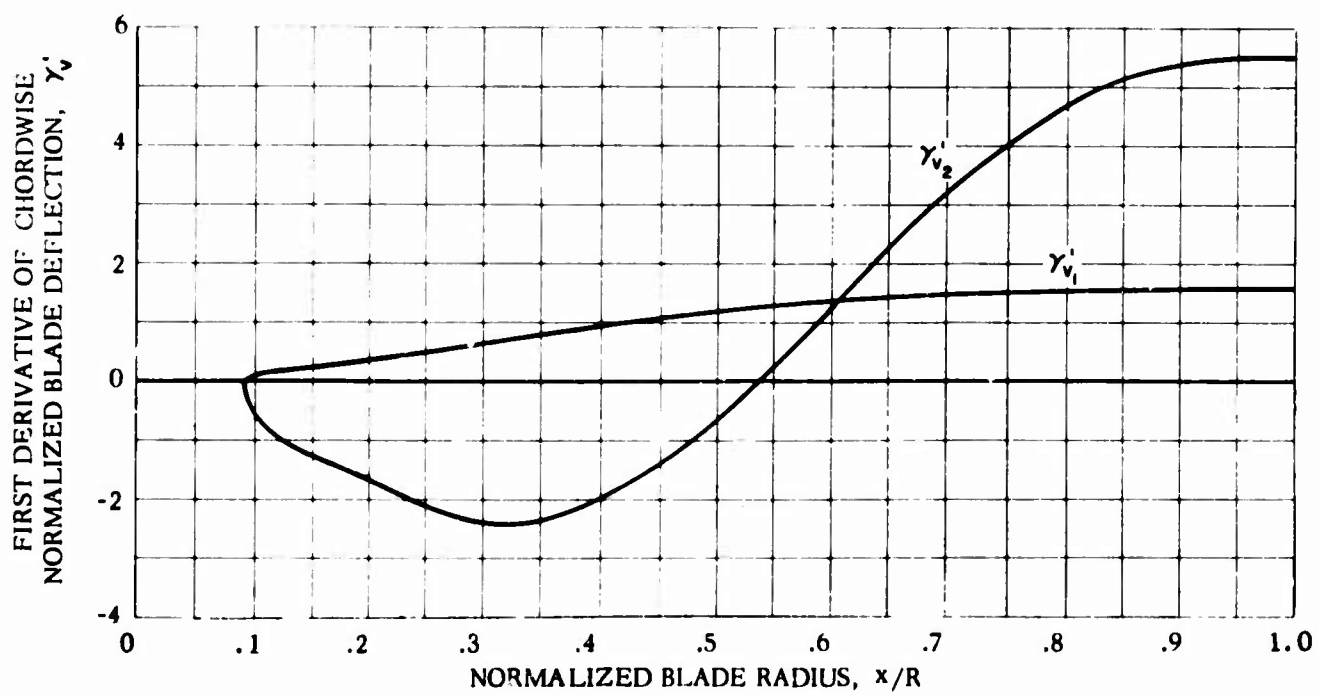
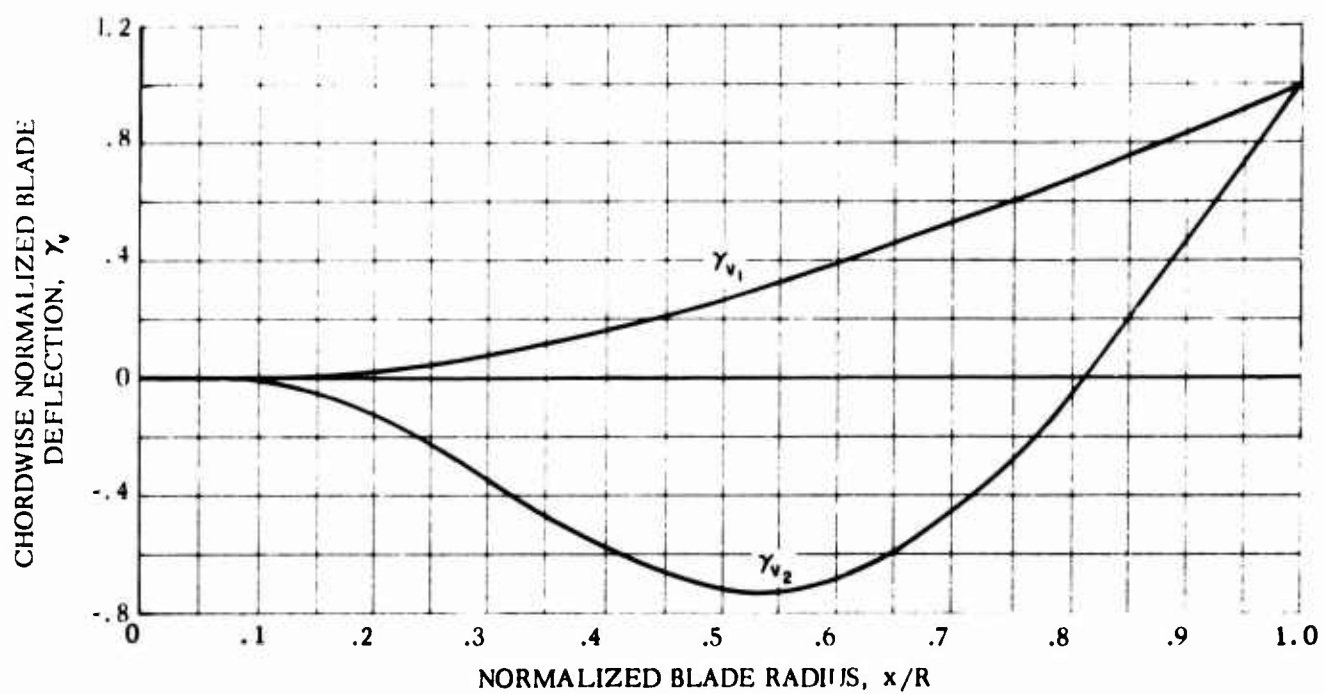


Figure 71. Continued

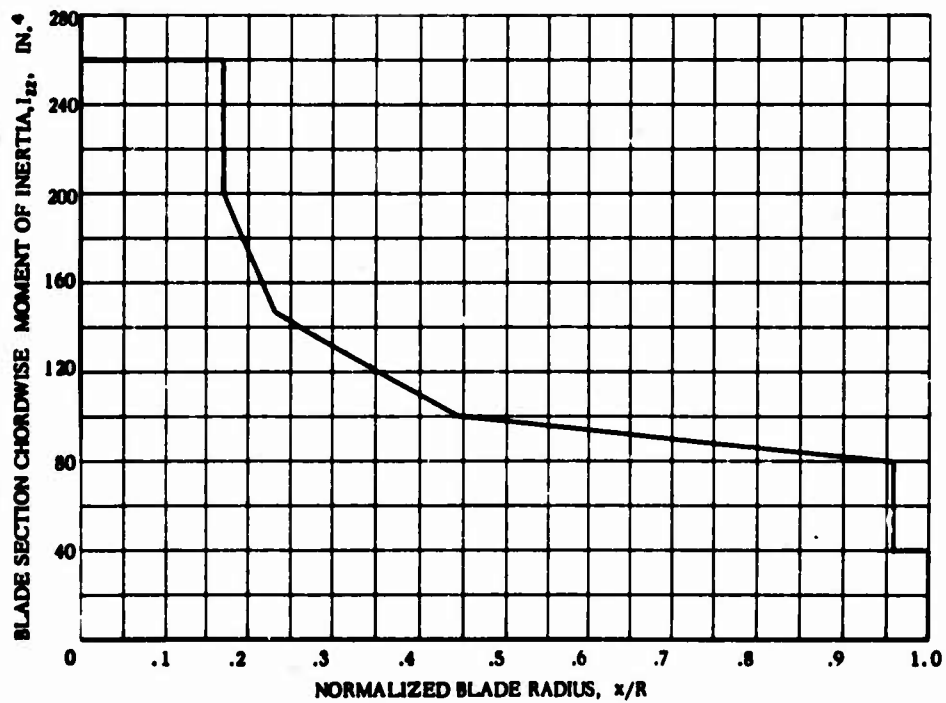
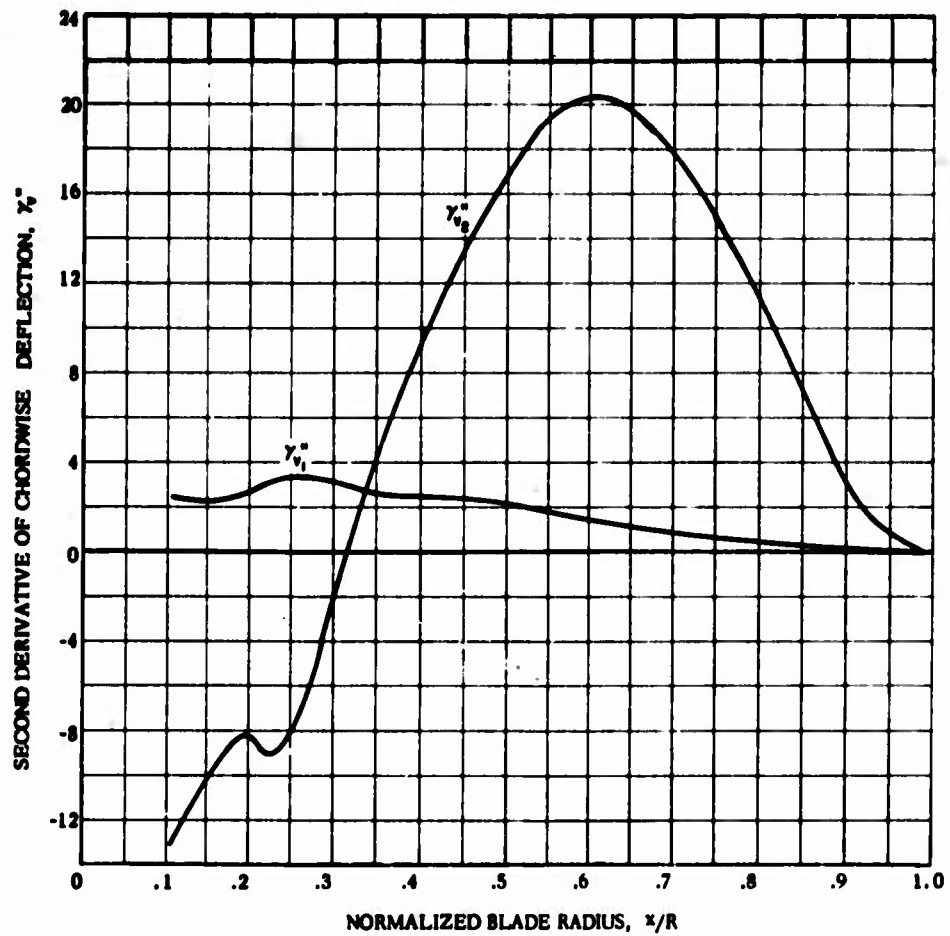


Figure 71. Continued

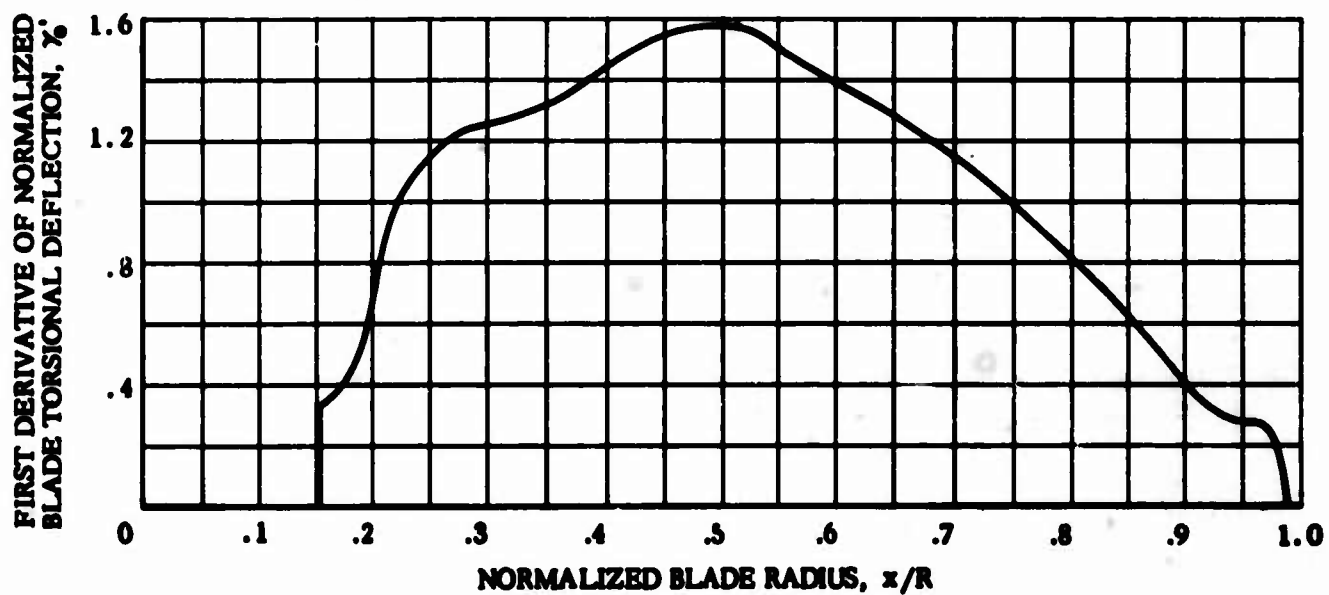
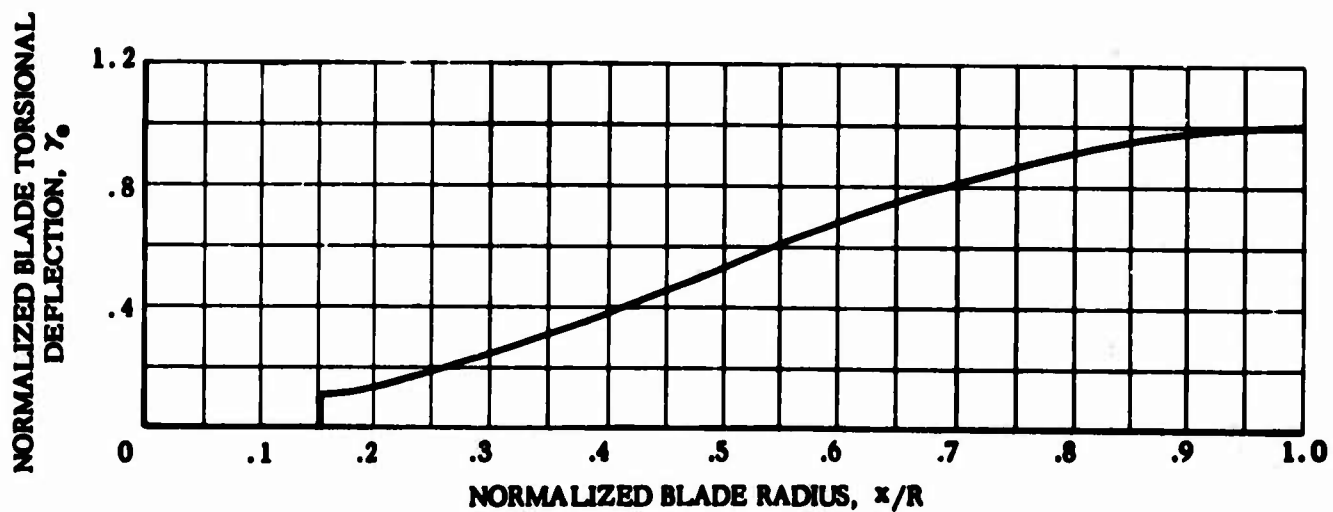


Figure 71. Continued

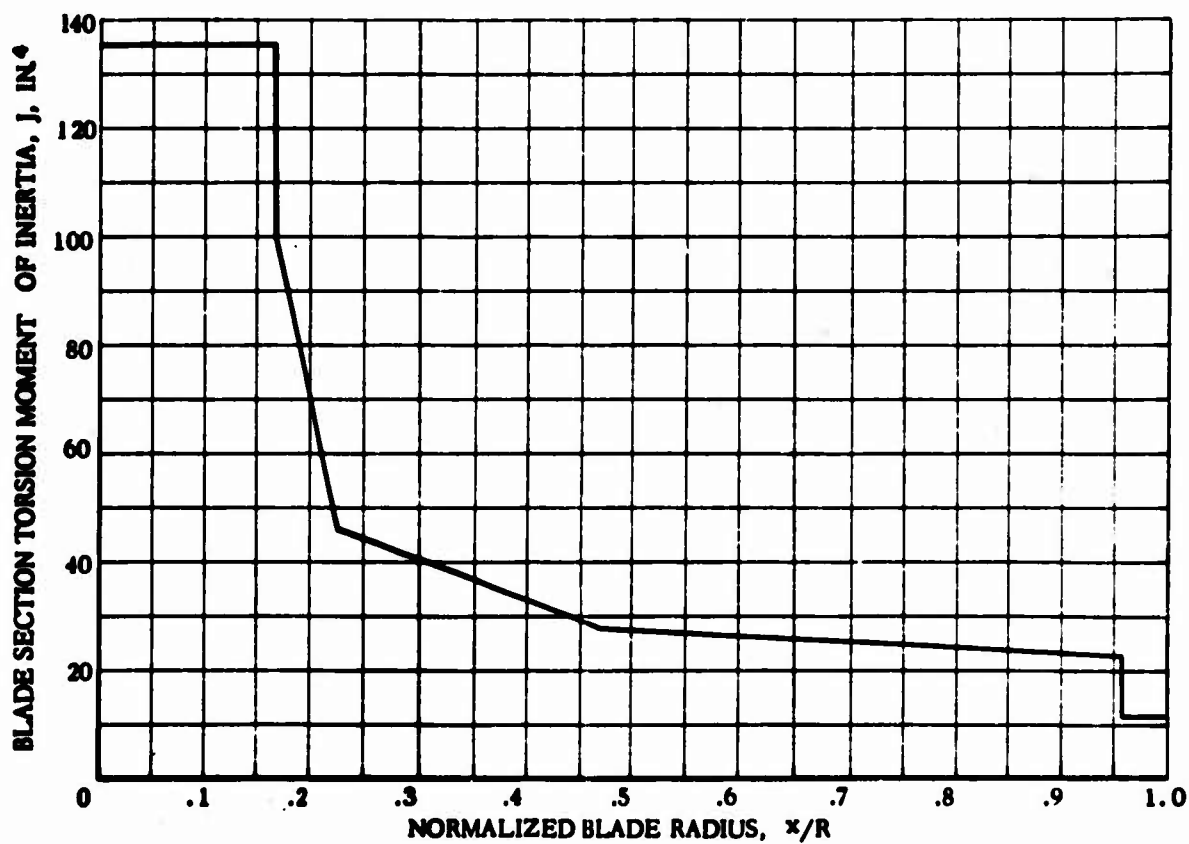
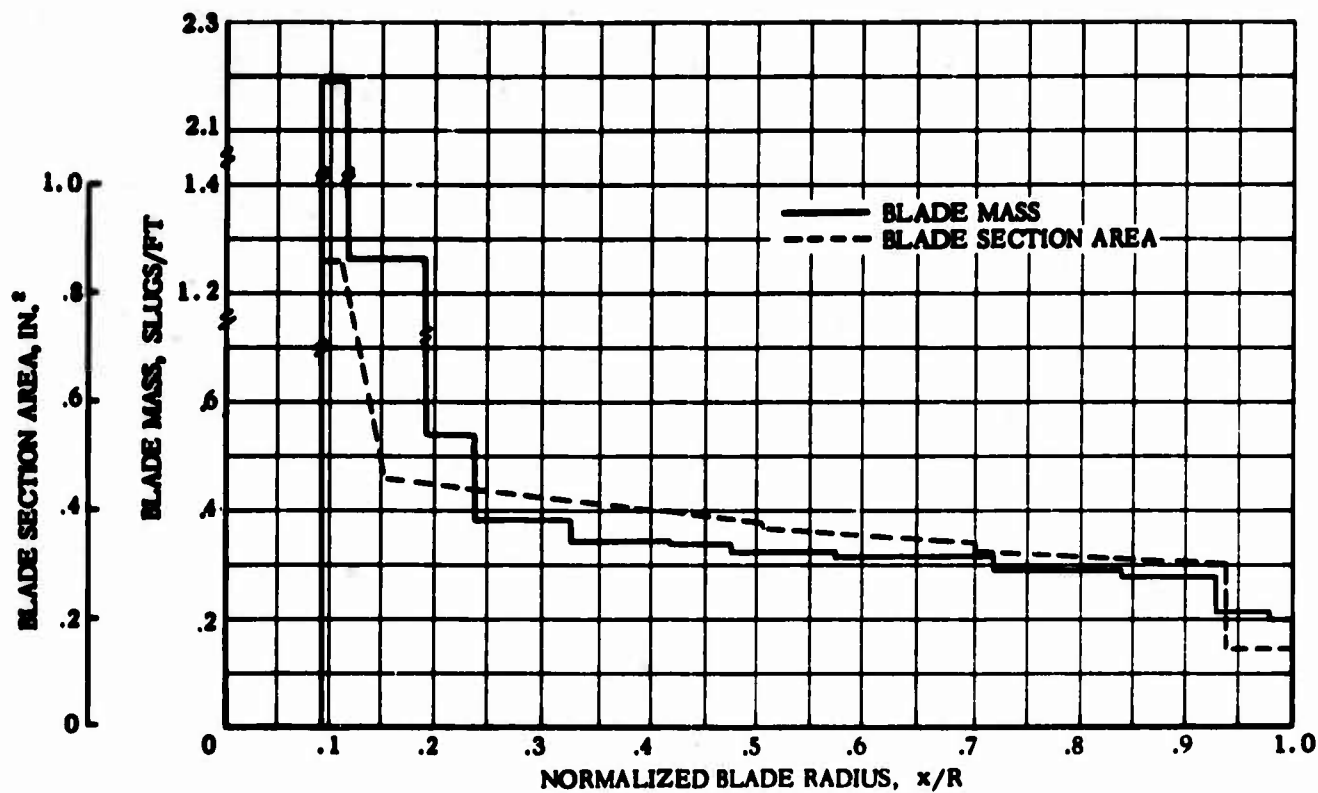


Figure 71. Concluded

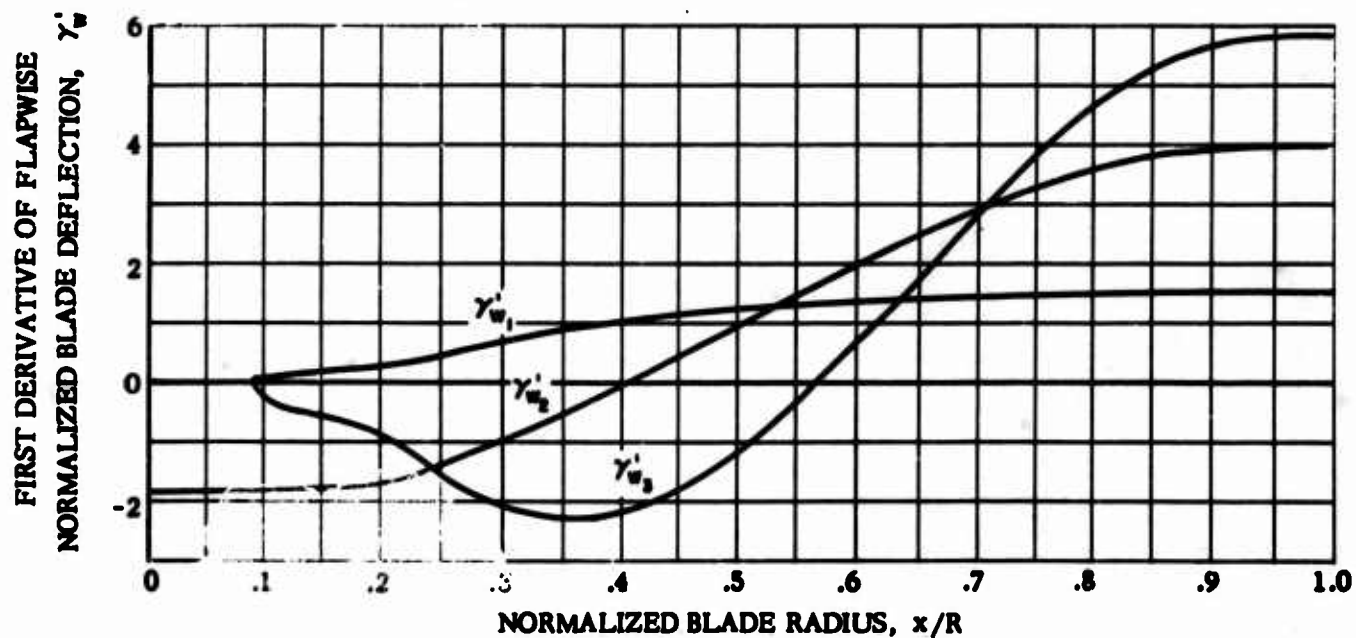
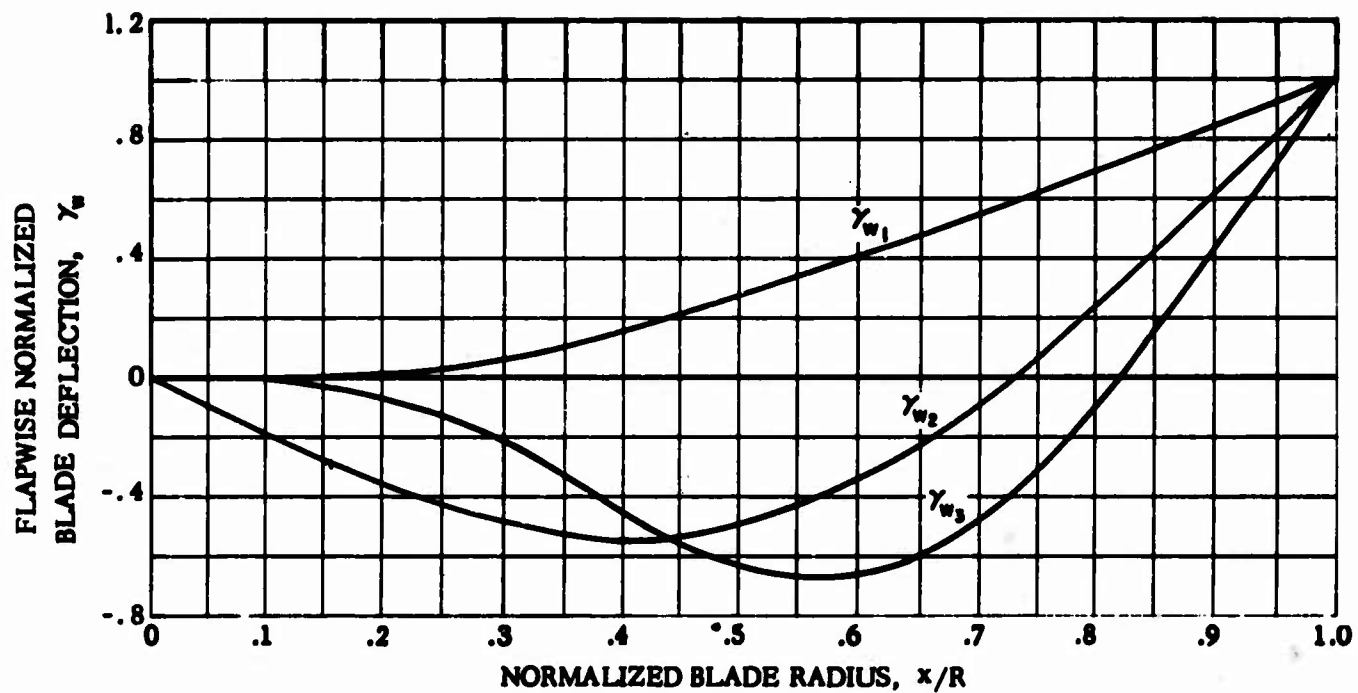
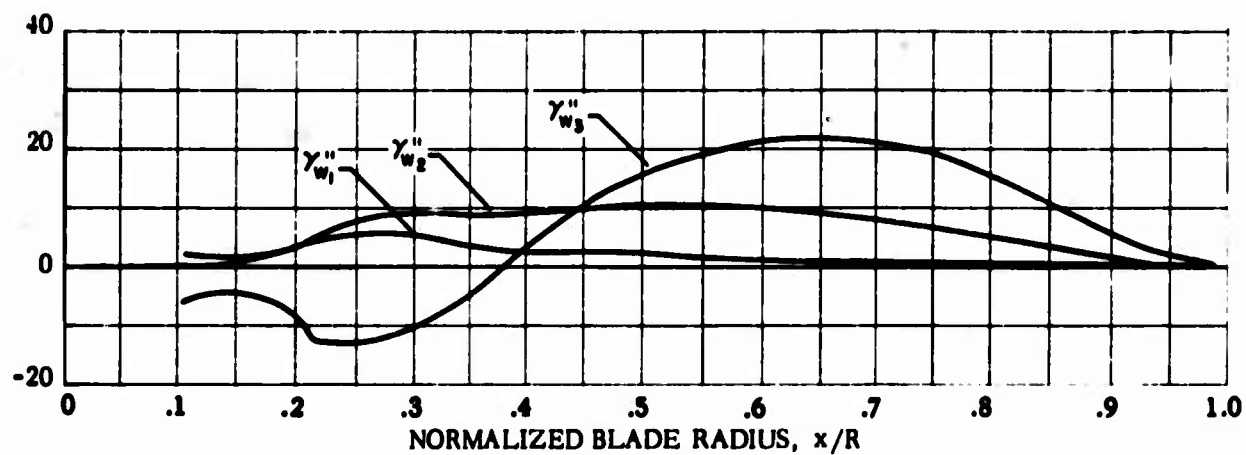


Figure 72. Floating Hub Rotor Blade Spanwise Structural and Physical Properties

SECOND DERIVATIVE OF FLAPWISE
NORMALIZED BLADE DEFLECTION, γ''



BLADE SECTION FLAPWISE MOMENT OF INERTIA, I_{yy} , IN.⁴

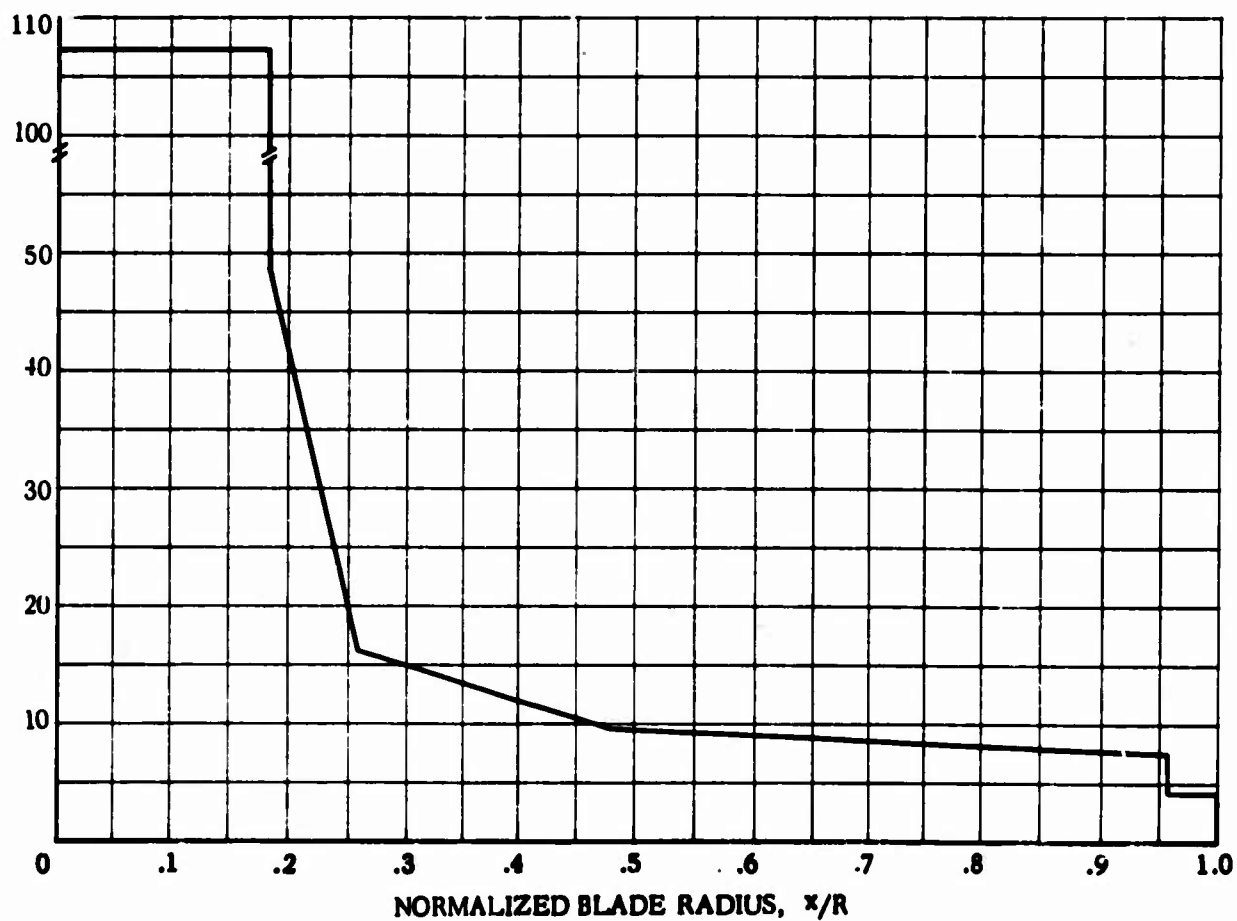


Figure 72. Continued

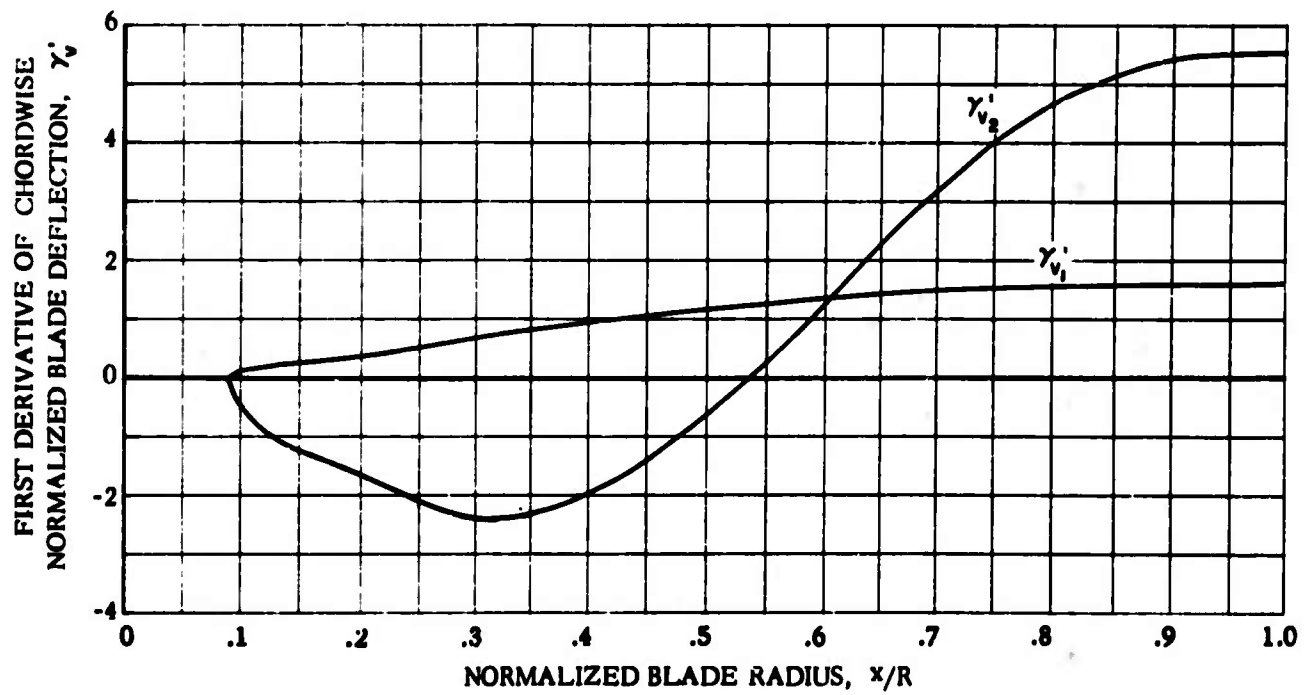
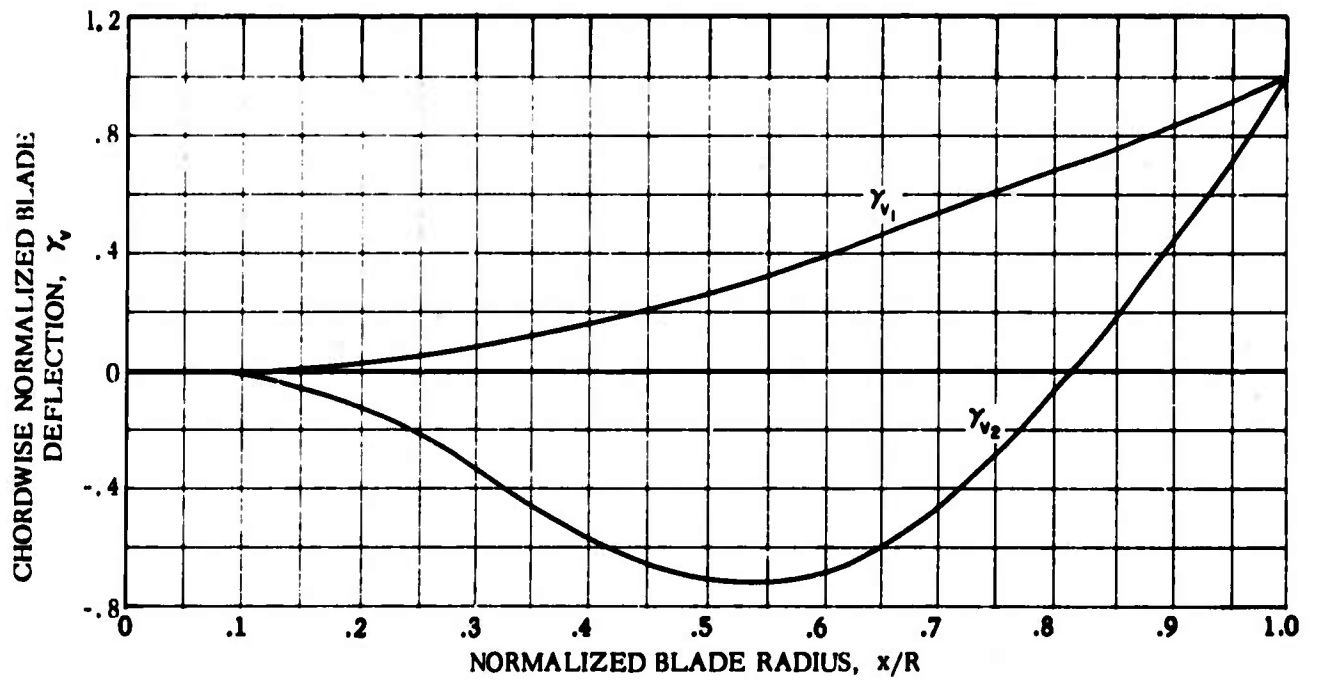


Figure 72. Continued

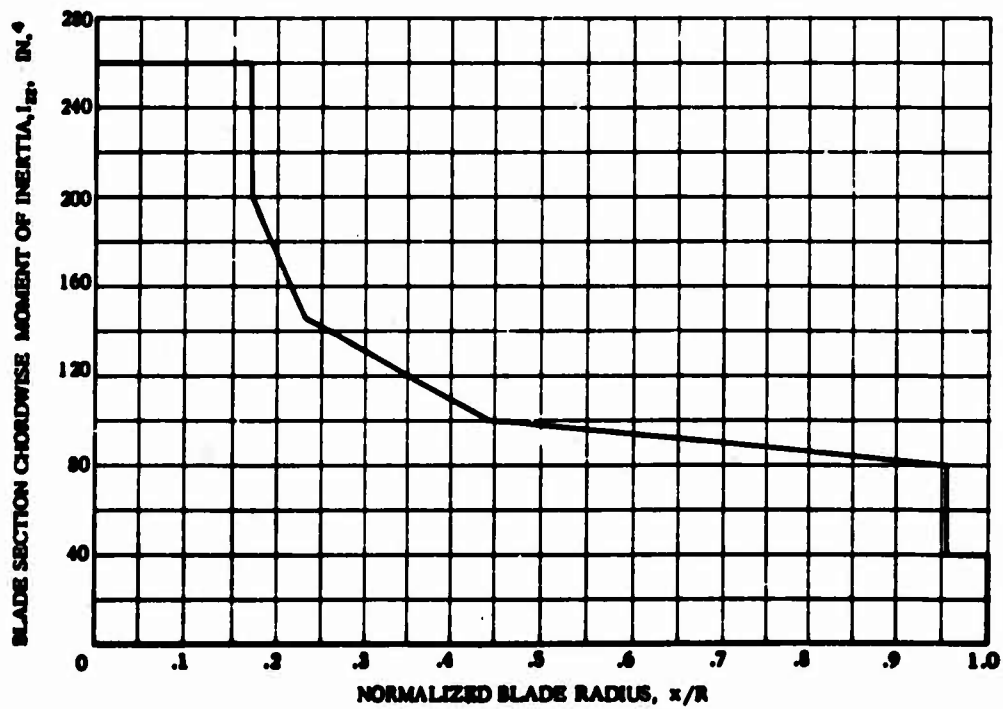
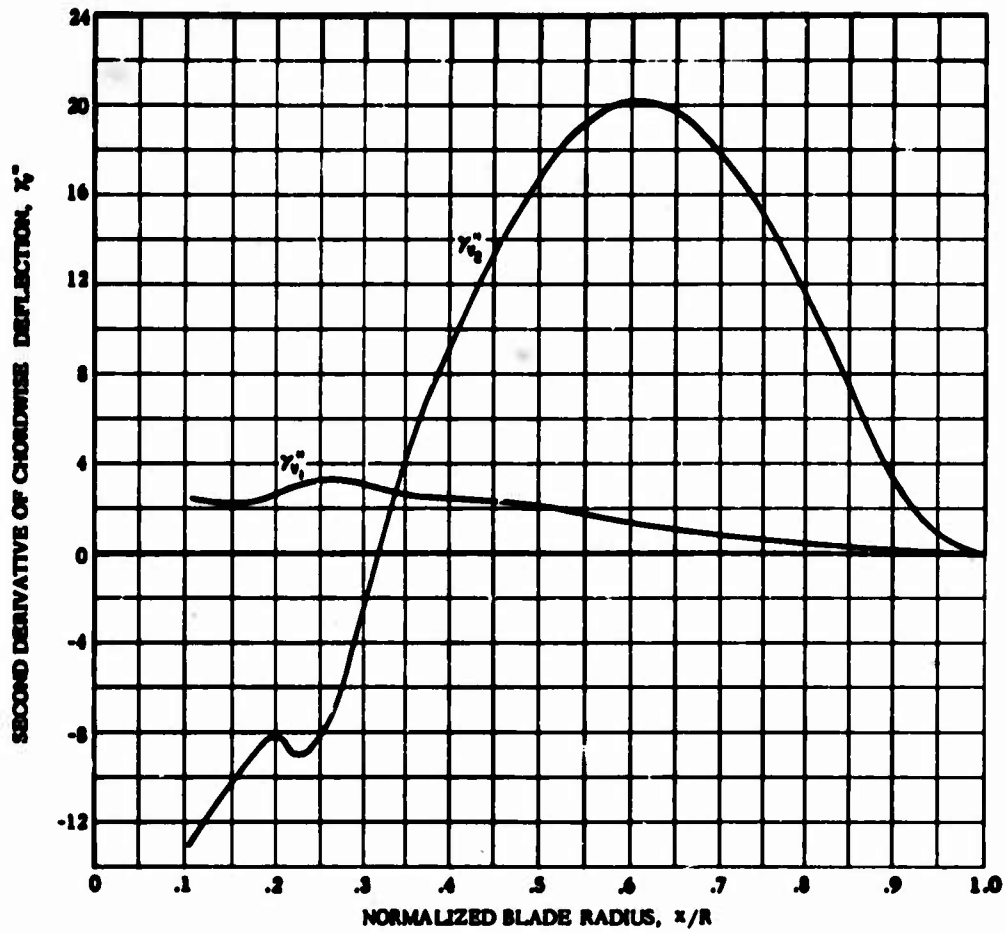


Figure 72. Continued

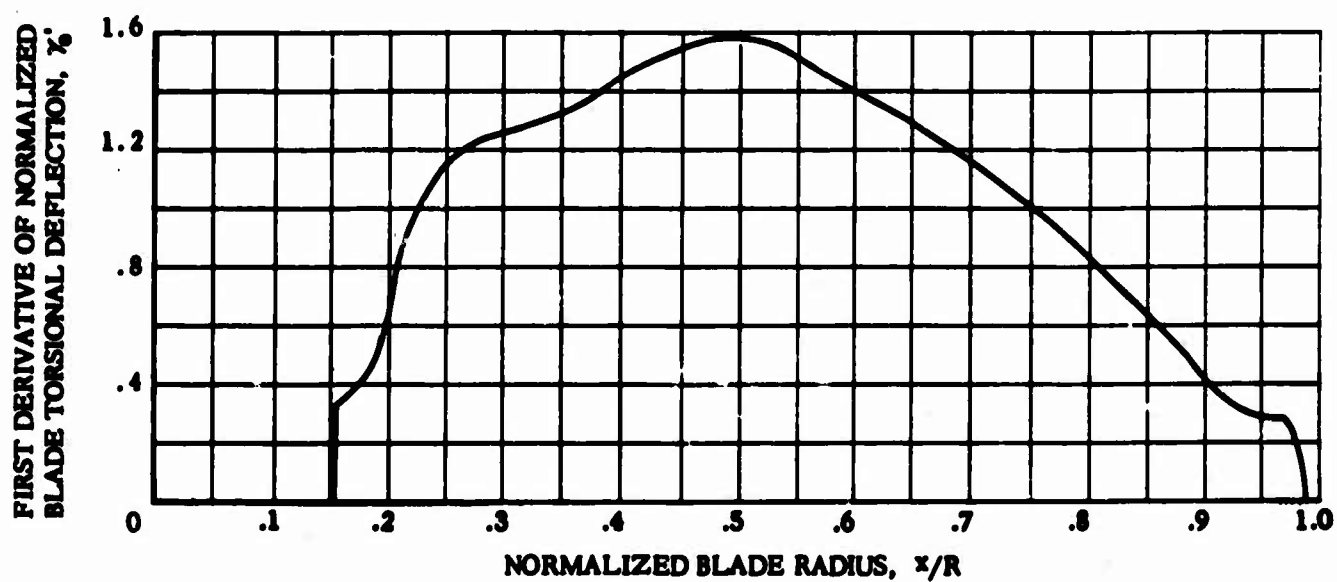
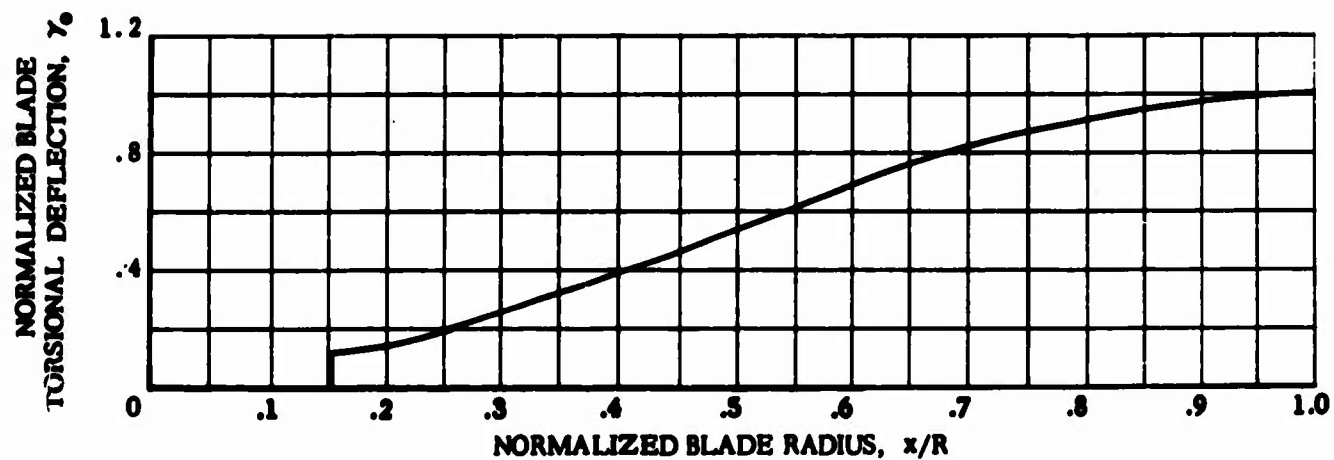


Figure 72. Continued

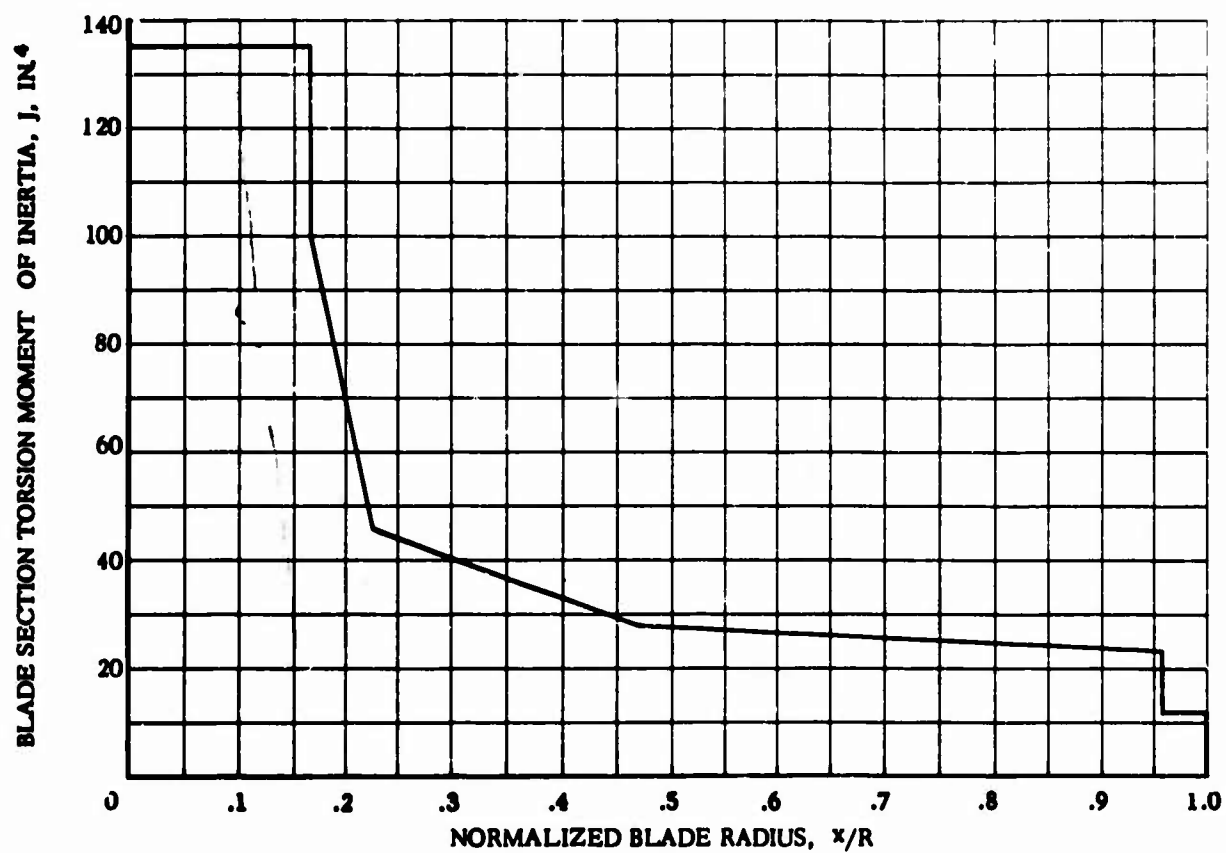
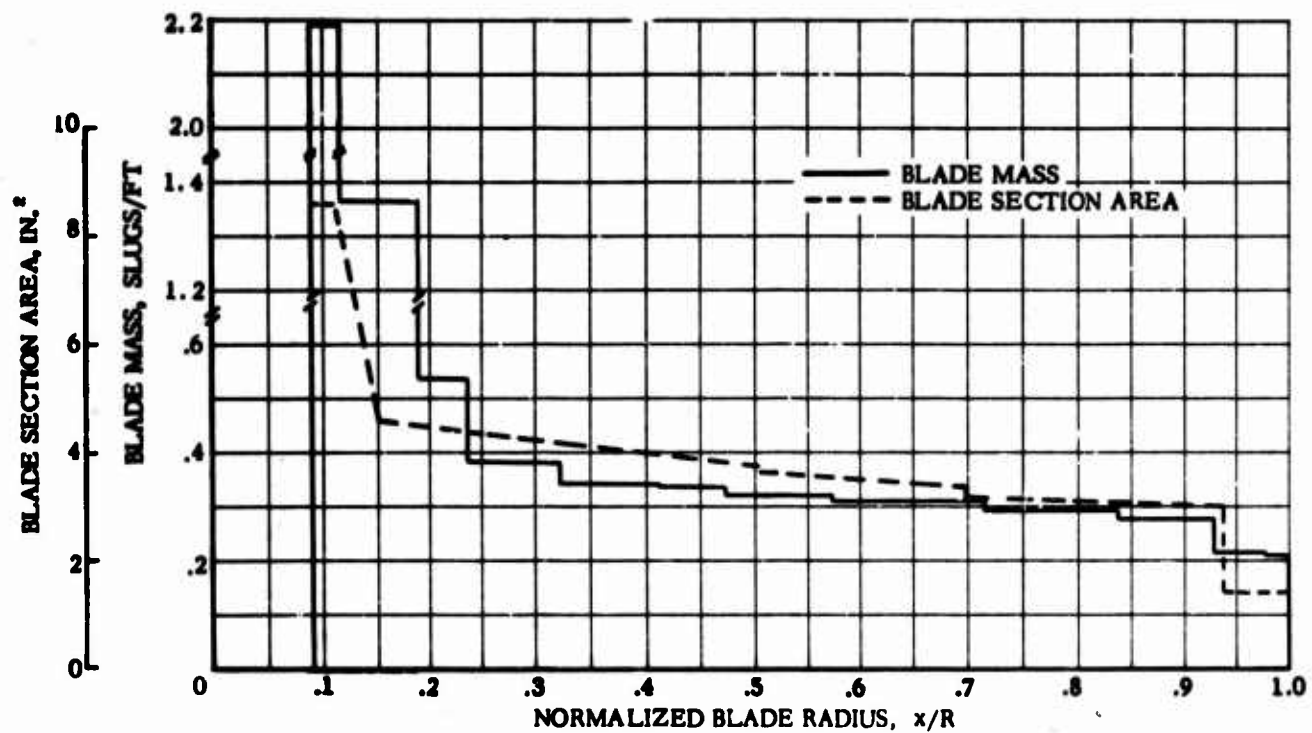


Figure 72. Concluded

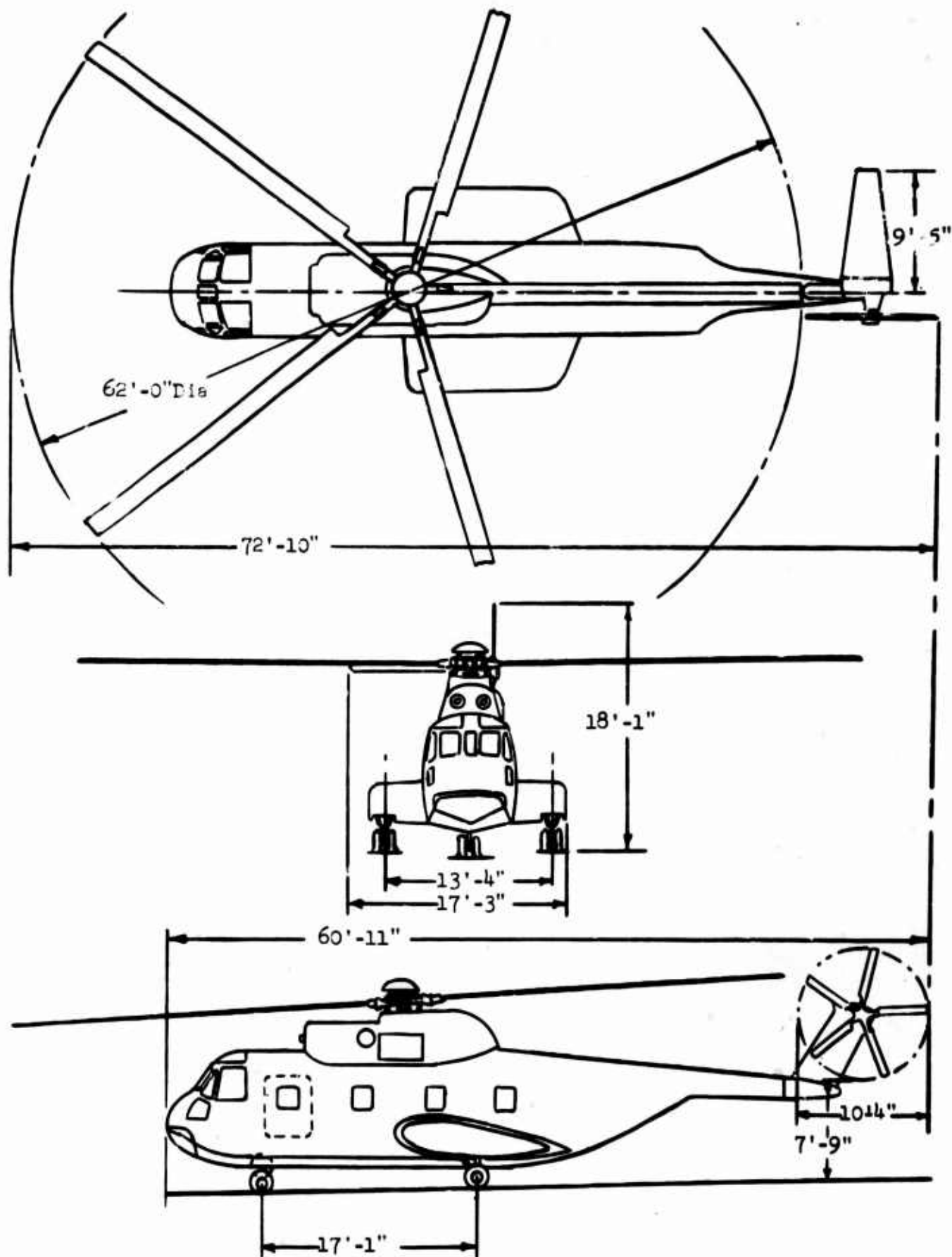


Figure 73. S-61R (CH-3C) Aircraft

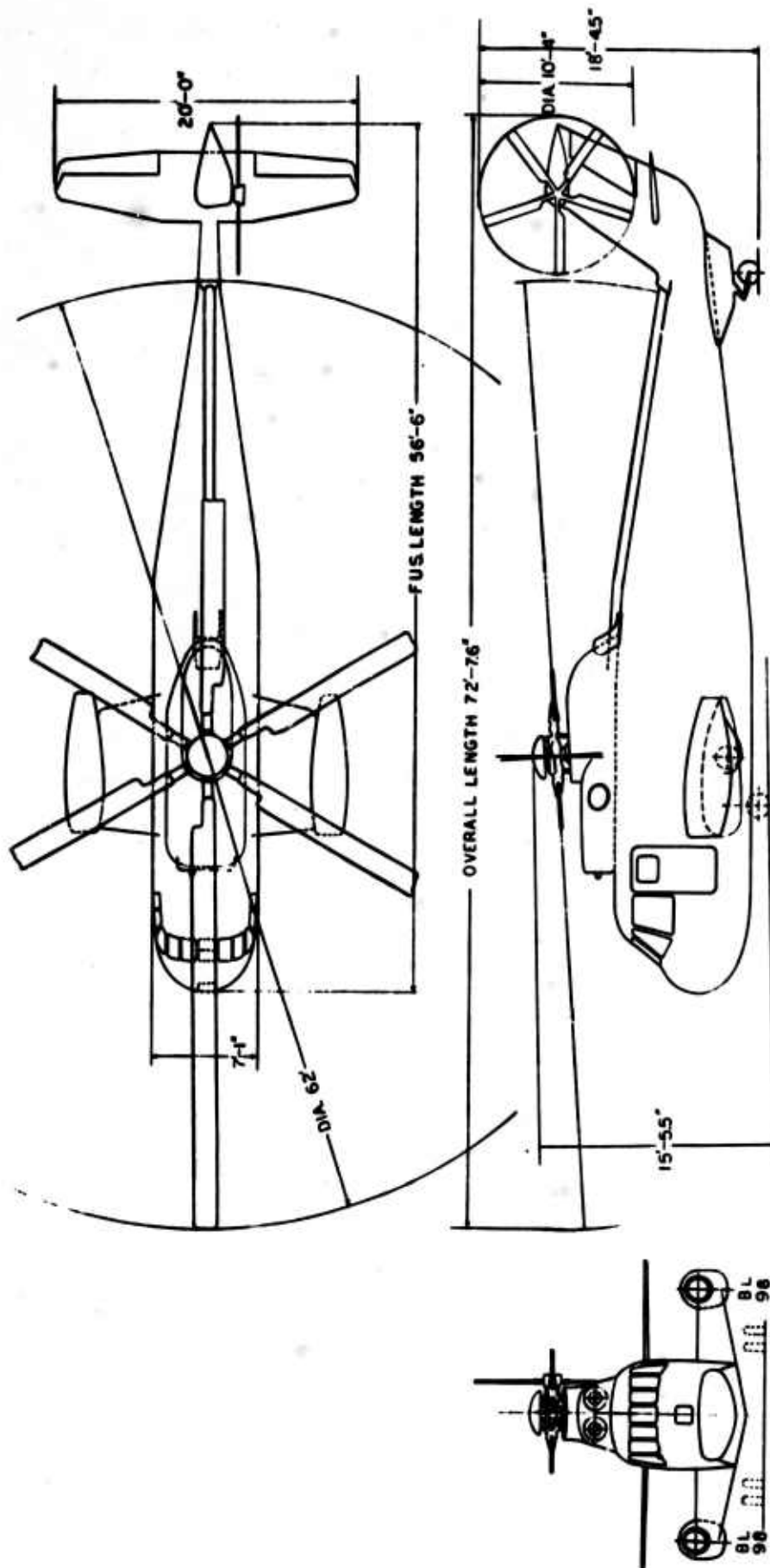


Figure 74. S-61F (NH-3A) Aircraft

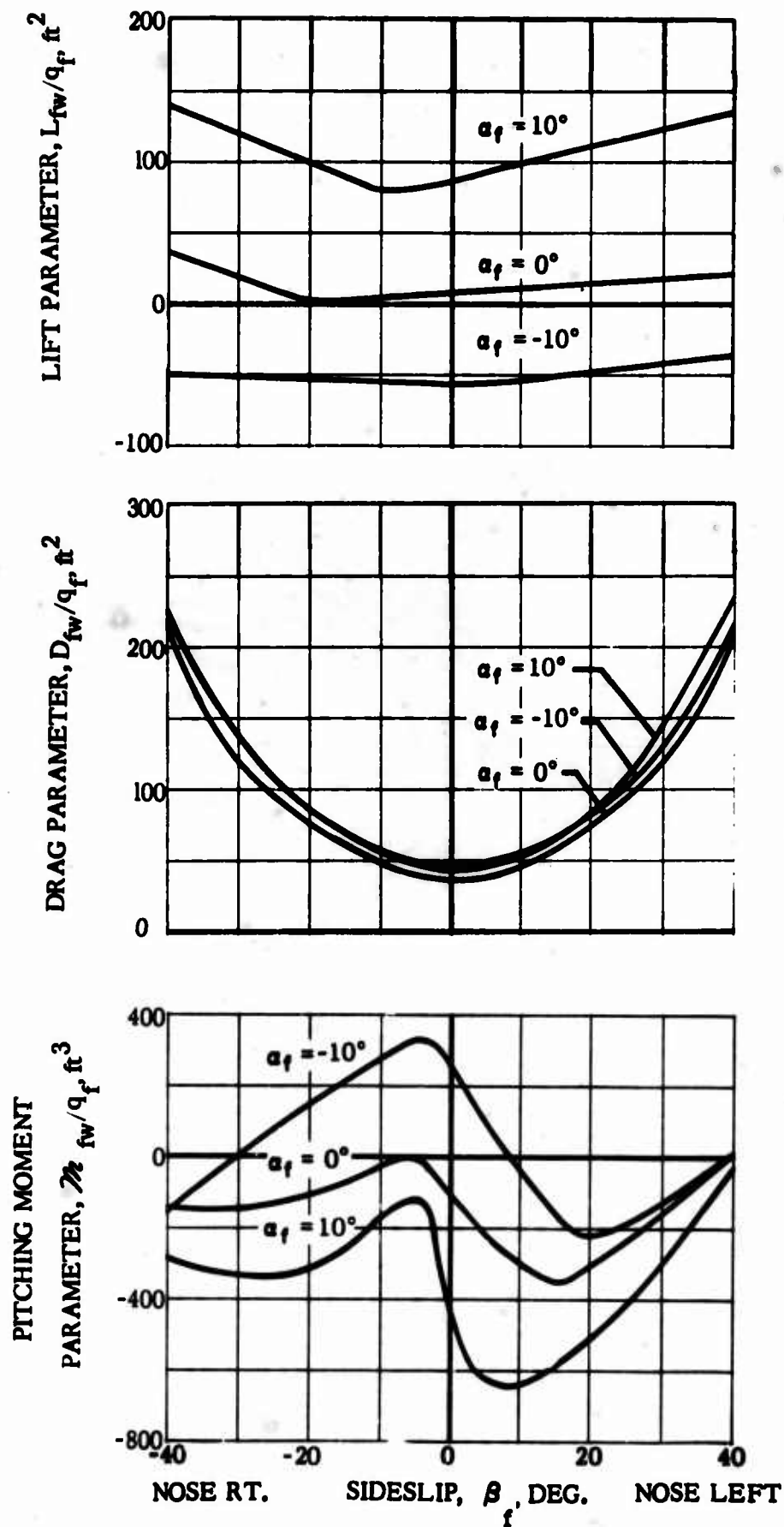


Figure 75. S-61R (CH-3C) Wind Tunnel Data (Wind Axis System)

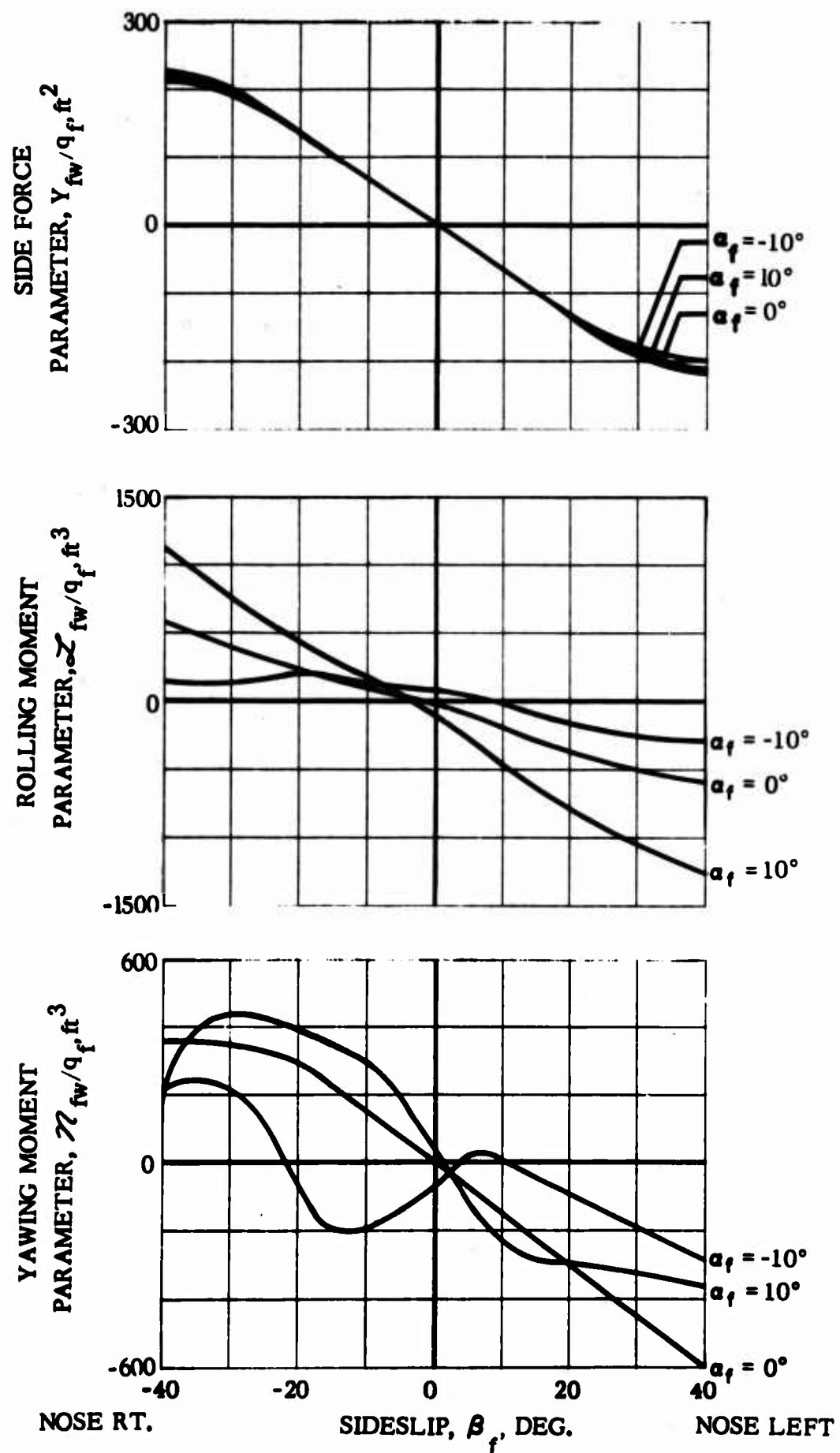


Figure 75. Concluded

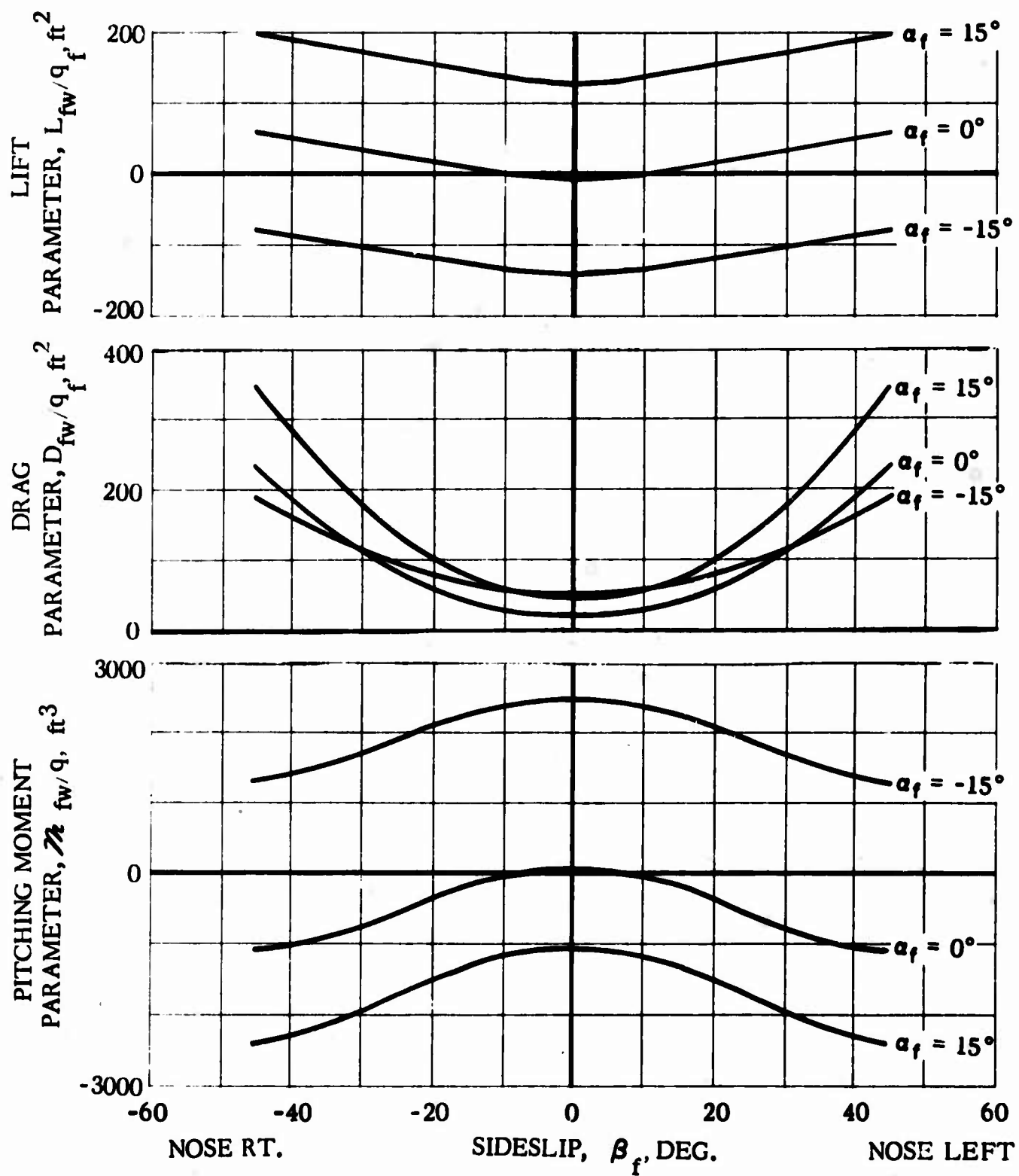


Figure 76. S-61F (NH-3A) Wind Tunnel Data (Wind Axis System)

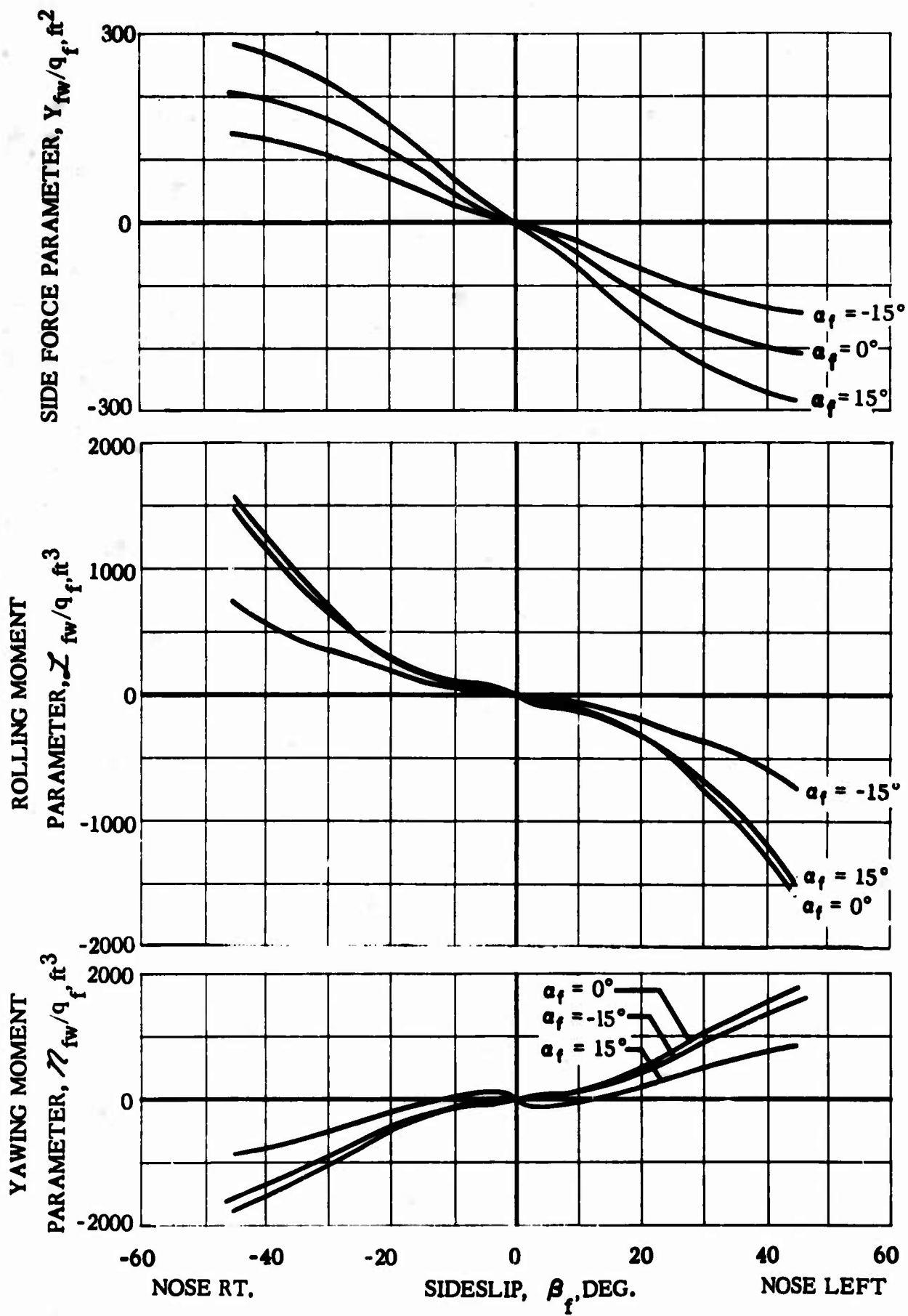


Figure 76. Concluded

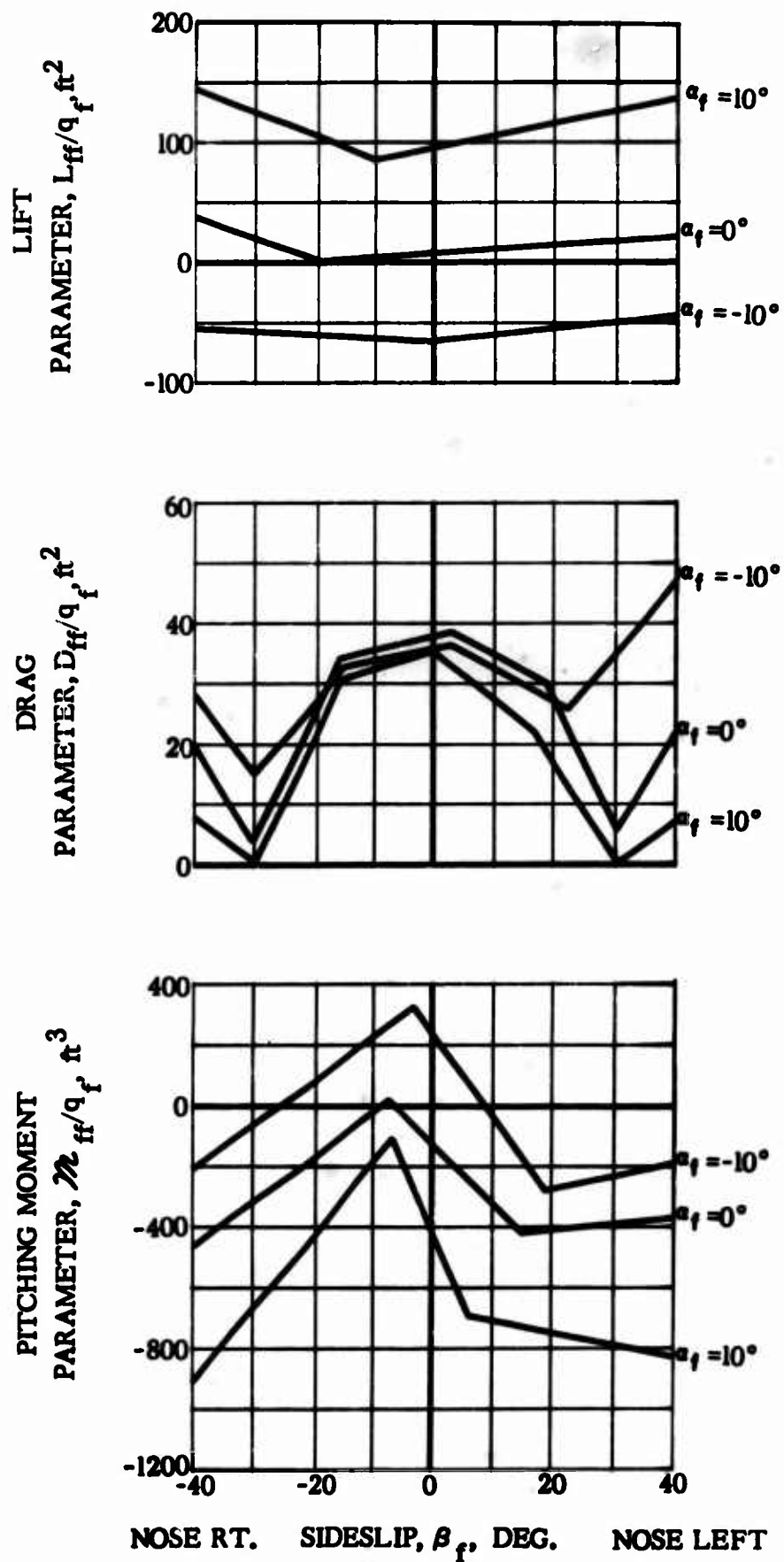


Figure 77. S-61R (CH-3C) Wind Tunnel Data (Body Axis System)

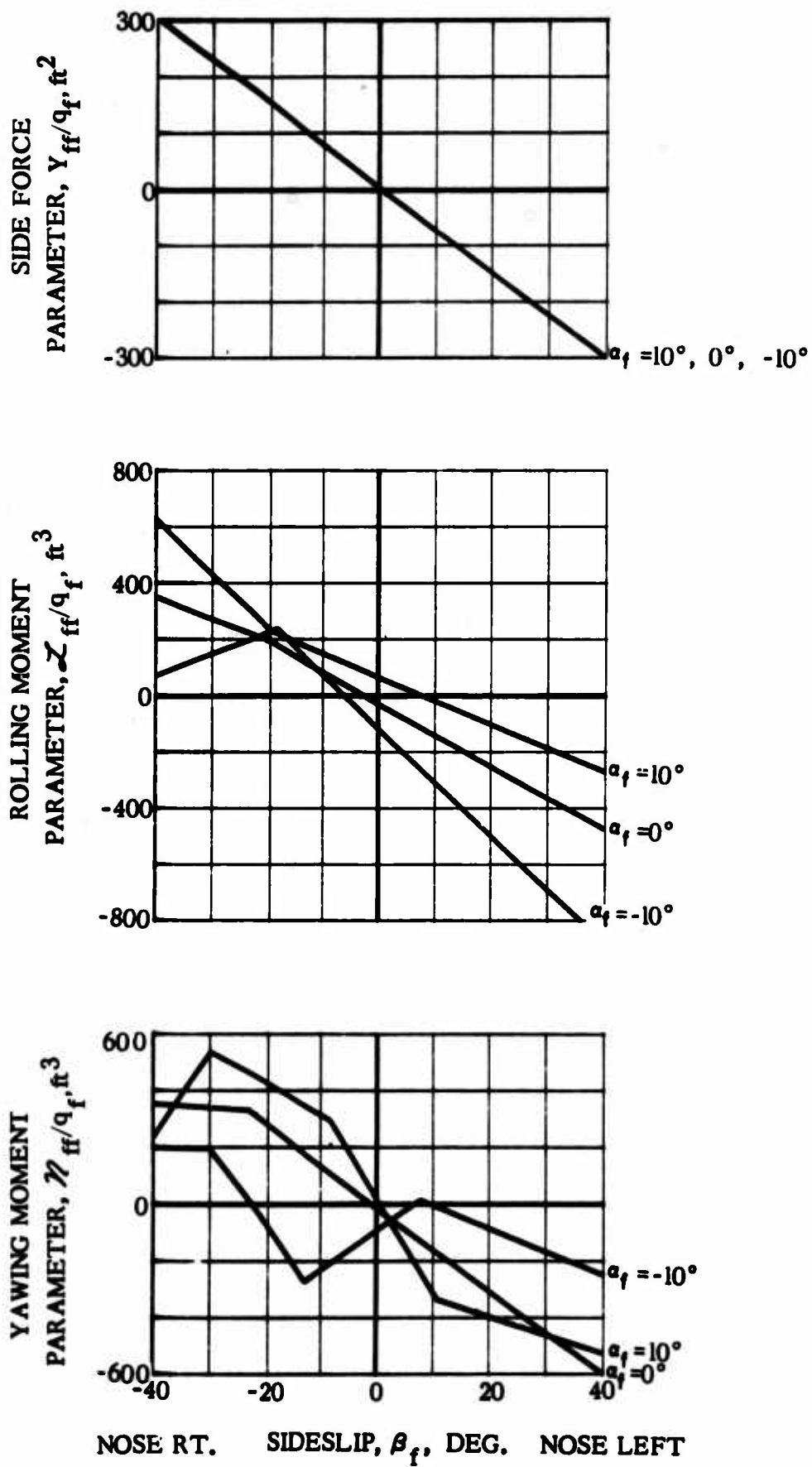


Figure 77. Concluded

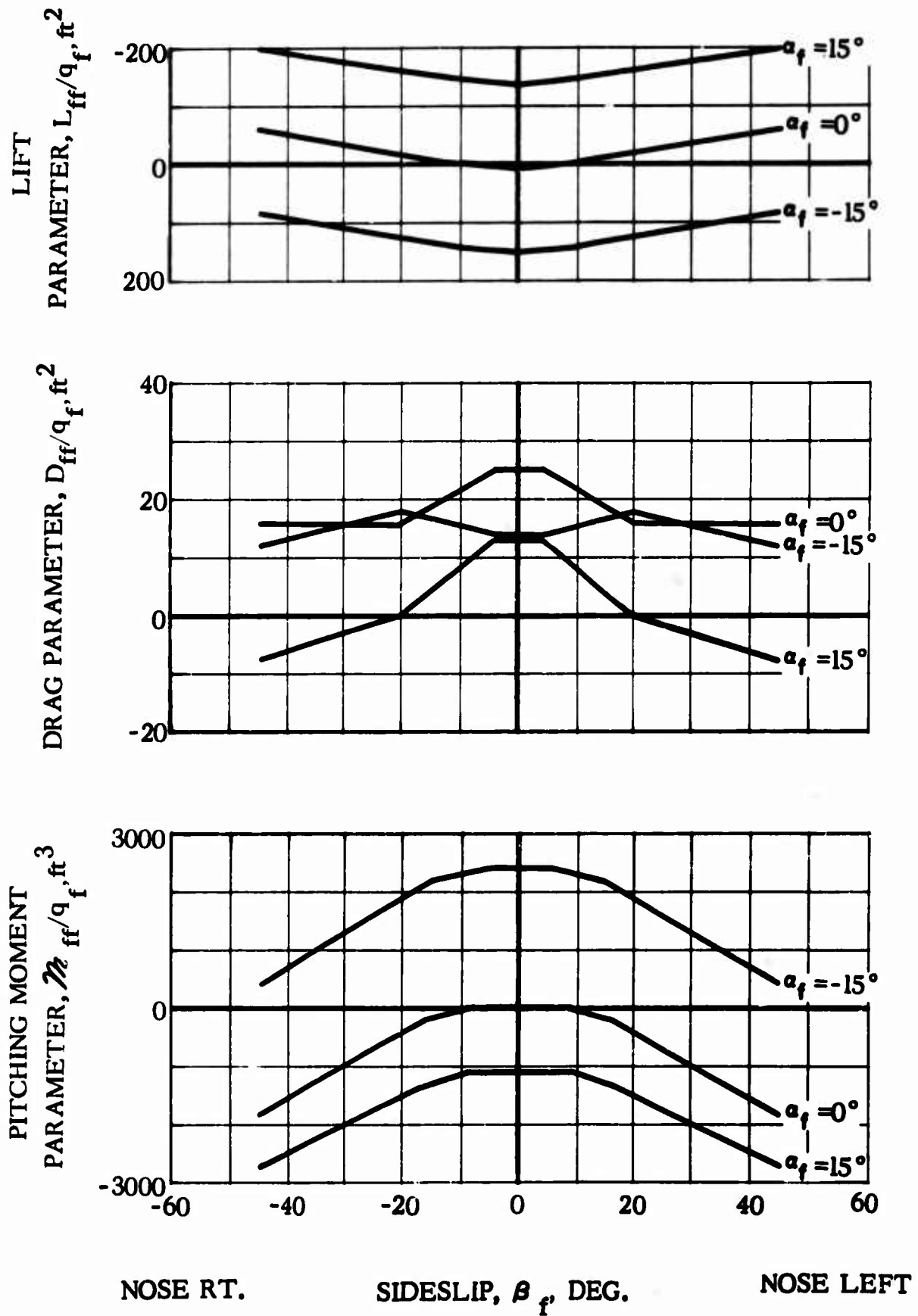


Figure 78. S-61F (NH-3A) Wind Tunnel Data (Body Axis System)

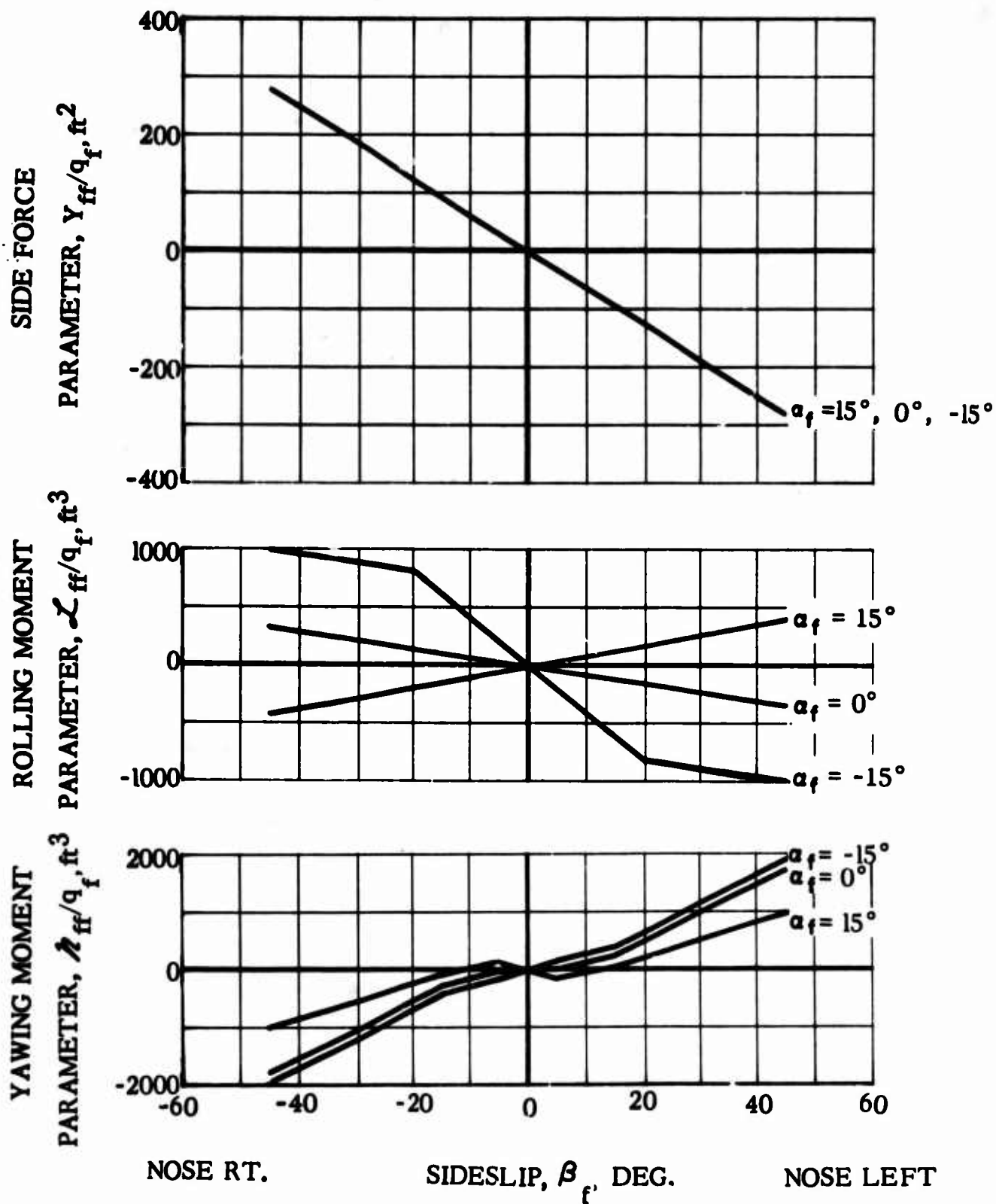


Figure 78. Concluded

APPENDIX II

EQUATIONS OF MOTION AND DESCRIPTION OF FLEXIBLE BLADE AND HYBRID COMPUTER SIMULATION

EQUATIONS OF MOTION

In anticipation of large transient aircraft motion following an abrupt loss of power, equations of motion of the fuselage were developed with no small angle assumptions. The rotor forces and moments were initially referenced to a shaft coordinate system and the fuselage wind tunnel data were initially referenced to a "wind tunnel" axis system. All forces and moments were then transferred to the body axis system for a final solution of the general equations of motion.

The origin of the body axis system is located at the aircraft center of gravity. The X-axis is positive forward along the fuselage horizontal reference line in the plane of symmetry. The Z-axis is also in the plane of symmetry but perpendicular to the X-axis and positive down. The Y-axis is perpendicular to the X-Z plane and positive to the right.

The inertial loading of the system is treated in the conventional manner. However, since the principal axes are very close to the aircraft reference axes, the products of inertia are considered reasonably small and, therefore, are not considered. The classic Euler equations were used to calculate motion in the space axis system for the inertia loads. The effect of rotor downwash on fuselage and horizontal tail angle of attack is included in this analysis.

The general body axis equations of motion are as follows:

Along Body X axis:

$$m (\dot{u}_{Xf} + q u_{Zf} - r u_{Yf}) = X_{MR} - D_{ff} - mg \sin \theta + \text{Propulsive Force}$$

Along Body Y axis:

$$m (\dot{u}_{Yf} + r u_{Xf} - p u_{Zf}) = Y_{MR} + Y_{ff} + T_T + mg \cos \theta \sin \phi$$

Along Body Z axis:

$$m (\dot{u}_{Zf} + p u_{Yf} - q u_{Xf}) = Z_{MR} - L_{ff} + mg \cos \theta \cos \phi$$

About the Body X axis:

$$\dot{p} I_X - q r (I_Y - I_Z) = h_{MR} Y_{MR} + L_{MR} + h_{TR} T_T + \mathcal{L}_{ff} + h_a Y_{ff}$$

About the Body Y axis:

$$\dot{q} I_Y - r p (I_Z - I_X) = I_{MR} Z_{MR} - h_{MR} X_{MR} +$$

$$M_{MR} + \mathcal{M}_{ff} - l_a L_{ff} + h_a D_{ff} + M_{damp} + M_{downwash}$$

About the Body Z axis:

$$\dot{r} I_Z - p q (I_X - I_Y) = - L_{MR} Y_{MR} + Q_{MR} -$$

$$L_{TR} T_T + \mathcal{N}_{ff} - l_a Y_{ff} + N_{damp}$$

The transformations of the various applied forces and angular relationships can be found in Appendix III along with further explanation and details of the above equations. A more simple Bailey analysis was used in the calculation of tail rotor thrust.

DESCRIPTION OF FLEXIBLE BLADE SIMULATION

The vibratory motion of the flexible rotor blades was simulated by a superposition of normal modes. This was accomplished by first deriving the differential equations of motion for the lateral and torsional deformation of a linearly twisted, mass balanced helicopter rotor blade operating in a maneuvering flight condition. The equations were initially derived from a consideration of the equilibrium of aerodynamic, dynamic, and elastic moments acting on a given blade section. The resulting moment equations were then differentiated to be expressed in terms of the local blade loadings. These differential equations were then solved by simulating the blades with a series of normal modes.

The flapwise, chordwise, and torsional elastic deflections were expressed as finite series summations of assumed radial shape functions (mode shapes), with each suitably scaled by time-dependent generalized coordinates. The number of terms retained constitutes three flapwise, two chordwise, and one torsional mode shape. The mode shapes used in this study correspond to the natural vibratory mode shapes of an untwisted blade mounted on a fixed hub and operating at zero pitch, flap, and lag angles and at the trim rotor speed.

The substitution of these mode shapes permits the three equations of flapwise, chordwise, and torsional loading to be expanded into a system of differential equations, with the generalized coordinates as unknowns. Further, because of the orthogonality properties of the particular mode shapes selected, modal dynamic coupling terms have been eliminated. Additional simplifications were achieved by replacing the structural and centrifugal stiffness terms with natural frequency terms. Chordwise structural damping was also included in the analysis. An equivalence of 5% structural damping was simulated by 2.5% viscous damping, Reference 4.

Rotor equations of motion were developed and programed so that only minor modifications were required for each configuration. For the hingeless rotor, several program expressions were altered; two degrees of freedom, flapping and lead-lag were removed; and flapping angle was replaced by a fixed coning angle of 4° . Since the blades are rigidly attached to the hub, the rotor speed degree of freedom equation was simplified by using only

aerodynamic torque. This procedure also eliminated any algebraic instability from dynamic coupling.

The floating hub rotor was simulated by a four blade rotor with two orthogonal teetering rotors. Initially, all elastic deflections were measured relative to a plane which was tangent to the hub. Due to an undesirable mathematic instability, the method was revised so that the average tilt of the rotor disk was used as a plane of reference. This procedure required the introduction of pinned-free as well as fixed-free bending modes, as shown in Figure 72. Due to the complexity of this change, the floating hub analysis was restricted to inelastic degrees of freedom. Thus, only helicopter and blade motion data were obtained for this configuration.

Some of the assumptions on which the derivation of the flexible blade equations of motion was based are as follows:

1. The blade section center of gravity is coincident with the intersection of the blade elastic axis and the principal axis of the section.
2. All elastic deflections and rotations are small.
3. Blade flapping and lagging angles are small, so that $\sin(\theta) = \theta$ and $\cos(\theta) = 1 - \frac{\theta^2}{2}$.
4. Fuselage angular and linear velocities are small compared with rotor angular velocity and tip speed, respectively.
5. Quasi-steady aerodynamic theory is applicable, and rotor inflow is uniform across the disk.
6. Radial flow effects are negligible.
7. Apparent mass aerodynamic forces are negligible.
8. Blade twist is both small and linear with radius.
9. The flapping and lagging hinges are offset from the center of rotation by less than 10% of the rotor radius.
10. The blade flapping and lagging hinges are coincident for the fully articulated rotors.
11. The change in radial position of a blade mass element due to elastic deformations is negligible when compared to rigid body blade motions for the articulated and floating hub rotors.
12. The thickness-to-chord and the chord-to-radius ratios of the blade are small.
13. Pitch-flap coupling affects only the blade aerodynamics.

14. The lag hinge offset for the zero offset rotor can be represented by an equivalent linear spring.

These simplifying assumptions are standard for rotor blade aeroelastic analyses and are considered adequate to qualitatively describe the effects of a power loss at high speeds. Correlation studies for the Sikorsky blade aeroelastic analysis have been discussed in References 2, 5, and 6. Comparisons of calculated data using constant inflow with flight test data indicated that calculated performance and one-half peak-to-peak flapwise blade stresses gave good agreement with flight-measured values at 140 knots. However, as concluded in Reference 2, a better definition of induced velocity was required to predict higher harmonic air loads and blade stresses with greater accuracy at all airspeeds. The Cornell Aeronautical Laboratory (CAL) variable inflow analysis, as used in Reference 1, did not produce peak-to-peak stress values matching the good correlation obtained using a constant inflow analysis at the high speed conditions. For high speed flight, then, the assumption of constant inflow was considered valid.

DESCRIPTION OF HYBRID COMPUTER SIMULATION

A hybrid computer, which included both a digital and analog computer, was used to solve the coupled equations of motion, in order to take full advantage of the more desirable features of each system. The hybrid facility located at the United Aircraft Research Laboratories was used for this study. This facility consists of a general purpose digital computer, Digital Equipment Corporation PDP-1, and a general purpose analog computer, Beckman Ease 2133. The two computers are logically linked for mode control and arithmetically linked by 20 high speed conversion channels in each direction.

The PDP-1 computer, used to solve the helicopter equations of motion and rotor dynamics, is a single address, single instruction, stored program machine with a word length of 18 bits. The memory unit contains a capacity for storing 14,336 words with a memory cycle time of 5 microseconds. The computer instructions that are available permit a wide range of logic operations and fixed point arithmetic. The 2133 analog computer was used to provide automatic controls for commanding trim, pilot inputs after power loss, and output data for time history recording. Some of the computer equipment includes 100 operational amplifiers and 150 coefficient potentiometers. In addition to the linear equipment, the computer also contains automatic potentiometer setting and component read-out equipment.

The dynamic response of the helicopter and the rotor blades can be separated into two frequency bands. The six elastic, flapping and lead-lag degrees of freedom constitute a high frequency range. The rotor speed and six helicopter degrees of freedom appear in the lower frequency range. The high frequency degrees of freedom were integrated on the digital computer by means of a Z transform technique, Reference 3. Also, a computer time scale of 1/100 of real time was selected to insure conversion of the higher bending modes. Simple Euler integration was found adequate, in this time frame, for the lower frequency degrees of freedom.

The rotor and helicopter equations of motion are solved by the digital computer as a three loop system. A simplified flow diagram of the computer program is presented in Figure 79. The program includes aerodynamic calculations for each of ten radial stations along the blade, forces, moments, and dynamics for up to six blades, and forces, moments, and dynamics for rotor speed and helicopter motion. Although the program is in closed loop form, it starts with the calculation of forces and moments and concludes with calculation of accelerations. In order to synchronize the digital computer with the analog operations, a digital clock maintains the program cycle at a one second time interval.

At the start of each clock interval, the program converts data from the analog computer into the digital computer. The data converted includes pilot control inputs and helicopter attitudes and velocities. During the computer time allocated for data conversion, the computer shares data transfer operations with the calculation of fuselage aerodynamics. The body axis component of velocity is used to calculate forward speed, angle of attack, and sideslip angle. With the aid of the fuselage wind tunnel data (Figures 77 and 78), the fuselage forces and moments are determined and then the tail rotor thrust is calculated. Square root operations in these calculations are accomplished by four iterations of the Newton Raphson square root technique, and all required arctangents are computed utilizing a three term Chebyshev polynomial.

Preliminary data are then calculated for use in the individual blade loop. These include flapping and lead-lag integration coefficients and a term for elastic torsion acceleration. Also, the gravitational force vector, weight, is resolved into the fuselage and shaft axes along with the aircraft translation and angular velocities and accelerations. Following the calculation of main rotor inflow, the rotor angular velocity is calculated with provisions for forcing the engine-supplied torque to zero or one half value for full and part power loss. A sudden loss of power was simulated by an exponential time decay with a time constant of 0.25 second.

The loop, in which the calculations for each blade are performed, is started by the calculation of azimuth angle corresponding to the current blade position. The local blade angle associated with specified control inputs is then determined, along with the blade segment velocities, angle of attack, shears, and moments.

Composite OOL2 airfoil data in the form of lift, drag, and pitching moment coefficient as a function of local angle of attack and Mach number, shown in Figure 80, are used to calculate the aerodynamic forces and moments for each blade segment. The calculations for each blade segment are repeated until the forces and moments are evaluated at the center of ten equally spaced segments, starting at blade radial station 0.23 and extending to the tip.

When the data for one blade have been determined, the blade flapping, lagging and elastic accelerations, velocities, and displacements are then calculated. The accelerations are integrated by means of difference equations which were derived from a Z transform equivalence of a second order

undamped system, Reference 3.

With the blade flapping and displacements known, the deflection of the blade tip, measured relative to a plane normal to the shaft, is then calculated. In this way the blade tip clearance over the tail cone can be established. The tip deflection is computed for any blade within 5° azimuth location of the tail. The deflection value in the time history traces is changed only when the blade enters the angular section of interest. The individual blade calculations are completed with the calculation of the blade root shear forces and bending moments. When the calculation of the data for all the blades has been completed, the total force and moments are calculated.

With the rotor calculations completed, the forces and moments generated by the fuselage, main rotor, tail rotor, and auxiliary jet engines are summed in the general equations of motion to determine the aircraft accelerations, velocities, and displacements. The program then returns to the outer loop beginning the calculation sequence again to complete the clock interval. If the aircraft is in a trimming mode, the controls are adjusted to reduce the aircraft accelerations to zero and to bring the forward speed to its trim value. At the same time pertinent data are transmitted to the six-channel Sanborn recorders for time history trace.

Due to the fact that the PDP-1 computer operates with fixed point arithmetic, and the digital-analog converters require fixed point data of a specified scale, predetermined scale factors had to be introduced into the computer program. Scaling factors were selected to permit as large a range as possible in parameters without severely restricting accuracy. These scale factors, Table IX, were based on flight test information of maximum values expected to be incurred on present day helicopters and do not necessarily represent physical limits. These scaling factors, therefore, limited the range of some of the parameters. The computer is programmed to go into a hold mode when these limits are exceeded. Minor scale changes were made during this study to insure that sufficient history data were acquired for analysis.

TABLE IX
SCALE FACTORS

Rotor Systems	CH-3C, a, b, c, e	d	f	g
θ_f, ϕ_f, ψ_f deg.	± 180	± 180	± 180	± 180
$\dot{\theta}_f, \dot{\phi}_f, \dot{\psi}_f$ deg./sec.	± 1	± 1	± 1	± 1
$\mu_{X_f}, \mu_{Y_f}, \mu_{Z_f}$	± 1	± 1	± 1	± 1
$\dot{\mu}_{X_f}, \dot{\mu}_{Y_f}, \dot{\mu}_{Z_f}$ 1/sec.	± 1	± 1	± 1	± 1
p, q, r rad./sec.	± 1	± 1	± 1	± 1
$\dot{p}, \dot{q}, \dot{r}$ rad./sec. ²	± 4	± 4	± 4	± 4
β rad.	$\pm .5$	$\pm .5$	--	$\pm .5$
$\dot{\beta}$ rad.	± 2	± 2	--	± 2
$\ddot{\beta}$ rad.	± 2	± 2	--	± 2
δ rad.	$\pm .5$	$\pm .5$	--	--
$\dot{\delta}$ rad.	± 1	± 1	--	--
$\ddot{\delta}$ rad.	$\pm .125$	$\pm .125$	--	--
μ_P	± 2	± 2	± 2	± 2
μ_T	± 2	± 2	± 2	± 2
θ_c rad.	$\pm .5$	$\pm .5$	$\pm .5$	$\pm .5$
$\dot{\theta}_c$ rad.	$\pm .5$	$\pm .5$	$\pm .5$	$\pm .5$
$\ddot{\theta}_c$ rad.	$\pm .5$	$\pm .5$	$\pm .5$	$\pm .5$
θ_o rad.	$\pm \pi$	$\pm \pi$	$\pm \pi$	$\pm \pi$
$\dot{\theta}_o$ rad.	± 4	± 4	± 4	± 4
$\ddot{\theta}_o$ rad.	± 4	± 4	± 4	± 4
$\theta_{s.75}$ rad.	± 1	± 1	± 1	± 1
$\dot{\theta}_{s.75}$ rad.	± 4	± 4	± 4	± 4
$\ddot{\theta}_{s.75}$ rad.	± 4	± 4	± 4	± 4

TABLE IX (Continued)

Rotor Systems	CH-3C,a,b,c,e	d	f	g
$(C_T/\sigma)_s$	$\pm .5$	$\pm .5$	$\pm .5$	$\pm .5$
$(C_H/\sigma)_s$	$\pm .5$	$\pm .5$	$\pm .5$	$\pm .5$
$(C_Y/\sigma)_s$	$\pm .5$	$\pm .5$	$\pm .5$	$\pm .5$
$(C_L/\sigma)_s$	$\pm .0312$	$\pm .0312$	$\pm .25$	$\pm .0312$
$(C_m/\sigma)_s$	$\pm .0312$	$\pm .0312$	$\pm .25$	$\pm .0312$
$(C_Q/\sigma)_s$	$\pm .0312$	$\pm .0312$	$\pm .25$	$\pm .25$
$(C_n/\sigma)_f$	$\pm .0312$	$\pm .0312$	$\pm .25$	$\pm .0312$
$(C_l/\sigma)_f$	$\pm .0312$	$\pm .0312$	$\pm .25$	$\pm .25$
$(C_m/\sigma)_f$	$\pm .0312$	$\pm .0312$	$\pm .25$	$\pm .25$
$(C_Q/\sigma)_e$	$\pm .0312$	$\pm .0312$	$\pm .25$	$\pm .25$
q_{w1}	$\pm .025$	$\pm .025$	$\pm .4$	$\pm .4$
q_{w2}	$\pm .00625$	$\pm .00625$	$\pm .1$	$\pm .1$
q_{w3}	$\pm .003125$	$\pm .003125$	$\pm .05$	$\pm .05$
$\overset{x}{q}_{w1}$	$\pm .05$	$\pm .05$	$\pm .8$	$\pm .8$
$\overset{x}{q}_{w2}$	$\pm .0125$	$\pm .0125$	$\pm .2$	$\pm .2$
$\overset{x}{q}_{w3}$	$\pm .00625$	$\pm .00625$	$\pm .1$	$\pm .1$
$\overset{xx}{q}_{w1}$	$\pm .40$	$\pm .40$	± 6.40	± 6.40
$\overset{xx}{q}_{w2}$	$\pm .10$	$\pm .10$	± 1.60	± 1.60
$\overset{xx}{q}_{w3}$	$\pm .05$	$\pm .05$	$\pm .80$	$\pm .80$
q_{v1}	$\pm .025$	$\pm .025$	$\pm .400$	$\pm .400$
q_{v2}	$\pm .003125$	$\pm .003125$	$\pm .050000$	$\pm .050000$
$\overset{x}{q}_{v1}$	$\pm .050$	$\pm .050$	$\pm .800$	$\pm .800$
$\overset{x}{q}_{v2}$	$\pm .00625$	$\pm .00625$	$\pm .10000$	$\pm .10000$

TABLE IX (Continued)

Rotor System	CH-3C,a,b,c,e	d	f	g
$q_{v_1}^{**}$	$\pm .40$	± 1.60	± 6.40	± 6.40
$q_{v_2}^{**}$	$\pm .050$	$\pm .200$	$\pm .800$	$\pm .800$
q_{θ}	$\pm .2$	$\pm .2$	$\pm .2$	$\pm .2$
q_{θ}^*	± 8	± 8	± 8	± 8
q_{θ}^{**}	± 8	± 8	± 8	± 8

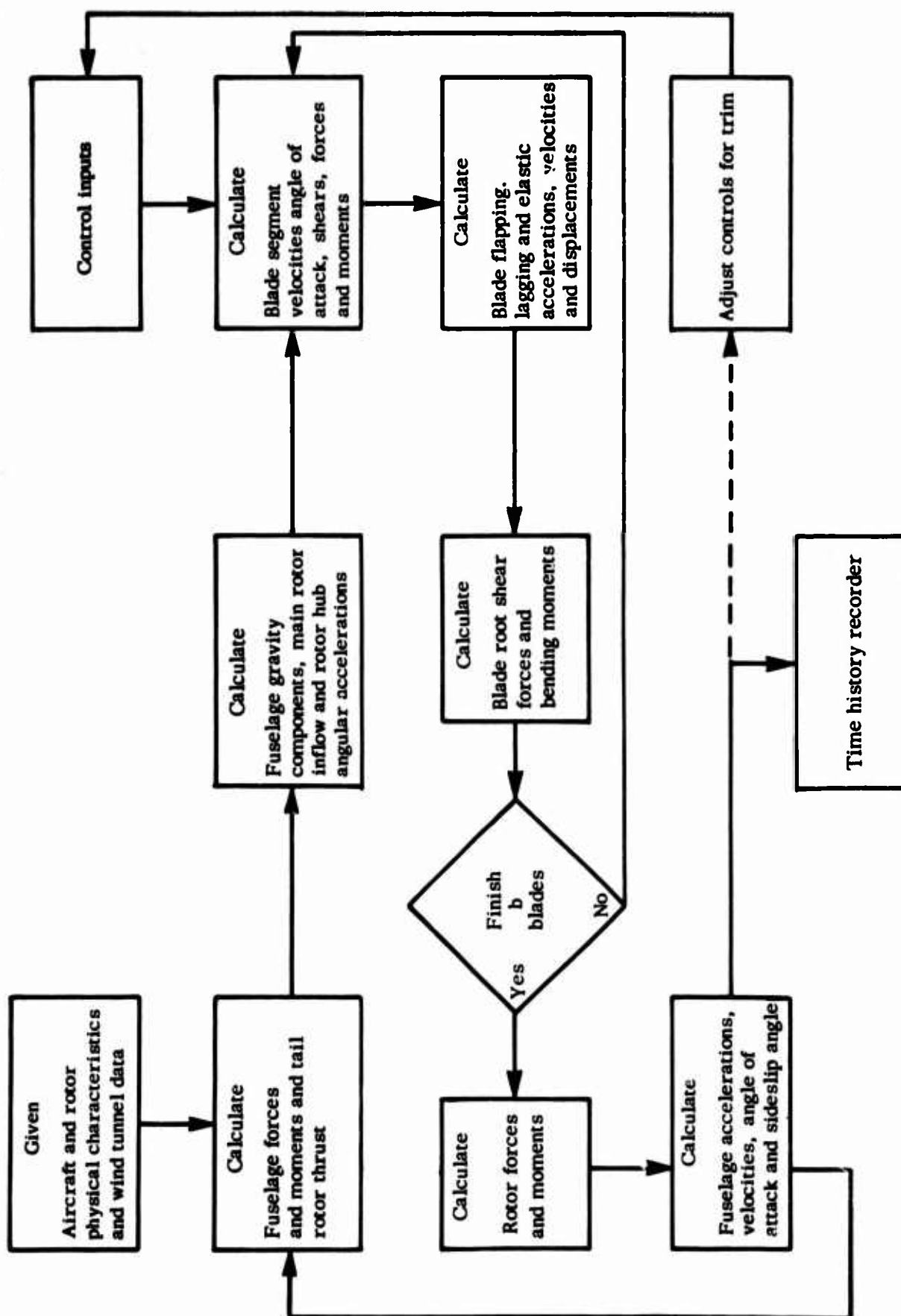


Figure 79. Hybrid Computer Flow Diagram

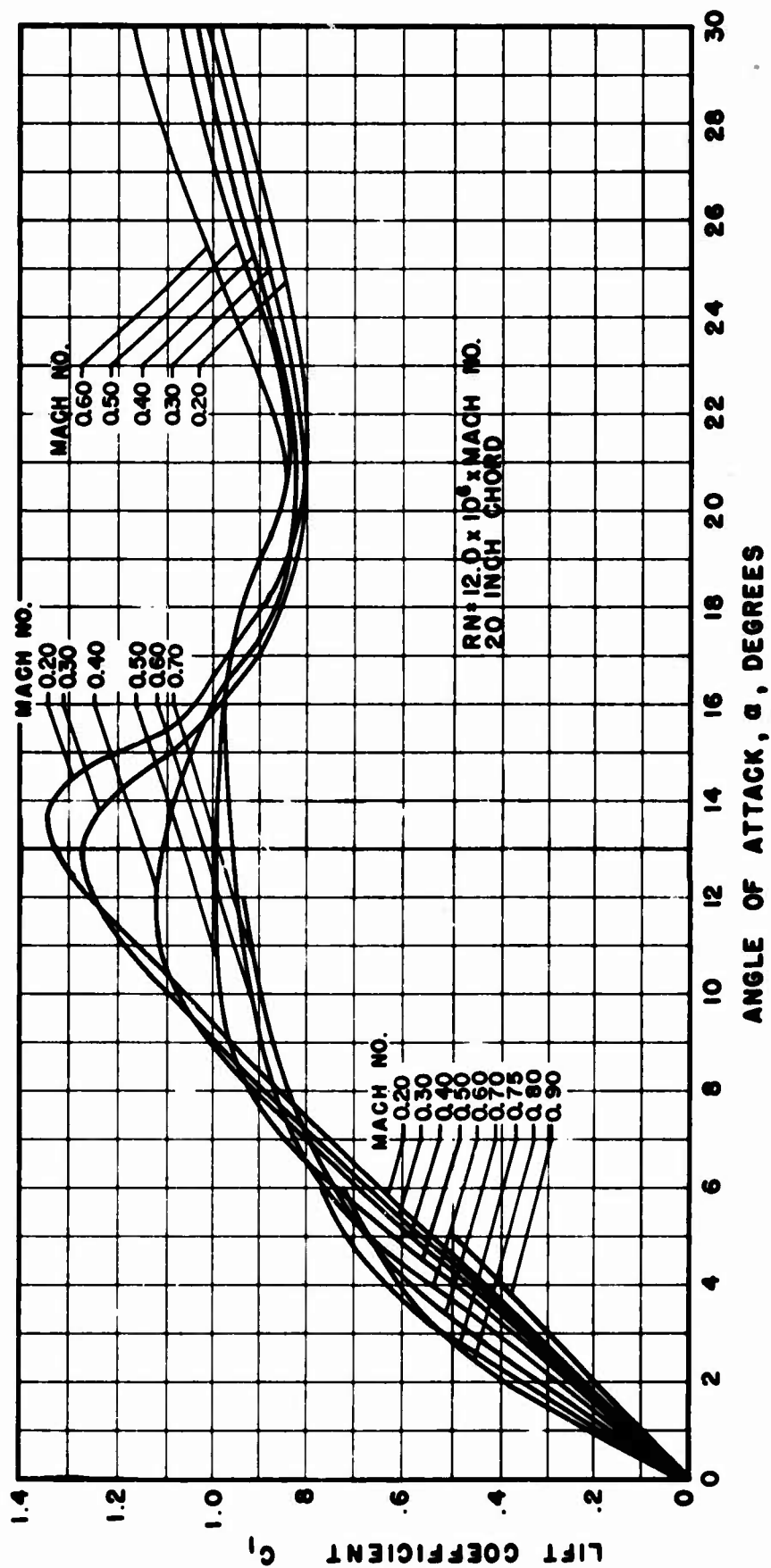


Figure 80. Composite OOL2 Airfoil Data, Sea Level, Standard Conditions

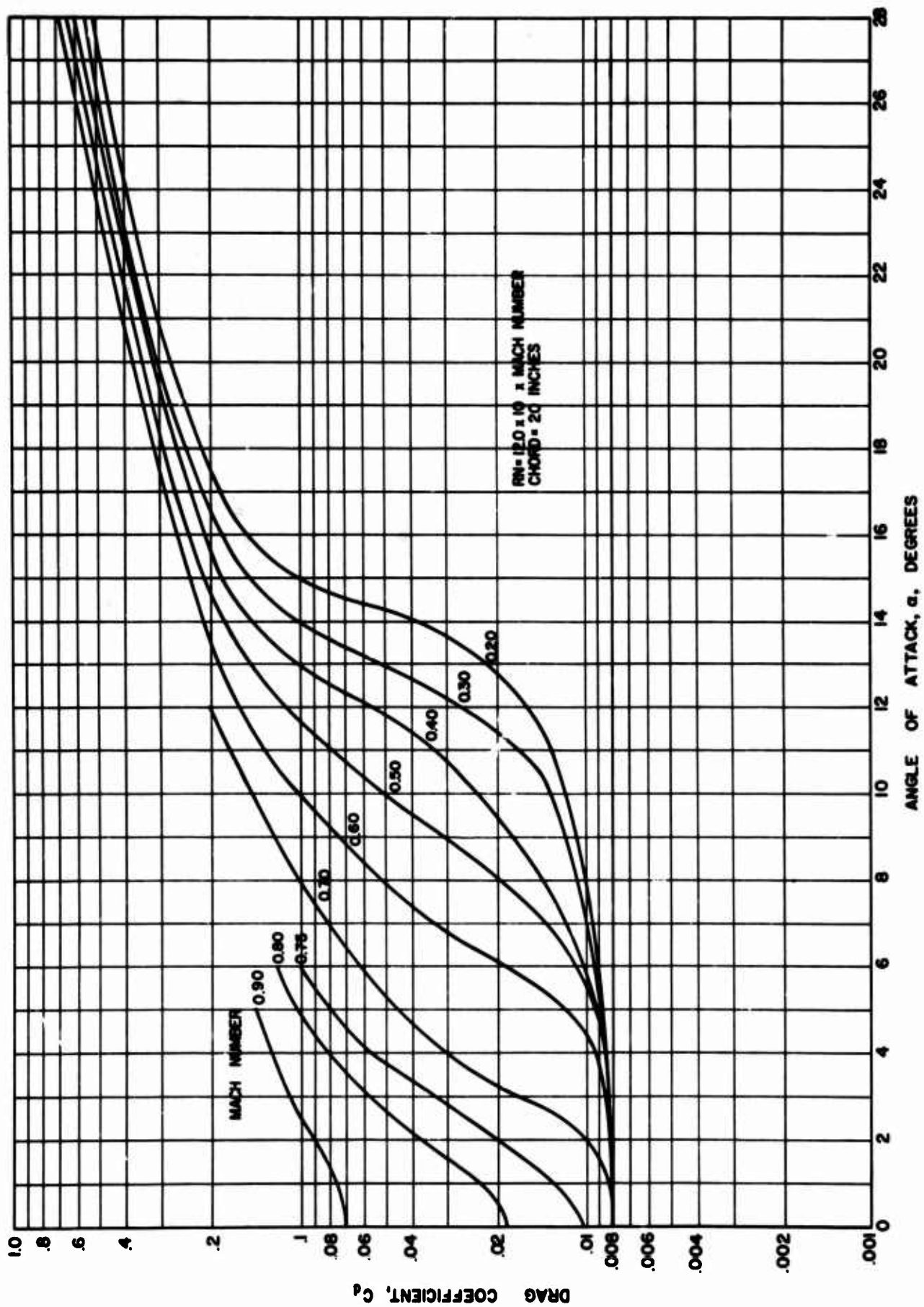


Figure 80. Continued

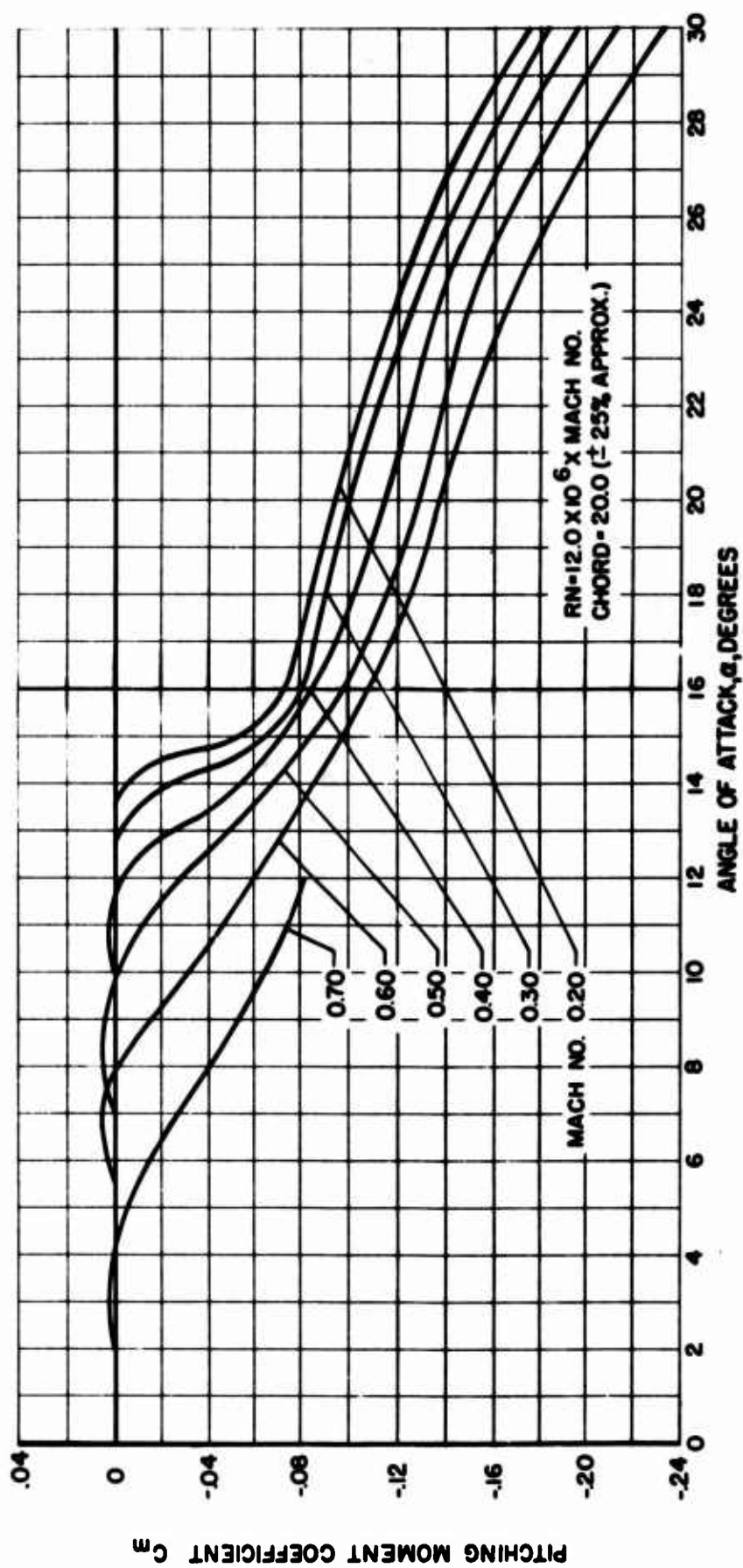


Figure 80. Concluded

APPENDIX III

PROGRAM EQUATIONS

This appendix presents the equations used in this study. The fuselage equations are given below in nondimensional form:

$$\dot{\mu}_{xf} = r\mu_{yf} - q\mu_{zf} + \frac{1}{K_1} \left(\frac{C_x}{\sigma} \right)_f - \frac{K_4}{K_1} \sin \theta - \frac{K_2}{K_1} \frac{D_{ff}}{q_f} \bar{\mu}_f^2 + \frac{1}{K_1} P_{xf}$$

$$\dot{\mu}_{yf} = p\mu_{zf} - r\mu_{xf} + \frac{1}{K_1} \left(\frac{C_y}{\sigma} \right)_f + \frac{K_3}{K_1} \left(\frac{C_T}{\sigma} \right)_t + \frac{K_4}{K_1} q'_{yf} + \frac{K_2}{K_1} \frac{Y_{ff}}{q_f} \bar{\mu}_f^2$$

$$\dot{\mu}_{zf} = q\mu_{xf} - p\mu_{yf} + \frac{1}{K_1} \left(\frac{C_z}{\sigma} \right)_f + \frac{K_4}{K_1} q'_{zf} - \frac{K_2}{K_1} \frac{L_{ff}}{q_f} \bar{\mu}_f^2$$

$$\dot{p} = -\frac{K_{59}}{K_6} q r + \frac{K_7}{K_6} \left(\frac{C_y}{\sigma} \right)_f + \frac{K_{63}}{K_6} \left(\frac{C_z}{\sigma} \right)_f + \frac{1}{K_6} \left(\frac{C_d}{\sigma} \right)_f + \frac{K_9}{K_6} \left(\frac{C_T}{\sigma} \right)_t + \bar{\mu}_f^2 \left(\frac{K_{12}}{K_6} \frac{\alpha_{ff}}{q_f} + \frac{K_{17}}{K_6} \frac{Y_{ff}}{q_f} \right)$$

$$\dot{q} = -\frac{K_{60}}{K_{13}} r_f P_f - \frac{K_7}{K_{13}} \left(\frac{C_x}{\sigma} \right)_f + \frac{K_{20}}{K_{13}} \left(\frac{C_z}{\sigma} \right)_f + \frac{1}{K_{13}} \left(\frac{C_m}{\sigma} \right)_f + \bar{\mu}_f^2 \left(\frac{K_{12}}{K_{13}} \frac{M_{ff}}{q_f} - \frac{K_{18}}{K_{13}} \frac{L_{ff}}{q_f} + \frac{K_{17}}{K_{13}} \frac{D_{ff}}{q_f} \right) + \frac{K_{15}}{K_{13}} \frac{\bar{\mu}_f^2}{\mu_{xf}} q_f - \frac{K_{65}}{K_{13}} \left(\frac{C_T}{\sigma} \right)_s \cos \beta_f$$

$$\dot{r} = -\frac{K_{61}}{K_{19}} p q - \frac{K_{63}}{K_{19}} \left(\frac{C_x}{\sigma} \right)_f - \frac{K_{20}}{K_{19}} \left(\frac{C_Y}{\sigma} \right)_f + \frac{1}{K_{19}} \left(\frac{C_n}{\sigma} \right)_f$$

$$+ \bar{\mu}_f^2 \left(\frac{K_{12}}{K_{19}} \frac{n_{ff}}{q_f} - \frac{K_{18}}{K_{19}} \frac{Y_{ff}}{q_f} \right) - \frac{K_{21}}{K_{19}} \left(\frac{C_T}{\sigma} \right)_f + \frac{K_D}{K_{19}} r \frac{\bar{\mu}_f^2}{\mu_{xf}}$$

where the constants (K) are defined in Table X and the axis systems are shown in Figure 81.

The fuselage angle of attack, sideslip, and velocity are given by:

$$\tan \beta_f = \frac{\mu_{yf}}{|\mu_{xf}|}$$

$$\tan \alpha_{ef} = \left[\frac{\mu_{zf} - \frac{D_w \cos \beta_f}{2}}{|\mu_{xf}|} \right]$$

$$\bar{\mu}_f = \sqrt{\mu_{xf}^2 + \mu_{yf}^2 + \mu_{zf}^2}$$

$$V = \Omega_0 R \bar{\mu}_f \frac{1}{1.688}$$

Fuselage attitude and rates are defined by the Euler angles.

$$\dot{\theta}_f = q \cos \phi_f - r \sin \phi_f$$

$$\dot{\phi}_f = p + \dot{\psi}_f \sin \theta_f$$

$$\dot{\psi}_f = \frac{r \cos \theta_f + q \sin \theta_f}{\cos \theta_f}$$

$$\theta_f = \int_0^T \dot{\theta}_f dt$$

$$\phi_f = \int_0^T \dot{\phi}_f dt$$

$$\psi_f = \int_0^T \dot{\psi}_f dt$$

The fuselage and rotor velocities and accelerations are related by means of the following equations:

$$\bar{v}_{x1} = -[\mu_{x_F} - \eta/\Omega_0(K_7 - K_{20}I_3) + \mu_{z_F}I_3]$$

$$\bar{v}_{z1} = -[\mu_{z_F} - \mu_{x_F}I_3 + \eta/\Omega_0(K_{20} + K_7I_3)]$$

$$\bar{v}_{y1} = \mu_{y_F} + \frac{1}{\Omega_0}(K_7\dot{p} - K_{20}\dot{r})$$

$$\bar{\omega}_{x1} = -\frac{1}{\Omega_0}[\dot{p} + \dot{r}I_3]$$

$$\bar{\omega}_{y1} = \eta/\Omega_0$$

$$\bar{\omega}_{z1} = \frac{1}{\Omega_0}[\dot{p}I_3 - \dot{r}]$$

$$\ddot{v}_{x1} = -\frac{1}{\Omega_0}[\dot{\mu}_{x_F} + \dot{\mu}_{z_F}I_3 - \dot{\eta}/\Omega_0(K_7 - K_{20}I_3)]$$

$$\ddot{v}_{y1} = \frac{1}{\Omega_0}[\dot{\mu}_{y_F} + \frac{1}{\Omega_0}(K_7\dot{p} - K_{20}\dot{r})]$$

$$\ddot{v}_{z_1} = -\frac{1}{\Omega_0} [\dot{\mu}_{z_F} - \dot{\mu}_{x_F} I_s + \dot{\vartheta}/\Omega_0 (K_{20} + K_7 I_s)]$$

$$\ddot{\omega}_{x_1} = -\frac{1}{\Omega_0^2} [\dot{r} + \dot{r} I_s]$$

$$\ddot{\omega}_{y_1} = \dot{\vartheta}/\Omega_0^2$$

$$\ddot{\omega}_{z_1} = \frac{1}{\Omega_0^2} [\dot{r} I_s - \dot{r}]$$

ROTOR EQUATIONS

The rotor flapping and lead acceleration are given by the following equations:

$$\begin{aligned} \ddot{\delta} = & \frac{1}{I_B} \int_{\bar{e}'}^{\bar{R}} \bar{S}_{A\gamma Sa} \bar{F}_a d\bar{F} - \frac{\bar{M}_B (\bar{F}_{ce})_B}{\bar{I}_B} \bar{L}_2' - \bar{f}_2' \\ & + \frac{\bar{M}_{LB}}{\bar{I}_B} - \delta \frac{\bar{M}_B (\bar{F}_{ce})_B}{\bar{I}_B} \bar{e} \end{aligned}$$

$$\begin{aligned} \ddot{\beta} = & \frac{1}{I_B} \int_{\bar{e}'}^{\bar{R}} \bar{S}_{A\gamma Sa} \bar{F}_a d\bar{F} - \frac{\bar{M}_B (\bar{F}_{ce})_B}{\bar{I}_B} \bar{L}_1' - \bar{f}_1' \\ & - \beta \left(\frac{\bar{M}_B (\bar{F}_{ce})_B}{\bar{I}_B} \bar{e} + 1 \right) \end{aligned}$$

The \bar{l} and \bar{f} terms are velocity and acceleration components, respectively, and are defined by the following equations:

$$\bar{l}_1' = \dot{\bar{v}}_{0x_1} - \beta d_2 + d_1 + \bar{e} d_3 + \bar{g}_{25}$$

$$\bar{l}_2' = -\delta d_2 + a_5 - \bar{v}_{0x_1} a_2 + \bar{w}_{z_1} a_3 + \bar{e} b_3 + \bar{g}_{45}$$

$$\bar{f}_2' = \delta [2\bar{\Omega} a_1 + a_4] + d_3 + 2\dot{\delta} a_2 + \beta [b_4^2 + 2\bar{\Omega} b_4]$$

$$\bar{f}_3' = b_3 - 2\dot{\beta} [a_2 + \beta(\bar{\Omega} + \bar{w}_{z_1})] - \beta a_4$$

$$a_1 = \bar{w}_{y_1} \cos \psi_R - \bar{w}_{x_1} \sin \psi_R$$

$$a_2 = \bar{w}_{x_1} \cos \psi_R + \bar{w}_{y_1} \sin \psi_R$$

$$a_3 = \dot{\bar{w}}_{y_1} \cos \psi_R - \dot{\bar{w}}_{x_1} \sin \psi_R$$

$$a_4 = \dot{\bar{w}}_{x_1} \cos \psi_R + \dot{\bar{w}}_{y_1} \sin \psi_R$$

$$a_5 = \dot{\bar{v}}_{0y_1} \cos \psi_R - \dot{\bar{v}}_{0x_1} \sin \psi_R$$

$$a_6 = \dot{\bar{v}}_{0x_1} \cos \psi_R + \dot{\bar{v}}_{0y_1} \sin \psi_R$$

$$a_7 = \bar{v}_{0y_1} \cos \psi_R - \bar{v}_{0x_1} \sin \psi_R$$

$$a_8 = \bar{v}_{0x_1} \cos \psi_R + \bar{v}_{0y_1} \sin \psi_R$$

$$b_1 = \bar{\Omega} + \bar{w}_{z_1}$$

$$b_2 = \bar{\Omega} + \bar{w}_{z_1} + \dot{\delta}$$

$$b_3 = \dot{\bar{\Omega}} + \dot{\bar{w}}_{z_1}$$

$$d_1 = \bar{\omega}_x \bar{v}_{oy} - \bar{\omega}_y \bar{v}_{ox}$$

$$d_2 = \bar{v}_{ox} (\bar{\omega}_y \cos \Psi_R - \bar{\omega}_x \sin \Psi_R) + \bar{v}_{oy} \cos \Psi_R + \bar{v}_{ox} \sin \Psi_R \\ - \bar{\omega}_z [\bar{v}_{oy} \cos \Psi_R - \bar{v}_{ox} \sin \Psi_R + \bar{e} (2\bar{\Omega} + \bar{\omega}_z)]$$

$$d_3 = 2\bar{\Omega} [\bar{\omega}_x \cos \Psi_R + \bar{\omega}_y \sin \Psi_R] - \bar{\omega}_y \cos \Psi_R + \bar{\omega}_x \sin \Psi_R$$

Blade flapwise, chordwise, and torsional modal amplitudes accelerations are given in the expressions below where the C coefficients are defined in Table XI.

Flapwise:

$$\ddot{q}_{wi}^{xx} = \frac{\Delta \bar{r}}{C_{ii}} \sum_{a=1}^N \{ \bar{r}_{wia} [\bar{S}_{AZ5a} m_{1a} - \bar{S}_{AY5a} m_{2a}] \} \\ + \frac{1}{C_{ii}} \left\{ \sum_{i'=1}^3 \bar{q}_{wi} [\bar{f}_{20} (C_2 - C_6)_{i,i'} + \bar{f}_{21} (C_4 - C_7)_{i,i'} \right. \\ + (\bar{\Omega}^2 - 1) (C_{28} - C_{29})_{i,i'}] + \sum_{p=1}^2 \bar{q}_{vp} [(\bar{f}_{20} \theta - \dot{\theta}_0^x) C_{3i,p} \\ + \bar{f}_{21} (\theta, C_8)_{i,p} + \bar{\Omega}^2 (\theta, C_{30})_{i,p}] + \sum_{i'=1}^3 \bar{q}_{wi} [-2\theta_1 (\frac{\omega_{wi}}{\Omega_0}) C_{9i,i'}] \\ + \sum_{p=1}^2 \bar{q}_{vp} [2\theta_1 (\frac{\omega_{vp}}{\Omega_0})^2 C_{8i,p} - C_{35} C_{27i,p}] \\ - m_8 \sum_{p=1}^2 \ddot{q}_{vp} C_{3i,p} - m_3 C_{10i} + m_4 C_{11i} + [\bar{f}_8 \cos \theta \\ + \bar{f}_2 \sin \theta] C_{13i} \} + m_6 \bar{q}_{wi} - \bar{q}_{wi} (\frac{\omega_{wi}}{\Omega_0})^2$$

$$\bar{f}_{20} = \bar{e} (\delta \bar{\Omega} - 2\bar{\omega}_z \bar{\Omega})$$

$$\bar{f}_{21} = \beta^2 \bar{\Omega}^2 - 2 \bar{\omega}_{z1} \bar{\Omega} - 2 \dot{\delta} \bar{\Omega} - \dot{\delta}^2 - \dot{\beta}^2$$

$$\bar{f}_e = b_3 - 2\beta[a_2 + \beta(\bar{\Omega} + \bar{\omega}_{z1})] - \beta a_4 + \dot{\delta}$$

$$\bar{f}_2 = \bar{f}_2' + \dot{\beta} + \beta \bar{\Omega}^2$$

$$m_{1a} = \cos \theta_0 - \theta_{0a} \sin \theta_0$$

$$m_{2a} = \sin \theta_0 + \theta_{0a} \cos \theta_0$$

$$m_3 = \bar{l}_1 \cos \theta_0 - \bar{l}_2 \sin \theta_0$$

$$m_4 = \bar{l}_2 \cos \theta_0 + \bar{l}_1 \sin \theta_0$$

$$m_6 = 2\beta \dot{\theta}_0 (\bar{\Omega} + \bar{\omega}_{z1} + \dot{\delta}) + \dot{\theta}_0^2$$

$$m_8 = 2\dot{\theta}_0 + 2\beta(\bar{\Omega} + \bar{\omega}_{z1} + \dot{\delta})$$

Chordwise:

$$\begin{aligned} \ddot{q}_{vp}^{xx} = & \frac{\Delta \bar{\Gamma}}{C_{14p}} \sum_{j=1}^N \left\{ d_{1vpj} [\bar{S}_{AY5a} m_{1a} + \bar{S}_{AZ5a} m_{2a}] \right\} \\ & + \frac{1}{C_{14p}} \left\{ \sum_{p'=1}^2 q_{vp'} [\bar{f}_{20} (C_{17} - C_{19})_{p,p'} + \bar{f}_{21} (C_{18} - C_{20})_{p,p'} \right. \\ & + (\bar{\Omega}^2 - 1) (C_{32} - C_{31})_{p,p'} - m_5 \bar{f}_{10} C_{34p,p'}] + \sum_{i=1}^3 q_{wi} [(\dot{\theta}_0^2 \\ & - \bar{f}_9 \cos^2 \theta_0 + \frac{m_5 \bar{f}_{10}}{2} - \theta_1 \bar{f}_{20}) C_{3i,p} - \bar{f}_{21} (\theta_1 C_5)_{i,p} \\ & \left. - \bar{\Omega}^2 (\theta_1 C_{30})_{i,p} + (m_5 \bar{f}_9 - m_9 \bar{f}_{10}) (\theta_1 C_{99})_{i,p} \right] \end{aligned}$$

$$\begin{aligned}
& + \sum_{i=1}^3 q_{wi} \left[-2\theta_1 \left(\frac{\omega_{wi}}{\Omega_0} \right)^2 C_{22i,p} + C_{25} C_{26i,p} \right] \\
& + \sum_{p'=1}^2 q_{vp'} \left[2\theta_1 \left(\frac{\omega_{vp'}}{\Omega_0} \right)^2 C_{21p,p'} \right] + m_6 \sum_{i=1}^3 \ddot{q}_{wi} C_{2i,p} \\
& - m_4 C_{15p} - m_3 C_{16p} - [\bar{f}_2 \cos \theta_0 - \bar{f}_6 \sin \theta_0] C_{33p} \\
& + \gamma'_{vp} \Big|_{\bar{r}=0} \bar{M}_{LD} + (\bar{f}_{20} - \bar{e} \bar{\Omega}^2) C_{23p} \\
& + (\bar{f}_{21} - \bar{\Omega}^2) C_{24p} \Big\} + m_7 q_{vp} - q_{vp} \left(\frac{\omega_{vp}}{\Omega_0} \right)^2 \\
& - 2(0.025) \bar{\omega}_{vp} \ddot{q}_{vp}
\end{aligned}$$

Torsion:

$$\begin{aligned}
C_{36} \ddot{q}_\theta &= \Delta \bar{r} \sum_{a=1}^N \gamma_{\theta a} \bar{M}_{caAa} + \theta_1 \left[\sum_i \sum_{i'} q_{wi} \ddot{q}_{wi'} C_{38i,i'} \right. \\
& + \sum_{p=1}^2 \sum_{p'=1}^2 q_{vp} q_{vp'} C_{39p,p'} \Big] - \sum_{i=1}^3 \sum_{p=1}^2 q_{wi} q_{vp} C_{46i,p} \\
& - C_{44} (\bar{f}_{23} + \ddot{\theta}_0^x) + \beta \gamma_{\theta LD} \bar{M}_{LD} + C_{37} \bar{\Omega}^2 \\
& - C_{36} \left(\frac{\omega_\theta}{\Omega_0} \right)^2 q_\theta
\end{aligned}$$

Terms common to the above equations are given by the following expressions:

$$\begin{aligned}
\bar{f}_9 &= -2\beta (\bar{\Omega} + \bar{\omega}_{z_1} + \dot{\delta}) - \beta (\ddot{\Omega} + \ddot{\omega}_{z_1} + \ddot{\delta}) \\
\bar{f}_{10} &= [\bar{\Omega} + \bar{\omega}_{z_1} + \dot{\delta}]^2 \\
m_5 &= 2 \sin \theta_0 \cos \theta_0
\end{aligned}$$

$$m_7 = m_6 - [(\bar{\Omega} + \bar{\omega}_2 + \dot{\delta}) \sin \theta_0]^2 + (\bar{\Omega} + \bar{\omega}_2 + \dot{\delta})^2 - 1$$

$$m_9 = 1 - 2 \sin^2 \theta_0$$

$$\bar{f}_{22} = [\bar{\Omega} + \bar{\omega}_2 + \dot{\delta}]^2 - 1$$

$$\begin{aligned} \bar{f}_{23} = a_4 + (\bar{\Omega} + \dot{\delta}) \left[\frac{1}{2} m_5 (\bar{\Omega} + \dot{\delta}) + \beta (1 - m_9) \right] \\ + a_1 \bar{\Omega} (1 + m_9) \end{aligned}$$

The lag damper moment, including both viscous damper and a spring force, is given by the following expression:

$$\begin{aligned} \bar{M}_{LD} = & [C_0 \ddot{\theta}_0 \cos \theta_0 + K_0 \sin \theta_0] \sum_{i=1}^3 (\dot{\delta}'_{wi})_{\bar{r}=0} q_{wi} \\ & - [K_0 \cos \theta_0 - C_0 \ddot{\theta}_0 \sin \theta_0] \sum_{p=1}^2 (\dot{\delta}'_{vp})_{\bar{r}=0} q_{vp} \\ & - C_0 \left[\cos \theta_0 \sum_{p=1}^2 (\dot{\delta}'_{vp})_{\bar{r}=0} \ddot{q}_{vp} \right. \\ & \left. - \sin \theta_0 \sum_{i=1}^3 (\dot{\delta}'_{wi})_{\bar{r}=0} \ddot{q}_{wi} \right] - C_0 \dot{\delta} - K_0 \delta \end{aligned}$$

The blade root end shear forces include aerodynamic as well as dynamic terms as follows:

$$\begin{aligned} \bar{S}_{x_3} = & -\beta \sum_{a=1}^N \Delta \bar{r} \bar{S}_{Az5a} - \delta \sum_{a=1}^N \Delta \bar{r} \bar{S}_{Ay5a} - \bar{M}_B \{ a_6 \\ & + \omega_2 a_7 + \bar{v}_{02} a_1 - \bar{e} b_1^2 + \bar{g} x_3 \} - \bar{M}_B (\bar{r}_{c_6})_B \{ \\ & -\beta \ddot{\beta} - \dot{\beta}^2 - \delta \ddot{\delta} - \dot{\delta}^2 - 2\delta \dot{b}_1 + \beta a_3 - \delta b_2 \end{aligned}$$

$$\begin{aligned}
& + 2\beta a_1 + b_1^2 \left(\frac{\beta^2}{2} + \frac{\delta^2}{2} - 1 \right) \} - s_3 \sum_{i=1}^3 \ddot{q}_{w_i}^{xx} C_{10i} \\
& - 2(s_1 + s_5) \sum_{i=1}^3 \ddot{q}_{w_i} C_{10i} + (\ddot{\beta}^{xx} \cos \theta_0 - \ddot{\delta}^{xx} \sin \theta_0 \\
& - b_1 s_3 + b_1^2 s_3) \sum_{i=1}^3 \ddot{q}_{w_i} C_{10i} + s_4 \sum_{p=1}^2 \ddot{q}_{v_p}^{xx} C_{15p} \\
& + 2(s_2 + s_6) \sum_{p=1}^2 \ddot{q}_{v_p} C_{15p} + (\ddot{\delta}^{xx} \cos \theta_0 + \ddot{\beta}^{xx} \sin \theta_0 \\
& - b_1 s_7 - b_1^2 s_4) \sum_{p=1}^2 \ddot{q}_{v_p} C_{15p}
\end{aligned}$$

$$\begin{aligned}
\bar{S}_{z_3} = & (1 - \frac{\beta^2}{2}) \sum_{a=1}^N \Delta \bar{r} \bar{S}_{A z s_a} - \bar{M}_B \left\{ \ddot{v}_{0z_1} - \bar{e} [a_3 \right. \\
& - a_2 (\bar{\Omega} + b_1)] + d_1 + \bar{g}_{z_3} \} - \bar{M}_B (\bar{r}_{c6})_B [d_3 + \omega_{z_1} a_2 \\
& + \ddot{\beta}^{xx}] - \cos \theta_0 \sum_{i=1}^3 \ddot{q}_{w_i}^{xx} C_{10i} + s_7 \sum_{i=1}^3 \ddot{q}_{w_i} C_{10i} \\
& - \sin \theta_0 \sum_{p=1}^2 \ddot{q}_{v_p}^{xx} C_{15p} - s_8 \sum_{p=1}^2 \ddot{q}_{v_p} C_{15p}
\end{aligned}$$

$$\begin{aligned}
\bar{S}_{y_3} = & (1 - \frac{\delta^2}{2}) \sum_{a=1}^N \Delta \bar{r} \bar{S}_{A y s_a} - \beta \delta \sum_{a=1}^N \Delta \bar{r} S_{A z s_a} - \bar{M}_B \{ a_5 \\
& - \ddot{v}_{0z_1} a_2 + \omega_{z_1} a_3 + \bar{e} b_3 + \bar{g}_{y_3} \} - \bar{M}_B (\bar{r}_{c6})_B \{ \ddot{\delta}^{xx} \\
& - 2\ddot{\beta} a_2 + b_3 - 2b_1 (\beta \ddot{\beta} + \delta \ddot{\delta}) - \delta b_1^2 \} \\
& - \cos \theta_0 \sum_{p=1}^2 \ddot{q}_{v_p}^{xx} C_{15p} + (s_7 + 2b_1 s_4) \sum_{p=1}^2 \ddot{q}_{v_p} C_{15p} \\
& + 2b_1 (s_2 + \frac{1}{2} s_6) \sum_{p=1}^2 \ddot{q}_{v_p} C_{15p} + \sin \theta_0 \sum_{i=1}^3 \ddot{q}_{w_i}^{xx} C_{10i}
\end{aligned}$$

$$-(2b_1 s_3 - s_0) \sum_{i=1}^3 \ddot{q}_{\theta} w_i C_{10i}$$

$$-2b_1 (s_1 + \frac{1}{2} s_5) \sum_{i=1}^3 q_{\theta} w_i C_{10i}$$

$$s_1 = -\ddot{\beta} \cos \theta_0 + \ddot{\delta} \sin \theta_0$$

$$s_2 = \ddot{\delta} \cos \theta_0 + \ddot{\beta} \sin \theta_0$$

$$s_3 = -\beta \cos \theta_0 + \delta \sin \theta_0$$

$$s_4 = \delta \cos \theta_0 + \beta \sin \theta_0$$

$$s_5 = (\bar{\Omega} + \bar{\omega}_{z_1}) \sin \theta_0$$

$$s_6 = (\bar{\Omega} + \bar{\omega}_{z_1}) \cos \theta_0$$

$$s_7 = 2 \ddot{\theta}_0 \sin \theta_0$$

$$s_8 = 2 \ddot{\theta}_0 \cos \theta_0$$

The rotor blade segment forces are represented as:

$$\bar{S}_{Az5a} = \frac{1}{2} \frac{\rho R c}{m_0} U (U_T C_l + U_P C_D)$$

$$\bar{S}_{Ay5a} = \frac{1}{2} \frac{\rho R c}{m_0} U (U_P C_l - U_T C_D)$$

$$\bar{M}_{caAa} = \left(\frac{1}{2} \frac{\rho c^2}{m_0} C_{m c/4} \right) U_a^2 + \bar{\eta}_{p c/4} \bar{S}_{Az5a}$$

$$-\frac{\pi}{2} \left(\frac{1}{2} \frac{\rho c^2}{m_0} \right) U_a R$$

$$\bar{K} = -\bar{y}_{\theta_{3/4C}} (\gamma_{\theta a} \ddot{q}_0 + \ddot{\theta}_0) \quad u_{Ta} \geq 0$$

$$= \bar{y}_{\theta_{3/4C}} (\gamma_{\theta a} \ddot{q}_0 + \ddot{\theta}_0) \quad u_{Ta} < 0$$

Blade segment velocities are given by the following equations:

$$\begin{aligned} u_p = & \lambda_0 (1 - \frac{\beta^2}{2}) + \beta (a_7 \delta + a_8) + a_1 (\bar{e} + \bar{r}_a) \\ & - \bar{r}_a (a_2 \delta + \beta) - \cos \theta_0 \left[\sum_{i=1}^3 \delta_{wia} \ddot{q}_{wi} \right. \\ & + \theta_0 \left(\sum_{p=1}^2 \delta_{vpa} \ddot{q}_{vp} + \bar{y}_{\theta_{3/4C}} \right) - a_5 \sum_{i=1}^3 \delta'_{wia} \ddot{q}_{wi} \\ & + \sin \theta_0 \left[\ddot{\theta}_0 \sum_{i=1}^3 \delta_{wia} \ddot{q}_{wi} - \sum_{p=1}^2 \delta_{vpa} \ddot{q}_{vp} \right. \\ & \left. \left. + a_8 \left\{ \sum_{p=1}^2 \delta'_{vpa} \ddot{q}_{vp} + \bar{y}'_{\theta_{3/4C}} \right\} - \bar{y}_{\theta_{3/4C}} \delta_{\theta a} \ddot{q}_{\theta} \cos \theta_0 \right] \right] \end{aligned}$$

$$\begin{aligned} u_T = & a_7 (1 - \frac{\delta^2}{2}) - a_8 \delta + (\bar{e} + \bar{r}_a) \left[\delta - \beta (a_2 + \bar{\Omega} \frac{\beta}{2}) \right] \\ & + (\bar{e} + \bar{r}_a) b_1 + \cos \theta_0 \left(\sum_{p=1}^2 \delta_{vpa} \ddot{q}_{vp} - a_8 \left[\sum_{p=1}^2 \delta'_{vpa} \ddot{q}_{vp} \right. \right. \\ & \left. \left. + \bar{y}'_{\theta_{3/4C}} \right] \right) - \sin \theta_0 \sum_{i=1}^3 (\delta_{wia} \ddot{q}_{wi} - a_5 \delta'_{wia} \ddot{q}_{wi}) \end{aligned}$$

$$u = u_p \sin \phi_\omega + u_T \cos \phi_\omega$$

$$\bar{y}_{9/4c} = \bar{y}_{9c/4} - \frac{1}{2} \frac{c}{R}, \quad u_T \geq 0$$

$$= \bar{y}_{9c/4}, \quad u_T < 0$$

$$h_{2a} = a_B \left[\sum_{p=1}^2 \gamma'_{vpa} q_{vp} + \bar{y}'_{9/4c} \right]$$

$$h_{3a} = \sum_{p=1}^2 \gamma_{vpa} \check{q}_{vp}$$

$$h_{4a} = \sum_{i=1}^3 \gamma_{wia} q_{wi}$$

$$h_{5a} = \sum_{i=1}^3 \gamma_{wia} \check{q}_{wi}$$

$$h_{6a} = a_B \sum_{i=1}^3 \gamma'_{wia} q_{wi}$$

$$h_{7a} = \sum_{p=1}^2 \gamma_{vpa} q_{vp}$$

$$M_a = \left(\frac{\Omega_o R}{V_{\infty D}} \right) \mu_a$$

where the blade segment angle of attack is given by:

$$\alpha_r = \theta_o + \theta_B + \phi_\omega + \gamma_{\theta a} q_\theta$$

$$\phi_\omega = \tan^{-1} \left(\frac{u_p}{u_T} \right)$$

and θ_o is the actual geometric pitch of the blade at the three quarter radial station, $r/R = 0.75$.

$$\theta_0 = (\theta_s)_{.75} - \tan \delta_3 \left[\beta + \sum_{i=1}^3 (\delta'_{wi})_{\bar{r}=0} q_{wi} \right] + k_{\theta, \delta} \left[\delta + \sum_{p=1}^2 (\delta'_{vp})_{\bar{r}=0} q_{vp} \right] + k_{\theta, \beta} \left[\beta + \sum_{i=1}^3 (\delta'_{wi})_{\bar{r}=0} \ddot{q}_{wi} \right]$$

$$\dot{\theta}_0 = (\dot{\theta}_s)_{.75} - \tan \delta_3 \left[\dot{\beta} + \sum_{i=1}^3 (\delta'_{wi})_{\bar{r}=0} \dot{q}_{wi} \right] + k_{\theta, \delta} \left[\dot{\delta} + \sum_{p=1}^2 (\delta'_{vp})_{\bar{r}=0} \dot{q}_{vp} \right] + k_{\theta, \beta} \left[\ddot{\beta} + \sum_{i=1}^3 (\delta'_{wi})_{\bar{r}=0} \ddot{q}_{wi} \right]$$

$$\ddot{\theta}_0 = (\ddot{\theta}_s)_{.75} - \tan \delta_3 \left[\ddot{\beta} + \sum_{i=1}^3 (\delta'_{wi})_{\bar{r}=0} \ddot{q}_{wi} \right] + k_{\theta, \delta} \left[\ddot{\delta} + \sum_{p=1}^2 (\delta'_{vp})_{\bar{r}=0} \ddot{q}_{vp} \right]$$

The inelastic blade pitch is given by the following equation:

$$(\theta_s)_{.75} = \theta_c - [A_{1s} \cos \psi_R + B_{1s} \sin \psi_R] + .75 \theta$$

$$(\dot{\theta}_s)_{.75} = \dot{\theta}_c - [\ddot{A}_{1s} + B_{1s} \bar{\Omega}] \cos \psi_R + [A_{1s} \bar{\Omega} - \ddot{B}_{1s}] \sin \psi_R$$

$$(\ddot{\theta}_s)_{.75} = \ddot{\theta}_c + [(A_{1s} \bar{\Omega} - 2 \ddot{B}_{1s}) \bar{\Omega} - \ddot{A}_{1s} - B_{1s} \ddot{\Omega}] \cos \psi_R + [(2 \ddot{A}_{1s} + B_{1s} \bar{\Omega}) \bar{\Omega} - \ddot{B}_{1s} + A_{1s} \ddot{\Omega}] \sin \psi_R$$

The pitch of the blade along the blade radius is given by:

$$\theta_b = (\bar{r}_a + \bar{e} - .75) \theta$$

The various gravity vector terms are defined as follows:

$$g'_{zf} = \cos \theta_f \cos \phi_f$$

$$g'_{xf} = -\sin \theta_f$$

$$g'_{yf} = \sin \phi_f \cos \theta_f$$

$$\bar{g}_{z_1} = \frac{g}{\Omega_o^2 R} (I_s \sin \theta_f - \cos \theta_f \cos \phi_f)$$

$$\bar{g}_{x_1} = -\frac{g}{\Omega_o^2 R} (\sin \theta_f + \cos \theta_f \cos \phi_f I_s)$$

$$\bar{g}_{y_1} = \frac{g}{\Omega_o^2 R} \sin \phi_f \cos \theta_f$$

$$\bar{g}_{z_2} = \bar{g}_{z_1}$$

$$\bar{g}_{x_3} = \bar{g}_{x_1} \cos \Psi_R + \bar{g}_{y_1} \sin \Psi_R$$

$$\bar{g}_{y_3} = \bar{g}_{y_1} \cos \Psi_R - \bar{g}_{x_1} \sin \Psi_R$$

$$\bar{g}_{z_5} = \bar{g}_{z_1} - \beta(\bar{g}_{x_3})$$

$$\bar{g}_{y_5} = \bar{g}_{y_1} \cos \Psi_R - \bar{g}_{x_1} \sin \Psi_R - \delta(\bar{g}_{x_3})$$

Rotor inflow is defined as:

$$\lambda = -\bar{v}_{z_1} - \frac{1}{2} \frac{(C_T/\sigma) \sigma}{\sqrt{\bar{v}_{o_{x_1}}^2 + \bar{v}_{o_{y_1}}^2 + \lambda^2}}$$

Rotor shaft forces and moments are given by the following equations:

$$\left(\frac{C_H}{\sigma}\right)_s = \frac{m_o}{\rho b c R} \sum_1^b [\bar{S}_{x_3} \cos \Psi_R - \bar{S}_{y_3} \sin \Psi_R]$$

$$\left(\frac{C_Y}{\sigma}\right)_s = \frac{m_o}{\rho b c R} \sum_1^b [\bar{S}_{x_3} \sin \Psi_R + \bar{S}_{y_3} \cos \Psi_R]$$

$$\left(\frac{C_T}{\sigma}\right)_s = \frac{m_o}{\rho b c R} \sum_1^b \bar{S}_{z_3}$$

$$\left(\frac{C_l}{\sigma}\right)_s = -\frac{m_o}{\rho b c R} \bar{e} \sum_1^b (\bar{S}_{z_3} \sin \Psi_R)$$

$$\left(\frac{C_m}{\sigma}\right)_s = -\frac{m_o}{\rho b c R} \bar{e} \sum_1^b (\bar{S}_{z_3} \cos \Psi_R)$$

These forces are then transformed into fuselage forces and moments.

$$\left(\frac{C_x}{\sigma}\right)_f = \left(\frac{C_T}{\sigma}\right)_s I_s - \left(\frac{C_H}{\sigma}\right)_s$$

$$\left(\frac{C_y}{\sigma}\right)_f = \left(\frac{C_Y}{\sigma}\right)_s$$

$$\left(\frac{C_z}{\sigma}\right)_f = -\left(\frac{C_T}{\sigma}\right)_s - \left(\frac{C_H}{\sigma}\right)_s I_s$$

$$\left(\frac{C_l}{\sigma}\right)_f = \left(\frac{C_l}{\sigma}\right)_s - \left(\frac{C_q}{\sigma}\right)_e I_s$$

$$\left(\frac{C_m}{\sigma}\right)_f = \left(\frac{C_m}{\sigma}\right)_s$$

$$\left(\frac{C_n}{\sigma}\right)_f = \left(\frac{C_q}{\sigma}\right)_e + \left(\frac{C_l}{\sigma}\right)_s I_s$$

The nondimensional rotor speed is calculated using the following equation:

$$\bar{\Omega}(nT) = \bar{\Omega}(nT-T) + \Omega_{o,T} \ddot{\bar{\Omega}}(nT)$$

where the acceleration of the rotor is calculated using the following equation:

$$\ddot{\bar{\Omega}} = \frac{(m_e R^3 \bar{e}^2 M_B b) \left[\frac{M_B (\bar{r}_{cg})_B^2}{\bar{I}_B} - 1 \right] \ddot{\bar{\Omega}} + \rho b c R^4 \left[\left(\frac{C_q}{\sigma}\right)_s - \left(\frac{C_q}{\sigma}\right)_e \right]}{\frac{m_e R^3 b M_B^2 \bar{e}^2 (\bar{r}_{cg})_B^2}{\bar{I}_B} - [I_{HUB} + m_e R^3 b \bar{e}^2 \bar{M}_B]}$$

Prior to the simulated loss of the rotor driving torque the following equation is used:

$$(C_q/\sigma)_e = (C_q/\sigma)_s$$

At the time of the simulated power failure, one of the following two equations is used:

Full power loss:

$$(C_q/\sigma)_e(nT) = \left(\frac{T_0 - T}{T_0}\right)(C_q/\sigma)_e(nT - T)$$

Part power loss:

$$(C_q/\sigma)_e(nT) = \left(\frac{T_0 - T}{T_0}\right)(C_q/\sigma)_e(nT - T) + \left(\frac{T}{T_0}\right)(\overline{C_q/\sigma})_e$$

The rotor blade azimuth station part power loss is calculated using the following equation:

$$\psi_R(nT) = \psi_R(nT - T) + \Omega_0 T \bar{\Omega}(nT)$$

The local blade bending moments were calculated using the following equations:

$$M_f = \frac{EI_{yy}}{R} \sum_i^3 \gamma_{wi}'' q_{wi}$$

$$M_c = \frac{EI_{zz}}{R} \sum_i^2 \gamma_{wi}'' q_{vi}$$

$$M_\theta = \left(\frac{GJ}{R}\right) \gamma_\theta' q_\theta$$

Other quantities calculated were the chordwise bending moment in the vicinity of the lag damper,

$$M_{LD} = \frac{EI}{R} \sum_1^2 \gamma_{wi}'' q_{vp}$$

and the deflection of the tip of any blade within 5 degrees azimuth position of the tail:

$$D_T = R \left(\beta + \sum_{i=1}^3 q_{wi} \right)_v$$

Tail Rotor Equations

The tail rotor thrust is calculated using the following Bailey theory equations, which include the effect of delta three:

$$\left(\frac{C_T}{\sigma} \right)_T = \left[K_{22} \lambda_T + (K_{25} + K_{26} \mu_{xt}^2) (\theta_t - K_{58} \left\{ \frac{C_T}{\sigma} \right\}_t) \right] \bar{\Omega}^2$$

$$\lambda = -\mu_{yf} + K_{56} r - \frac{\sigma_T (C_T/\sigma)_T}{\sqrt{2} \mu_{xt}^2 + \lambda_T^2}$$

$$\mu_{xt}^2 = K_{57}^2 \mu_{xf}^2$$

Two additional equations were used to calculate the change in altitude following a loss in power and normal load factor, and are given by the following equations, respectively:

$$\Delta Z = \Omega_0 R \int (\mu_{xf} \sin \theta_f - [\mu_{yf} \sin \phi_f + \mu_{zf} \cos \phi_f] \cos \theta_f) dt$$

and

$$m_z = g'_{zf} - \frac{\dot{\mu}_{zf} \Omega_0 R}{g}$$

NONARTICULATED ROTOR CONVERSION

The above equations were modified for the hingeless rotor and the floating hub portion of this study.

Hingeless Rotor Modification

The lead-lag and flapping equations were eliminated, and flapping angle was replaced by a fixed coning angle.

$$\delta = \dot{\delta} = \ddot{\delta} = 0$$

$$\beta = \dot{\beta} = \ddot{\beta} = 0$$

$$\beta = \beta_B$$

The rotor acceleration was calculated using the following equation,

$$\ddot{A} = \left[\frac{m_0 R^3}{I_H + m_0 R^3 b (I_B + \bar{M}_B \bar{e}^2)} \right] \left[\sum_{f=1}^b (\bar{e} \bar{S}_{Y3A} + \bar{\Delta} r \sum_{a=1}^{10} \bar{r}_a \bar{S}_{AY5a}) \right] + \left(\frac{\rho b c R}{m_0} \right) \left(\frac{c_f}{\sigma} \right) e$$

and the blade segment velocities were modified to result in the following equations:

$$u_T = a_7 + (\bar{e} + \bar{r}_a) \left[b_1 \beta \left(a_2 + \frac{\bar{r}_2 \beta}{2} \right) \right] \\ + (h_{3a} - h_{2a}) \cos \theta_0 - (h_{5a} - h_{6a}) \sin \theta_0$$

Blade flapwise, chordwise, and torsional modal amplitude accelerations were modified to include the following effect of Coriolis acceleration and structural damping:

To the right hand side of the flapwise equation the following term was added:

$$\frac{1}{c_{1i}} \left[-c_{12i} (\bar{f}_2 \cos \theta_0 - \bar{f}_8 \sin \theta_0) \right]$$

The quantities

$$\frac{1}{c_{14p}} \left[c_{3p11} b_1 (2.86 \bar{q}_{w,} \dot{\bar{q}}_{w,}^x) - c_{47p} (\bar{f}_8 \cos \theta_0 \right. \\ \left. + \bar{f}_2 \sin \theta_0) \right] - 0.05 \bar{w}_{vp} \dot{\bar{q}}_{vp}^x$$

were added to the chordwise equation, and to the S_{y3} equation, the following term was added:

$$+ c_{10,1} b_1 (2.86 \bar{q}_{w,} \dot{\bar{q}}_{w,}^x) \cos \theta_0$$

The moment at the root of the blade was calculated using the following internal moment equations:

$$\bar{M}_{z_3} = [\cos \theta_0 + 0.75 \theta, \sin \theta_0] \sum_i^p C_{s1i} \rho v_i \\ - [\sin \theta_0 - 0.75 \theta, \cos \theta_0] \sum_i^i C_{s2i} \rho w_i$$

$$M_{y_3} = -[\cos \theta_0 + 0.75 \theta, \sin \theta_0] \sum_i^i C_{s2i} \rho w_i \\ - [\sin \theta_0 - 0.75 \theta, \cos \theta_0] \sum_i^p C_{s1i} \rho v_i$$

so that the rotor moments can now be written as:

$$\left(\frac{C_Q}{\sigma}\right)_s = -\frac{m_0}{\rho b C_R} \sum_i^b [\bar{e}(S_{y_3}) + \bar{M}_{z_3}]$$

$$\left(\frac{C_D}{\sigma}\right)_s = -\frac{m_0}{\rho b C_R} \sum_i^b [\bar{e}(S_{z_3}) - \bar{M}_{y_3}] \sin \psi_r$$

$$\left(\frac{C_m}{\sigma}\right)_s = -\frac{m_0}{\rho b C_R} \sum_i^b [\bar{e}(S_{z_3}) - \bar{M}_{y_3}] \cos \psi_r$$

Floating Hub Modifications

The floating hub rotor system was represented by two orthogonal teetering rotors.

The flapping equation was changed from the previous equation to the following:

$$\beta^{xx} = \frac{1}{\bar{I}_B + \bar{M}_B \bar{Q}^2} \int_{\bar{Q}}^{\bar{R}} \bar{S}_A z s_a (\bar{Q} + \bar{r}_a) dr \\ - \frac{\bar{M}_B (r_{CG})_B}{\bar{I}_B} \bar{f}_1' - \bar{f}_2' - \beta \left(\frac{\bar{M}_B (r_{CG})_B}{\bar{I}_B} \bar{Q} + 1 \right)$$

Before integration, the flapping accelerations for opposing blades were made to conform to the teetering condition:

$$\ddot{\beta}_2(\psi) = \frac{\ddot{\beta}_1(\psi) - \ddot{\beta}_1(\psi + 180^\circ)}{2}$$

$$\ddot{\beta}_2(\psi + 180^\circ) = -\ddot{\beta}_2(\psi)$$

$$\ddot{\beta}_2(\psi + 90^\circ) = \frac{\ddot{\beta}_1(\psi + 90^\circ) - \ddot{\beta}_1(\psi + 270^\circ)}{2}$$

$$\ddot{\beta}_2(\psi + 270^\circ) = -\ddot{\beta}_2(\psi + 90^\circ)$$

The flapping velocity and angle for the floating hub then becomes,

$$\dot{\beta}_2(\psi) = \int \ddot{\beta}_2(\psi) dt$$

$$\dot{\beta}_2(\psi + 180^\circ) = -\int \ddot{\beta}_2(\psi) dt = -\dot{\beta}_2(\psi)$$

$$\dot{\beta}_2(\psi + 90^\circ) = \int \ddot{\beta}_2(\psi + 90^\circ) dt$$

$$\dot{\beta}_2(\psi + 270^\circ) = -\int \ddot{\beta}_2(\psi + 90^\circ) dt = -\dot{\beta}_2(\psi + 90^\circ)$$

$$\beta(\psi) = \int \dot{\beta}(\psi) dt + \beta_B$$

$$\beta(\psi + 180^\circ) = -\beta(\psi) + \beta_B$$

$$\beta(\psi + 90^\circ) = \int \dot{\beta}_2(\psi + 90^\circ) dt + \beta_B$$

$$\beta(\psi + 270^\circ) = -\beta(\psi + 90^\circ) + \beta_B$$

where β_0 is a built-in coning angle.

Blade segment velocities were expressed as follows:

$$\begin{aligned} u_p = & \lambda_0 \left(1 - \frac{\beta^2}{2} \right) + \beta(a_0) + (\bar{e} + \bar{r}_a) [a_1, -\dot{\beta}] \\ & - [h_{5a} + \dot{\theta}_0 (h_{7a} + \bar{y}_{9 \ 3/4c}) - h_{6a}] \cos \theta_0 \\ & + [\dot{\theta}_0 h_{4a} - h_{3a} + h_{2a}] \sin \theta_0 \end{aligned}$$

$$\begin{aligned} u_T = & a_7 + (\bar{e} + \bar{r}_a) [b_1, -\beta(a_2 + \bar{\omega} \beta/2)] \\ & + [h_{3a} - h_{2a}] \cos \theta_0 - [h_{5a} - h_{6a}] \sin \theta_0 \end{aligned}$$

For the floating hub configuration without the elastic degrees of freedom the rotor moments become:

$$(C_Q/\sigma)_s = -\frac{m_0}{\rho b C_R} \sum_i [\bar{e} \bar{S}_{Y3A} + \int \bar{S}_{AY5a} \bar{r} dr]$$

$$(C_P/\sigma)_s = 0$$

$$(C_m/\sigma)_s = 0$$

TABLE X

K CONSTANTS

$$T.F. = \rho b c \Omega^2 R^3$$

$$K_1 = \frac{G.W.}{T.F.} \cdot \frac{\Omega_0 R}{g}$$

$$K_2 = \frac{1}{T.F.} \frac{1}{2} \rho (\Omega R)^2$$

$$K_3 = \frac{b_{TR} C_{TR} \Omega_{OTR}^2 R_{TR}^3}{b c \Omega_0^2 R^3}$$

$$K_4 = \frac{G.W.}{T.F.}$$

$$K_6 = \frac{I_x}{T.F.(R)}$$

$$K_7 = \frac{WLMR - WLCG}{12 R}$$

$$K_9 = \frac{WLTR - WLCG}{12 R} \cdot \frac{b_{TR} C_{TR} \Omega_{OTR}^2 R_{TR}^3}{b c \Omega_0^2 R^3}$$

$$K_{12} = \frac{1}{T.F.(R)} \frac{1}{2} \rho (\Omega R)^2$$

$$K_{13} = \frac{I_y}{T.F.(R)}$$

$$K_{15} = \frac{M_{IT}}{\alpha_0} \cdot \frac{FSHT - FSCG}{24 b c \Omega_0 R^3}$$

$$K_{17} = \frac{WLAD - WLCG}{12 R} \frac{1}{T.F.} \frac{1}{2} \rho (\Omega R)^2$$

$$K_{18} = \frac{FSAD - FSCG}{12 R} \frac{1}{T.F.} \frac{1}{2} \rho (\Omega R)^2$$

$$K_{19} = \frac{I_z}{T.F.(R)}$$

$$K_{20} = \frac{FSMR - FSCG}{12 R}$$

$$K_{21} = \frac{FSTR - FSCG}{12 R} \cdot \frac{b_{TR} C_{TR} \Omega_{OTR}^2 R_{TR}^3}{bc \Omega^2 R^3}$$

$$K_{22} = \frac{a}{4} B^2$$

$$K_{25} = \frac{a}{6} B^3$$

$$K_{26} = \frac{a}{4} B$$

$$K_{56} = \frac{K_{21}}{K_3} \frac{1}{\Omega}$$

$$K_{57} = \frac{\Omega R_{MR}}{\Omega R_{TR}} \left(\frac{q_t}{q} \right)^{1/2}$$

$$K_{58} = \frac{\gamma_{TR}}{a} \cdot \frac{1}{1.2} \delta_3$$

$$K_{59} = K_{19} - K_{13}$$

$$K_{60} = K_6 - K_{19}$$

$$K_{61} = K_{13} - K_6$$

$$K_{63} = \frac{BLMR - BLCG}{12 R}$$

$$K_{65} = (\epsilon_{KT} - \epsilon_{KF}) \frac{\partial M}{\partial \alpha} \frac{1}{4 \pi R^3}$$

$$K_0 = - \frac{\partial N_{VT}}{\partial \beta} \frac{(FSVT - FSCG)}{24 bc \Omega R^3}$$

TABLE XI

C CONSTANTS

The blade constants appearing in the various equations of motion are defined below:

$$C_0 = \frac{C}{m_0 \Omega_0 R^3}$$

$$C_{1i} = \int_0^{\bar{r}_T} \bar{m} \chi_{wi}^2 d\bar{r}$$

$$C_{2i,i'} = \int_0^{\bar{r}_T} \bar{m} \chi_{wi} \chi_{wi'} d\bar{r}$$

$$C_{3i,p} = \int_0^{\bar{r}_T} \bar{m} \chi_{wi} \chi_{vp} d\bar{r}$$

$$C_{4i,i'} = \int_0^{\bar{r}_T} \bar{m} \chi_{wi} \chi_{wi'} \bar{r} d\bar{r}$$

$$C_{5i,p} = \int_0^{\bar{r}_T} \bar{m} \chi_{wi} \chi_{vp} \bar{r} d\bar{r}$$

$$C_{6i,i'} = \int_0^{\bar{r}_T} \chi_{wi} \chi_{wi'} \int_{\bar{r}}^{\bar{r}_T} \bar{m} d\bar{\xi} d\bar{r}$$

$$C_{7i,i'} = \int_0^{\bar{r}_T} \chi_{wi} \chi_{wi'} \int_{\bar{r}}^{\bar{r}_T} \bar{m} \bar{\xi} d\bar{\xi} d\bar{r}$$

$$C_{8i,p} = \int_0^{\bar{r}_T} \chi_{wi} \int_{\bar{r}}^{\bar{r}_T} \bar{m} \chi_{vp} d\bar{\xi} d\bar{r}$$

$$C_{9i,i'} = \theta_i \int_0^{\bar{r}_T} \chi_{wi} \left[\int_{\bar{r}}^{\bar{r}_T} \bar{m} \chi_{wi'} \bar{\xi} d\bar{\xi} - \bar{r} \int_{\bar{r}}^{\bar{r}_T} \bar{m} \chi_{wi'} d\bar{\xi} \right] d\bar{r}$$

$$C_{10i} = \int_0^{\bar{r}_T} \bar{m} \chi_{wi} d\bar{r}$$

$$C_{11i} = \int_0^{\bar{r}_T} \bar{m} \chi_{wi} \theta_B d\bar{r} \triangleq \theta_i [C_{12i} - 0.75 C_{10i}]$$

$$C_{12i} = \int_0^{\bar{r}_T} \bar{m} \chi_{wi} \bar{r} d\bar{r}$$

$$C_{13i} = \int_0^{\bar{r}_T} \bar{m} \chi_{wi} \bar{r} \theta_B d\bar{r} \triangleq \theta_i \int_0^{\bar{r}_T} \bar{m} \chi_{wi} \bar{r}^2 d\bar{r} - 0.75 \theta_i C_{12i}$$

$$\begin{aligned}
C_{14p} &= \int_0^{\bar{r}_T} \bar{m} \gamma_p^2 d\bar{r} \\
C_{15p} &= \int_0^{\bar{r}_T} \bar{m} \gamma_p d\bar{r} \\
C_{16p} &= \int_0^{\bar{r}_T} \bar{m} \gamma_p \theta_B d\bar{r} \hat{=} \theta [C_{47p} - 0.75 C_{15p}] \\
C_{17p,p'} &= \int_0^{\bar{r}_T} \bar{m} \gamma_p \gamma_{p'}' d\bar{r} \\
C_{18p,p'} &= \int_0^{\bar{r}_T} \bar{m} \gamma_p \gamma_{p'}' \bar{r} d\bar{r} \\
C_{19p,p'} &= \int_0^{\bar{r}_T} \gamma_p \gamma_{p'}'' \int_{\bar{r}}^{\bar{r}_T} \bar{m} d\bar{\xi} d\bar{r} \\
C_{20p,p'} &= \int_0^{\bar{r}_T} \gamma_p \gamma_{p'}'' \int_{\bar{r}}^{\bar{r}_T} \bar{m} \bar{\xi} d\bar{\xi} d\bar{r} \\
C_{21p,p'} &= \theta \int_0^{\bar{r}_T} \gamma_p \left[\int_{\bar{r}}^{\bar{r}_T} \bar{m} \gamma_{p'} \bar{\xi} d\bar{\xi} - \bar{r} \int_{\bar{r}}^{\bar{r}_T} \bar{m} \gamma_{p'} d\bar{\xi} \right] d\bar{r} \\
C_{22i,p} &= \int_0^{\bar{r}_T} \gamma_p \int_{\bar{r}}^{\bar{r}_T} \bar{m} \gamma_{w_i} d\bar{\xi} d\bar{r} \\
C_{23p} &= \int_0^{\bar{r}_T} \gamma_p \left[\bar{e}_A'' \int_{\bar{r}}^{\bar{r}_T} \bar{m} d\bar{\xi} - 2 \bar{e}_A' \bar{m} - \bar{e}_A \bar{m}' \right] d\bar{r} \\
&\quad + \int_0^{\bar{r}_T} \gamma_p \left[\Delta \bar{e}_{cw}'' \int_{\bar{r}}^{\bar{r}_T} \bar{m}_{cw} d\bar{\xi} - 2 \Delta \bar{e}_{cw}' \bar{m}_{cw} - \Delta \bar{e}_{cw} \bar{m}_{cw}' \right] d\bar{r} \\
C_{24p} &= - \int_0^{\bar{r}_T} \gamma_p \left[- \bar{e}_A'' \int_{\bar{r}}^{\bar{r}_T} \bar{m} \bar{\xi} d\bar{\xi} + 2 \bar{e}_A' \bar{m} \bar{r} + \bar{e}_A (\bar{m}' \bar{r} + \bar{m}) \right] d\bar{r} \\
&\quad - \int_0^{\bar{r}_T} \gamma_p \left[- \Delta \bar{e}_{cw}'' \int_{\bar{r}}^{\bar{r}_T} \bar{m}_{cw} \bar{\xi} d\bar{\xi} + 2 \Delta \bar{e}_{cw}' \bar{m}_{cw} \bar{r} + \Delta \bar{e}_{cw} (\bar{m}_{cw}' \bar{r} + \bar{m}_{cw}) \right] d\bar{r} \\
C_{25} &= \frac{2 \theta}{m_0 \Omega_0^2 R^4} \\
C_{26i,p} &= \int_0^{\bar{r}_T} \gamma_p \left[E I_{x_p} \gamma_{w_i}' \right]'' d\bar{r} \hat{=} - \int_0^{\bar{r}_T} \gamma_{w_i}' (E I_{z_p}' \gamma_{w_i}' + E I_{z_p} \gamma_{w_i}'') d\bar{r} \\
C_{27i,p} &= \int_0^{\bar{r}_T} \gamma_{w_i} \left[E I_{x_p} \gamma_{w_i}' \right]'' d\bar{r} \hat{=} - \int_0^{\bar{r}_T} \gamma_{w_i}' (E I_{x_p}' \gamma_{w_i}' + E I_{x_p} \gamma_{w_i}'') d\bar{r}
\end{aligned}$$

$$C_{20,i,i'} = -\bar{e} C_{2,i,i'} - C_{4,i,i'}$$

$$C_{29,i,i'} = -\bar{e} C_{6,i,i'} - C_{7,i,i'}$$

$$C_{30,i,p} = -\bar{e} C_{3,i,p} - C_{5,i,p}$$

$$C_{31,p,p'} = -\bar{e} C_{19,p,p'} - C_{20,p,p'}$$

$$C_{32,p,p'} = -\bar{e} C_{17,p,p'} - C_{18,p,p'}$$

$$C_{33,p} = \theta_1 \left[\int_0^{\bar{r}_T} \bar{m} \gamma_p \bar{r}^2 d\bar{r} - 0.75 C_{47,p} \right]$$

$$C_{34,p,p'} = \theta_1 \int_0^{\bar{r}_T} \bar{m} \gamma_p \gamma_{p'} (\bar{r} + \bar{e} - 0.75) d\bar{r}$$

$$C_{35} = \frac{2\theta_1(EI_{y_0})_{ret}}{m_0 \Omega_0^2 R^4}$$

$$C_{36} = \int_0^{\bar{r}_T} \bar{m} \bar{k}_{z_0}^2 \gamma_\theta^2 d\bar{r}$$

$$C_{37} = \int_0^{\bar{r}_T} \gamma_\theta \left[\bar{k}_A^2 \theta_1 \int_{\bar{r}}^{\bar{r}_T} \bar{m} (-\bar{e} - \bar{\xi}) d\bar{\xi} \right] d\bar{r}$$

$$C_{38,i,i'} = -2 \int_0^{\bar{r}_T} \gamma_\theta \gamma_{w_i}' \gamma_{w_i}'' \left(\frac{EI_{y_0} - EI_{z_0}}{m_0 \Omega_0^2 R^4} \right) d\bar{r}$$

$$C_{39,p,p'} = -2 \int_0^{\bar{r}_T} \gamma_\theta \gamma_{v_p}' \gamma_{v_p}'' \left(\frac{EI_{z_0} - EI_{y_0}}{m_0 \Omega_0^2 R^4} \right) d\bar{r}$$

$$C_{44} = \int_0^{\bar{r}_T} \bar{m} \bar{k}_{z_0}^2 \gamma_\theta d\bar{r}$$

$$NO \quad C_{45}$$

$$C_{46,i,p} = \int_0^{\bar{r}_T} \gamma_\theta \gamma_{w_i}'' \gamma_{v_p}'' \left(\frac{-EI_{y_0} + EI_{z_0}}{m_0 \Omega_0^2 R^4} \right) d\bar{r}$$

$$C_{47,p} = \int_0^{\bar{r}_T} \bar{m} \gamma_{v_p} \bar{r} d\bar{r}$$

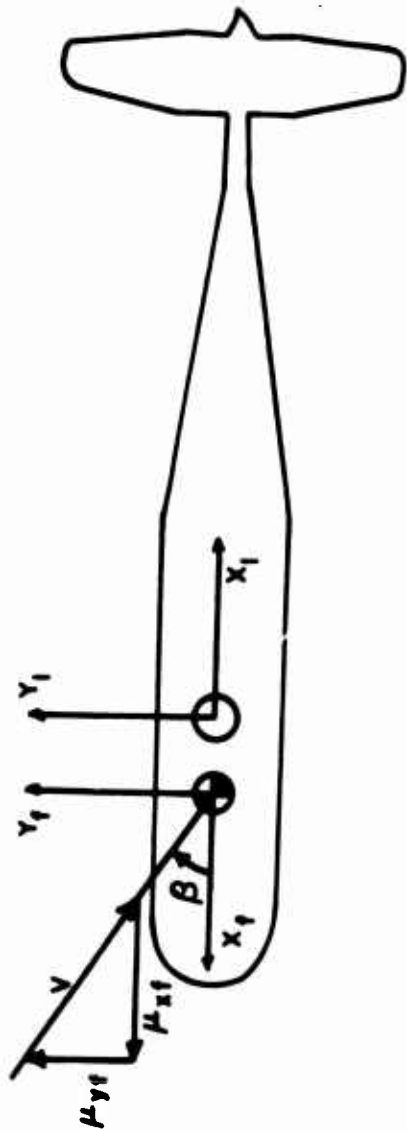
NO C_{48} or C_{49}

$$C_{50} = \frac{(GJ)_{\bar{r}=0}}{m_0 \Omega_0^2 R^4} (\gamma'_\theta)_{\bar{r}=0}$$

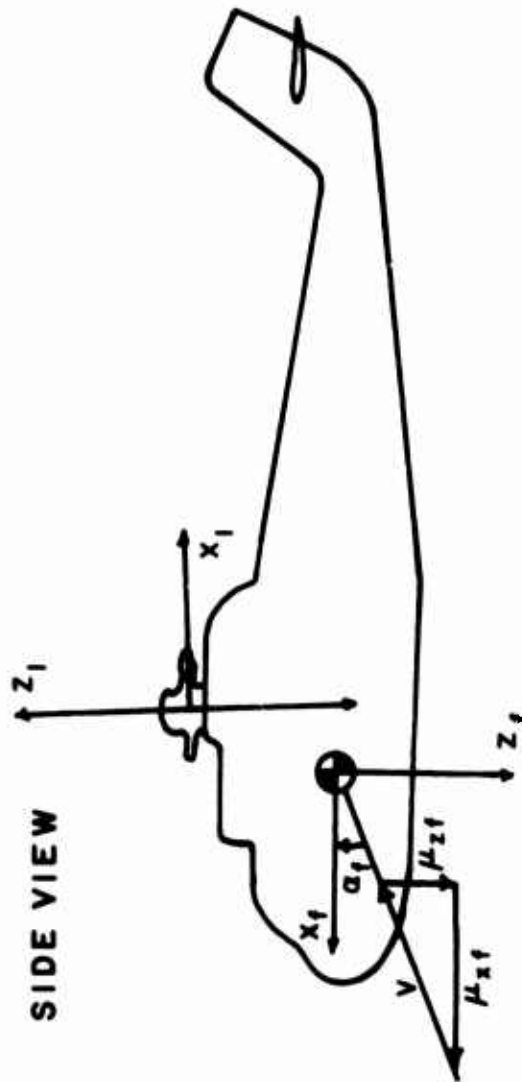
$$C_{51p} = \frac{(EI_{z_0} \gamma''_{vp})_{\bar{r}=0}}{m_0 \Omega_0^2 R^4}$$

$$C_{52i} = \frac{(EI_{y_0} \gamma''_{wi})_{\bar{r}=0}}{m_0 \Omega_0^2 R^4}$$

TOP VIEW



SIDE VIEW



REAR VIEW

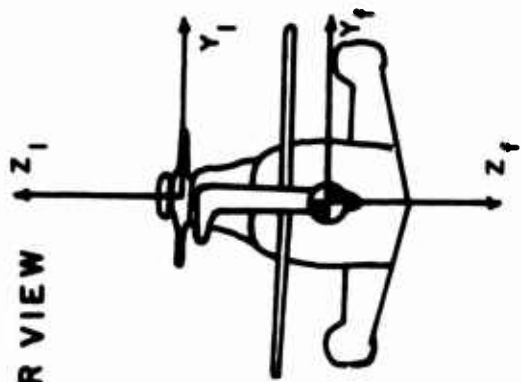
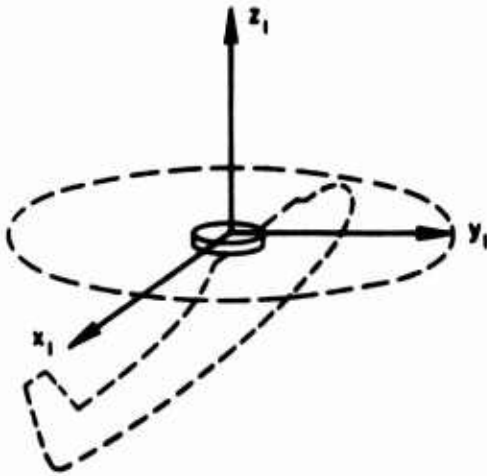
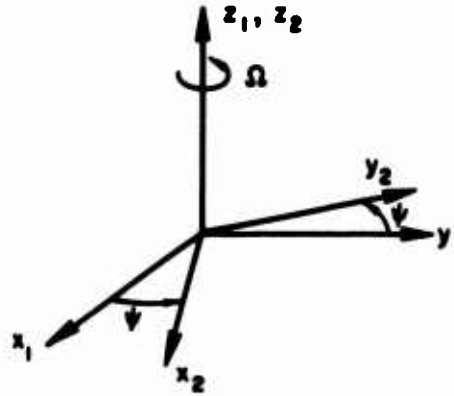


Figure 81. Fuselage and Rotor Head Axis Systems

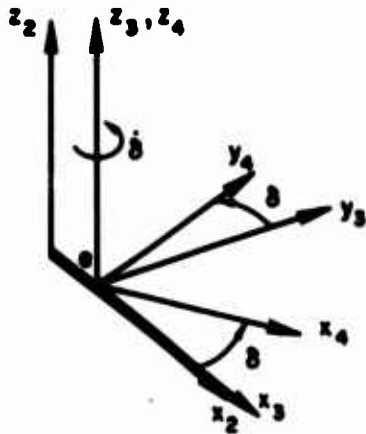
NONROTATING HUB



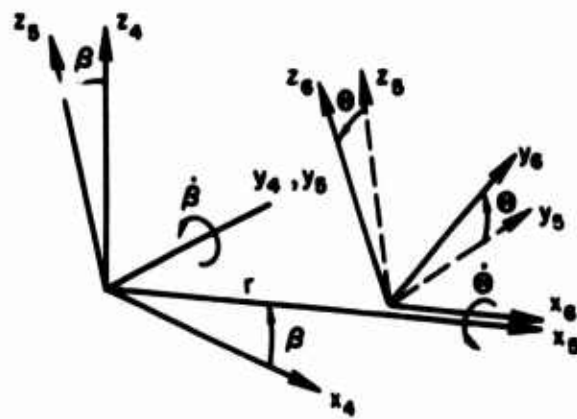
ROTATING HUB



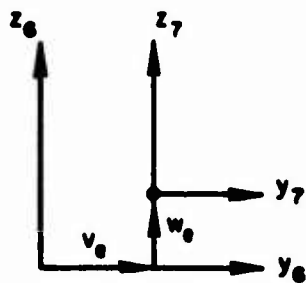
OFFSET AND BLADE LEAD ANGLE



RIGID BLADE AND PITCHED SECTION



BENDING TRANSLATION



BLADE SECTION

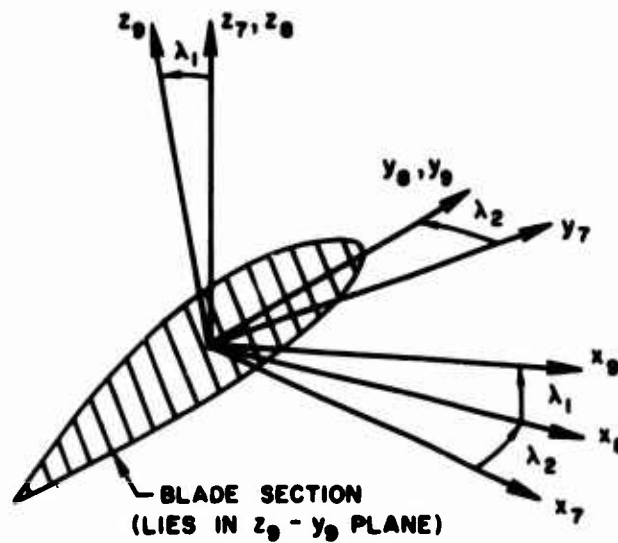


Figure 81. Concluded

BLANK PAGE

UNCLASSIFIED

Security Classification

DOCUMENT CONTROL DATA - R&D

(Security classification of title, body of abstract and indexing annotation must be entered when the overall report is classified)

1. ORIGINATING ACTIVITY (Corporate author) SIKORSKY AIRCRAFT DIVISION UNITED AIRCRAFT CORPORATION STRATFORD, CONNECTICUT		2a. REPORT SECURITY CLASSIFICATION UNCLASSIFIED	
		2b. GROUP	
3. REPORT TITLE SINGLE ROTOR HELICOPTER DYNAMICS FOLLOWING POWER FAILURE AT HIGH SPEEDS			
4. DESCRIPTIVE NOTES (Type of report and inclusive dates) FINAL			
5. AUTHOR(S) (Last name, first name, initial) COOPER, DEAN E. HANSEN, KNUTE C. KAPLITA, THADDEUS T.			
6. REPORT DATE June 1966		7a. TOTAL NO. OF PAGES 237	7b. NO. OF REFS 6
8a. CONTRACT OR GRANT NO. DA 44-177-AMC-195(T)		9a. ORIGINATOR'S REPORT NUMBER(S) USAAVLABS Technical Report 66-30	
b. PROJECT NO.			
c. Task No. 1D121401A14203		9b. OTHER REPORT NO(S) (Any other numbers that may be assigned this report) SER-50414	
d.			
10. AVAILABILITY/LIMITATION NOTICES Distribution of this document is unlimited.			
11. SUPPLEMENTARY NOTES		12. SPONSORING MILITARY ACTIVITY U.S. ARMY AVIATION MATERIEL LABORATORIES FORT EUSTIS, VIRGINIA	
13. ABSTRACT This program was conducted to investigate the effects of a loss of power on a single rotor helicopter at high speeds. A normal mode flexible blade analysis was combined with generalized helicopter equations of motion on a hybrid computer to predict the effects of rotor design variables and corrective control inputs on the transient response of a helicopter following a loss of main rotor power. At high forward speeds (200 to 235 knots) a loss of power can seriously affect the safety of single rotor helicopters unless there is a rapid and appropriate application of main rotor and tail rotor control. Rotor propulsive force, hinge offset, and rotor blade inertia were found to be important design considerations which effect helicopter and blade motion and loading following a loss of power. The aircraft response is due primarily to the fuselage aerodynamic characteristics associated with the sideslip and yaw motion generated by the unbalanced tail rotor yawing moment. The loss of power is less critical when a partial loss of power occurs or for a reduced rotor propulsive force.			

UNCLASSIFIED

Security Classification

14. KEY WORDS	LINK A		LINK B		LINK C	
	ROLE	WT	ROLE	WT	ROLE	WT
1. Single Rotor Helicopter Dynamics Following Power Failure. 2. Helicopter Rotors - Blade Bending Moments. 3. Helicopter Dynamics						

INSTRUCTIONS

1. ORIGINATING ACTIVITY: Enter the name and address of the contractor, subcontractor, grantee, Department of Defense activity or other organization (*corporate author*) issuing the report.

2a. REPORT SECURITY CLASSIFICATION: Enter the overall security classification of the report. Indicate whether "Restricted Data" is included. Marking is to be in accordance with appropriate security regulations.

2b. GROUP: Automatic downgrading is specified in DoD Directive 5200.10 and Armed Forces Industrial Manual. Enter the group number. Also, when applicable, show that optional markings have been used for Group 3 and Group 4 as authorized.

3. REPORT TITLE: Enter the complete report title in all capital letters. Titles in all cases should be unclassified. If a meaningful title cannot be selected without classification, show title classification in all capitals in parenthesis immediately following the title.

4. DESCRIPTIVE NOTES: If appropriate, enter the type of report, e.g., interim, progress, summary, annual, or final. Give the inclusive dates when a specific reporting period is covered.

5. AUTHOR(S): Enter the name(s) of author(s) as shown on or in the report. Enter last name, first name, middle initial. If military, show rank and branch of service. The name of the principal author is an absolute minimum requirement.

6. REPORT DATE: Enter the date of the report as day, month, year; or month, year. If more than one date appears on the report, use date of publication.

7a. TOTAL NUMBER OF PAGES: The total page count should follow normal pagination procedures, i.e., enter the number of pages containing information.

7b. NUMBER OF REFERENCES: Enter the total number of references cited in the report.

8a. CONTRACT OR GRANT NUMBER: If appropriate, enter the applicable number of the contract or grant under which the report was written.

8b, 8c, & 8d. PROJECT NUMBER: Enter the appropriate military department identification, such as project number, subproject number, system numbers, task number, etc.

9a. ORIGINATOR'S REPORT NUMBER(S): Enter the official report number by which the document will be identified and controlled by the originating activity. This number must be unique to this report.

9b. OTHER REPORT NUMBER(S): If the report has been assigned any other report numbers (*either by the originator or by the sponsor*), also enter this number(s).

10. AVAILABILITY/LIMITATION NOTICES: Enter any limitations on further dissemination of the report, other than those imposed by security classification, using standard statements such as:

(1) "Qualified requesters may obtain copies of this report from DDC."

(2) "Foreign announcement and dissemination of this report by DDC is not authorized."

(3) "U. S. Government agencies may obtain copies of this report directly from DDC. Other qualified DDC users shall request through _____."

(4) "U. S. military agencies may obtain copies of this report directly from DDC. Other qualified users shall request through _____."

(5) "All distribution of this report is controlled. Qualified DDC users shall request through _____."

If the report has been furnished to the Office of Technical Services, Department of Commerce, for sale to the public, indicate this fact and enter the price, if known.

11. SUPPLEMENTARY NOTES: Use for additional explanatory notes.

12. SPONSORING MILITARY ACTIVITY: Enter the name of the departmental project office or laboratory sponsoring (*paying for*) the research and development. Include address.

13. ABSTRACT: Enter an abstract giving a brief and factual summary of the document indicative of the report, even though it may also appear elsewhere in the body of the technical report. If additional space is required, a continuation sheet shall be attached.

It is highly desirable that the abstract of classified reports be unclassified. Each paragraph of the abstract shall end with an indication of the military security classification of the information in the paragraph, represented as (TS), (S), (C), or (U).

There is no limitation on the length of the abstract. However, the suggested length is from 150 to 225 words.

14. KEY WORDS: Key words are technically meaningful terms or short phrases that characterize a report and may be used as index entries for cataloging the report. Key words must be selected so that no security classification is required. Identifiers, such as equipment model designation, trade name, military project code name, geographic location, may be used as key words but will be followed by an indication of technical context. The assignment of links, rules, and weights is optional.

UNCLASSIFIED

Security Classification

3602-66